Synchronous Monitoring Adaptive Real Time (SMART) Analysis System for Energy Efficient Building

Cheng Kean Keong[1], Aravind C. V.[2*]

[1]*Research Student, School of Engineering, Taylor's University, Malaysia*

[2] *Senior Lecturer, School of Engineering, Taylor's University, Malaysia*

[*]aravindCV@ieee.org

Abstract

From the economic and sustainable use of energy aspects, an optimal operational of equipment inside the building is required. In this paper, the theory, method and impact of the Synchronous Monitoring and Real Time (SMART) analysis system is presented. The test vicinity taken for this approach is based on the analysis of energy usage and the bill pay by the Taylor's University Lakeside Campus, Malaysia. The approach was scaled down to a test area which restricted to a room design and employing the new methodology to optimize the energy usage. The design of this system is based on analyzing the waste of energy caused by utilities usage factors and the equipment health factor. The system design proposes a real time monitoring of not just load but also the health condition of various equipment, as they are the major source for operational inefficiency. By performing utilities usage control using SMART system, the electricity saving is estimated to be 22.13 %.

Keywords: Energy Efficient, SMART, SCADA, Energy Saving, Energy Management.

1. Introduction

Electrical energy consumption continues to increases as a result of uprising human economic activities. Malaysia's industrial sector takes up the largest portion of 45 %, whereas commercial and residential contributed to 33 % and 21 % consumption respectively [1]. Commercial building in Malaysia used most electricity for Heating Ventilation and Air Conditioning (HVAC) system (64%) but it is somehow found to be poorly designed [2]. As a result, the system often performs out of the rated condition which affects the stability of the power grid. Besides, forgetful or irresponsible users tend to leave not-in-use electrical utilities such as air conditioner and light being switched on. In order to increase the electrical system efficiency, the building electrical system is to be monitored, analyzed and controlled in real time [3]. The proposed solution is Synchronous Monitoring Adaptive Real Time (SMART) analysis system. The system is designed and implemented using National Instrument LABVIEW® Reconfigurable I/O Architecture platform. Taylor's University Lakeside Campus (TULC) is selected as the test facility but any other commercial building is suited for implementation. There are five blocks which enclose HVAC system, lift drives and other

critical load that contributes to 64 % of the dynamic load capacity. Figure 1 shows the Google image bird-eye view of TULC which consists of 5 building blocks. Blocks C, D and E are the test target for this research because these 3 blocks are mainly comprised of classroom where daily activities are constant. Whereas, Block A and B are administration building and event hall where electricity usage is not constant and much lower than Block C, D and E combined.

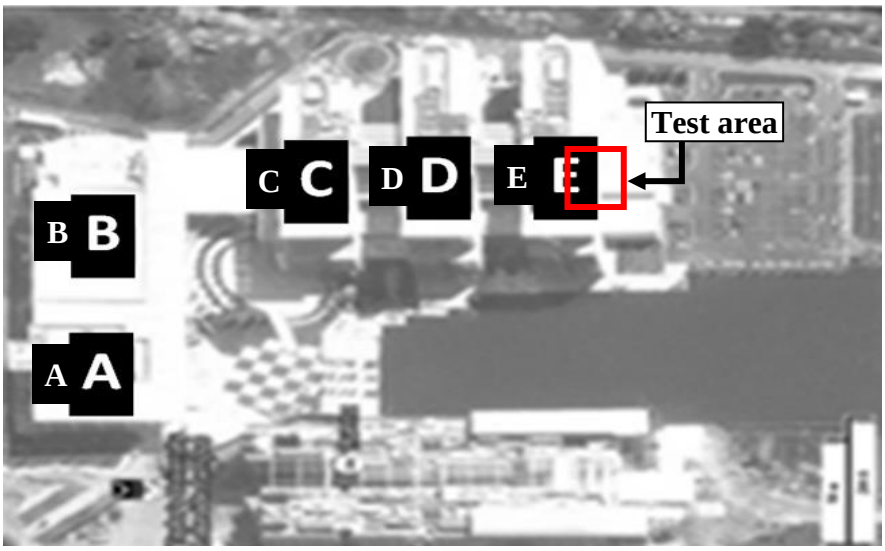

Fig. 1. Taylor's University Lakeside Campus (TULC) as test facility [4]

Figure 2 shows the recordings on the consumption economic analysis of TULC for 2013. TULC paid RM 5500k in year 2013 for electricity usage. This number is expected to increase for the coming years with the growing number of user. Thus, [5] suggested the operational efficiency can be increased by manage the load with an appropriate electricity usage management system.

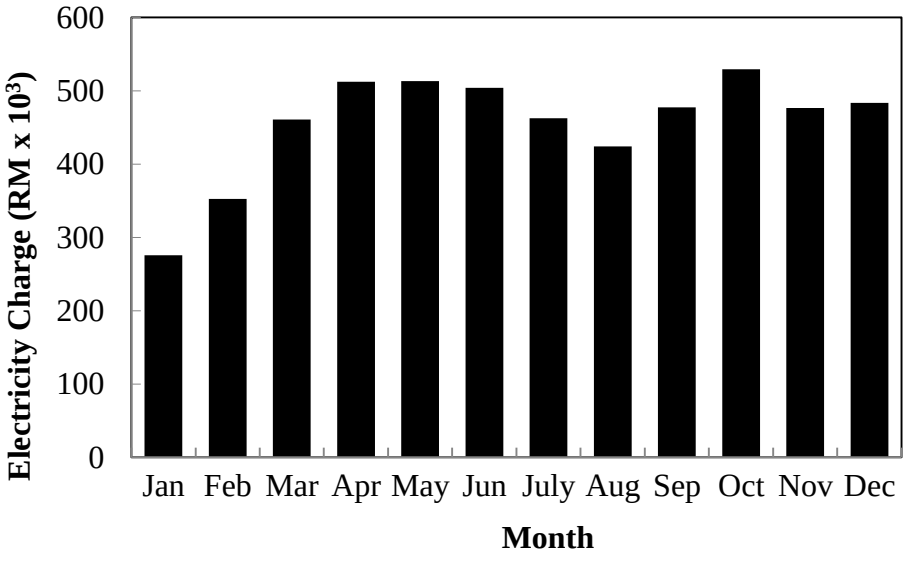

Fig. 2. TULC's economic analysis for year 2013 [6]

2. Methodology

2.1 Overall System Configuration

The main concept of the SMART system is to increases the energy efficient of a building as a whole by synchronously monitoring the equipment condition and managing the utilities usage. The system comprises of two networks. Firstly, the power network which controls the operation of the dynamic load mainly air conditioner based on its health condition. In this case, a motor is taken as the representation of dynamic load. The vibration data is acquired into Labview Sound and Vibration Assistant using USB-6009 Data Acquisition hardware for octave and power spectrum analysis. The second network is to control the utility circuit that switch on or off the light and air conditioner. The concept is illustrated in Figure 3.

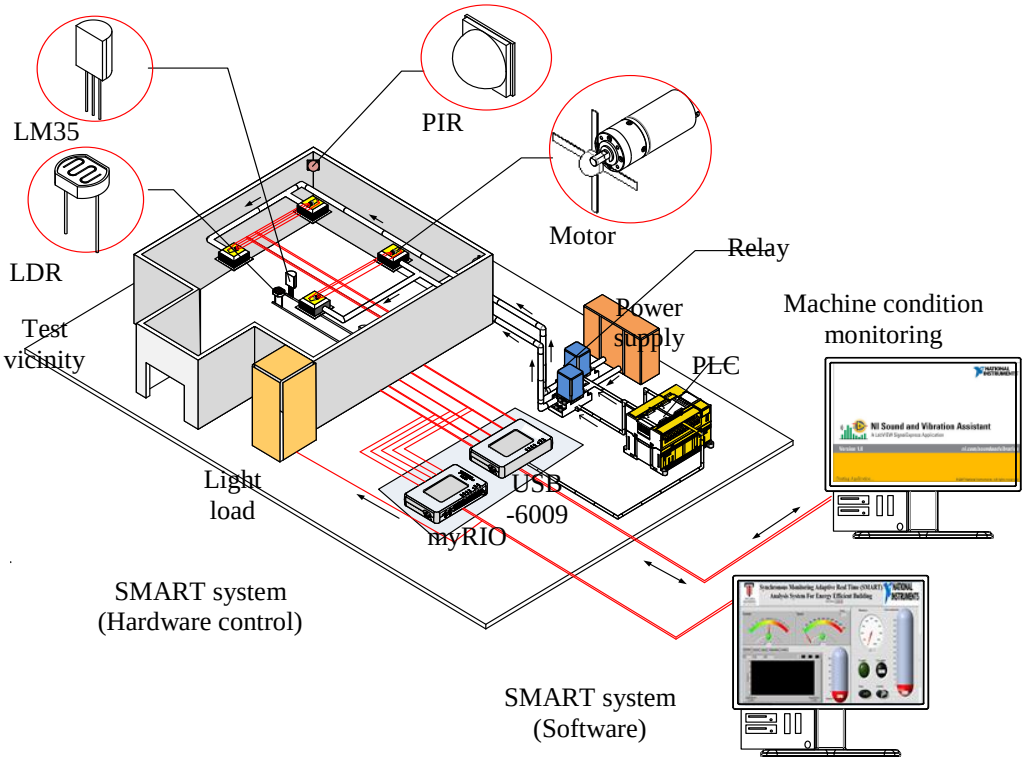

Fig. 3. Overall system concept

Figure 4 shows the condition monitoring method for dynamic load. The vibration data is captured and analyzed using Labview Sound and Vibration Assistant. This helps operator to identify motor malfunction condition for further isolation of the equipment in order to reduce the power loss to a greater extent. In order to test utility control operation effectively, a room is taken as test area for light and air conditioner control. Temperature transducer LM35, Light Dependent Resistor (LDR) and Passive Infrared (PIR) motion sensors are used for temperature, illuminance and motion detection respectively. The control criteria are based on Ministry of Human Resources Malaysia guidance where the suitable light level is above 400 Lux and temperature is 20^{o}C to 26^{o}C for routine office work. The system will switch off the utilities if no motion is detected in 10 minutes as the time interval between classes are usually less than 10 minutes. The control logic cc is as shown in Figure 5.

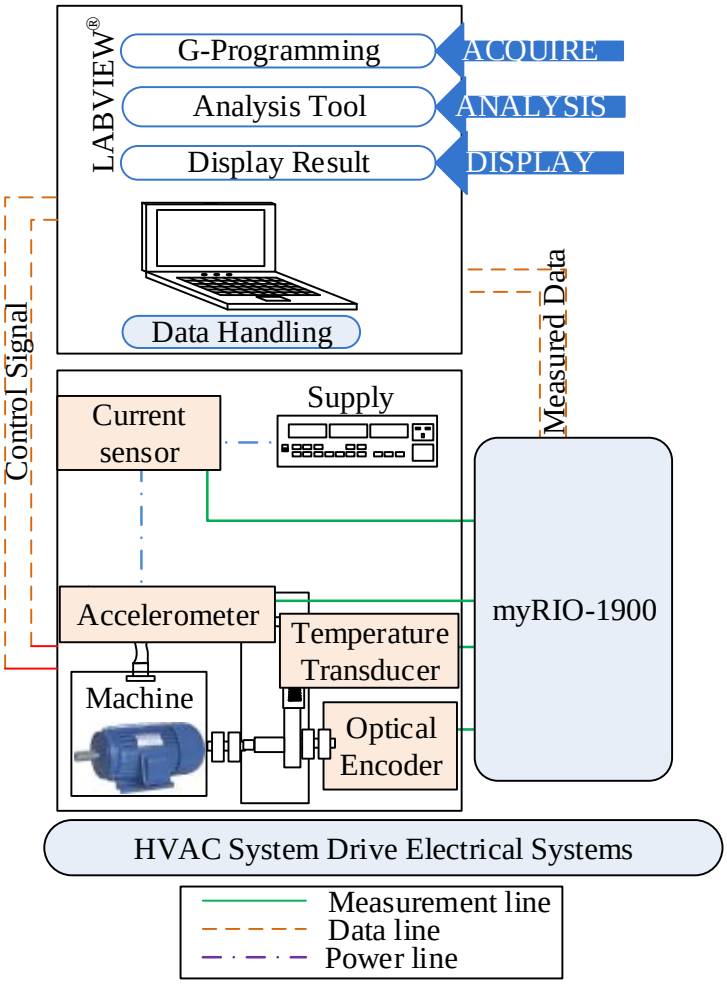

Fig. 4. Condition monitoring system (High Voltage AC system)

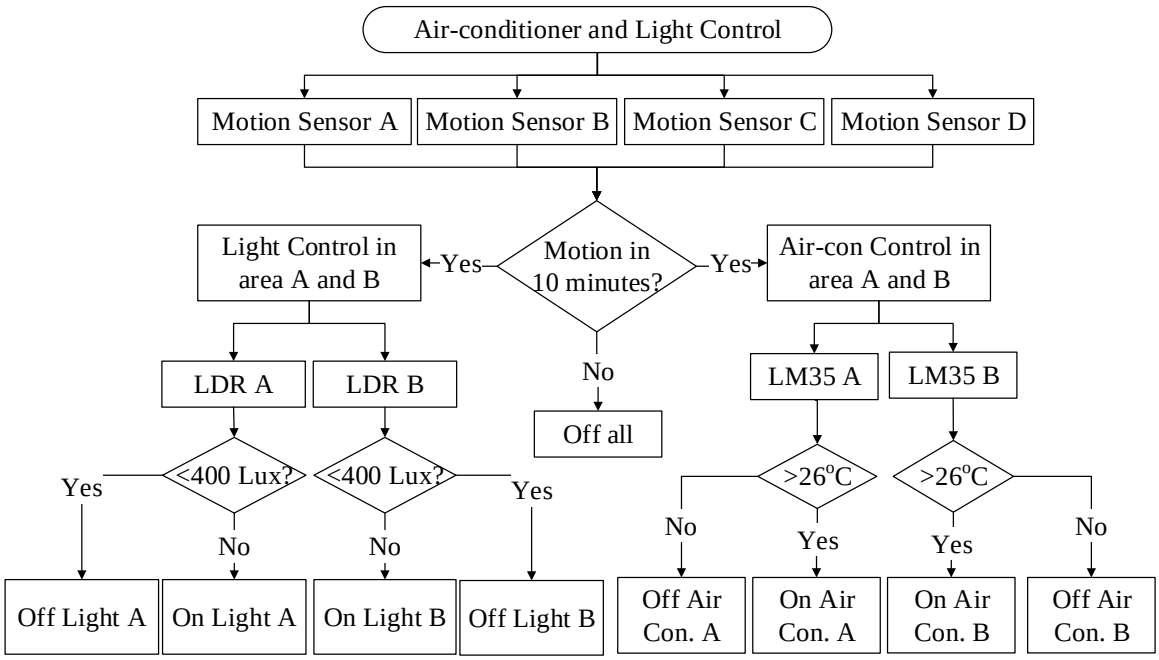

Fig. 5. Overall system concept (shown for two unit control)

2.3 Physical System Model

For testing purpose, the test area is scaled-down to a mock-up model which is mounted on a piece of plywood with proper wiring and electrical grounding as showed in Figure 6. LED is used to represent the lighting load and motor is adopted to represent the dynamic load which is air conditioner in this case. The main parts of the system involved laptop, sensors, and myRIO-1900. The sensors used for condition monitoring of dynamic load included current transducer, accelerometer, temperature transducer and optical encoder for current, vibration, temperature and speed measurement respectively; whereas for utility control, temperature transducer, LDR, and PIR motion sensor are employed. The design of the SMART Analysis System Human Machine Interface (HMI) included all the desired parameters which are shown in Figure 7.

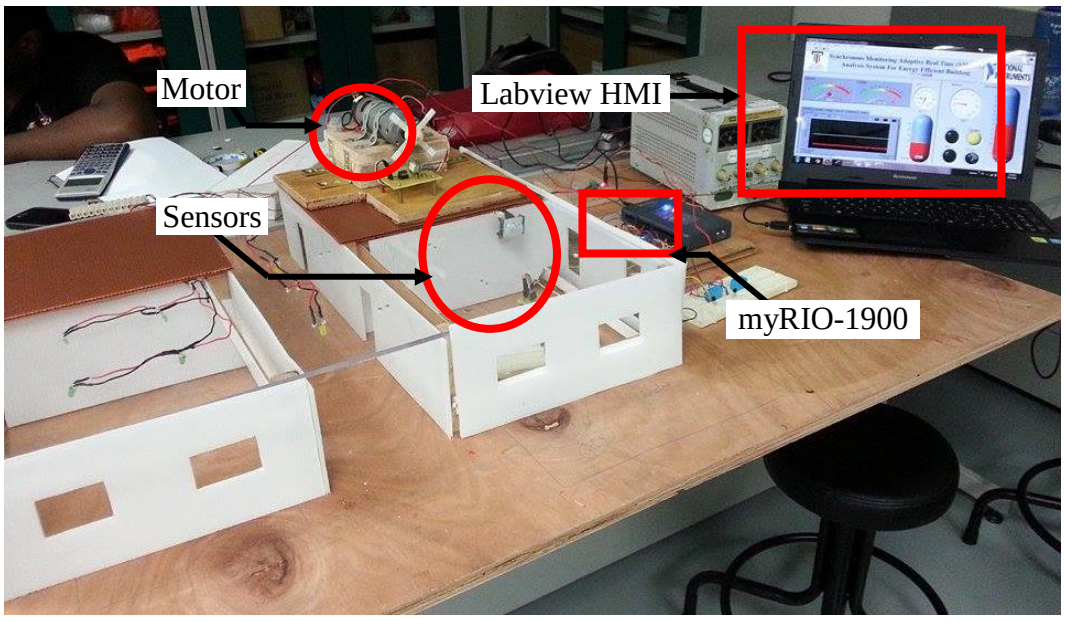

Fig. 6. Experimental set-up

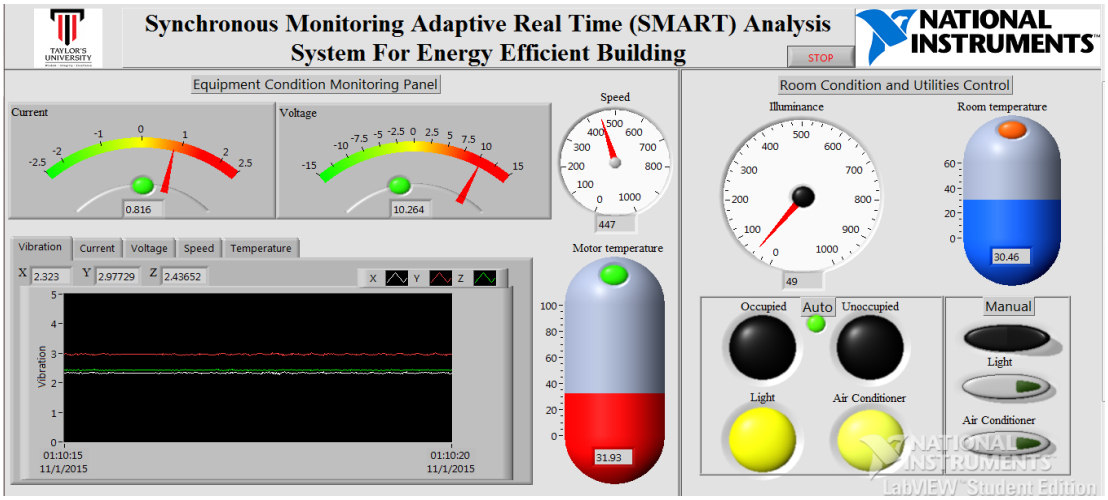

Fig. 7. Human Machine Interface (HMI) of SMART analysis system

3. Results and Discussion

3.1 Utility Operation Control

Four possible conditions are considered and tested for utility operation control. The utility being considered here are light and air conditioner where represented with hardware using LEDs and a motor. According to Ministry of Human Resources Malaysia, the suitable illuminance is above 400 Lux and temperature is 20°C to 26°C.

Case 1: No motion for 10 minutes
After 10 minutes without any detected motion, the system switched off the motor and light which can be seen in the HMI and hardware response in Figure 8 (a) and (b) even though the illuminance and temperature are not in suitable range.

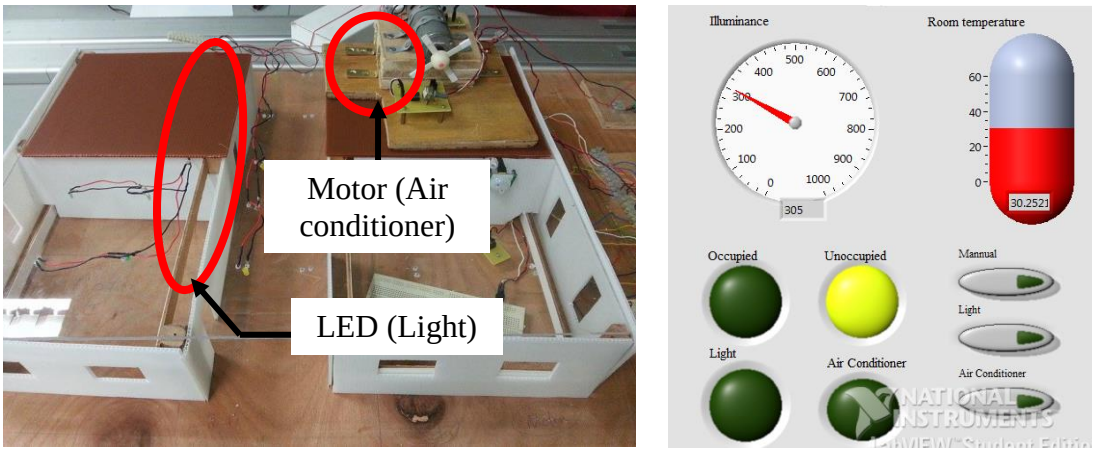

(a) (b)

Fig. 8. (a) Hardware: LED and motor off (b) HMI: Light and air conditioner off

Case 2: Motion detected; Illuminance < 400 Lux; Temperature >26°C
When the system detected motion and with illuminance below 400 Lux and temperature above 26°C, both air conditioner (motor) and light (LED) are switched on as shown in Figure 9 (a) and (b).

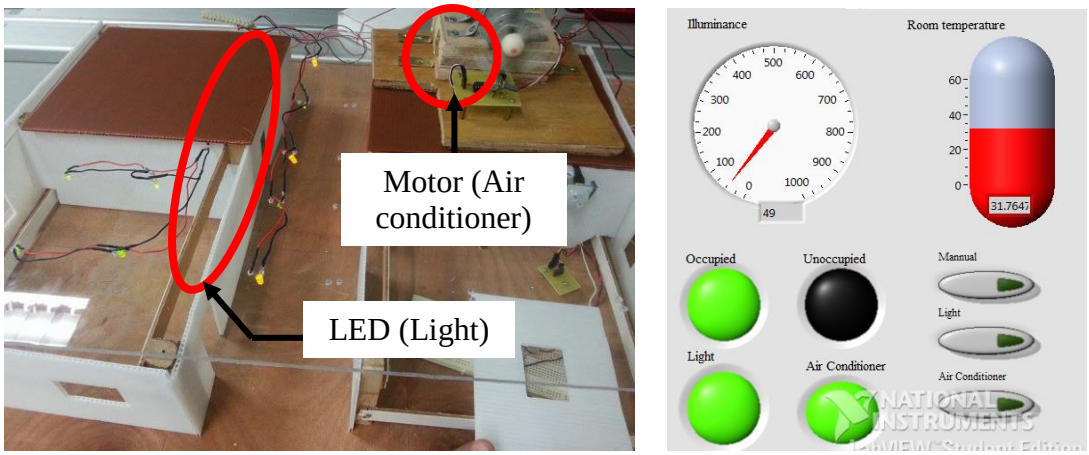

(a) (b)

Fig. 9. (a) Hardware: LED and motor on (b) HMI: Light and air conditioner on

Case 3: Motion detected; Illuminance > 400 Lux; Temperature > 26°C

In a condition that illuminance is above 400 Lux and temperature is more than 26 °C, the light (LED) is switched off and air conditioner (motor) switched on as illustrated in Figure 10 with human occupancy detected.

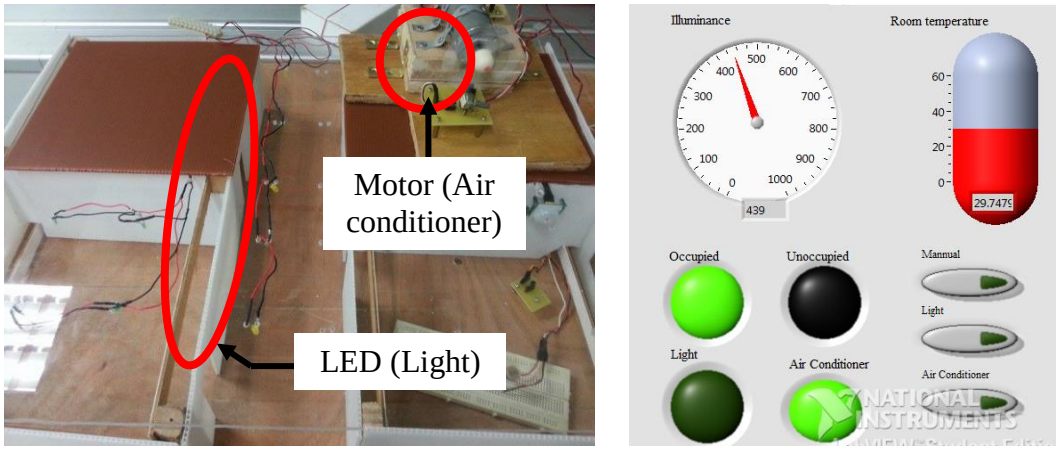

(a) (b)

Fig. 10. (a) Hardware: LED off and motor on (b) HMI: Light off and air conditioner on

Case 4: Motion detected; Illuminance > 400 Lux; Temperature < 35°C (Adjusted for test)

The threshold of air-conditioner to switch off is 26 °C which is difficult achieve under laboratory condition, thus, the threshold is adjusted in the program to 35°C for testing purpose. As a result, the system switched off the air conditioner (motor) as the measured temperature is 30 °C and occupancy is detected. Apart from that, the light is switched off since the illuminance is 439 Lux.

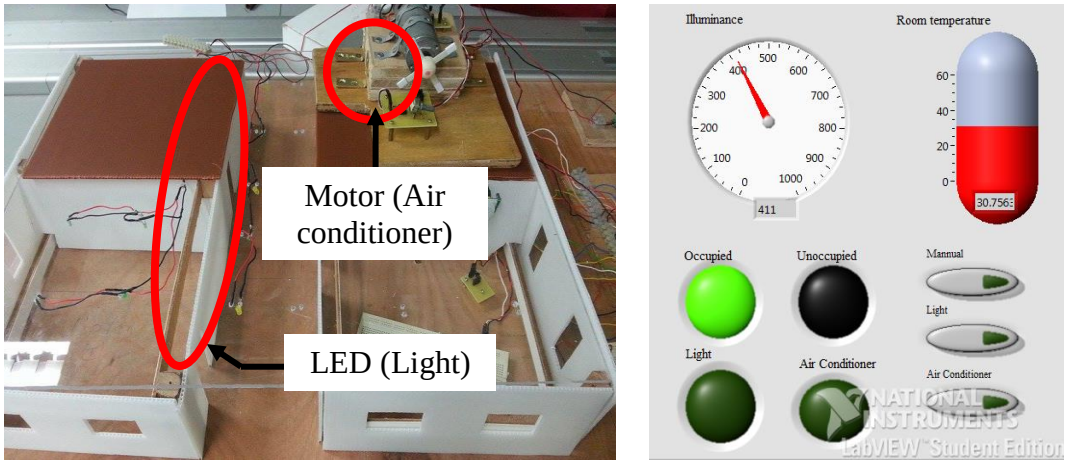

(a) (b)

Fig. 11. (a) Hardware: LED and motor off (b) HMI: Light and air conditioner off

These control actions could greatly reduce the energy usage without compromise the comfort level of user. Besides, the alteration of threshold demonstrated adaptability and flexibility of the system to meet user specific requirement.

3.2 Dynamic Load Vibration Analysis

The dynamic load where in this case is the motor that represented the air conditioner is analyzed using Labview Sound and Vibration Analysis Assistant. Order analysis on the motor vibration is performed with octave spectrum and power spectrum. The result from octave spectrum in Figure 12 (a) showed that harmonic exhibits vibration at 20 Hz as 1st order, 80 Hz (4 x 20 Hz) as 4th order and 140 (7 x 20 Hz) Hz as 7th order. The vibration caused at 20 Hz and 80 Hz (Low order) are due to imbalance, miss alignment or loose coupling. Whereas 140 Hz 7th order (High order) harmonic is due to blade defects. Others harmonics are caused by the fault of loose mount. On the other hand, Figure 12 (b) shows the power spectrum/loss data from the vibration level. Isolation on the peak sustained vibration conditions helps to operational benefit of the consumer. By doing so, the harmonic contributed to the power grid can be minimized and increases the overall efficiency of the grid.

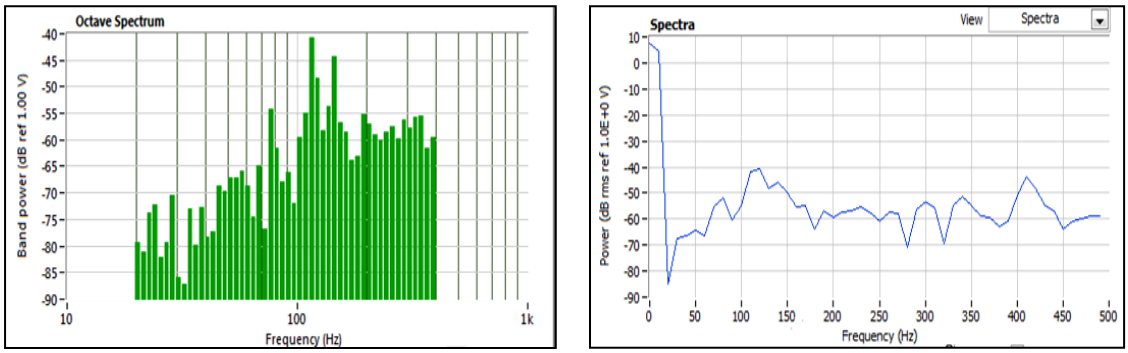

(a) (b)

Fig. 12. (a) Octave spectrum of the vibration data (b) Power spectrum of the vibration data

3.3 Energy Recovery Analysis

The SMART system is focused on Blocks C, D and E as their energy usage are similar in nature where daily operation took place mainly in classroom; whereas Block A and B are made up of administration office and event hall. Electricity usage in Blocks C, D and E (RM 3493789 in 2013) are much higher compared to Blocks A and B (RM 1977593 in 2013). The electricity capacity of TULC is mainly ventilation, air-conditioner, lighting and general equipment. Air-conditioner and lighting load are found to be 80 % of the total capacity. Therefore, contribution of air-conditioner and lighting load in Block C, D and E for year 2013 is found as,

$$80\% \times RM\,3493789 = RM\,2795031$$

Thus, controlling usage of these two utilities can increased the electricity efficiency significantly. Since Block C, D and E mostly consist of classroom, the operation start at 8 am to 6 pm. However, the utilities (Air-conditioner and light) are left in switched-on condition after users left. It is only being switched off by facility management staff at around 8 pm. Thus, the utilities usage duration is 12 hours even though the demand for classes is only 10 hours. Besides, some of the classrooms are not fully utilized from the 8 am to 6 pm duration. Therefore, the actual demand for the utilities is estimated to be only 8 hours.

By performing utilities operation control using SMART system, the extra 4 hours of electrical energy wastage can be vastly reduced. Taking year 2013 electricity usage as

example, energy or kWh charge is 80% of the total electricity charge. The energy saving is estimated to be 15 to 20 % less and the new monthly kWh charge with SMART system is presented in Figure 13. In the process, maximum demand or kW charge that made up the remains 20 % of the bill is expected to decrease by 5 % to 10 % with the SMART system implementation. A graph that illustrated the new saving for each month in 2013 is presented in Figure 14. Overall, the forecast saving is RM 773292 per year or 22.13 % for Block C, D and E electricity expenses. Moreover, the user comfort level is maintained at the acceptable standard specified by Ministry of Human Resources Malaysia.

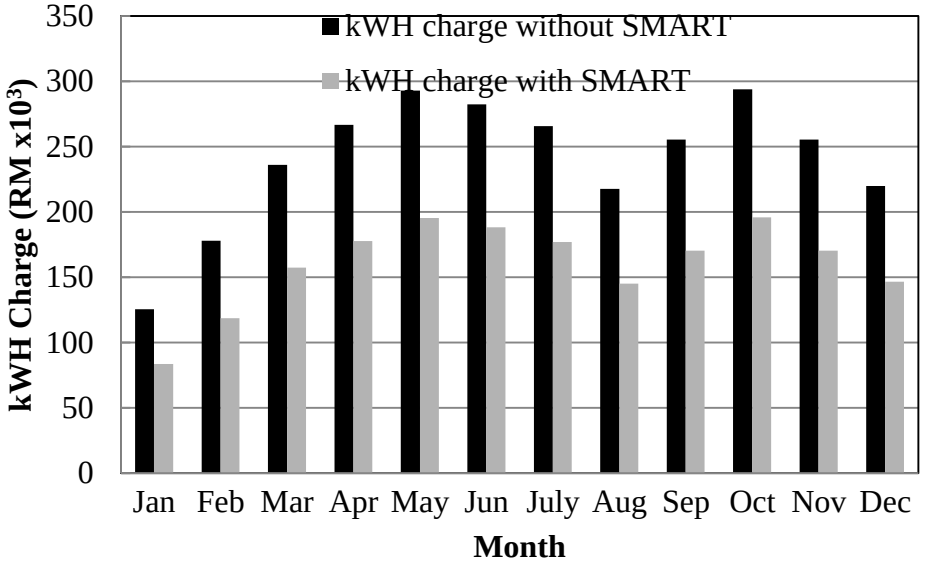

Fig. 13: kWh charge with and without SMART system

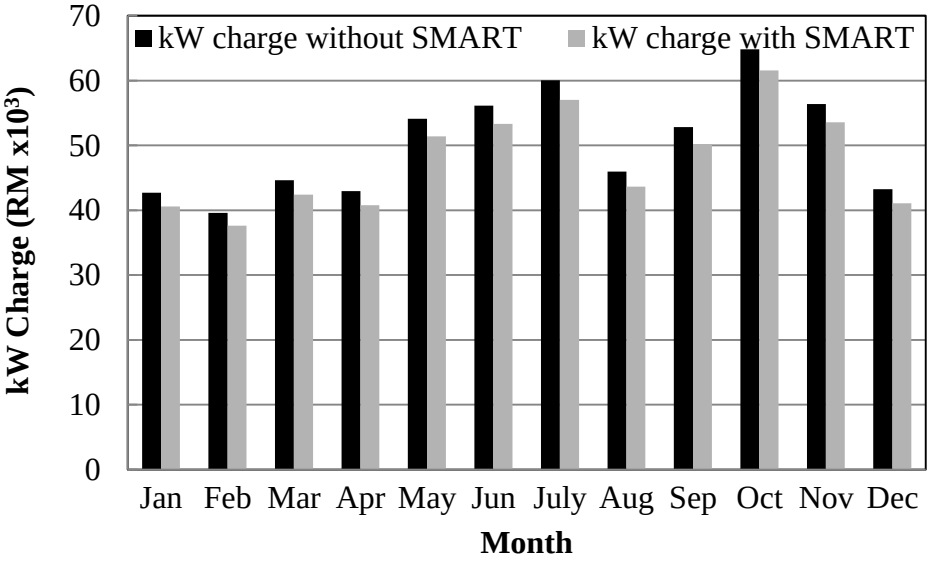

Fig. 14: kW charge with and without SMART system

4. Conclusion

In this paper, the theory, method and impact of the Synchronous Monitoring and Real Time (SMART) Analysis System are presented. The test area is scaled down to a room design and employed the methodology proposed in this paper to optimize the energy usage. The design system has two circuits control. The dynamic load control where it isolates the faulty machine by performs regular condition monitoring of the dynamic load. Through USB data acquisition, the sensors data are analyzed and alerts the operator for isolation or maintenance. The other control is for utilities circuit which controls the operation based on physical environment condition. An algorithm is programmed into the FPGA chip of the myRIO unit for this operation. As a result, SMART system can enhance the operational control which leads to higher energy efficiency and the sustainability to a larger extent.

References

[1] Center for Climate and Energy Solutions. "Buildings and Emissions: Making the Connection," Internet: http://www.c2es.org/technology/overview/buildings, 2009, [16th January 2015]

[2] H. Z. Xin and S. P. Rao. "Active Energy Conserving Strategies of the Malaysia Energy Commission Diamond Building," *Procedia Environmental Science*, vol. 17, pp. 775–784, 2013.

[3] W. John, **C. V. Aravind**, K. R. Rajparthiban and P. Sugendran. "Conditional Power Monitoring of Domestic Loads through Human Machine Interface," *Asian Journal in Electrical Sciences*, vol. 2, no. 2, pp. 8-13, July-Dec. 2013.

[4] **C. V. Aravind**, M. Al-atabi, J. Ravishankar, A. Malik, Arkar and E. Ambikairajah. "Eco-tourism Sustainability through PV Technology: A Comprehensive Review," *Journal of Engineering Science and Technology*, vol. 8, no. 6, pp. 654-668, Dec. 2013.

[5] **C. V. Aravind**, M. Al-Atabi and B. Arasan. "The Case of the Energy Solution to the Eco-tourism Model for Sustainable Development using PV/T Technology," *International Journal of Scientific and Engineering Research*, vol. 5, no. 4, pp. 174–177, 2014.

[6] R. G. I. Olisa, **C. V. Aravind** and M. Ihwan. "Real-Time Human Machine Interface Controllers for Industrial Drives," in *ASEAN 2011 Virtual Instrumentation Contest*, Kuala, Lumpur, 2011.

[7] K. K. Cheng and **C. V. Aravind**. "Testing of Motion, Temperature and Current Sensors in a Synchronous Monitoring Adaptive Real Time System," presented in *2nd International Conference on Green Technologies in Power Generation, Communication Instrumentation*, Chennai, India, Feb. 2015.

[8] K. K. Cheng and **C. V. Aravind**. "Testing of Motion, Temperature and Current Sensors in a Synchronous Monitoring Adaptive Real Time System," *International Journal of Applied Engineering Research*, vol.10, no.17, pp.12843-12846.

[9] W. Y. Chan. "Machine Condition Monitoring for Vibration Analysis using Labview," *Bachelors Thesis*, UCSI University, 2009.

A New Permanent Magnet Synchronous Machine for Small Battery Operated Vehicle

Chong Wei Hsiung, Aravind CV*

Computer Intelligence Applied Research Cluster
Taylor's University School of Engineering, Malaysia

*chongweihsiung@gmail.com, *aravindcv@ieee.org*

Abstract

For the use of motor in electric vehicle, permanent magnet motors are the "go to" machines as it is able to provide a high torque and high torque is a standard requirement for electric vehicles[1-2]. The torque produced by these machines are the resultant forces at the air gap of the machines where there is a flux linkage between the machine's stator windings and the rotors permanent magnets. By reducing the air gap length between the stator and rotor, it will certainly improves the flux linkage of the machine, however, there is a limit as reducing this air gap will increase the cogging torque of the machine which may result in the reduce in efficiency of them machine as the motor may require more power to overcome it. A New Permanent Magnet Synchronous Machine for Small Battery Operated Vehicle is proposed to improve torque performance for a surface permanent magnet machine. The key to this proposed structure is the dual stators and the placement of the permanent magnets in the rotor. Consequently, this dual stator structure is to generate a higher by not only utilising the flux linkage at stators yokes, but increase the number of coil winding for the machine. Meanwhile, the air gap length is also reduced as to improve the magnetic flux linkage between both stators and the rotor. Using a finite element method the static torque characteristic for the machine is evaluated. The average torque for the proposed motor structure is found to be 14.745 Nm with a motor constant square density of 42.5×10^3 $Nm^2/A^2/W/m^3$ at its synchronous speed with the injection of 1A current to the coil winding

Keywords: Double stator, air gap flux linkage, Surface permanent magnet motor, finite element analysis, motor constant square density.

1. Introduction

The buzz of this centuries with regard to our environment have been on climate change, global warming, melting of the earth polar ice caps, rising sea levels, etc. An overwhelming majority of climate scientists have agreed that this is the results of mankind's actions and is a global treat if left unattended, which will result in irreversible consequences such as extinction of certain species vital to the animal kingdom, displacement of the human population living along the coast of every continent, increase of global temperature, etc. According to the United Nation Environmental Program (UNEP) report on greenhouse gasses emission in 2012, it have shown that transport vehicles such as car, motorcycles, ships, etc. are the 3rd highest contributors to greenhouse gases such as carbon dioxide (CO_2) into our atmosphere [3]. On top of "transport vehicles" being mention behind only to the power sectors and the industrial sectors in the title for the most greenhouse gases emitter, vehicles in general have been estimated to release 1.7-2.5 Giga-tonne of CO_2 equivalent volume of greenhouse gasses.

To overcome this issue, commercial available vehicles such as cars and motorcycles have started manufacturing electrical alternative known as Electrical Vehicles (EV) or Hybrid Electric Vehicles (HEV). These vehicles are meant to reduce commercial transport vehicles dependence on fossil fuel. These cars produce less greenhouse gasses during its operations and have been improved to have feature such as regenerative braking systems. Such a system basically converts mechanical energy lose during braking to electrical energy which is stored in battery packs to improves efficiency of HEV and EVs as less heat energy is dissipated during braking when compared to a conventional vehicles [4].

The function of the Novel small brushless motor that is describe in this report is design to suit a small electric vehicle such as a bicycle. The motor is first designed and then analyze with numerical and mathematical tools. The results obtain from the analysis is then compared with a motor done by a previous party which have the same volume with the proposed designed motor. These comparison of torque density between the two machines are done with the same condition such same power supplied, same material, same electrical circuit and etc. This is to ensure the torque density of the motor is improved solely with the change in design.

As for the objective of the project it is aimed to devise a ***novel fractional horsepower brushless motor*** for ***torque density improvement*** using principles of electro-magnetic and to ***optimize*** the propose ***design*** through ***numerical simulation and analysis for*** electric vehicle application**.**

2. Theoretical Frame Work

2.1 Machine Design

The figures below shows the components for the proposed model design where **Fig 1** shows the exploded view for the Double Stator Surface Permanent magnet machine. While **Table 1** are the parameters for the machine. This machine have is design such that it have 18 stator coil winding connected with a star configuration and a 20 pole rotor as shown in **Fig 2**.

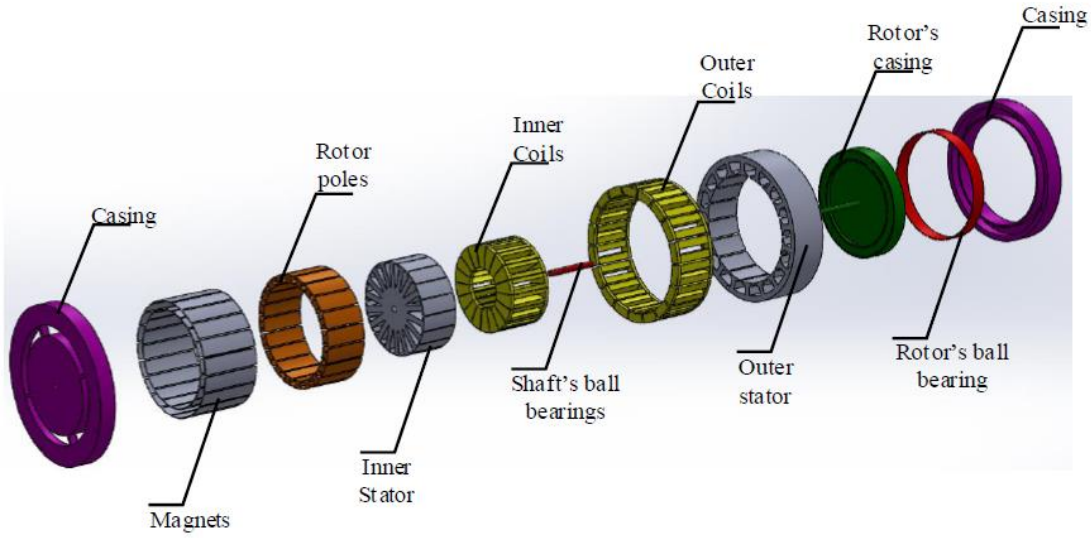

Figure 1: Exploded view of the machine.

Table 1: Proposed design specifications

Parameters	Values
All	
Outer Diameter of Machine	200 mm
Stack Length	50 mm
Inner Stator	
Number of slots	18
Diameter Outer Surface	122.8mm
Diameter Inner Surface	8mm
Diameter Outer Coil	111.6mm
Diameter Inner Coil	76mm
Outer Stator	
Number of slots	18
Diameter Outer Surface	200mm
Diameter Inner Surface	148.8mm
Diameter Outer Coil	184mm
Diameter Inner Coil	160.1mm
Rotor	
Number of poles	20
Diameter of Outer surface	147.8mm
Diameter of Inner surface	123.8mm
Inner stator Air-gap	0.4mm
Outer stator Air game	0.4mm

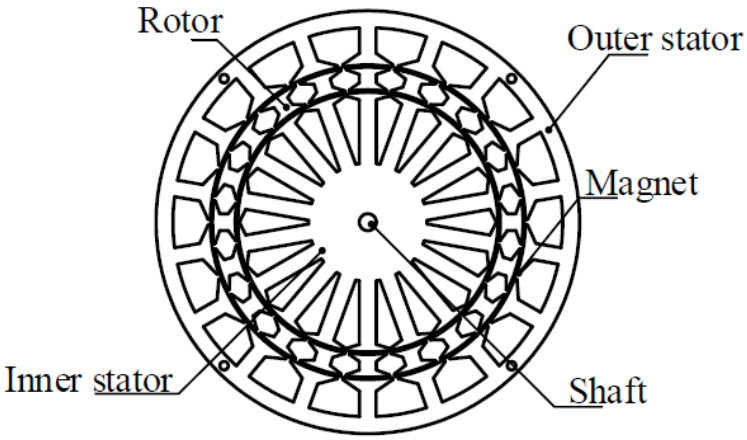

Figure 2: Proposed design main components

Double stator design is chosen such that it is to allow the machine to be able to have an increase in torque as explained in section 2.2 and as for surface permanent magnet (SPM) machine, it is to allow the machine to lose its heat during operation more efficiently when compared to interior permanent magnet machine [5]. However, the down side of a SPM machine is it may increase the cost of maintenance as the magnet may break off from the rotor when operating in high speed [6], since the rotor are not secured inside the rotor.

2.2 Electromagnetic Torque Production Theory

Permanent magnet motors operating principles are based off the attraction and repulsive force of a magnets and electromagnets [7]. These forces are because of the interaction of magnetic field between the electromagnet stator winding and the permanent magnet within the rotor [7]. To achieve this, the number of stator pole within the machine is divided by 3 to evenly distribute the 3 phase power supply throughout the motor coil windings. When currents are injected to the coils a flux is produced, govern by Fleming's left hand rule, the interaction between the stator and rotor magnets either attract with one another or repel one another. Thus for the DC machine, it rotates because the motor's rotor is trying to reach an equilibrium position [8]. However, due to the constant change in magnetic flux in the stator coil, the machine's rotor is forced to rotate.

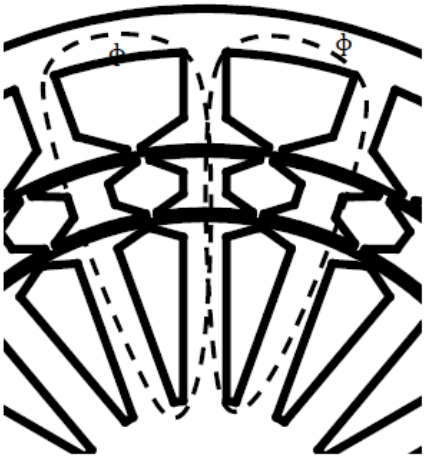

Figure 3: Operating principles of DSSPM motor

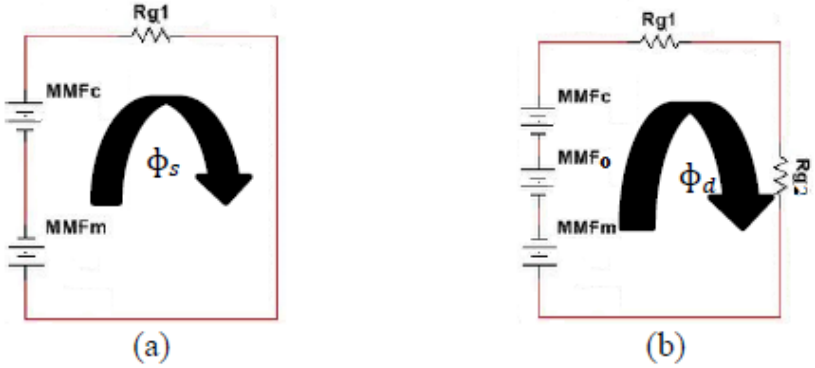

Figure 4: Equivalent electrical circuit to formulate flux in single stator machine (a) and double stator machine (b).

The air-gaps reluctance between rotor and stator are represented as resistors while the magneto-motive force (MMF) of the coils are represented as battery. For the flux generated, it is represented as the flow of current. Thus, from the equivalent circuit the equation for flux can be determine:

$$\phi_s = \frac{MMF_c - MMF_m}{R_{g1}} \quad (1)$$

$$\phi_{ds} = \frac{F_{total}}{R_{oag} + R_{iag}} \quad (2)$$

Since,

$$R_{oag} = \frac{R_{g1}}{2} \quad (3)$$

$$R_{oag} = R_{iag} \quad (4)$$

$$\phi_{ds} = \frac{F_{total}}{\frac{R_{g1}}{2}} \quad (5)$$

For the equation above, ϕ and ϕ represents the flux for single stator and double stator respectively, Ʀ 1 represent the air gap reluctance between inner stator and rotor while Ʀ 2 represents the air gap reluctance between outer stator and rotor. As for , it represents the MMF by the inner coil, 0 represents the MMF by the outer coil and is the MMF from the magnet. Since the volume of both the machines are identical, an assumption is made, that the MMF by the coils in both cases remains constant ("" + = "" =). Thus, as shown in equation 1 and 5, ϕ would be more than ϕ as there is a decrease in reluctance since the flux is inversely proportional to reluctance. Therefore justifying the reason for increasing the number of stator to two in the design.

2.3 Comparison evaluation of Torque between machines

To compare the torque between 2 machines, a unit known as the motor constant square density is used (G), as shown in equation,

$$G = \frac{(K_m)^2}{V} \quad (6)$$

Where, K_m is the machine constant is in $(Nm/A/W^{-(1/2)})$ unit and V is the volume of the machine (m^3). To find the machine constant equation 7 is used.

$$K_m = \frac{K_T}{\sqrt{P}} \quad (7)$$

Where, K_T is the torque constant (Nm/A) and P is the input power to the coil winding $[W]$. As for the torque constant, it is given as in Equation (8).

$$K_T = \frac{T_{avg}}{I} \quad (8)$$

And T_{avg} is the fundamental torque (Nm) and I is the maximum current input to the machine (A). The use of "G" allows the comparison between machine of different volume since the motor constant square density takes into account the torque, power supplied and volume of the machine.

5. Finite Element Analysis Method

Finite Element Analysis (FEA) tool is used as a design and simulation tool for analysis of the proposed model. This tool is used to help determine the motor constant square density as well as help determine magnetic flux density within the machine. The figure below (**Fig 5**) shows the flux density at different rotor positions for 0^0, 6^0, 12^0, 18^0, 24^0 and 30^0 degree which is shown in **Fig 5** (a) – (f) respectively. However, the analysis of the flux density within the machine as shown below neglects the mutual inductance effect in the machine. Since the performance of the motor in this paper focuses on the geometry of the machine, the FEA tool is able to provide an accurate analysis of the magnetic flux within the machine, direction of flux flow, torque performance and the magnetic flux density with respect to the changes in the design. Based on these results, it is then evaluated to ensure the magnetic flux are fully utilize with the change to its geometry/design.

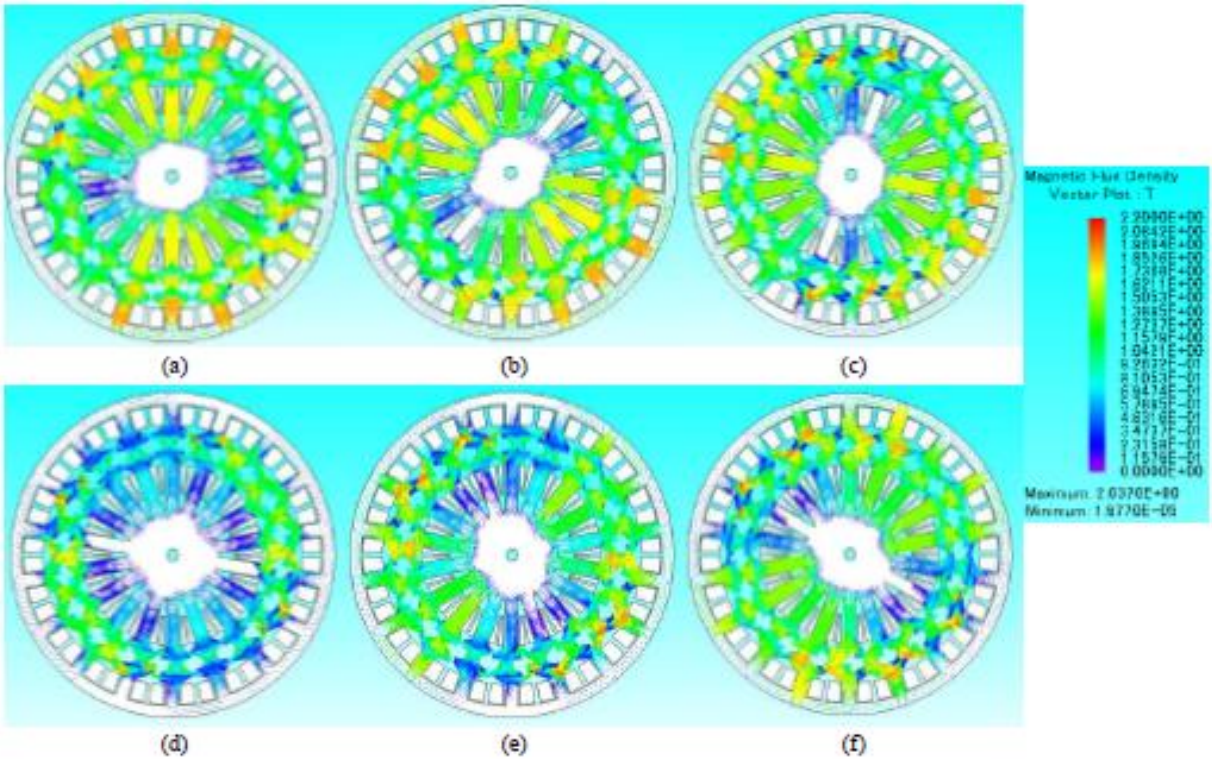

Figure 5: Flux Flow for Various Rotational between Angle 0-30 degrees

Other than the design of the machine being a huge factor to the magnetic flux density of the machine, material used in the machine is also vital. **Table 2** shows the type of material for the main components of the DSSPM machine.

Table 2: Type of Material used for DSSPM machine in FEA tool

DSSPM Main Component	Type of material
Outer Stator core	Steel(50jn400)
Inner Stator core	Steel(50jn400)
Rotor core	Steel(50jn400)
Magnets	NEOMAX-42
Coils	Copper wire(SWG 25)

3. Methodology

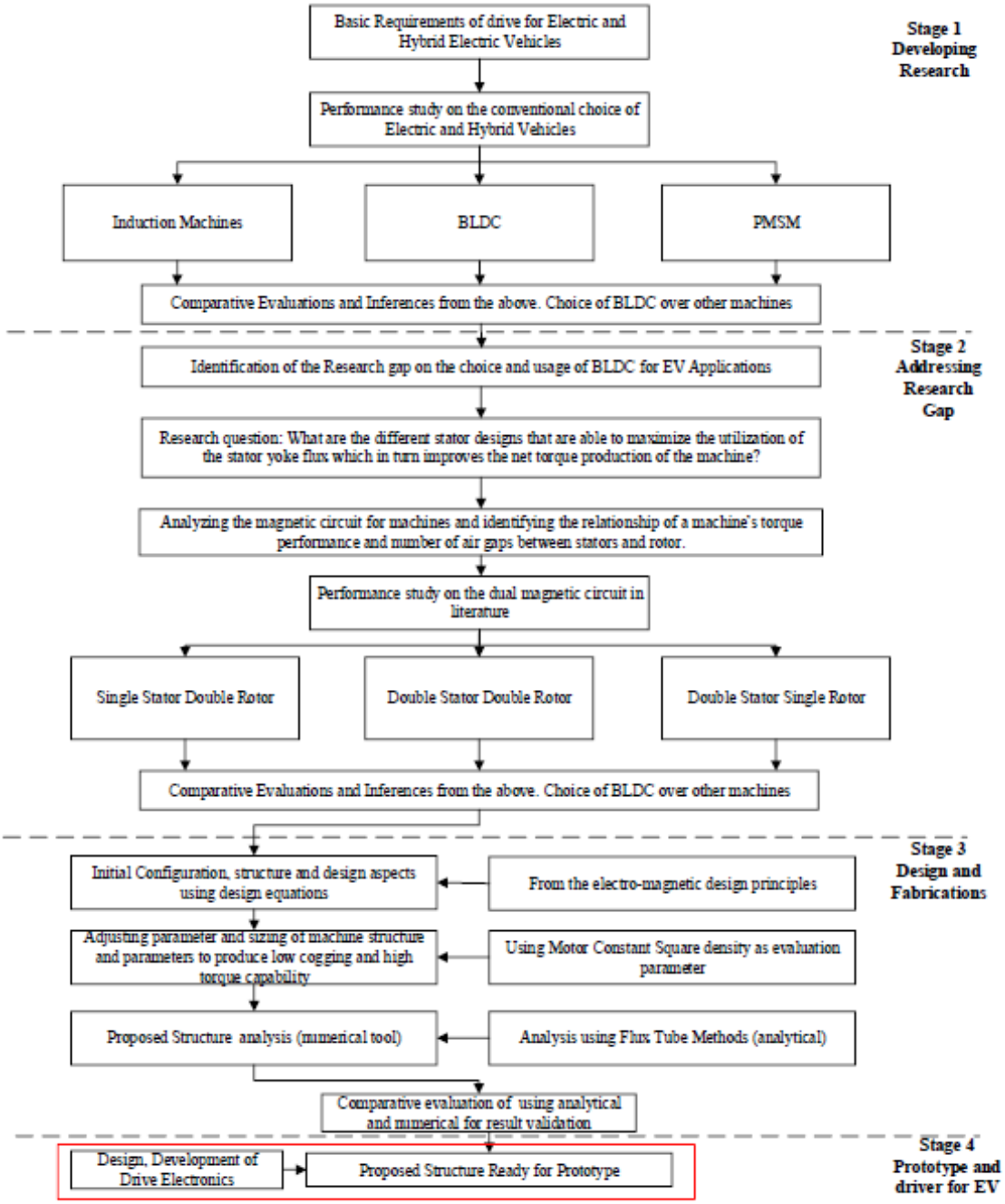

4. Results and Discussion

To analyse the machine, the static torque characteristic of the machine is used to determine the average torque of the machine. The proposed design is simulated in an Finite Element Analysis (FEA) tool where the design is provided with a current of 1 ampere DC source and rotated at its' synchronous speed of 300 rpm. The static torque characteristic is as shown in **Fig 7** where is maximum torque is at 24.13Nm and with the help of Origin® software, it is found that the DSSPM machine have an average torque of 14.74Nm. The torque can be further analyse for different current values and is shown in **Fig 8** and **Table 3**.

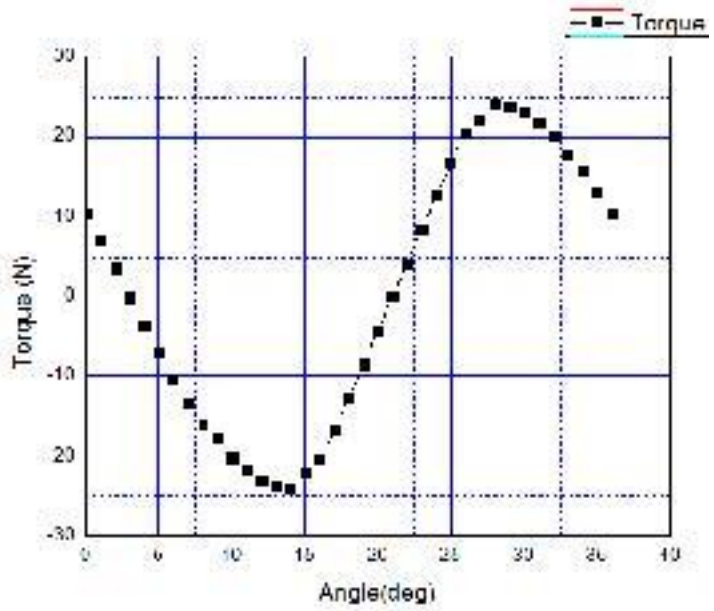

Figure 7: Static Torque Characteristics for 1 pole pitch

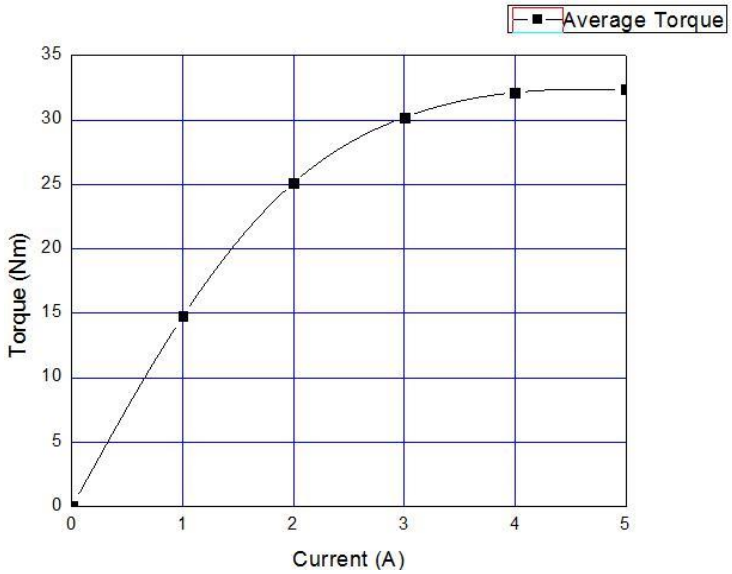

Figure 8: Current-Torque Characteristics**.**

Table 3: Motor constant square density at Synchronous Speed.

$I[A]$		1	2	3	4
V	$[m^3]$	1.571×10^{-3}	1.571×10^{-3}	1.571×10^{-3}	1.571×10^{-3}
T_{avg}	$[Nm]$	14.75	25.12	30.20	32.13
K_t	$[Nm/A]$	14.75	12.56	10.07	8.03
K_m	$[Nm/A/W^{-(1/2)}]$	7.102	3.025	1.616	0.967
G	$[Nm^2/A^2/W/m^3]$	32.11×10^3	5.824×10^3	1.662×10^3	0.595×10^3

Thus, from the **Fig 8**, the average torque of the machine tend to increase with the increase in current. However, the average torque value also tend to plateau beginning at 4A onwards. Hence showing that the machine is able to provide a maximum average torque of 32.13Nm. As for the motor constant square density, it will decline with the increase with current as seen in **Table 3** as well.

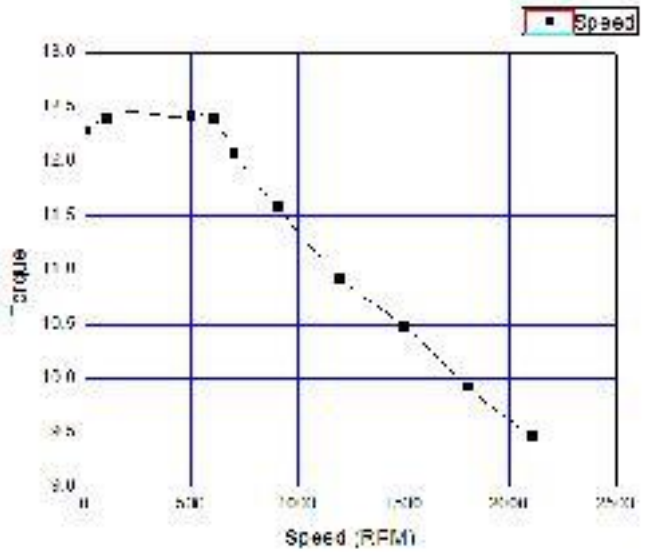

Figure 9: Speed-Torque Characteristics**.**

As for **Fig 9**, the graph shows the speed torque characteristic for the machine when injected with 3 phase current source with an amplitude of 1A ampere where the voltage have been calculated to be 3.04 volts since the total resistance of the coils are calculated to be 4.31Ω and the current source RMS value is 0.7071A.

5. Conclusion

The static measurement characteristic of the double stator surface permanent magnet machine show a motor constant square density of 261.87[^{2}/ ^{2}/ / ^{3}] at 5A. However, as stated before, the drawback of this machine is that the magnet which are mounted on the surface the rotors are prone breaking off the surface of the rotor during high speed application which may require a higher cost in its maintenance. Thus, for future work, the ideal speed and type of adhesive used to secure the magnet is to be research on to prevent the magnet from coming of the surface of the rotor.

6. Reference

[1] Naumov V, Baumann R Gross T(2006) An evaluation of inter vehicle ad hoc network based on realistic vehicular traces. In: Proceedings of ACM MOBIHOC'06, Florence, pp108-119.

[2] Lochert C et al. (2003) A routing strategy for vehicular ad hoc network in city environments, IVS'03, pp156-16.

[3] A. Nagoor Kani, "A Simplified Text in Electrical Machine Design 2nd Edition" in Electric Machinery, Chennai: RBA Publications, vol. 1, pp. 7-35, Nov. 2012.

[4] T. D. Strous, Polinder, "Design of a Permanent Magnet Radial Flux Concentrated Coil Generator for a Range Extender Application," Electrical Power Processing, vol. 3, pp. 12-30, Nov. 2011.

[5] C.V. Aravind, "Design and Development of Double-Rotor Switched Reluctance Motor Using Magnetic Circuit Analysis," IEEE Trans. on Motor Using Magnet Circuit Analysis, pp. 1-186, Jan. 2013.

[6] Lam Pin Wen, Aravind CV, Reynold Hariyadi, "Design of a Novel Double-Rotor Flux Assisted Machine for Electric Vehicle Applications" *International Conference on Electrical Power Engineering and Applications (ICEPEA2014)*, Langkawi, Malaysia, 2014. (Under review)

[7] Krishnamurthy, M, Fahimi, B, Edrington, "Comparison of Various Converter Topologies for Bipolar Switched Reluctace Motor Drives" In Power Electronics Specialists Converence, PESC'05, pp. 1858-1864, 2005.

[8] J.R., Hendershot Jr. and T, Miller. (2010). "Design of Brushless Permanent-Magnet Machines." Venice, Florida: Motor Design Books LLC, pp.9, 83,123-125.

Design and Simulation of Harmonics Filter for PT Gajah Tunggal Tbk

Omar Mohammed Omar Basharahil[1*], Reynato Andal Gamboa[1], Taufik Ridwan[2]

[1]*Taylor's University Lakeside Campus, Malaysia*

[2]*PT. Gajah Tunggal Tbk, Indonesia*

[*]O_M_B90@hotmail.com

Abstract

The new power conversion technologies along with the employment of power electronics devices in both commerce and industries have substantial contribution in raising harmonics level in the electrical power systems resulting in serious issues that damage the electrical machines and hence increase the financial loss. This research was coordinated with an industry that encounters high harmonics level, which results in serious damages in generators, transformers and capacitor banks. This industry is called PT Gajah Tunggal Tbk, Indonesia. Hence, this research proposes a filter to be used as a solution to mitigate the harmonics issues encountered by PT Gajah Tunggal Tbk, Indonesia. The THD at the bus of the company's main distribution board 7 is 22.8%. In this study, the single line diagram (SLD) of MDB7 was obtained from the industry and built in ETAP software with full specifications of machines and components. Subsequently, harmonics analysis was conducted in ETAP to analysis THD in the SLD and the ETAP result of THD is 23.38%. Besides, the 5^{th} harmonics order was identified as highly contributor order in raising the THD in bus of MDB7. Furthermore, A single tuned filter was sized to mitigate the 5^{th} order harmonics using some values from the load flow analysis in ETAP and a flow chart on design & simulation was developed. In addition, after implementation of the filter the results showed that the 5^{th} order harmonics was eliminated and the percentage of the THD has dropped from 23.39 to 4, which is within IEEE 519 limits. Lastly, mathematical analysis on impedance diagram and sizing LC filter is presented.

Keywords: Harmonics, Filter, Power, ETAP, Total Harmonics Distortion.

1. Introduction

Harmonic distortion is one of the significant problems that most industries face nowadays due to the huge volume of electric power conversion required for multiple applications [1]. Harmonics in a simple term is the distortion of sinusoidal waveform by other frequencies raised. Harmonics in voltage or current generate multiple frequencies of the fundamental frequency and these multiple frequencies are known as harmonics order [2]. Therefore, as the harmonics order increases, the output waveform becomes more complex. This complexity causes the distributions in the electrical systems. Moreover, the increase of nonlinear loads made harmonics distortion common in most industries [3]. A load is considered as nonlinear load when its impedance changes with applied voltage (sinusoidal waveform) resulting in non-sinusoidal current. The non-sinusoidal current contains harmonics, which interact with system impedance and lead to voltage distortion. This distortion causes many troubles and losses in the system that contributes in reducing electrical device's lifetime as well as lowering system performance.

Industrial facilities are the main source of harmonics production. In industries, there are sources from which harmonics are generated and developed such as transformers, rotating machines, fluorescent lumps and electric furnaces. Power converters are also part of harmonics generation as these devices change the voltage from one form to another such DC-AC, AC-DC, DC-DC and AC-AC. These converters develop harmonics in the system during conversion process (rectifying, inverting, chopping etc) [4]. Due to the increasing of these converters in industries they are considered as primary source of harmonics distortion in distribution systems.

Power systems are designed to operate normally at the fundamental frequency. Hence, when a distorted waveform with multiple frequencies (harmonics) flows into the system, it causes the system to operate abnormally due to heating and overloading conditions created. Such conditions may cause failure to electrical equipment. Furthermore, Excessive harmonics current can also cause maloperation to the control and protection equipment in system as these equipment are designed to operate under normal condition. What is more, induced noise from harmonics can produce interference the negatively impacts the communication system. Ac motors can also be affected by harmonics, as hysteresis losses are propositional to frequency 5. Thus, when the higher frequency is introduced the losses at the ac motor core increase resulting in temperature rise in the core. In addition, resonance between impedances of inductor and capacitor can be raised with the presence of harmonics current, which can also result in over voltages at different parts of the system. As a result, all of these effects contribute in reducing equipment lifetime. Therefore, the institution of electrical and electronics engineers (IEEE) has released IEEE Std 519-1992 document which includes voltage harmonics limits at different buses voltage at PCC [6]. According to IEEE 519, the THD and IHD of voltage should not exceed 5% and 3% respectively for a system with bus voltage of 69kv and below.

There are several methods and techniques to reduce harmonics level in power systems. They are as following:

- Harmonics filtering
- Harmonics cancellation
- Network topology reconfiguration
- Increase of supply mode stiffness
- Phase balancing
- Series reactors

As filtering techniques are one of the most common methods for control of harmonic distortion in industry, this research aims to use harmonics filtering technique as a solution to mitigate harmonics level to an acceptable level in PT Gajah Tunggal Tbk, Indonesia [7]. PT Gajah Tunggal Tbk is a manufacturing industry that experiences high harmonics level in its electrical power systems resulting in many machines failures and damages.

The power supply in the industry consists of two different sources, which are synchronous generators (13 units) and PLN (national electricity company in Indonesia). These two sources supply all the loads in this industry where PLN supplies 78% of the total power demand and the rest of demand is supplied by the generators. This research focuses on one of the main distribution boards (MDB) in the company, which is MDB7 that encounters total harmonics distortion (THD) of 22.8% as shown in the digital display in Fig. 1. According to IEEE, the acceptable THD in a power system should not exceed 5%. Therefore, 22.8% THD is an unacceptable harmonics level that causes serious consequences in the system. 22.8% THD is developed from the MDB7 load. MDB7 distributes power to nonlinear loads that contain many induction motors driven by variable frequency drives (VFD). Thus, harmonics generation comes from these nonlinear loads and the VFDs in the load are considered as the primary contributors in developing THD up to 22.8% as they are made up of rectifiers and inverters [8]. Consequently, this industry has experienced many failures and damages in the capacitor bank, transformers and generators. In this paper, the proposed solution is to design and simulate a single-tuned harmonics filter that will reduce the THD to an acceptable level to provide clean effective and stable power system without disturbances using ETAP software.

Figure 1. THD in MDB7 digital display.

1.1 Objectives

The main objectives of this project are as following:

- To analyze proliferation, source and effects of harmonics level in PT Gajah Tunggal Tbk industry that experiences intolerable harmonics level.
- To analyze the single line diagram of the industry to check the individual harmonics distortion (harmonic order) that has highest contribution to the THD of the system using ETAP software.
- To design and simulate harmonics filter using ETAP software to mitigate that particular harmonics order to an acceptable level.

2. Methodology

The single line diagram obtained from the company was built in ETAP software with full specifications. However, the SLD had to be simplified due to some limitation in ETAP license and the simplified network shown in Fig. 2.

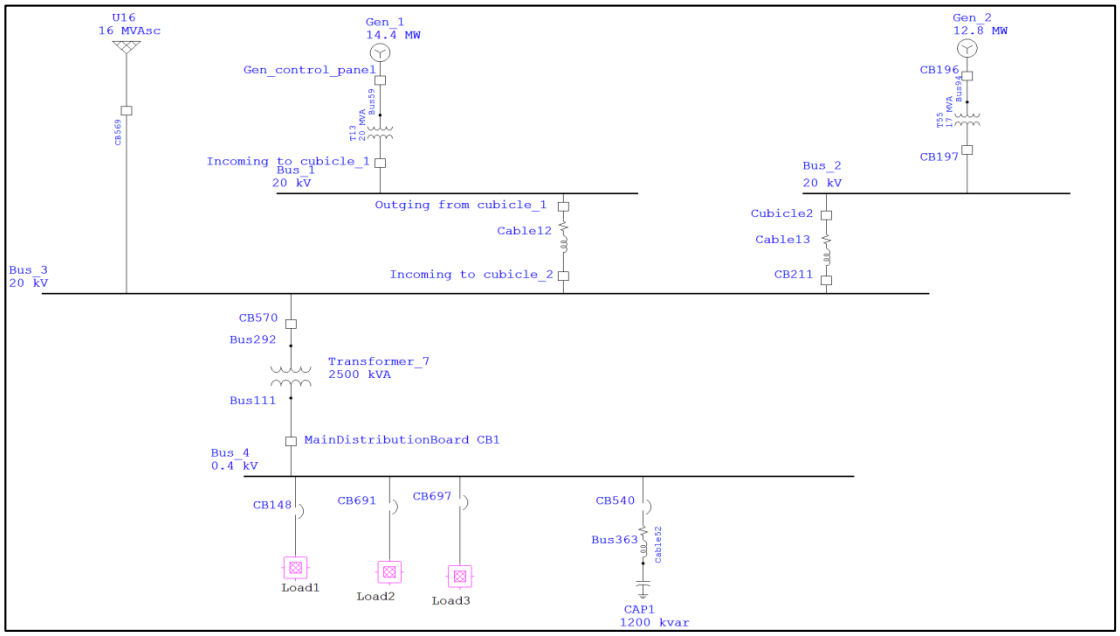

Figure 2. The simplified SLD in ETAP.

2.1 Design and Simulation

In this research, the analysis, design, simulation and results have been accomplished using ETAP software. Therefore, after building the SLD in ETAP, the design and simulation begin. The steps taken to design and simulate the filter in ETAP are summarized in a flow chart as shown in Fig. 3.

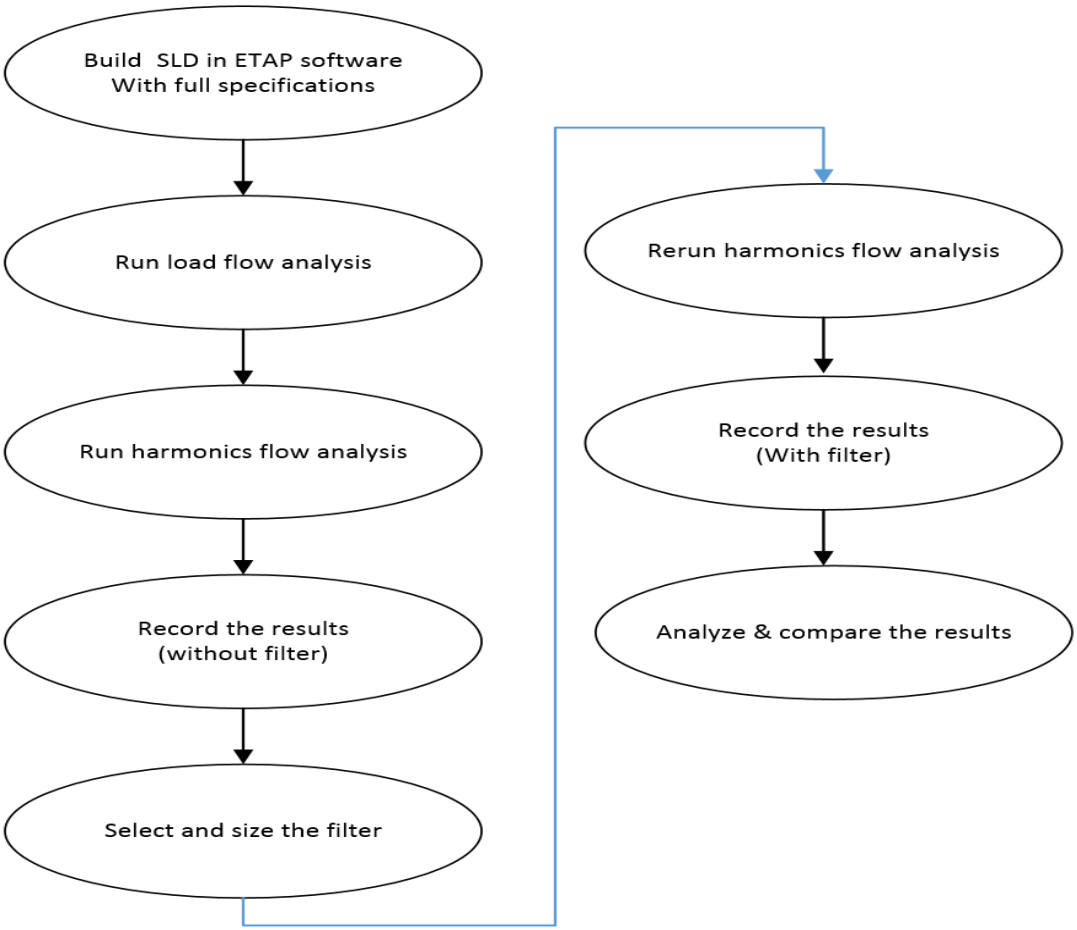

Figure 3. Flow chart of design and simulation in ETAP.

First of all, the load flow analysis is conducted to clear any fault in the system such as overload, overvoltage, under voltage, under excitation etc. Load flow also, helps to better understand the electrical network parameters. The main reason of running load flow in this study is to get the load MVA of the system and the exciting system power factor. Load MVA of and the exciting system power factor are used later to size the filter. To run load flow analysis, the sequence in Fig. 4 is followed. First the load flow analysis icon at the top left is clicked to switch from edit mode to load flow analysis. After that, the analysis is run by clicking the on the first icon at the to right. Once load flow is running, the load MVA and system power factor can be obtained as shown in Fig. 4.

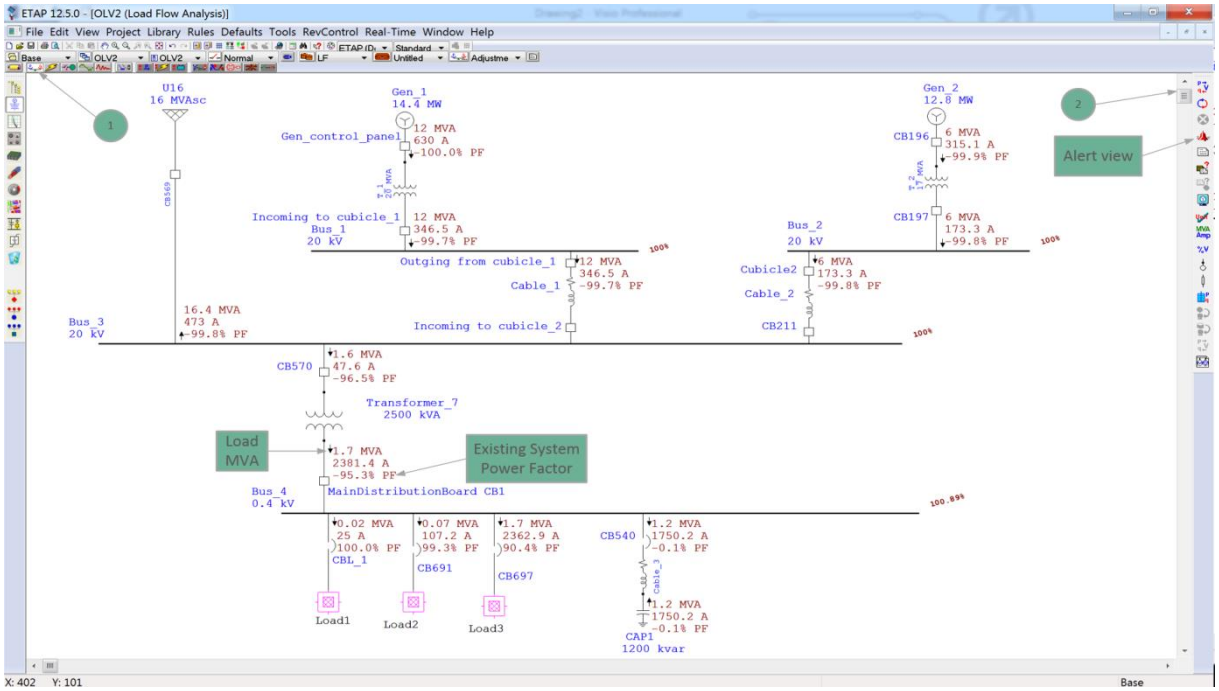

Figure 4. Running load flow.

Next, harmonics flow analysis is conducted to analyze the system. To start the analysis, the THD at bus_4 (the bus corresponding to MDB7 bus at the company) is checked and compared to the THD at the MDB7 bus. The THD at the MDB7 bus is 22.8% as captured from the company digital display shown in Fig. 1. Fig. 5 shows that the THD obtained by ETAP is 23.38%. After that, the results are recorded for later comparison after filter implementation. Since the THD obtained by ETAP is almost the same as the real value of THD at the company MDB7, the system is then analyzed to determine the harmonics order the highly contributes in raising the THD at MDB7. The analysis includes 5^{th}, 7^{th}, 11^{th} and 13^{th} harmonics orders. After analyzing the system in ETAP, it was found that the 5^{th} harmonics order has the highest contribution among the rest as shown in Table. 1. Since the harmonics order that needs to be mitigated is identified, hence filter design process will begin.

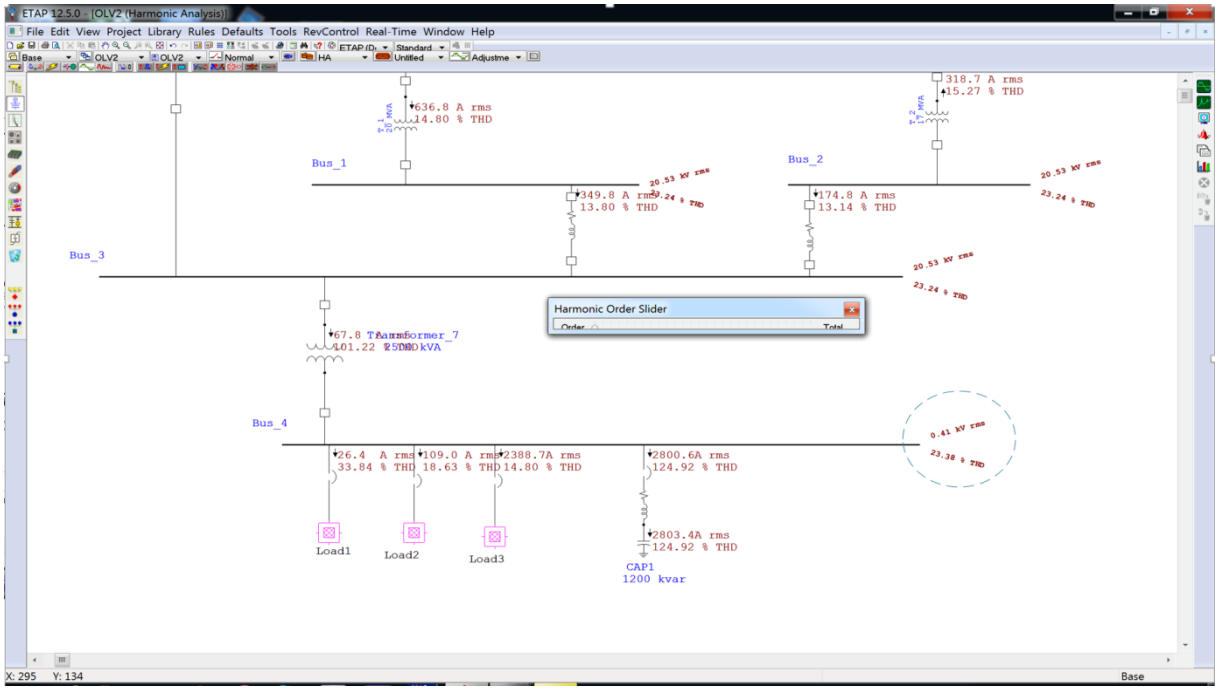

Figure 5. Running harmonics flow analysis.

Table 1: ETAP IHD of harmonics orders at bus 4 before the filter.

Bus \ Harmonic order	5^{th} (IHD)	7^{th} (IHD)	11^{th} (IHD)	13^{th} (IHD)	THD (%)
Bus_4 (MDB7)	23.11	2.27	1.94	1.57	23.38

Then, the filter is sized to mitigate 5^{th} harmonics order. To size the filter, the load harmonics current has to be determined; hence Eq. (1) is used.

$$I_{rms} = \sqrt{I_{load1}^2 + I_{load2}^2 + I_{load3}^2 + I_{Cap}^2} \quad (1)$$

After that, the filter type is selected. ETAP has several types of passive filters but the one selected for this project is single-tuned as it has good result in filtering out odd harmonics. Besides, the data obtained from the load flow analysis and the calculated total harmonics current are inputted as shown in Fig. 6. As a result, ETAP will calculate the required Kvar, capacitance and inductor reactance. Lastly, harmonics load analysis is rerun to record and analyze the results with the filter installed in the system.

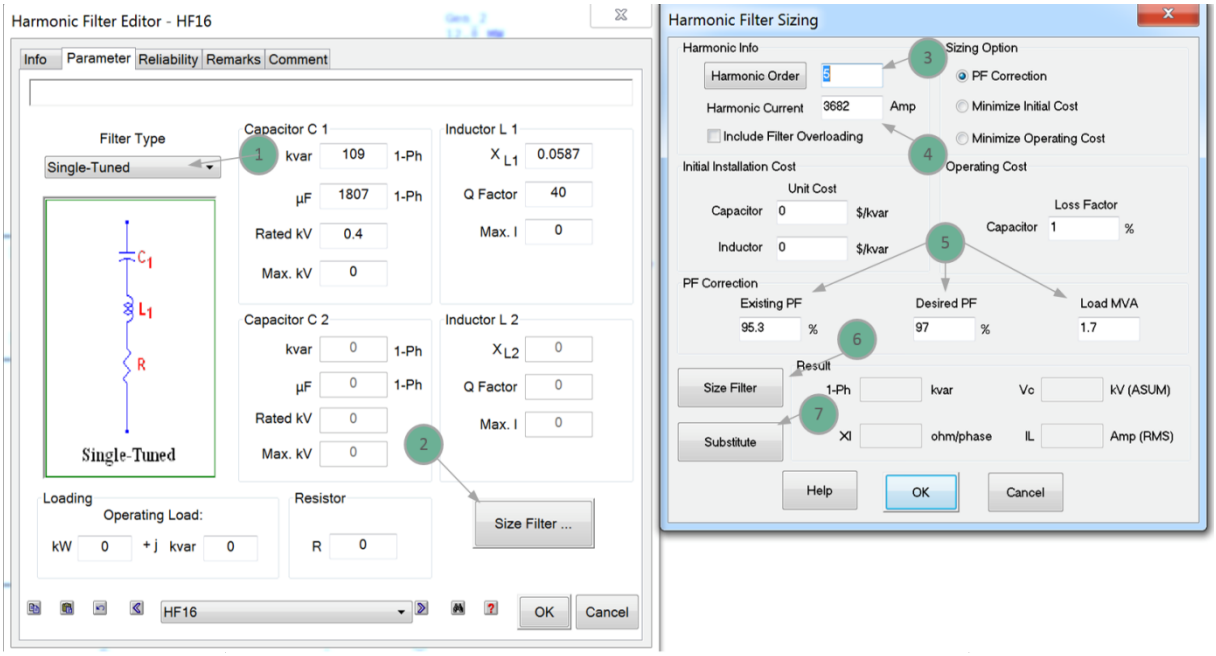

Figure 6. Harmonics filter editor.

2.2 Mathematical Analysis

Mathematical analysis includes the procedures of sizing an LC filter along with equations used. However these calculations were not applied to the existing SLD and that is due to its complexity but the method is presented.

Before sizing the filter, SLD in Fig. 2 will be represented in impedance diagram to simplify it and get the impedances of the supply (Z_S) and the load (Z_L). To do that, all components (machines and cables) in the SLD should be represented by impedance. Hence, each component will be converted from actual value into per unit value. The purpose of per unit values is to bring all the system quantities into common base by expressing them as fractions of predefined base unit. This helps to easily simplify the system and get the total impedance. The first step to start the calculation is to choose base values (MVA_{Base} and KV_{Base}) so that all the components in the system is referred to that base. Eq. (2) can be used to find the per unit value for generators, transformers and motors. For cables, Eq. (3) is used first to find he base impedance and then it is substituted in Eq. (4) to get the per unit impedance of the cable.

$$Z_{pu} = Z_{pu_{Given}} \left(\frac{KV_{B_{Given}}}{KV_{B_{New}}}\right)^2 \left(\frac{MVA_{B_{New}}}{MVA_{Given}}\right) \quad (2)$$

where, $Z_{pu_{Given}}$ is the per unit value of the machine [Ω], MVA_{Given}, $KV_{B_{Given}}$ are base values of the machine and $MVA_{B_{New}}$, $KV_{B_{New}}$ are the base values chosen.

$$Z_B = \frac{KV^2}{MVA_B} \quad (3)$$

where, KV is the line to line voltage of the cable and MVA_B is the base value chosen.

$$Z_{pu} = \frac{Z_{pu_{Given}}}{Z_B} \tag{4}$$

After the above equations are applied to all components in the SLD in Fig. 2, the SLD can be represented as impedance diagram as shown left side diagram of Fig. 7. Now that all the values are in per unit, the diagram can be simplified by simply adding the impedances with consideration of series and parallel connection. After simplification the Z_S and Z_L are known and the simplified diagram is shown as right side diagram of Fig. 7.

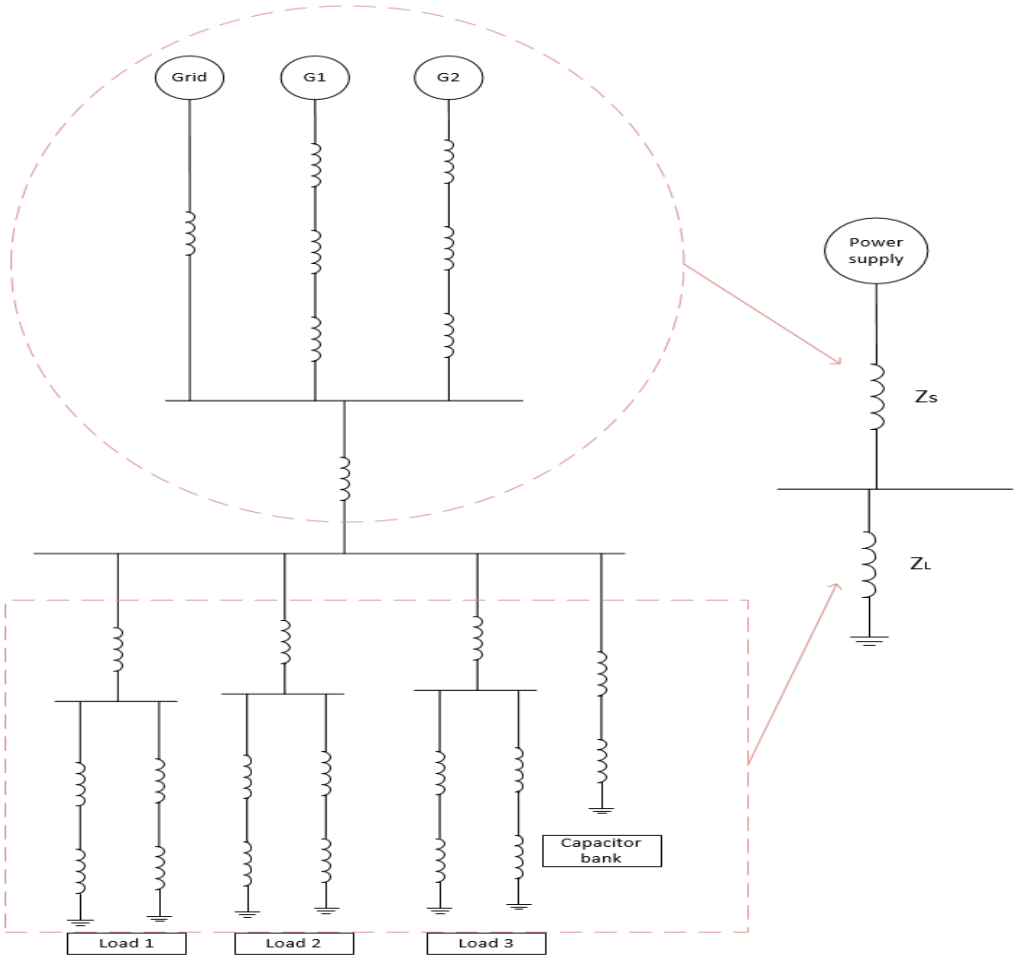

Figure 7. Impedance diagram before and after simplification.

Normally, the current in AC network will flow into different branches of the power system depending on the impedance ratio in the branches. Likewise, the flow of harmonics current in the system depends upon the impedance of the system. Since the power supply is always of low impedance, most of harmonics current generated from the load will flow back to supply. Therefore, sizing harmonics filter depends on

the impedance of the system. In other words, harmonics filter has to be designed with impedance that is lower than the impedance of the supply so that it can divert most of the harmonics current. Fig. 8 shows the simplified impedance diagram with a filter connected in parallel with load.

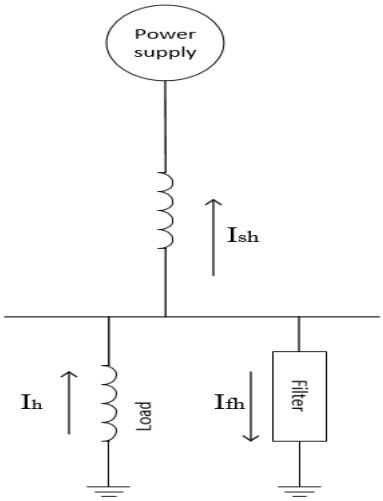

Figure 8. Simplified impedance diagram with filter.

To size the filter, the impedance of filter has to be lower than the impedance of supply. In this case LC filter is considered. Hence, the two parameters involved in sizing the filter are inductance and capacitance. Eq. (5) and (6) are the reactance of inductor and capacitor respectively. Since the frequency and the harmonics order depended on the application the filter is design for hence the inductance and capacitance are the two unknowns in both equations. Therefore, Eq. (7) and (8) are used to find the unknowns using base impedance of the system. Once the inductance and capacitance are found they are substituted back in their respective equations to find the reactance of inductor and capacitor. Furthermore, the reactance of inductor and capacitor are substituted in Eq. (9) to calculate impedance of the filter (Z_F). Since the filter used is LC, the resistance is zero. When the Z_F is found, it can be compared with impendence of supply (that can be found from the impedance diagram calculation) to make sure that Z_F is less than Z_S.

$$X_L = 2\pi f\ (H.O)(L) \tag{5}$$

where f is the frequency, H.O is harmonic order and L is the inductance.

$$X_C = \frac{1}{2\pi f(Harmonic\ order)(C)} \tag{6}$$

where C is the capacitance.

$$L = \frac{Z_B}{2\pi f} \tag{7}$$

$$C = \frac{1}{2\pi f(Z_B)} \tag{8}$$

$$Z_B = (X_L - X_C) \quad (9)$$

3. Results and discussion

3.1 Harmonics Analysis Without Filter

Fig. 9 shows harmonics order versus voltage spectrum for bus bar 4 without the implementation of the filter. From Fig. 9, it is observed that the individual harmonics distortion of 5^{th} order harmonics in bus 4 is 23.11% and the THD is 23.38%. This shows that THD at the bus 4 exceeds IEEE-519 limits. While the IHDs of orders harmonics range from 1.5% to 2.5%. This indicates that the 5^{th} order harmonics is the highest contributor in generating harmonics in the system. Furthermore, the three loads connected to bus 4 are nonlinear loads as they contain many induction motors driven by variable frequency drives. The VFD converts the sinusoidal waveform into DC waveform and then into AC square waveform to smoothly control the current going to the motor, hence during the conversion process the waveform gets distorted and harmonics level rises. Fig. 10 shows the distorted waveform over one cycle.

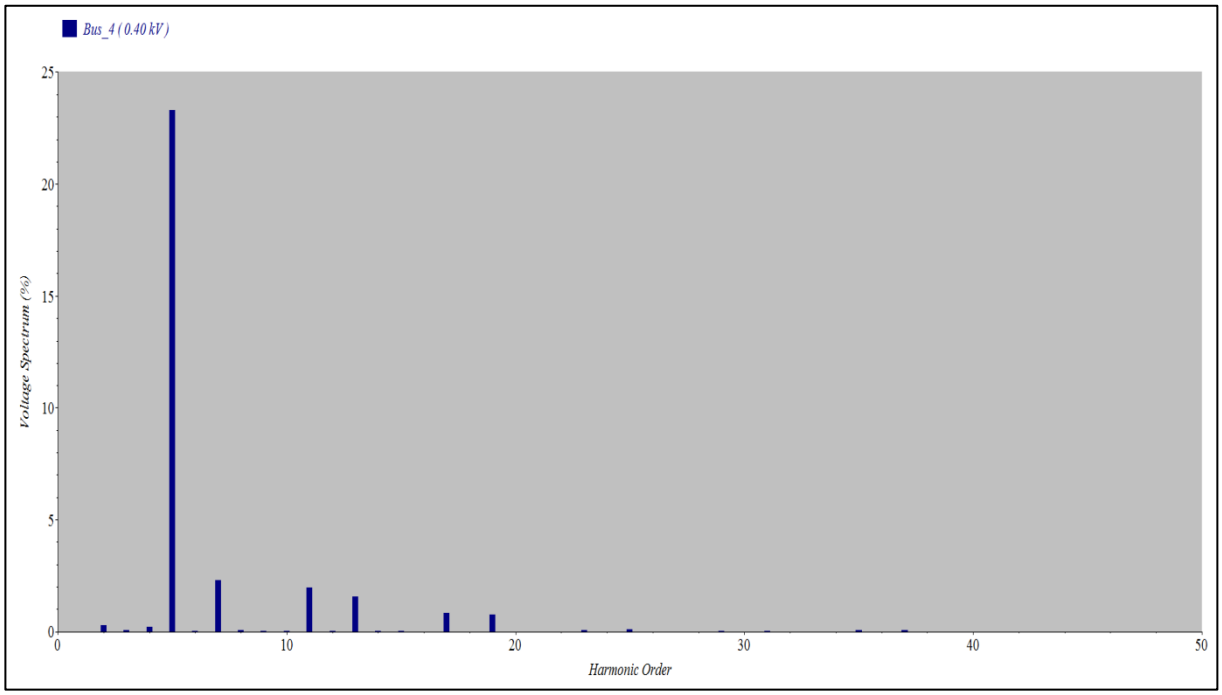

Figure 9. Harmonics order versus voltage spectrum (without filter).

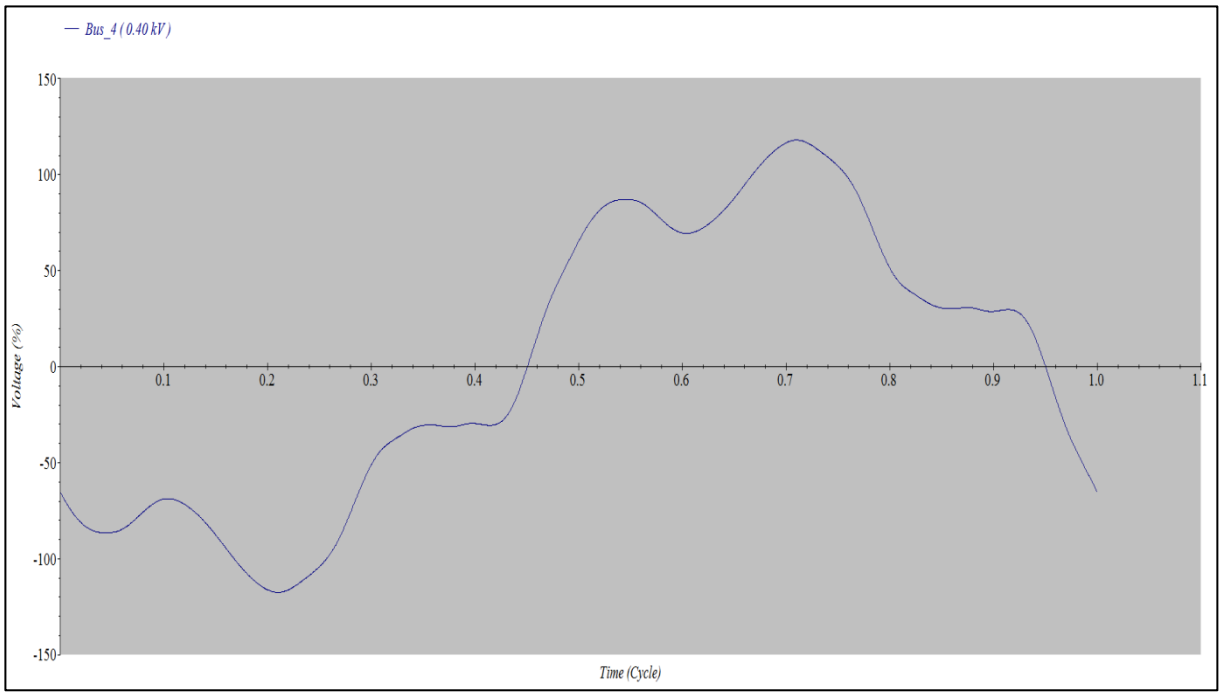

Figure 10. Time (cycle) Versus voltage % (without filter).

The current always follows the easiest path that has low impendence. Therefore, the excessive harmonics current due to nonlinear loads will flow back to the system looking for lower impendence path. Hence the current will flow to generators through transformers 7 as generators have lower impedance resulting in overloading transformer 7 (the step-down). Furthermore, the purpose of the capacitor bank connected to bus 4 is to correct the power factor however it is overvoltage due to the harmonics current at bus 4. As a result, some machines got damaged as reported by the company.

The individual harmonics distortion of 5^{th}, 7^{th}, 11^{th} and 13^{th} obtained by ETAP are tabulated in Table. 2.

Table 2. IHD of 5^{th}, 7^{th}, 11^{th} and 13^{th} harmonics order at bus 4 before the filter.

Harmonic order / Bus	5^{th} (IHD)	7^{th} (IHD)	11^{th} (IHD)	13^{th} (IHD)	THD (%)
Bus 4 (MDB7)	23.11	2.27	1.94	1.57	23.38

3.2 Filter Location

The designed filter is implemented in the bus 4 so that is in parallel with loads and capacitor bank as shown in Fig. 11. Therefore, the filter will divert the current flowing back to the system. Hence, the THD at bus 4 will be dropped.

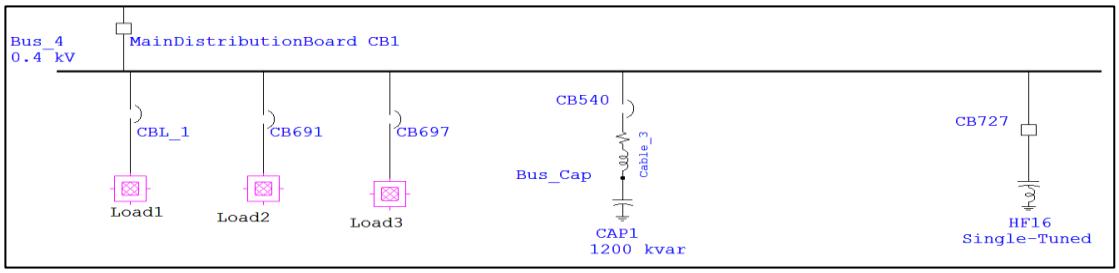

Figure 11. Implementing the filer in bus 4.

3.3 Harmonics Analysis With Filter

Fig. 12 shows harmonics order versus voltage spectrum for bus bar 4 with the implementation of the single-tuned filter. From Fig. 12, it is spotted that the IHD of the 5th order has dropped to almost zero. Hence, the THD has reduced from 23.38% to 4% as shown in Table. 3. This means the single tune filer has diverted most of the harmonics current, which makes the percentage of THD at bus 4, falls within IEEE-519 limits. As a result, the implementation of single-tuned harmonics filter results in clearing the transformer 7 overloading and capacitor bank overvoltage. Moreover, the distorted waveform before the filter has improved as shown in Fig. 13.

Table 3. IHD of 5th, 7th, 11th and 13th harmonics order at bus 4 after the filter.

Harmonic order / Bus	5th (IHD)	7th (IHD)	11th (IHD)	13th (IHD)	THD (%)
Bus_4 (MDB7)	-	2.85	1.98	1.55	4

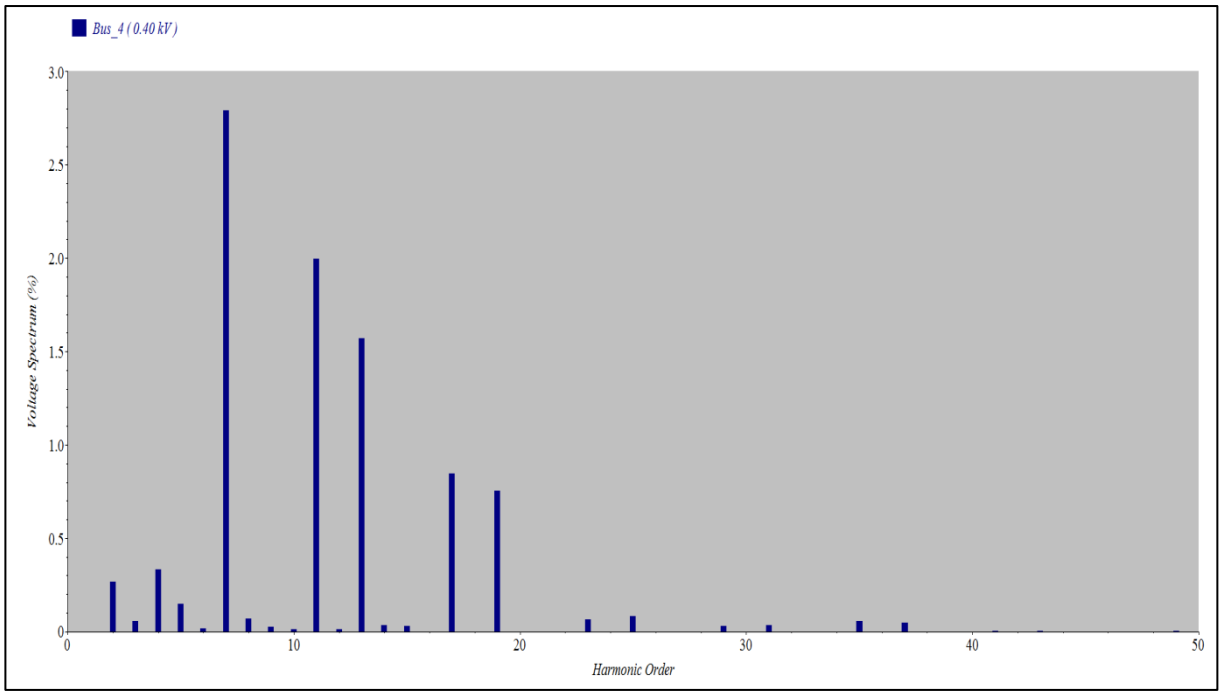

Figure 12. Harmonics order versus voltage spectrum (with filter).

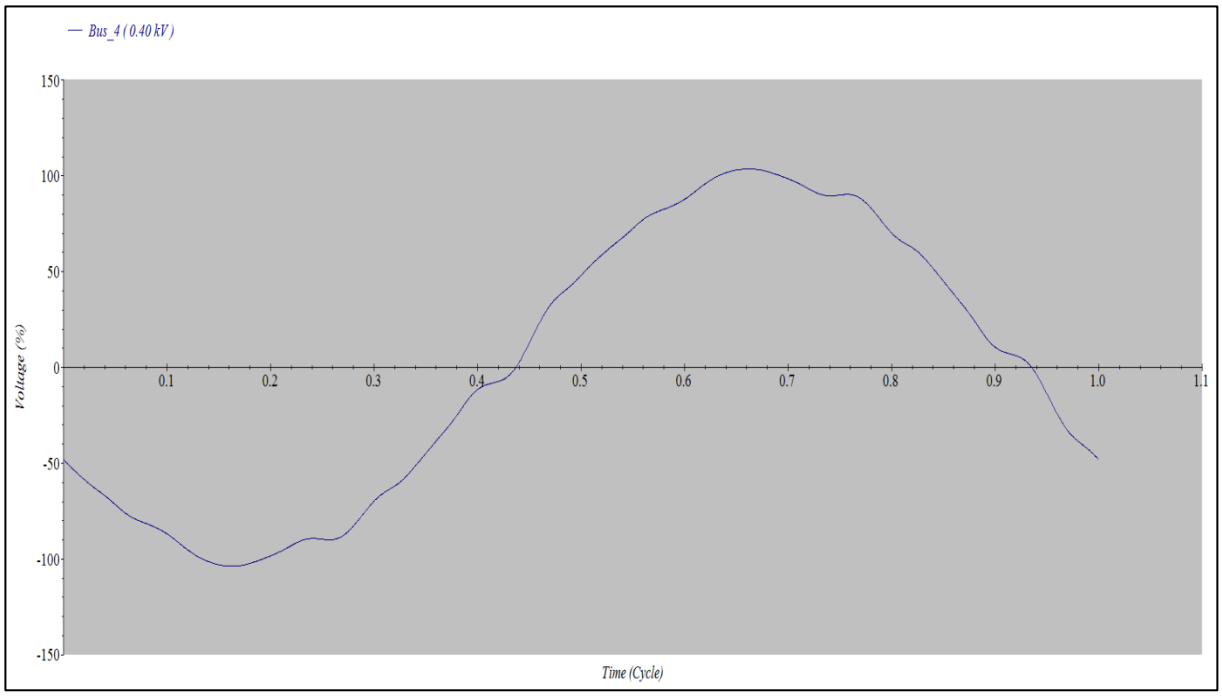

Figure 13. Time (cycle) Versus voltage (%) (with filter).

From the two cases above, the implementation of single-tuned harmonics filter can reduce the THD to an acceptable level as stated by IEEE-519. Besides, it clears the abnormal operation conditions due to harmonics such as overload and overvoltage. Thus, the electrical machines can be protected and a stable operation condition can be maintained.

4. Conclusion

This project aims to propose a single tuned passive filter for PT. Gajah Tunggal Tbk, Indonesia to mitigate the high harmonics level. As reported by the company the current total harmonics distortion in the system is 22.8%. According to IEEE 519, the voltage (THD) limits for a voltage bus below 69kv is 5% and 3% for (IHD). Therefore, the proposed filter was designed and simulated on ETAP software to bring this this level with IEEE 519 limits. Before sizing the filter, the ETAP value of THD (23.38%) was verified with the actual THD (22.8%) in the company. After the verification, the result showed both value are almost the same. From the harmonics flow analysis on ETAP, it was found that the 5^{th} order harmonics has the highest contribution in raising harmonics hence; the filter was tuned to 5^{th} order harmonics. Also, load MVA, existing system power factor and harmonics current were considered in sizing the filter. Furthermore, the results showed that the implementation of the proposed filter has dropped the total harmonics distortion in the system from 23.38% to 4%. Moreover, this research conducted mathematical analysis on impedance diagram calculation. Mathematical analysis also includes the procedures of sizing an LC filter. However these calculations were not applied to the existing SLD due to its complexity. In addition, due to the limitation of ETAP license, the maximum number of buses that could be used in the software are 25 while the SLD contains more than 150 buses hence the SLD was simplified to meet the 25 buses. As a result, the results obtained by ETAP might not be accurate. For future work, further analytical calculation using Fourier series on the equivalent load should be conducted to verify ETAP results.

Reference

[1] S. D. Upadhye and Y. R. Atre, "Determination of the design parameters of passive harmonic filters using nonlinear optimization," in *Industrial and Commercial Power Systems Technical Conference, 1998 IEEE*, 1998, pp. 155-164.

[2] A. H. Chowdhury, W. M. Grady, and E. F. Fuchs, "An investigation of the harmonic characteristics of transformer excitation current under nonsinusoidal supply voltage," *Power Delivery, IEEE Transactions on*, vol. 14, pp. 450-458, 1999.

[3] A. Mansoor, W. M. Grady, R. S. Thallam, M. T. Doyle, S. D. Krein, and M. J. Samotyj, "Effect of supply voltage harmonics on the input current of single-phase diode bridge rectifier loads," *Power Delivery, IEEE Transactions on*, vol. 10, pp. 1416-1422, 1995.

[4] F. C. D. L. ROSA, *HARMONICS AND POWER SYSTEMS*. Hazelwood, Missouri, U.S.A.: Taylor & Francis Group, LLC, 2006.

[5] S. E. S, P. E. K, K. Chatterjee, and S. Bandyopadhyay, "An Active Harmonic Filter Based on One-Cycle Control," *IEEE Transactions on Industrial Electronics*, vol. 61, pp. 3799-3809, Aug2014.

[6] T. M. Blooming, N. Carolina, and D. J. Carnovale, "Eaton Electrical," *Distribution*, pp. 1–9, 1992.

[7] E. Ngandui, "Characteristics of the measured current harmonics produced by clusters of variable speed drives," in *Electrical and Computer Engineering, 2004. Canadian Conference on*, 2004, pp. 1347-1351 Vol.3.

[8] P. Bagheri and W. Xu, "A Technique to Mitigate Zero-Sequence Harmonics in Power Distribution Systems.pdf," *IEEE Transactions on Power Delivery*, vol. 29, p. 9p, Feb 2014.

Generalized Design of New Electrical Machines Using Integrated Numerical Tool

Huang Poh Huai[1*], Aravind C.V.[1]

[1] *School of Engineering, Taylor's University, Lakeside Campus, Box.47500 Subang Jaya, Malaysia.*

[*] *huangpohhuai@hotmail.com*

Abstract

Electrical machine plays a very important role in ensuring comfort in life since most of the household appliances available in the market today are equipped with electrical machines whether in the form of motor, generator or transformer. Designing an electrical machine could be very tedious. This encourages engineers to adapt numerical tools to aid in electrical machine design. Improvement in technology has allowed computational tool like MATLAB to perform machine parameters calculation. Such approach provides repeatability and time saving. Despite that, MATLAB is not useful when dealing with electrical machine of new design and the behavior of new machine could not be predicted. This work aims to come out with a generalized design of electrical machines using integrated numerical tool. This work demonstrated a comprehensive and systematic design and analysis of SynRM by using numerical tools. The machine parameters are evaluated out using developed MATLAB GUI and the machine is modelled out using modelling tool. Condition setting (material, mesh, rotational speed) is performed and electromagnetic analysis is carried out using numerical tools to predict the behavior of the machine based on electromagnetic analysis (flux flow, flux density) and electromechanical analysis (speed, torque). The average torque results is analyzed and the speed torque characteristic of the machine is generated. The model is used to generate S block function that is compatible with Simulink. This allows further analysis on the controller of the machine. This work intends to provide a comprehensive and systematic analysis of electrical machine to ease the cost fabrication for physical testing.

Keywords: Numerical Tool, FEA, Electrical Machine Design, CAD

1. Introduction

Electrical machine play a very important role in ensuring comfort in life as most of the electrical appliances available in the market today are equipped with electrical machines. Designing an electrical machine is a very tedious processes since many aspects are taken into consideration when evaluating the design parameter of the machines.

Traditionally, Paper and pen approach was adapted to evaluate the parameters involved in electrical machine design. This however is not practical since such approach is time consuming and the parameters are evaluated each and every time when the design of the machine is changed.

Improvement in technology has allowed computational tool like MATLAB to perform machine parameters calculation. Such approach provides repeatability and time saving. MATLAB GUI based system is extensively used in electrical machine design as presented by M. Karacor et al. [1], Aravind C.V. et al. [2], and Petropol Serb et al. [3]. The GUI based systems are used to evaluate the important machine parameters involved when designing electrical machines.

Besides, Simulink tools in MATLAB is extensively used to perform electrical machine simulation and control as presented by Saffet Ayasun et al.[4], Viliam Fedal et al.[5] and Mircea Catrinoiu [6]. The Simulink tools allow the development of the drive system of an electrical machine and provide graphical simulation for electrical machine provided that the mathematical model of the machine is already derived or the machine is available in the database.

Despite that, MATLAB is not beneficial when dealing with machine designs that is new where the mathematical modelling of the machines are not derived or not available in the Simulink database. The complication of the machine make the derivation of mathematical modelling harder. Therefore, electromagnetic analysis could not be performed and the behavior of a newly developed machine could not be predicted.

A possible solution to this is to integrate Finite Element Analysis (FEA) tools to MATLAB to provide a fidelity new design, analysis and control of the machine. FEA tool allows electromagnetic analysis to be done. Such FEA tools include JMAG©, MAGNET, EMWORK and Electro. For this study, JMAG© is used as it is extensively used in the motor industry [7] [8] and interfacing of this software with MATLAB is possible. Electromagnetic analysis is demonstrated by Aravind C.V [9], Lam Pin Wen [10], and Reynold [11] in their respective machines. This paper discussed about the generalized design of electrical machines using integrated numerical tool. This generalized design procedure could be applied for any new electrical machine design, optimization and controller/sensor simulation.

2. Research Methodology

Comprehensive electrical machine design involves 3 stages, which are initial machine's geometries design stage, the optimization stage and the control stage. All the stages are carried out using integration of numerical tool to perform calculations and simulations.

In the initial machine's geometries design stage, MATLAB GUI based system are adapted. A MATLAB GUI is designed to evaluate important machine geometries. These include the machine diameter, length, loadings, number of slots and number of poles. The

machine geometries is evaluated based on the power rating of the machine, the supply voltage and the desired speed of rotation of the machine.

After the machine parameters are evaluated, the machine is modelled out using JMAG© editor and conditions setting is performed on the model. These include the rotational speed of the rotor, material settings and mesh configuration. Electromagnetic analysis is performed to generate the speed-torque characteristic of the machine. The RT-Model of the machine is then generated.

Simulink could then run the mdl file generated when RT-Model is generated. This would allow a new novel machine to be added to Simulink workspace without the need of mathematical modelling of the machine to be derived. By using Simulink, machine control could be simulated and it is possible to validate a machine for desired application. The design methodology of this research is shown in fig. 1.

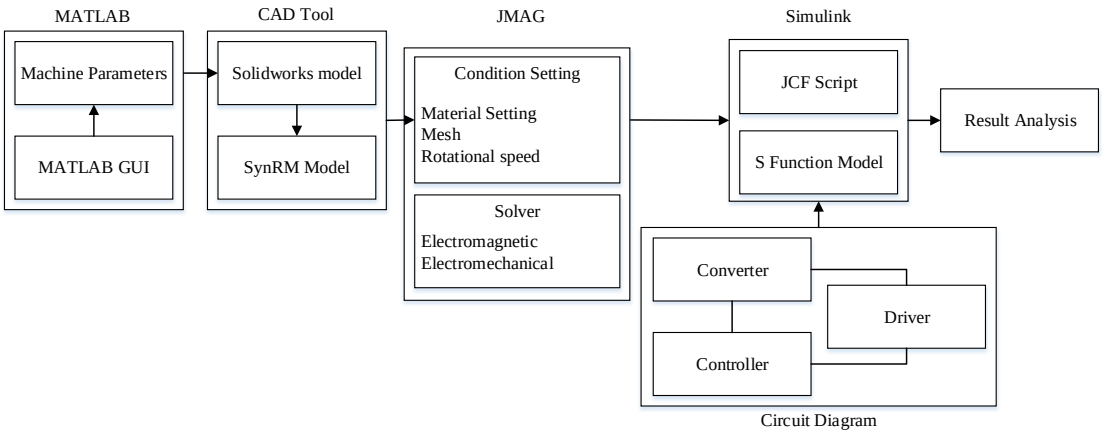

Figure 1. Design Methodology

2.1 Machine Configuration

The 12 slots 4 poles Synchronous Reluctance Motor (SynRM) shown in fig. 2 is used for this study. The motor consists of 2 structures, which are the rotor and the stator. The SynRM is designed using CAD tool based on the geometries of the machine evaluated by developed MATLAB GUI. The dimension of SynRM is shown in table 1.

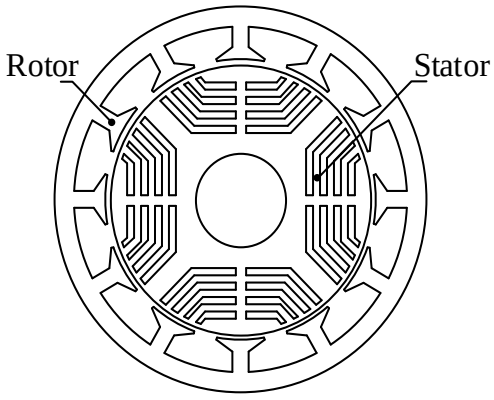

Figure 2. SynRM Structure[12]

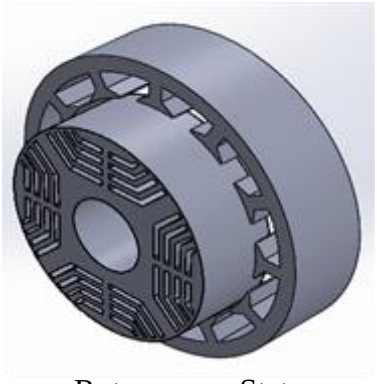

Figure 3. SynRM Exploded View[12]

Table 1. SynRM Main Dimension

Parameter	Unit(mm)
Outer rotor diameter	80
Outer rotor inner diameter	65
Air gap length	0.5
Stack Length	50
Turns per pole	58
Rated current (I)	5 A
Resistance (I)	1.04Ω

After SynRM is modelled out using the numerical tool, conditions setting are performed on the structure based on the configurations shown in table 2. The winding configuration of the machine is shown in fig. 4.

Table 2. SynRM Condition Setting in JMAG©

Properties		Value
Full Model Conversion	Stack Length	50mm
Step Control	Type	Regular Interval
	Steps	33
	Division	11520
Stator Core, Rotor Core	Material	JFE Steel: 50JN400
	Lamination	98 %
Magnet	Material	NEOMAX-42
	Number of Poles	4
Coil	Material	JSOL: Copper
Rotation Motion	Target	Rotor Core
	Displacement Type	0-1600(400 increment)
Rotation Motion	Rotation Axis	Upward
Torque: Nodal Force	Target	Rotor Core
Mesh Properties	Mesh Type	Slide Mesh
	Rotational Mesh	On

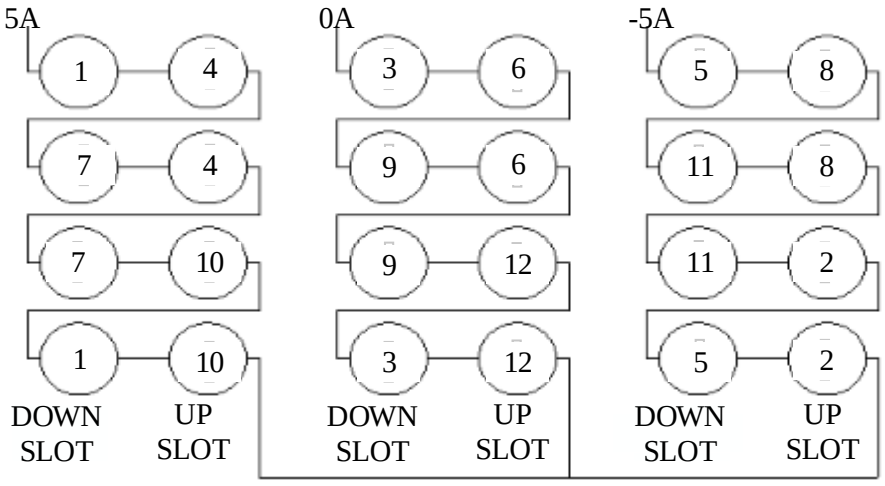

Figure 4. SynRM Winding Configuration

After the electromagnetic analysis is performed on the model, the model is converted to JMAG RT model in which a Mathwork data file would be generated during the process of conversion to JMAG RT. The Mathwork data file is a Simulink block file that consists the mathematical modelling of the novel electrical machine which is not available in Simulink database. This would allow further machine controller analysis in block diagram simulation.

2.2 Performance Measurement

To evaluate the performance of any electrical machine, motor constant square density (G) is calculated. It determine the performance of the machine based on the torque, power and volume. Motor constant square density is given as in Eq. (1).

$$G = \frac{(K_m)^2}{V} \tag{1}$$

where K_m is the machine constant $[Nm/A/W^{-\frac{1}{2}}]$ and V is the volume of the machine $[m^3]$. The machine constant is determined by Eq. (2).

$$K_m = \frac{K_T}{\sqrt{P}} \tag{2}$$

where K_T is the torque constant $[Nm/A]$ and P is the power input $[W]$.
The torque constant is given as in Eq. (3).

$$K_T = \frac{T_{avg}}{I} \tag{3}$$

where $T_{avg}$is the average torque $[Nm]$ and I is the current input to the machine $[A]$.

4. Results and Discussions

To perform calculation of machine geometries, the GUI based design as shown in fig. 5 is developed. The GUI is designed to take in some inputs from the user. These inputs are the power rating of the machine, the rotational speed of the machine, the supply voltage and design specification which includes minimum cost (L/τ =1.75), good power factor (L/τ=1.25),

good efficiency (L/τ=1.5) and good overall design (l/τ =1). From the given input, the GUI would evaluate the required machine geometries which consist of the machine sizing, number of pole required, number of slots, electric and magnetic loading and the number of conductors required. With these information, SynRM could be designed in FEA tool without the need for user to perform tedious paper calculations.

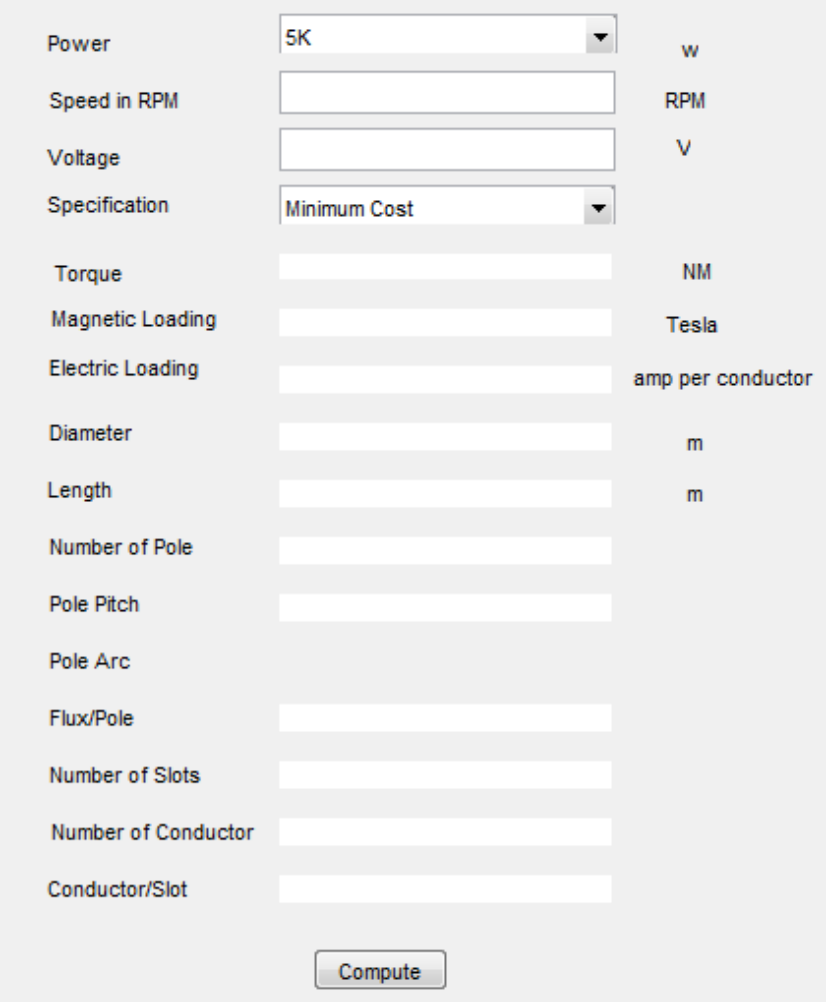

Figure 5. MATLAB GUI for Electric Machine Parameters Calculation

After the machine is modelled out based on the machine geometries output from the GUI developed, conditions setting are performed and the model is meshed in order to perform FEA on electromagnetic analysis. The meshed model is illustrated in fig. 6. The rotational periodic mesh allows a rotating machine to be meshed evenly without the need to separate meshing and therefore improve the accuracy of the results.

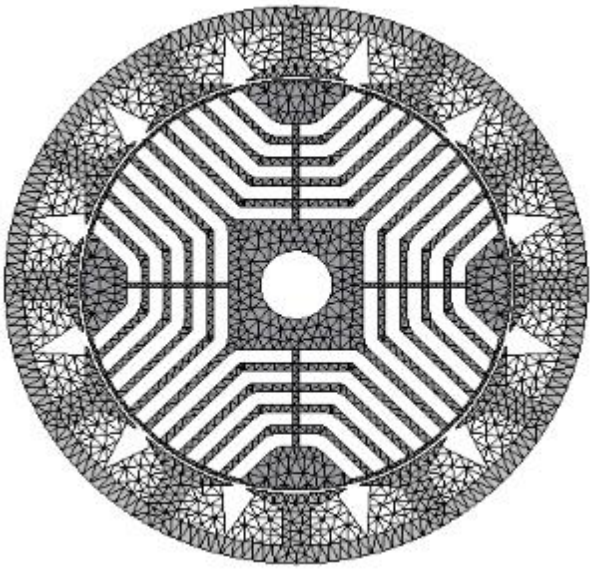

Figure 6. SynRM Mesh Structure

Electromagnetic analysis is performed on the model by using FEA tool. The flux flow in the machine is shown in fig. 7 and the flux density is shown in fig. 8. The Flux Density Contour plot is shown in fig. 9.

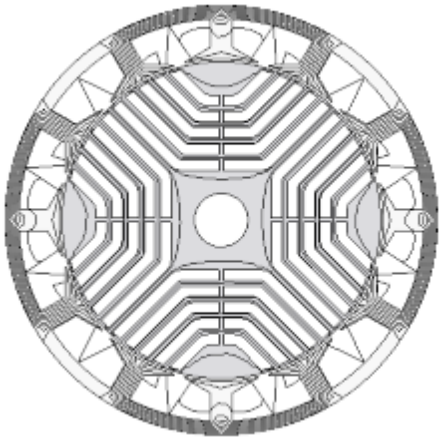

Figure 7. Magnetic Flux Flow in SynRM

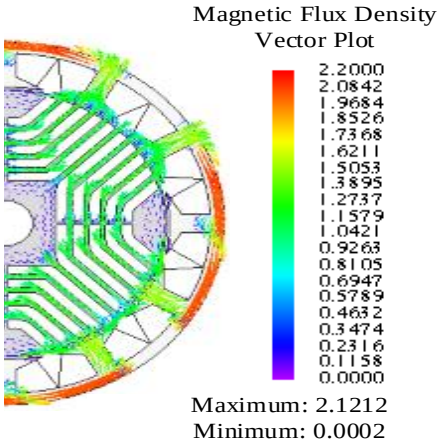

Figure 8. Magnetic Flux Density in SynRM

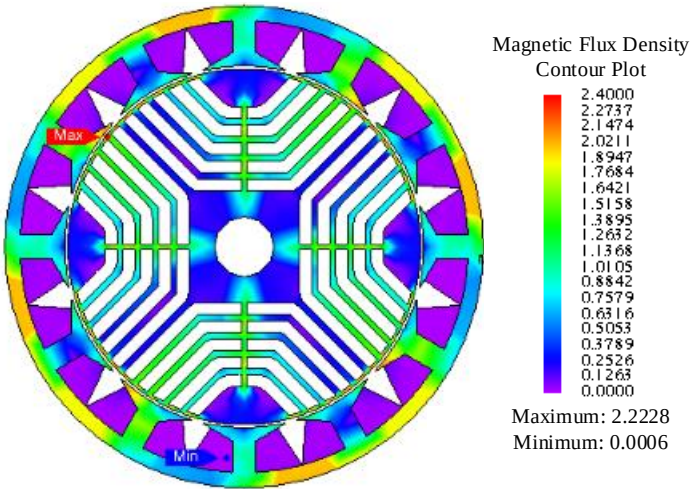

Figure 9. Magnetic Flux Density Contour Plot in SynRM

From fig. 7, the winding machine is excited to form 4 flux path. This shows that the winding configuration of the machine is correct. The flux flow is directed by the barrier design to minimize the flux leakage. From fig. 8 and fig. 9, the flux density is highest at the stator side and this is because the windings are winded over the stator and when the windings are excited, the stator become electro magnetized and therefore lead to high flux density at stator side compared to the rotor side. However, excessive flux would contribute to heating issue. The flux density is minimum when closer to the shaft as there is no magnetic source at the rotor side. The graph of torque vs rotation angle in SynRM is shown in fig. 10 while the graph of rotational speed vs average torque in SynRM is shown in fig. 11.

From fig. 10, in a 4 poles machine, the torque waveform is sinusoidal in one pole pitch period which is 90 *deg*. This indicate that the rotation of the rotor is sync with the supply. Therefore, the motor would operate on optimum condition with 50 Hz supply frequency. From Fig. 11, the speed is inversely proportional to the torque production. Such characteristic is very common for Brushless DC machine.

Rotation Angle Vs Torque in SynRM

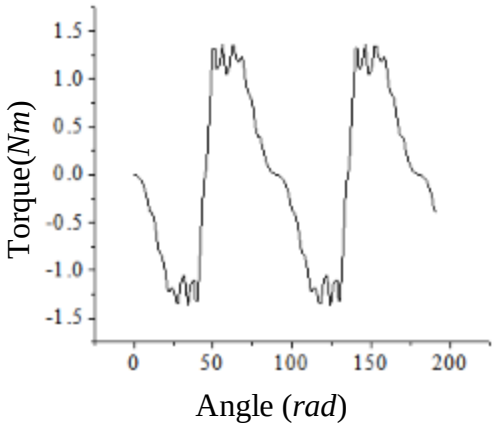

Figure 10. Rotational Angel-Torque Characteristic of SynRM

Rotational Speed Vs Torque in SynRM

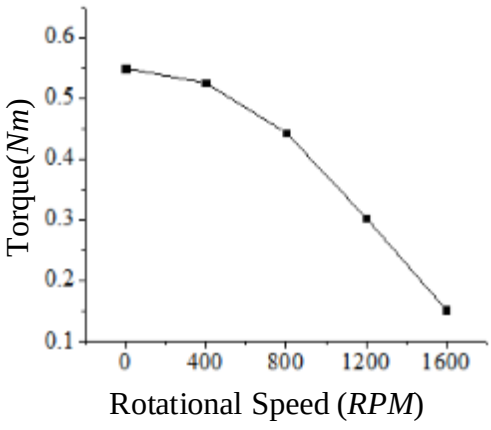

Figure 11. Speed-Torque Characteristic of SynRM

Table 3. SynRM Motor Constant Square Density

Motor		12s 4p SynRM
I	$[A]$	5
V	$[\times 10^{-4} m^3]$	2.513
T_{avg}	$[Nm]$	0.525
P	$[W]$	25
K_T	$[Nm/A]$	0.105
K_m	$[Nm/A/W^{-(1/2)}]$	0.021
G	$[Nm^2/A^2/W/m^3]$	1.75

The motor constant square density of SynRM is evaluated as shown in table 3. The torque characteristic is relatively high compared to a conventional SynRM without magnet [13]. After performing the electromagnetic analysis, JMAG RT model conversion is perform and the Simulink block shown in fig. 12. The S block function allows the user to perform multiple simulations which include the loss in the machine, controller operation and the performance of machine under different temperature. The S block function is used to perform BLDC drive system as shown in fig. 12. This allows new machine to be tested in the drive system that is available in the Simulink.

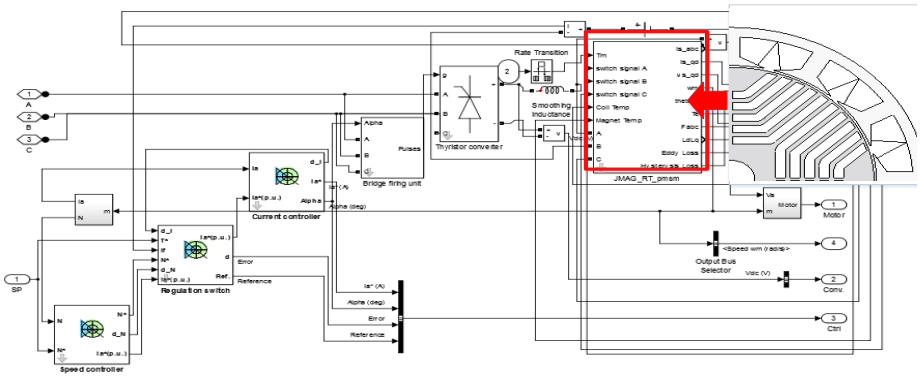

Figure 12. Simulink S Block of SynRM

5. Conclusion

In conclusion, the proposed generalized design of new electrical machines using integrated numerical tool provides a more thorough process in which new electrical machine could be designed and optimized using combination of FEA tool and numerical tool, and controlled using Simulink block diagram simulation. FEA tool is limited to machine design analysis while Simulink is limited to the machines that are already available in the database. A more comprehensive design approach is adapted in which the designed machine is optimized, and tested with different control condition in Simulink before it is fabricated. This would provide a better design experience and reduce the cost of performing physical test on a machine design or the controller to be coupled with the machine.

The main drawback of such approach is the conversion of JMAG model to JMAG RT model requires mass computational power. This however is not a main concern as it yields

decent accuracy and the processing power of computer in the market are increased exponentially with time.

To conclude this, generalized design of new electrical machines using integrated numerical tool are very helpful and provide virtual domain to perform analysis of a new electrical machine. Future improvement include block simulation of the controller with the Simulink block of the machine generated by JMAG RT. Besides, 3-dimensional simulation of the machine could be taken into consideration to improve further the accuracy of the results.

References

[1] M. Karacor, F.E. Kuyumcu, "Matlab GUI based SRM design program," *Electrical Machines and Power Electronics", ACEMP '07. International Aegean Conference,* pp.846-849, 2007.

[2] Aravind C.V., Grace I., Rozita T., Rajparthiban R., Rajprasad R., Wong Y.V., "Universal computer aided design for electrical machines", *Signal Processing and its Applications (CSPA), 2012 IEEE 8th International Colloquium*, pp.99-104, 2012.

[3] Petropol-Serb G.D., Petropol-Serb I., Campeanu A., Petrisor A., "Using GUI of Matlab to create a virtual laboratory to study an induction machine", *EUROCON, 2007. The International Conference on "Computer as a Tool,"* pp.2355-2360, 2007.

[4] Saffet Ayasun, Gultekin Karbeyaz, "DC Motor Speed Control Methods Using MATLAB/Simulink and Their Integration into Undergraduate Electric Machinery Courses", Computer Application In Engineering Education(CAEE) Wiley Interscience, vol 15, issue 4, pp. 347-354, 2007.

[5] Viliam Fedák, Tibor Balogh, Pavel Záskalický, "Dynamic Simulation of Electrical Machines and Drive Systems Using MATLAB GUI."*InTech MATLAB- A Fundamental Tool for Scientific Computing and Engineering Application*, vol. 1, chap. 14, pp. 317-342 2012.

[6] Mircea Catrinoiu, "MATLAB / Simulink Model of a System for Determining the Angle of Internal Synchronous Generators", *U.P.B. Sci. Bull, vol. 75, issue 3, pp. 199-208, 2013.*

[7] Yuichi Shibukawa, Natee Limsuwan, David Reigosa, Robert D. Lorenz, "Novel Design of Flux-Intensifying Interior permanent Magnet Synchronous Machine", *Paper presented by Nissan Motor Co. Ltd at JMAG Users Conference* , 2010.

[8] Nobuyuki Suzuki, "Coupled Analysis of an IPM Motor", *Paper Presented by Toshiba Corporation at JMAG Users Conference*, 2010.

[9] C. Aravind, "Design and development of double-rotor switched reluctance motor using magnetic circuit analysis," *IEEE Trans. On Motor Using Magnet Circuit Analysis*, pp. 1 – 186, 2013.

[10] Lam Pin Wen, Aravind CV, Reynold Hariyadi, "Comparative Evaluation of a Novel Field Assisted Permanent Magnet Machine with Conventional IPM using Motor Constant Square Density" *International Conference on Electrical Power Engineering and Applications (ICEPEA2014)*, Langkawi, Malaysia, 2014. (Under review)

[11] Reynold Hariyadi, Aravind CV, Lam Pin Wen, "Comparative Evaluation of a Novel Field Assisted Permanent Magnet Machine with Conventional IPM using Motor Constant Square Density", *International Conference on Electrical Power Engineering and Applications (ICEPEA2014)*, Langkawi, Malaysia, 2014. (Under review)

[12] Roshanfekr P, Thiringer T., Lundmark S., Alatalo M., "Comparison of an Interior Mounted Permanent Magnet Synchronous Generator with a Synchronous Reluctance Generator for a Wind Application", *World Academy of Science, Engineering and Technology, International Science Index 79*, vol. 7, issue 7, pp. 1571 – 1575, 2013.

[13] R.N.Firdaus, M.Norhisam, N,Mariun, I.Aris, M.Nirei, H.Wakiwaka, "Torque Characteristic of Single Brushless DC Permanent Magnet Motor", *Journal of the Japan Society of Applied Electromagnetics and Mechanics*, vol.19, Supplement, 2011.

Optical Wireless Communication System

Joshua Chieng Lie Yang, Irda Hassan

Taylor's University, Malaysia

chieng.joshua@gmail.com

Abstract

The growing demand of bandwidth in this modern internet age has been testing the existing telecommunication infrastructures around the world. With broadband speeds moving towards the region of Gbps and Tbps, many research has begun on the development of using optical wireless technology as a feasible and future methods to the current wireless technology. Unlike the existing radio frequency wireless applications, optical wireless uses electromagnetic spectrums that are unlicensed and free. With that, this project aim to understand and gain better understanding of optical wireless communication system by building an experimental and simulated model. The quality of service and system performance will be investigated and reviewed. This project employs laser diode as the propagation medium and successfully transferred audio signals as far as 15 meters. On its quality of service, results of the project model reveal that the bit error rate increases, signal-to-noise ratio and quality factor decreases as the link distance between the transmitter and receiver increases. OptiSystem was used to build the simulated model and MATLAB was used to assist signal-to-noise ratio calculations. By comparing the simulated and experimental receiver's power output, the experimental model's efficiency is at 66.3%. Other than the system's performance, challenges and factors affecting the system have been investigated and discussed. Such challenges include beam divergence, misalignment and particle absorption.

Keywords: Optical Wireless Communication, (OWC), Free Space Optics (FSO), Quality of Service (QoS), Bit-Error-Rate (BER), Q-Factor.

1. Introduction

The optical wireless communication system mainly comprises of three major parts: the transmitter, receiver and propagation channel. OWC is also known as Visible Light Communication (VLC) or Free Space Optical (FSO) has been propagating signals through at a wavelength between 380nm to 740nm for VLC and 750nm to 1600nm for laser through free and open spaces [1]. Similar with fibre optics, OWC system sends signals from the transmitter to receiver in the form of light. Though fibre optics propagates through glass fibre medium, OWC propagates light through air. OWC should not be confused with RF. Although it shares the same term of being wireless, but OWC is an optical technology that uses properties of light such as IR or laser to propagate [2]. Hence, many industry players are favouring the usage of IR because it brings numerous advantages such as IR is not affected by certain regulations on RF and OWC requires no spectrum licences, thus saving acquiring cost [3]. OWC is promising as a solution for the "last mile" bottleneck in wireless communications. As for radio frequency (RF), it is facing a soon to be congested spectrum, emerging security and terrorism issues, lower data rate and high cost of installation [3].

In the market today, many users are subscribing to RF wireless LAN products as WiFi hotspots commercially or at residential. However, RF wireless LAN uses the unregulated "free" spectrum region of 2.4 GHz and it has limited channel bandwidth [4]. As for fibre optical technology, it does offer good QoS but unable to reach everyone especially in the rural areas and has no mobility advantage because it is a wired technology [5]. OWC system has applications ranging from short range to ultra-long range. Currently, OWC systems are being used by military and space operations. A few vendors have started providing OWC system to industrial and commercial players as well. It is projected that by 2020, RF technologies power consumption will dominate the global network. However, optical link has the best bit rate and the lowest normalised energy consumption compared to the rest of RF wireless communication standards [6]. The main reason behind optical link's efficiency is due to having optical properties as baseband, resulting in a simpler transmitter and receiver architecture [6]. Whereas for RF systems, its complex transceiver architecture causes substantial dissipation loss of power [6]. In the recent years, there has been an emerging research and applications of integrating both optical and RF wireless network also known as radio over fibre (RoF). RoF systems are capable of reaching data rates up to 500 Mbps but the transmission is still limited by the low carrier frequency [7].

1.1 Advantages of OWC over Radio

The term "wireless" is not just limited to radio frequency (RF) applications only, but infrared (IR) also known as OWC are utilizing other regions of the electromagnetic spectrum as well. Due to the tremendous growth in broadband data demands, OWC technology has been accelerated in terms of research and development. Some of the most common OWC systems are IR LEDs and laser diodes (LD) as propagation mediums; photodiodes like PIN and avalanche diodes are amongst the common receivers used. Line of Sight (LOS) link type such as intensity modulation (IM) with direction detection (DD) is the most widely used modulation in

OWC systems [8]. OWC systems offer numerous advantages over its RF counterpart, such as [8]:

- Abundance of unregulated bandwidth (200 THz in the 700 – 1500 nm range).
- No licensing fees needed to use the spectrums.
- No multipath fading when IM and DD is used.
- Very secure connectivity. It requires a matching transceiver carefully aligned to complete the transmission.
- Small, light, compact smaller size components and relatively low cost.
- Well defined cell boundaries and no interchannel interference.
- Use one wavelength to cover a large number of cell, therefore no frequency reuse problem as in RF.
- No need to dig up underground and is easily installed.
- Minimal absorption effects at 800-890 nm and 1500 nm.
- Health-friendly (no RF radiation hazards).
- Lower power consumption compared to RF.
- Lower probability of intercept and antijamming characteristics.
- Highly directional and cone-shaped propagation compared to RF radiate signals in all directions.

RF based technology does offer wireless broadband coverage in outdoors and indoors. However, it has limitations on the number of users per access point. Moreover, RF wireless LANs usually uses the unregulated or 'free' spectrum bands at 2.4 GHz. Other proposed unregulated bands like 17 GHz and 60 GHz technologies are under development [9]. Although RF are great in providing wide coverage but it lacks in terms of data rates due to lower carrier frequencies. As much as RF has diffraction and scattering issues, it can provide full coverage between rooms and walls. On the contrary, OWC system uses wide range of unlicensed spectral band range at 700 – 10,000 nm. It is therefore more cost effective to implement and has data rates exceeding 2.5 Gbps per wavelength up to 5 km range [10]. OWC might be more sensible in applications that require more than 100 Mbps because of its multiple user-sized cells, improved carrier reuse capabilities due to its abrupt cell boundary and reduced interference [10]. To make broadband networks more effective, OWC and RF can be seen as complementary rather than competition in technologies.

1.2 Challenges and Gaps of OWC System

OWC system may have major advantages to the communication landscape, however it poses several challenges. According to Debbie Kedar and Shlomi Arnon [11], there are certain challenges and possible solutions to urban optical wireless communication systems. They have identified that OWC faces challenges such as the LOS alignment with the receiver and transmitter module due to external weather conditions such as sway of wind or weak earthquakes. For instance, two tall buildings using OWC system on top of their buildings to establish connections. Sometimes, these buildings are bound by dynamic wind causes to sway along it during the day or even the slight thermal expansion or shrinking of building's frame might cause small misalignment for the transmitter and receiver. Every misalignment of the devices poses a threat to OWC's QoS [12]. As this phenomena occurs randomly, the performance of the system will be affected at uncertain time. Because OWC employs

"point and shoot" approach, and errors of alignment will introduce signal fading. One possible solution is to develop a pointing error mechanism that able to feedback the alignment error and readjust its transmission and receiving behaviour with intelligent protocols, more research has to be done on this area [12].

Besides that, Ahmed Nabih Z. R. [13] mentioned that weather conditions like rain, snow, fog or even clouds may absorb the light wave propagation and small water particles from the rain can also cause particles scattering. This will caused the OWC system performance to be affected like particle scattering will result in signal attenuation and distortions. Therefore, it is important to maintain a clear line of sight between the transmitter and receiver, especially when LOS link type is used. Sometimes, the LOS can also be interfered by foreign objects such as birds or airplanes, making it a possible threat for temporary downtime of transmission.

Ambient light and artificial light can result in background noise which can degrade receiver's performance. Moreira et. al. performed testing on various ambient light sources and developed a model to describe background noises [14]. One of the largest noise source is the sun itself. Sunlight is unmodulated and has wide spectral width. It is the major noise source in any photo detection devices. However, artificial light source noise does not produce background current (micro-amperes) as high as the sun (mili-amperes) but it still does contribute to noise background [14]. Bocouvalas [15] and other researchers have done significant amount of work on experimenting optical source noises and proposed advanced signal processing filters to remove many types of such noises and improve overall performance.

The research question for this project: What is the impact of Optical Wireless Communication System to the quality of service (QoS) such as bit error rate, signal-to-noise ratio, Q-factor, receiver's voltage output, identify challenges and suggestions for improvement?

2. Methodology

The hardware's results will be obtained by collecting the receiver's output and feed it to the multimeters and digital oscilloscopes. By manipulating the propagation distance between the transmitter and receiver, the receiver's output voltage, current and signal waveforms will be collected. Due to the limited equipment in the engineering lab, Optiwave OptiSystem software will be used to produce a simulated circuit and calculate the model's BER. As for SNR, MATLAB software will be used to calculate it. The following subchapters will discuss more details.

2.1 System Model

The transmitter circuit is intended to be designed such a way that it can transmit wirelessly to the receiver. The input signal is an audio signal that will fed by the audio generator. The laser is responsible to transmit the light at a distance. The photo transistor at the receiver's end supposed to be directed Line of Sight (LOS) link to the transmitter's laser beam.

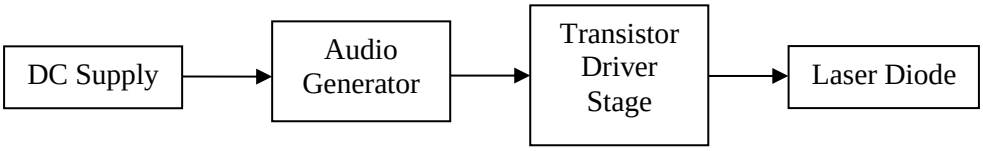

Figure 1. The audio is transmitted by a laser diode

The receiver circuit is proposed to use phototransistor to receive laser signals from the transmitter. As the received signals produce voltages, it is further amplified with the signal amplifiers. Then it will be converted back to audio signals and to be heard by the speaker. The speaker has an in built gain or volume dial to further boost the signal amplification.

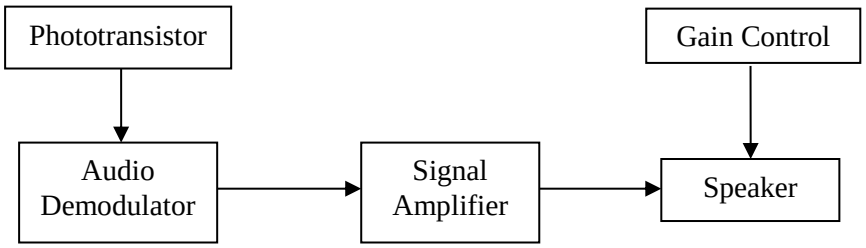

Figure 2. The audio is being received by the photo transistor

Table 1 shows the fixed parameters for both the experimental and software OWC model to reduce fluctuations of the results.

Table 1. OWC system parameters for this project.

Transmitter Front End (Laser + Modulator)		Receiver Front End (Photodetector + Amplifiers)	
Operating Wavelength	650 nm	*Type of Photodetector (PD)*	PIN Photodetector (Solar Cell)
Class	Class 3A	*PD Responsivity*	0.233A/W
Average Optical Output Power	5 mW	*PD active area*	0.5 cm^2
Bit Rate	320 kbps	*Amplifier Frequency Response*	100 Hz – 10 Khz
Input Signal	Audio Song (Pseudo-Random NRZ bits)	*Amplifier Power Output*	200 mW
Transmitter Aperture Diameter	0.2 cm	*Receiver Aperture Diameter*	0.8 cm

After identifying the project hardware specifications. Figure 3 introduces the experimental model of the OWC system and Figure 4 introduces the simulation model of the OWC system using OptiSystem software.

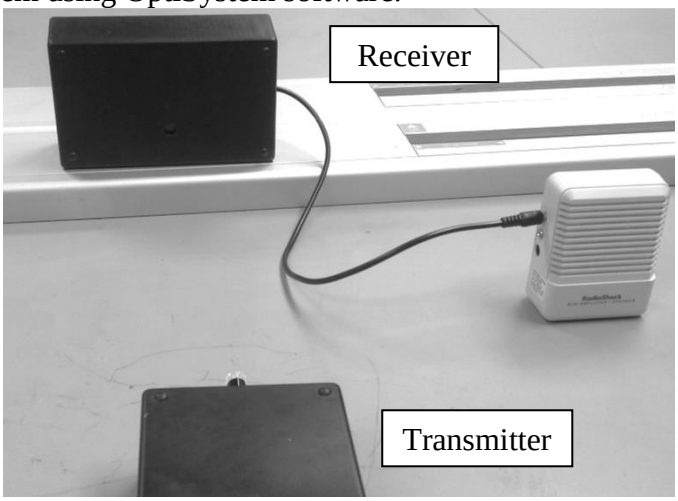

Figure 3. Experimental model of OWC system

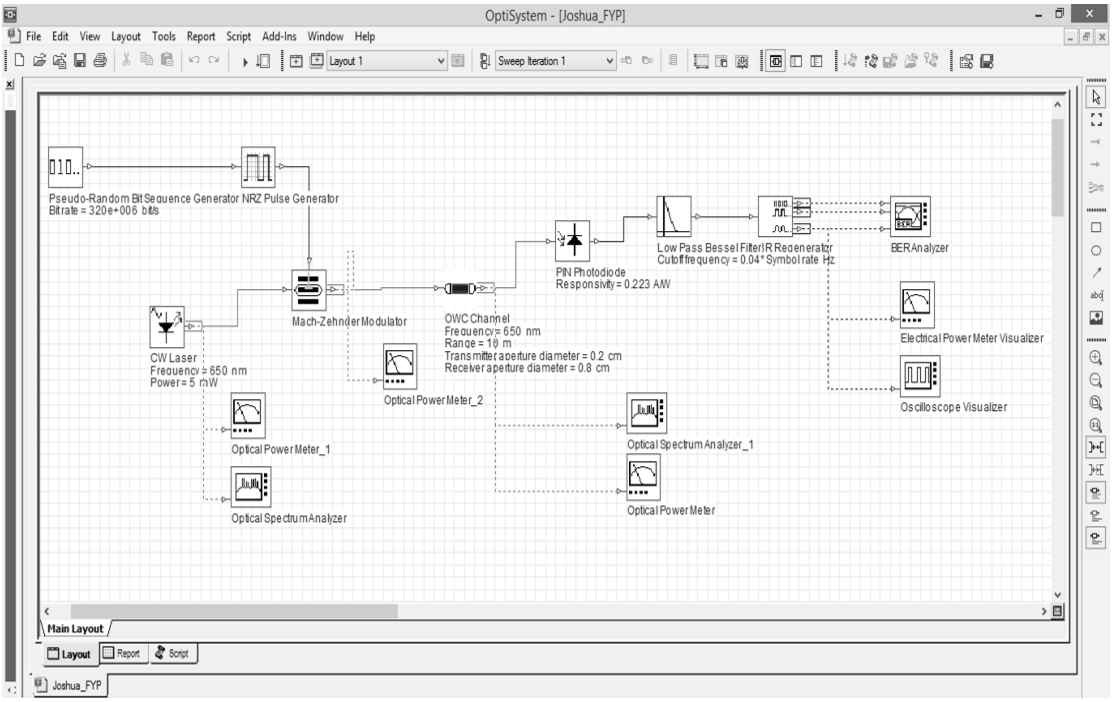

Figure 4. OWC System in OptiSystem

2.2 System Efficiency between Simulated and Experimental Model

Comparison will be made between the simulated data by using OptiSystem and experiment data. The manipulated variable will be the propagation link distance given a 320 kbps audio signal. The responding variable will be the output power produced at the PIN photodetector. Once the comparison is made, the efficiency of both the transmitter and receiver circuit can be calculated in terms of output (refer eq. 1). Repeat the whole process again by manipulating the propagation distance between the transmitter and receiver from 0.5 meter to 15 meters.

$$system\ efficiency, \eta = \frac{P_O\ experimental}{P_O\ simulated}\ x\ 100\% \quad (1)$$

2.3 Signal-To-Noise Ratio (SNR)

Signal-to-noise ratio is a measure of how a certain signal is being corrupted by noise. Defined as the ratio of signal power to the noise power along the signal, a ratio of more than 1 indicates more signal than noise. In communication system, higher SNR is favourable. Eq. 2 shows that the SNR in decibels (dB) [16]. For this project, SNR will be calculated with MATLAB by using Eq. 2 [16] because there is a limitation of tools to measure background noise power.

$$\mathrm{SNR_{dB}} = 10 \log_{10} \left(\frac{P_{\mathrm{signal}}}{P_{\mathrm{noise}}} \right) \quad (2)$$

2.4 Quality Factor (Q-Factor)

In optical communication, the common existence of signals are power and noise. That is why SNR is an important parameter for any communication systems. Q-factor is a dimensionless measurement where it simply indicates quality factor of the system whether it is underdamped or overdamped [17]. Given SNR, Q-factor is able to be calculated as shown in Eq. 3 [18]. T is the bit period and B_{opt} is the bandwidth of the optical filter used. In Optisystem, the Q-factor are calculated based on this equation.

$$Q = \frac{\mathrm{SNR}\sqrt{2TB_{\mathrm{opt}}}}{1 + \sqrt{1 + 2\mathrm{SNR}}} \quad (3)$$

2.5 Bit Error Rate (BER)

Bit error rate is usually a standard data given by any transmission devices. BER is the number of bit errors received by the total bits of the transmission media. These bit errors are usually due to noises or other interferences. The BER formula for this OWC system is shown in Eq. 4 [18]. This project will be built and simulate in OptiSystem software in order to get the BER and the Q-Factor using the BER analyser tool as shown in Figure 5 and 6.

$$\mathrm{BER} = \mathrm{erfc}(Q/\sqrt{2})/2 \quad (4)$$

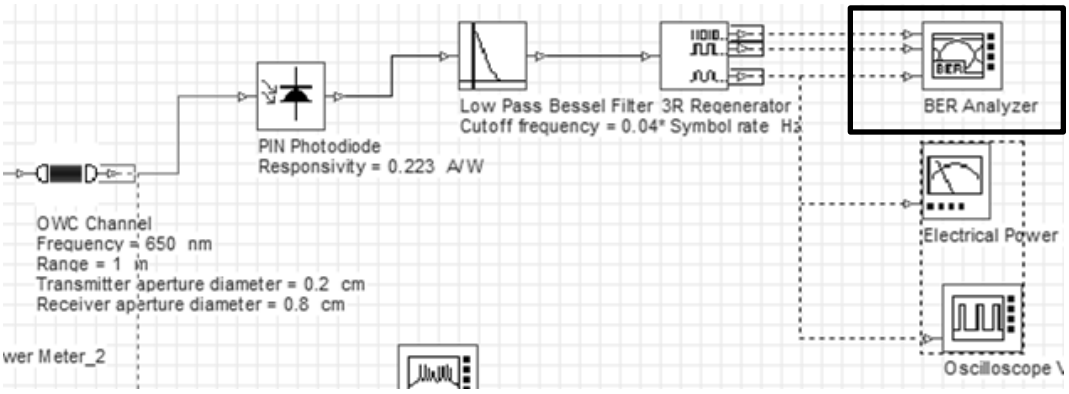

Figure 5. BER analyzer tool is connected to the simulation model output.

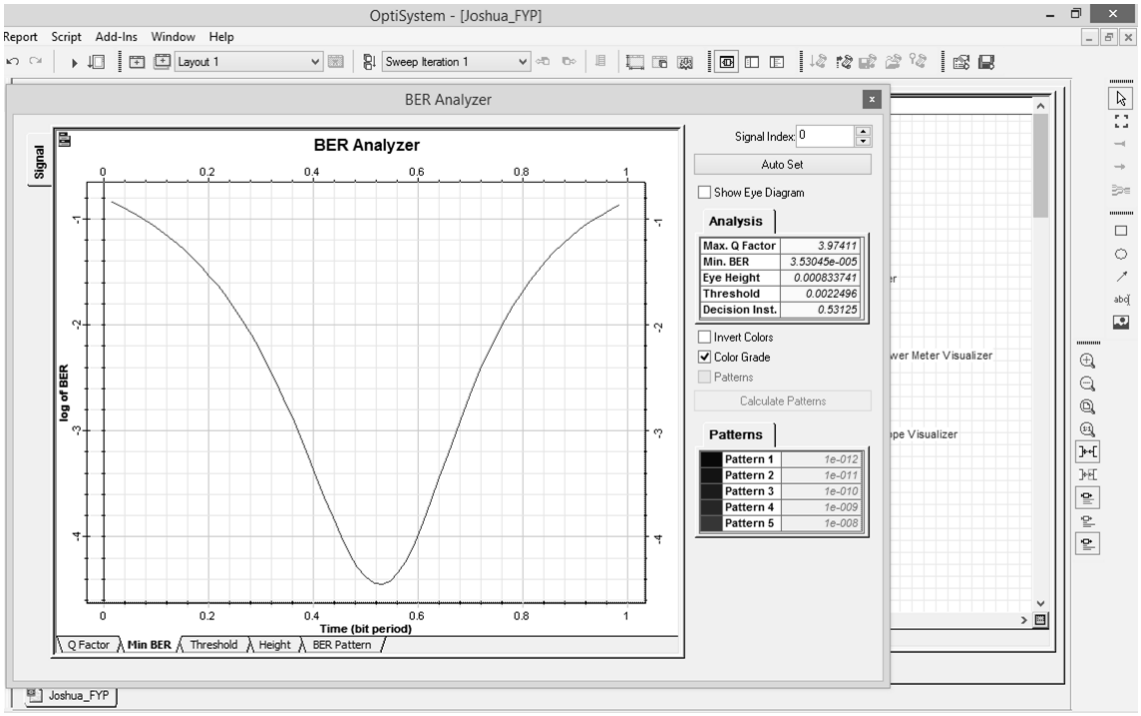

Figure 6. BER Graph in the Analyzer Tool

3. Results & Discussion

The project prototype has successfully built and various experiments have been done to obtain the data for analysing. After performing experiments with the project prototype, the model is being built and simulated in OptiSystem software to further validate, verify and compare the actual experimental results. More details will be discussed in the subchapters.

3.1 Receiver's Power Output vs. Link Distance

An audio signal that has a bit rate of 320 kbps was made as input of the transmitter. The laser then transmit light to the receiver at a distance ranging from 0.2 m to 15 m. A multimeter was tapped onto the output of the receiver's circuit for data collection. Once the experiment is done, a simulated model was performed using OptiSystem 12. The power output of the simulated design is also being recorded.

Table 2 shows the results of receiver's output power from experiments and simulations.

Table 2. Output results of receiver

Link Distance (m)	Output Power from Experiment (mW)	Output Power from Simulation (mW)	System Efficiency (%)
0.2	3.35	4.91	68.3
1.0	2.63	4.18	63.1
3.0	2.17	3.20	67.9
5.0	1.88	2.78	67.5
7.0	1.49	2.22	66.8
9.0	1.30	2.03	64.2
11.0	0.98	1.50	65.8
13.0	0.63	0.94	67.0
15.0	0.39	0.60	66.1

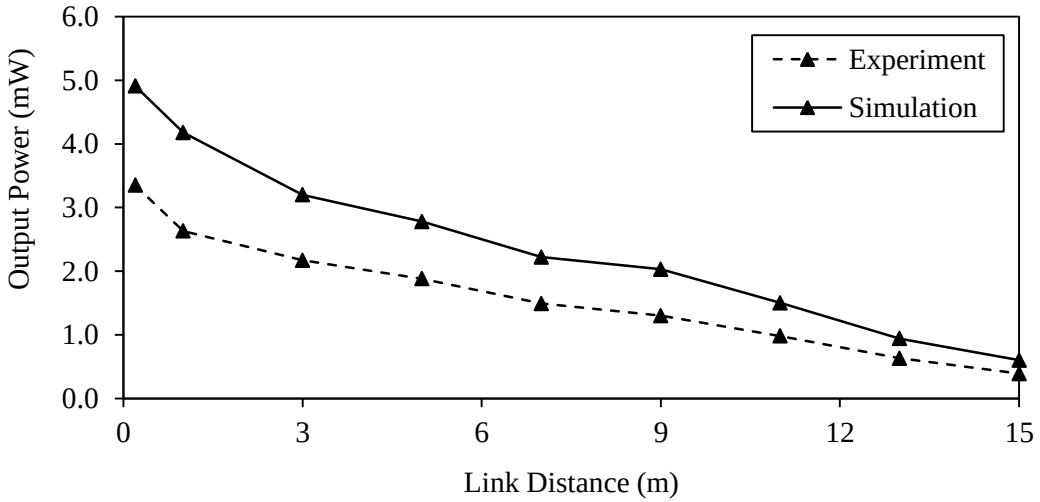

Figure 7. Receiver's output power vs. link distance

From Table 2 and Figure 7, results has shown that the receiver's power output is experiencing a decrease as the propagation link distance increase; just as expected in the initial proposal. At 0.2 m, the experimental receiver managed to give an output of 3.35 mW, the highest recorded; while the simulation model gives 4.91 mW. Bear in mind that the transmitter is sending a signal power 5 mW. At close proximity, the sound amplifier gives a very clear and loud audio sound. This is a classic trend in any audio wireless signal system where it shows that power signals become weak as propagation

distance increases. At 9 m and beyond, the power loss became very obvious when the sound amplifier produced a very faint and soft audio sound. Unless the transmitter

source increases its signal power, the receiver will suffer from poor signal power reception. In the case of laser, it is challenging to increase transmitting power because of the eye safety regulations that are in place. A higher power laser may cause harm and damage to human eyes.

By comparing the simulated and experimental output, the overall system efficiency is at 66.3%. Generally, hardware components are bound by power losses such as heat dissipation, power supply fluctuations, minor current and voltage leakage, conversion rate of input signal to output signal. However, the major factor of such drop in efficiency is the atmospheric effect. Dust particles found in atmosphere can cause particle absorption and scattering. Thus, the drop in receiver's ability to achieve maximum 5 mW power given by the transmitter.

3.2 SNR vs. Link Distance

To aide calculations, MATLAB algorithms has been used to find out the SNR at link distance of 0.2 m to 15 m. Table 3 tabulated the results from MATLAB's command window and Figure 6 show the results of SNR vs. link distance curve.

Table 3. SNR vs. Link Distance

Link Distance (m)	SNR (dB)
0.2	291.2
1.0	260.9
3.0	227.9
5.0	208.8
7.0	195.6
9.0	188.6
11.0	180.7
13.0	174.3
15.0	168.16

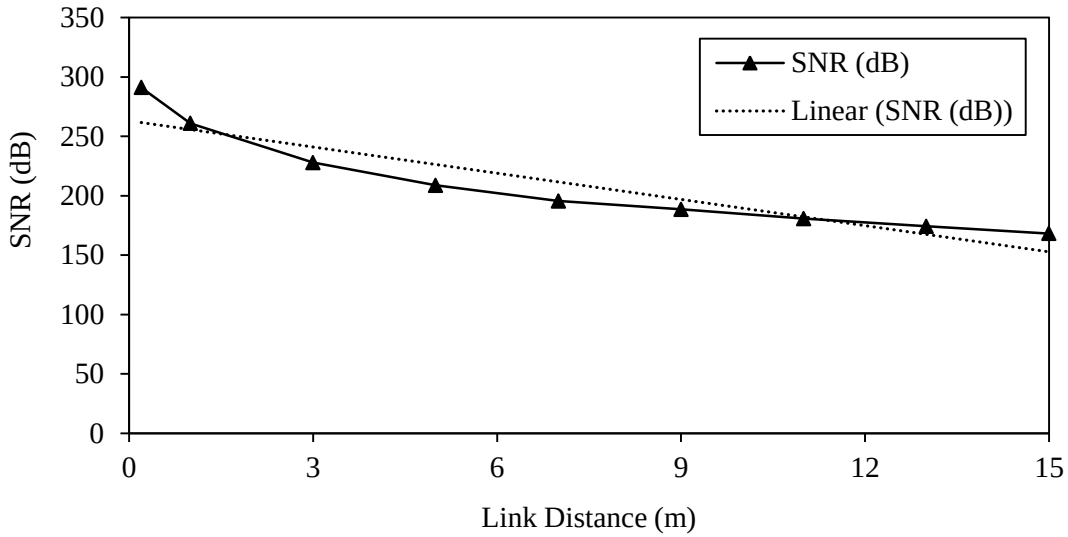

Figure 8. SNR vs. Link Distance

The SNR results demonstrated in Table 3 and Figure 8 that SNR decreases as the link distance increases. As explained in the research methodology, it is known that SNR is the ratio of signal power over noise power. Logically as the link distance increases, the receiver's output power would decrease too. As a result, the signal power diminish quickly and the noise power steadily increases. Hence, the SNR has decreased in respect of link distance just as expected. Poor SNR is a major concern in communication systems, therefore it is a priority to find ways improving the performance. Other than keeping both the transmitter and receiver distance at closer range, the introduction of signal processing filters at both ends are good methods to curb noise signals.

3.3 Q-Factor vs. Link Distance

Quality Factor (Q-factor) is a very useful parameter to indicate the performance of any communication systems. As mentioned in the research methodology, Q-factor at different link distance is being recorded by using the OptiSystem model. The BER Analyzer tool measured both BER and Q-Factor. Table 4 shows the results of this OWC system Q-factor at distance of 0.2 m to 15 m.

Table 4. Q-Factor vs. Link Distance

Link Distance (m)	Q-Factor
0.2	4.09
1.0	3.97
3.0	3.95
5.0	3.96
7.0	3.97
9.0	3.95
11.0	3.91
13.0	3.92
15.0	3.91

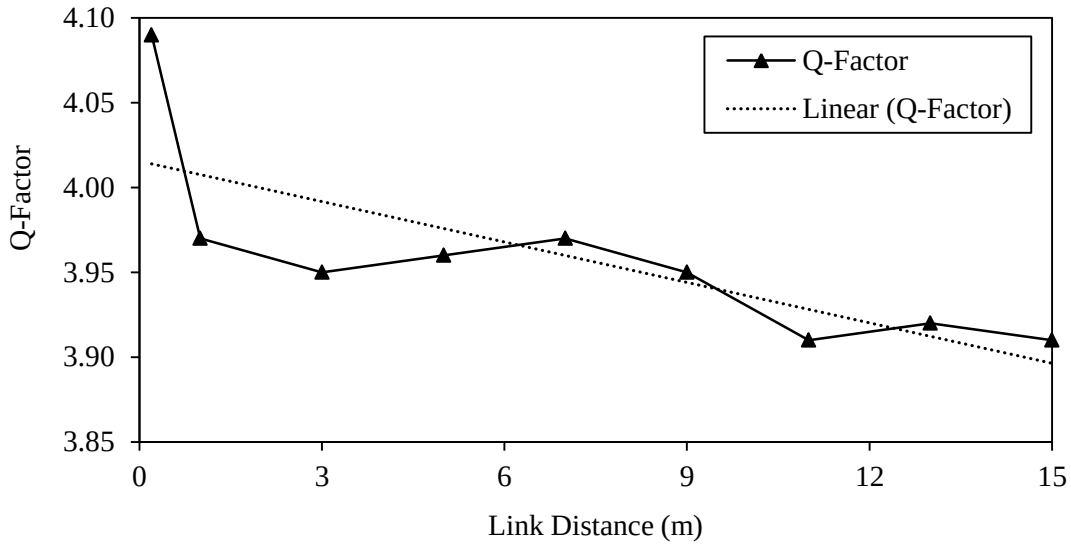

Figure 9. Q-Factor vs. Link Distance

The Q-Factor of this OWC system reflects the same trend as the BER and SNR. As explained in the previous chapter, Q-factor is a way of measure the quality performance of any communication system. Just as expected in the initial proposal, the Q-factor decreases as link distance. However at 0.2 m to 15 m, the Q-factor decreases at a very small rate. Just like the BER results (refer 3.4), the laser optical properties do not have immediate impact towards the system performance at such ranges of link distance. According to the simulated model, the system's non-functional point is at 600 meters. That is when the Q-Factor approaches 0.

3.4 BER vs. Link Distance

With the implementation of this OWC system in OptiSystem, the BER of this OWC system is able to be collected. Simply by connecting a BER Analyser Tool to

the model's output, readings such as the eye diagram, BER and Q-Factor are able to be displayed.

Table 5. Output Results of BER vs. Link Distance (0.2m-15m)

Link Distance (m)	Bit Error Rate (x $10^{-5)}$
0.2	2.13
1.0	2.23
3.0	2.53
5.0	2.65
7.0	2.75
9.0	2.75
11.0	3.36
13.0	4.47
15.0	4.59

From Table 5, it is clearly seen that the BER increases as the distance increases. In simple explanation, higher BER indicates that the data signal has higher probability of error in its propagation. This is not favourable in all communication systems. However in this project, the BER is still within the range of 10^{-5} at 0.2 m to 15 meters. It was initially expected to increase exponentially but it shows that it increased steadily instead. This is due to the property of laser diode at a narrow 1 nm optical bandwidth, which is less prone to particle scattering and fading signals compared to IR LEDs. Figure 10 illustrates the trend of the BER vs. Link Distance from 0.2 m to 15 m. It shows a linear increase in the BER as link distance increases.

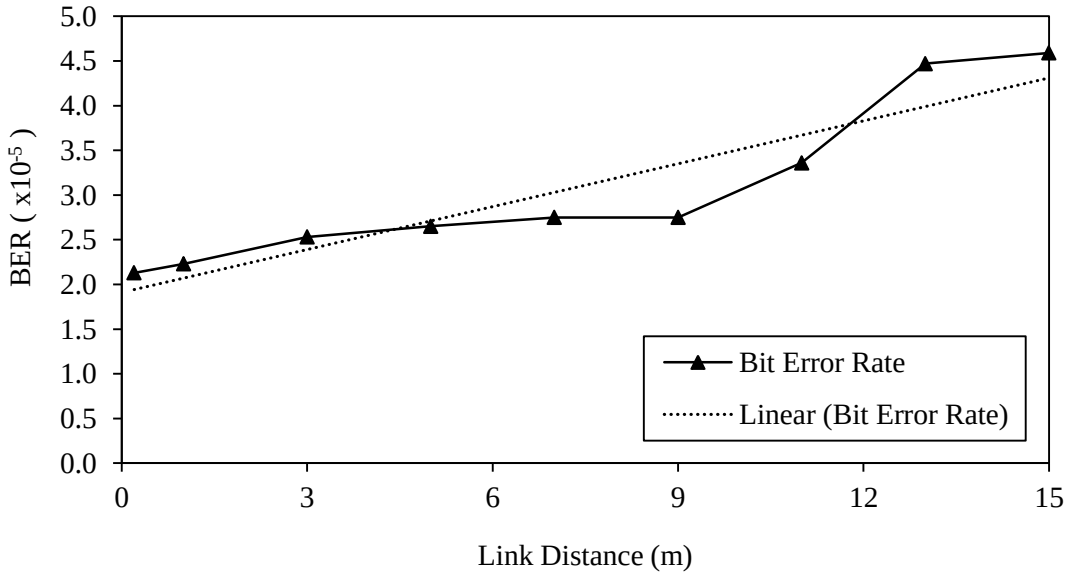

Figure 10. BER vs. Link Distance (0.2m-15m)

Since the range of 0.2 m to 15 m did not display a significant decrease in performance, a larger link distance range (250 m – 600 m) has been investigated. In order to investigate the maximum distance when the BER is 1 for this system, the simulated model in OptiSystem was used. When BER is 1, it signifies that the probability of error in this system is unavoidable. According to Figure 11 output results, it is found that the maximum distance for this system to achieve BER=1 is 600 meters. From the results, it is inevitable that BER increases as link distance increases.

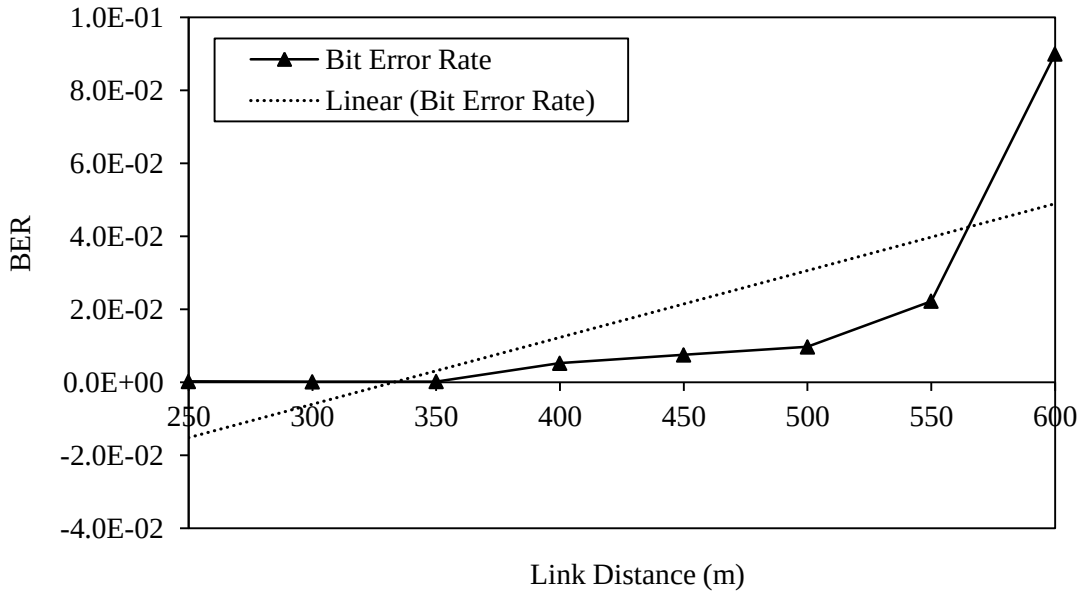

Figure 11. BER vs. Link Distance (250m-600m)

3.5 Beam Divergence, Misalignment and Particle Absorption

In LEDs and Lasers, the optical source is subjected to beam divergence due to its optics property. Likewise, this experimental model has faced the same issue but with minimal impact to its output results due to the low laser power output at 5mW. Figure 12 shows the beam divergence at 0.2 m and 15 meters. It can be seen that the laser beam aperture diameter has increased from 1 centimetre to 2.5 centimetres as link distance increases at 0.5 meter to 15 meters. One of the method to overcome this challenge is to increase the receiver's photodetector active area to receive larger aperture lasers. Throughout the experiment, there were difficulties to align the laser propagation especially when the link distance increases. No signal or weak signal is received whenever misalignment of laser occurs.

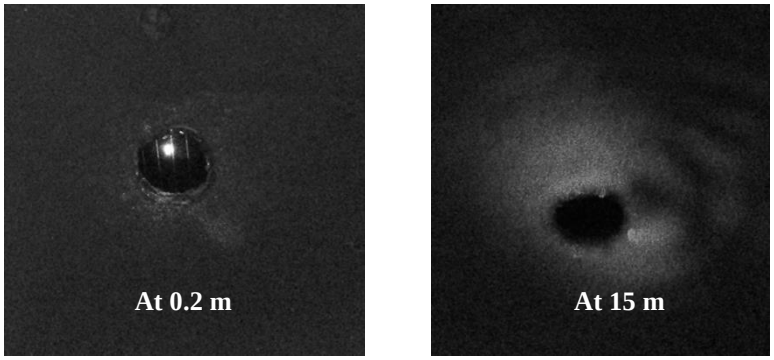

Figure 12. Laser beam divergence occur at 0.2 m and 15 m at the receiver.

For experimental and investigation purposes, water spray has been introduced during the propagation of signal between the transmitter and receiver. As the water is being sprayed perpendicularly to the propagated laser path, the receiver's sound amplifier produced distorted signals and fading signals such as hissing and thunder sounds. Such distortion is caused by particle absorption. Where photons' energy did not successfully channel to the receiver but absorbed by the particles in the atmosphere such as dust and water droplets. Figure 13 shows the water spray is being introduced to the system for experimentation.

Figure 13. Water is being sprayed at the laser beam propagation path.

4. Conclusion

This OWC system has clearly demonstrated the expected outcome that was initially raised in the project proposal. From the results collected, it can be seen that the efficiency of experimental vs. simulation model is at 66.3%. As the link distance increases, the BER increased, SNR and Q-Factor decreased. These outcomes are in line with hypothesis. According to the OptiSystem simulated model, this OWC system has a break down limit at 600 meters; where the BER is at 1 and Q-Factor at 0. There are also some challenges faced during the experiment. Laser beam divergence is a common issue and usually a larger receiver active area is one of the immediate ways to overcome it. Particle absorption phenomena has also been demonstrated in this experiment, as well as noise signals from the ambience light can be heard as link distance increases. It is proposed that the implementation of signal processing noise filters can help to improve signal quality. In order to overcome random errors

throughout the experiment, a few attempts of data recording has also been done. The average mean of the results are used in this report. Table 6 shows a summary table of all the results collected in this project.

Table 6. Summary of OWC results

Link Distance (m)	Output Power from Experiment (mW)	Output Power from Simulation (mW)	Bit Error Rate (x 10^{-5})	SNR (dB)	Q-Factor
0.2	3.35	4.91	2.13	291.2	4.09
1.0	2.63	4.18	2.23	260.9	3.97
3.0	2.17	3.20	2.53	227.9	3.95
5.0	1.88	2.78	2.65	208.8	3.96
7.0	1.49	2.22	2.75	195.6	3.97
9.0	1.30	2.03	2.75	188.6	3.95
11.0	0.98	1.50	3.36	180.7	3.91
13.0	0.63	0.94	4.47	174.3	3.92
15.0	0.39	0.60	4.59	168.16	3.91

Acknowledgment

Warm expression and sincere appreciation to Taylor's University, School of Engineering and its staffs who assist to accomplish the project. Throughout this final year project, time and effort has been invested by the project supervisor. Warmest thanks and regards to the lecturer in charge.

References

[1] T. Garlington, 'Analysis of Free Space Optics as a Transmission Technology', *U.S. Army Information Systems Engineering Command*, no., p. 2, 2005.

[2] H. Elgala, R. Mesleh and H. Haas, 'Indoor optical wireless communication: potential and state-of-the-art', *IEEE Communications Magazine*, vol. 49, no. 9, pp. 56-62, 2011.

[3] Z. Ghassemlooy and A. Boucouvalas, 'Indoor optical wireless communication systems and networks', *International Journal of Communication Systems*, vol. 18, no. 3, pp. 191-193,2005.

[4] Global IP Traffic Forecast and Methodology Cisco Systems, 2006C2011, 2008.

[5] A. Dodd, The essential guide to telecommunications. Upper Saddle River, NJ: Prentice Hall, 2012.

[6] N. Mohamad, A. Wakiran, M. Iswandi and A. Salleh, 'Development of Optical Wireless Audio System Using Infrared Light Communications', *IOSR Journal of Electronics and Communication Engineering*, vol. 8, no. 6, p. 1, 2013.

[7] H. Hodson, 'Radio-over-fibre could give wireless internet access to the masses', New Scientist, vol. 215, no. 2882, p. 18, 2012.

[8] K Kikuchi, Coherent optical communications: Historical perspectives and future directions, High Spectral Density Optical Communication Technologies, M Nakazawa, K Kikuchi, and T Miyazaki, eds , Berlin: Springer-Verlag, 2010, pp 11–49.

[9] A K Majumdar and J C Ricklin, Free-Space Laser Communications: Principles and Advances, New York: Springer, 2008.

[10] L Noel, D Wake, D G Moodie, D D Marcenac, L D Westbrook and D Nesset, Novel techniques for high-capacity 60 GHz fiber-radio transmission systems, IEEE Transactions on Microwave Theory and Techniques, 45, 1416–1423, 1997.

[11] D. Kedar and S. Arnon, 'Urban optical wireless communication networks: the main challenges and possible solutions', Communications Magazine, IEEE, vol. 42, no. 5, pp. 2--7, 2004.

[12] J M Kahn and J R Barry, Wireless infrared communications, Proceedings of IEEE, 85, 265–298, 1997.

[13] Z. R. Ahmed Nabih., 'Optical Wireless Link Budget Analysis for Optical Wireless Communication Networks', *International Journal of Advanced Research in Computer Science and Electronics Engineering*, vol. 1, no. 10, , p. 2, 2012.

[14] A J C Moreira, R T Valadas and A M d O Duarte, Optical interference produced by artificial light, Wireless Networks, 3, 131–140, 1997.

[15] A C Boucouvalas, Indoor ambient light noise and its effect on wireless optical links, IEE Proceedings—Optoelectronics, 143, 334–338, 1996.

[16] *Optical Signal-to-Noise Ratio and the Q-Factor in Fiber-Optic Communication Systems*, 1st ed. Maxim Integrated, 2015, p. 2.

[17] A. Rashed, 'High efficiency wireless optical links in high transmission speed wireless optical communication networks', *International Journal of Communication Systems*, p. 1, 2013.

[18] J. Zweck, I. Lima Jr., Y. Sun, A. Lima, C. Menyuk and G. Carter, 'Modeling Receivers in Optical Communication Systems With Polarization Effects', *Optics & Photonics News*, vol. 14, no. 11, p. 30, 2003.

Design of a Passive Parallel Leg Exoskeleton for Load Carrying Augmentation

Kin-Ming Chan*, Mushtak Al-Atabi

School of Engineering, Taylor's University Lakeside Campus, Malaysia

* *Email: ckming0511@gmail.com*

Abstract

Exoskeletons for load-carrying augmentation have undergone significant progress in recent decades and been brought into commercialization and clinical trials. However, they are commonly active systems which include the use of actuators and external power, coupled with electronic control assist. For the task of load carrying, they might be more complicated than necessary, hence research into passive exoskeletons attempts to bridge this gap. The paper presents a passive parallel leg exoskeleton to augment load-carrying ability of a user. A saw-tooth cam mechanism is adapted into the mechanical design of the exoskeleton, inspired by a retractable pen mechanism. During stance phase of walking, the mechanism allows the exoskeleton leg to form a rigid link, allowing load transfer to the ground and subsequently during swing phase, the rigid link decouples to enable leg swing. The paper provides a brief review of current state-of-the-art of lower-limb exoskeletons developed for load-carrying, design methodology for proposed exoskeleton, operation principle of saw-tooth cam mechanism, a discussion on the mechanical design and ends with current progress and work to be done.

Keywords: Exoskeleton, Passive Leg, Load-carrying, Saw-tooth cam mechanism, Mechanical Design

1. Introduction

Exoskeletons can be broadly defined as mechanical devices or wearable robotics that are designed and fitted externally to the human body, with the aim of increasing or restoring the physical ability of the user. Combining human intelligence and machine power, it gives rise to a system with machine power but guided directly by human intelligence, allowing the operator to achieve physical feats he would not otherwise been capable of. For an able-bodied operator, it facilitates increase of joint strength (to support heavy loads) or increase of physical endurance (allowing greater operation time)

They allow a person to carry heavier loads, run faster, jump higher and work longer while expending less energy. Furthermore, they are able to traverse irregular, non-paved terrains where wheeled vehicles cannot, enabling rapid deployment to disaster areas for relief work such as clearing of heavy debris. Since legged locomotion is able to adapt to a wider variety of terrains, it is hence an attractive method of transportation.

The goal of the research undertaken is to investigate and implement an alternative design of a fully-passive leg exoskeleton to help support backpack load during walking. This is done by designing and evaluating a leg exoskeleton that adapts a saw-tooth cam mechanism, whose principle has not been applied in a leg exoskeleton as of the time of writing.

2. Literature Review

The literature review described focuses mainly on portable, stand-alone devices that operate in parallel with the human legs, as opposed to those that operate in series with the wearer. Only devices that provide some means of augmenting power/enhancing load-bearing at one or more joints of the leg are considered. Additionally, devices that utilize passive elements as means of improving walking ability under load are presented.

2.1 Active Exoskeletons

Figure 1 (from left) BLEEX [1], Sarcos XOS2 [2]; HAL [3]

2.1.1 Berkeley Lower Extremity Exoskeleton (BLEEX)

The Berkeley Lower Extremity Exoskeleton (BLEEX) developed at University of California, Berkeley is designed to augment load carrying capacity of humans [1]. It consists of two powered anthropomorphic legs, a power unit and a back-pack like frame. It features three degrees of freedom at the hip, one at the knee and three at the ankle. Of these, four are actuated: hip flexion/extension, hip abduction/adduction, knee flexion/extension and ankle flexion/extension. Of the non-actuated joints, the ankle abduction/adduction and hip rotation joints are spring loaded and ankle spring joint is free-spinning [4].

For the control scheme, BLEEX minimizes use of sensory information from human/exoskeleton interaction, relying mainly on sensory information from the exoskeleton itself. It is able to balance on its own, but the wearer must provide a forward guiding force to direct the system during walking. BLEEX can support a load of up 75 kg while walking at 0.9 m/s and go up to 1.3 m/s without the load.

2.1.2 Hybrid Assistive Limb (HAL)

The Hybrid Assistive Limb (HAL) developed by University of Tsukuba [5] [3] is used for performance augmenting and rehabilitative purposes. Mechanical power is provided to augment joint torque when doing work; reducing joint pain during locomotion and restoring joint strength in paralyzed and weakened joints. The flexion/extension at the joints is powered at the hip and knees via a DC motor placed directly on the joints.

HAL uses electrical signals sent to the muscles from the brain to anticipate the wearer's movement. Both an EMG-based system and walking pattern-based system allow it to move fractions of a second before the wearer, providing seamless interaction between human and robot. Weighing in at 21 kg [6], it is able to increase the user's capacity to lift and press loads. Wearing the suit, a healthy adult male can lift 80 kg while leg press capability is increased from 100 kg to 180 kg.

2.1.3 Sarcos XOS-2

Under the DARPA EHPA [7] programme, an energetically autonomous, full-bodied exoskeleton was developed by Sarcos Robotic Technologies. Dubbed the XOS-2, it employs the use of rotary hydraulic actuators at the joints as opposed to the linear hydraulic actuators commonly used. Force sensing between the wearer and exoskeleton is utilized to implement a "get out of the way" control scheme.

It is reportedly capable of a number of feats [6] such as supporting an entire load of 84 kg, carrying one person on the back while standing with only one leg, walking at 1.6 m/s while carrying 68 kg on the back and 23 kg on the arms, walking through 23 cm of mud, as well as twisting, squatting and kneeling.

2.2 Passive Exoskeletons

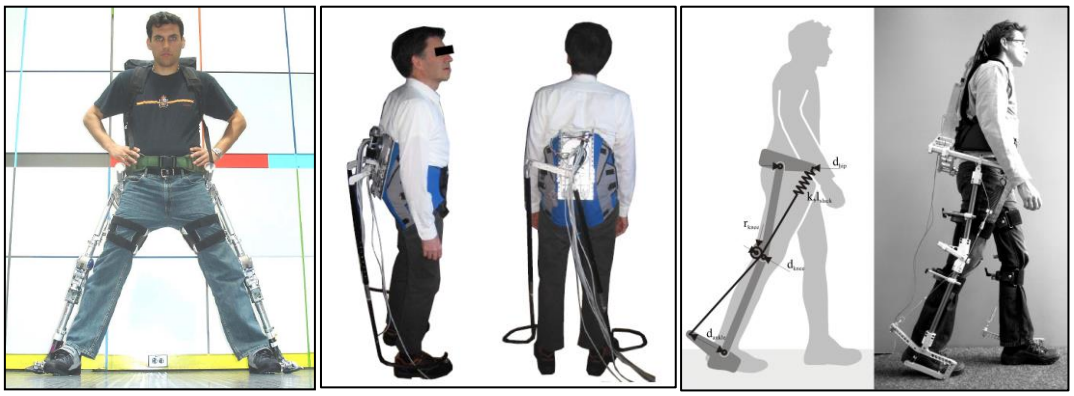

Figure 2 (from left) MIT quasi-passive exoskeleton [8], MoonWalker [9] , Passive Exoskeleton with Artificial Tendons [10]

2.2.1 MIT Quasi-Passive Leg Exoskeleton

A quasi-passive exoskeleton concept was developed by the Biomechatronics Group at the Massachusetts Institute of Technology (MIT), which aims to exploit the passive dynamics of human walking in order to create lighter and more efficient exoskeleton devices [8]. The exoskeleton structure runs parallel to the legs, transferring payload forces to the ground. Actuators for adding power at the joints are not utilized, harnessing instead the controlled release of energy stored in springs during phases of the walking gait. Quasi-passive elements (springs and variable damper) were chosen based on analysis of the kinetics and kinematics of human walking. Passive hip and ankle springs are employed to store and release energy throughout the gait cycle. To reduce knee muscular effort, a variable damper is implemented at the knee to support body weight throughout early stance.

Experimental work demonstrated that a working device successfully supported a 34kg load during walking at 1 m/s. Additionally, the structure transferred on average 80% of the payload to the ground during single-support phase of walking. However, in terms of the metabolic energy cost, experimental testing showed a 64% increase in metabolic energy required when compared to a backpack of the same weight without the exoskeleton. This disproved their hypothesis that a reduction in metabolic energy cost will be achieved with their quasi-passive leg exoskeleton when compared to unassisted loaded walking

2.2.2 Biomimetic Under-actuated Leg Exoskeleton

Another variant of the MIT leg exoskeleton [11] [12] [13] was developed using the same principle of harnessing the passive dynamics of walking with the aim of creating a lighter, more efficient exoskeleton for load-carrying augmentation. Different from [8], the hip springs are replaced with an actuator. The joint components of the exoskeleton in the sagittal plane consist of a force-controllable actuator at the hip, a variable-damper mechanism at the knee and a passive spring at the ankle. A state-machine control strategy was written based on joint angle and ground-exoskeleton force sensing. Positive, non-conservative power is added at the hip during the walking cycle to help propel the mass of the human and payload forward. At the knee, the damper mechanism is turned on at heel strike as the exoskeleton leg is loaded and turned off during terminal stance to allow knee flexion. The spring at the ankle engages

in controlled dorsiflexion to store energy that is later released to assist in powered plantarflexion.

With a 34 kg payload, the exoskeleton transfer 90% and higher loads to the ground depending on the phase of gait. Furthermore, wearers report that the exoskeleton greatly reduces the stress on the shoulders and back. Despite a significant fraction of the payload transferred through the exoskeleton structure, an increase metabolic cost was still found. Results highlighted the benefit of ankle elastic energy storage and knee variable-damping in exoskeleton design, and further the need for a lighter, more efficient hip actuator.

2.2.3 MoonWalker

The MoonWalker [9] is a quasi-passive lower limb exoskeleton developed to sustain part of the user's bodyweight. It can be used for rehabilitation, to help people having weak legs or those suffering from a broken leg to walk. It can also be used as an assistive device helping people carrying heavy loads. Its main characteristic is a passive force balancer that provides the force to sustain bodyweight. An actuator is also required, but only to shift the force the same side as the leg in stance and requires low energy to work.

It is able to exert an upwards vertical force on the user's pelvis in order to lighten the forces on user's leg due to bodyweight. A prototype is built, proving the conceptual design to the functional level only. However, it remains to be verified that the device reduces load on leg muscles and joints by supporting a portion of the user's bodyweight.

2.2.4 Passive Exoskeleton with Artificial Tendons

In the Netherlands, a passive exoskeleton was developed to minimize joint work during walking. Passive structures, called artificial tendons [10], acting in parallel with the leg are utilized. These artificial tendons are elastic elements that are able to store and redistribute energy over the human joints. The model for these artificial tendons is similar to one proposed by Bogert [14].

The artificial tendon is an elastic cable that spans multiple joints (hip, knee and ankle joints) and is attached at one end at the foot and the other at the pelvis. At the joints in between, the tendon is offset by a lever at the ankle and hip and by a lever with attached pulley. These offsets cause the artificial tendon to change length when joint angles change and subsequently induce a force and torque to aid leg motion.

In simulation, the maximal reduction in energy expenditure at the joint was estimated at 40 percent. In an experimental evaluation, normal walking was found to be most efficient and while walking with the exoskeleton, the artificial tendons only resulted in negligible small decrease in energy expenditure.

2.3 Lower-limb Exoskeletons for Load Carrying

Active powered exoskeletons for load-carrying such as BLEEX [1], HAL [5] and XOS-2 **[2]** have been demonstrated and brought into commercialization [6] and initial clinical trials. Commonly, actuators and external power supplies are required, which increases their weight, impacting on their efficiency and operation range. In addition, complex electronic

control systems are required to drive and control such systems, further increasing their complexity. While shown to be able to increase the load-carrying capability of the user, the advantages in terms of reduction in metabolic energy are largely unreported. Hence, questions arise on whether a simpler design can be utilized for load-carrying, as an active system may be more complex than necessary.

Research into passive or quasi-passive exoskeleton aims to achieve the same objective for enhanced load-carrying, but without the use of heavy actuators and external power supply. State of the art in (quasi)-passive exoskeleton are exoskeletons that compensate gravity such as gravity-balancing leg orthosis [15] and MoonWalker [14]; match joint moments such as the designs by MIT [8] [13] or utilize passive exo-tendons [10] [16] where long springs spanning multiple joints temporarily store and redistribute energy over the joints. However, it is noted that the current state of progress is focused on getting metabolic or energy savings from normal unloaded walking, before scaling to load carrying applications.

Published results for passive exoskeletons thus far have not shown an absolute or significant reduction in metabolic rate and a mismatch between theoretical model and reality persists. However, their research suggests benefits in having passive design elements that store and release energy during gait cycle. Design challenges that lead to poor exoskeleton performance [8] include; misalignment of joints between operator and hardware, kinematic constraints from attachments such as harnesses and cuffs, design not optimized for load-carrying gait, added forces to the operator that resist motion and addition of power in suboptimal manner (i.e. mistiming, too little, too much).

3. Design Methodology

3.1 Parameter Setting

For load-carrying exoskeletons, active systems have been demonstrated to augment load-carrying capability. For passive systems, only the MIT leg exoskeletons [12] [13] have been designed to carry loads. Other passive systems such as MoonWalker and XPED2 are primarily developed to reduce metabolic energy or force requirements at the joint, and thus are not considered in Table 1 as they have not been demonstrated to carry external loads.

Table 1 Comparison of Different Load-Carrying Exoskeletons

Examples	Type	Exoskeleton Weight (kg)	Load Supported(kg)	Payload/Weight ratio
BLEEX	Full-body (Active)	28	75	2.68
HAL-5	Full-body (Active)	21	80	3.33
MIT Quasi-Passive	Lower-limb (Quasi-Passive)	15.5	34	2.19
MIT Under-actuated	Lower-Limb (Active)	13.4	34	2.54
Proposed Design	Lower Limb (Passive)	≤ 15	≥ 30	≥ 2.00

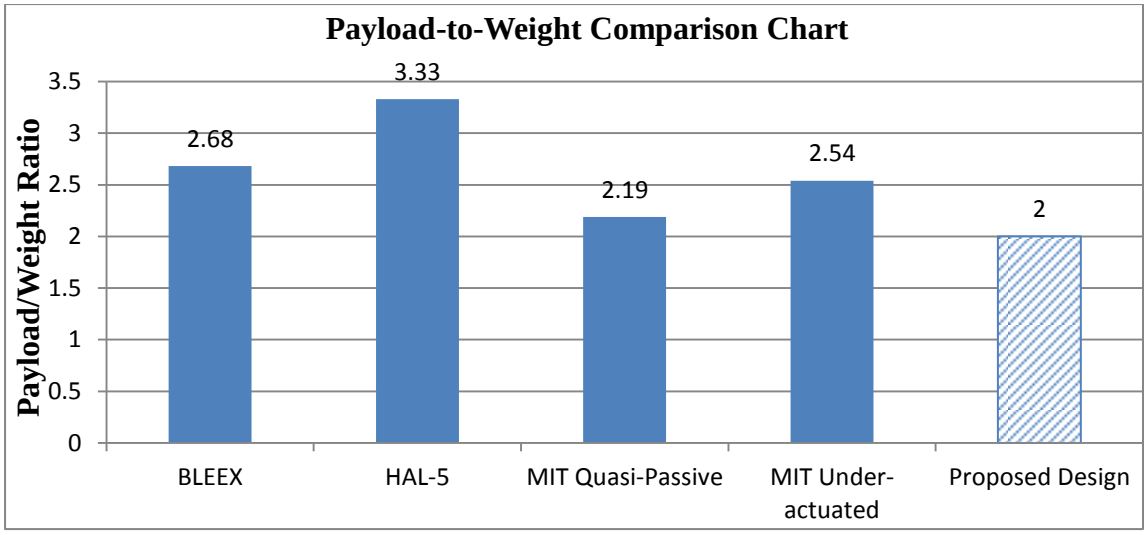

Figure 3 Payload-to-Weight Ratios for Different Devices

A relation could be established between the weight and load-bearing capacity of the similar exoskeletons (refer Graph 1). It is noted that their payload-to-weight ratio hovers around 2.7 on average. A conservative payload-to-weight ratio of 2 is thus suggested for the proposed exoskeleton.

3.2 Biomechanics of Walking

A gait cycle (GC) is defined in terms of an interval of time during which one sequence of regularly recurring succession of events is completed. In other words, gait cycle can be thought as the time between successive foot contacts of the same limb and is often described in percentage time elapsed. One cycle being when the reference foot contacts the ground and ends with subsequent floor contact of the same foot [17].

Further, each (GC) is divided into 2 periods: stance and swing (refer Fig. 3). Stance designates the entire period during which the foot is on the ground and begins with initial contact. The term swing applies to the time the foot is in the air for limb advancement. Swing begins as the foot is lifted from the floor (toe off). The generic normal distribution of the floor contact periods approximates 60% for stance and 40% for swing.

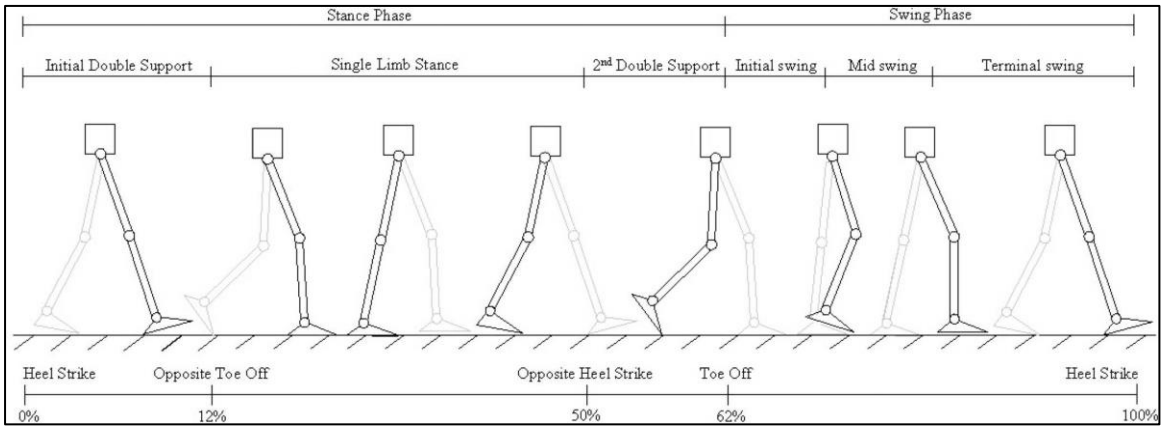

Figure 4 Human Walking Gait Cycle, adapted from [17]

Generally, support of body weight on one limb occurs during single limb support of stance phase. Subsequently, transfer of body weight from one limb to another occurs when both feet are in contact with the ground during double limb support. It can be inferred that when carrying loads, the loads are transferred to the legs for support during these phases of stance.

3.3 Saw-tooth Cam Mechanism

The saw-tooth cam mechanism in a retractable pen (refer Fig. 4) exhibits a distinct pattern of locking and unlocking, where the nib of the pen extends and retracts with each click of the push button. Molded onto the pen housing is a series of saw-tooth profiles, separated by a slot in between them. A number of fins are also molded onto the guide pin. The guide pin rests on the ink cartridge which in turn is continuously biased upward by a spring at the fitted at other end of the housing.

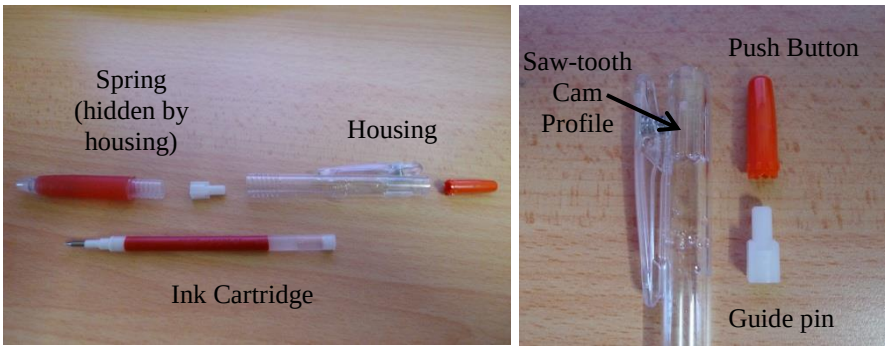

Figure 5 Components of Retractable Pen

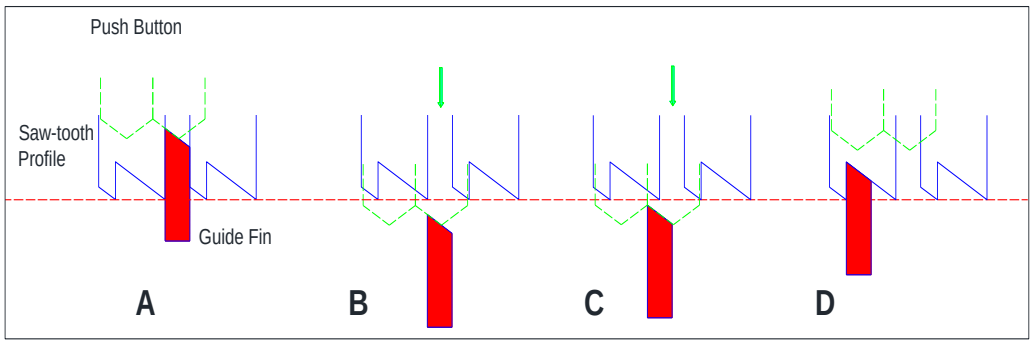

Figure 6 Saw-tooth Mechanism Sequence

Referring to Fig. 5, in the retracted position (A), the fins of the guide pin slide through the slots, allowing the nib to retract from the bottom end. When the push button is pressed downward (B), the guide pin is pushed downwards until the point it extends beyond the saw-tooth profile. The fins will then slide up the angled notches of the push-button (C), effectively causing guide pin to rotate one position. As the push button is released (D), the spring-biased guide pin move upwards, and its fins latches onto the saw-tooth profile of the housing, sliding up the angled surface and eventually coming to a stop. At this stage, the ink cartridge is prevented from being pushed by the spring upwards into the pen housing, setting the nib in the extended position from bottom end.

4. Mechanical Design

During stance phase of walking while carrying a load, a rigid link should be formed in the exoskeleton structure to enable load transfer to the ground. By simply having a rigid rod attached in parallel to the legs, the wearer will be unable to bend the knee, resulting in an unnatural gait. There is a need to be able to de-couple the stance and swing phase, so that the exoskeleton knee can be locked to form a rigid link during stance phase for load-bearing; and unlocked during swing phase to enable the leg to bend and swing. The saw-tooth mechanism in a retractable pen is thus studied and applied in the mechanical design, as it exhibits a distinct locking and unlocking mechanism.

4.1 Prototype description

The prototype is designed using SolidWorks (refer Fig. 6), adapting the saw-tooth mechanism and matching it with the human gait. Component sizing was done based on measurements of author's leg dimensions and gait parameters. The prototype consists of a waist unit connected with two leg structures. The waist unit will have a shoulder and belt harness to connect the exoskeleton to the wearer, the exoskeleton legs are connected via simple pin-joints to the waist unit and a backpack unit can be mounted onto the waist unit. A leg structure (refer Fig. 8) consists of a 3-piece cam sleeve (containing the saw-tooth profile), a load road with rotatable ridged bushing and a spring-loaded annular cam. A spring is mounted at the top of cam-sleeve to continuously bias the annular cam downwards. The load rod connects directly via a simple pint joint to a modified safety shoe. The exoskeleton is designed to weight below 15 kg, while being capable of supporting a load of at least 30 kg (refer Table 1).

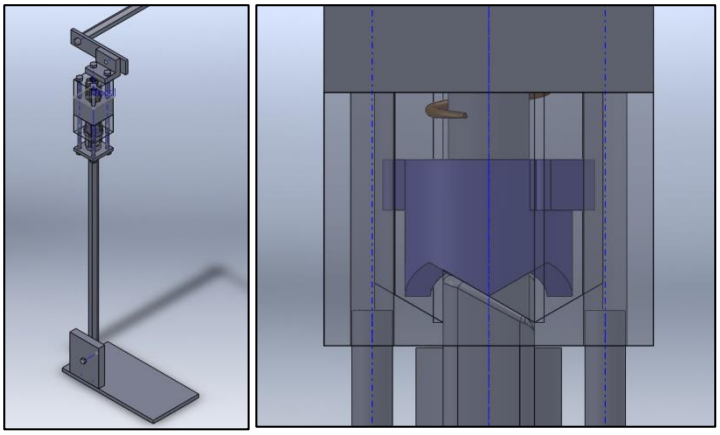

Figure 7 CAD Design of Leg Exoskeleton (saw-tooth mechanism shown on right)

4.2 Principle of Operation

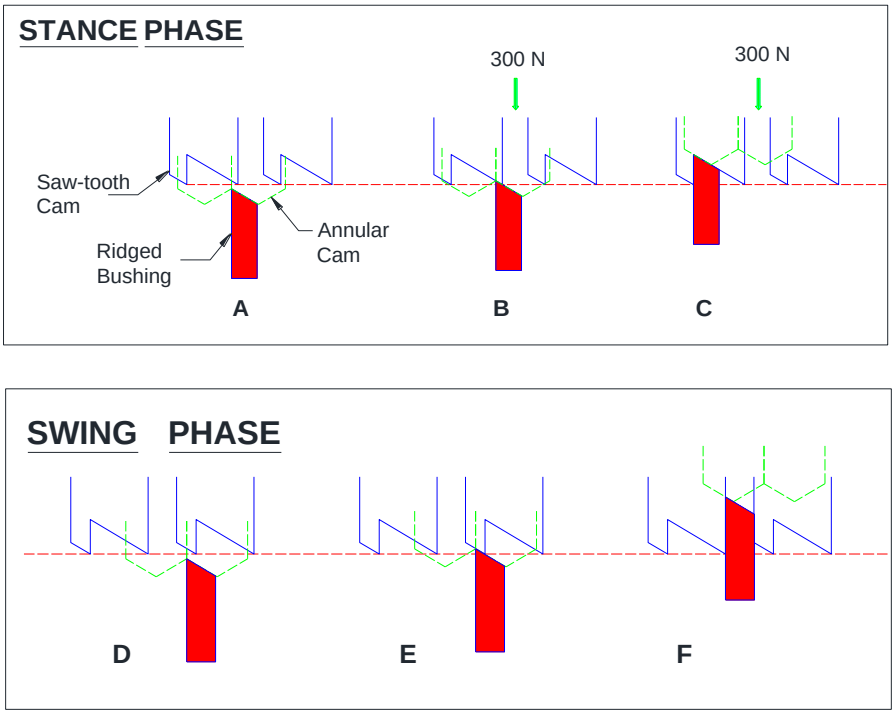

Figure 8 Sequence Events for Load-bearing in Exoskeleton

Referring to Fig. 7, during stance phase: (A) Just before heel strike, the spring-loaded annular cam slides past saw-tooth cam, consequently pushing the ridges of ridged bushing out of slot. (B) At heel strike, a payload (approximately 30 kg) transmitted through waist unit pushes down the cam sleeve (which contains the saw-tooth cam profile). The spring-loaded annular cam which is in contact with ridge is compressed between cam-sleeve pushing down and level ground contact. (C) Annular cam along with longitudinal ridges are pushed up as leg pivots over ground. Eventually, the ridge latches onto the saw-tooth profile and continues to slide circumferentially along its angled surface before coming to a stop at the trough. Load is transferred through structure to the ground during engagement of ridge with saw-tooth cam.

For swing phase: (D) During toe-off, payload no longer pushes down on ridge (as load support has already shifted to next leg). Spring-loaded annular cam is then free to slide back to its neutral position past the saw-tooth cam. At the same time, the annular cam pushes down the ridge. (E) As knee bends and foot lifts off ground, annular cam with ridged bushing moves together upwards. As they continue to move upwards, the ridge comes into contact with second angled surface of saw-tooth profile. (F) Ridge slides circumferentially into cam slot, allowing leg to bend.

5. Current Progress

As of time of writing, manufacturing of the components is still in progress with right leg components having been completed through CNC machining. Initial test fit of the ridged bushing with saw-tooth profile indicated a tight engagement, which is beneficial in forming a rigid link during stance phase of walking. Additionally, it was found that the internal components had a tendency to tilt and jam within the internal bore of cam-sleeve, hinting on possible centering issues of the components.

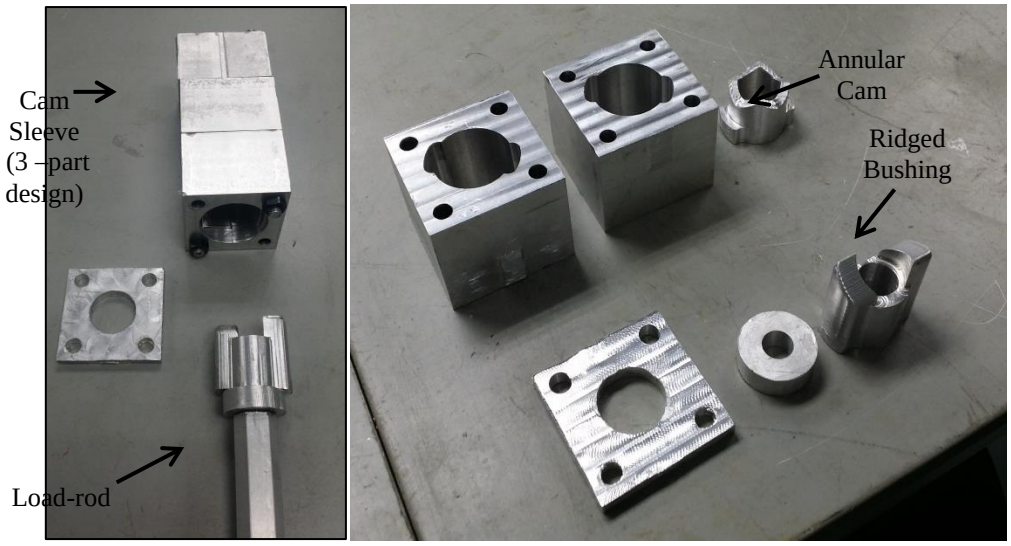

Figure 9 Fabricated Components of Exoskeleton Leg

6. Conclusions and Further Work

The report covers the first phase of a research project aimed at developing a fully-passive leg exoskeleton to augment the load-carrying capacity of the wearer. The intermittent locking and unlocking mechanism of a saw-tooth cam mechanism was studied and its application for a passive leg exoskeleton has been advanced into detailed design and manufacturing. It remains to be verified that the device helps to support a portion of the payload.

Future work will focus improving the exoskeleton, validating the design and evaluating its performance. Therefore, the following steps are planned:

- Minimizing mass and inertia of the device, and improving degree of freedom while walking with the device.
- Conducting stress analysis on load-bearing components of the device in order to optimize strength-to-weight ratio and ensure safety of design
- Testing of the device with a wearer and measuring the proportion of loads transferred through the exoskeleton leg, supported by proper experimental methodology. Currently, a load cell is planned to be fitted in-line with the load rod to detect loads transferred and will be logged by a National Instrument DAQ unit.

References

[1] K. H and S. R, "The Berkeley Lower Extremity Exoskeleton," *ASME Journal of Dynamic Systems, Measurement and Control*, vol. 128, pp. 14-25, March 2006.

[2] Raytheon, "Sarcos XOS-2," 2011. [Online]. Available: http://www.raytheon.com/newsroom/technology/rtn08_exoskeleton/ . [Accessed 4th Nov 2012].

[3] H. Kawamoto, S. Lee, S. Kanbe and Y. Sankai, "Power assist method for HAL-3 using EMG-based feedback controller," in *Proc. IEEE Int. Conf.* , Systems, Man, Cybernetics, 2003, pp. 1648-1653.

[4] A. Zoss, H. Kazerooni and A. Chu, "On the mechanical design of the Berkeley lower extremity exoskeleton (BLEEX)," *Intelligent Robots and Systems, IEEE International Conference,* pp. 3465-3472, IEEE, 2005.

[5] H. Kawamoto and Y. Sankai, "Power assist system HAL-3 for gait disorder person," in *Proc. Int. Conf. Comput. Helping People Special Needs (ICCHP) (Lecture Notes on Computer Science), vol 2398*, Berlin,

Germany: Spinger-Verlag, 2002.

[6] E. Guizzo and H. Goldstein, "The rise of the body bots," *IEEE Spectrum*, vol. 42, no. 10, pp. 50-56, Oct. 2005.

[7] E. Garcia, J. Sater and J. Main, "Exoskeletons for human performance augmentation (EHPA): A program summary," *J. Robot. Soc. Japan*, vol. 20, no. 8, pp. 44-48, 2002.

[8] A. Valiente, *Design of a quasi-passive parallel leg exoskeleton to augment load carrying for walking*, Master's thesis, Dept. Mech. Eng., Massachusetts Inst. Technol., Cambridge, Aug. 2005.

[9] S. Krut, M. Benoit, E. Dombre and F. Pierrot, "MoonWalker, a Lower Limb Exoskeleton able to sustain Bodyweight using a passive Force Balancer," in *IEEE Internationl Conference on Robotics and Automation*, Anchorage, Alaska, USA, 2010.

[10] W. van Dijk, H. van der Kooij and E. Hekman, "A Passive Exoskeleton with Artificial Tendons - Design and Experimental Evaluation," in *IEEE International Conference on Rehabilitation Robotics*, ETH Zurich Science City, Switzerland, 2011.

[11] C. Walsh, *Biomimetic design of an underactuated leg exoskeleton for load-carrying augmentation*, Master's thesis, Dept. Mech. Eng., Massachusetts Ints. Technol., Cambridge, Feb. 2006.

[12] C. Walsh, D. Paluska, K. Pasch, W. Grand, A. Valiante and H. Herr, "Development of a lightweight, underactuated exoskeleton for load carrying augmentation," in *Proc. IEEE Int. Conf. Robot. Autom.*, Orlando, FL, 2006, pp. 3485-3491.

[13] C. Walsh, K. Pasch and H. Herr, "An autonomous, underactuated exoskeleton for load-carrying augmentation," in *Proc. IEEE/RSJ Int. Conf. Intell. Robots Syst. (IROS)*, Beijing, China, 2006, pp. 1410-1415.

[14] A. van der Bogert, "Exotendons for assistance of human locomotion," *BioMedical Engineering OnLine*, vol. 2, p. 17, 2003.

[15] S. Banala, S. Agrawal, A. Fattah, V. Krisnamoorthy, H. Wei-Li, J. Scholz and K. Rudolph, "Gravity-Balancing Leg Orthosis and Its Performance Evaluation," *IEEE Transactions on Robotics*, vol. 22, p. 1228, 2006.

[16] W. van Dijk and H. Van der Kooij, "XPED 2: A Passive Exoskeleton with Artificial Tendons," *Robotics & Automation Magazine, IEEE*, vol. 21, no. 4, pp. 55-61, Dec. 2014.

[17] J. G. J. Rose, "Kinematics of Normal Human Walking," in *Human Walking*, Lippincott Williams & Wilkins, 2006, pp. 36-50.

[18] H. Herr, "Exoskeletons and Orthoses: Classification, Design Challenges and Future Directions," *Journal of NeuroEngineering and Rehabilitation*, vol. 6:21, June 2009.

[19] B. R. &. H. E. Laboratory, "BLEEX," 2011. [Online]. Available: http://bleex.me.berkeley.edu/research/exoskeleton/bleex/. [Accessed Nov 3rd 2012].

[20] "Hybrid Assistive Limb (HAL)," Cyberdyne Japan, 2011. [Online]. Available: http://www.cyberdyne.jp/english/robotsuithal/index.html. [Accessed 3rd November 2012].

[21] IEEE Spectrum, "The Rise of the Body Bots," 1 Oct 2005. [Online]. Available: http://spectrum.ieee.org/biomedical/bionics/the-rise-of-the-body-bots. [Accessed 15 May 2013].

[22] Australian Orthotic Prosthetic Association, "What is an Orthosis?," 2013. [Online]. Available: http://www.aopa.org.au/careers/what-are-orthoses-and-prostheses. [Accessed 13th Oct 2014].

[23] N. Yagn, "Apparatus for facilitating walking, running and jump". U.S. Patent 420179 & 438830, 1890.

[24] S. Zarrodny, "Bumpusher - A powered aid to locomotion," U.S. Army Ballistic Research Laboratory, Aberdeen Proving Ground, MD, Tech. Note 1524, 1963.

[25] R. Mosher, "Handyman to Hardiman," in *Soc. Autom. Eng. Int. (SAE)*, Detroit MI, Tech. Rep. 670088, 1967.

[26] K. Gilbert, "Exoskeleton prototype project: Final report on phase I," General Electric Company, Schenectady, NY, GE Tech. Rep. S-67-1011, 1967.

[27] K. Gilbert and P. Callan, "Hardiman I prototype," General Electric Company, Schenectady, NY, GE Tech. Rep. S-68-1081, 1968.

[28] J. Moore, "Pitman: A powered exoskeleton suit for infantryman," Los Alamos Nat. Lab., Los Alamos, NM, Tech. Rep. LA-10761-MS, 1986.

[29] B. Fick and J. Makinson, "Hardiman I prototype for machine augmentation of human strength and endurance: Final report," General Electric Company, Schenectady, NY, GE Tech. Rep. S-71-1056, 1971.

[30] C. Chu, "Passive Exoskeleton". United States Patent 7,445,138 B2, 4 Nov 2008.

[31] U. Dallas, "Walking in Graphs," [Online]. Available: http://www.utdallas.edu/atec/midori/Handouts/walkingGraphs.htm. [Accessed 1 April 2015].

An Empirical Model for Forced Convection Condensation on Horizontal Integral Fin Tubes - Optimisation of Empirical Constants.

Z.H. Ong, Namasivayam. S, Briggs. A, Sivanesan. S

Taylor's Graduate School, School of Engineering, Taylor's University Lakeside Campus, 47500 Selangor, Malaysia
David.ong828@gmail.com

Abstract

A new theoretical approach on the development of semi-empirical model for forced convection condensation on integral fin tubes is presented in this paper. Most of the experimental data are extracted from previous researchers and the theoretical data are calculated with the enhanced version of the semi empirical model. Results for both theoretical and experimental were captured in a range of flowing pure vapour velocities up to 62 m/s for steam and 22 m/s for ethylene glycol and valid only for finned and smooth tubes with fin height from 0.5 to 1.6 mm, fin spacing from 0.25 to 2.0 mm, fin thickness 0.25 and 0.5 mm and inner diameter of 12.7 mm. The chosen semi-empirical model is enhanced by showing the improvement of correlation between theoretical and experimental data. The constants found in the semi-empirical model were tested in several stages which critically affected the correlation between theoretical and experimental data. Hence, a new method of enhancing the data correlation is presented in this research. This correlation includes the effect of gravity, surface tension and vapour shear on the vapour-side heat-transfer coefficient. Consequently, the semi empirical model is able to predict a majority of 2800 data points to within ±25%.
Keywords: Condensation, Finned tube, Heat transfer, Semi empirical model, Steam

1. Objective

The aim of this research is to improve the correlation of the semi empirical model by Namasivayam (2006) for forced convection condensation on integral fin-tubes by optimizing the empirical constants. Besides, a new method of enhancing the correlation will be introduced that include the effect of gravity, surface tension and vapour shear on the vapour-side heat transfer coefficient. Hence, the correlation outcome from the enhanced model has to be less than 32% of percentage difference which is only valid for finned and smooth tubes

with fin height from 0.5 to 1.6 mm, fin spacing from 0.25 to 2.0 mm, fin thickness 0.25 and 0.5 mm and inner diameter of 12.7 mm.

2. Introduction

The illustration of condensation heat transfer has generally been the essential component in a wide range of engineering applications such as refrigeration, air conditioning and power generation. Heat transfer for laminar film condensation of pure vapours on solid surfaces such as vertical and horizontal plates and horizontal tubes can be categorized into two different manners such as dropwise and filmwise. Vapour-side, heat-transfer coefficients are much higher for dropwise condensation than for filmwise but dropwise condensation is difficult to maintain for long periods because it contains higher density than filmwise that tend to drop away into liquid form while filmwise remains. Due to the fact that it is easier to maintain and achieved through a wide range of fluids, condensers are designed to operate under filmwise conditions. However, there are some cases where both manners can occur on different parts of the same surface.

The idea of fin tubes in enhancing the heat transfer coefficient is well established and available commercially nowadays such as in shell and tube heat exchanger. Tube surfaces are enhanced with added extra surfaces in order to improve vapour-side heat transfer coefficient that can be predicted for vertical and horizontal plates and horizontal tubes for free convection condensation and forced convection condensation. The model by Namasivayam (2006) developed for condensation on nine single horizontal integral-fin tubes with high vapour velocities is able to predict a majority of 2800 data points with inclusion of wide range of heat fluxes, vapour velocities, test fluids and tube geometries to within ±25% and a percentage difference of 32%. The resulting correlation from the theoretical and experimental data has the potential to be enhanced by manipulating the empirical constants of the model, thus allowing a prediction of 2800 data points with a percentage difference lesser than 32%.

3. Theoretical Studies

Four relating theoretical models will be reviewed in this section in line sequence which includes the models of Namasivayam (2006), Cavallini *et al*. (2006) and Briggs and Rose (2009).

Nusselt (1916) was the first investigator to develop the theory of condensation heat transfer. In free convection condensation, two heat transfer models were generated for a vertical flat plate and for a horizontal tube. The models shown below are formed with uniform vapour-side, temperature difference and by neglecting inertia, pressure gradient and convection in the condensate film and shear stress at the condensate surface.

For a vertical flat plate,

$$Nu_{\mathrm{L}} = 0.943\left[\frac{\rho(\rho-\rho_{\mathrm{v}})gh_{\mathrm{fg}}L^3}{\mu k\Delta T}\right]^{0.25} \quad (1)$$

and for a horizontal tube,

$$Nu_{\mathrm{d}} = 0.728\left[\frac{\rho(\rho-\rho_{\mathrm{v}})gh_{\mathrm{fg}}d^3}{\mu k\Delta T}\right]^{0.25} \quad (2)$$

In forced convection condensation, the vapour approach velocity is sufficiently high enough to create shear stress to thin the condensate film leading to a decrease in vapour-side resistance and enhanced heat transfer.

Nomenclature, Namasivayam (2006)

A_{d}	outside surface area of smooth tube with diameter d	q	heat flux on outside of test tube
A_{f}	surface area of fin flanks	q_{flank}	heat flux to fin flank in unflooded part of tube
A_{finned}	constant in Equation 6.4	q_{finned}	heat flux for finned tube
A_{i}	smooth tube inside surface heat-transfer area with inside diameter, d_{i}	q_{tip}	heat flux to fin tip
A_{o}	smooth tube outside surface heat-transfer area with fin root diameter, d_{o}	s	fin spacing at fin root
A_{plain}	constant in Equation 6.4	t	fin thickness at fin tip
A_{r}	surface area of interfin spacing	$\overline{U}_{\mathrm{flank}}$	effective vapour velocity at the fin flank
A_{s}	surface area associated with half fin channel	$\overline{U}_{\mathrm{root}}$	effective vapour velocity at the fin base/root
A_{t}	surface area of fin tip	$\overline{U}_{\mathrm{tip}}$	effective vapour velocity at the fin tip
A_{ts}	cross sectional area of test section	β	fin tip half-angle
A_1	smooth tube surface heat-transfer area with diameter, d_1	ΔT	temperature difference across the condensate film
B	fin spacing at fin tip		
c_P	specific isobaric heat capacity of condensate	ϕ_{f}	condensate retention angle / flooding angle measured from the top of a horizontal finned tube
D	diameter of smooth tube or fin root diameter of finned tube	ε	heat-transfer enhancement ratio, heat flux for finned tube based on fin root diameter divided by

d_i	inside tube diameter	heat flux for smooth tube with same fin root
d_o	fin tip diameter of finned tube	diameter, at same vapour-side temperature
d_1	$(d_o+d)/2$	difference and vapour velocity
F	dimensionless parameter, $(\mu g d h_{fg}/kU_v^2\Delta T)$	
f_f	proportions of the fin flank covered by retained liquid	
f_s	proportions of the fin root covered by retained liquid	
f_x	component of gravity acting in the x-direction	
G	dimensionless parameter, $(k\Delta T/\mu h_{fg})\ (\rho\mu/\rho_v\mu_v)^{0.5}$	
g	specific force of gravity	
h	fin height	
h_v	mean vertical fin height as define by Rose (1994)	
k	thermal conductivity of condensate	
K	constant in Equation ???	
L	length of flat plate	
Nu	vapour-side Nusselt number	
n	constant in Equation 3	
Q	total heat-transfer rate	

The effect of forced-convection condensation of a pure vapour on horizontal smooth tube or fin tube has been studied extensively theoretically and experimentally. Namasivayam (2006) proposed a model similar to that used by Cavallini *et al*. (1996) that includes both the free and forced convection conditions and is shown below.

$$Nu = (Nu_{g\sigma}{}^{n} + Nu_{u}{}^{n})^{\frac{1}{n}} \tag{3}$$

In Equation 3 above, $Nu_{g\sigma}$ represents the Nusselt number for condensation on fin tubes under free-convection conditions where the effects of vapour shear are insignificant and Nu_u represents the Nusselt number for condensation on fin tubes under forced-convection conditions where vapour shear dominates gravity and surface tension.

The effect of vapour shear towards the condensate in between fins may lead to a decrease in the amount of retained condensate at very high vapour velocity. The decrease of condensate amount provided additional surface area for heat transfer which increased the enhancement ratio when vapour velocity increase. The heat transfer rate to the whole tube can be calculated from the relevant heat fluxes and surface areas on different section of the tubes with suitable corrections for condensate retention. This yielded the following results.

$$Q = C_1\pi d_o t q_{tip} + \frac{\phi_f}{\pi}\left(C_2(1-f_f)\frac{\pi\left(d_o{}^2 - d^2\right)}{2} q_{flank} + C_3(1-f_s)\pi b d q_{root} \right) \tag{4}$$

Where C_1, C_2 and C_3 are the empirical constants which are valued of 1, 0.41 and 0.41 respectively giving a percentage difference for all the data within 32%.

Cavallini. *et al* (2006) presented a method to determine the heat transfer coefficient of fluids flowing into horizontal smooth tubes with internal diameters above 3 mm. This method has been proposed as simply as possible and is ready to use in heat exchanger modeling and design applications. A more emphasized on the accuracy, the model has been tested over a wide range of experimental database with reduced experimental uncertainties. To obtain an easy structure, only two equations are included respectively which are related to the ΔT – independent and to ΔT - dependent fluid flows.

Nomenclature, Cavallini. *et al* (2006)

α	Heat Transfer Coefficient, $Wm^{-2}K^{-1}$
x	Thermodynamic vapor quality
ρ	Density, $kg\ m^{-3}$
μ	Dynamic viscosity, $kg\ m^{-1}s^{-1}$
Pr	Prandtl Number, $=\mu\ c_p/\lambda$
J_G	$xG/[gD\rho_G(\rho_L-\rho_G)]^{0.5}$
J_G^T	Transition dimensionless gas velocity
A	ΔT independent flow regime
D	ΔT dependent flow regime
LO	Liquid phase with total flow
$STRAT$	Fully stratified flow regime

Note that, all the parameters that influence the condensation heat transfer have been included. For ΔT-independent flow regime, the heat transfer coefficient α_A is;

$$\alpha_A = \alpha_{LO}[1 + 1.128x^{0.8170}(\rho_L/\rho_G)^{0.3685}(\mu_L/\mu_G)^{0.2363} \times (1-\mu_G/\mu_L)^{2.144}Pr_L^{-0.100}] \quad (5)$$

For ΔT-dependent flow regime, the heat transfer coefficient α_D is;

$$\alpha_D = [\alpha_A(J_G^T/J_G)^{0.8} - \alpha_{STRAT}](J_G/J_G^T) + \alpha_{STRAT} \quad (6)$$

The model has been developed from an extensive analysis of 425 experimental heat transfer data points. The structure allows to clearly pointing out the influence of the various parameters such as geometrical, thermodynamic and thermophysical. The model has been validated by compared to HCFCs, HFCs, HCs, carbon dioxide, ammonia, and water (pure fluids or near azeotropic mixtures) with a total number of 4471 data points. An average deviation of $e_R = +1\%$, an absolute mean deviation $e_{AB} = +15\%$, and a standard deviation $\sigma_N = 18\%$ are obtained from the comparisons. With the Bell and Ghaly (1973) correction,

the model also applied to zeotropic mixtures (HFC and HC fluids), resulting in a total of 1007 points in the deviations $e_R = +5\%$, $e_{AB} = +12\%$ and $\sigma_N = +19\%$.

Briggs and Rose (2009) presented a model for forced-convection condensation on integral-fin tubes. This model is compared to nearly 3000 data points for 18 tubes and 4 fluids with approach the combined effects of surface tension, vapour shear and gravity.

Nomenclature, Briggs and Rose (2009)

A,a	Empirical constants in equations 10 and 11	$\emptyset_{obs}$	Observed retention angle measured from top of tube
α	Vapor-side, heat transfer coefficient,$q/\Delta T$	*s*	Spacin between fins at fin root
α_0	Vapor-side, heat transfer coefficient for free convection	p	Pressure
α_v	Vapor-side, heat transfer coefficient for force convection	p	Fin pitch
α_{Nu}	Vapor-side, heat transfer coefficient calculated using Nusselt (1916) approach	*k*	Thermal conductivity
α_t	Vapor-side, heat transfer coefficient for fin tip	d_0	Diameter at fin tip
α_r	Vapor-side, heat transfer coefficient for fin root	*A,a*	Empirical constants
ε_0	Enhancement ratio for free convection	$\tilde{R}e_t$	Two-phase Reynolds number based on fin tip,
e_t^a		m	
e_r^a		*n*	Empirical constant in equation (7)
t	Fin thickness at fin tip	*h*	Radial fin height
d	Diameter of smooth tube or fin root diameter of finned tube		

The equation for vapour-side heat transfer coefficient is shown below.

$$\alpha = (\alpha_0^n + \alpha_v^n)^{1/n} \quad (7)$$

Where, $\alpha_0$is the heat-transfer coefficient for stationary vapour and can be calculated by equation as shown below

$$\alpha_0 = \varepsilon_0 \alpha_{Nu} \quad (8)$$

ε_0 is found from the model of Rose (1994) but with observed flooding angle and $\alpha_{Nu}$is the heat transfer coefficient for a plain tube (with fin-root diameter) calculated using Nusselt (1916) model.

On the other hand,α_v is the heat transfer coefficient for forced convection.

$$\alpha_v = \alpha_t \left(\frac{t}{p}\right)\left(\frac{d_0}{d}\right) + \alpha_r \left(\frac{\emptyset_{obs}}{\pi}\right)\left(\frac{s}{p}\right) \quad (9)$$

Where

$$\alpha_r = \left(\frac{k}{d_0}\right) A\tilde{R}e_t^a \,, \tag{10}$$

$$\alpha_r = \left(\frac{k}{d}\right)\left(1 - exp\left(-\left(\frac{s}{h}\right)^m\right)\right) A\tilde{R}e_r^a, \tag{11}$$

In the equations, $\tilde{R}e_t$ and $\tilde{R}e_r$ are the two-phase Reynolds numbers based on the fin tip and fin root diameters respectively. Equations (12 and 13) are based on the model by Shekriladze and Gomelauri (1966) for forced-convection condensation. The term $\left(1 - exp\left(-\left(\frac{s}{h}\right)^m\right)\right)$ in equation 14 consider the reduced effect of vapour shear at the fin root. For positive values of m, tends to unity and zero for large and small values of *s/h*, respectively. The model contains 4 empirical constants which are namely m, A, n, and a. These constants can be found by minimizing the sum of squares of residuals in heat transfer coefficients. However, the empirical correlation from the model is not satisfactory and is obeyed only for data that is used to determine the constants. The correlations for refrigerants are not good enough but it gives satisfactory agreement with data for steam.

4. Experimental Studies

A total of four relevant condensation experimental works have reviewed in this section. Murase *et al*. (2005) presented a method to measure the effect of inundation during condensation of steam in tube banks. This experimental study included the results from enhanced wire-wrapped tubes, smooth tubes and finned tubes.

Artificial inundation has been used where liquid is supplied above a single horizontal test condenser tube to simulate condensate draining from higher tubes. All the tests were carried out at atmospheric pressure with constant vapour velocity and constant coolant flow rate.

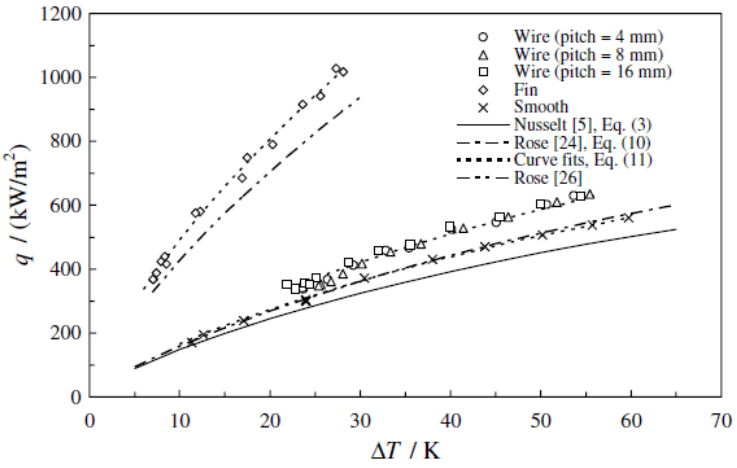

Figure 3: Dependence of heat flux on vapour-to-surface temperature difference without inundation.

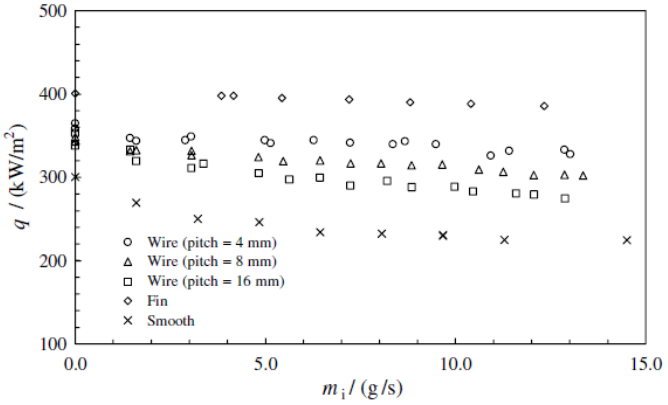

Figure 4: Dependence of heat flux on inundation rate.

The best enhancement (ratio of heat transfer coefficient for finned tube divided by that for smooth tube at the same coolant flow rate and would depend on the coolant flow rate used) was found for the low-finned tube with the enhancement ratio of 4. The enhancement ratio was found for wire-wrapped tube is only around 1.3 and almost similar for the three winding pitches tested. While for inundation, the finned tube was found the best performance tube with heat-transfer coefficient virtually unaffected up to the highest inundation rate used, equivalent to a depth of around 20 tubes in a bank. For wire-wrapped tubes, the inundation performance increased with decreasing winding pitch. The heat transfer coefficient for the tube with smallest winding pitch was around 50% higher than that for smooth tube at the highest inundation rate.

Fitzgerald. *et al*. (2010) had conducted an experimental work for forced-convection filmwise condensation of ethylene glycol flowing vertically downward over two single horizontal instrumented integral fin tubes and one plain tube. Both tubes have fin height of 1.6 mm and fin root diameter 12.7 mm, with fin thickness and spacings of 0.3 mm and 0.6 mm, respectively for one of the tubes and 0.5 mm and 1 mm, respectively for the other.

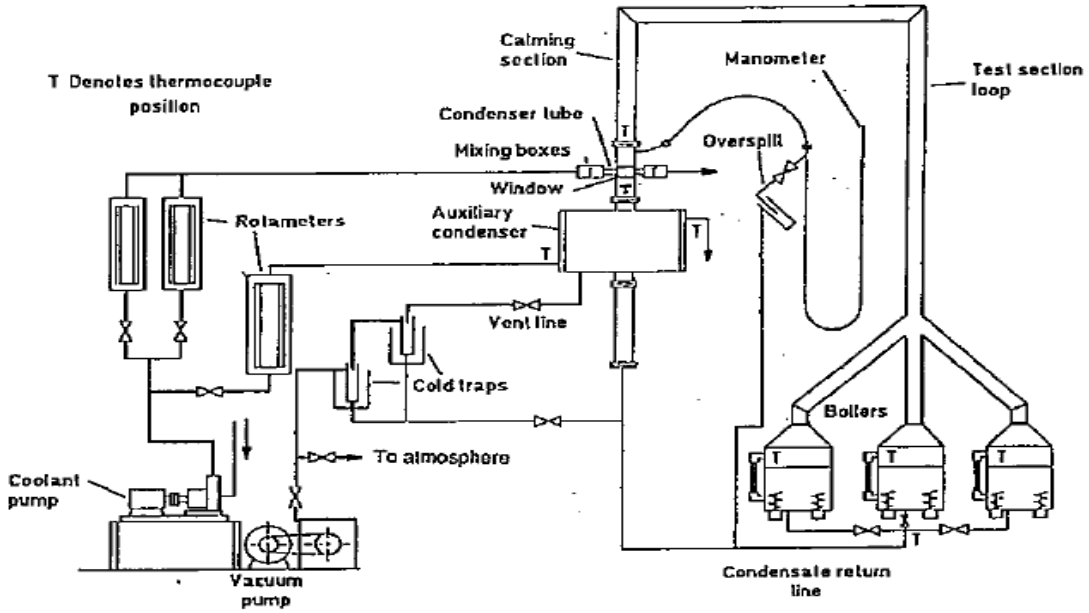

Figure 5: Experimental apparatus (Fitzgerald. *et al*. (2010))

A stainless steel closed loop condensation test rig is illustrated in Figure 5. The generated vapour by three electrical boilers flow vertically downwards through a calming section before approaching the condenser tube test section. Excessive vapour in the test section will flow to an auxiliary condenser that the condensate will return to the boiler by gravity. A circular glass viewing port attached at the test section for observation purpose.

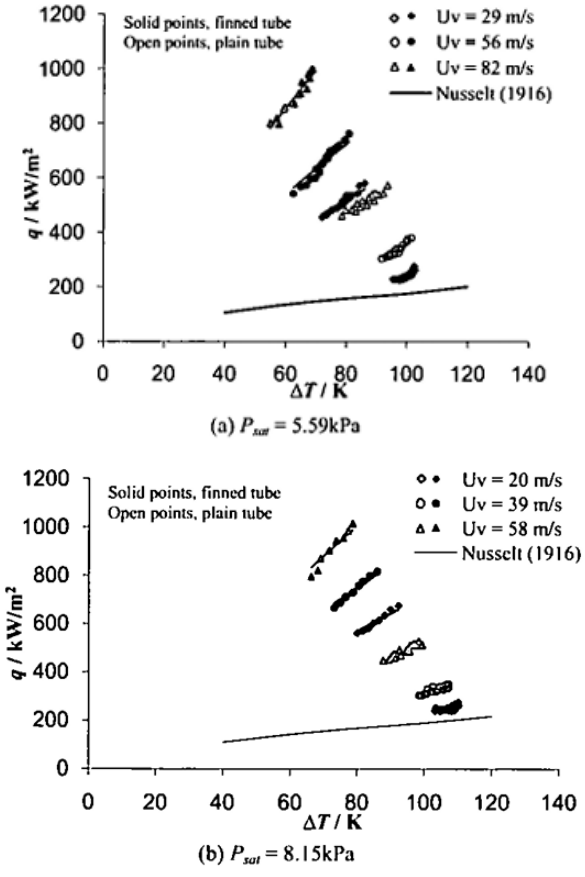

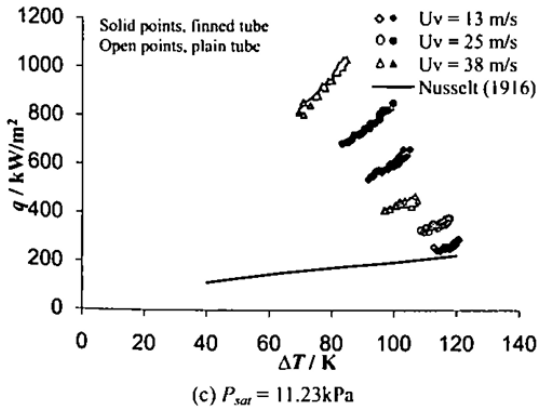

Figure 6: Variation of heat flux with vapour-side temperature difference integral-fin tubes (s=0.6 mm, *t* = 0.3 mm, *h* = 1.6 mm, dr = 12.7 mm) and plain tube.

The experimental result shows the enhanced effect of the vapour shear on the vapour-side heat transfer coefficient. Vapour velocity enhanced the finned tube more than the plain tube. Hence, the enhancement ratios decreased as vapour velocity increases. The retention angle moves from its original position as predicted by the Honda theory and becomes asymptotic at around 90 degree angle as vapour velocity is increased.

Another condensation experiment on horizontal fin tubes was simulated by Fitzgerald. *et al.* (2011). The simulation was conducted with three different testing liquids (water, ethylene glycol and R113) that was supplied to the tube with small holes (see figure 7) between fins along the top generator of the tubes.

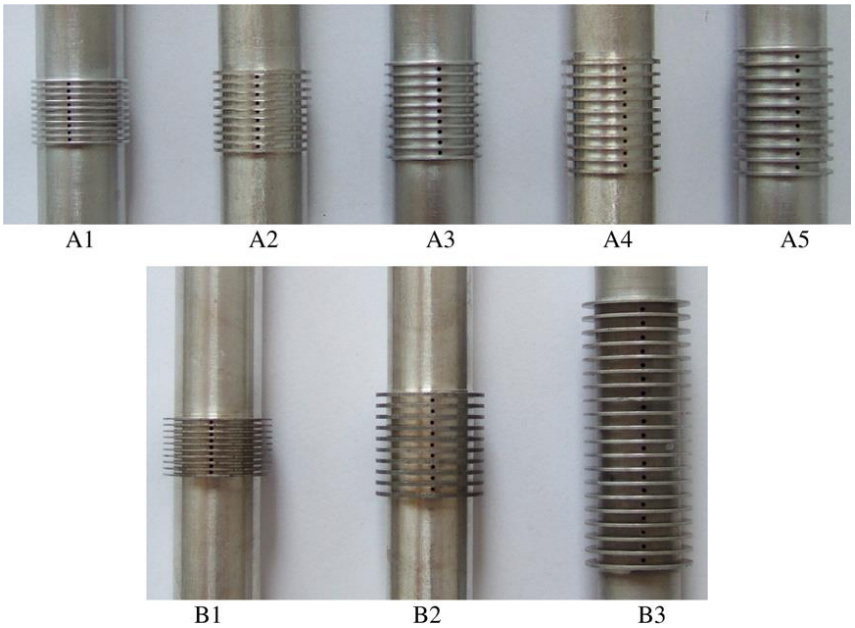

Figure 7: Finned tubes for simulated condensation measurements. (Fitzgerald. *et al.* (2011))

Eight different fin dimension tubes with a range of fin heights 0.8 and 1.6 mm and fin spacings 0.5 to 1.5 mm. All the tubes had fin root diameter 12.7 mm and fin thickness of 0.5

mm except one which had 0.3 mm. were tested in this experiment. One end of the tube was connected to a fluid reservoir with a flexible tube and a valve to control the flow rate. A plane Perspex window was located in the tunnel wall opposite the test tube for visual and photographic observation purpose to determine the retention angle.

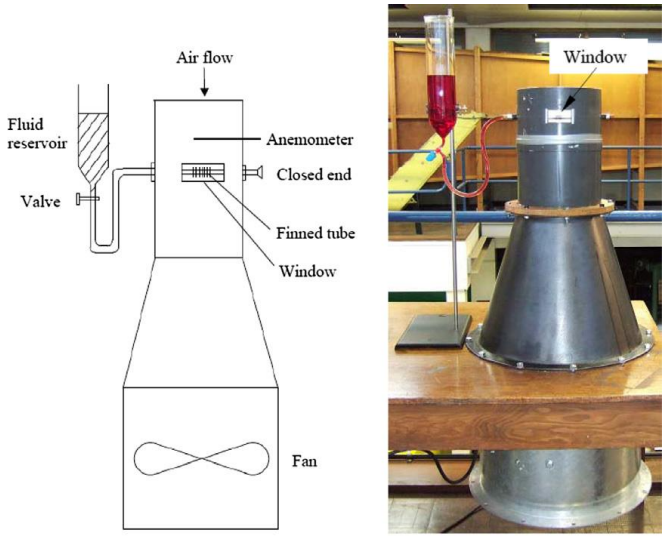

(a) Schematic of the rig (b) Photo of the rig

Figure 8: Schematic diagram and photo of the apparatus for simulated condensation experiment. Fitzgerald. *et al.* (2011)

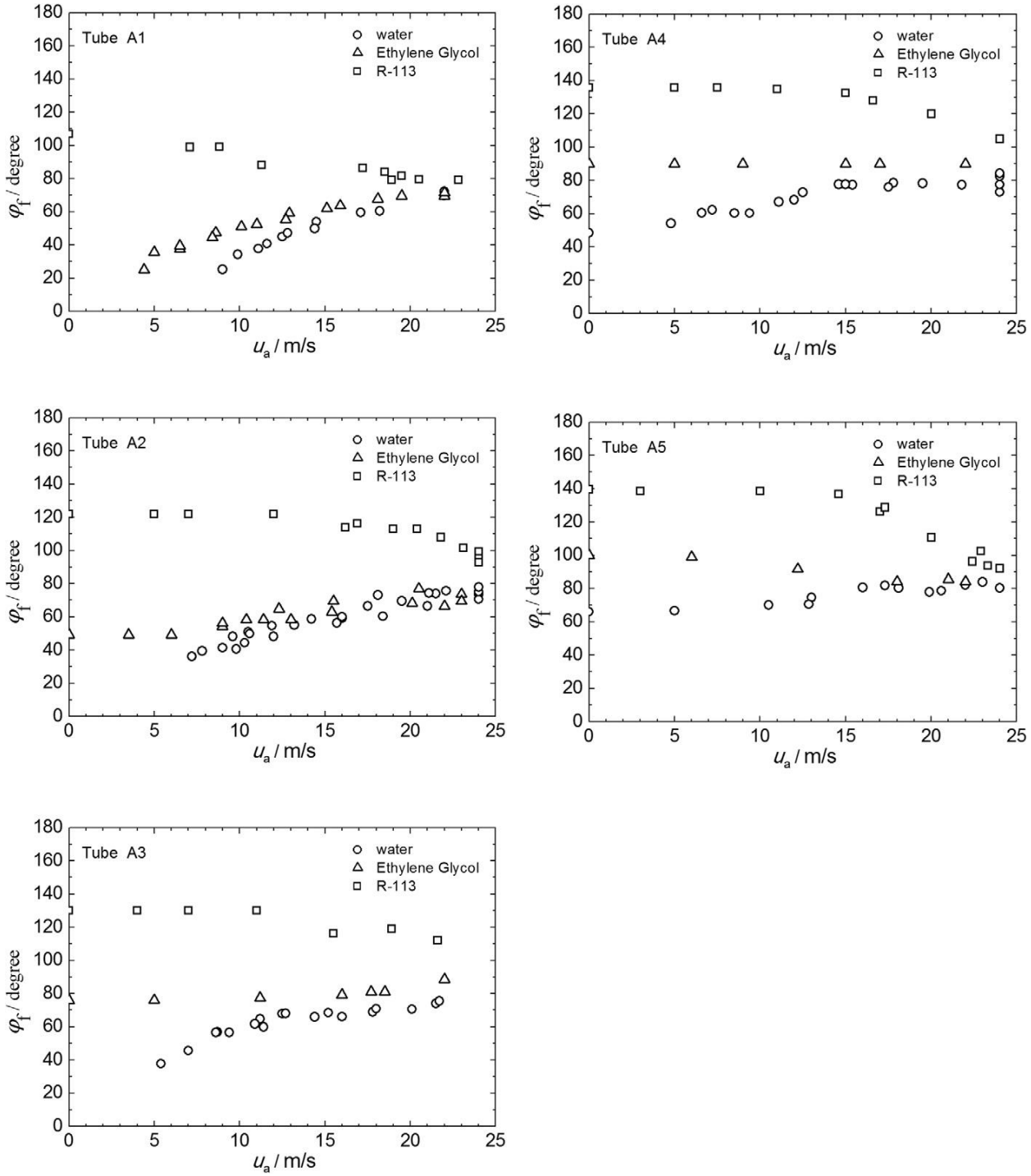

Figure 9: Retention angle against air velocity for tubes A1-A5.

The retention angle at zero air velocity is less than about 90 degree and increases with increasing velocity. Conversely, the retention angle at zero air velocity is greater than about 90 degree falls progressively with increasing air velocity. For all the cases, the retention angle approached a value of around 80 to 90 degrees with increasing air velocity. In the case of quiescent vapour the retention angle is determined by a balance of the surface tension pressure drop across the meniscus of the retained condensate and the gravity force on retained

liquid column which can be readily calculated with well of accuracy. However, in the presence of significant vapour velocity and consequent shear stress on the liquid surface the problem is affected both by the pressure variation around the tube and distortion of the meniscus.

Ali and Ali (2014) presented a semi empirical correlation on condensate retention on horizontal integral fin tubes with the effect of vapour velocity.

Nomenclature

A	Constant in equation 13	d_i	Internal diameter of tube
a	Constant in equation 13	ϕ_f	Condensate retention angle
b	Constant in equation 13	σ	Surface tension of condensate
c	Constant in equation 13	ρ_c	Density of condensate
v	Velocity of air	ρ_a	Density of air
s	Fin spacing		
t	Fin thickness		
h	Fin height		
g	Force of gravity		
R_o	Fin tip radius		
d_o	Fin tip diameter		
d_r	Fin root diameter		

Three different testing fluids (water, ethylene glycol and R-141b) were used in the condensation simulation in a vertical wind tunnel. Eight tubes of different dimensions were used with fixed fin root diameter and internal diameter of tubes which kept at 12.7 mm and 8.0 mm respectively.

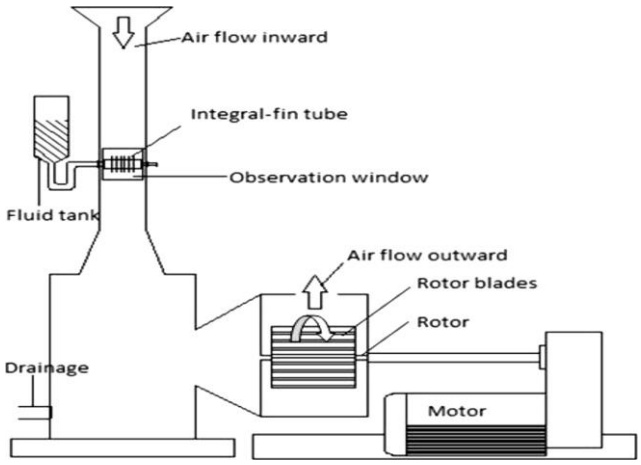

Figure 10: Schematic of experimental apparatus.

In the experiment, the retention angle is a strong function of fluid properties, geometric properties and vapour Reynolds number, as retention angle increase with increased vapour Reynolds number for fluids which have higher surface tension. On the other hand, retention

angle decreases with increasing vapour Reynolds number for fluids which have lower surface tension (i.e. refrigerants).

The average vertical height of condensate retention during free convection condensation from the bottom of the tube is the function of the geometric and fluid properties and also including the effect of vapour velocity on the condensate retention where shown below.

$$H_{avg} = f(v, \sigma, p_c, p_a, g, s) \quad (12)$$

By applying dimensional analysis ;

$$H_{avg} = A \times s \times \left(\frac{\sigma}{v^2 s p_c}\right)^a \times \left(\frac{sg}{v^2}\right)^b \times \left(\frac{p_a}{p_c}\right)^c \quad (13)$$

Where, A, a, b and c are the semi-empirical constants which can be found by minimizing the sum of square of residuals. The retention angle is then can be calculated by,

$$\emptyset_f = \cos^{-1}\left[\frac{1}{R_0}\left\{A \times s \times \left(\frac{\sigma}{v^2 s p_c}\right)^a \times \left(\frac{sg}{v^2}\right)^b \times \left(\frac{p_a}{p_c}\right)^c\right\} - 1\right] \quad (14)$$

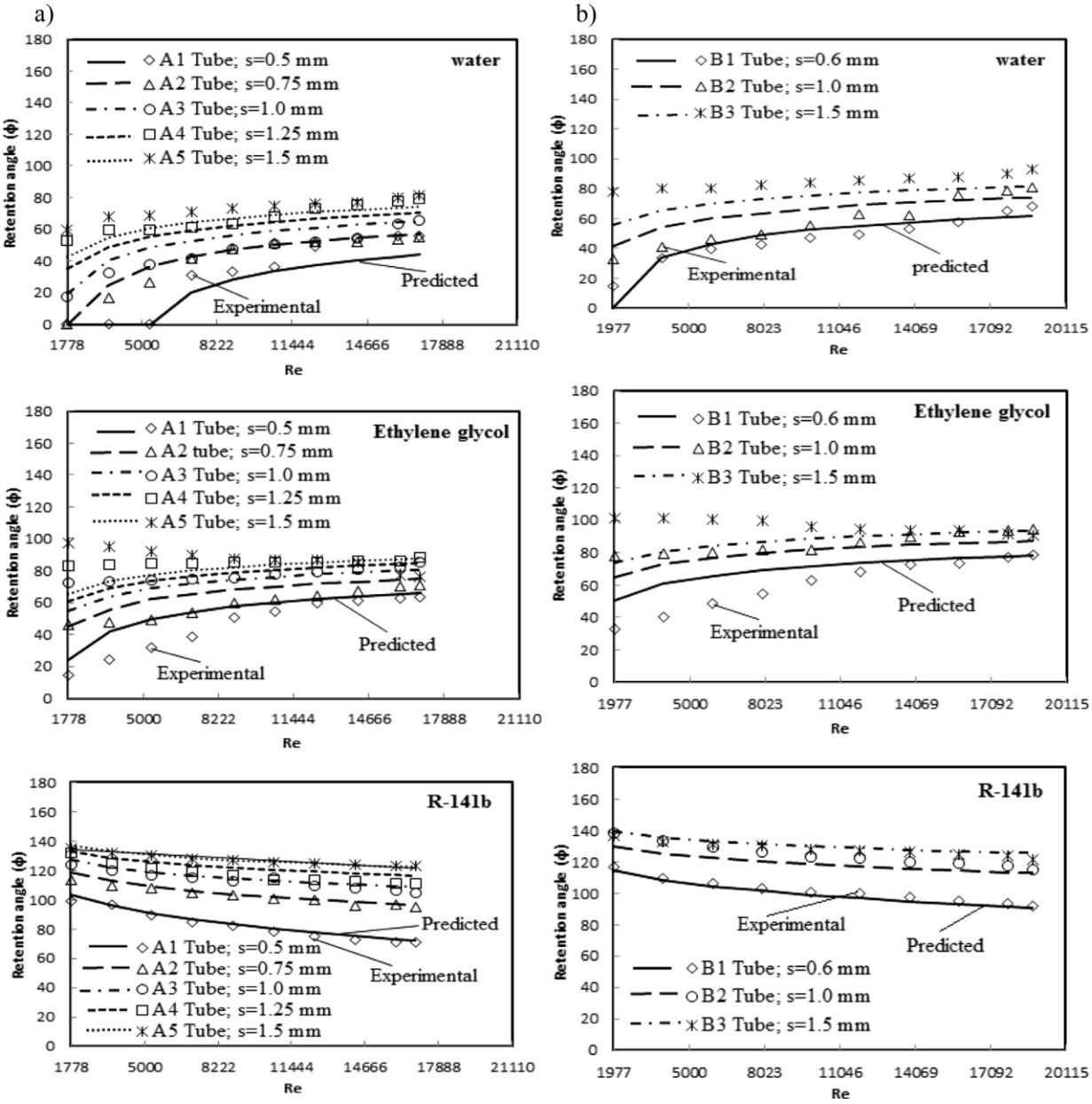

Figure 11: Comparison of experimental and predicted results.

The semi empirical model showed an excellent agreement with the experimental data. For water and ethylene glycol, 90% of the data calculated experimentally fluctuated within a range of 15% when compared to theoretical valve. The fare rate of fluctuation was found for R-141b. The model also showed very good agreement with the experimental data produced by Fitzgerald. *et al* for water and ethylene glycol. Most of the data agreed with theoretical valves to within a rate of $\pm$20% and for R-113 to within $\pm$5%.

5. Optimization of model

The semi empirical model of Namasivayam (2006) is the main model to be rectified and enhanced in this research. Outcomes of the comparison between theoretical and experimental values by the model have been well accepted. However, this outcome can be further improved by optimizing the model empirical constant values in equation 20. In this investigation, Nu_{calc} indicated as the theoretical model which proposed by Namasivayam (2006) and $Nu_{\exp}$ is the experimental model that followed the basic of Nusselt number for a cylindrical object. The temperature difference and heat flux values are extracted from the previous experimental works done by Namasivayam (2006) and both models required the same temperature difference and heat flux values in order to facilitate comparisons.

$$Nu_{calc} = (Nu_{g\sigma}{}^{n} + Nu_{u}{}^{n})^{\frac{1}{n}} \tag{15}$$

Where,

$$Nu_{g\sigma} = (\varepsilon).Nu_{\text{smooth}} \tag{16}$$

And

$$\varepsilon = \left[\begin{array}{l} \dfrac{d_0}{d}\dfrac{t}{b+t}\left\{\dfrac{d}{d_0} + \dfrac{0.143\sigma d}{0.728^4\,\tilde{p}gt^3}\right\}^{0.25} \\ + \left(\dfrac{\phi_f}{\pi}\right)\dfrac{1-f_f}{\cos\beta}\left\{\dfrac{d_0{}^2 - d^2}{2d(b+t)}\right\}\left\{\dfrac{\left(\dfrac{0.943}{0.728}\right)^4\dfrac{d}{h_v} + }{\dfrac{0.143\sigma d}{0.728^4\,\tilde{\rho}gh^3}}\right\}^{0.25} \\ + \left(\dfrac{\phi_f}{\pi}\right)(1-f_s)2.97\dfrac{s}{b+t}\left\{\dfrac{(\xi(\phi_f))^3}{0.728^4} + \dfrac{0.143\sigma d}{0.728^4\,\tilde{\rho}gs^3}\right\}^{0.25} \end{array} \right] \tag{17}$$

Where,

$$\begin{aligned} \xi(\phi_f) &= 0.874 + 0.1991\times10^{-2}\phi_f - 0.2642\times10^{-1}\phi_f{}^2 \\ &+ 0.5530\times10^{-2}\phi_f{}^3 - 0.1363\times10^{-2}\phi_f{}^4 \end{aligned} \tag{18}$$

$$\phi_{\mathrm{f}} = \cos^{-1}\left(\frac{4\sigma}{\rho g s d_{\mathrm{o}}}(1-\psi)-1\right) \text{ for } s < 2h \tag{19}$$

Where,

$$\psi = K\left(\frac{\rho_{\mathrm{v}} U_{\mathrm{v}}{}^{2}}{\rho g s}\right)^{m} \tag{20}$$

And Nu_{smooth} is found from the Nusselt (1996) model as follows.

$$Nu_{\mathrm{smooth}} = 0.728\left[\frac{\rho(\rho-\rho_{\mathrm{v}})g h_{\mathrm{fg}} d^{3}}{\mu k \Delta T}\right]^{0.25} \tag{21}$$

Equation 16 as shown above represents the free convection condition in the model where vapour velocities are neglected. Conversely for forced convection condition, the equation included the effect of vapour velocities and is shown below in equation (19).

$$Nu_{\mathrm{u}} = \frac{qd}{k\Delta T} = \frac{Q}{\pi(s+t)k\Delta T} \tag{22}$$

Where,

$$Q = C_1 \pi d_{\mathrm{o}} t q_{\mathrm{tip}} + \frac{\phi_{\mathrm{f}}}{\pi}\left(C_2(1-f_{\mathrm{f}})\frac{\pi\left(d_{\mathrm{o}}{}^{2}-d^{2}\right)}{2} q_{\mathrm{flank}} + C_3(1-f_{\mathrm{s}})\pi b d q_{\mathrm{root}}\right) \tag{23}$$

Equation proposed above indicated the heat transfer rate to the whole fin tube with the concern of heat flux, flooding angle and the proportion in each condensation area.
For the fin flank flooding proportion,

$$f_{\mathrm{f}} = \frac{1-\tan(\beta/2)}{1+\tan(\beta/2)} \cdot \frac{2\sigma\cos(\beta)\tan(\phi_{\mathrm{f}}/2)}{\rho g d h \phi_{\mathrm{f}}} \tag{24}$$

and the fin root flooding proportion,

$$f_s = \frac{1-\tan(\beta/2)}{1+\tan(\beta/2)} \cdot \frac{4\sigma\tan(\phi_f/2)}{\rho g d s \phi_f} \quad (25)$$

For heat flux on fin tip,

$$q_{tip} = \left[\frac{0.9^2 \rho k^2 \Delta T^2 \overline{U}_{tip}}{\mu d_o}\right]^{\frac{1}{2}} \quad (26)$$

In the present case for the fin tip, since

$$\overline{U}_{tip} = U_\infty \quad (27)$$

For heat flux on fin root,

$$q_{root} = \left[\frac{\rho k^2 \Delta T^2 \beta(\phi_f)\overline{U}_{root}}{\mu d}\right]^{\frac{1}{2}} \quad (28)$$

where,

$(\square_f) = 1.4177+0.0172\square_f - 0.0477\square_f^2$ (29)

and the effective vapour velocity at fin root $\overline{U}_{root}$ is,

$$\overline{U}_{root} = U_\infty\left(1-\exp\left(-\left(\frac{s}{h}\right)\right)\right) \quad (30)$$

in this case, $\overline{U}_{root} \to U_\infty$ for large values of *s/h* and $\overline{U}_{root} \to 0$ for small values of s/*h*.

For heat flux on fin flank,

$$q_{\text{flank}} = \left[\frac{2\rho k^2 \Delta T^2 \overline{U}_{\text{flank}}}{\mu d_o \phi_f} \right]^{\frac{1}{2}} \quad (31)$$

For this case,

$$\overline{U}_{\text{flank}} = \left(\overline{U}_{\text{tip}} + \overline{U}_{\text{root}}\right)/2 \quad (32)$$

On the other hand, experimental results are predicted in a basic way by assuming the heat transfer to a cylindrical object instead of a fin tube as shown below.

$$Nu_{\text{exp}} = \frac{qd}{k\Delta T} \quad (33)$$

Namasivayam (2006) found the empirical constant values for C1, C2 and C3 are 1, 0.41 and 0.41 respectively for all three testing fluids that gave a percentage difference for all the data to within 32%. At the beginning stage of the development, numerical test were made to enhance the correlation between Nusselt theoretical and experimental.

Comparing between Figures 12 and 13, results are largely improved from 48% to 7.8% of percentage differences which made by the changes of empirical constants in equation 7. The finalized values for C1, C2 and C3 are 0.4, 4 and 1.81 respectively for steam at near atmospheric pressure. The other two test results for steam at low pressure and ethylene glycol were also be tested in this development. The improvement of percentage differences shown well from 54.8% to 26.8% for steam at low pressure with finalized empirical constant values of C1=0.53, C2=2.17 and C3=2.44. On the other hand, the finalized C1, C2 and C3 gave very minor improvement on ethylene glycol at low pressure from 22.6% to 21.9% with values 0.04, 0.77 and 0.06 respectively.

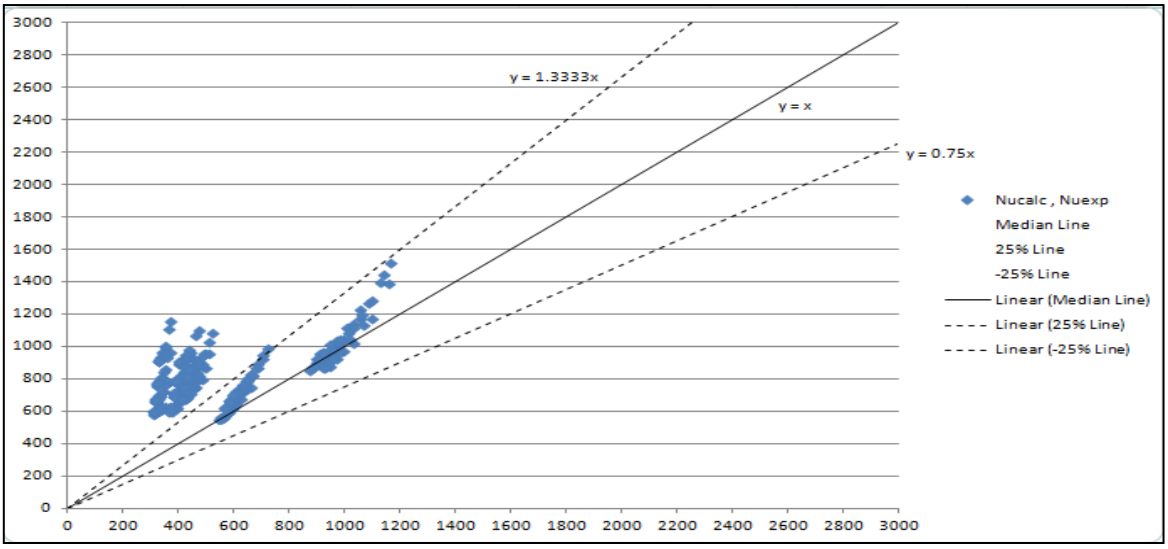

Figure 12: Nusselt experimental vs Nusselt calculated for steam at near atmospheric pressure (Model of Namasivayam. S (2006)).

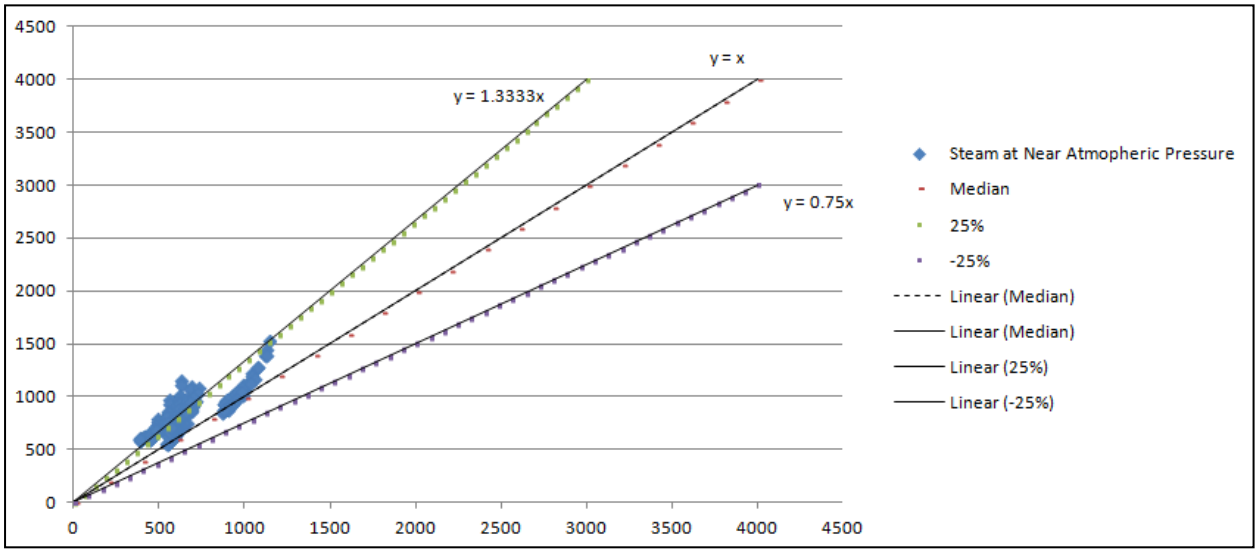

Figure 13: Nusselt experimental vs Nusselt calculated for steam at near atmospheric pressure (Current investigation)

The finalized empirical constant values for each testing fluid are found by numerical test in various different combinations in several sections in order to determine the best or lowest percentage differences in the heat transfer analysis. The finalized C1, C2 and C3 values are presented below.

Table 14: The finalized empirical constant values for each testing fluids.

Steam at atmospheric pressure				
C1	C2	C3	Std. Dev	Overall % Diff
1	0.41	0.41	243.258483	43.09207668
0.4	4	1.81	169.3822206	8.173122185
Steam at low pressure				
C1	C2	C3	Std. Dev	Overall % Diff
1	0.41	0.41	332.821876	54.83255767
0.53	2.17	2.44	253.5903084	26.7862015
Ethylene glycol at low pressure				
C1	C2	C3	Std. Dev	Overall % Diff
1	0.41	0.41	106.5070446	22.65720928
0.04	0.77	0.06	100.3411049	21.88616545

The results from the summary above shown well improvement for steam at near atmospheric pressure and low pressure. However, for the ethylene glycol at low pressure the improvement shown very mild with only from 22.7% to 21.9%. In general, this can be concluded that this strategy of improving the correlation between Nusselt theoretical and Nusselt is in the right track. The empirical constant values somehow needed to be tested again with similar method in order to determine the overall best values of C1, C2 and C3 that fit into these three testing fluid. The values and graphical analysis are shown below in table 15 and figures (16 & 17) accordingly.

Table 15: The finalized empirical constant values applicable for all three testing fluids.

	Namasivayam (2006)	Current Investigation
C_1	1	0.37
C_2	0.41	2.32
C_3	0.41	1.7
Average Std Dev	153.58	125.24
Overall % Difference	31.40	23.38

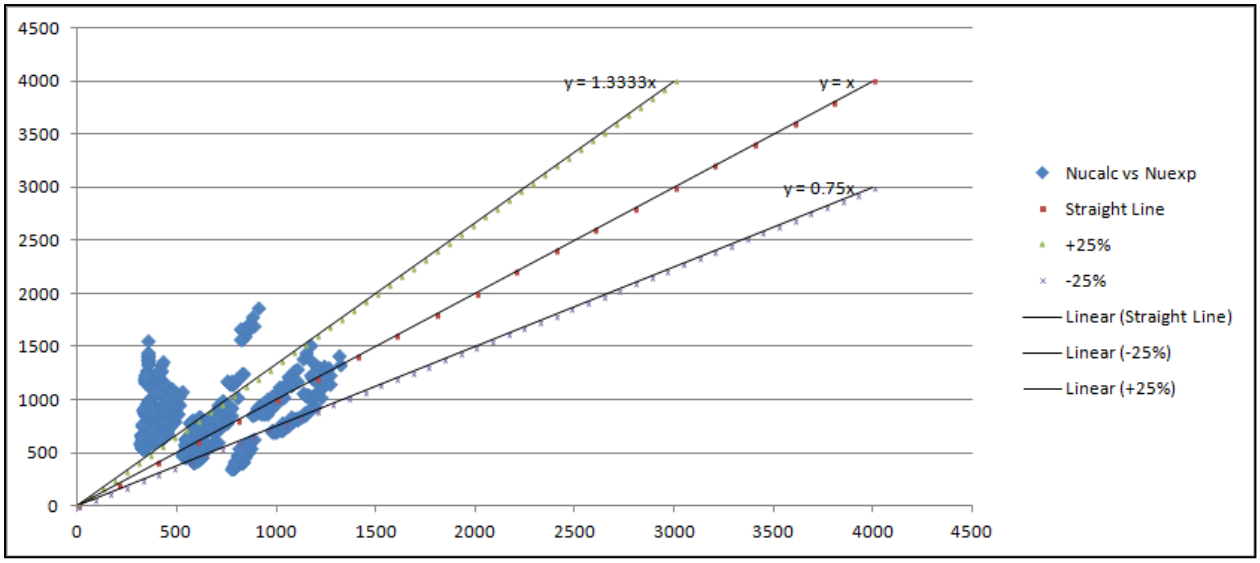

Figure 16: Nusselt experimental vs Nusselt calculated (Model of Namasivayam. S (2006)).

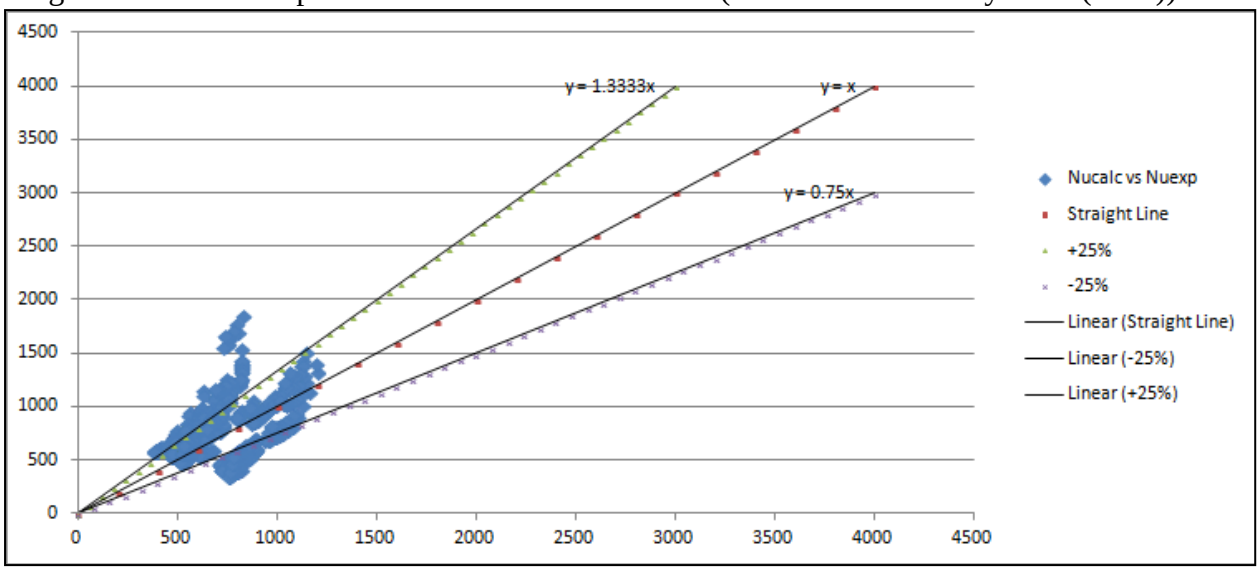

Figure 17: Nusselt experimental vs Nusselt calculated (Current investigation).

Conclusion:

New developed empirical constants are presented for forced-convection condensation on integral-fin tubes for steam at near atmospheric pressure, steam at low pressure and ethylene glycol at low pressure. Relevant studies have been revised and referred which are very supportive for this research. Both theoretical and experimental methods by previous researchers are very similar. The model by Namasivayam (2006) shown better potential to be enhanced which can be done directly through a series of testing. The results from the beginning stage of test showed promising improvement for the correlation that between

theoretical and experimental and validation of the model improvement method. Furthermore, the finalized empirical constant values for all three testing fluids have been done and presented as well. The values of C1, C2 and C3 were determined are 0.37, 2.32 and 1.7 respectively provided the improvement of percentage difference from 31% to 23% in the comparison of theoretical and experimental heat transfer analysis.

The percentage difference showed the agreement level between theoretical and experimental works. Hence, the lower percentage differences the better agreement. This is a good introduction for academic and engineering industries that work on fin tube condensation condition in optional way.

References:

Ali. H. M., and Ali. A., (2014) *Measurement and semi empirical correlation for condensate retention on horizontal integral-fin tubes: Effect of vapour velocity,* Applied Thermal Engineering 71, 24-33.

Al-Badri. A. R., Gebauer. T., Leipertz. A., and Fröba. A. P., (2013) *Element by element prediction model of condensation heat transfer on a horizontal integral finned tube, International Journal of Heat and Mass Transfer 62,* 463-472

Bell. K. J., and Ghaly. M. A., (1973) *An Approximation Generalized Design Method for Multicomponent/Partial Condenser, A1ChE Symp. Ser*., vol. 69, pp. 72-79.

Cavallini. A, Doretti. L, Longo.G.A, Rossetto. L, A., (1996) *New Model for Forced-Convection Condensation on Integral-Fin Tubes, Trans*. ASME J. Heat Transfer 118, 689-693.

Cavallini. A, Del.C. D, Doretti. L, Matkovic. M, Rossetto. L, Zilio. C., (2006) *Condensation in Horizontal Smooth Tubes: A New Heat Transfer Model for Heat Exchanger Design, Heat Transfer Engineering, 27(8), 31-38.*

Fitzgerald. C. L., Briggs. A., Rose. J. W., and Wang. H., (2011) *Effect of Vapour velocity on condensate retention between Fins during condensation on low-finned tubes, International Journal of Heat and Mass Transfer 55*, 1412-1418

Fitzgerald. C. L., Briggs. A., Rose. J. W., and Wang. H., (2010) *Effect of Vapour Velocity on Condensation of Ethylene Glycol on Horizontal Integral Fin Tubes: Heat Transfer and Retention Angle Measurements, Proc.* ASME International Heat Transfer Conference 14th, 89-96.

Murase. T., Wang. H. S., and Rose. J. W., (2005*) Effect of inundation for condensation of steam on smooth and enhanced condenser tubes, International Journal of Heat and Mass Transfer 49*, 3180-3189.

Namasivayam. S., (2006) *Condensation on Single Horizontal Integral – Fin Tubes –Effect Of Vapour Velocity And Fin Geomerty*., Ph.D. Thesis, Univ of London.

Nusselt, W., (1916), *Die Oblerflachenkondensation des Wasserdampfes*, Z. Vereines Deutsch. Ing., 60, 541 - 546, 569 - 575.

Rose. J. W., and Briggs. A., (2009*) Condensation on Integral-Fin Tubes with Special Reference to Effects of Vapor Velocity*., Heat Transfer Research., vol. 40, 1, 57-78.

Rose, J. W., (1994) *An Approximate Equation for the Vapour-side Heat Transfer Coefficient for Condensation on Low Finned Tubes*., Int. J. Heat Mass Transfer, 37, 865-875.

Shekriladze, I. G. and Gomelauri, V. I., (1966) *Theoretical study of laminar flow condensation of flowing vapor,* Int. J. Heat Mass Transfer, vol. 9, pp. 581-591.

Analytical modeling of fibro-granular composite materials as sustainable acoustic absorber

Hasina Mamtaz[1*], Mohammad Hosseini Fouladi[2], Mushtak Al-Atabi[3], Satesh Narayana Namasivayam[4]

School of Engineering, Taylor's University, Taylor's Lakeside Campus, No.1 Jalan Taylor's, 47500 Subang Jaya, Selangor, DE, Malaysia.

[*]hasina_ctg@yahoo.com

Abstract
Application of natural fiber reinforced composites showed its effectiveness as sustainable acoustic absorbers. Current research was initiated to investigate the acoustic absorption characteristics of the composite structure of fiber and bio-granular materials, namely fibro-granular material. Analyses were based on three empirical models such as, Delany-Bazley, Biot-Allard and Johnson-Champoux-Allard models for predicting the acoustical properties of fibro-granular composite materials. Flow resistivity is an influential and intrinsic parameter which plays a significant role in describing the potential effectiveness of any porous sound absorbing material. The choice of analyzing the above mentioned models was for the involvement of this intrinsic parameter. Other four important parameters- porosity, tortuosity, viscous and thermal characteristic lengths are involved in the latter two models. The pore size of the testing sample which is controlled by the ratio of granular materials in the composites has significant impact in predicting four parameters later on. The airflow resistivity is also controlled by the pore size of the sample so as the ratio of the granular materials in the composite structure as well. Acoustic absorption plots were developed by using MATLAB R2014b (Version8.4), in terms of three analytical models. Based on outcome, the paper concluded that the above mentioned models constitute good tools in order to design a fibro-granular sound absorber for acoustic absorption purpose. Supplementary data from relevant published research was provided in the paper for validation of the acoustic properties of fibro-granular materials. The estimation helped to conclude the potential of a fibro-granular composite to confront any synthetic fiber composite as an acoustic absorbing material. Furthermore, the paper reported the invention of new fibro-granular acoustic absorber is an efficient way of solving three major environmental problems which are noise pollution, environmental pollution and waste management.

Keywords: Natural materials, Physical properties and Acoustic absorption.

1. Introduction

The importance of noise control engineering is the demand of addressing rapid growing concern for environmental problem and human health issue. Application of natural fiber and granular acoustic materials is still progressing to replace the synthetic porous material to provide an alternative green technology. Because of the biodegradability, sustainability and cost efficiency of natural acoustic materials, the new materials of certain waste and by-product materials were offered by many researchers to be considered as the new sound absorbent materials. The stimulation of this study was stemmed to support the green environmental campaign and to find the possible tools of acoustic absorbers in composition of natural fibers and bio-granular materials.

A new empirical model for loose granular media was developed by Voronina and Horoshenkov [11]. Their model related characteristic impedance and propagation constant with characteristic particle dimension, porosity, tortuosity and the specific density of grain base. The study reported a reliable prediction of acoustic performance of loose granular mix of grain base 0.4-3.5mm and specific densities between 200-1200 kg/m^3, in the frequency range 250-4000 Hz. Due to continuous growth of population and developing society, over the past few decades highway construction and automobile production have increased immensely. This leads to the production of more tires which tends to have short lives. As a result, heaps of waste tires are piling up around the world in every year. This causes serious environmental and financial problem[12]. The rubber crumbs granulates produced from the scrap tires were reported as potential acoustic material with a broadband absorption spectrum[13]. Swift, Bris [14] investigated the acoustic properties of rubber granular materials at different sizes and the effect of the composition ratio of binders on its acoustic absorption. They reported that the size of the granulates is a potential factor in manufacturing of an optimal acoustic absorber. For consolidated granulates of grain sizes between 0.5-1mm showed the maximum acoustic absorption with peak in low frequency region. For unconsolidated material the same performance was considered for larger grain size which is greater than 2mm, with the condition of applying binder at suitable ratio. Khan [23] developed an effective acoustic absorber of rubber particulates, plastic and fibrous material porous structure. The study suggested that the production of desired acoustic properties made out of fibro-granular materials is possible by controlling the size of particulates, the ratio of binder to water and the level of compaction in the extruder.

The traditional granular material limestone chips, is a well-known porous sound absorbing material. The flow resistivity information of limestone chips at the size range of 0.2-4 mm revealed as almost the same as glass fiber and rock wool[7]. Rusu and Vasile [22] studied the sound absorption capacity of a composite material of pine saw dust and recycled rubber as sound absorber. The value of sound absorption coefficient is calculated by using Delany-Bazley model for the composite of pine saw dust particle of size 1-4mm and rubber particles size of 1-2mm. The study reported the good sound absorption properties of the composite material of pine sawdust, recycled rubber particles and polyurethane binder at wideband frequency range. Ersoy and Küçük [15] investigated the waste substances from tea leaf fiber and compared the acoustic performance with woven textile cloth. They reported that at frequency range 500-3000 Hz, the tea leaf waste showed almost equal sound absorption as six layers of woven cloth at 10mm thickness. Comprehensive studies were conducted by Hosseini [16-19] to investigate the acoustic characteristics of fresh and industrial coir fiber by implementing different techniques such as rigid backing, air gap

backing, perforated plate facing etc. In terms of all techniques coir fiber was found as naturally good sound absorber at medium and high frequency regions.

Rice husk and rice straw are two enormous quantities of agricultural residual wastes, which exist due to the cultivation of rice crop. The potential of these two products was reported to be used as an important resource of renewable energy after pre-treatment process. But sadly every year this energy gets wasted by open burning while disposed for the next crop[20]. Mahzan, Zaidi [9] identified the rice husk as a potential acoustic material and found the value of sound absorpttion coefficient 0.889 at the frequency 250 Hz. The study reported that, rice husk exhibited better acoustic performance than wood shavings and rubber granular materials when the ratio of ricehusk to virgin polyurethane was 25:75 in the composite. It showed the better acoustic performance than the rubber granular and wood shavings materials. The study also identified, the effect of composite stiffness was the reason for higher sound absorption at low frequency region. Furthermore, Mahzan, M Ahmad Zaidi [21] studied the effectiveness of coir fiber-recycled rubber composite as promising sound absorption material. The effect of second hand rubber and polyurethane resin as a binder were investigated in two composite structures at various compositions to investigate the possible substitution of industrial and metal fiber. The result showed higher absorption coefficient for mid to high frequency range which was 1400-6300 Hz for both the samples. It was found that the lower content of binder influence the density and porosity value of the material. Therefore, it was concluded that due to the lower content of polyurethane, the composite density gained higher and porosity dropped to lower value which resulted in higher absorption coefficient of the coconut coir composite.

The aim of this research was to investigate the acoustic absorption characteristics of fibro-granular composites through the implementation of suitable analytical models. The study also investigated the possible ways to establish the link between physical and acoustical properties of fibro-granular material for the enhancement of low frequency acoustic absorption.

1.1 Fibrous Material

Based on the microscopic configuration of porous absorbing materials, they can be classified as cellular, fibrous or granular [1]. All fibrous materials are porous materials[2], which are comprised of a group of continuous filaments. In the interstices of filaments, there are tunnel like openings in the material, where air is trapped. When sound waves are incident on the surface of the material, they propagate through the interconnected pores of the porous media. Whilst propagating the collision between air particles and pore walls, energy of the air molecules is converted into heat due to the thermal and viscous losses at the pores walls and tunnel. As a result, acoustic energy is converted into heat energy. At low frequency this change is isothermal and at high frequency it is adiabatic [3, 4] Fig.1 shows the structure of fibrous material with its microscopic arrangement.

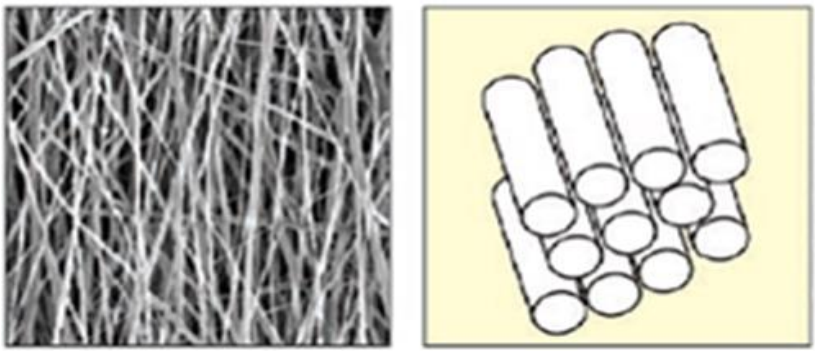

Figure.1 Structure of fibrous material [4]

The main raw material was chosen for this study is coconut coir fiber. Coir fibers are highly abundant across all part of the world. Most importantly, it is an important agricultural waste in Malaysia. It is a tropical plant of *Arecaceae* (palm) family and the scientific name of the fruit is *Cocos Nucifera.* The coarse, stiff, reddish brown fibers of coconut are obtained from their husk. The main constituents of coir fibers are cellulose, hemicelluloses and lignin. The maximum percentage of content in the fibers is lignin, which makes the fibers strong and highly durable compared to other natural fibers. The cellulose content is present on the wall of fiber cell which makes the cell wall thicker and the reason of water absorption. The individual fiber cell is hollow and the presence of the hollow cavity in fibers decreases its bulk density and makes it light and delicate to serve as an acoustic and thermal insulator [5].

1.2 Granular Material

The recycled granular materials are widely accepted as acoustic absorption materials for their sustainability, longevity, non-combustible and moisture resistant quality. The grains themselves in a granular absorbent contain pores where the sound absorption takes place due to viscosity. Granular materials can be classified as consolidated and unconsolidated or loose granular materials. In consolidated granular materials the particles are relatively rigid and macroscopic and their dimensions are greater than those of the internal voids by many orders of magnitude. Unconsolidated materials are the assemblages of loosely packed individual particles. The example of some granular absorbing materials are granular clays, sands, gravel, limestone chips and soil which are perfect in controlling outdoor sound propagation[6, 7]. The solid structure in rigid porous materials is perfectly rigid and stationary. The granules are separated by the interconnected voids where the air is held. Air is a viscous fluid and the sound absorption takes place due to the viscous friction of air with the pores wall. The sound energy converted into heat energy in isothermal heat transfer process, at low and high frequency region. Besides viscous effect the energy scattered from the granules also has significant effect in sound absorption of granular materials [4]. The enhancement of the sound absorption of recycled granular materials is possible more properly by forming wedges than flat boards[8]. Fig. 2 shows the structure of granular materials with its typical microscopic arrangement.

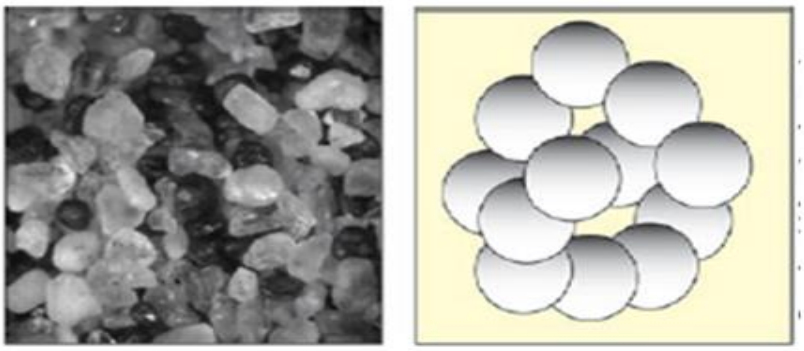

Figure 2. Structure of granular materials[4]

The secondary raw material that was chosen for this study is rice husk, which is considered as biomass granular material. Paddy is a commonly cultivated crop in almost all parts of the world. Rice is produced from paddy through rice milling process and rice husk is the by-product of the process. It has highly moisture resistible, incombustible and anti-fungal material qualities. Rice husk waste was investigated as an efficient acoustic absorber at low frequency region. It was reported that dried rice husk together with polyurethane binder showed significant value of sound absorption coefficient at low frequency region compare to wood shaved materials. The absorption peak was found at frequency 250 Hz for 25% rice husk-polyurethane composite with a value of 0.889 [9]. It is a great resource as a raw bio-granular material for producing composite materials. In order to improve the mechanical properties of natural fiber composites, rice husk waste was found to be an effective filler in fiber- matrix composite [10].

2. Methodology

Three models were investigated for the formulation of analytical model of acoustic wave propagation through the natural fibro-granular materials at normal incidence. The first approach is based on the simple method Delany-Bazley model, which is easy for fast approximation. The second approach is based on elastic frame Biot-Allard model where the frame or fiber is considered as elastic cylindrical fiber, hence both frame and fluid are in motion. The third approach is rigid frame Johnson-Champoux-Allard model where the solid frame structure is considered as rigid. First model is based on one and only intrinsic parameter- flow resistivity. Later two models are based entirely on a set of five measurable non-acoustic parameters, which are porosity, flow resistivity, tortuosity, viscous characteristic length and thermal characteristic length. For estimation of the sound absorption coefficient of any porous materials, all these five physical geometrical parameters are extremely influenced by bulk density of the material. Bulk density was defined from the mass and volume of the material. Combined flow resistivity and porosity of the fibro-granular composite materials were implemented in the formulation of three models, in order to link the physical and acoustical parameters for the enhancement of low frequency acoustic absorption.

The fibrous and bio-granular waste materials that were chosen for this analysis are coir fiber and rice husk respectively. To calculate all five physical parameters including the combined flow resistivity of coir fiber and rice husk, the predicted weight of coir fiber and rice husk are assumed as 56.27mg [18] and 16mg respectively. The weight of rice husk is determined on the basis of its average weight 1.6mg per piece [34]. Data collected from relevant published studies were elaborated to compare the

value of sound absorption coefficient between the calculated and published one. MATLAB R2014b (Version 8.4) was used to plot the sound absorption coefficient in the frequency range between 0-5000 Hz based on calculated data.

2.1 Delany-Bazley Model

An empirical formula of homogenous and isotropic porous materials was developed by Delany-Bazley [24] for the estimation of the characteristic impedance (Z_c) and wave propagation constant (k). The fast approximation Delany-Bazley technique depends only on one intrinsic property of the material which is, flow resistivity to a certain range of $1000 \leq \sigma \leq 50000$ MKS rayl m^{-1} and porosity close to 1.
The characteristic impedance (Z_c), the propagation constant (k) and surface acoustic impedance (Z) can be obtained in terms of flow resistivity (σ) as [25, 26]:

$$Z_c = \rho_0 c_0 \left[1 + 0.057 b^{-0.754} - i(0.087 b^{-0.732})\right] \quad (1)$$

$$k = \frac{2\pi f}{Co}\left[0.189\, b^{-0.595} + \mathrm{i}(1 + 0.0978 b^{-0.7})\right] \quad (2)$$

$$Z = Z_c \coth(k.d) \quad (3)$$

Where,
$Z_0 = \rho_0 c_0$ =Impedance of the air
ρ_0 = Air density
c_0 = Speed of sound in air
f = Sound wave frequency
d = Thickness of porous layer
$b = \frac{\rho_0 f}{\sigma}$ =Dimensionless parameter; the model is applicable only for $0.01 \leq b \leq 1.0$

2.2 Biot-Allard Model

The second approach of this study is Allard model[27] and his extension to Biot [28], which is an elastic frame method for the porous material saturated with viscous fluid. Hence the frame (fiber) is assumed as elastic cylindrical fiber, which deals with the study of frame - fluid interaction. Therefore, both frame (fiber) and fluid (air) are in motions. The frame geometry dependent viscous characteristics length (Λ) can be stated as:

$$\Lambda = \frac{1}{2\pi r l} \quad (4)$$

$$l = \frac{1}{\pi r^2 * \frac{\rho_{bulk}}{\rho_{fiber}}} \quad (5)$$

Where,
l= Total length of fiber per unit volume
r= Cross sectional radius of fiber
ρ_{bulk} = Bulk density of porous material
ρ_{fiber} = Density of fiber

$\frac{\rho_{bulk}}{\rho_{fiber}}$ = Fraction of fiber exists in porous material

The frequency dependent bulk modulus of fluid, $K_f(\omega)$ inside the pores, which is assumed to be the only parameter to characterize the air filling pores, is defined as [27]:

$$K_f(\omega) = \frac{\gamma p_0}{\gamma-(\gamma-1)\left[1+\frac{8\eta}{j\Lambda'^2 B^2\omega\rho_0}\left(1+j\rho_0\frac{\omega B^2\Lambda'^2}{16\eta}\right)^{1/2}\right]^{-1}} \quad (6)$$

Where,
η = Viscosity of air
Λ' = Thermal characteristic length
ω = Angular frequency
γ = Ratio of specific heat at constant pressure to specific heat at constant volume;
p_0 = Atmospheric pressure
B^2= Prandtl no.

Allard [27] derived the elasticity coefficients, P, Q and R in terms of Biot's experiments as follows:

$$P = \tfrac{4}{3}N + K_b + \frac{(1-\varphi)^2}{\varphi}K_f \quad (7)$$

$$Q = K_f(1-\varphi) \quad (8)$$

$$R = K_f\varphi \quad (9)$$

The bulk modulus of frame K_b can be evaluated as:

$$K_b = \frac{2N(\nu+1)}{3(1-2\nu)} \quad (10)$$

Where,
N = Shear modulus
ν = Poisson coefficient

The dynamic rigidity of the elastic solid was characterized by shear modulus and Poisson coefficient. The derivation of the kinetic energy helps in evaluation of the equation of motion in elastic medium. The parameters ρ_{11}^*, ρ_{12}^* and ρ_{22}^* which help to identify the inertial coupling between frame and fluid can be estimated as [27]:

$$\rho_{11}^* = \rho_{bulk} + \rho_a - j\sigma\varphi^2\frac{G(\omega)}{\omega} \quad (11)$$

$$\rho_{12}^* = -\rho_a + j\sigma\varphi^2\frac{G(\omega)}{\omega} \quad (12)$$

$$\rho_{22}^* = \varphi\rho_0 + \rho_a - j\sigma\varphi^2\frac{G(\omega)}{\omega} \quad (13)$$

Where,

$$G_\omega = \left(1 + \frac{4j\alpha_\infty^2 \eta \rho_0 \omega}{\sigma^2 \Lambda^2 \varphi^2}\right)^{1/2} \quad (14)$$

$\rho_a = \rho_0 \varphi(\alpha_\infty - 1)$ = Inertial coupling term. (15)

α_∞ is the tortuosity of the frame, which is defined as [29]:

$$\alpha_\infty \approx \frac{1}{\sqrt{\varphi}} \quad (16)$$

According to Biot [28] there are two compression waves and one shear wave which propagate in porous media. One compression wave is air borne, which mostly transmits in air and another one is frame borne which propagates in both fluid and frame. A rotational wave called shear wave is also frame borne which is considered when the sound waves propagate at oblique incidence. The study only analyzed the propagation of sound at normal incidence, hence two compression waves are considered here.

Therefore, to calculate the ratio of frame and fluid velocity, the squared wave numbers of two compression waves can be evaluated as:

$$\delta_1^2 = \frac{\omega^2}{2(PR - Q^2)} \left[P \rho_{22}^* + R \rho_{11}^* - 2Q \rho_{12}^* - \sqrt{\Delta} \right] \quad (17)$$

$$\delta_2^2 = \frac{\omega^2}{2(PR - Q^2)} \left[P \rho_{22}^* + R \rho_{11}^* - 2Q \rho_{12}^* + \sqrt{\Delta} \right] \quad (18)$$

Where,

$$\Delta = (P \rho_{22}^* + R \rho_{11}^* + 2 Q \rho_{12}^*)^2 - 4\left(PR - Q^2\right)(\rho_{11}^* \rho_{22}^* - \rho_{12}^{*2}) \quad (19)$$

The squared wave numbers are useful to calculate the ratio of frame and fluid velocity as:

$$\mu_i = \frac{P\delta_i^2 - \omega^2 \rho_{11}^*}{\omega^2 \rho_{12}^* - Q\delta_i^2} \quad (20)$$

As two compression waves simultaneously propagate in both media, four characteristic impedances related to the propagation in air Z_i^a or frame Z_i^f can be evaluated as:

$$Z_i^a = \left(R + \frac{Q}{\mu_i}\right) \frac{\delta_i}{\varphi \omega} \quad (21)$$

$$Z_i^f = (P + Q\mu_i) \frac{\delta_i}{\omega} \quad (22)$$

Where, $i = 1, 2$ in case of equations (21) and (22).

The surface acoustic impedance at normal incidence (Z) of the material with thickness d, which is the function of above characteristics impedances, can be calculated as:

$$Z = -j \frac{\left(Z_1^f Z_2^a \mu_2 - Z_2^f Z_1^a \mu_1\right)}{D} \quad (23)$$

Where, D can be defined as:

$$D = (1 - \varphi + \varphi\mu_2)\left[Z_i^f - (1-\varphi)Z_i^a\mu_1\right]tg\delta_2 d + (1 - \varphi + \varphi\mu_1)\left[Z_2^a\mu_2(1-\varphi) - Z_2^f\right]tg\delta_1 d \quad (24)$$

Thus the Biot-Allard formulation for the sound propagation of normal incident wave in elastic material has been modeled. Even though the modeling of this formulation was more complicated compared to Delany-Bazley model, but this technique is useful in detecting the resonances within the frame of porous material.

2.3 Johnson-Champoux-Allard Model

The third approach of this study is rigid frame Johnson-Champoux-Allard Model. In this model, the solid phase of the frame remains motionless, hence the modeling of this technique was easier than Biot-Allard technique. In this model five non-acoustical parameters- flow-resistivity, porosity, tortuosity, viscous characteristics length and thermal characteristics length are involved in the expression of the effective density (ρ_ω) and the bulk modulus $K(\omega)$ of the fluid of rigid framed porous materials , which can be expressed as [27, 30, 31],

$$\rho(\omega) = \alpha_\infty\rho_o\left[1 + \frac{\sigma\phi}{j\omega\rho_o\alpha_\infty}\sqrt{1 + \frac{4\,\alpha_\infty^2\eta\rho_o\omega}{\sigma^2\Lambda^2\omega^2}}\right] \quad (25)$$

$$K(\omega) = \frac{\gamma P_o}{\gamma - (\gamma-1)\left[1 - j\frac{8k}{\Lambda'^2 N_p\rho_o\omega}\sqrt{1 + j\frac{\Lambda'^2 N_p\rho_o\omega}{16k}}\right]^{-1}} \quad (26)$$

Where,
γ= Ratio of the specific heat capacities of air
P_0= Atmospheric pressure
N_p= Prandtl number of the air
ω= Angular frequency

The expression for characteristic impedance $Z_c(\omega)$, the complex wave number $k_c(\omega)$, surface acoustic impedance Z can be estimated as [27, 32]:

$$Z_c(\omega) = \frac{1}{\phi}\sqrt{\rho(\omega).K(\omega)} \quad (27)$$

$$k_c(\omega) = \omega\sqrt{\rho(\omega)/K(\omega)} \quad (28)$$

$$Z = Z_c(\omega).\coth(k_c(\omega)) \quad (29)$$

Having surface acoustic impedance (Z) on the basis of three above mentioned models, the sound absorption coefficient (α) at normal incidence of the porous layer while backed with a rigid wall can be calculated as:

$$\alpha = 1 - \left|\frac{Z - Z_0}{Z + Z_0}\right|^2 \quad (30)$$

The quantity derived from equation (30) is directly linked through the above mentioned equations in three formulations to the five physical parameters namely porosity, tortuosity, flow resistivity and two characteristics lengths. The values of sound absorption coefficients that have been calculated through each formulation were investigated and compared in the later part of this study.

3. Results and discussions

The effectiveness of a porous material depends on the value of its sound absorption coefficient which is close to one, with an absorption plane on a large frequency range. In order to predict the sound absorption coefficient of any fibro-granular composite materials, the study investigated the composite structure of coir fiber and rice husk materials for acoustic absorption purpose.

Bulk density of any porous material can be determined by its mass per unit volume. Flow resistivity of fibrous material (σ_f) having bulk density ($\rho_{bulk(f)}$) and flow resistivity of loose granular material(σ_g) having characteristic particle dimension (*D*) can be estimated as [11, 33]:

$$\sigma_f = 490 \frac{\rho_{bulk(f)}^{1.61}}{d_{fiber}} \quad (31)$$

$$\sigma_g = \frac{400(1-\varphi_g)^2(1+\varphi_g)^5\mu}{\varphi_g D^2} \quad (32)$$

$$D = \sqrt{V_g/0.5233} \quad (33)$$

Where,
V_g = Number of granular particles per unit volume
d_{fiber} = Diameter of fiber
μ = Dynamic viscosity of air

Flow resistivity of new fibro-granular material (σ_{fg}) is-

$$\sigma_{fg} = \sigma_f + \sigma_g \quad (34)$$

Porosity of new fibro-granular material (φ_{fg}), having specific densities and bulk density was estimated as [32]:

$$\varphi_{fg} = 1 - \frac{\rho_{bulk(fg)}}{\rho_f + \rho_g} \quad (35)$$

Where,
ρ_f = Specific density of fibrous material
ρ_g = Specific density of granular material
$\rho_{bulk(fg)}$ = Bulk density of fibro-granular material

The values of physical parameters $\sigma, \varphi, \propto_{\infty}$, Λ and Λ' for the fresh coir fiber(C.F) collected from relevant published data [18] were illustrated in row-1 of Table-1. The calculated values of same parameters for the new fibro-granular material which is coir fiber-rice husk (C.F-R.H) were demonstrated in row-2 of the following Table-1. This comparison study in Table-1 was for the purpose of the validation of the theoretical outcome of the current study of C.F-R.H composite material with the relevant study of fresh C.F material [18] at 45mm thickness for both samples.

Table 1. Comparison between the physical parameters of fibrous and fibro-granular materials

Materials	Mass of the sample for 100mm diameter (gm)	Flow resistivity σ (Nsm^{-4})	Porosity φ	Tortuosity $\propto_{\infty}$	Viscous characteristics length Λ (μm)	Thermal characteristics length Λ' (μm)
C.F	56.3	6298	70%	1.19	20	40
C.F-R.H	72.27	6754	76%	1.15	26.32	52.64

Fig. 3, 4, and 5 were illustrated with the calculated acoustical absorption lots using the Delany-Bazley model, Biot-Allard model and Johnson-Champoux-Allard models respectively.

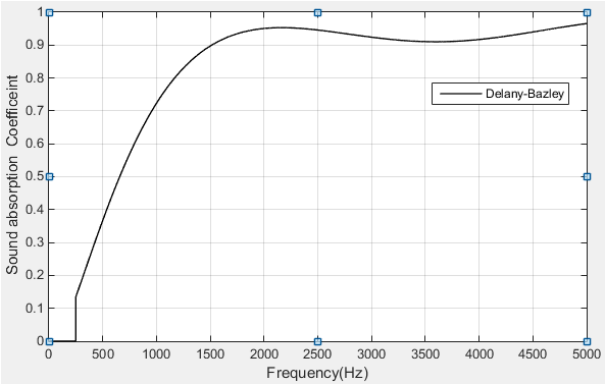

Figure-3: Acoustic absorption coefficient of 45mm thickness of fresh coir fiber-rice husk, fibro-granular composite material using Delany-Bazley model.

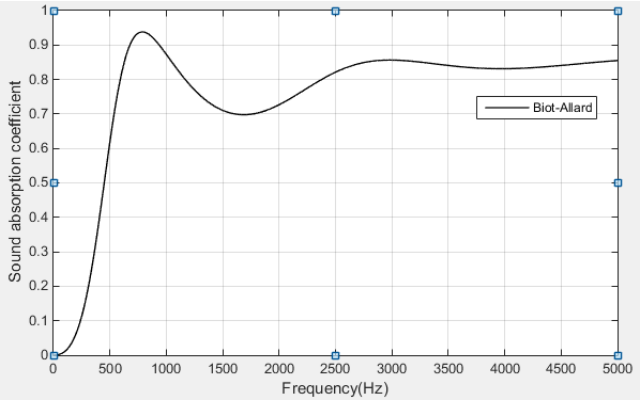

Figure 4. Acoustic absorption coefficient of 45mm thickness fresh coir fiber-rice husk, fibro-granular composite material, using Biot-Allard model.

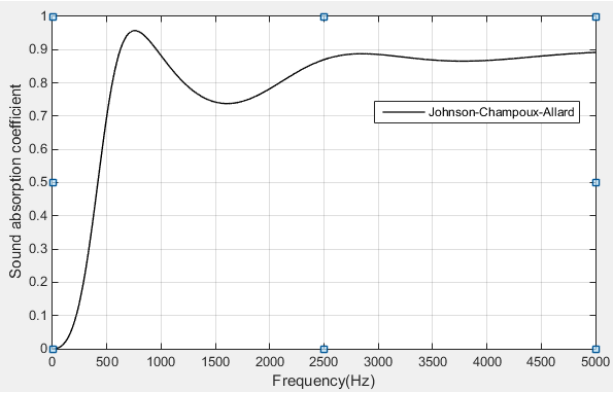

Figure 5. Acoustic absorption coefficient of 45mm fresh coir fiber-rice husk, fibro-granular composite material using Johnson-Champoux-Allard model

The comparison study of the calculated acoustic absorption coefficients in terms of all three analytical models was illustrated in figure-6.

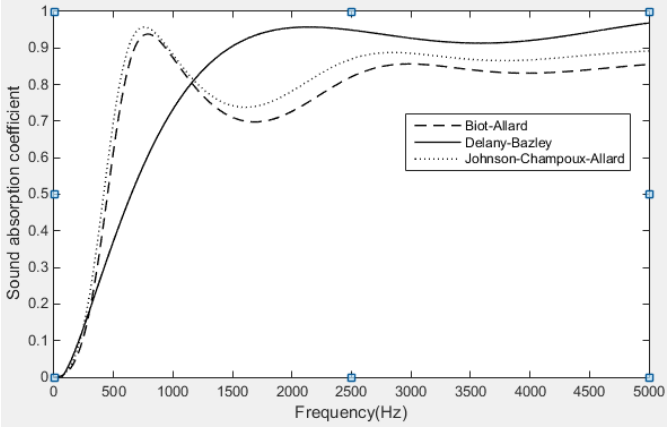

Figure-6: Comparison of calculated acoustic absorption coefficients of coir fiber-rice husk, fibro-granular composite material for three models. Thickness=45mm, $\rho_{f=}$ 537kg/m^3 , $\rho_{bulk(f)} = 159$ kg/m^3, $\rho_{g=}$ 302kg/m^3, $\rho_{bulk(g)} = 45.29$ kg/m^3 and $d_{fiber} = 273$µm.

The value of acoustic absorption coefficient was calculated by using new physical parameters of fibro-granular materials which are demonstrated in the equations (34) and (35). The study showed good approximation of the solution for the value of acoustic absorption coefficient in terms of three models. The first approach Delany-Bazley showed the overall absorption pattern at broadband frequency without any précised information about peaks and resonance of the frame. The outcome of second approach Biot-Allard was close to third approach Johnson-Champoux-Allard model truly showed the overall pattern including the well predicted resonances at certain frequencies of the frame structure. There is no considerable difference between the outcomes of both Biot-Allard and Johnson-Champoux-Allard model. The calculated result for the value of acoustic absorption coefficient for the first approach Delany-Bazley model was found 0.7 at frequency range below 1000 Hz, for second approach Biot-Allard model the absorption peak was found at frequency 787 Hz and the value of sound absorption coefficient is 0.94. For third approach Johnson-Champoux-Allard model, the peak was found at 757 Hz and the value of sound absorption coefficient is 0.96. The outcomes of second and third approaches clearly showed the resonances of acoustical absorption at lower frequencies. Hence the models were proved to be used as efficient tools for the enhancement of low frequency acoustic absorption of fibro-granular materials.

In the current analysis fresh coir fiber was chosen to measure the value of acoustic absorption coefficient. The possible reason is, the fresh fiber shows better sound absorption performance at low frequency region due to its moisture absorption capability compare to the industrially prepared fiber mixed with binder. The bio-granular composite that was chosen for this analysis is rice husk. To calculate the value of the absorption coefficient, the weight of rice husk is assumed as 1.6mg per piece. The effectiveness of rice husk and buckwheat husk as sound absorbing materials was revealed by Sakamoto, Takauchi [34]. Where the of bulk density of rice husk and buckwheat husk were reported 105 kg/m^3 and 135 kg/m^3 and average weight per piece were reported as 1.6mg and 3.8mg respectively. From various experimental and theoretical overviews it was concluded that the size of granular material in the range of 2-4mm exhibits better acoustic performance. The average length of rice husk of medium grain is 3-6mm and average diameter is 1500μm[35]. However, Hosseini [17] suggested to use improved industrially treated fibers in real world application due to their better stiffness, less moisture and larger life expectancy. Introduction of bio-granular materials in a composite increases the bulk density and flow resistivity of the sample. The materials with higher flow resistivity exhibits as better sound absorber medium[36].

4. Conclusion

- The new fibro-granular material confirmed their potential to be used as effective acoustic materials for sound absorption purpose.
- The acoustical absorption performance of the fibro-granular material can be modelled by using three formulations namely Delany-Bazley, Biot-Allard and Johnson-Champoux-Allard model as theoretical tools.
- The acoustical behaviour of the material can be predicted by Delany-Bazley model for overall frequency band without any resonance. A very good agreement has been achieved between the relevant published data for natural fiber and the calculated data for fibro-granular composite material by using both Biot-Allard and Johnson-Champoux Allard model. These two models are useful to predict the peaks and resonances in the overall frequency band.

- The new physical parameters such as, combined flow resistivity and porosity have been confirmed their potential contribution in the acoustic performance of new fibro-granular material by linking with the material's acoustical parameters.
- Introduction of granular materials increase the flow resistivity of the composite which leads the enhancement of absorption coefficient. Furthermore introduction of bio-granular materials acts as a compensator for any industrial natural fiber composite for their lower moisture content.
- Utilization of waste materials as acoustic materials solves the problem of its management and environment pollution. Furthermore they are exhibited as potential acoustic absorbers to be used in many indoor and outdoor applications.

References

[1] Sagartzazu, X., Hervella-Nieto, L. and Pagalday, J.(2008). Review in sound absorbingmaterials. *Archives of Computational Methods in Engineering,*15(3), 311-342.

[2] Beranek, L.L., Vér, I.L. (1992). *Noise and vibration control engineering*, Newyork, Wiley.

[3] Jayaraman, K.A.(2005). *Acoustical absorptive properties of nonwovens*, Doctoral dissertation, North Carolina State University.

[4] Arenas, J.P. and Crocker, M.J.(2010). Recent trends in porous sound-absorbing materials. *Sound & vibration*, 44(7) 12-18.

[5] Waifielate, A.A. and Abiola B.O.(2008). *Mechanical Property Evaluation of Coconut Fibre*, Doctoral dissertation, Blekinge Institute of Technology Karlskrona, Sweden.

[6] Sikora, J. and Turkiewicz, J.(2010). Sound absorption coefficients of granular materials. *Mechanics and Control*, 29(2010) 149-157.

[7] Iannace, G., Ianniello, C., Maffie, L., Romano, R.(1999). Steady-state air-flow and acoustic measurement of the resistivity of loose granular materials. *The Journal of the Acoustical Society of America*, 106(3),1416-1419.

[8] Cox, T.J., D'Antonio, P.(2009) *Acoustic absorbers and diffusers: theory, design and application*, London and Newyork, Taylor & Francis.

[9] Mahzan, S., Zaidi, A., Mujahid, A., Ghazali, M.I., Yahya, M.N., Ismail, M.(2009) Investigation on sound absorption of rice-husk reinforced composite. *MUCEET*(pp.19-22). Malaysian Technical Universities Conference on Engineering and Technology, Pahang, Malaysia.

[10] Satapathy, A., Jha, A.K., Mantry, S., Singh, Sk. Patnaik, K.(2010). Processing and characterization of jute-epoxy composites reinforced with SiC derived from rice husk. *Journal of Reinforced Plastics and Composites*, 29(18), 2869-2878.

[11] Voronina, N. , Horoshenkov, K.(2003). A new empirical model for the acoustic properties of loose granular media. *Applied Acoustics*, 64(4), 415-432.

[12] Santini, A., Morselli, L., Passarini, F., Vassura, I., Di Carlo, S., Bonino, F.(2011) End-of-Life Vehicles management: Italian material and energy recovery efficiency. *Waste management,* 31(3) 489-494.

[13] Pfretzschner, J.(2002) *Rubber crumb as granular absorptive acoustic material.* Institute de Acustica Serrano, Madrid, Spain.

[14] Swift, M., Bris, P., Horoshenkov, K.(1999). Acoustic absorption in re-cycled rubber granulate. *Applied Acoustics,* 57(3), 203-212.

[15] Ersoy, S., Küçük, H.(2009). Investigation of industrial tea-leaf-fibre waste material for its sound absorption properties. *Applied Acoustics,* 70(1), 215-220.

[16] Hosseini, F.M., Nor, M.J.M., Ayub, M., Ghassem, M.(2012). Enhancement of coir fiber normal incidence sound absorption coefficient. *Journal of Computational Acoustics,* 20(01), 1-31.

[17] Hosseini, F.M., Ghassem, M., Ayub, M.(2011). Implementation of coir fiber as acoustic absorber material. *Noise & Vibration Worldwide,* 42(9), 11-16.

[18] Hosseini, F.M., Ayub, M., Nor, M.J.M.(2010). Analysis of coir fiber acoustical characteristics. *Applied Acoustics,* 72(1), 35-42.

[19] Hosseini, F.M., Nor, M.J.M., Ayub, M., Leman, Z.A.(2010). Utilization of coir fiber in multilayer acoustic absorption panel. *Applied Acoustics,* 71(3), 241-249.

[20] Lim, J.S., Manan, Z.A., Alwi, S.R.W., Hashim, H.(2012). A review on utilisation of biomass from rice industry as a source of renewable energy. *Renewable and Sustainable Energy Reviews,* 16(5), 3084-3094.

[21] Mahzan, S., Ahmad Zaidi,A.M., Arsat, N., Hatta, M.N.M., Ghazali, M.I., Rasool Mahideen, S.(2010). Study on sound absorption properties of coconut coir fibre reinforced composite with added recycled rubber. *International Journal of Integrated Engineering,* 2(1), 29-34.

[22] Rusu, T., Vasile, O.,(2012). Investigation Composite Materials for its Sound Absorption Properties. *Romanian Journal of Acoustics & Vibration,* 9(2), 123-126.

[23] Khan, A., (2008). *Vibro-acoustic products from re-cycled raw materials using a cold extrusion process: a continuous cold extrusion process has been developed to tailor a porous structure from polymeric waste, so that the final material possesses particular vibro-acoustic properties*, Doctoral dissertation, University of Bradford, England.

[24] Delany, M., Bazley, E.(1970). Acoustical properties of fibrous absorbent materials. *Applied Acoustics,* 3(2), 105-116.

[25] Lee, F.-C., Chen, W.-H.(2001). Acoustic transmission analysis of multi-layer absorbers. *Journal of Sound and Vibration,* 248(4), 621-634.

[26] Dunn, I., Davern, W.(1986). Calculation of acoustic impedance of multi-layer absorbers. *Applied Acoustics,* 19(5), 321-334.

[27] Allard, J. (1993). *Sound propagation in porous media: modelling sound absorbing materials.* London, Elsevier.

[28] Biot, M. (1962). Generalized Theory of Acoustic Propagation in Porous Dissipative Media. *The Journal of the Acoustical Society of America,* 34(9A), 1254-1264.

[29] Attenborough, K.(1993). Models for the acoustical characteristics of air filled granular materials. *Acta. Acust.,* 1, 213-226.

[30] Champoux, Y., Allard, J.F. (1991). Dynamic tortuosity and bulk modulus in air-saturated porous media. *Journal of Applied Physics,* 70(4), 1975-1979.

[31] Johnson, D.L., Koplik, J., Dashen, R.(1987). Theory of dynamic permeability and tortuosity in fluid-saturated porous media. *Journal of fluid mechanics,* 176(3), 379-402.

[32] Kino, N., Ueno, T., Suzuki, Y., Makino, H. (2009) Investigation of non-acoustical parameters of compressed melamine foam materials. *Applied Acoustics,* 70(4), 595-604.

[33] Ballagh, K. (1996). Acoustical properties of wool. *Applied Acoustics,* 48(2), 101-120.

[34] Sakamoto, S., Takauchi, Y., Yanagimoto, k., Watanabe, S. (2011). Study for Sound Absorbing Materials of Biomass Tubule etc. *Journal of Environment and Engineering,* 6(2), 352-364.

[35] Abdullah, M., Husain, Z., Pong, S.Y. (2003) Analysis of cold flow fluidization test results for various biomass fuels. *Biomass and Bioenergy,* 24(6),487-494.

[36] Seddeq, H.S. (2009). Factors influencing acoustic performance of sound absorptive materials. *Australian Journal of Basic and Applied Sciences,* 3(4), 4610-4617.

Hybrid VLC using Visible Light and Radio Frequency Spectrum

Ching Han Tan,
Taylor's Graduate School, Lakeside Campus
*email: tanch28@gmail.com
Florence Choong Chiao Mei
Taylor's Graduate School, Lakeside Campus (Supervisor)
YanDan Lin
FuDan University (Co-Supervisor)

Abstract

Visible light communication (VLC) has attained considerable attention in the past decade due to exponential growth in radio frequency (RF) communication usage. With the ever expansion in users of smart phones and other tablet based devices, this has cause a concern in the depletion of radio frequency spectrum. Visible light communication (VLC) spectrum of 400 to 790 THz range, can boost 390 THz additional frequencies for data communication purpose. At the same time with the increasing Lighting infra-structure converting to solid states Light Emitting Diodes (LEDs), it can save more energy usage versus radio frequency (RF). The hybrid VLC is to use this advantage and to maintain the connectivity to the current Wireless Fidelity (WiFi) infrastructure. In this paper, hybrid VLC technology is surveyed. The new scenario of Light fidelity (LiFi) is explored towards 5th Generation communication in indoor high definition applications. This eventually will lead to realization of ubiquitous VLC application. This paper presents a comprehensive overview of different techniques used for Hybrid VLC. Major key issues and challenges in Hybrid VLC schemes are critically examined and outlined.

Keywords: VLC (Visible light communication), RF (Radio frequency), WiFi (Wireless Fidelity), LiFi (Light fidelity), Hybrid VLC.

1. Introduction

Visible light communications appeared a few centuries earlier than radio frequency communications. Each civilization has its own examples of using signaling fires to convey the news of victory, invasion or other auspicious event. Visible light communication (VLC) spectrum of 400 to 790 THz range, can boost 390 THz additional frequencies for data communication purpose. At the same time with the increasing Lighting infra-structure converting to solid states Light Emitting Diodes (LEDs), it can save more energy usage versus radio frequency (RF). Fig.1 shows the electromagnetic spectrum. Visible light is 10,000 times more bandwidth than radio frequency [1, 2].

In the past decades, solid state lighting has grown rapidly. In 2014, Nobel prize for Physics was awarded to the three inventors of Blue LEDs due to its energy saving impact. In the near future, majority of fluorescent lightings will be replaced by light-emitting diodes (LEDs) that can be modulated at a higher rate As a result, research on utilising these light sources for both illumination and communications is catching up actively. Japan originated the visible light communication consortium (VLCC). Over the years, several standards of visible light communication (VLC) were generated in order to pave the way for a greener sustainability environment.

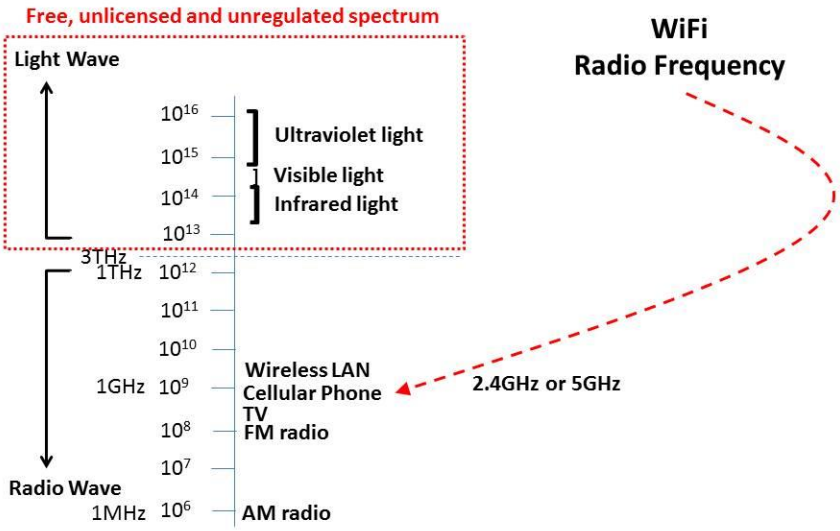

Fig.1.Electromagnetic Spectrum [1, 20]

The research Questions emerged are: (i) What is the future possible direction of telecommunication? (ii) What modulation schemes can be optimized in the communication environments? (iii) How to effectively ensure energy efficiency for both lightings and communications? This paper will address the possible solutions for the above.

2. Literature Review

The literature review of visible light communication can be classified under 3 major topics: (i) Pure VLC, (ii) Multiple-input-Multiple-output (MIMO) schemes and (iii) Hybrid VLC.

Most of the studies are focused in the pure visible light communication system development and implementations. Less attention is given to the practical aspect of it. Hence the aim in this paper will be to investigate its adaptation to complement the radio frequency spectrum especially the hybrid Visible light communications.

2.1 Pure Visible Light communication (VLC)

H. L. Minh et al., 2010 [8], reported that there are two types of white LEDs used for general illumination, i.e. Red-green-blue (RGB) Light emitting Diodes and Blue emitter with combination of yellowish phosphor. The latter is a better choice for lighting because of its lower complexity. Its disadvantage was its limited modulation bandwidth. Blue filter therefore has to be added to filter out its phosphor component in order to alleviate its low modulation bandwidth. However, this incurs a power penalty. This is because energy in other parts of the visible light spectrum are blocked. Equalizer with complex modulation schemes is employed to increase the data transmission. Light dimming is the other challenge for the high speed VLC that will impact the link performance. There are two types of dimming, i.e. amplitude reduction and pulse width modulation (PWM). Firstly, link target performance could be maintained by raising the link power. Secondly, data transmission with PWM dimming, could operate in burst mode as well as coordination with duty cycle of dimming pulses. Hence, the average data transmission throughput is reduced.

G. Yun et al., 1992 [4], described a configuration using spot-diffusing, fly-eye receivers and multiple line of sights for indoor visible light wireless communications. Simple geometric models design was suggested as suitable light sources with power budgeted fly-eye design amongst ambient light interference. A demonstration of spot diffusing idea is done through experiment. Indoor wireless communication systems consisted of two types: Directive beam configuration (DBC) and diffused illumination configuration (DIC). In DBC, two collimated light beams connected each user terminal to the local area network. They will be for down-linking and up-linking respectively. Diffused illumination configuration (DIC) employed wide beam illumination of the entire region of the walls and ceiling. A wide angle receiver accepted from the walls and ceiling. DIC eliminated the alignment requirement due to its simplicity in operation. But this leads to a high transmission power and a low data rate. In reverse, a DBC system with narrow transmission beams can have a higher bit rate because of the small Field-of view (FOV) transmission paths and receivers. The line-of-sight (LOS) can be blocked. The optical antenna systems needed high mechanical stability for alignment.

This to some extent, makes a DBC system less competent. In this paper, a new approach which was called spot diffusion multi- LOS configuration was proposed. The required power level of a diffused system can be reduced. At the same time, the broadcast feature and a similar robustness can be kept. The optical power was broadcasted onto a small

area of the reflecting surfaces. Examples for area are walls or the ceiling. Diverted or Collimated beams were send through the transmitter.

Diffusing spot is the illuminated area. Light is diffused or reflected to all the internal terminals of the users. There is some advantages of spot diffusing when compared to DIC. The receivers can now have a narrow FOV with greater area of energy concentrators. As a collimated beam is used between the diffusing spot and the transmitter, the channel loss is independent from the length for this channel.

J. Rufo et al., 2010 [10] described a prototype of visible light communication system using white LEDs. This video broadcasting setup can reach a 2 Mbps bit rate. From a distance of more than 3 m, the SNR of receiver is more than 40 dB. The bit error rate is very low. This system of video transmission gave illumination levels ranged from 15% to 85% of the normal lamp power value. Further works should be oriented towards RGB LEDs versus phosphor ones. Hence, real-time video on Ethernet transmission can be achieved. Here, also there is no real analogue video transmission. New OFDM modulation technique should also be used.

D. O'Brien, 2013 [3], described OFDM schemes with equalization in digital domain, i.e. with pre-equalization for transmitter and post-equalization for receiver. The results achieved were 40Mbit/s with NRZ-On-Off Keys over several meters for pre-equalization and 100Mbit/s NRZ-OOK for post-equalization. The indoor MIMO was also investigated. Four LEDs communicated with four receivers. There are space of 0.1m from the terminal of the receiver. The transfer functions between the detectors and individual sources was measured by the 'In-operation training' software sequences. A channel or H matrix was created with the above combination. Each receiver recorded the independent data transmitted. The inverse of the H matrix is multiplied to estimate the transmitted data. The H matrix with full rank is then inverted. There are several distinct advantages for visible light communication (VLC) arose from high data rates based on low bandwidth channels. Standards for control of lighting systems and lightings are developing. Hence, VLC must be compatible with these standards as communication is its sub-function.

Z.H.Yu et al., 2014 [14], introduced the use of delta-sigma modulators in VLC. OFDM system converted continuous magnitude OFDM symbols into LED driver signals. The proposed system has the communication theory advantages of OFDM along with the practical analogue and optical advantages of simple two level driver signals. Orthogonal frequency division (OFDM) can easily support multiple access, which is critical for multiple user broadcasting [16]

P. Wolniansky et al.,1998[11], showed high spectral efficiencies is achievable in the rich scattering wireless channel. The V-Blast and Blast detection scheme were described in detail. It was pointed out that spectral efficiencies of these magnitudes are essentially impossible to obtain using traditional approaches with the use of a single transmitter. This is because the required constellation loading would be enormous. It has been demonstrated

spectral efficiencies of 20 to 40 bps/Hz under real world indoor conditions. It was exceeding any experiments that were not aware of using normal modulation technique.

2.2. Multiple-input-multiple-output (MIMO) communication

H. Minh, et al., 2010 [8], described Multiple-input-multiple-output (MIMO) systems that can provide higher Gbit/s transmitter capacity by parallel data transmitting and continuous channel matrix updating with separate data at the receiving end.

S. Jivkova et al., 2004 [12], stated that multi-spot diffuse multiple-input–multiple-output (MSD-MIMO) links are free from multipath dispersion virtually with high-speed communications. This non- line-of-sight links with poor power efficiency is its characteristics. The quality of service in indoor VLC systems is their vulnerability to blockage and shadowing. An opaque object can completely blocked or partially shadow an optical link. This is because light does not penetrate opaque barriers. Sitting people can cause blockage. Therefore, the maximum radiation angle at the transmitter can be concluded less than 45 degree with restricted communication cell size. MSD-MIMO links are vulnerable to shadow but robust against blockage. In a typical office with a height of 3m, shadowing probability caused by standing people is less than 2% . The majority of the shadowing with less than 0.1 dB in 99% of the cases, is insignificant For indoor environment, there are 3 types of MIMO configuration: diffuse, multi-spot diffusing and line of sight. Multi-Spot-Diffusing (MSD) was used to reduce temporal dispersion and to enable terminal mobility. Hence, a configuration known as MSD-MIMO system is a hybrid configuration that combines their advantages to feature line-of-sight (LoS) links and classical diffuse.

V. Rivera-Alvarez et al., 2005 [13], described MIMO technology aimed to improve the bit error rate (BER) quality or deployment of multiple spatial ports and adequate signal processing techniques at both ends of the system. Orthogonal space-time block coding is emphasized. Space-time coding methodology in mobile systems reduced the complexity of the receiver structure. In a multiple antenna transmitter, one may expand the degrees of freedom for the Vector space-time signal design. The advantage of constellation rotations and the introduction of quasi-orthogonal STBC were explored.

2.3. Hybric Visible light communication

C.C.Lee et al.,2013 [1] had described their simulated results. Hybrid system achieved power consumption by 68% and reduced cost by 3% when compared to fluorescent lights with RF technology. However, LEDs with RF technology can reduced power consumption by 49% and achieved device cost saving as high as 47% . Thus, hybrid VLC has paved the way for greater cost saving and energy efficiency. It has demonstrated to be a feasible solution.

Xu B. et.al, 2013 [15], showed a Hybrid VLC-OFDMA network model is linked to the server via wired connections. Analytical and simulation results showed large improvements in the capacity performance of the hybrid, when compare to OFDMA system. Hence, this research will focus further on the investigation of Hybrid VLC.

N.Rajagopal et al., 2014 [17], described VLC between smart-phone camera and LED light has gain recognition for indoor localization applications. This paper provided adaptive duty cycling as a scheme for mixing camera communication with higher speed data. The camera communication with more extreme duty cycles increased the data speed with reduced performance. A wakeup circuit to support aggressive duty cycling of low power embedded devices such as wireless sensors has also been shown.

W.Guo et al., 2015 [18], proposed a parallel transmission Multiple access communication (MAC) protocol for an indoor hybrid wireless network using VLC and RF. Combining the CSMA/CA algorithm and the concept of parallel transmission, the protocol can solve the multiple access problems for nodes in the hybrid network. It uses a two-dimensional Markov chain model to construct the channel reservation model and also gives the throughput theory analyzing algorithm of parallel channel. According to the numerical results, the proposed mechanism improves the throughput and efficiency of the hybrid network.

3. Methodology in Hybrid Visible Light Communication (VLC)

A typical visible light communication can be depicted in Fig.2. Two different scenario associated with VLC are showed in indoor environment. The radiating source is a transmitter. Modulation can be done on its intensity. Transmitter diffused indirectly light with reflection from intermediate surfaces or propagates via a Line-of-sight (LOS) path as shown in Fig. 2(a) and 2 (b) respectively. A lens or other optical apparatus concentrates light on the receiver. Hence, it created a signal proportional to the optical power incident on it. This is called Direct detection (DD) or intensity modulation (IM) system. This constituted fundamentally to the majority of VLC research. The intensity enveloped detector effectively formed a receiver. This 10^{14} Hz visible light carrier frequency is too high to be detected by DD receivers.

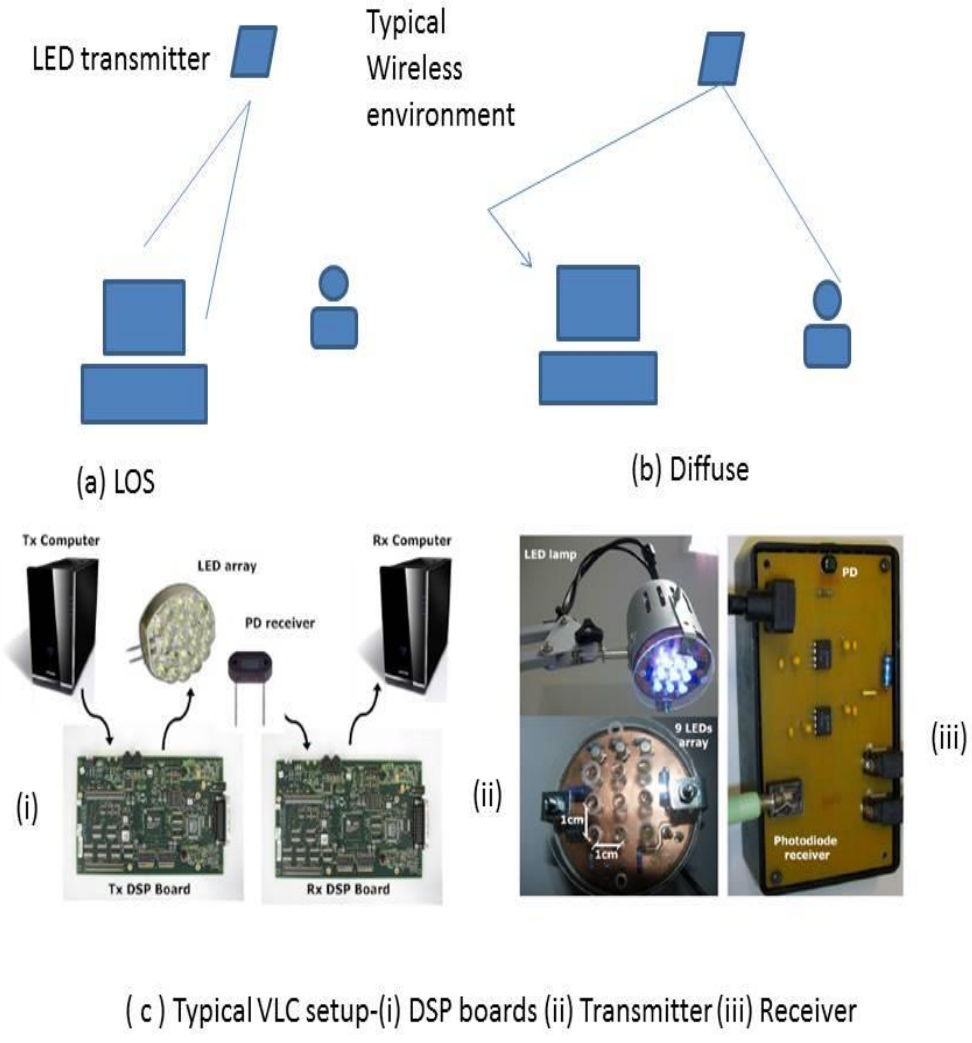

Figure 2: Typical optical wireless environment[5]

The diagrams of the transmitter and the receiver are shown in Fig.3 with their brief descriptions [19, 20].

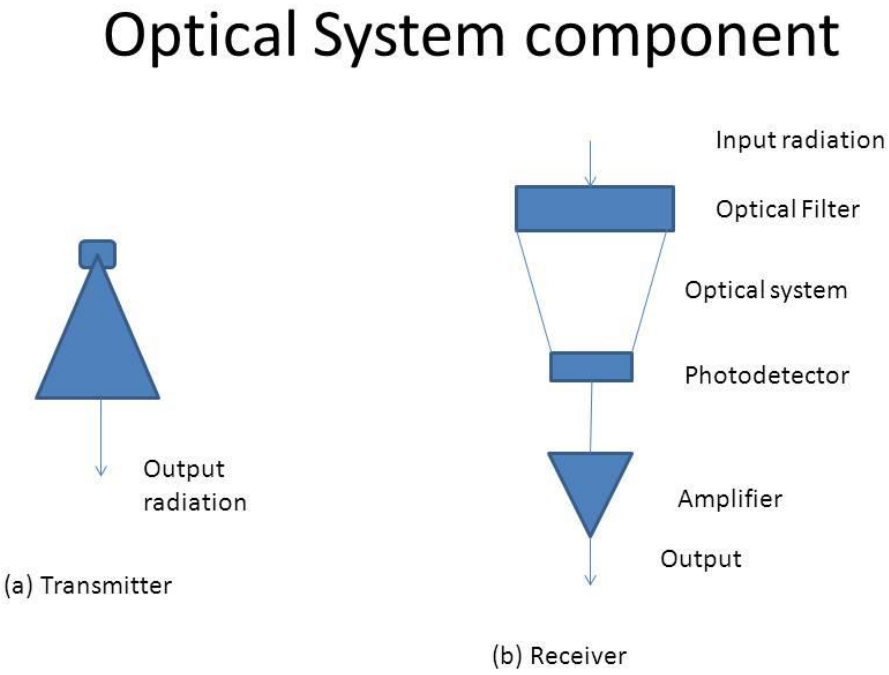

Figure 3: Optical system components (a) Transmitter (b) Receiver

3.1 VLC Transmitter:

Radiation sources may come from LEDs or semiconductor lasers. A drive current controlled the optical output power of these apparatus with modulated Information. Low cost LEDs with modest bandwidth are used as high power sources. Typically high-power white light sources are utilized for VLC. A yellow phosphor coating excited blue LED generated the light. White light is created by the yellow and blue lights illumination jointly. Blue driver current emitter with direct modulation has a faster time constant versus the yellow emission. Therefore, the yellow component is blocked at the receiver and the blue "channel" is used for communications. Eye safety is an issue especially in the context of lasers. The emission pattern can be controlled safely through diffusing elements source [20].

3.2 VLC Receivers:

Light passes through an optical filters to the receiver. Both artificial illumination and natural daylight sources posed as noise sources on the VLC signal. Relatively narrowband radiation from the transmitter passes through the optical filter. It rejects the optically broadband unwanted light which fell externally to the useful band. For VLC, blue LED light passes through the filter. Light is concentrated onto a photo-detector through a lens. Photo-detectors changes the optical power with proportion to the current. This current is usually transformed to a voltage through a trans -impedance amplifier. Before data recovery, it further amplified.

The receiver constraints determined the performance of VLC systems rather than that of transmitter. The goal of the optical collection element is to maximize field of view. In other words, the range of incident angles over the receiver is sensitive to incoming light over the collection area. Therefore, the area of the photo-detector is directly proportional to the

system's capability in collecting light. However, detector's capacitance increases with its area. Thus, It limits the achievable bandwidth. Complexity tradeoffed the design of VLC receivers. [20].

3.3. The channel:

Single propagation path is associated with LOS channels. There are no practical channel bandwidth limitations. The receiver and transmitter designs caused limitations. DD/IM channels has no identifiable interference effects even if coherent sources are used (e.g.lasers). Diameter of most photodetectors is several hundred micrometers. Therefore, the integrating effect of the photo-detector covered any potential spatial multipath interference effects.

In non-LOS channels, multipath propagation posed problem to the inter-symbol interference (ISI). Most surfaces are Lambertian scatter in indoor situations [18]. The light reemitted and absorbed effectively into all angles of emission with equal brightness. The radiation angle of incidence onto walls destroys the omnidirectional scattering. Similar quantum of power was detected in any direction by a receiver. Diffuse environment created the scattering of light by multiple surfaces, Different delays in propagation at the receiver is radiated by multiple copies of the transmitted signal. The power in each of them will be integrated or summed by the photo-detector at the receiver. There is a few delayed paths by channel-induced dispersion. Its Fourier transform consisted of a low pass nature. It will have severe resultant bandwidth limitation. This dispersion scenarios can be found in many literatures [20].

3.4 Modulation:

Visible light communication (VLC) used extensively simple modulation schemes like Pulse position modulation (PPM) and on-off keying (OOK). It is different from RF systems in that there is a tradeoffs between power and bandwidth efficiencies. The difference is the unipolar nature of the optical signal. Direct current (DC) offset from source is needed for bipolar scheme. When compared to OOK, quadrature amplitude modulation (QAM) schemes have a biasing penalty. This erodes QAM scheme benefits. However, it is more bandwidth efficient [25].

To achieve data rates greater than 500 Mb/s using a single LED, Orthogonal frequency division modulation (OFDM) has been used [22]. "Bias-free" OFDM has strikes a balance between power and bandwidth efficiency. Emitter with linearity and dynamic range limits the performance achievable [24].

One notable source is from research works done by Prof. Herald Haas [5]. He is recognized world- wide to be the pioneer in visible light communication. His team in University of Edinburgh, Scotland, U.K. has achieved many successes as far as harnessing this new technology. His prototype consisted of a transmitter with two parts. Firstly, a digital signal processing (DSP) development board is to generate analog signal and interface with the transmitter computer. Secondly, an analog section of LEDs array and the driver electronics [5]. The receiver consisted of an analog photodiode (PD). Then a dc blocking stage via a transmitter amplifier is linked to a preamplifier stage. OFDM signal was decoded by another DSP board. It will then interface to receiver computer [5].

Fig. 4 depicted the physical layer's building blocks. A convolutional encoder for data protection using forward error correction (FEC) coding algorithm in the system. Frequency and time interleaving algorithms are used for burst error protection. The model is similar to

that of a classical OFDM system. The difference appears with the IFFT (inverse fast Fourier transform) operation. It is related to the optical carrier intensity modulation (IM) technique. LED intensity modulated the OFDM baseband signal. It should avoid any complex values. A CP (cyclic prefix) of guard interval is added to avoid multipath induced inter-state-interference (ISI). A linear convolution OFDM signal is to be converted to a circular convolution. Simple frequency domain equalizer can be used at the end. Moreover, symbol equalization and time synchronization can be realized using the pilot carriers and training sequences [5]. When generating the training sequences, it must fulfill a complex conjugate requirements. Then the pilot carriers can be assigned. Fast Fourier transform (FFT) operation will be used to convert the OFDM signal back to frequency domain after the CP removal.

The training sequence formed the OFDM frame which consists of one OFDM symbol. Subsequently it was followed by 20 OFDM symbols of data sub-carriers. Estimation of channel is by the training sequence. A conventional OFDM zero forcing (ZF) equalizer can be used to realize frequency domain equalization. A Viterbi algorithm of hard decision decoded and estimated de-interleaved bit stream [5].

Orthogonal frequency division modulation (OFDM) is becoming the chosen modulation technique for wireless communication. OFDM can provide high data rates to radio channel impairments with sufficient robustness. An OFDM scheme consisted of a large number of overlapping, narrow band, orthogonal sub-carriers or sub-channels. It divided the transmission bandwidth and transmitted in parallel. There is a very compact spectral utilization. The separation of the subcarriers is theoretically minimum. The attraction of OFDM will be its handling of the multi-path interference at the receiver.

Robustness can be achieved against frequency selective fading by using powerful error correcting codes together with frequency and time interleaves. The reduction in efficiency of ISI can be done through insertion of an extra guard interval between consecutive OFDM symbols. Therefore, an equalizer is not needed in the receiver.

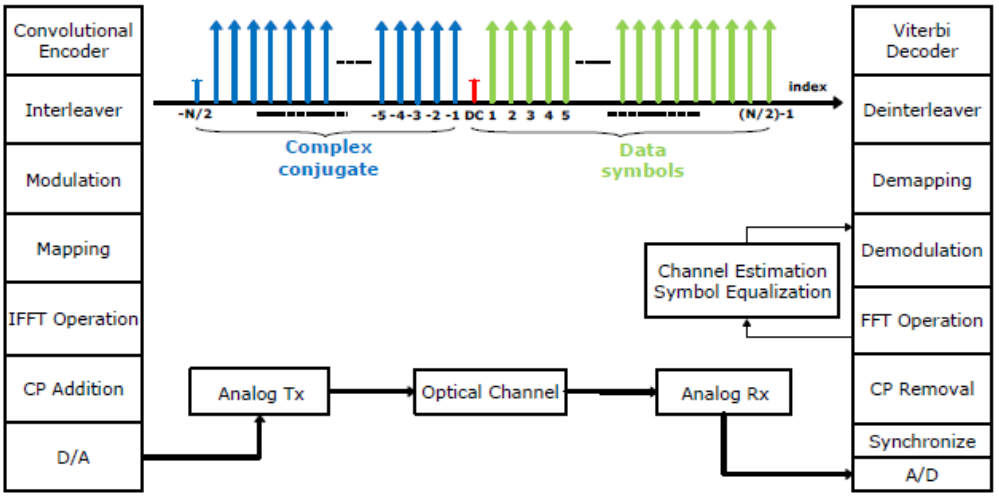

Fig.4: The Building block of VLC OFDM [5]

Example of a typical VLC scheme's Block diagram is as shown in Fig.5 [16]. Other methods will vary the modulator technique to achieve the required performance in Signal-to-noise (SNR) ratio, bit rate ratio and other typical efficiency ratio.

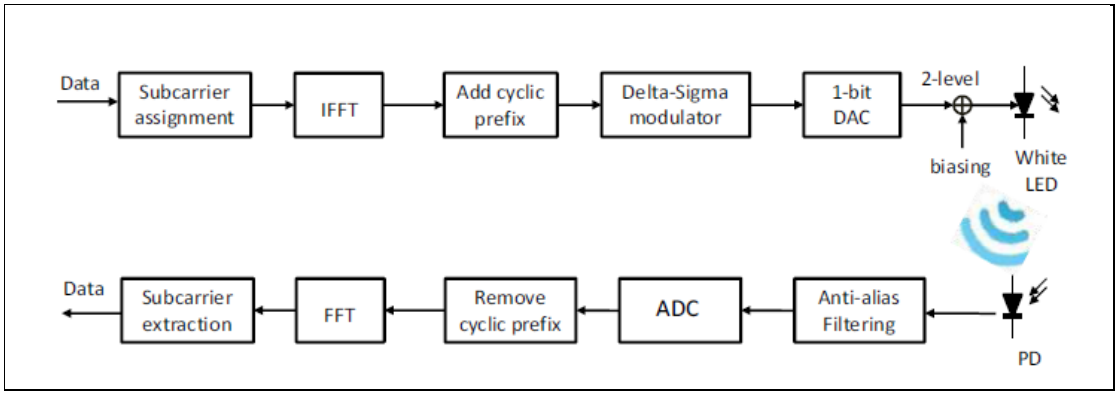

Fig.5: The Block diagrams of VLC [16]

Another paper of Prof. H. Haas [2], described a strictly unipolar orthogonal frequency division multiplexing (OFDM) design which requires no biasing and is able to demonstrate significant energy advantage.

4. Research Challenges

Multiple receivers and transmitters with high data rate are required for VLC systems. High gain beam-steering should be used to track them. Their architectures includes image based cellular, quasi diffuse, angle diversity assisted and tracking aids.
Multiple LEDs plotted on the target coverage area in VLC with the aid of MIMO-like architectures. This design philosophy for both IR and visible lights sources is particularly promising. The fabrication of transmitters or large arrays of sources are relatively straightforward. Massive multifunctional MIMO (MF-MIMO) systems is feasible with hundreds of detectors or receiver arrays [20].

There is a growing interest in Optical MF-MIMOs for VLC. When each source has a limited bandwidth, The signals of multiple sources based on MIMO concept may be combined for overall data rate increments. Moreover, “rich scattering” environment does not create by the DD/IM channel. Typically, a full rank channel matrix is resulted as in RF wireless communications. Lambertian scattering from surfaces normally tends to render similar elements of the channel matrix with each other with no useful angle of arrival information. Hence, LOS MIMO systems imaging often rely on auxiliary elements and other lenses to create on detector array an approximate image of the source array. Maximizing attainable quantum design of channel matrix with robustness to misalignment of detectors and sources is employment of some diffractive elements. The ease to shape the optical field is its benefit. Design based on a spatial modulation is an alternative proposal for isolation of MIMO transmitters. The activated transmitter index itself also conveys implicit information. The whole concept of diverse MIMO solutions may also be used in the visible light communications (VLC) . The non-coherent unipolar nature of the channel substantially affects the performance and analysis of different schemes [20].

System with 1.25 Gb/s operation has been demonstrated [14]. Experiments with 10 Gb/s partial link transmission also attempted. Hence, it is feasible for higher data rates. Large coverage area combined with high rates constitutes the major challenge. This is because the link margin requires a low path-loss for such systems to operate reliably. MIMO systems are able to mitigate this impediment to a certain extent. The basic receiver sensitivity is still worse than for RF in magnitude. [16] investigated parametric amplification. [17] conceived optical amplification using fiber and [18] conceived semiconductor amplifiers. Free-space

radiation into a waveguide with high amplifier gain is the requirement. Designing high-bandwidth and high sensitivity receivers is going to gain the most in the near future.

5. New development of Hybrid VLC

The wide spread of mobile broadband services and wireless fidelity (WiFi) [24] meant that future VLC system will coexist with established RF communications. It is still a relatively opened research question to use the systems cooperatively. Very high data-rate connections with a combination of RF and VLC hotspot can be reliable. It is also an advantage for visually observable hotspots in VLC. Further good point is its mobility. An optical downlink availability in hybrid VLC for large data transfer shows the potential promise of the technique.

Services providing continuous streaming (e.g. video) and constant cloud connectivity (e.g. cloud file synchronization) are particularly onerous on data capacity requirements. Technologies such as fiber optics can increase transmission along part of the network delivery path, the limited capacity of existing wireless local area networks (WLANs) can severely limit transmission rates within the home or office. Li-Fi (Light Fidelity) technology utilized LEDs to serve as dual role in providing lighting and data communication in an energy efficient way based on visible light communications [26]

Table 1 summarizes the basic characteristic of VLC and a comparison between RF and optical wireless systems. VLC has opened up new wireless bandwidths. It is owned by the lighting rather than the communication providers. It is potentially attractive as a low cost overlay where the lighting infrastructure can be reused. It has to be compliment to RF wireless solutions so that the best overall network can be provided to the users. LiFi uses complex heterogeneous optical semiconductor components with low-cost electronics. RF communications utilizes the complexity resides in electronic processing. Future systems will aim for resolving these difficulties and those imposed by the associated channel characteristics.

There may be a “cross-over frequency” amongst higher carrier frequencies between their domains. LOS propagation may be encountered in both cases. Thus, the associated blockage and coverage issues are expected to be similar. The electronic convenience of LiFi is an advantage. It is more realistic to combine the coherent techniques with high data rate detection algorithms in optical MIMO fiber transmission systems. The low power, license-free services, that may be allocated in the higher frequency bands. This is useful to expand the coverage into indoor spaces. These LiFi systems will operate by modulating the visible light, thus creating visible LiFi hotspots physically. The power cable directly linked together the LED transmitters with the mains. Numerous transmitters of LED based transmit prepossesing cooperative VLC linkage to the mains. The advantage is that there will be a sufficiently close optical hotspot for supporting VLC receivers. The LiFi hotspots may be expected to spread to street and traffic lights, shops and etc. Naturally, the LiFi hotspots’ tele-traffic may also be fed into the asynchronous digital subscriber line (ADSL) based telephone lines. The resultant heterogeneous network architecture may be contrasted with the hierarchical cellular structure as in Figure 6 [27, 28].

Table 1: Comparison of Optical and RF wireless [20]

Attribute	RF Wireless	Optical wireless
Link Margin	Excellence, due to coherent detection and noise processes	Poor due to incoherent detection at receiver and noise mechanism
Spatial Confinement	Typical propagation loss Through walls.1 dB/cm	Confined by internal spaces
Regulation	Subject to licensing and regulation	Subject to eye safety regulation, currently no licensing
Availability of spectrum	Limited and expensive	1000s of Thz of spectrum available
Ability to control radiation patterns	Challenging owing to constraints on antenna size in most appliances.	High degree of control using lenses and diffractive elements
Propagation	Scattering/reflection and diffraction create broad area coverage	Ray propagation allows very tight confinement of radiation
Interface with fixed network	Need optoelectronic interface of directed RF to connect with fibre network	Possibility of using light from fibre network to create transparent interface

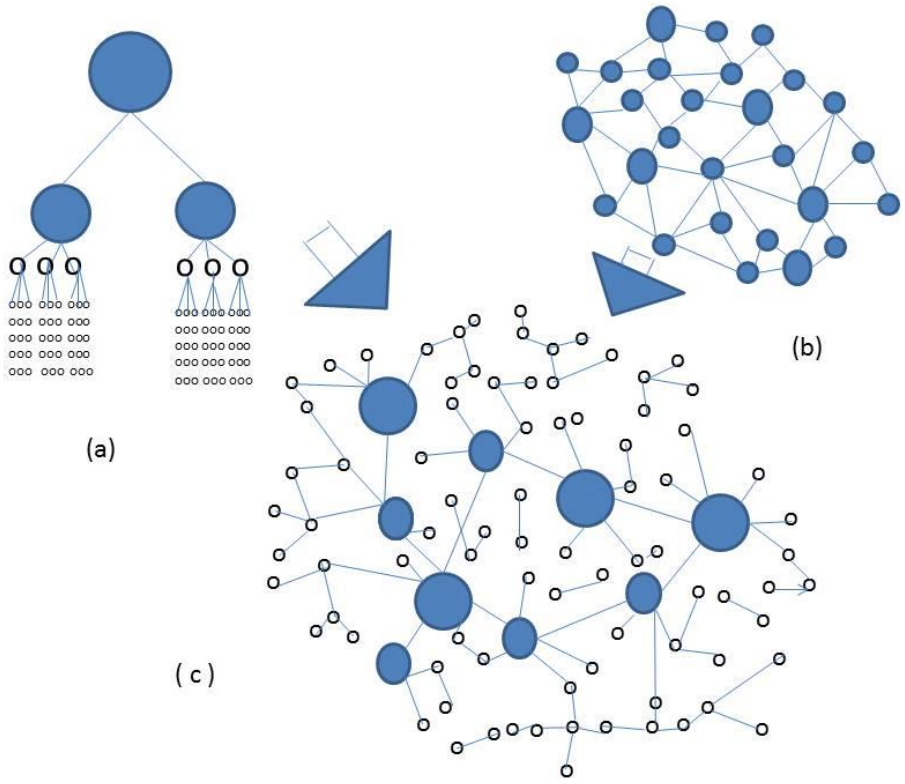

Figure 6: Network architecture-(a) cellular (b) Ad-hoc (c) Heterogeneous/Hybrid

Fig.7. Future telecommunication networking scenario[5]

Due to the complementary nature of visible light and radio frequency wireless, the combined use of both illumination and transmission in coverage and capacity would have advantages over a single media. Hence, the seamlessly transitional hybrid visible light communication scheme can be the future telecommunication way of life as in Fig.7.

7. Conclusions

From the past three decades, there is a thousand fold in bit rate improvement. New and powerful wireless services have been introduced. These power thirsty and bandwidth hungry multimedia services has absorbed the bitrate increase. Moreover, smartphones and tablet computers with increased popularity has resulted in unprecedented penetration of wireless communications. In the next decade, the amount of tele-traffic is expected to substantially increase with new frequency bands requirement. The RF bands has migrated from 450 MHz, 900 MHz, 2 GHz, 5GHz, 60 GHz and go above the terahertz visible light domain.

The fifth generation networks (5G) will not be an extension of today's fourth generation mobile Networks (4G). 4G networks today achieves a maximum speed of 1Gbit/s and a delay of about 50ms theoretically. To make next generation mobile networks possible, telco operators will have to deploy new network technology such as hybrid visible light communication technology described in this paper. Therefore, the superfast visible light communication (VLC) network of greater than 10Gbit/s and a latency delay of very few milliseconds will be ideal candidate to achieve this ambition plan. Telco operators will have to create dense clusters of small mobile phone cells or tap into the VLC LiFi spectrum that works like WiFi. Fifth generation (5G) will have to be ready for ever increasing data volumes of mobile users and the proliferation of data from the smart sensors and device that will propel the Internet of Things.

Acknowledgment (optional)

The author would like to thank O.Y.L.Technology S/B and Taylor's University for their support of this paper. Special Thanks to Dr.Florence Choong Chiao Mei and Dr. Yandan Lin for their assistants and guidance in the research work and important suggestions.

References

[1] C. C. Lee, C. S. Tan, H. Y. Wong, M. Yahya, "Performance evaluation of Hybrid VLC Design using device cost over data throughput criterion", SPIE Conference on Ultrafast Imaging and Spectroscopy (2013).
[2] D. Tsonev and H. Haas , "Avoid Spectral Efficiency Loss in Unipolar OFDM for Optical Wireless Communication.", EPSRC (2014).
[3] D. O'Brien, "Visible light communications: achieving high data rates", ERC (2011).
[4] G. Yun and M. Kavehrad, "Spot diffusing and fly-eye receivers for indoor infrared wireless communications," in Proc. IEEE Int. Conf., pp. 262–265. (1992).
[5] H. Elgala, R. Mesleh and H. Haas, "Indoor Broadcasting via white LEDs and OFDM.", IEEE (2009).
[6] H. Elgala, Raed Mesleh and Harald Haas, "An LED Model for Intensity-Modulated Optical Communication Systems", IEEE Photonics Technology Letters (2013).
[7] H. Haas and S. McLaughlin, "Next generation mobile access technologies.", Cambridge University press (2007).
[8] H. L. Minh, Z. Ghassemlooy, D. O'Brien, G. Faulkner, "Indoor Gigabit Optical Wireless Communications: Challenges and Possibilities", ICTON pp. 1-6 (2010).
[9] Ingram M.A. and Acosta G., "OFDM simulation Using Mathlab.", SARL,Georgia Institute of Technology", (Aug. 2000).
[10] J. Rufo, J. Rabadan, F. Delgado, C. Quintana, and R. Perez-Jimenez, "Experimental Evaluation of Video Transmission Through LED Illumination Devices.", IEEE Transactions on Consumer Electronics, Vol. 56, No. 3, pp. 1411-1416 (Aug. 2010).
[11] P. W. Wolniansky, G. J. Foschini, G. D. Golden and R.A. Valenzuela, "VBLAST: an architecture for realizing very high data rates over the rich scattering wireless channel," in Proc. URSI International Symposium on Signals, Systems, and Electronics, Palazzo dei Congressi, Pisa, Italy, pp. 295 (Sept. 1998).
[12] S. Jivkova, B. A. Hristov, and M. Kavehrad, "Power-Efficient Multispot-Diffuse Multiple-Input–Multiple-Output Approach to Broad-Band Optical Wireless Communications", IEEE (2004).
[13] V. Rivera-Alvarez, D. Torres-Román and V. Kontorovitch, "On MIMO Space-Time Coded Systems: Unleashing the Spatial Domain", 2nd International Conference on Electrical and Electronics Engineering (ICEEE) and XI Conference on Electrical Engineering (CIE) (2005).
[14] V. Tarokh, H. Jafarkhani, and A. R. Calderbank, "Space-time block code from orthogonal designs," IEEE Trans. Inform. Theory, vol. 45, pp. 1456-1467 (July 1999).
[15] B. Xu, X.R.Zhu, T. C. Song and Y.Q.Ou, "Protocol design and capacity analysis in Hybrid network of visible light communication and OFDMA systems.", IEEE (2013).
[16] Z. H. Yu, A. J. Redfern and G. T. Zhou, "Using Delta-Sigma Modulators in visible Light OFDM systems.", WOCC (2014).
[17] N.Rajagopal, P.Lazik and A.Rowe, "Hybrid Visible Light Communication for cameras and low-Power Embedded devices", Carnegie Mellon University (2015).
[18] W.Guo, Q.Li; H. Yu and J.Liu, "A parallel Transmission MAC Protocol in Hybrid VLC-RF Network", Engg and Tech (2015).

[19] A.Servincer, A. Bhattarai, M. Bilgi, M. Yuksel and N. Pala, "Lightnets: smart lighting and mobile optical wireless networks- a survey." IEEE (2013).
[20] L.Hanzo, H.Haas, S. Imre, D.O'Brien, and L. Gyongyosi, "Wireless Myths, Realities, and Futures: From 3G/4G to Optical and Quantum Wireless', IEEE (2012).
[21] V.Jungnickel, V.Pohl, S.Nonnig, and C. von Helmolt, "A physical model of the wireless infrared communication channel", IEEE (2002).
[22] A.J. Lowery and J.Amstrong, "10 Gbit/s multimode filter link using power efficient OFDM", Op Express (2005).
[23] J. Vucic, C. Kottke, S. Nerreter, K.D. Langer, and J.W. Walewski, "513 Mbit/s visible light communication link based on DMT-modulation of a white LED." J. Lightw. Tech., (2010)
[24] J. Armstrong and A. Lowery, "Power efficient optical OFDM", Elect. Lett. Vol.28.no.6, pp.370-372, (2006)
[25] S. Dimitrov and H. Haas, "On the clipping noise in an ACO-OFDM optical wireless communication system" Proc. IEEE conf. (2010)
[26] L. Hanzo, J.Akhtman, L.Wang and M.Jiang, "MIMO for LTE, WIFI and WIMAX: CoHerent Versus Non-coherent and CooperativeTurbo Transceivers", Chichester, U.K., Wiley/IEEE Press (2010)
[27] J. Hou and D. O'Brien, "Vertical handover decision making algorithm using fuzzy logic for the integrated Radio and OW system.",IEEE Trans Wireless Commun., Vol 5, no.1, pp 176-185 (2006)
[28] J.Akhtman an L.Hanzo, "Heterogeneous networking: An enabling paradigm for ubiquitous wireless communications", Proc. IEEE, vol.98, pp 135-138 (2010)

Edge Detection of the Scoliotic Vertebrae using X-Ray Images

P. Mohankumar, LEONG Wai Yie
School of Engineering, Taylor's University, Taylor's Lakeside Campus, No 1 Jalan Taylor's, 47500 Subang Jaya
mohanphysionix06@gmail.com, waiyie@gmail.com

Abstract

Bones such as skull, rib cage and pelvis provides protection to our internal organs. Bones also act as a mineral storage reservoir for calcium and phosphorus. It also helps in the blood cell production. A proper well grown bones give a perfect posture to the human body. In other case, if the bone has an improper growth, it might lead to an abnormal posture or an awkward posture. Scoliosis is a condition where the scoliotic vertebrae is wedge shaped and differ with the shape of a normal vertebrae. Treatment for scoliosis depends majorly on cobbs angle which can be measured using spine X-rays. Recent development in the medical imaging techniques brought us to a new research area in image processing which includes medical image enhancement, detailed visualization of internal organs & tissues and edge detection. Bone edges are important feature in an X-ray image. The purpose of application of segmentation in medical imaging is to develop a detailed framework on human anatomy, whose primary objective is to outline the anatomical structures. Whereas edge detection is a technique which extracts vital features like corners, lines, angles and curves from an image. In this study, we are going to deal with the edge detection technique on scoliotic vertebrae. The objective of this paper is to compare the performance of edge detectors using filters and operators.

Keywords: X-rays, Edge detection.

1. Introduction

Bones are the basic blocks of human body [1]. It gives the shape and structure to our human body. Bone density depends on several variables. They are: Age, Gender, Location in the body, its Mineral content, Water and Diseases. These variables are inter-related to each other. For instance, mineral content and density will vary depending on the bone's location in the body. As humans get old, their bones become osteoporotic. Their strength decreases, which means they are more susceptible to fracture. Osteoporosis is a disease which leads to a decrease in bone mass. It is mostly found in geriatrics patients. Bone is considered to be a responsive material. The formation and resorption of bone occur in a cyclic manner. Our body responds to different stress levels from different parts of the body in different areas of bone to ensure that, the right amount of healthy tissues of bone is present, so that the bone can be continuously reshaped.

A stress of 25–40 MPa is sufficient to maintain the correct levels of bone [1]. If the bone is under stress for a prolonged duration, bone formation and resorption process is disturbed and leads to wastage in bone tissues. Due to this, bones become thinner. This can be an issue for patients who are bedridden for a long duration and with the astronauts after a long stay in the space. Similar effect occurs during osteoporosis too. In osteoporosis osteoblast gets reduced, leading to thinner and weaker bones. Whereas scoliosis is a condition, where mal alignment of the vertebral bones and improper stress distribution (trabecular system) lead to a wedge shaped vertebrae.

The objective of this study is to do edge detection in patients with scoliotic vertebrae using x-rays. In early stages of image processing, identifying any features in an image that are relevant to estimating the structure and properties of the objects in that image was the primary motive. Edges are a significant local change in an image. Edges are one such feature which typically occurs in the boundary between two different regions or colours in an image. Edge detection method is the first step in recovering information from images. Due to its importance, edge detection continues to be an active research area [2]. Hence, this study will be helpful to understand and identify the edge detection methods in x-rays.

Edge detection is an image processing technique, mainly used for finding the boundaries of objects, within the different regions in the image. It works by detecting the discontinuation in the brightness of the image and the boundaries of objects in a scene. In an image, an edge is a curve that follows a path of rapid change in image intensity. Edge detection is used to identify the edges in an image. Discontinuities in the image intensity can be either step or line discontinuities. In step discontinuities, the image intensity abruptly changes from one value on one side of the discontinuity to a different value on the opposite side. While in the line discontinuities, the image intensity abruptly changes value but then returns to the starting value within some short distance. However, step and line edges are rare in real images. Because of low-frequency components or the smoothing introduced by most sensing devices, sharp discontinuities rarely exist in real signals. Step edges become ramp edges and line edges become roof edges, where intensity changes are not instantaneous but occur over a finite distance. Illustrations of these edge profiles are shown in Figure

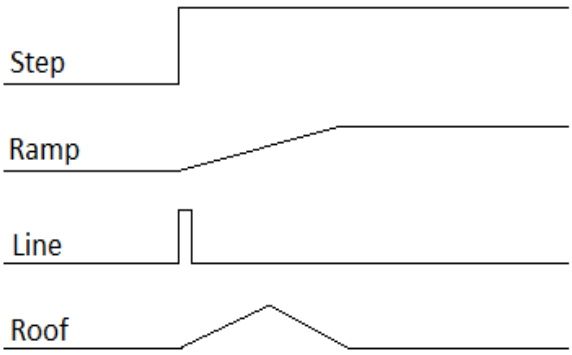

Figure 1: Types of edge profiles

2. Review of Literature

2.1 Edge Detection on X-rays

Several studies were done to find the edge detection of an image. Certain studies were done on the X-ray images too. Padma Priya B, Ashmaa R and Shiny Mol S (2014) conducted a study on X-ray image acquisition and analysis. They used edge detection techniques for various dental X-rays [3]. Dr. S.K. Mahendran (2012) done a study on edge detection algorithms for computer aided fracture detection systems, where, he analyzed the applicability of five different edge detection algorithms for detecting the edges of X-ray images [4]. Shubhangi D.C, Raghavendra S. Chinchansoor and P.S. Hiremath (2012) conducted a study on edge detection of femur bones in X-ray images. It was a comparative study of edge detectors [5]. Cristina Stolojescu-Crisan (2012) from Politehnica University of Timisoara done a study on edge detection techniques for X-ray image segmentation on hand X-rays [6]. Gautam Appasaheb Kudale and Mahesh D. Pawar (2010) conducted a study on analysis of various edge detection methods for X-ray images [7].

2.2 Cobb angle detection

Tri Arief Sardjono, Michael H.F. Wilkinson, Albeert G. Veldhuizen et al., (2013) conducted a study on automatic cobb angle determination from radiographic images [8]. Raka Kundu, Prasanna Lenka and Amlan Chakrabarti (2012) done a study on cobb angle quantification for scoliosis using image processing techniques, where they found the cobb angle using different filters and hough transform [9].

3. Methodology

Subjects with history of scoliosis in the age group between 5 to 35 years were selected. Informed consent was obtained prior. Baseline assessment like age and sex were noted for all the subjects participated in this study. After the baseline assessment, X-rays were obtained from the patients, for edge detection. These algorithms have been coded in order to detect the edge of the X-ray images of spine. There are several methods to detect the edge of the X-ray images of spine using the gradient method. In this study ddifferent types of edge detection

methods like Sobel operator, Prewitt operator, Robert operator, Log operator and Canny operator were used to analyze x-ray images. The original image is given below:

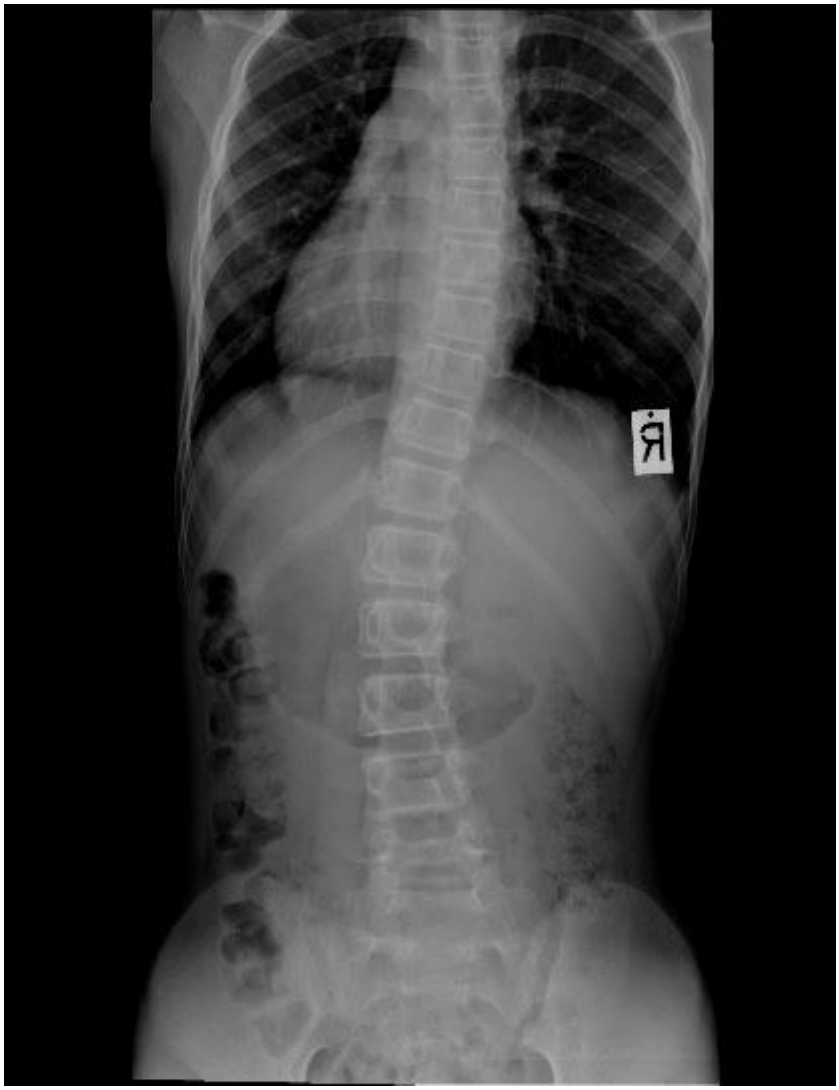

Figure 2: Original X-ray image

3.1 Sobel operator

The sobel operator uses a 3x3 convolution, which is the x and y direction of an image. It is discovered at the first derivative level. The horizontal and vertical pixel masks for sobel operator is shown below. The sobel operator calculates the opposite of the gradient of the input image. The formula to find the gradient magnitude is:

$$|G| = |G_x|\,|G_y| \qquad (1)$$

where G_x and G_y are given by the formulae:

$G_x = (a_2 + ca_3 + a_4) - (a_0 + ca_7 + a_6)$

$G_y = (a_0 + ca_1 + a_2) - (a_6 + ca_5 + a_4)$

Where c is a constant with a value 2.

The horizontal and vertical pixel masks for sobel operator is given below:

-1	0	1
-2	0	2
-1	0	1

1	2	1
0	0	0
-1	-2	-1

Edge detection is applied to the figure 2 using sobel operator.

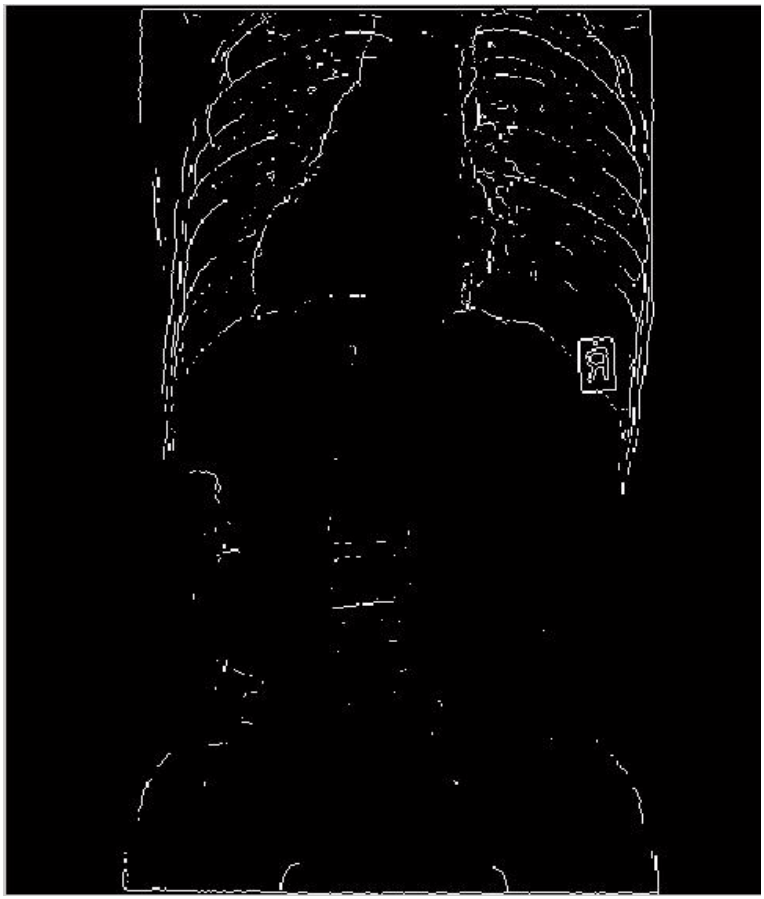

Figure 3: Edge detection using Sobel operator

The algorithm of the edge detection must include gray scale function to convert the color image to gray scale before proceeding to edge detection to avoid any occurrence of error.

3.2. Prewitt operator

Prewitt operator is a discrete differentiation operator, which computes an approximation of the gradient of the image. It is based on the central difference concept. Prewitt is more sensitive to noise effect. The properties of Prewitt operator are similar to sobel operator. Prewitt operator is similar to Sobel operator except that the constant $c = 1$. The convolution mask of prewitt operator is given below:

-1	0	1
-1	0	1
-1	0	1

1	1	1
0	0	0
-1	-1	-1

Prewitt operator is based on the central difference concept and is given by:

$$\frac{\partial I}{\partial x} \approx [\, I\,(x+1, y\,) - I\,(x-1, y\,) / 2] \qquad (2)$$

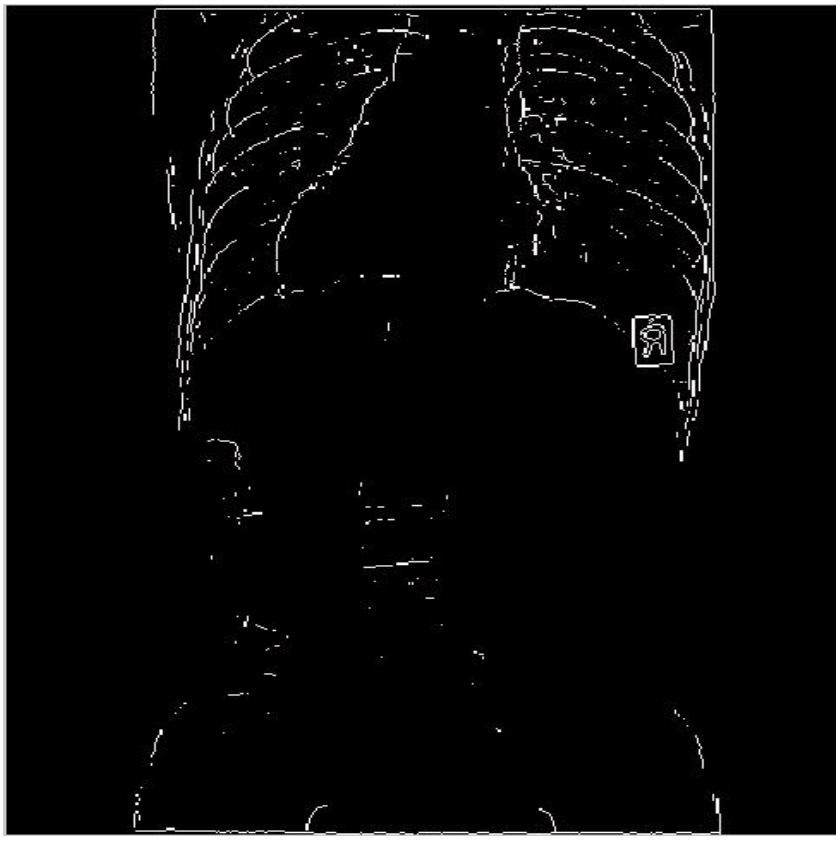

Figure 4: Edge detection using Prewitt operator

3.3. Robert operator

Robert operator uses 2 x 2 convolution masks. It uses (+1, -1) operator that will calculate the value for (*i*, *j*) pixel. Robert operator performs the discrete differentiation. The spatial gradient of an input image can be calculated absolute by computing the sum of squares of the differences between diagonally neighboring pixels. Robert operator provides a simple approximation to the gradient magnitude. The gradient can be defined as:

$$\nabla I(u, v) = G(u, v) = \sqrt{Gu^2 + Gv^2} \qquad (3)$$

Where $I(u, v)$ is a point in the original image, $G_u\,(u, v)$ is a point in an image formed by convolving with first kernel and $G_v\,(u, v)$ is a point in an image formed by convolving with the second kernel. The convolution mask of robert operator is given below:

1	0
0	-1

0	-1
1	0

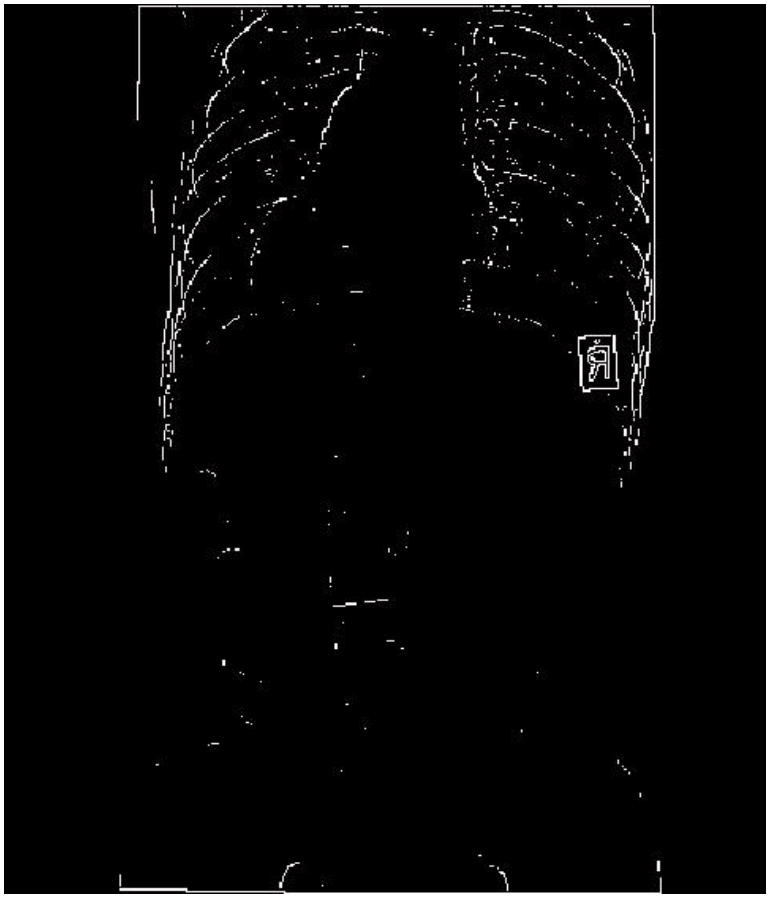

Figure 5: Edge detection using Robert operator

3.4. Laplacian of Gaussian (LOG)

The laplacian of gaussian (LOG) filter is used to filter out the noise in the image. LOG is used as an enhancement to the image. Enhancement is done by transforming edges into zero crossings. This is done by using 3x3 mask. Detection is done by finding a zero crossings. The laplacian $L(x, y)$ of image with pixel intensity values $I(x, y)$ is given by:

$$L(x, y) = \partial^2 I / \partial x^2 + \partial^2 I / \partial y^2 \quad (4)$$

Three commonly used small kernels are shown below.

0	1	0
1	-4	1
0	1	0

1	1	1
1	-8	1
1	1	1

-1	2	-1
2	-4	2
-1	2	-1

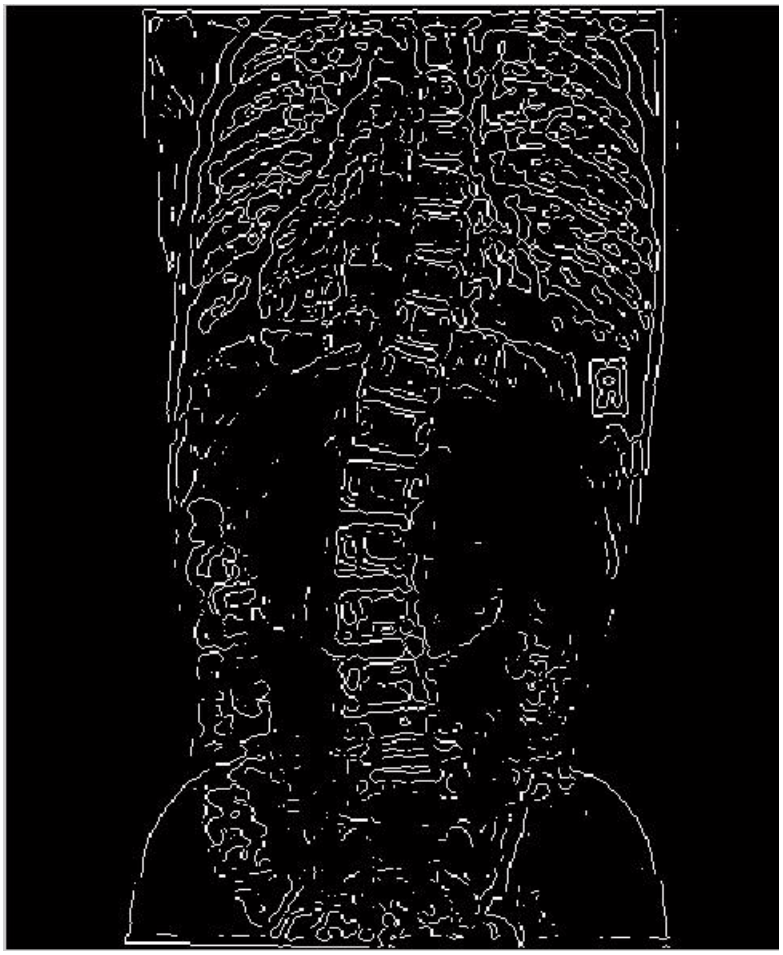

Figure 6: Edge detection using LOG operator

3.5. Canny operator

Canny edge detection method is a more robust gradient based edge detection algorithm. The canny edge detector is the first derivative of a Gaussian and closely approximates the operator that optimizes the product of signal to noise ratio and localization. In canny, edge detection is done on multiple stages. Noise reduction is one of the primary step to smooth the image. Then the edge gradient can be determined by returning the value of first derivative in horizontal, vertical and diagonal directions of a particular image. Finally, the edge strength of each edge pixel is set to zero if its edge strength is not larger than the edge strength of the two adjacent pixels in the gradient direction. The remaining pixels after this process are labeled as candidate edge pixels.

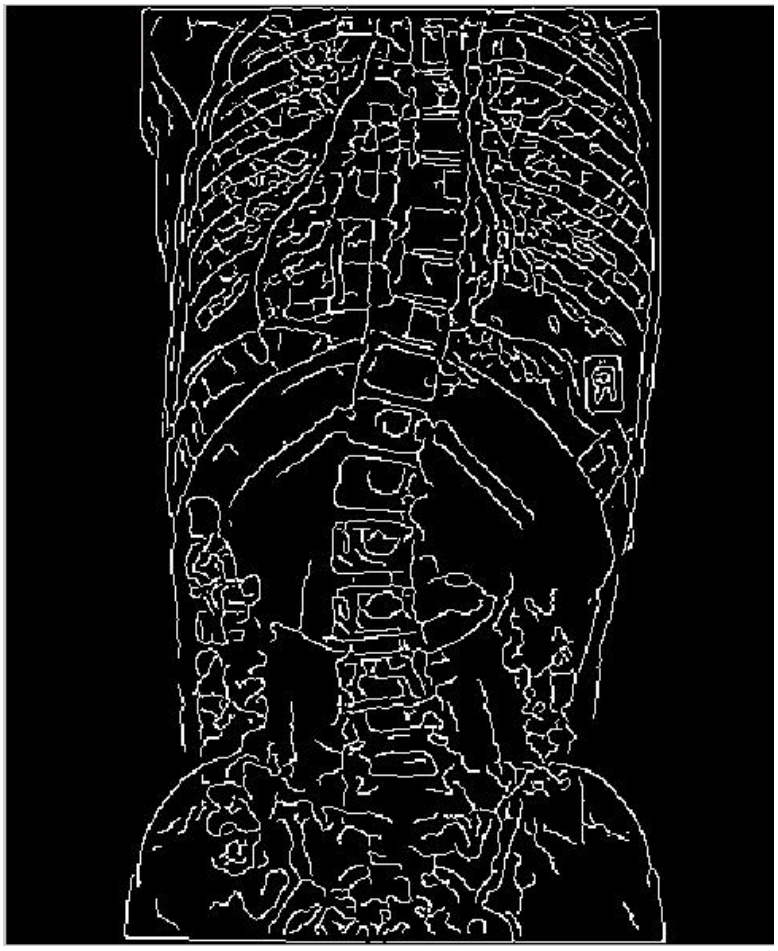

Figure 7: Edge detection using Canny operator

4. Results

In Figure 3, 4 and 5, the Sobel, Prewitt and Robert operators were used to detect the edge of the image. Prewitt operator is basically a discrete differentiation operator which involves in evaluating an approximation of the gradient in the scene. By comparing the results from Figure 3, Figure 4 and Figure 5, it is clearly seen that the difference in these three Figures are minor. That being said, the properties of the Prewitt operator is close to the Sobel operator which resulting the edges that can be detected in both horizontal and vertical direction. On the other hand, Figure 6 and Figure 7 delivers a better edge detection image with corresponding to the previously discussed Sobel, Prewitt and Robert operators. Figure 6 refers to the edge detection using laplacian of gaussian filter. Whereas Figure 7 refers to the edge detection on X-ray spine image using the built-in Canny operator in MATLAB software. When comparing the Figure 6 and 7, Figure 7 (Canny) provides more detailed edge detection than the Figure 6 (LOG). This is because the Canny operator detects a wide range of edges in image using multi-stage algorithm.

5. Conclusion

By comparing the obtained results from different types of operators, the Canny operator clearly has a better advantage in edge detection when compared to the Sobel operator and Prewitt operator as Canny operator has a wider range of detection in edge detection. The importance of edge detection is that it can help in predicting and comparing

the bone density of the scoliosis patients before operation and after operation [10]. All the algorithms proposed in this report are simple and easy to implement and at the same time, it increases the efficiency of analyzing and synthesizing medical radiographic images. All the above mentioned operators were used and tested on a Spine X-rays only. It is advisable and recommended to the readers that to try these operators on other several types of X-rays.

References

1) M.Palaniswamy, W.Y.Leong (2015). Healthcare Technology: Scoliosis CT Scan Processing and Detection, *IET Newsletter MAY 2015*, pp6-7.
2) Davis, E. (1990). *Machine Vision - Edge Detection.* Retrieved December 2014
3) B, P. P., R, A., & S, S. M. (2014, August). X-Ray Image Acquisition and Analysis. *International Journal for Research in Emerging Science and Technology, 1*(3).
4) Mahendran, D. S. (2012, November). A Comparative Study on Edge Detection Algorithms for Computer Aided Fracture Detection Systems. *International Journal of Engineering and Innovative Technology, 2*(5), pp190-193.
5) D.C, S., Chinchansoor, R. S., & P.S, H. (2012, March). Edge Detection of Femur Bones in X-ray images - A comparative study of Edge Detectors. *International Journal of Computer Applications, 42*(2), 13-16.
6) Stolojescu, C., & Crisan. (2012). *Edge detection techniques for X-ray image segmentation.* 'Politehnica' University of Timisoara, Department of Communication. Romania: Proceedings of 13th Symposium of Mathematica and its Application. Retrieved December 2014
7) Kudale, G. A., & Pawar, M. D. (2010). Study and Analysis of Various Edge Detection Methods for X-Ray Images. *International Journal of Computer Science and Application Issue*, 15-19.
8) Sardjono, T. A., Wilkinson, M. H., Veldhuizen, A. G., & Pumama, K. E. (2013). Automatic Cobb Angle Determination From Radiographic Images. *SPINE, 38*(20), 1256-1262.
9) Kundu, R., Ratnesh kumar, P. L., & Chakrabarti, A. (2012). Cobb Angle Quantification for Scoliosis Using Image Processing Techniques. *International Journal of Computer Applications*, 6-10
10) M.Palaniswamy, W.Y.Leong (2014). *Mechanical Properties of the Human Vertebrae Between Normal, Post Corrective and Post-Operative*. 2014 IEEE International Symposium on Robotics and Manufacturing Automation.

3D Modelling with CT and MRI Images of a Scoliotic Vertebrae

P. Mohankumar, LEONG Wai Yie
School of Engineering, Taylor's University, Taylor's Lakeside Campus, No 1 Jalan Taylor's, 47500 Subang Jaya
mohanphysionix06@gmail.com, waiyie@gmail.com

Abstract

Scoliosis is a lateral or sideways deviation of the spine or vertebral column. Scoliosis can be treated by postural correction, providing braces or by surgery. Even after treating scoliosis with the help of brace or surgery, the normal spine range of motion is not achieved in most cases. After treating scoliosis either by brace or surgery, the normal posture might be achieved. But, it is important to know whether the patient is able regain his/her functionality. The mechanical properties of the vertebrae and intervertebral disc pressure after the application of brace and surgery are unknown and yet to be explored. In order to explore it, we come up with the thought of creating a 3D model of vertebrae. Because scientists and researchers depend upon cadaver specimens to try new fixations where the number of people willing to donate their body for research purpose is very low or nil in most of the countries. Without a sufficient number of cadaver specimens, the research progress remains still or very slow. Thus, creating a 3D model of vertebrae could yield more importance and convenience to do spine research. A 3D model of human spine can help in 3D printing too. In this study, we propose a simple method where the 3D model of scoliotic vertebrae can be created with the help of DICOM files.

Keywords: Scoliotic vertebrae, DICOM, InVesalius, Magics.

1. Introduction

It has been postulated that density of the bone decreases as the age increases [1]. Which leads to decrease in the mechanical properties, function and stability in bones. Human spine consists of 33 vertebrae. 7 cervical, 12 thoracic, 5 lumbar, 5 fused sacral vertebrae and 4 fused coccygeal vertebrae [1]. Each vertebrae is separated by an intervertebral disk, which acts as a shock absorber between each of the vertebrae in the spinal column when there is impact from activity. When the spine is affected by means of spinal deformity, the shape and properties of the vertebrae and intervertebral disc are also affected.

The mechanical properties of the human vertebrae are of great importance. It plays a vital role in maintaining the Range of Motion (ROM) and stability. The mechanical properties of vertebrae include stress, strain, shear, and torsion of the bone. These mechanical properties varies between the normal individuals and in the patients with spinal deformities. There are many structural changes in the human vertebral column, which are considered as spinal deformities. They are: Herniated disc, Spinal arthritis, Spina bifida Ankylosing spondylitis, Spondylosis, Spinal curvature issues like Scoliosis, Lordosis and Kyphosis. In this, scoliosis is quite common among the general population. Some are congenital and some are idiopathic. These abnormalities can be confirmed by using radiographic methods like x-ray, CT scan and MRI scan (Digital Imaging and Communication in Medicine - DICOM files).

Several studies were done on obtaining the mechanical properties of human vertebrae using cadaver models and digitizer. Only very few studies were done on obtaining the 3D model using the CT and MRI scan files (DICOM files). This gives the urge to conduct a study on 3D modelling with CT and MRI images.

Appearance of the scoliotic vertebrae differs from the normal vertebrae. Scoliotic vertebrae are wedge shaped. Because of this wedge shaped vertebrae, the normal pressure (0.7 kg/cm^2) exerted on the intervertebral disc is altered and concentrated on either side of the disc [1]. It may lead to further secondary complications. Due to this abnormalities, mechanical properties of the vertebrae and intervertebral disc pressure might vary between the normal persons and patients with spinal deformities (scoliosis). It can be treated by providing braces or by surgery. Braces are provided only for the young patients (teenagers) having congenital scoliosis or with the cobbs angle lesser than 40 degree. Because the bone is not completely developed and can be corrected with the help of braces itself. Whereas corrective surgeries are performed in adults for both the congenital and acquired scoliosis. With the advancement in medical field, scoliosis corrective surgeries are performed for teenagers in the recent years. Even after treating the spinal deformities like scoliosis or kyphosis with the help of brace or surgery, the normal spine range of motion is not achieved. The mechanical properties of the vertebrae after the application of surgery is unknown and yet to be explored. Thus an easy and noninvasive method is necessary to know the mechanical properties of the vertebrae.

The objective of this study is to provide a 3D model of a human spine using the DICOM files to understand the mechanical properties of the human scoliotic vertebrae.

2. Review of Literature

2.1 Studies done using cadaver

Many studies were done in the earlier days to find the mechanical properties of the human spine. Arno Bisschop, Jaap H. van Dieen and Idsart Kingma (2013) conducted a study on torsion biomechanics of the spine following lumbar laminectomy: a cadaver study, where they found the torsion biomechanics of spine using Instron [2]. Another study done by Hakan Bozkus, Ergun Bozdag and Ercan Tanyeli (2004) done a biomechanical pilot study on surface strain and stress analysis of mid-cervical vertebrae bony compartments using Strain gages [3]. M.M. Trexler, A.M. Lennon, Q.T. Luong and A.C. Wickwire (2011) used modified split Hopkinson pressure bar to find the shear loading in soft materials and biological tissues [4]. Ling H.Y and Tan S.H used Dual-energy X-ray Absorptiometry (DEXA) to find the effect of bone density on the mechanical properties of human vertebrae [5]. Kim-Kheng Lee, Tian-Xia, Qiu, Ee-Chon Teo (2002) done a 3-D finite element modeling of lumbar spine (L2/L3) using a digitizer. They used touch probe digitizer to extract the geometrical data of the lumbar spine. Using a software called Surfacer 7.0, the three dimensional data was processed and finite element mesh was constructed using ANSYS software [6]. All these studies were done on vertebrae obtained from human cadaver. None of those studies were conducted on a live human being. Only a very few studies were done with live human beings.

2.2 Studies done on live human beings:

Qinghua Meng and Chunyu Bao (2009) done a study on biomechanical characteristics of lumbar vertebrae for speed skating athlete using finite element analysis. In this study, a continuous scanning to the volunteer's upper edge of fourth vertebrae to the lower edge of the fifth lumbar vertebrae was fulfilled through spiral CT scan. The CT images were processed in medicinal picture processing software in dicom format. The bony tissues were distinguished from CT images through region growing. The three dimensional geometrical model of L4-L5 was established by 3D calculation through region growing to segment the different regions. They found that "when speed skaters were skating, the stress on the disc mainly concentrated on annulus fibrosus" [7].

2.3 Studies done using radiographs:

Hendrik Schmidt, Annette Kettler, Frank Heuer and Ulrich Simon (2007) conducted a study on intradiscal pressure, shear strain and fiber strain in the intervertebral disc under combined loading using finite element analysis. A finite element model of human lumbar spine segment was generated based on CT scan. The model is transferred to finite element package in ANSYS and meshed [8].

3 Methodology

3.1 Selection of Subjects

Subjects with the history of scoliosis in the age group between 10 to 45 years were selected. Study was clearly explained to the subjects. Baseline assessment like age, sex, height, weight and date of treatment completion were noted for all the subjects participating in the study. The details obtained from the subjects are kept confidential and will be never shared with others. Some data were collected from in and around the scan centres of the state Tamilnadu, India.

3.2 Method

After finishing the baseline assessment, CT and MRI scan files (Digital Imaging and Communications in Medicine - DICOM) were obtained from the subjects. Then these DICOM files were used in InVesalius software, version 3.0 [9]. InVesalius is an open source software for reconstruction of computed tomography and magnetic resonance images. It generates a 3D medical imaging reconstruction based on a sequence of DICOM files.

The folder with DICOM files were imported into the InVesalius software and the region of interest is selected. The mask properties, surface properties and the threshold properties are adjusted according to the need. Once the properties are set, a 3D surface is created and it is exported in STL file format. Refer figure 1.

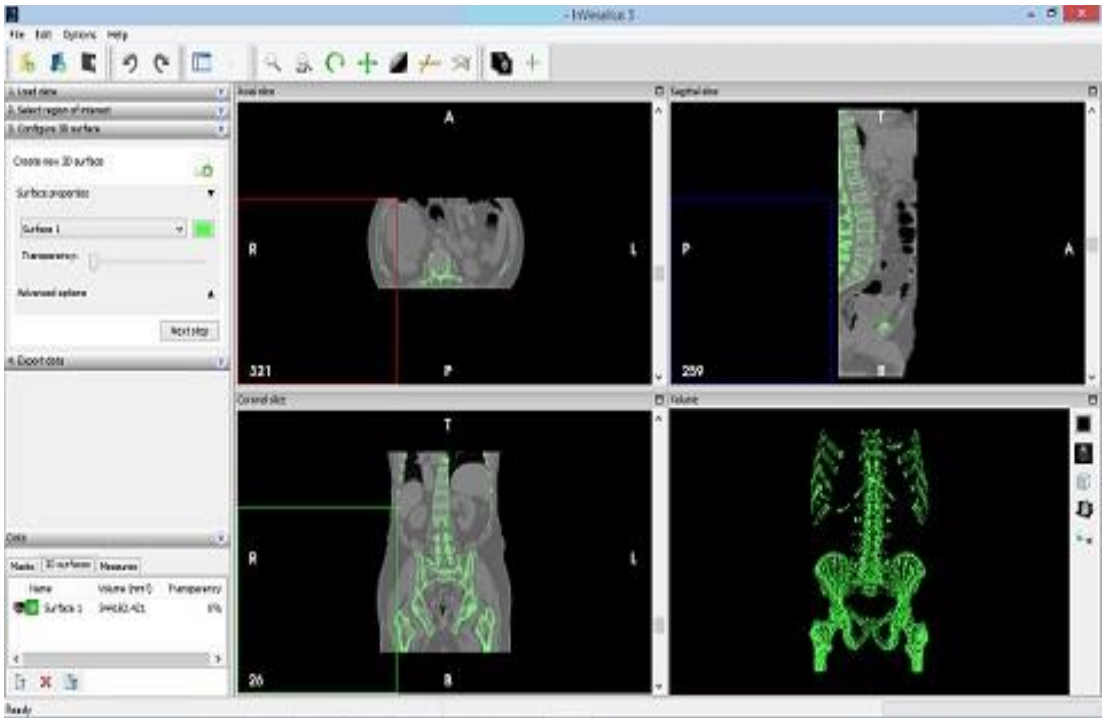

Figure 1: Processing in InVesalius

Once the 3D surface is created it is then imported in Magics software version 18 [10]. Magics is a data preparation software package and STL editor. It can guide

through every step of additive manufacturing or 3D printing workflow. The file exported from InVesalius is imported into Magics. Refer figure 2.

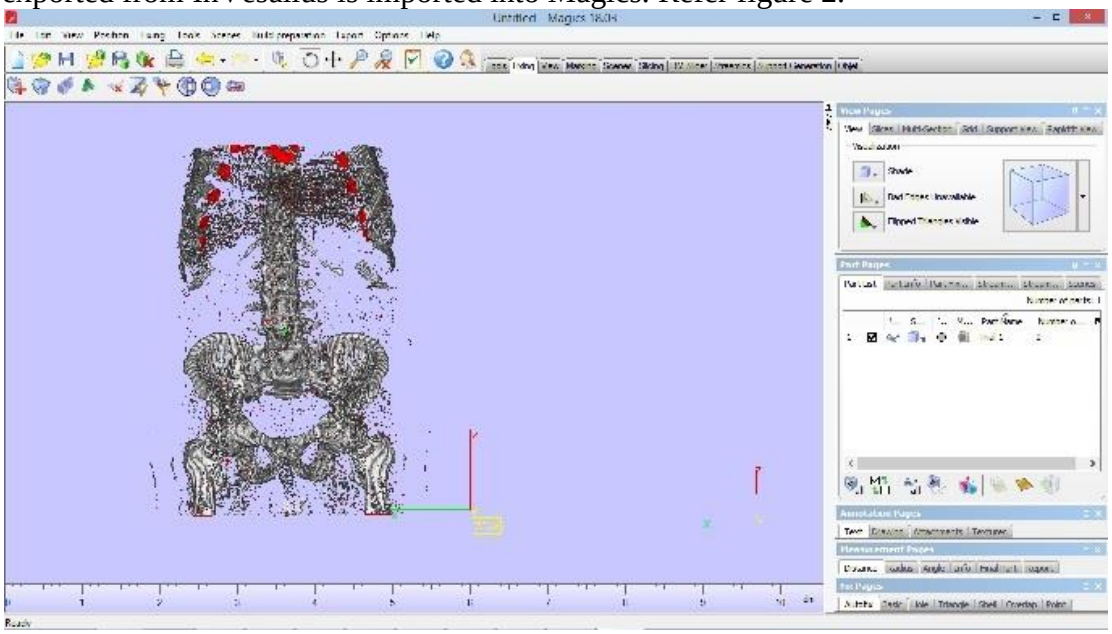

Figure 2: Before processing in Magics

The imported STL file is edited in Magics. Shells, holes, triangles, overlaps, stitching, etc., are edited to get the final 3D model of human vertebrae. Refer figure 3.

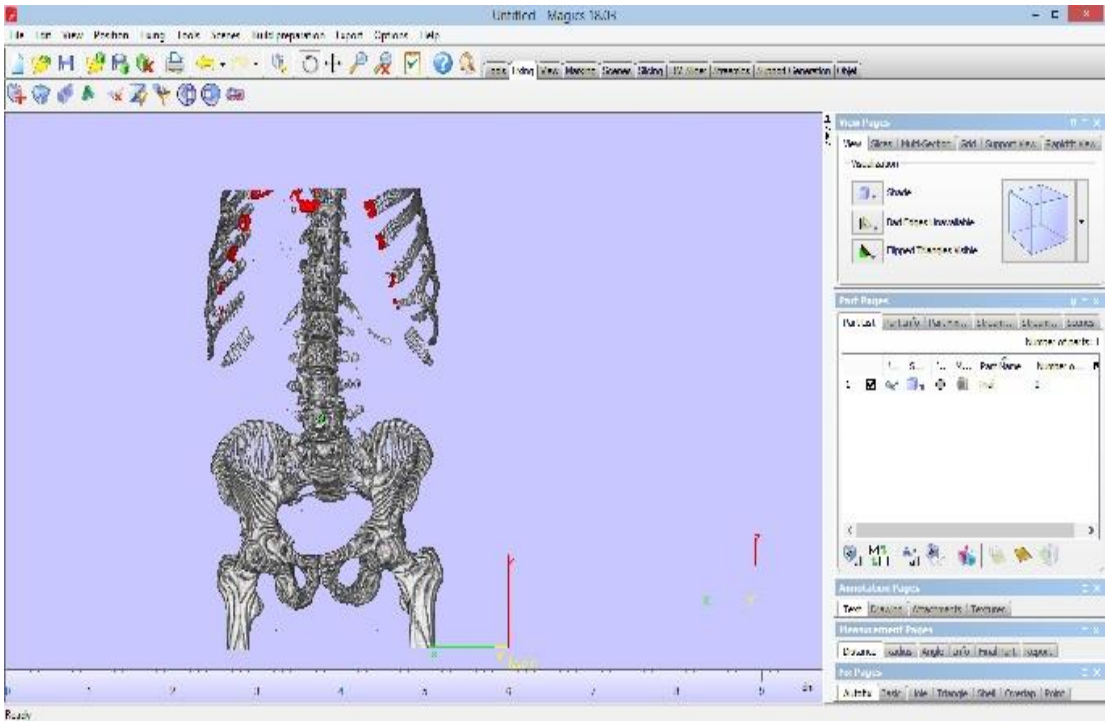

Figure 3: After processing in Magics

The followed method is given as a flowchart below. Refer figure 4.

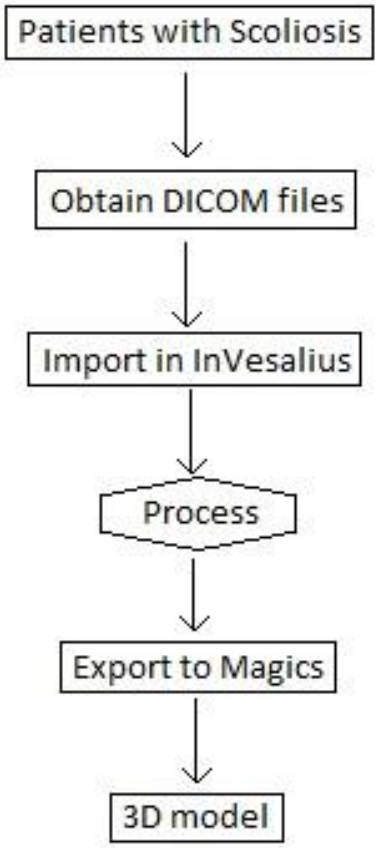

Figure 4: Proposed method

4. Results and Discussion

The imported file in Magics initially looked like a corrupted, noisy, untidy 3D model. The edges and the curves were not clearly visible. After processing in Magics, after fixing several issues, a clear 3D model of human spine is obtained with a diminished corruption. But much better than the previous model. This 3D model, when incorporated with its tissue properties can be used to find the mechanical properties of scoliotic vertebrae using the Finite Element Analysis. Unlike the olden days, here after the dependency on the cadaver will be diminished for medical research purpose, since the 3D model serves a much better option. Previously, Janko D. Jovanovic and Miomir Lj. Jovanovic (2010) created a finite element modeling of the vertebrae with its geometrical and material properties retrieved from the CT scan data. The CT images of the vertebra was exported in common medical file format called DICOM (Digital Imaging and Communication in Medicine). The scanned images have CT numbers, which is converted to density of the bone tissue by Computed Tomography (QCT). Using the program Mimics (materialize software) CT images were processed to generate the geometric model of the vertebra. Their results showed that the model was capable of giving detailed quantitative information on the

biomechanical behavior of the vertebra and could be considered as a useful tool in risk evaluation of osteoporotic fracture of vertebra [11]. Ai-Min Wu, Zhen-Xuan Shao, Jian-Shun Wang, Xin-Dong Yang et al., (2015) conducted a study on the accuracy of a method for printing 3D spinal models. They concluded that the 3D model provide a protocol for printing accurate 3D models for surgeons and researchers. The resulting 3D printed model is inexpensive and easily obtained for spinal fixation research [12-14].

5. Conclusion

This method of creating a 3D model with the help of DICOM files could serve as a much better option to the researchers rather than depending on cadavers or digitizers. With a completely developed 3D model of a scoliotic vertebrae, its mechanical properties can be identified by finite element analysis. This 3D model also helps in 3D printing of vertebrae. Thus future researchers can use this method to do 3D printing.

References

1. Alison Middleditch and Jean Oliver. (2005). *Funtional Anatomy of the Spine*, 2nd edition.
2. Arno Bisschop, Jaap H van Dieen, Idsart Kingma, Albert J. van der Veen …. Barend J. van Royen (2013). Torsion biomechanics of the spine following lumbar laminectomy: a human cadaver study. *European Spine Journal* 22: 1785-1793.
3. Hakan Bozkus, Ergun Bozdag, Ercan Tanyeli, Emin Sunbuloglu, Murat Hanci. (2004). Surface Strain and Stress Analysis of the Mid-Cervical Vertebrae Bony Compartments: A Biomechanical Pilot Study. *Turkish Neurosurgery*, Volume: 14, No: 1-2, 1-11
4. M.M. Trexler, A.M. Lennon, Q.T. Luong, A.C. Wickwire, J.C. Roberts and A.C. Merkle. (2011). Modified split hopkinson pressure bar technique for characterizing soft materials and biological tissue under shear loading. *Injury Biomechanics Research*, Proceedings of the Thirty Seventh International Workshop. Epub Jun 23.
5. Ling H. Y. and TAN S. H. Effect of bone density on the mechanical properties of human bone. School of Mechanical and Production Engineering, Nanyang Technological University, 50 Nanyang Avenue, Singapore. Retrived from: http://www3.ntu.edu.sg/eee/urop/congress2003/Proceedings/.../LingHY.pdf.
6. Kim-Kheng Lee, Tian-Xia, Qiu, Ee-Chon Teo. 3D Finite Element Modeling of Lumbar Spine (L2-L3) using Digitizer. *International Journal of Information Technology*, Volume 8, No. 2. September 2002.
7. Qinghua Meng, Chunyu Bao. (2009). Study on Lumbar Vertebrae Biomechanical Characteristics for Speed Skating Athlete based on Finite Element Method. *International Journal of Sports Science and Engineering*, Volume – 03, No. 03, pp. 169 - 174.
8. Hendrik Schmidt, Annette Kettler, Frank Heuer, Ulrich Simon, Lutz Claes and Hans-Joachim Wilke. (2007). Intradiscal Pressure, Shear Strain and Fiber

Strain in the Intervertebral Disc under combined loading. *SPINE* Volume 32, Number 7, pp 748-755.

9. *INVESALIUS*. (2015, 5 7). Retrieved 4 2015, from INVESALIUS: http://www.cti.gov.br/invesalius/
10. *Materialise*. (2015, 5 7). Retrieved 5 7, 2015, from Materialise: http://software.materialise.com/magics
11. Janko D. Jovanovic, Miomir Lj. Jovanovic. (2010). Finite element modeling of the vertebra with geometry and moterial properties retrived from CT-scan data. Facta universitatis, *Mechanical engineering*, volume 8, no 1, page 19-26.
12. Ai-Min Wu, Zhen-Xuan Shao, Jian-Shun Wang, Xin-Dong Yang, ……, Zhong-Ke Lin et al., (2015). The Accuracy of a Method for Printing Three-Dimensional Spinal Models. DOI: 10.1371/journal.pone.0124291.
13. M.Palaniswamy, W.Y.Leong (2015). Healthcare Technology: Scoliosis CT Scan Processing and Detection, *IET Newsletter MAY 2015*, pp6-7.
14. M.Palaniswamy, W.Y.Leong (2014). *Mechanical Properties of the Human Vertebrae Between Normal, Post Corrective and Post-Operative*. 2014 IEEE International Symposium on Robotics and Manufacturing Automation.

Preliminary Study of Mechanical Properties in Thermoplastic Starch (TPS) / Coffee-Waste-Derived Fillers Composites

Y.M. CHAN[1*], S.W. PHANG[1], T.T. TEE[2], T.S. LEE[2], T.B. SOO[2]
[1]*Environmental Research Group, Department of Chemical Engineering, Taylor's University Lakeside Campus, Malaysia.*
[2]*Department of Chemical Engineering, Faculty of Engineering and Sxience, University Tunku Abdul Rahman, Jalan Genting Kelang, 53300 Setapak, Kuala Lumpur, Malaysia.*
**Corresponding Author E-mail: yenmin91@gmail.com*

Abstract
Thermoplastic starch (TPS) has been studied to replace the conventional petroleum-derived plastics in the last decade for its biodegradability, low production cost, availability and is a renewable agricultural resources. However, it has limited performance due to its hydrophilic nature, poor mechanical properties and poor long-term stability. Blending fillers into TPS matrix has shown improvements in the mechanical properties of TPS such as cellulose, clay, fiber, fly ash and carbon nanotubes for widening the range of their applications. Most of the fillers that have been studied are not readily biodegradable or incompatible with the hydrophilic characteristic of TPS. Hence, this research aimed to introduce a brand new bio-filler, grinded used-coffee-waste into the combination of *cassava* starch and glycerol via solution casting method in order to improve the compatibility between the fillers with TPS. Critical mechanical properties of the TPS composites, maximum tensile stress, elongation at break and Young's modulus were evaluated using tensile test machine according to ASTM D882-12. Presence of coffee fillers demonstrated sharp increments in elongation at break up to 106 % but slight decrement in both maximum tensile stress and Young's modulus with 0.67 MPa and 4.11 MPa respectively. The elongation at break of the TPS composites increased with the loading levels of coffee fillers from 1 to 5 wt. %, while maximum tensile strength and Young's modulus showed adverse effect with the increase of coffee loading levels. Optimal mechanical properties was exhibited by the specimen with formulation of 1 wt. % of coffee filler and 40 wt % of glycerol, which demonstrated maximum tensile stress of 1.82 MPa, Young's modulus of 12.45 MPa and elongation at break of 51%.

Keywords: Thermoplastic starch, Coffee-waste-derived fillers, Mechanical properties, Solution casting.

1. Introduction

The daily usage of plastics in the modern society cannot be overlooked due to their plentiful applications ranged from food and merchandise packaging industries to medical technologies. The current plastic films are derived from petroleum and the non-biodegradable characteristic has become their intrinsic deficiency which result in a vast environmental accumulation and pollution problem that lasts for centuries. According to the report from Environmental Protection Agency (EPA) in United States, plastics has made up 12.4 % of municipal waste in year 2010, which is accounted for 24 times of the amounts generated in year 1960, and only 8.2 % of plastic waste was recovered [1].

Hence, in the last decade, there are increased interests and research efforts on developing the biodegradable and renewable plastic films to substitute the petroleum-based films, which is generally known as bioplastics. A recent report presented by Shen et al. [2] revealed that the bioplastics market is gradually growing at a rate of 30 % annually to capture the plastics market. Starch for this context has becoming a promising natural renewable resources to produce bioplastics due to its abundant availability, extremely low cost and biodegradable nature. It composes two structural classes, amylose, the linear poly (α-1,4-glucopyronosyl) polysaccharide molecules and amylopectin, the branched molecules, with abundant of α-1,6-glucopyronosyl linked branch points, as shown in figure 1 [3]. There is a vast hydrogen bonds network in starch as it is a multi-hydroxyl polymer and hence, starch is not readily to be used as a bioplastic alone. However, it poses similar characteristics to the conventional plastics with the addition of suitable plasticizers, such as glycerol, sugars and sorbitol, prepared under the conditions of high temperature with moderate shearing [4]. During the gelatination process, the bonds of hydrogen chains are broken, and the structure of starch molecules are disrupted, leading the starch becomes plasticized.

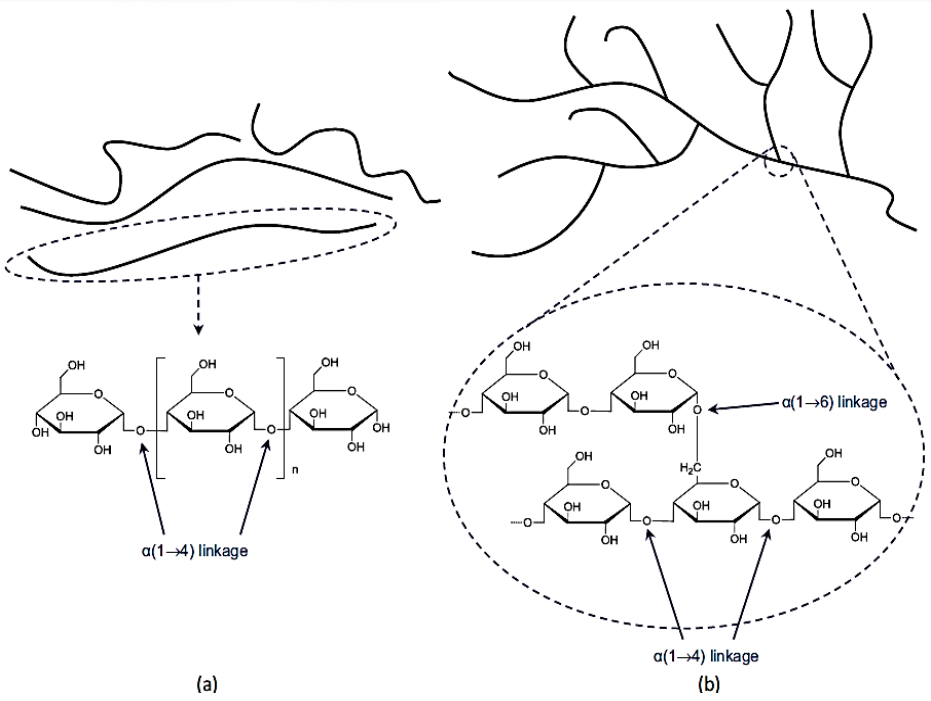

Figure 1. Molecular structure of amylose (a) and amylopectin (b) [5].

The plasticized starch is known as thermoplastic starch (TPS). Utilization of suitable plasticizer is critical for the synthesis of TPS. In this context, water is reported as a good plasticizer as a gelatinization temperature at a range of 60-70 ºC is given by adequate amount of water, particularly 10-30 wt. % with the destruction of crystalline organization due to the swelling of the granules in starch [6]. However, water is not encouraged to be used as plasticizer solely for its high dependence of final properties to the ambient humidity as well as high volatility that produces a brittle TPS in return. Glycerol is hence applied in this research for its hydroxyl-rich properties and compatibility with *cassava* starch as its application is successfully reported by several studies [7-9]. According to Janssen and Moscicki [8], glycerol is the most excellent plasticizer in reducing the friction between starch molecules. In addition, it has been generated in a large quantities as the by-products in biofuel industries and therefore the utilization of glycerol can address environmental issue simultaneously. The ideal ratio of starch to glycerol (w/w) was claimed to be 70:30 according to Zullo and Iannace [7]. The same result was presented by Pushpadass el al. [9] as the optimal conditions of TPS in terms of tensile strength and Young's modulus are achieved by the addition of 35 wt. % of glycerol. Despite the potential of starch to be the substitution for conventional plastic films, it has limited performance due to its major drawbacks such as hydrophilic nature, poor mechanical properties and poor long-term stability. Incorporation of foreign body that compatible with the TPS matrix is believed to reinforce the films as it has been proven by some of the fillers such as cellulose nanofillers, nanoclay and carbon nanotubes.

Cellulose nanofillers had brought significant improvement in mechanical properties to the reinforced TPS composites by providing good adhesion in the matrix [10]. This statement is proven by Martins et al. [11] who used bacterial cellulose produced from *Acetobacter Xylinum* as the reinforcement fillers with the loading level from 1 to 5 wt. %. The Young's modulus and tensile strength increasing with the cellulose contents shows 30 times higher than that of non-reinforced TPS. On the other hand, TPS composites with the addition of only 0.055 wt. % of multi-walled carbon nanotubes (MWCNTs) shows increments of 35 % in ultimate tensile strength, up to 70 % in stiffness and 80 % in elongation before failure in a recent works done by Famá et al. [12]. MWCNTs achieved good compatibility with the TPS matrix due to excellent dispersion and adhesion between the phases as proven by SEM micrographs. Another research from Huang et al. [13] reported the improvements in mechanical properties of TPS composites with the addition of nanoclay, activated montmorillonite (MMT) minerals. The tensile stress is increased from 4.5 MPa to 24.9 MPa with the addition of 10 wt% of MMT while the optimum tensile strain, 134.5 % is achieved by the addition of 5 wt% of MMT. In spite of the potential demonstrated by the mentioned fillers in improving the mechanical properties of TPS composites, high priced and complex preparation process of the fillers turns out to be the major drawbacks which are not economically feasible and hence limit the potential of reinforced TPS in substituting the conventional petroleum-based plastics.

Grinded coffee waste for this context is considered as a good candidate to be utilized as the bio-filler for TPS composite because it is abundant, low cost, biodegradable, and is a renewable resource. Spent coffee grounds have become a major waste in food industries as 650 kg of spent coffee grounds are produced from the processing of one ton of green coffee, leading to an annual generation of 6.0 million tonnes [14]. Hence, valorization of grinded coffee waste in TPS composites can address the environmental issue brought by spent coffee grounds. In addition, the

constituents of grinded coffee waste, namely carbohydrates (38-42 %), melanoidins (23 %), lipids (11-17%), protein (10%), minerals (4.5-4.7 %), caffeine (1.3-2.4 %) and etc. show a great potential to share the chemical similarities with starch and hence improve the compatibility with TPS [15]. As cellulose and hemicellulose are the main ingredients of the formation of carbohydrates due to the polymerization of sugars according to Mussato et al. [16], improvement of mechanical properties of TPS composites can be estimated by blending in coffee waste, providing that cellulose had been proven as an effective filler in the enhancement of properties of TPS. On the other hand, melanoidins, the nitrogen-containing brown pigments consist of carboxyl group, as shown in Figure 2 as well as numerous hydroxyl groups with sugar derived skeleton which are predicted to develop strong hydrogen bonds with starch molecules of TPS, and hence improve the compatibility of coffee waste in TPS matrix [17]. Another major constituents, lipids consist of three fatty acyl residues with glycerol served as the backbone for the molecules [18]. As glycerol is an effective plasticizer for TPS, lipids are assumed to exhibit good interaction with the starch molecules in TPS matrix. In overall, the core objective of this research is to introduce a brand new bio-filler, grinded coffee waste into TPS via solution casting method, and to study the effect of incorporation of coffee fillers in polymer matrix as well as its compatibility in enhancing the mechanical properties.

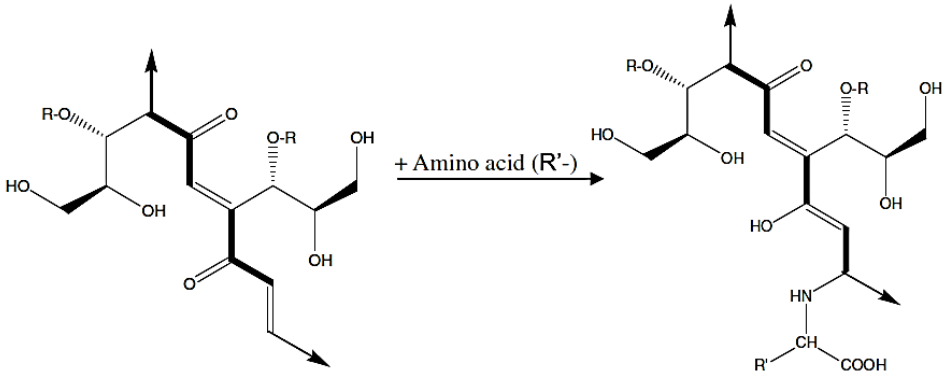

Figure 2. Carbohydrate-based melanoidin structure [19].

2. Experimental

2.1 Materials

The *cassava* starch, normally denoted as tapioca starch that containing around 17 % of amylose was purchased from SCS Food Manufacturing Sdn. Bhd. and utilized as the main ingredient for the preparation of TPS. Tapioca is abundantly cultivated in Malaysia and hence *cassava* starch was served as the native starch in this research in order to reduce the feedstock cost. The plasticizer, glycerol with 98 % of purity was purchased from R & M Marketing (Essex, U.K) and it was used without pre-treatment or further purification [20]. The grinded coffee waste was kindly supplied by Starbucks Sdn. Bhd. in Taylor's Lakeside Campus for the convenient purpose. The grinded coffee waste was washed with distilled water to remove impurities and dried in oven with 70 ºC for 24 hours until a constant weight was obtained and sieved with a sieve shaker to obtain a particle size of 500 µm. The dried starch and grinded coffee waste were kept in desiccator prior to use.

2.2 Design of Experiments

The research was mainly based on experimental and quantitative study. Experiments were carried out with respect to two different parameters, namely, loading level of glycerol and grinded coffee waste filler. Full factorial design was applied for this context as the parameters were manipulated into three different levels, namely low, medium and high. Consequently, there were altogether 9 runs for the experiments according to 3^2 full factorial design. The loading level of glycerol was ranged from 40 to 60 wt. % as this particular loading level of glycerol was believed to produce the desirable properties of TPS [6], [21], [22]. The loading level of coffee filler on the other hand was ranged from 1 to 5 wt. %. This range was set according to the similar research works as grinded coffee waste was a novel filler [23], [24]. Three replicates were tested for each experiments to get the average results in order to increase the accuracy. The composition of each formulation and controlled sample is as shown in Table 1.

Table 1. Formulation of TPS/grinded coffee waste filler composites.

Formulation	Loading level of glycerol (wt. %)	Loading level of coffee filler (wt. %)
TPS	50	0
T1-1	40	1.0
T1-2	40	3.0
T1-3	40	5.0
T2-1	50	1.0
T2-2	50	3.0
T2-3	50	5.0
T3-1	60	1.0
T3-2	60	3.0
T3-3	60	5.0

2.3 Preparation of TPS/coffee-waste-derived Fillers Composites Films

TPS composites films were prepared using solution casting method. 20 g of *cassava* starch was added into 800 ml of distilled water with 40, 50 and 60 wt. % of glycerol and 1, 3 and 5 wt. % of coffee waste fillers according to the corresponding run of experiments. The suspensions were heated at 70 ºC and 800 rpm using magnetic plate stirrer (SMHA-3 WiseStir) for 1 hour. The suspensions were then poured into Teflon-coated carbon steel plates and left to dry in the oven at 70 ºC for 24 hours in order to obtain the TPS composites films. The TPS composites films were left to cool until room temperature and kept in polyethylene zip lock bags with silica gels for further testing purpose.

2.4 Tensile Testing of TPS Composites Films

Maximum tensile strength, elongation at break and Young's modulus of the TPS composites films were determined using Tensile Tester Machine STM-SERVO according to ASTM D882-12 (Standard Test Method for Tensile Properties of Thin Plastic Sheeting) with a 5 kN load cell. During the tensile test, the specimens were gripped at one end of the tensile testing machine and pulled until failure with a crosshead speed of 50 mm/min, as suggested by ISO 527 standards (1993). Before

testing, the cast TPS composites films were cut randomly into strips with dimension of 8 x 5 mm while the thickness of the specimens were measured at four point along its length using a digital micrometer. The original gauge length, L_0 was set as 6 mm and the cross-sectional area of the specimens was calculated and recorded in order to obtain the load per unit area of the specimens.

3. Results and Discussion

3.1 Tensile Testing

The results of three vital mechanical properties, maximum tensile stress, Young's modulus and elongation at break obtained from tensile testing are tabulated using graphical method with boxplots to indicate the standard deviations of the data, as shown in Figure 3, 5 and 7. Dotted lines in the graphs show the mean reading given by controlled samples for comparison purpose. In order to comprehend the significance of each factors contributing in the mechanical properties of TPS composites, Minitab 17 software was employed in this research to further analyse the individual effects of loadings of coffee filler and glycerol by plotting main effects plots as shown in Figure 4, 6 and 8.

3.1.1 Maximum Tensile Stress

Based on Figure 3, the incorporation of grinded coffee waste into TPS matrix did not exhibit a positive effect in enhancing the maximum tensile stress as the results given by most of the TPS/coffee filler composites were slightly lower than the controlled samples. However, TPS composites with the lowest loadings of coffee filler and glycerol, T1-1 yielded an increase in maximum tensile stress up to 0.95 MPa. Hence, it could be considered as the optimum loading levels for both the coffee filler and glycerol in terms of enhancing the maximum tensile stress of TPS composites. In contrary, TPS composites with the highest loadings of coffee filler and glycerol, T3-3 demonstrated the lowest maximum tensile strength, 0.21 MPa. This result is in concordance with the studies performed by Hietala et al. [25] that revealed aggregates of the filler, cellulose nanofibres in the TPS matrix when the loadings were higher than the optimum level, leading to the decline in tensile strength. In addition, it could be observed that the results showed an adverse effect by increasing the loading level of coffee fillers from 1 to 5 wt. %, regardless of the loading level of glycerol. Therefore, lower loading level of coffee filler was preferable in increase the maximum tensile strength of TPS composites. The effect given by the loading level of glycerol on the other hand was not noteworthy as similar trend of results were obtained at different loadings of glycerol.

It was clearly evident that the optimum loadings of coffee fillers in enhancing the maximum tensile stress was only 1 wt. % according to the main effects plot of as shown in Figure 4. Maximum tensile stress decreased significantly when the loadings of coffee filler increased from 1 to 5 wt. %. The results obtained were not preferable as the maximum tensile stress lies between the ranges of 0.3 to 0.4 MPa, which were lower than that of controlled sample. It could be due to the large particle size of coffee filler that impede the even distribution of components in the polymer matrix, and hence weaken the hydrogen bonding between the molecules of native starch and the fillers itself. Based on the research performed by Muller et al. [24], physical contact of fillers in the polymer matrix would affect the mechanical properties to some extent

as several breakpoint could be formed around the filler particles. Hence, it could be deduced that the decrease in maximum tensile stress of TPS/coffee fillers composites was due to the structural effect of the fillers' particles and the mere physical contact of the particles in the polymer matrix [26].

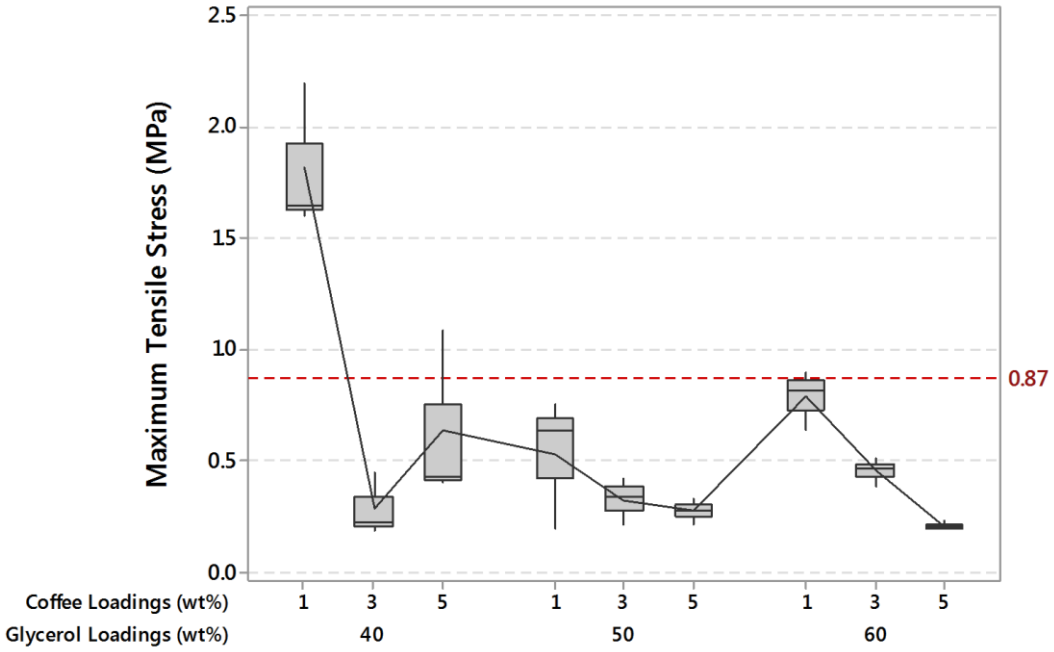

Figure 3. Maximum tensile stress of various formulations.

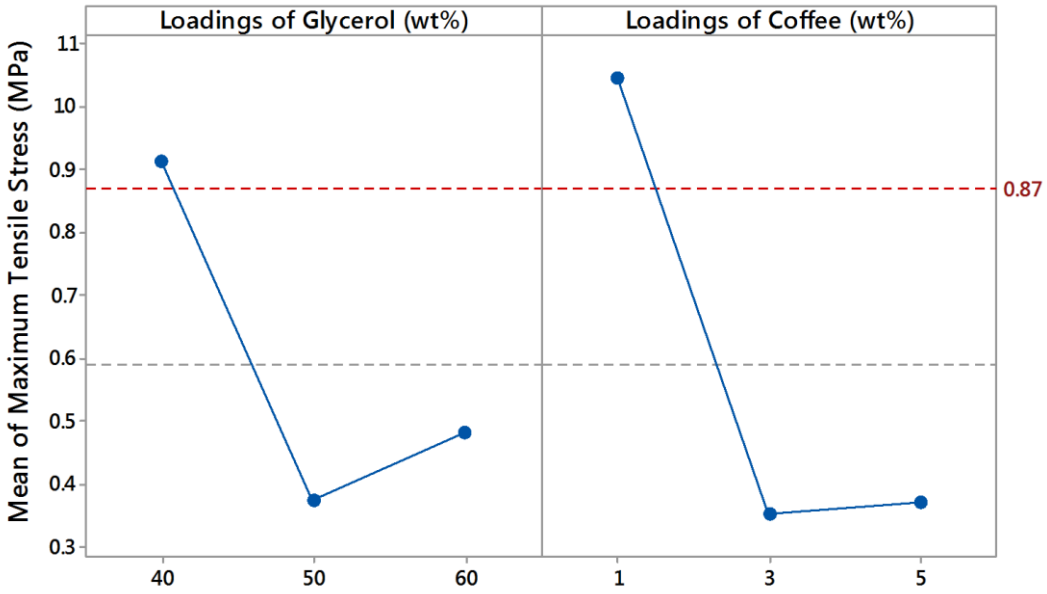

Figure **Error! No text of specified style in document.**. Main effects plot for maximum tensile stress.

On the other hand, the optimum loadings of glycerol was 40 wt. % in improving the maximum tensile stress. The maximum tensile stress of the TPS composites decreased significantly with increasing concentrations of glycerol from 40 to 60 wt. %. The results is in concordance with the studies performed by Pushpadass

et al. [27] in which the tensile strength declined with the increasing of glycerol concentrations in TPS/LDPE composites. The higher loadings of glycerol in TPS/coffee filler composites might form a weak boundary layer between starch and coffee fillers due to phase separation of starch [27]. Increased of free volume in the TPS composites network due to the increasing loadings of glycerol leading to poor interactions between the starch chains as well, attributed to the decreasing values of maximum tensile stress [28].

3.1.2 Young's Modulus

According to Figure 5, the trend of results in Young's modulus was very similar to that of maximum tensile stress as previously observed. Presence of grinded coffee waste fillers had brought down the Young's modulus of TPS composites likewise. Similar to that of maximum tensile stress, formulation with the highest loadings of coffee filler and glycerol, T3-3 exhibited the lowest Young's modulus, which is 0.33 MPa. Formulation with the lowest loadings of coffee filler and glycerol, T1-1 again demonstrated an increase in Young's modulus up to 8.01 MPa, and hence proving that the optimum level of loadings of coffee filler and glycerol had been achieved. Conversely, no specific trend was observed for the effect of increasing the loadings of coffee filler and glycerol in Young's modulus by only observing Figure 5. Hence, further analysis that required to study the effect of individual factors to the responses in detail is as shown in Figure 6.

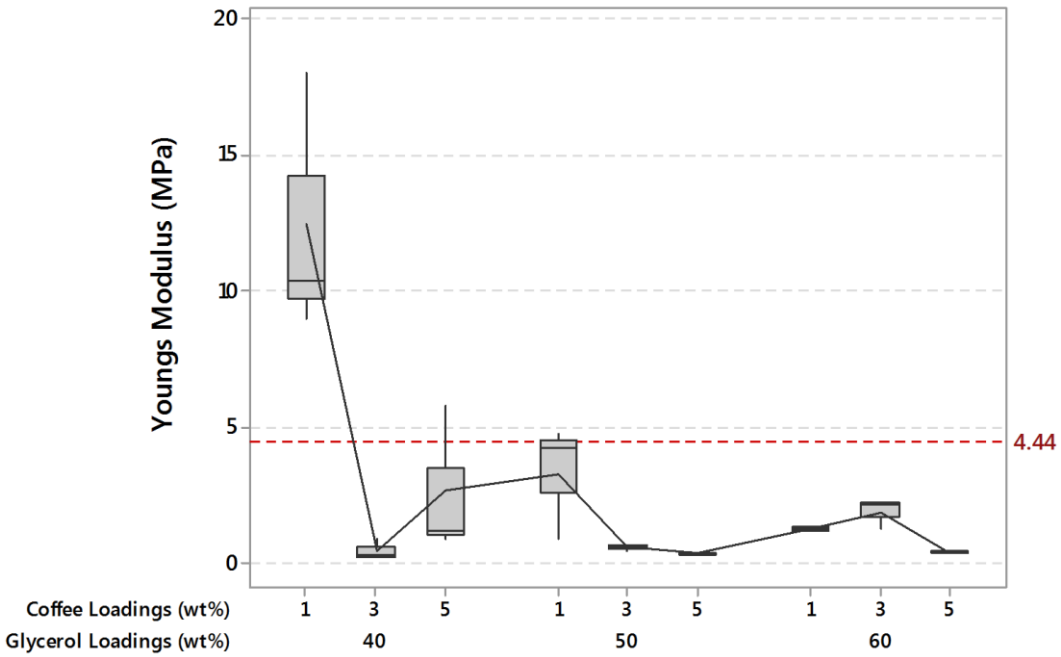

Figure 5. Young's modulus of various formulations.

Similarly, the main effect plots for Young's modulus as shown in Figure 6 displayed the same trend of graphs with that of maximum tensile strength. Increasing the loadings of coffee fillers from 1 to 5 wt. % again demonstrated adverse effect to the Young's modulus as the lowest value demonstrated by T3-3 was inferior to the controlled sample by 75%. The decrease in Young's modulus could be due to the formation of physical contacts among the large fillers content, as discussed earlier in

section 3.1.1. Apart from that, aspect ratio represented by the ratio of surface area to volume of the fillers also brought great effect to the mechanical properties of polymers [29]. Low aspect ratio given rise by the large particle size of coffee fillers had worsen the surface reactivity at molecular level distribution in polymer matrix [30]. Therefore, it showed a decreasing trend in Young's modulus when the loadings of coffee fillers were higher. As for the effect of loadings of glycerol, similar trend of results with that of maximum tensile stress was observed. The increase of loading level of glycerol had weaken the Young's modulus of TPS composites significantly. The reason attributed to this effect had been discussed in section 3.1.1 as well.

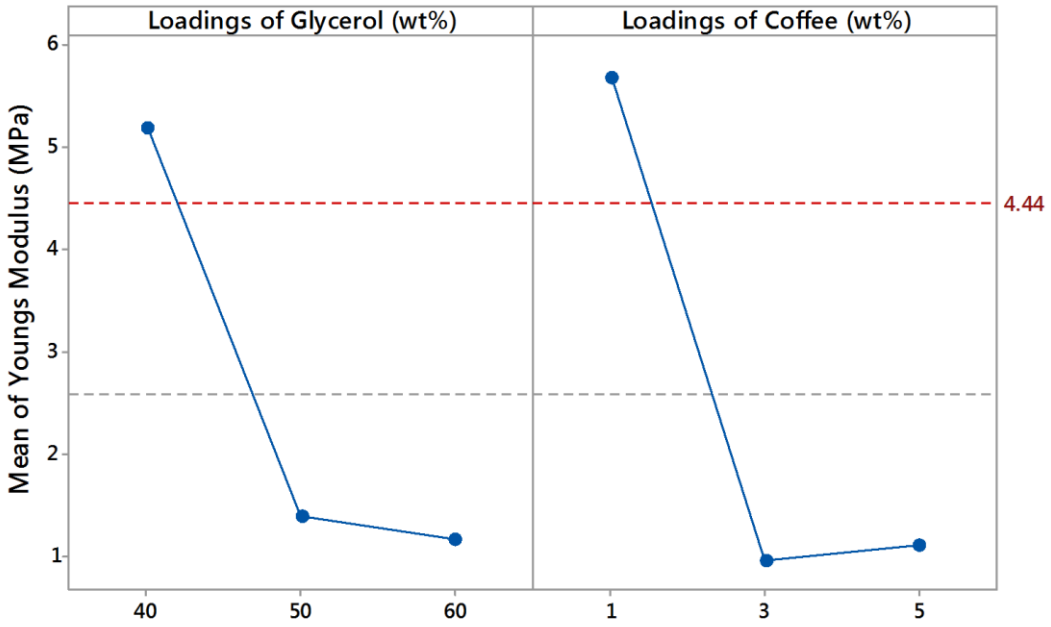

Figure 6. Main effects plot for Young's modulus.

3.1.3 Elongation at Break

It was clearly evident from Figure 7 that blending of grinded coffee waste filler enhanced the elongation at break of TPS composites since all formulations demonstrated an increase in elongation at break compared to the controlled samples. Generally, the reduction in elongation at break is very common for polymer reinforcement as it is inversely related with tensile strength [5]. Incorporation of coffee fillers into TPS matrix demonstrated this phenomenon in the other way round, whereby the results showed enhancement in elongation at break of the materials with the decrement of maximum tensile stress. Based on Figure 7, highest elongation at break that up to 140 % was exhibited by the formulation T2-3 while the lowest elongation at break with the value of 42 % was given by the formulation T3-2. As the standard deviation of the data was so huge and no specific trend could be observed from the results with just based on Figure 7, main effects plot is required to further justify the effects of loadings of coffee fillers and glycerol in the enhancement of elongation at break of TPS composites.

Based on Figure 8, elongation at break of the TPS films were subjected to a slight increment when the concentration of glycerol was increased from 40 to 50 wt.

% after which it dropped drastically when the concentration was further increased to 60 wt. %. Hence, the optimum loadings of glycerol was 50 wt. % and it started to exhibit adverse effect when it went beyond this threshold limit. Upon this threshold limit, weak boundary layer as well as poor interactions between the starch chains taken place due to the increased of free volume in the TPS composites [28]. After all, Glycerol for this context was observed as a good plasticizer making the TPS films more ductile. Besides, it could be clearly seen that the elongation at break of TPS/coffee fillers composites increased significantly with the increasing of loadings of coffee fillers from 1 to 5 wt. %, with 5 wt. % as the optimum loading level. The introduction of coffee fillers in TPS composites was more prominent in increasing the elasticity of the materials rather than tensile strength and Young's modulus. The constituents of spent coffee grounds might have led to this behaviour due to the interactions between the lipids contents with the TPS matrix. As glycerol acted as the backbones of lipids molecules in coffee waste and at the same time a good plasticizer in increasing the ductility of TPS composites, the lipids contents in coffee waste served as the main contributor for this behaviour to be observed [18].

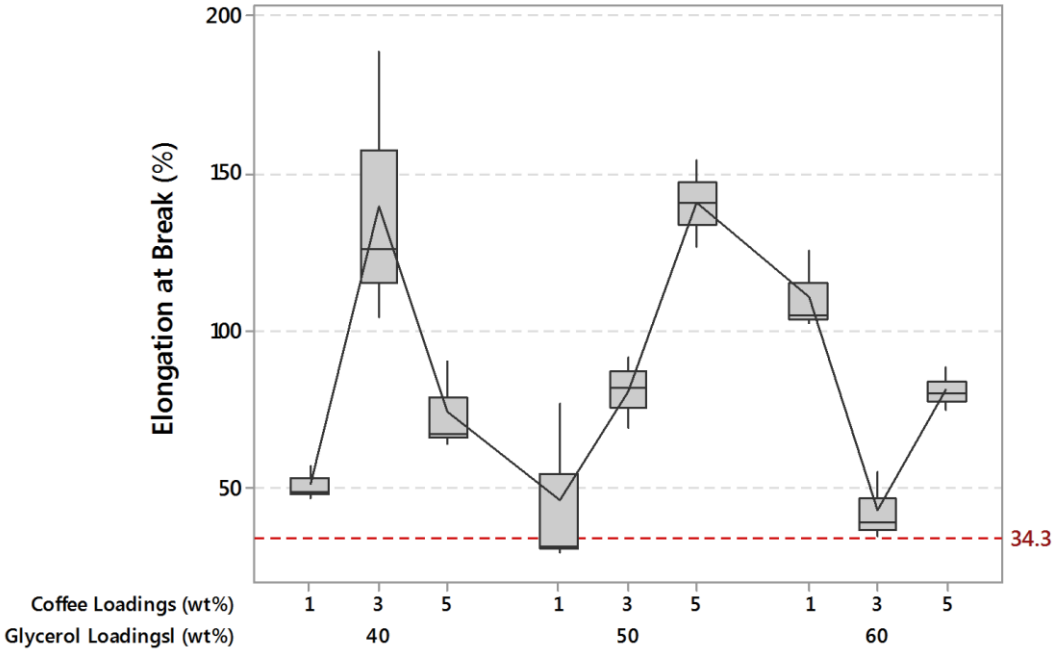

Figure 7. Elongation at break of various formulations.

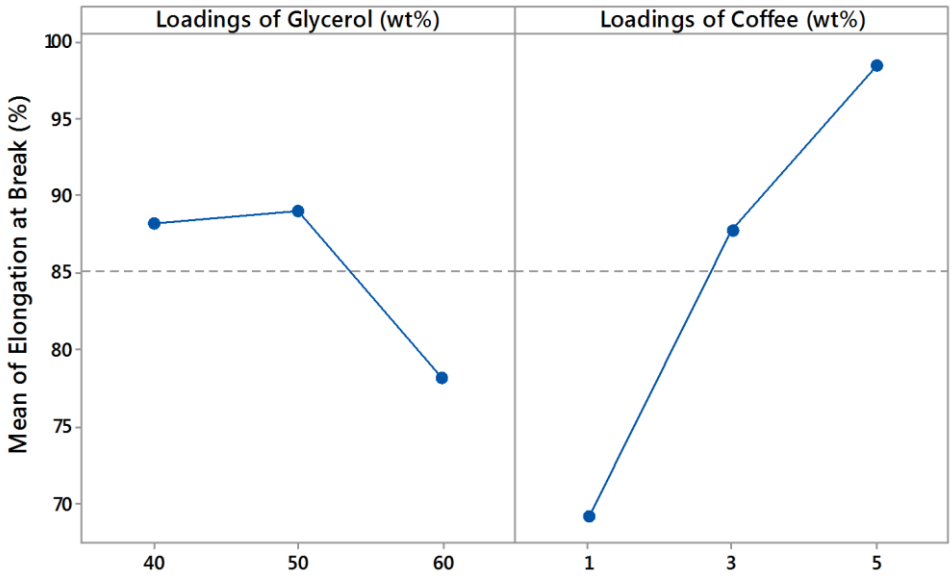

Figure 8. Main effects plot for elongation at break.

As this research was only served as a preliminary study for the effect of introduction of coffee filler into TPS films, the particle size of coffee fillers was remained as micron scale instead of nano scale, which was 33 times larger than that of *cassava* starch. The large particle size of coffee fillers might have impeded the embedment of the fillers in TPS matrix and hence worsen the mechanical properties of TPS composites in terms of maximum tensile stress and Young's modulus. The large particle size of coffee filler inevitably caused uneven distribution of the materials in the TPS matrix, which in turns influenced the hydrogen bonding between the starch granules and the fillers. The compatibility of coffee filler with TPS matrix in terms of degree of adhesion and dispersion has to be further analysed using SEM. It was very common to obtain a negative result for the introduction of brand new filler into TPS films, whereby the incorporation of fly ash, a brand new filler showed incompatibility with the hydrophilic characteristic of TPS, proven to worsen the mechanical properties of TPS composite with the research performed by Ma et al. [31].

In addition, the fairly large standard deviations existed in the results as shown in the boxplots for each mechanical properties also contributed to the inaccuracy of the outcomes. The estimated errors for each formulations could be observed from the error bars attached to the boxplots. These errors might be due to the deficiency in testing method as most of the specimens subjected to tensile testing experienced a breaking point nearby the edge of the grips instead of at the middle part of the specimens. Hence, it yielded the inaccuracy and errors in the outcomes obtained. These errors could be reduced by using different method in preparing the test specimens, which is the hot-pressing of 60 g of TPS casts films into TPS sheets of thickness of 1 mm and followed by molding of the TPS sheets into standard dumbbell shapes for tensile testing.

4. Conclusions

Incorporation of brand new bio-filler, grinded coffee waste filler into TPS composites films were successfully synthesised via solution casting method with various loadings of coffee fillers and glycerol. The critical mechanical properties, maximum tensile stress, Young's modulus and elongation at break of TPS/coffee-waste-derived fillers composites were evaluated in compliance with international standards as well as compared with non-reinforced control samples to analyse the individual effects of coffee fillers and glycerol on the TPS.

Presence of coffee filler greatly improved the elongation at break accompanied with slight decrement in maximum tensile stress and Young's modulus of the TPS composites. The elongation at break were increased to a maximum of 140 %, while the maximum tensile stress and Young's modulus were declined to 0.21 MPa and 0.37 MPa respectively. However, the positive effect exhibited by coffee filler alone in enhancing the elongation at break of the TPS films showed the potential in producing an elastic material for certain applications such as plastic wrap, simple packaging materials for one time usage and etc. Large particle sizes of coffee fillers might be the main contributor to the decrement in both the tensile strength and Young's modulus. The individual effect of loadings of glycerol on the other hand was insignificant for both maximum tensile stress and Young's modulus, but the elongation at break was improved with increasing loading of glycerol up to 50 wt. % after which adverse changes were observed when the loading was further increased to 60 wt. %. The optimum loadings of coffee fillers and glycerol were found to be 1 wt. % and 40 wt. % respectively in enhancing the mechanical properties of TPS composites as the formulation with this loading level exhibited improved mechanical properties as compared to non-reinforced control samples.

References

[1] U. EPA, "Minucipal solid waste generation, recycling, and disposal in the United States: facts and figures for 2010," *Solid Waste Emerg. Response*, vol. 5350P, p. 12, 2011.

[2] L. Shen, J. Haufe, M. K. Patel, and G. Science, "Product overview and market projection of emerging bio-based plastics," Netherlands, 2009.

[3] D. R. Lu, "Starch-based completely biodegradable polymer materials," *Express Polym. Lett.*, vol. 3, no. 6, pp. 366–375, May 2009.

[4] A. Curvelo, A. De Carvalho, and J. Agnelli, "Thermoplastic starch–cellulosic fibers composites: preliminary results," *Carbohydr. Polym.*, vol. 45, 2001.

[5] F. Xie, E. Pollet, P. J. Halley, and L. Avérous, "Starch-based nano-biocomposites," *Prog. Polym. Sci.*, vol. 38, no. 10–11, pp. 1590–1628, Oct. 2013.

[6] Robert Shanks and I. Kong, "Thermoplastic Starch," in *Thermoplastic Elastomers*, A. Z. El-Sonbati, Ed. InTech, 2012, pp. 238–250.

[7] R. Zullo and S. Iannace, “The effects of different starch sources and plasticizers on film blowing of thermoplastic starch: Correlation among process, elongational properties and macromolecular structure,” *Carbohydr. Polym.*, vol. 77, no. 2, pp. 376–383, Jun. 2009.

[8] L. Janssen and L. Moscicki, “Thermoplastic starch as packaging material,” *Acta Sci. Pol., Tech. Agrar.*, vol. 5, no. 1, pp. 19–25, 2006.

[9] H. A. Pushpadass and M. A. Hanna, “Age-induced changes in the microstructure and selected properties of extruded starch films plasticized with glycerol and stearic acid,” *Ind. Agric. Prod. Cent.*, vol. 48, no. 18, pp. 8457–8463, 2009.

[10] R. Bodîrlău, C. Teacă, and I. Spiridon, “Green composites comprising thermoplastic corn starch and various cellulose-based fillers,” *BioResources*, vol. 9, no. 1, pp. 39–53, 2013.

[11] I. Martins, S. Magina, and L. Oliveira, “New biocomposites based on thermoplastic starch and bacterial cellulose,” *Sci. Technol.*, vol. 69, pp. 2163–2168, 2009.

[12] L. M. Famá, V. Pettarin, S. N. Goyanes, and C. R. Bernal, “Starch/multi-walled carbon nanotubes composites with improved mechanical properties,” *Carbohydr. Polym.*, vol. 83, no. 3, pp. 1226–1231, Jan. 2011.

[13] M. Huang, J. Yu, and X. Ma, “High mechanical performance MMT-urea and formamide-plasticized thermoplastic cornstarch biodegradable nanocomposites,” *Carbohydr. Polym.*, vol. 63, no. 3, pp. 393–399, Mar. 2006.

[14] S. Obruca, P. Benesova, S. Petrik, J. Oborna, R. Prikryl, and I. Marova, “Production of polyhydroxyalkanoates using hydrolysate of spent coffee grounds,” *Process Biochem.*, vol. 49, no. 9, pp. 1409–1414, Sep. 2014.

[15] P. Esquivel and V. M. Jiménez, “Functional properties of coffee and coffee by-products,” *Food Res. Int.*, vol. 46, no. 2, pp. 488–495, May 2012.

[16] S. I. Mussatto, L. M. Carneiro, J. P. a. Silva, I. C. Roberto, and J. a. Teixeira, “A study on chemical constituents and sugars extraction from spent coffee grounds,” *Carbohydr. Polym.*, vol. 83, no. 2, pp. 368–374, Jan. 2011.

[17] R. Shi, Z. Zhang, Q. Liu, Y. Han, L. Zhang, D. Chen, and W. Tian, “Characterization of citric acid/glycerol co-plasticized thermoplastic starch prepared by melt blending,” *Carbohydr. Polym.*, vol. 69, no. 4, pp. 748–755, Jul. 2007.

[18] L.-C. Wu and C.-M. Cheng, “Flow-injection enzymatic analysis for glycerol and triacylglycerol.,” *Anal. Biochem.*, vol. 346, no. 2, pp. 234–40, Nov. 2005.

[19] H.-Y. Wang, H. Qian, and W.-R. Yao, “Melanoidins produced by the Maillard reaction: Structure and biological activity,” *Food Chem.*, vol. 128, no. 3, pp. 573–584, Oct. 2011.

[20] R. Bodirlau, C.-A. Teaca, and I. Spiridon, “Influence of natural fillers on the properties of starch-based biocomposite films,” *Compos. Part B Eng.*, vol. 44, no. 1, pp. 575–583, Jan. 2013.

[21] È. Mylla, R. Partanen, and J. Seppa, “Effect of glycerol on behaviour of amylose and amylopectin films,” *Carbohydr. Polym.*, vol. 50, pp. 355–361, 2002.

[22] A. L. Da Róza, A. J. F. Carvalhob, A. Gandinia, and A. A. S. Curveloa, “The effect of plasticizers on thermoplastic starch compositions obtained by melt processing,” *Carbohydr. Polym.*, vol. 63, no. 3, pp. 417–424, 2006.

[23] M. Bootklad and K. Kaewtatip, “Biodegradation of thermoplastic starch/eggshell powder composites.,” *Carbohydr. Polym.*, vol. 97, no. 2, pp. 315–20, Sep. 2013.

[24] P. Müller, K. Renner, J. Móczó, E. Fekete, and B. Pukánszky, “Thermoplastic starch/wood composites: interfacial interactions and functional properties.,” *Carbohydr. Polym.*, vol. 102, pp. 821–9, Feb. 2014.

[25] M. Hietala, A. P. Mathew, and K. Oksman, “Bionanocomposites of thermoplastic starch and cellulose nanofibers manufactured using twin-screw extrusion,” *Eur. Polym. J.*, vol. 49, no. 4, pp. 950–956, Apr. 2013.

[26] K. Renner, C. Kenyo, J. Moczo, and B. Pukanszky, “Micromechanical deformation processes in PP/wood composites: Particle characteristics, adhesion, mechanisms,” *Compos. Part A Appl. Sci. Manuf.*, vol. 41, pp. 1653–1661, 2010.

[27] H. Pushpadass, P. Bhandari, and M. Hanna, “Effects of LDPE and glycerol contents and compounding on the microstructure and properties of starch composite films.,” *Carbohydr. Polym.*, vol. 82, no. 4, pp. 1082–1089, 2010.

[28] D. Lourdin, H. Bizot, and P. Colonna, “Antiplasticization in starch-glycerol films?,” *J. Appl. Polym. Sci.*, vol. 63, pp. 1047–1053, 1997.

[29] G. Faludi, J. Hari, K. Renner, J. Moczo, and B. Pukanszky, “Fiber association andnetwork formation in PLA/lignocellulosic fiber composites,” *Carbohydr. Polym.*, vol. 34, pp. 67–73, 2013.

[30] M. A. S. Azizi Samir, F. Alloin, and A. Dufresne, “Review of recent research into cellulosic whiskers, their properties and their application in nanocomposite field.,” *Biomacromolecules*, vol. 6, no. 2, pp. 612–26, 2014.

[31] X. Ma, J. Yu, and N. Wang, “Fly ash-reinforced thermoplastic starch composites,” *Carbohydr. Polym.*, vol. 67, no. 1, pp. 32–39, Jan. 2007.

Preparation and Characterization of Plasticized Polylactic Acid / Microcrystalline Cellulose Composite

Wai Kit Len[1*], Ming Meng Pang[1], Kim Yeow Tshai[2]

[1]*School of Engineering Taylor's University, Lakeside Campus, No1, Jalan Taylor's, 47500 Subang Jaya, Malaysia*

[2]*University of Nottingham Malaysia Campus, Department of Mechanical, Materials & Manufacturing Engineering, Jalan Broga, 43500 Semenyih, Selangor Darul Ehsan, Malaysia*

[*]email of the corresponding author: lenwaikit@gmail.com

Abstract

Polylactic acid (PLA) is a biobased and biodegradable polymer which is widely used in packaging applications. However, one of its disadvantages is the brittleness and poor elongation at break. This study proposed the combination of the novel plasticizer (coconut oil) versus conventional plasticizer (polyethylene glycol), treated and untreated microcrystalline cellulose (MCC) into the PLA matrix. MCC was treated by using ultrasonic machine to aid the dispersion in the PLA. The compounding of PLA composite was carried out in an internal mixer at 180^{o}C, 50rpm. The composites were pressed into thin sheet (1 mm thickness) by using compression molding at 180^{o}C, 150 bar. The characterization tests for PLA composites were comprised of tensile test, thermal tests (Differential Scanning Calorimetry, Thermo Gravimetric Analysis) and scanning electron microscopy (SEM) test. Presence of coconut oil (5 to 10wt%) in MCC filled PLA showed improvement in tensile elongation property in the range of 1 to 59% as compared to neat PLA. The coconut oil plasticized PLA also reported better elongation properties than PEG plasticized PLA with 22.8% vs 14.8%. Treated MCC showed higher thermal stability as compared to untreated MCC in the plasticized PLA, with onset decomposition temperature recorded at 350°C vs 302°C. This could be due to better dispersion of the treated MCC in the composites which further improve the crystallinity. SEM images also showed more uniform and homogenous distribution of the treated MCC in the PLA. Overall, the coconut oil plasticized PLA showed better flexibility in terms of higher elongation at break as compared to unplasticized PLA and the addition of MCC into the PLA matrix showed improvement in the thermal stability and modulus property of the composite.

Keywords: Polylactic acid, Coconut oil, Microcrystalline cellulose, Polyethylene glycol

1. Introduction

Polylactic acid (PLA) is a biobased polymer produced from biomass such as corn and sugar beet. PLA is also a biodegradable plastic which is widely used in many applications such as medical, textile and packaging (Al-mulla et al. 2005). PLA has good mechanical properties (tensile strength and modulus), processibility, biocompatibility and less energy dependence. However, it has disadvantages due to its brittleness and hydrophobicity (Halász et al. 2013).

The function of plasticizer is to improve the flexibility of polymers and reduce the friction during processing (Rahman et al. 2004). Apart from that, it helps to enhance its elongation at break. Plasticizers can be categorized as either internal or external plasticizer. Internal plasticizers are added during the polymerization process to form covalent bonds with the polymer while external plasticizer are added in to resin during compounding to form a weaker bond with the polymer resin. External plasticizer is more in favorable because it gives satisfactory combination properties and flexibility for manufacture to formulate the material as compare to internal plasticizer which need to be added during polymerization process (Rahman et al. 2004). In this study, coconut oil and PEG are both considered as external plasticizer used to improve the flexibility of the PLA.

Cellulose is plentiful on the Earth. It is a biodegradable polymer which can be added into PLA to reduce the material cost, enhance the mechanical and thermal properties of the polymer blends. However, cellulose has its own drawback because it is highly attracted to water (hydrophilic). It may display poor compatibility with hydrophobic matrices when it is added (Halász et al. 2013).

In this study, the area that will be explored is the incorporation of novel plasticizer, coconut oil into the PLA/MCC blends. The study focused on the performance of the coconut oil plasticizer against the conventional plasticizer of polyethylene glycol and the effect of the MCC treatment with ultrasonic machine.

Objectives:

The main objective of this research paper is to investigate the type of plasticizer that can be used in preparation of biocomposite, compare the properties of treated and

untreated MCC and to study the effect of addition of plasticizer and MCC on the mechanical and thermal properties of PLA.

2. Methodology

2.1 Materials

The materials used are polylactic acid 3051D (PLA), polyethylene glycol (PEG400), coconut oil and microcrystalline cellulose (MCC). PLA was obtained from Nature Works LLC with glass transition temperature of 55-60^{o}C and melting temperature of 150-165^{o}C. Polyethylene glycol, microcrystalline cellulose and coconut oil were obtained from Synertec Enterprise at Kuala Lumpur, Malaysia.

2.2 Method

2.2.1 Melt blending

Melt blending process was carried out in order to mix the MCC, plasticizer and the PLA according to the formulation in Table 1. This process use internal mixer (Haake Polylab System E93) at temperature 180^{o}C and speed 50 rpm (Chun et al. 2013). Once it has the set temperature and speed, the mixture of PLA-compound was put inside for about 7 to 8 minutes. The plasticizer and MCC dosage of 5 and 10wt% respectively are selected based on the previous literature outcomes (Dai et al., 2014;Frone et al., 2013;Halász et al, 2013;Sungsanit et al. 2012;Tariq et al., 2014;Tsou et al., 2014; Kulinski et al., 2005).

2.2.2 Compression Molding

Compression molding process was done to produce the sheet. The mixture of PLA-MCC is compressed at temperature 180^{o}C and pressure 150 bar by using hot press machine (Moore E53) (Chun et al. 2013). Once the machine has reached the set temperature, the compound is put inside. It undergoes a pre-heating process for about 4 minutes before the pressure being applied for 8 minutes. Then, the machine is let to cool down to 70^{o}C before the sheet can be taken out. The polymer sheet obtained will be in 12cm x13 cm in size with 0.2cm thickness.

`

2.2.3 Ultrasonic Machine

The MCC which is put inside a beaker wrap with aluminium foil will be placed into another big beaker filled with water. MCC is then treated in an ultrasonic bath using ultrasonic machine at 50 Hz for 30 minutes.

Table 1: Formulation of polylactic acid, plasticizers and microcrystalline cellulose.

Neat PLA
PLA + PEG (10wt %)
PLA + PEG (10wt %) + MCC (10%)
PLA + Coconut Oil (10wt %)
PLA + Coconut Oil (10wt %) + MCC (10wt %)
PLA + Coconut oil (10wt %) + treated MCC (5wt %)
PLA + Coconut oil (10wt %) + treated MCC (10wt %)
PLA + Coconut oil (5wt %) + treated MCC (10wt %)

2.3 Equipment used

2.3.1 Tensile test

Tensile test was carried out using Instron Tensile Test Machine 3366 according to the standard ASTM D638-10 with a 1kN load cell at temperature, 23±2 ^{o}C and relative humidity 50±5 %. The crosshead speed for the tensile test was set at 5 ± 25% m/s. Samples were cut into dumbbell-shaped type IV specimen as shown in Figure 3.3. The measured force-displacement data as obtained from the Universal Testing Machine was extracted for computation of the nominal stress-strain response of the composite (Chun et al. 2013).

2.3.2 Differential Scanning Calorimetry

DSC was used to measure the crystallinity and heat resistance of PLA composites. The samples were heated up from room temperature to 200^{o}C. It was then cooled at the rate of 10^{o}C/min in a nitrogen atmosphere (Chun et al. 2013).

2.3.3 Thermo Gravimetric Analysis

TGA was used to measure the decomposition temperature of the PLA composite. The samples are heated up from 30^{o}C to 800^{o}C at rate 10 ^{o}C/min (Chun et al. 2013).

2.3.4 Scanning Electron Microscopy

Field emission SEM (model FEI Quanta 400F FESEM) was used to observe the surface and fracture morphology of the specimens. Specimens were sputtered-coated with a thin layer of gold to avoid electrical charging during examination (Chun et al. 2013).

3.0 Results and Discussion

3.1 Tensile Testing

The tensile tests were performed for analysis to determine the tensile properties of the samples. The tensile tests were performed on all the formulations according to standard test method for tensile properties, ASTM 638-10 using Instron Tensile Test Machine 3366.

Table 3.1 shows the summary of the analysis for 8 samples. Three important mechanical properties were evaluated from this test – Young's modulus, maximum tensile strength and elongation at break for pure PLA and plasticized PLA (either plasticized with CO or PEG). In this research study, the addition of plasticizer, CO on the PLA show improvement in terms of elongation at break and modulus strength compared to pure PLA and PEG plasticized PLA. Refer to formulation 1, 2, and 4, formulation 4 (PLA/10wt% CO) demonstrated elongation at break, 22.8±6.12% and modulus strength, 404±4.37MPa whereas formulation 1 (pure PLA) and formulation 2 (PLA/10wt% PEG), only demonstrated elongation at break, 22.6±3.78% and 14.8±4.39%, modulus strength, 393±14.1 and 330±21.5 MPa, respectively. Hence, it can be clearly inferred that the effect of plasticizer on the PLA show better elongation at break and modulus strength but not the tensile strength of the composite. From the results, it show that CO is a better plasticizer than PEG.

The effects of MCC loading (0 and 10wt %) on the tensile properties of plasticized PLA (either plasticized with CO or PEG) are shown in Figure 3.1 As can be seen in Figure 3.1, the incorporation of MCC loading of 10wt % showed significant improvement in terms of elongation at break about 2.6% on PLA/CO compared to PLA/PEG which drop about 1.6%. Overall, as illustrated in Figure 3.1, the coconut oil plasticized PLA composites show better elongation at break than the PEG plasticized PLA composites. The incorporation of MCC into the PLA matrix are supposed to show improvement in the tensile modulus. However, refer to Table 3.1, there is no significant improvement in the tensile modulus even with the loading of 10% MCC into plasticized PLA. This could be due to the interference of the plasticizer in the composites which provides flexibility to the material. Refer to formulation 6 and 7, the addition of 10% TMCC indeed showed higher modulus strength than the 5% TMCC (359

MPa Vs 344 MPa). The increase in modulus with increasing MCC loading in PLA can be explained by increased in hydrogen bonding, stiffening effect and high crystallinity index of the filler which is a typical characteristics filler/polymer composites.

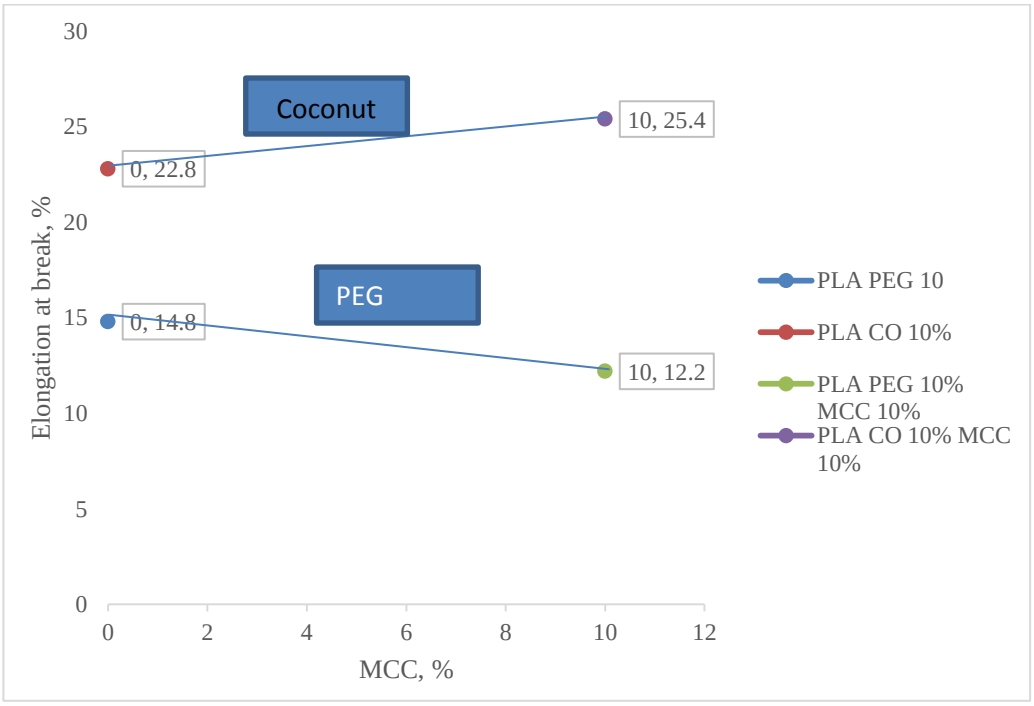

Figure 3.1 Comparison of elongation at break with and without MCC

The tensile strength of composite deteriorates when there is addition of plasticizer and MCC. It can be observed that the maximum tensile strength for neat PLA and PLA/10% CO/10% MCC exhibited the value of 56.2 and 22.2 MPa respectively. Refer to Table 4.1, formulation 4 (PLA plasticized with 10%CO) exhibited higher tensile strength, 46.5MPa compared to formulation 2 (PLA plasticized with 10%PEG), 31.9MPa. This finding is in agreement with previous study, where the adding of plasticizer (e.g., PEG) does increase the elongation at break but not the tensile strength. However, CO still performed better than PEG in the tensile properties. It can be inferred that type of plasticizers, CO do affect the tensile properties.

It is reported that high amount of natural filler would decrease the tensile properties and the brittleness was able to improve with optimum amount of plasticizer based on the literature review. According to the results in Table 3.1, the addition of treated MCC in small content (5wt%) exhibited improvement in terms of tensile strength and elongation at break when compared to treated MCC of 10wt% loading. Refer to formulation 5 and 6 in Table 3.1, the treated and untreated MCC in the CO plasticized PLA composites do not show significant different in the tensile properties.

Table 3.1 Summary of Tensile Test

No.	Sample	Max Tensile Strength, MPa	Elongation at Break, %	Tensile Modulus, MPa
1	Neat PLA	56.2±1.37	22.6±3.78	393±14.1
2	PLA+PEG 10%	31.9±2.09	14.8±4.39	330±21.5
3	PLA+PEG 10%+MCC 10%	26.8±2.07	12.2±1.53	349±9.88
4	PLA+CO 10%	46.5±1.53	22.8±6.12	404±4.37
5	PLA+CO 10%+MCC 10%	22.2±0.47	25.4±5.34	346±5.12
6	PLA+CO 10%+TMCC 10%	22.7±0.48	15.7±4.31	359±7.96
7	PLA+CO 10%+TMCC 5%	23.2±0.65	35.9±6.95	344±5.18
8	PLA+CO 5%+TMCC 10%	25.8±0.38	22.7±8.78	379±3.86

3.2 Thermo Gravimetric Analysis (TGA)

In order to investigate the thermal properties of the PLA/Plasticizers/MCC composites, thermo gravimetric analysis (TGA) were performed. Figure 4.6 shows the TGA curve (weight% vs temperature ^{o}C) of four formulations of treated and untreated PLA/MCC composites with conventional PEG and coconut oil. The thermal degradation data of PLA/MCC composites are tabulated in Table 3.2, using the temperature at which weight loss of the samples occurs and the residual weight at 600^{o}C.

Table 3.2 Thermal properties of PLA/Plasticizer/MCC composites

Sample	Decomposition temperature, ^{o}C	Residual weight % at 600^{o}C
	T_{onset}	
PLA/PEG 10%/MCC 10%	280	8.59
PLA/CO 10%/MCC 10%	302	5.24
PLA/CO 10%/TMCC 10%	350	7.0
PLA/CO 5%/TMCC 10%	350	7.5

Figure 3.2 clearly shows an improvement in thermal stability of CO in PLA/MCC composites compared to conventional PEG in PLA/MCC composites. From the TGA curve, it can be observed that the onset decomposition temperature (T_{on}), for all coconut plasticized PLA composites (~302-350^{o}C) show higher thermal stability than PEG plasticized PLA composite (280^{o}C). This could be attributed to the higher decomposition temperature of pure coconut oil at 200^{o}C against the pure PEG decomposition temperature at 80^{o}C (Raju et al. 2007).

According to (Giita Silverajah et al. 2012), the neat PLA onset decomposition temperature was recorded as 260^{o}C. This means the addition of MCC into PLA can improve the crystallinity of the PLA. This is also supported by (Halász & Csóka 2013) where the MCC dose of greater than 1-5% will show better thermal stability. The treated MCC is expected to exhibit better performance as compared to untreat MCC because the treated MCC formed very fine particles, with higher surface area for adhesion. The residual weight % displayed by PLA/PEG/MCC and PLA/CO/MCC, TMCC composite are almost the same where 90% of the sample were burned. This behavior is probably due to the presence of a higher amount of crystalline cellulose from MCC produced which has an intrinsically flame resistant property.

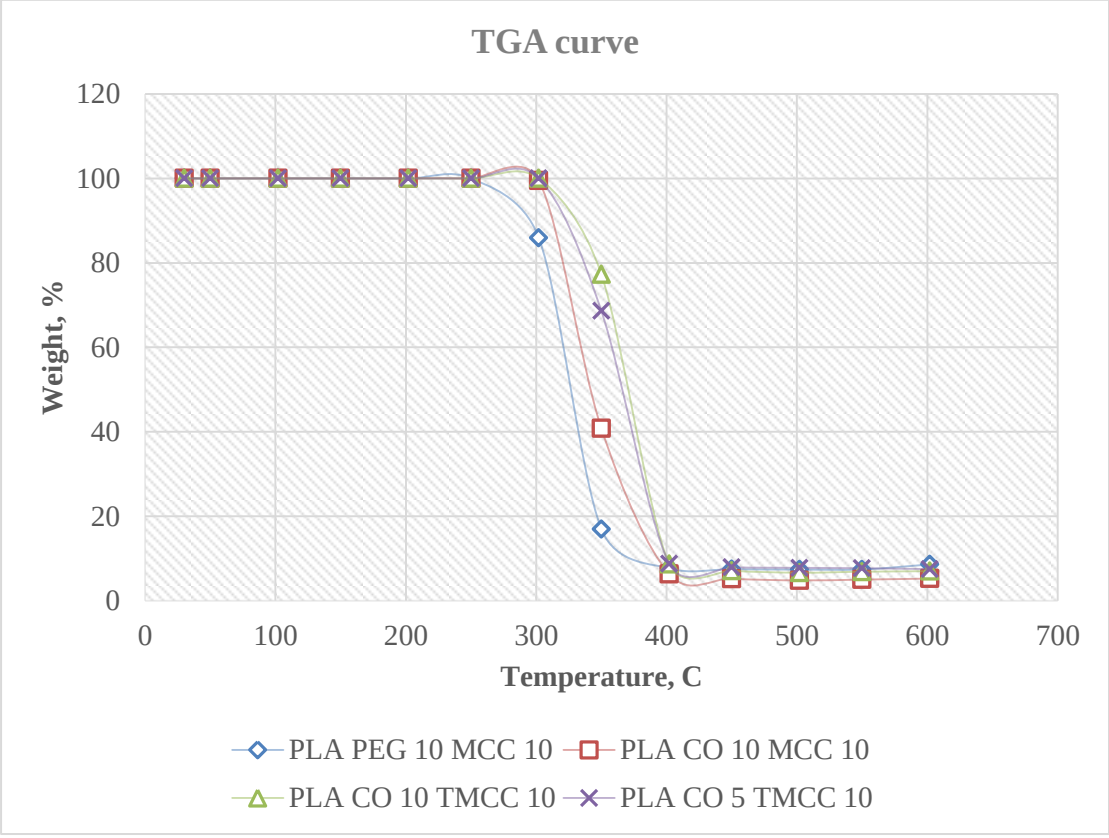

Figure 3.2 TGA curve

3.3 Differential Scanning Calorimetry (DSC)

Refer to the DSC curve (Figure 4.7), it can be clearly seen that there are two thermal transition phases for all the 3 PLA composites. First thermal transition happened at 50 C, which is the glass transition temperature for the matrix PLA. Second thermal transition happened at 155 C, which is the melting point for the matrix PLA. Glass transition temperature, T_g refer to the temperature range where a polymer changes its state from a hard, rigid or glassy to a more rubbery state (Transition n.d.).

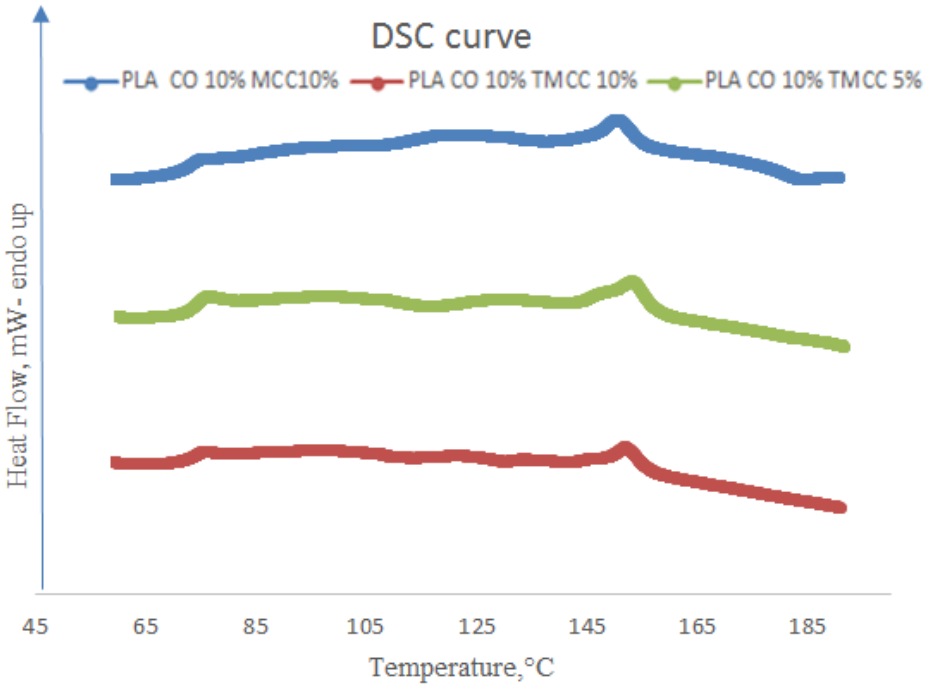

Figure 3.2 DSC curve of three samples

3.4 Scanning Electron Microscopy (SEM)

The tensile fractured surface of the specimens were examined using scanning electron microscope (SEM) with an acceleration voltage of 20kV under 100, 500 and 1000 times magnification (Matta et al. 2014).SEM images of fractured cross-sectional area under 500

times magnification were shown in Figure 3.3 (a), (b), (c) and (d). From SEM images, all the formulations showed homogenous surface morphology between PLA matrix, plasticizers and MCC. MCC was dispersed uniformly across the PLA polymer matrix. There is a good dispersion of molecules throughout the polymer matrices between the components. As illustrated in Figure 10 c and d, the higher loading of natural filler TMCC (10%) showed more compact image compared to TMCC (5%).

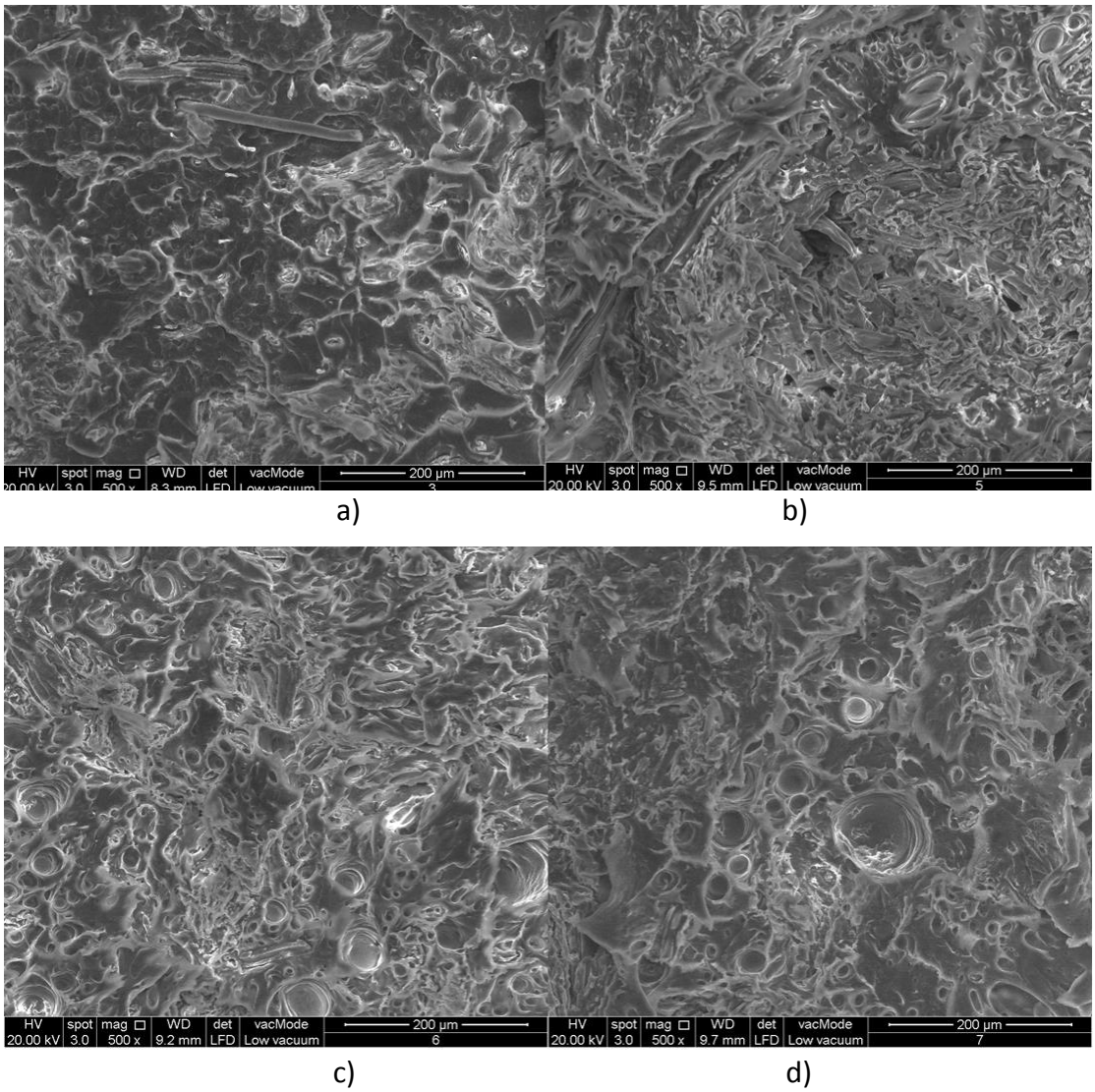

Figure 3.3 a) PLA/PEG 10%/MCC 10%, b) PLA/CO 10%/MCC 10%, c) PLA /CO 10%/TMCC 10% d) PLA/CO 10%/TMCC 5%

4. Conclusion

Plasticized PLA (either CO or PEG) with 5 and 10w wt% MCC biocomposite sheet were successfully synthesized through sample compounding in internal mixer followed by hot pressing. Control sample, pure PLA were also produced for comparison with CO and PEG plasticized PLA composite respectively. Tensile tests, SEM tests, TGA and DSC tests were performed accordingly in compliance with international standard on all the specimens.

Overall, coconut oil shows better performance in tensile properties and thermal stability as compared to PEG plasticizer. The onset decomposition temperature for the PLA/Coconut/TMCC is the highest at 350^{o}C. This could be due to the treatment of the ultrasound which enhance the structure and dispersion of the MCC in the PLA matrix. The addition loading of MCC into the PLA matrix indeed increase the thermal stability of the PLA due to the crystalline structure of the filler itself.

Acknowledgment

The authors would like to thank Taylor's University Malaysia (Grant: TRGS/ERFS/2/2013/SOE/008) and University of Nottingham Malaysia Campus for its financial and equipment supports.

References

Al-mulla, E.A.J., Azowa, N. & Ibrahim, B., 2005. Poly (Lactic Acid) as a Biopolymer-Based.

Ashori, A. & Nourbakhsh, A., 2010. Performance properties of microcrystalline cellulose as a reinforcing agent in wood plastic composites. *Composites Part B: Engineering*, 41(7), pp.578–581.

Choi, W.Y., Lee, C.M. & Park, H.J., 2006. Development of biodegradable hot-melt adhesive based on poly-ε-caprolactone and soy protein isolate for food packaging system. *LWT - Food Science and Technology*, 39(6), pp.591–597.

Chun, K.S. & Husseinsyah, S., 2013. Polylactic acid/corn cob eco-composites: Effect of new organic coupling agent. *Journal of Thermoplastic Composite Materials*.

Dai, X. et al., 2014. How does epoxidized soybean oil improve the toughness of microcrystalline cellulose filled polylactide acid composites? *Composites Science and Technology*, 90, pp.9–15.

Frone, A.N. et al., 2013. Morphology and thermal properties of PLA-cellulose nanofibers composites. *Carbohydrate polymers*, 91(1), pp.377–84.

Giita Silverajah, V.S. et al., 2012. A Comparative Study on the Mechanical, Thermal and Morphological Characterization of Poly(lactic acid)/Epoxidized Palm Oil Blend. *International journal of molecular sciences*, 13(5), pp.5878–98.

Halász, K. & Csóka, L., 2013. Plasticized Biodegradable Poly(lactic acid) Based Composites Containing Cellulose in Micro- and Nanosize. *Journal of Engineering*, 2013, pp.1–9.

Kulinski, Z. & Piorkowska, E., 2005. Crystallization, structure and properties of plasticized poly(l-lactide). *Polymer*, 46(23), pp.10290–10300.

Lim, L.-T., Auras, R. & Rubino, M., 2008. Processing technologies for poly(lactic acid). *Progress in Polymer Science*, 33(8), pp.820–852.

Rahman, M. & Brazel, C., 2004. The plasticizer market: an assessment of traditional plasticizers and research trends to meet new challenges. *Progress in Polymer Science*, 29(12), pp.1223–1248.

Range, N., Using, M. & Mass, I.R., Confused by the terms Biodegradable.

Rasal, R.M., Janorkar, A. V. & Hirt, D.E., 2010. Poly(lactic acid) modifications. *Progress in Polymer Science*, 35(3), pp.338–356.

Sungsanit, K., Kao, N. & Bhattacharya, S.N., 2012. Properties of linear poly(lactic acid)/Polyethylene glycol blends. *Polymer Engineering & Science*, 52(1), pp.108–116.

Tariq, F., Noori, M. & Ali, N.A., 2014. Study the mechanical and thermal properties of biodegradable polylactic acid / poly ethylene glycol nanocomposites. , 3(1), pp.459–464.

Tsou, C.-H. et al., 2014. Preparation and Characterization of Bioplastic-Based Green Renewable Composites from Tapioca with Acetyl Tributyl Citrate as a Plasticizer. *Materials*, 7(8), pp.5617–5632.

Mechanical Properties Investigation on Thermoplastic Starch (TPS)/ Montmorillonite Nano-clay (MMT)/ Alumina Trihydrate (ATH) Nanocomposites Film

Jun Wen Ho[1], Siew Wei Phang[1,2*], Lee Tin Sin[2], Soo Tueen Bee[2], Tiam Ting Tee[2]

[1]*School of Engineering, Taylor's University Lakeside Campus, Malaysia.*
[2]*Department of Chemical Engineering, Faculty of Engineering and Science, Universiti Tunku Abdul Rahman, Kuala Lumpur, Malaysia.*

*siewwei.phang@taylors.edu.my

Abstract
Starch has been selected to produce biodegradable polymer as it is an abundant, low cost, naturally renewable and biodegradable nature polymer. However, due to hydrophilic nature of pure TPS films, it has poor mechanical properties. Hence, fillers such as MMT, and ATH are introduced to improve the mechanical, thermal and flame retardant properties respectively. On the other hand, Citric acid (CA) is added to enhance the cross-linking effect between starch and fillers. Water is used as the main plasticiser and glycerol is used to further enhance the plasticising effect of the nanocomposites film. In this research, the main purpose is to determine the mechanical properties of the TPS/ MMT/ ATH blend. Preliminary test is carried out to determine the optimum ratio of glycerol and samples are prepared by solution casting method. The effects of each fillers are determined based on the experimental result from tensile tester machine STM-SERVO. The mechanical properties of TPS/ MMT/ATH nanocomposites film are determined by tensile strength, elongation at break and young's modulus. As a result, the nanocomposites film exhibited an improvement in tensile strength due to reinforcement of MMT and ATH. The elongation at break have reduced with introducing fillers in the nanocomposites films as intercalation of fillers into starch promotes the formation of restricted environment against the movement of polymer chains. On the contrary, the Young's modulus of the nanocomposites film shown measurable enhancement due to the polymer chains restricted.

Keywords: TPS/ MMT/ ATH nanocomposites, mechanical properties, tensile strength, cross-linking

1.0 Introduction

Plastic contributed considerable societal benefits in our daily lives. In fact, approximately 4% of the total oil production in the world is converted into plastics [1]. The usage of plastics gradually increases in the developing world due to its low unit cost and excellent performance specifications, the usage and annual production of plastics have exceed 300 million tons in the year 2010 [2]. In modern society, plastic plays an important role in the range of materials, almost every field involves plastics. For instance, plastics are utilised in packaging, public health, garment sector and also on external panel of cars. However, the current approaches in production, usage and disposal are not sustainable and created concerns for the environment, human and wildlife health. One of the major problems associated with production of plastics is the greenhouse gases (GHG) emission to atmosphere during the manufacturing of plastics. Besides, the drawbacks of utilising plastics also included the poor disposal method, which accumulated the waste in landfills. On the other hand, wildlife might be harm resulting from ingestion or entanglement in plastics. Also, during the production of plastic products, hazardous materials are released, which have the potential to endanger humans and wildlife [3]. Hence, compromise solution has to be found to overcome the current drawbacks of utilising plastics.

In order to reduce the GHG emission, one of the strategies adopted by several countries is to focus on the development of plastic that derived from biodegradable sources. On the other hand, the problems associated with handling and disposal of solid waste and interest in environmentally-friendly product has created a significant market opportunity for plant-based plastics. Currently, most of the synthetic plastics are derived from petrochemical, which are non-biodegradable, in another word; these materials are not able to be decomposed and it is difficult to recycle and reuse due to its complex composites [4]. Therefore, plant-based plastics has arisen as the alternative materials that have similar functionality to replace the conventional oil-based plastics. Plant-based plastics also known as biopolymer, which is derived from renewable sources such as starch.

Starch is an abundant, low cost, naturally renewable and biodegradable [5]. Starch is composed of repeating α-D-glucopyranosyl unit, which is the mixture of amylose, an essentially linear polysaccharide, and amylopectin, a highly branched polysaccharide as shown in Fig. 1. The properties of starch strongly depend on the ratio of amylose and amylopectin, typical cassava starch contains approximately 17% of amylose. In this research, cassava starch has been selected to produce starch-based plastics as it is renewable, low cost, and abundant in Malaysia. Cassava starch is also known as tapioca starch in Malaysia, it is obtained from the roots of the cassava plant. Compared to other types of starch, such as corn, potato and wheat starch, the characteristic of cassava starch are low level of residual materials, for instance, the amount of fat, protein and ash are relatively lesser.

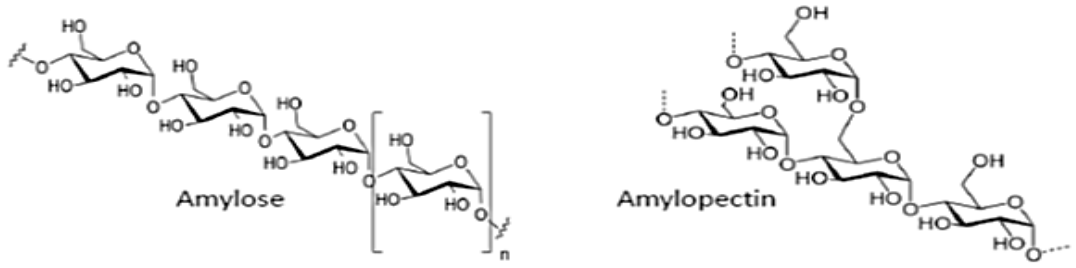

Figure 1. Structure of Amylose and Amylopectin

Few challenges existed in the starch-based plastics. For instance, due to the high hydrophilicity of starch, it has limited process ability and poor mechanical strength. Besides, starch tends to absorb the surrounding water vapour due to its characteristic in water absorption, which leads to poor long-term stability. Therefore, reinforcement of starch-based plastics is required to be carried out to eliminate the drawbacks. This research is conducted to addressed the challenges exist in the starch-based plastics, the following are the objectives that should be achieved throughout this research.

- To produce TPS/ MMT/ ATH nanocomposites films through solution casting method
- To determine the mechanical properties of the TPS/ MMT/ ATH blend
- To investigate and illustrate the effect of CA as cross-linking agent in TPS/MMT/ATH nanocomposites

As mentioned, granular starch has limited process ability, hence, it requires plasticiser for further process. The usage of plasticisers are able to enhance the film flexibility due to their ability in reducing the internal hydrogen bonding between the polymer chains. For instance, glycerol and water are used as the plasticiser in this research. In fact, water is the main plasticiser in the gelatinisation process. However, the effect of using water alone in starch-based plastics gelatinisation is very transient. Therefore, some less volatile plasticiser such as glycerol is introduced in the gelatinisation of starch. Glycerol has been selected as the plasticiser in this research as it is hydrogen bonding polar liquid [6], which is most suitable and it able to enhance the characteristic of starch by increase the molecular mobility of glucan chain. Besides, films that plasticised by glycerol is able to adsorbed faster and more water during storage as experimented by Mali et al. [7]. Based on the gelatinisation of cassava starch studies performed by Allen, the optimum gelatinisation temperature of starch-glycerol mixture is at 64.3 ºC [8], hence, during the preparation of TPS/ MMT/ ATH nanocomposites film, the solution is required to be heated to at least 65°C in order for the solution to be plasticised.

Due to the hydrophilic nature of pure TPS films, it carries poor mechanical properties. On the other hand, based on research performed by researchers in the similar field, the mechanical strength of the polymer blends have significant increment with the addition of montmorillonite nano-clay (MMT) [7, 8]. Hence, in this research, MMT is introduced to enhance the mechanical strength of the TPS film, the mechanical performance of the MMT in the polymer matrix is depending on the intercalation of MMT into the crystal lattice galleries. Excellent mechanical behaviour

of MMT in polymer matric is able to be achieved by perfect interaction between the organic and inorganic component. The optimum loading of MMT in the TPS/ MMT/ ATH nanocomposites film is crucial to be determined, in fact, adding of MMT able to increase the tensile strength of the nanocomposites film, however, there is a limitation, as further loading of MMT might bring adverse effect.

Thermal and flame retardant properties of nanocomposites film able to be enhanced by introducing the flame retardant filler. Studies on the alumina trihydrate (ATH) shows that ATH able to improve the fire resistance by retard the combustion of polymer matrix with reducing the melt dripping [11]. Besides, ATH is one of the flame retardant filler used in the polymers industry, compared to halogenated compounds flame retardant filler, ATH is more preferable as it does not release toxic smoke during the combustion process [12]. Based on the experimental outcomes performed by Cheng et al. [13], loading of both MMT and ATH in the nanocomposites film might results in flame retardant effect declined due to MMT unable to well integrate with ATH. Therefore, the loading level of ATH must be concerned when MMT is introduced in the polymer. The total weight percentage of ATH in the polymer composites should be high enough to avoid MMT suppressed the flame retardant ability of ATH.

Furthermore, citric acid (CA) is added into the nanocomposites films as the cross-linking agent to ensure all the components in the nanocomposites film are well-intercalated. According to studies, CA molecules act as a bridge between starch and clay molecule, it enhanced the intercalation process through hydrogen bonding [14]. On the other hand, as shown in Fig. 2, CA also able to enhance the plasticising effect by promote the fragmentation and dissolution of starch granule as claimed by Wang et al. [15].

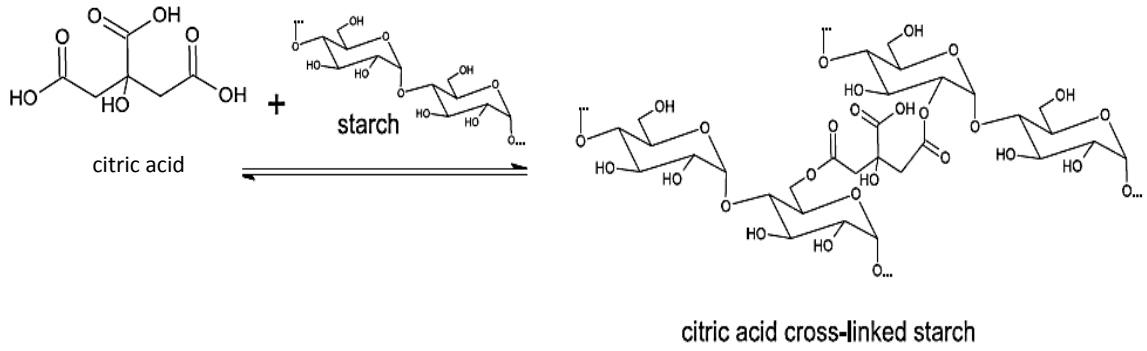

Figure 2. Cross-linking of Citric Acid with Starch

In this study, the mechanical properties such as elongation at break, young's modulus and tensile strength of the nanocomposites film are determined by Tensile Tester Machine STM-SERVO according to ASTM D882 standard.

2.0 Experimental Methodology

2.1 Materials

Native cassava starch powder with 17% of amylose is chosen in this research for the preparation of plant-based plastics due to its abundant availability, as cassava starch is widely cultivated and commercialised in Malaysia. For the main plasticiser – distilled water is obtained from Taylor's Engineering laboratory, and glycerol was chosen to further enhancing the plasticisation effect and it was purchased from Merck Sdn. Bhd., Malaysia. For the different fillers, in enhancing mechanical strength of the TPS/ MMT/ ATH nanocomposites, MMT which also denotes as Nanolin DK® Nano-clay was purchased from FCC®, Inc., China. On the other hand, ATH with 90% purity that enhanced the thermal properties and cross-linking agent, anhydrous CA ($C_6H_8O_7$) with 99% purity and density of 1.665 g/cm^3 was purchased from Evergreen Engineering Resources, Malaysia.

2.2 Design of Experiment

The factors and their levels are determined in the first step in design of experiment, then the experimental design approach is selected based on the factors. In this research, full factorial design of experiment is applied to investigate the effect of incorporation of TPS, MMT and ATH. Three main factors: loading of MMT, ATH and CA were considered in three levels. The three loading levels of the fillers are selected based on the literature reviews performed on journals and publication in the similar research field. The loading of MMT was chosen in the range of 1 to 3 wt.% [10, 11, 14], where the loading for ATH is selected in the range from 14 to 18 wt.% [9, 11]. On the other hand, the loading level for CA is varied from 1 to 5 wt.% [15, 16]. With three factors and three levels full factorial design, 27 runs are required for complete analysis, the formulation is shown in Table 1. Analysis software- Minitab 17 is used to calculate the interaction of the factors, and hence, main effect plots are generated.

2.3 Sample Preparation

2.3.1 Preliminary Test

Preliminary test is performed to determine the optimum amount of glycerol in the TPS/ MMT/ ATH nanocomposites in order to reduce the number of factors. As the amount of starch is fixed throughout the research, which is 10 phr, and the other factors such as MMT is crucial in determining the mechanical strength, ATH which is important in determining the effect of flame retardant properties and CA which is decisive in the effect of intercalation of fillers in the nanocomposites film. Hence, the amount of glycerol in the nanocomposites film is determined in the preliminary test to simplify the further work. The range of glycerol selected is based on the percentage proportion to the starch, and 40, 50 and 60 wt.% is selected based on the literature review performed. Besides, the nanocomposites films produced are observed in order to determine the optimum amount of glycerol. In fact, the redundant of glycerol will result in soft and mushy nanocomposites film where on the

contrary, insufficient of glycerol will produce brittle and fragile nanocomposites film. The technique applied in the preparation of TPS/ MMT/ ATH nanocomposites is solution casting method and the formulation is shown in Table 2. Detailed explanation on sample preparation can be refer to Section 2.3.1 Preparation of TPS/ MMT/ ATH Nanocomposites Film.

Table 1. Formulation of TPS/ MMT/ ATH nanocomposites film

Experiment	Starch	Nano-clay	Alumina Trihydrate	Citric Acid	Glycerol
	PHR[1]	PHR	PHR	PHR	PHR
1	10.00	0.16	2.50	0.16	5.00
2	10.00	0.32	2.50	0.16	5.00
3	10.00	0.48	2.50	0.16	5.00
4	10.00	0.16	2.50	0.48	5.00
5	10.00	0.32	2.50	0.48	5.00
6	10.00	0.48	2.50	0.48	5.00
7	10.00	0.16	2.50	0.80	5.00
8	10.00	0.32	2.50	0.80	5.00
9	10.00	0.48	2.50	0.80	5.00
10	10.00	0.16	3.00	0.16	5.00
11	10.00	0.32	3.00	0.16	5.00
12	10.00	0.48	3.00	0.16	5.00
13	10.00	0.16	3.00	0.48	5.00
14	10.00	0.32	3.00	0.48	5.00
15	10.00	0.48	3.00	0.48	5.00
16	10.00	0.16	3.00	0.80	5.00
17	10.00	0.32	3.00	0.80	5.00
18	10.00	0.48	3.00	0.80	5.00
19	10.00	0.16	3.50	0.16	5.00
20	10.00	0.32	3.50	0.16	5.00
21	10.00	0.48	3.50	0.16	5.00
22	10.00	0.16	3.50	0.48	5.00
23	10.00	0.32	3.50	0.48	5.00
24	10.00	0.48	3.50	0.48	5.00
25	10.00	0.16	3.50	0.80	5.00
26	10.00	0.32	3.50	0.80	5.00
27	10.00	0.48	3.50	0.80	5.00

Note: Concentration in the above table is in PHR, which is equivalent of loading 1, 2 and 3 wt.% of MMT is 0.16, 0.32 and 0.48 PHR, loading 14, 16, and 18 wt.% of ATH is 2.5, 3.0 and 3.5 PHR, loading of 1, 3 and 5wt.% of CA is 0.16, 0.48 and 0.8 PHR and loading of 27 wt.% of glycerol is 5 PHR.

[1] PHR is abbreviation for parts per hundred parts of resin, which is used in composites formulations, for instance, 10 PHR means 10 grams of an ingredient would be added to 100 grams of resin.

Table 2. Formulation of Preliminary Test

Experiment	Starch	Nano-clay	Alumina Trihydrate	Citric Acid	Glycerol
	PHR	PHR	PHR	PHR	PHR
1	10.00	0.32	3.00	0.48	4.00
2	10.00	0.32	3.00	0.48	5.00
3	10.00	0.32	3.00	0.48	6.00

Note: Concentration in the above table is in PHR, which is equivalent of loading 1, 2 and 3 wt.% of MMT is 0.16, 0.32 and 0.48 PHR, loading 14, 16, and 18 wt.% of ATH is 2.5, 3.0 and 3.5 PHR, loading of 1, 3 and 5wt.% of CA is 0.16, 0.48 and 0.8 PHR and loading of 23, 27 and 31 wt.% of glycerol is 4, 5 and 6 PHR respectively.

2.3.1 Preparation of TPS/ MMT/ ATH Nanocomposites Film

Solution casting method is utilised in this research to produce the TPS/ MMT/ ATH nanocomposites film. Solution casting method is started with measure the amount of starch, fillers and plasticisers required in the experiment, the formulation is shown in Table 1. 10 g of starch, 1, 2 and 3 wt.% of MMT, 14, 16 and 18 wt.% of ATH, and 1, 3 and 5 wt.% of CA which is in solid powder form are poured into a beaker. Fillers and cross-linking agent are mixed with starch before plasticisation is to ensure the fillers and cross-linking agent able to perfectly mixed together. As reported by Tang at el., the extent of intercalation of MMT increased when composites were prepared without earlier plasticisation, and it might due to plasticisers affected the attractive force between starch and MMT [17]. Hereafter, 400 ml of distilled water with 5 phr of glycerol as the plasticisers are gradually added into the beaker containing all the powder. Magnetic hot plate stirrer (SMHA-3 WiseStir) with operating speed of 600 rpm is used to mix the solution to achieve homogenous mixture, the solution are required to be heated up to 70°C due the effect of glycerol will only turn up after the specific temperature as mentioned earlier. After an hour of hot place stirring, the solution will became more viscous, which indicated the result of plasticisation. Then, the solution is poured on rectangular Teflon mould and oven that operated at 70°C is used to dry the solution for 24 hours. On the next day, the sample are removed from the Teflon mould. The limitation existed in the sample produced might subject to retrograde effect before testing and characterising, therefore samples are kept into a zipper bag with silica gels to avoid the samples from having further reaction with air.

2.4 Characterisation of TPS/ MMT/ ATH nanocomposites film

2.4.1 Mechanical Strength

The mechanical strength – tensile strength, Young's modulus and elongation at break of the TPS/ MMT/ ATH nanocomposites is determined by tensile tester machine STM-SERVO according to the ASTM D882 standard (Standard Test Method for Tensile Properties of Thin Plastic Sheeting). During tensile testing, the specimen was gripped at both ends of the tensile testing machine, elongation rate at 50 mm/min is subjected to the specimen until it break. Before testing, the specimens were cut into thin strip with dimension of 6 cm (L) × 5 mm (W),

and the thickness of the film is measured by digital micrometer. The cross-sectional area of the specimens is calculated by considered the length, width and thickness of the specimens.

3.0 Results and Discussions

3.1 Tensile Strength

The mechanical properties of TPS/ MMT/ATH nanocomposites film are determined by tensile strength, elongation at break and Young's modulus. The mechanical strength of the nanocomposites film is determined by tensile tester machine STM-SERVO according to ASTM D882 – "Standard Test Method for Tensile Properties of Thin Plastic Sheeting" [18]. The shape and dimension of the sample, specimen grip type, grip pressure and elongation rate for tensile testing is covered under this standard. The working mechanism of the machine is to pull both ends of the nanocomposites strip until it break. The tensile strength is determined based on the stress required to break the samples. On the other hand, the results obtained from tensile test are rather accurate due to it considered the cross sectional area of each sample, as the thickness of samples might vary from each and other. As the TPS/ MMT/ ATH nanocomposites film contains fillers and cross-linking agent, hence the effect of each filler and cross-linking on the tensile strength will be clearly discussed.

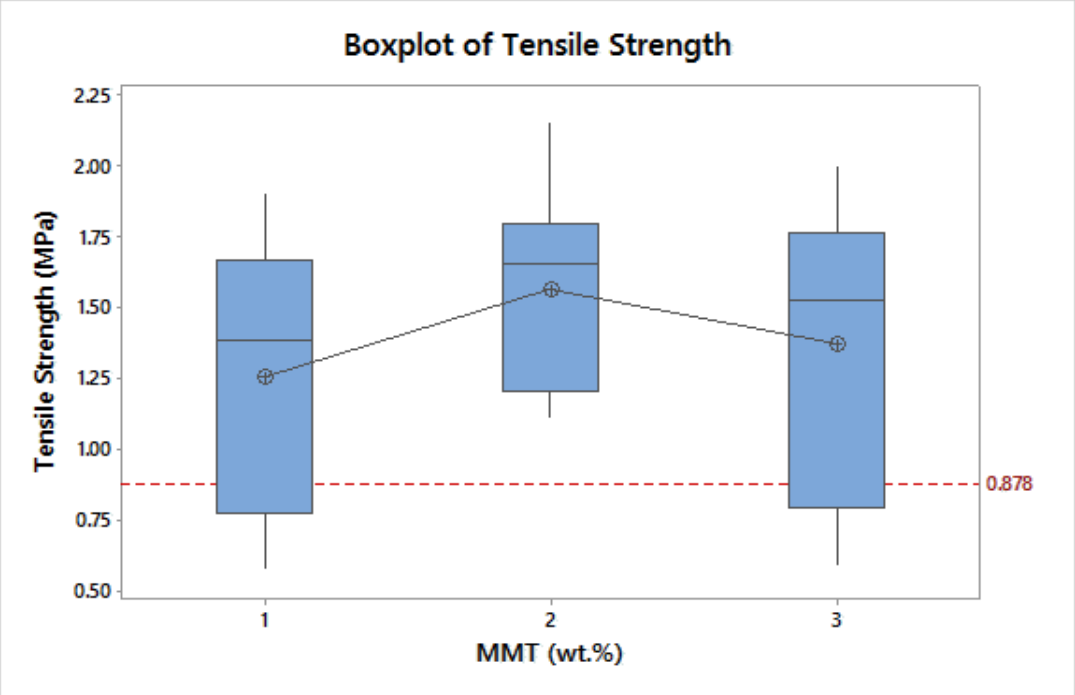

Figure 3. Boxplot of Tensile Strength against Loading of MMT

Based on the boxplot generated by Minitab 17 as shown in Fig. 3, it shown the mean tensile strength at various loading of MMT. The mean tensile strength of MMT loading level at 1, 2 and 3 wt.% are 1.252, 1.564 and 1.369 MPa respectively. The dotted line indicated the tensile strength of control sample which only contains starch and glycerol, and it has tensile strength of 0.878 MPa. The effect of MMT in the nanocomposites film is significant as the tensile strength have gradually increased with the loading of MMT. With loading of 1 wt.% of MMT, the mean tensile strength of the nanocomposites film increased 0.374 MPa, which is equivalent to 42.6% enhancement. As the loading level of MMT increases, the tensile strength increases, it is because present of MMT in the nanocomposites increased the stiffness, hence, more stress is required to break the samples.

The peak of tensile strength is obtained at loading of 2 wt.% of MMT, which is 2.15 MPa, compared to control sample, the enhancement is about 144.9%. As mentioned, pure starch-based plastics have poor mechanical strength, therefore, with loading of MMT, the tensile strength is greatly enhanced, which overcome the drawback of pure starch-based plastics. However, further increment of MMT to 3 wt.%, it shown adverse effect, where the mean tensile strength have decreased from 1.564 to 1.369 MPa. The adverse effect found in further increment of MMT might due to large amount of MMT particles tend to agglomerated into larger particles, which affect the intercalation effect of MMT particles in the polymer matrix. This phenomena also reported by other researchers in the similar field, Bee et al. found the LDPE/ EVA/ MMT blend has lower tensile strength with further increment of MMT to certain limit [11]. On the other hand, the TPS/ MMT nanocomposites research done by Majdzadeh-Ardakani et al. have the similar result, further increment of MMT brought deterioration effect on the samples [14]. Based on the results from tensile test, the loading of MMT is crucial in determining the tensile strength of the nanocomposites film, optimum loading of MMT is required to be found out in order to produce nanocomposites film with good tensile strength.

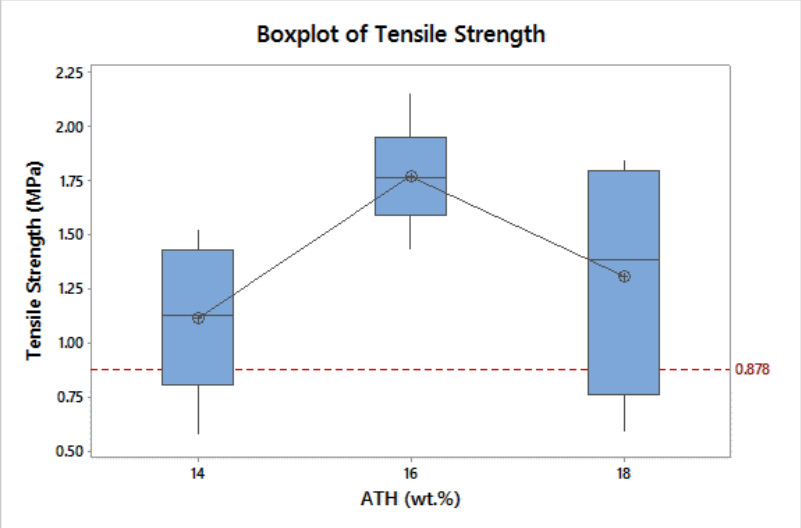

Figure 4. Boxplot of Tensile Strength against Loading of ATH

As compared to loading amount of MMT and CA, large amount of ATH loading is required in the nanocomposites to observe the effect of ATH. The mean tensile strength of nanocomposites film with various loading of ATH is shown in Fig. 4, the mean tensile strength of loading of ATH at 14, 16 and 18 wt.% are 1.109, 1.769, and 1.305 MPa respectively. As compared the control samples and loading level of ATH at 14 wt.%, the mean tensile strength of the nanocomposites film has increased 0.66 MPa which is equivalent to 59.5%. Somehow, the results obtained in this research are accordance to previously published work, as reported by Beyer and Kilialis [12], [19], loading of ATH enhanced the mechanical strength of the nanocomposites, and sometimes, high loading of ATH deteriorated the mechanical strength. Likewise, loading of ATH in this research shown contribution to tensile strength of the nanocomposites film although the main function of ATH is to enhance the flame retardant properties. Similar concept to loading of MMT, the particles size of ATH is larger than MMT, however, with the cross-linking agent, ATH is well-intercalated into the nanocomposites film, which increased the strength of the sample, indirectly, more stress is required to break the nanocomposites strip during the tensile test. In spite of that, the tensile strength of nanocomposites film is decreased at loading of ATH at 18 wt.%, this is due redundant amount of ATH suppressed the effect of cross-linking agent in the nanocomposites film, consequently, it lead to poor intercalation of fillers in the nanocomposites, with poor intercalation, the nanocomposites film is structurally weak, and hence, the tensile strength decreased.

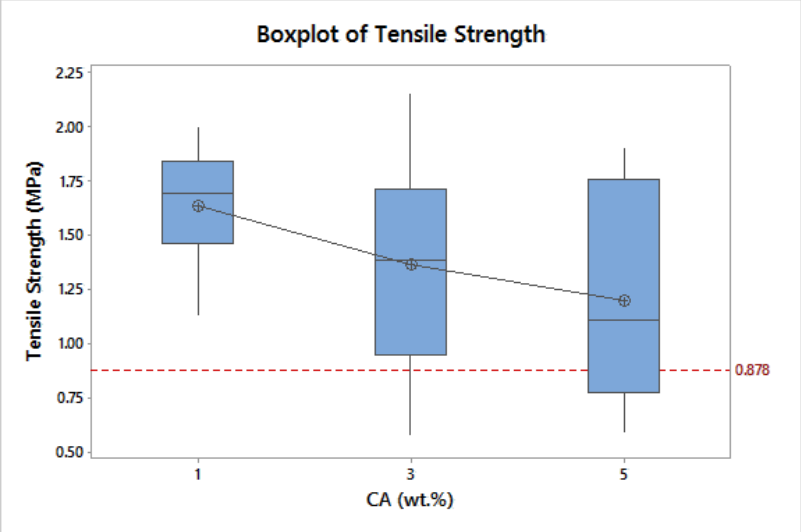

Figure 5. Boxplot of Tensile Strength against Loading of CA

Blending of CA as cross-linking agent into TPS/ MMT/ ATH nanocomposites film is novel and no similar research have been done. The effect of loading CA into the nanocomposites film with respect to tensile strength in shown in Fig. 5, the mean tensile strength of loading of CA at 1, 3 and 5 wt.% are 1.631, 1.361, and 1.139 MPa respectively. The cross-linking effect of CA in the nanocomposites film is shown in every loading of CA from 1 to 5 wt.%. Based on the result, it is believed that the d-spacing of MMT is enlarged

with the present of CA, larger the d-spacing of MMT, the better effect of intercalation as other components able to bind into MMT easily. Moreover, due to acidic nature of CA promote the fragmentation and dissolution of starch granule, the smaller pieces of starch granule are easily permeated by plasticers and fillers, thus, better intercalation and better mechanical strength. Based on the result obtained in individual effect plot, loading of CA at 1 wt.% exhibited highest mean tensile strength, and the mean tensile strength gradually decreased with further increment of CA. Thus, it can be said that the high loading level of CA might cause the starch badly acidolysis, which deteriorated the rigid structure of starch. Therefore, it is suggested that the loading of CA can be reduces accordingly in further studies, and the effect of lower loading of CA should be observed.

3.2 Elongation

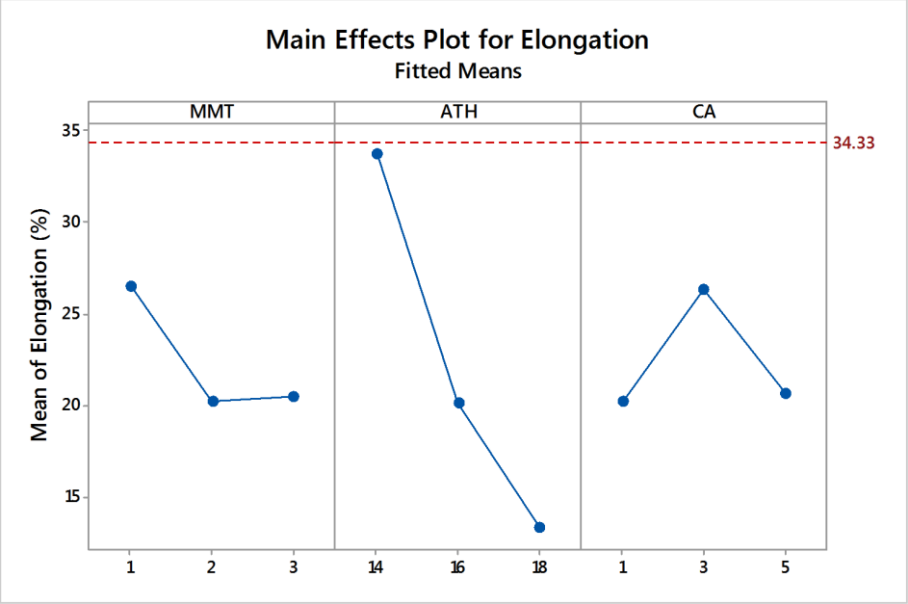

Figure 6. Main Effect Plots of Fillers with Respect to Elongation

The mean elongation with respected to loading of MMT, ATH and CA is shown in Fig. 6. The dotted line indicates the control sample without fillers and cross-linking agent, the elongation at break of the control sample is obtained as 34.44%, and it shown the highest percentage of elongation at break. The intercalation of MMT and ATH into starch promoted the formation of restricted environment against the movement of polymer chains as reported by Bee et al. [11], and hence, as the polymer chains are restricted and not able to move freely, the elongation ability of the polymer reduced.

Similar trend is obtained for both loading of MMT and ATH, the mean elongation at break of the samples are significantly decreased with higher loading of fillers. At low loading level of both MMT and ATH, the mean elongation are 26.54 % and 33.80% respectively. Compared low loading of MMT and ATH, the mean elongation of MMT is lower than ATH,

this is due to the particles size of MMT are way smaller than ATH, hence, the ability of intercalated of MMT into starch is much greater than ATH, consequently, the elongation at break of samples reduces. Moreover, at high loading level of MMT and ATH, the mean elongation are reduced to 20.54 and 13.37% respectively. At higher loading, MMT and ATH particles tend to agglomerated and formed larger particles, in this case, poor intercalation existed between starch and fillers, which lead to the stress acting on the sample is not even and weak point present in the particular area where the starch and fillers are not binded.

For loading of CA, as the main function of CA is to enhance the intercalation between the starch and fillers, as the intercalation effect is better, the weak point will be eliminated. Based on Fig. 6, it shows that the mean elongation is enhanced from loading of CA at 1 to 3 wt.%, which is 20.24 to 26.35%, thus, the effect of introducing CA in the nanocomposites film is again shown. However, at further loading of CA to 5 wt.%, the mean elongation is reduced to 20.70%. As mentioned, introduced of MMT and ATH into starch restricted the movement of the polymer chains, hence, even the components in the nanocomposites film are well intercalated, it is believed that the elongation ability of the nanocomposites film will still be affected.

3.3 Young's Modulus

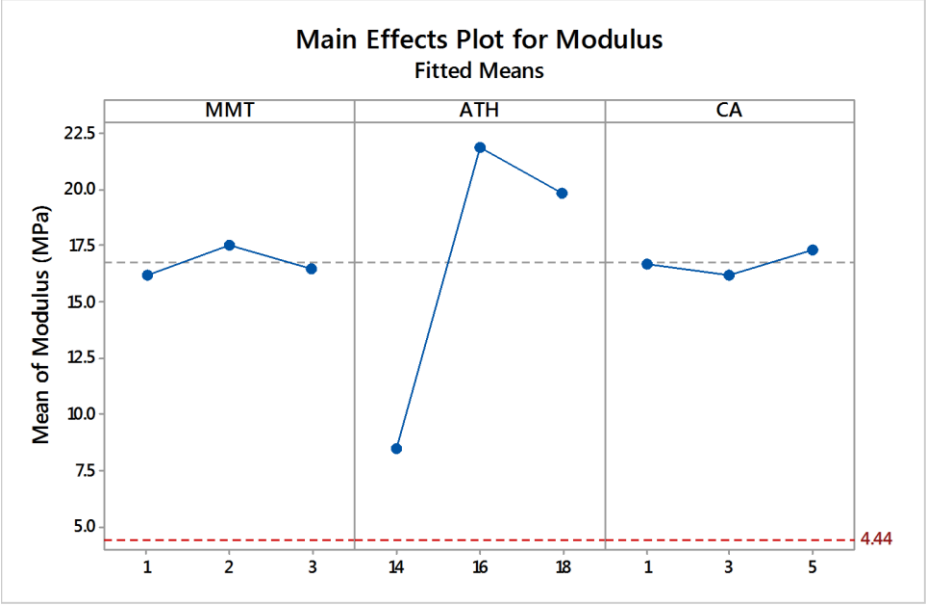

Figure 7. Main Effect Plots of Fillers with Respect to Young's Modulus

Mean of Young's modulus of loading of MMT, ATH and CA are shown in Fig. 7. The Young's modulus is the measure of stiffness of the materials, hence, higher the Young's modulus, the stiffness of the material increased. The dotted line in Fig. 7 shown the Young's modulus of the control sample which do not contain fillers and cross-linking agent, the Young's modulus for control sample is comparably low, which is only 4.44 MPa. As refer to

Fig. 7, as the loading of MMT increased from 1 to 2 wt.%, the mean Young's modulus increased from 16.23 to 17.56 MPa. On top of that, compared the control sample with loading of MMT at 1 wt.%, the Young's modulus have increased from 4.44 to 16.23 MPa, which is about 265.5%. The Young's Modulus value is increased when introduced and increased the loading level of MMT into the nanocomposites film, and this is due to strong interaction present between the polymer matrix and the MMT silicate layer via formation of hydrogen bond as well as strong hydrophilicity of the clay edges [20]. In spite of that, at further loading of MMT from 2 to 3 wt.%, adverse effect of MMT is found, the mean Young's modulus have dropped from 17.56 to 16.50 MPa. Although the variation is small, however, the adverse effect of MMT found in the experiment might due to at high loading of MMT into the nanocomposites film, the MMT particles tend to agglomerated, which causes the present of weak point.

Noticeable effect of ATH is found on the mean Young's modulus, from loading of 14 to 16 wt.% of ATH, the mean Young's modulus increased from 8.47 to 21.95 MPa. Besides, at further loading of ATH to 18 wt.%, the mean Young's modulus is 19.90 MPa. As compared to mean Young's modulus of MMT and CA, the variation of ATH is much higher, it might due to the loading of ATH into the nanocomposites film is much greater than both MMT and CA, thus, ATH possess significant effect on the Young's modulus. Similar theory with MMT, with loading of ATH, the linear polymer chains are disrupted. Moreover, the increment in Young's modulus also indicated CA enhanced the intercalation between the fillers and starch, as such MMT particles able to effectively fit and intercalate into the interfacial between ATH and starch matrix, therefore, the mobility of polymer chains have been restricted. Nevertheless, the retrograde of mean of Young's modulus is found at further loading of ATH, which again shown the effect of cross-linking is unable to improve the intercalation effects at high loading of MMT and ATH, where the particles of MMT and ATH are agglomerated into larger particles. On the other hand, the mean Young's modulus for loading level of CA at 1, 3 and 5 wt.% are 16.69, 16.23 and 17.38 MPa respectively. The individual effect of CA is not significant as compared to ATH, it is believed no matter how well intercalate existed between the fillers and starch, the linear polymer matrix is still disrupted, hence, the effect of cross-linking do not have great effect on the Young's modulus.

4.0 Conclusion

In a nutshell, this study has illustrated the investigation on the mechanical properties such as tensile strength, elongation at break and Young's modulus of the TPS/ MMT/ ATH nanocomposites films. It is found that both MMT and ATH able to contribute to the tensile strength of the nanocomposites films. Besides, at high loading of MMT and ATH, the particles tend to agglomerated into larger particles, which deteriorated the mechanical strength of the nanocomposites films, hence, the loading levels of fillers are crucial in determining the mechanical strength of the nanocomposites films. In addition, the effect of

CA as cross-linking agent is significant in this study, better intercalation effect is found with introducing CA into the nanocomposites films. Moreover, the elongation at break have reduced with introducing fillers in the nanocomposites films as intercalation of MMT and ATH into starch promotes the formation of restricted environment against the movement of polymer chains. On the contrary, with the polymer chains restricted, the Young's modulus of the nanocomposites film shown measurable enhancement. Last but not least, with introduced fillers and cross-linking agent into starch-based plastics, the drawbacks are eliminated, thus, the applications of this plastic are opened to wider areas.

References

[1] Y. J. Chen, "Journal of Chemical and Pharmaceutical Research , 2014 , 6 (1): 226-231 Bioplastics and their role in achieving global sustainability," vol. 6, no. 1, pp. 226–231, 2014.

[2] R. C. Thompson, C. J. Moore, F. S. vom Saal, and S. H. Swan, "Plastics, the environment and human health: current consensus and future trends.," *Philos. Trans. R. Soc. Lond. B. Biol. Sci.*, vol. 364, no. 1526, pp. 2153–66, Jul. 2009.

[3] H. H. Impacts, "Plastic Waste : Ecological and Human Health Impacts," no. November, 2011.

[4] J. H. Song, R. J. Murphy, R. Narayan, and G. B. H. Davies, "Biodegradable and compostable alternatives to conventional plastics.," *Philos. Trans. R. Soc. Lond. B. Biol. Sci.*, vol. 364, no. 1526, pp. 2127–39, Jul. 2009.

[5] L. Ren, M. Jiang, L. Wang, J. Zhou, and J. Tong, "A method for improving dispersion of starch nanocrystals in water through crosslinking modification with sodium hexametaphosphate," *Carbohydr. Polym.*, vol. 87, no. 2, pp. 1874–1876, Jan. 2012.

[6] R. Shanks and I. Kong, "Thermoplastic Starch," 2011.

[7] S. Mali, L. S. Sakanaka, F. Yamashita, and M. V. E. Grossmann, "Water sorption and mechanical properties of cassava starch films and their relation to plasticizing effect," *Carbohydr. Polym.*, vol. 60, no. 3, pp. 283–289, May 2005.

[8] J.F. Chabot, "Effect of chemical modification on the ultrastructure of corn, waxy maiza and tapoica starches.pdf." .

[9] X. Zhang, F. Guo, J. Chen, G. Wang, and H. Liu, "Investigation of interfacial modification for flame retardant ethylene vinyl acetate copolymer/alumina trihydrate nanocomposites," *Polym. Degrad. Stab.*, vol. 87, no. 3, pp. 411–418, Mar. 2005.

[10] F. a. Aouada, L. H. C. Mattoso, and E. Longo, "New strategies in the preparation of exfoliated thermoplastic starch–montmorillonite nanocomposites," *Ind. Crops Prod.*, vol. 34, no. 3, pp. 1502–1508, Nov. 2011.

[11] S.-T. Bee, A. Hassan, C. T. Ratnam, T.-T. Tee, L. T. Sin, and D. Hui, "Dispersion and roles of montmorillonite on structural, flammability, thermal and mechanical behaviours of electron beam irradiated flame retarded nanocomposite," *Compos. Part B Eng.*, vol. 61, pp. 41–48, May 2014.

[12] G. Beyer, "Flame retardant properties of EVA-nanocomposites and improvements by combination of nanofillers with aluminium trihydrate," *Fire Mater.*, vol. 25, no. 5, pp. 193–197, 2001.

[13] K. Cheng, C. Yu, W. Guo, S. Wang, T. Chuang, and Y. Lin, "Thermal properties and flammability of polylactide nanocomposites with aluminum trihydrate and organoclay," *Carbohydr. Polym.*, vol. 87, no. 2, pp. 1119–1123, 2012.

[14] K. Majdzadeh-Ardakani, A. H. Navarchian, and F. Sadeghi, "Optimization of mechanical properties of thermoplastic starch/clay nanocomposites," *Carbohydr. Polym.*, vol. 79, no. 3, pp. 547–554, Feb. 2010.

[15] N. Wang, X. Zhang, N. Han, and S. Bai, "Effect of citric acid and processing on the performance of thermoplastic starch/montmorillonite nanocomposites," *Carbohydr. Polym.*, vol. 76, no. 1, pp. 68–73, Mar. 2009.

[16] E. Olsson, M. S. Hedenqvist, C. Johansson, and L. Järnström, "Influence of citric acid and curing on moisture sorption, diffusion and permeability of starch films.," *Carbohydr. Polym.*, vol. 94, no. 2, pp. 765–72, May 2013.

[17] X. Tang, S. Alavi, and T. J. Herald, "Effects of plasticizers on the structure and properties of starch–clay nanocomposite films," *Carbohydr. Polym.*, vol. 74, no. 3, pp. 552–558, Nov. 2008.

[18] ASTM, "ASTM D882: Standard Test Method for Tensile Properties of Thin Plastic Sheeting," *ASTM Stand.*, p. 12, 2012.

[19] P. Kiliaris and C. D. Papaspyrides, "Polymer/layered silicate (clay) nanocomposites: An overview of flame retardancy," *Prog. Polym. Sci.*, vol. 35, no. 7, pp. 902–958, Jul. 2010.

[20] S.-T. Bee, A. Hassan, C. T. Ratnam, T.-T. Tee, and L. T. Sin, "Investigation of nano-size montmorillonite on electron beam irradiated flame retardant polyethylene and ethylene vinyl acetate blends," *Nucl. Instruments Methods Phys. Res. Sect. B Beam Interact. with Mater. Atoms*, vol. 299, pp. 42–50, Mar. 2013.

Effect of Process Variables on Extraction of *Orthosiphon Stamineus* Leaves

G.H.Koay[1*], Rajesh Nithyanandum[2]

[1]*Department of Chemical Engineering, School of Engineering, Taylor's University, Malaysia*
[2]*Department of Chemical Engineering, School of Engineering, Taylor's University, Malaysia*

[*]Corresponding author: geokhwa.koay@gmail.com

Abstract

The objective of this study was to study the effect of the process variables on the extraction of *Orthosiphon stamineus* leaves. The leaves were extracted using digital water bath at operating temperatures of 30 ^{o}C, 35 ^{o}C and 40 ^{o}C and different sample to solvent ratio of 1:1. 1:5 and1:10. Evaluation of colour characteristics of plant extracts and evaluation of microscopy were discussed and compared. The experimental results showed that 40 ^{o}C of operating temperature and 1:1 sample to solvent ratio give the best yield of extraction among the chosen conditions. Moisture content of powdered *Orthosiphon stamineus* leaves were determined using oven drying method. Antioxidant activities of the leaves were determined using the DPPH radical scavenging activity assay method. Extraction operated at 40 ^{o}C achieves the highest DPPH scavenging activity, 91.2% compared to extraction operated at 30 ^{o}C and 35 ^{o}C. 1:1 sample to solvent ratio of leaves extracts have stronger radical scavenging effect, 91.6% compared to sample to solvent ratio of 1:5 and 1:10. As a result, *Orthosiphon stamineus* is a natural source of antioxidants. The strong antioxidant activity of it has turned it to become one of the most popular herbs in Malaysia.

Keywords: *Orthosiphon stamineus*, misai kucing, water bath extraction, sample to solvent ratio

1. Introduction

Nowadays, there is an increasing interest in using herbal medicines for various diseases. Herbal medicines are one of the dietary supplements that made from traditional medical plants. These traditional medical plants have phytochemicals that can treat diseases effectively. One of the main reasons is because of the increasing exposure of consumers to the potential side effects of the synthetic and conventional drugs in the market [1]. Besides, herbal medicines made from traditional medical plants are similar to the synthetic and conventional drugs due to its similarity of the treatment process to the human body [2].

Besides, herbal medicines are more affordable compared to the modern pharmaceuticals that getting more and more expensive nowadays. Thus, people especially from low-waged families always prioritize the herbal medicines for the treatment of diseases instead of the synthetic and conventional drugs in the market. According to the World Health Organization (WHO) estimation in year 2008, there was 80% of the population of some Asian and African countries consume herbal medicines for their primary health care [3]. It is believed that there are more and more people around the world are relying on herbal medicines for primary health care currently. There are even some universities are offering courses on herbalism and Chinese medicines. It is clearly shown that herbalism is getting more popular among the society especially in Malaysia.

In Malaysia, *Orthosiphon stamineus* is one of the traditional medical plants that has been used as herbal medicine and other parts of Asia since ages ago. It is called as "Misai Kucing" in Malay or "Cat's Whiskers" in English in Malaysia and it belongs to the family of *Lamiaceae* [4]. It is also introduced as "Java Tea" locally in Malaysia for bladder and kidney disorders. It is reported that the leaves of this plant have been used to treat various kind of diseases such as cancer, arthritis, hypertension and etc [5]. It has been found that *Orthosiphon stamineus* contains some bioactive compounds, such as phenolic contents, terpenoids, several essential oil and etc [6, 7, 8]. Besides, it is also believed to have antiallergic, antihypertensive, anti-inflammatory, antioxidant and diuretic properties [4, 7, 9, 10]. The most important content among the bioactive compounds available is the phenolic contents which consist of caffiec acid derivatives, lipophilic flavones, flavonol glycosidase and polymethoxylated flavones [7]. There are four main compounds in *Orthosiphon stamineus* extract are sinensetin (SEN), eupatorin (EUP), and 3-hydroxy-5,6,7,4-tetramethoxyflavone (TMF) [7].

Extraction is the common technique used to recover the bioactive compounds available in the plant. Extraction requires the usage of solvents, either organic or inorganic. Furthermore, there are many factors that affect the extraction, such as extraction techniques, type of solvent, extraction time, extraction temperature, sample to solvent ratio and etc [11]. Water bath extraction is used in this study because it is simple and easiest way to extract plant. In the other hand, there are several factors that

influence the choice of solvent as well, such as quantity and quality of bioactive compounds to be extracted, rate of extraction, diversity of different compounds extracted, toxicity of the solvent and etc [12,13]. Thus, ethyl acetate is used as a solvent because of its low cost, low toxicity and agreeable odor [14]. Besides, ethyl acetate is frequently used for the extraction of the plant as well [15]. There are studies reported that ethyl acetate extract can be used safely for the treatment of some bacterial infection [16].

2. Materials and Method

2.1 Plant material and chemical reagent

The *Orthosiphon stamineus* leaves were obtained from a local nursery (Everflora Nursery & Lanscape). Ethyl acetate was purchased from PubChem (USA).

2.2 Preparation of leaves

Orthosiphon stamineus leaves were washed with tap water before with distilled water. The sample was dried in an oven (Memmert, Germany) at 70 ^{o}C for one day to remove its moisture content. The dried leaves were then ground using an electric blender (Pensonic PB-3205DJ).

2.3 Effect of Process Variables on Extraction

Choice of solvent used in extraction is one of the most important issue that being concerned because it decides the results of the extraction. In other words, the quality and quantity of the plant extracts are directly and largely dependent on the selection of solvent used in the extraction process. To ensure the heath and safety of the herbal plants products, low toxicity of the solvent is the only concern property of solvent used in extraction [17]. The solvent used in extraction must be non-toxic or within the toxic level that won't affect the human health and life. This is because the end products, which are the herbal plant medicines, will contain some of the remaining solvent from the extraction. Consumers nowadays are getting more interests on using herbal medicines for various diseases because of the side effects that brought by the synthetic medicines and drugs that are available in the market. Therefore, the toxicity of solvent used is the key point to ensure the safety of the end products.

In this study, ethyl acetate was used as a solvent in extraction because of its low cost, low toxicity and acceptable odour. Besides, ethyl acetate is one of the polar solvents that are commonly used for the extraction of a plant [17]. Raymond S. Mouokeu et. al, 2011 reported that ethyl acetate is safely used for treatment of some bacterial infections by the antibacterial and dermal toxicological profiles obtained from the *Crassocephalum bauchiense (Hutch*.) extracts [18]. Showkat Ahmad Ganie et. al, 2011 also reported that the antioxidant and protective effect were not reduced on Carbon Tetrachloride Induced Rat Liver Injury after using ethyl acetate as a solvent in the extraction of *Podophyllum hexandrum* Rhizome [19].

Solvent was added to the prepared leaves sample before the extraction was carried out. In this study, 50 ml of ethyl acetate was added to 5 g of the powdered leaves in a conical flask. Then, the sample was extracted using a digital water bath (Daniel Digital Water Bath) at 35 ^{o}C for 3 hours by Rajesh Nithyanandam et. al, 2012 method with slight modifications. Digital water bath extraction was used in this study because it is simple and easiest way to extract plant. The supernatant was separated from the residue using a Whatman No.1 filter paper. The extracted solution was stored in a closed container (Scott Duran Laboratory Bottle) and kept at 6 ^{o}C before any analysis being carried out. The extraction was repeated with temperature of 30 and 40 ^{o}C to investigate the effect of temperature on extraction. Additionally, the extraction was repeated with 1:1 and 1:5 samples to solvent ratio to investigate the effect of sample to solvent ratio on extraction.

2.5 DPPH Radical Scavengin Activity

The stable free radical diphenylpicrylhydrazyl (DPPH) was used to estimate the antioxidant activity of the plant extracts. According to Rajesh Nithyanandam et. al, 2011, DPPH can reacts with compounds that have the ability to donate a hydrogen atom. Therefore, the hydrogen donating abilities of *Orthosiphon Stamineus* leaves extract were obtained from the change in the absorbance at 517 nm by the Rajesh Nithyanandam et. al, 2011 method. To measure the free radical scavenging, samples in methanol solution were prepared by adding 10 mg of plant extract solution in 30 ml of methanol. Then, the samples were centrifuged for 10 min using a ScanSpeed 1236 Bench Top Centrifuge. Aliquots of supernatant were dissolved in 3 ml of 25 mg/l DPPH in methanol. The samples were left to react at room temperature for 40 min. After that, a Halo RB-10 UV Spectrophotometer was used to measure the change in absorbance of the samples after 40 min. Methanol was used as the blank and DPPH of different concentration (0-100 mg/l) was used to produce a standard calibration curve. All the measurements were done in triplicate.

The DPPH radical scavenging activity of the samples was calculated using the following equation:

$$DPPH\ scavenging\ activity\ (\%) = \frac{Abs_{517} DPPH\ solution - Abs_{517} sample}{Abs_{517} DPPH\ solution} x100 \qquad (1)$$

2.6 Evaluation of Colour Characteristics of Plant Extracts

The extracted solutions obtained from Section 2.3 were placed on white A4 paper to compare the colour of the extracted solutions with different operating temperatures and sample to solvent ratio. The result was compared with the DPPH radical scavenging activity and evaluation of microscopy technique.

2.7 Evaluation of Microscopy Technique on Authentication of Plant Extracts

The extracted solutions obtained from Section 2.3 were placed under a Swift Digital Microscope M10DB-MP. Observations were recorded and images of the samples

were captured and saved. The result was compared with the DPPH radical scavenging activity and evaluation of colour characteristics of the plant extracts.

3. Results and Discussion

3.1 DPPH Radical Scavenging Activity

In this study, ethyl acetate was used as a solvent in extraction because of its low cost, low toxicity and acceptable odour. Besides, ethyl acetate is one of the polar solvents that are commonly used for the extraction of a plant [17]. Raymond S. Mouokeu et. al, 2011 reported that ethyl acetate is safely used for treatment of some bacterial infections by the antibacterial and dermal toxicological profiles obtained from the *Crassocephalum bauchiense (Hutch*.) extracts [18]. Showkat Ahmad Ganie et. al, 2011 also reported that the antioxidant and protective effect were not reduced on Carbon Tetrachloride Induced Rat Liver Injury after using ethyl acetate as a solvent in the extraction of *Podophyllum hexandrum* Rhizome [19].

There are several types of methods and modifications have been used to determine the antioxidant activity of plant extracts. In this study, the DPPH assay method was used to determine the radical scavenging effects of oxidants. Lacine Aksoy et. al, 2013 states that DPPH assay method is fast, simple and high reliability [20]. Other than that, DPPH assay method does not need to use a special process or reaction and apparatus. The stable free radical diphenylpicrylhydrazyl (DPPH) was used to estimate the antioxidant activity of the plant extracts. According to Rajesh Nithyanandam et. al, 2011, DPPH can reacts with compounds that have the ability to donate a hydrogen atom. [21]. Therefore, the hydrogen donating abilities of *Orthosiphon Stamineus* leaves extract were obtained from the change in the absorbance at 517 nm by the Rajesh Nithyanandam et. al, 2011 method. Soares et al.,1997 reported that the DPPH free radical easier to accept an electron or hydrogen atom from antioxidant molecules to become stable at its maximum wavelength at 517 nm [28]. To measure the free radical scavenging, samples in methanol solution were prepared by adding 10 mg of plant extract solution in 30 ml of methanol. Then, the samples were centrifuged for 10 min using a ScanSpeed 1236 Bench Top Centrifuge. Aliquots of supernatant were dissolved in 3 ml of 25 mg/l DPPH in methanol. The samples were left to react at room temperature for 40 min. After that, a Halo RB-10 UV Spectrophotometer was used to measure the change in absorbance of the samples after 40 min. Methanol was used as the blank and DPPH of different concentration (0-100 mg/l) was used to produce a standard calibration curve. All the measurements were done in triplicate.

Table 1 shows the calibration table of DPPH in different concentration and Figure 1 shows the calibration curve of DPPH in different concentration.

Table 1: Calibration table of DPPH in different concentration.

Concentration (mg/L)	Absorbance (nm)
20	0.124
40	0.142
60	0.167
80	0.200
100	0.221

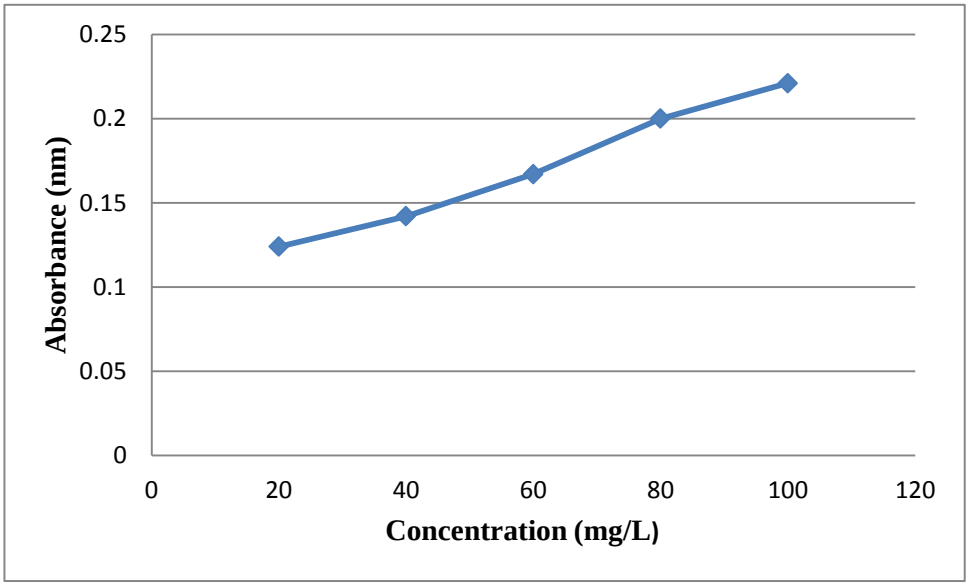

Figure 1: Calibration Curve of DPPH in different concentration.

Besides, effect of process variable was evaluated on the extraction and the antioxidant activity in this study. In this study, 50 ml of ethyl acetate was added to 5 g of the powdered leaves in a conical flask. Then, the sample was extracted using a digital water bath (Daniel Digital Water Bath) at 35 ^{o}C for 3 hours by Rajesh Nithyanandam et. al, 2012 method with slight modifications [21]. Digital water bath extraction was used in this study because it is simple and easiest way to extract plant. The supernatant was separated from the residue using a Whatman No.1 filter paper. The extracted solution was stored in a closed container (Scott Duran Laboratory Bottle) and kept at 6 ^{o}C before any analysis being carried out. The extraction was repeated with temperature of 30 and 40 ^{o}C to investigate the effect of temperature on extraction. Additionally, the extraction was repeated with 1:1 and 1:5 samples to solvent ratio to investigate the effect of sample to solvent ratio on extraction. Figure 2 shows the DPPH scavenging activity of the plant extracts with variation in temperature such as 30 ^{o}c, 35 ^{o}C and 40 ^{o}C. . Figure 3 shows the DPPH scavenging activity of the plant extracts with variation in sample to solvent ratio of 1:1, 1:5 and 1:10.

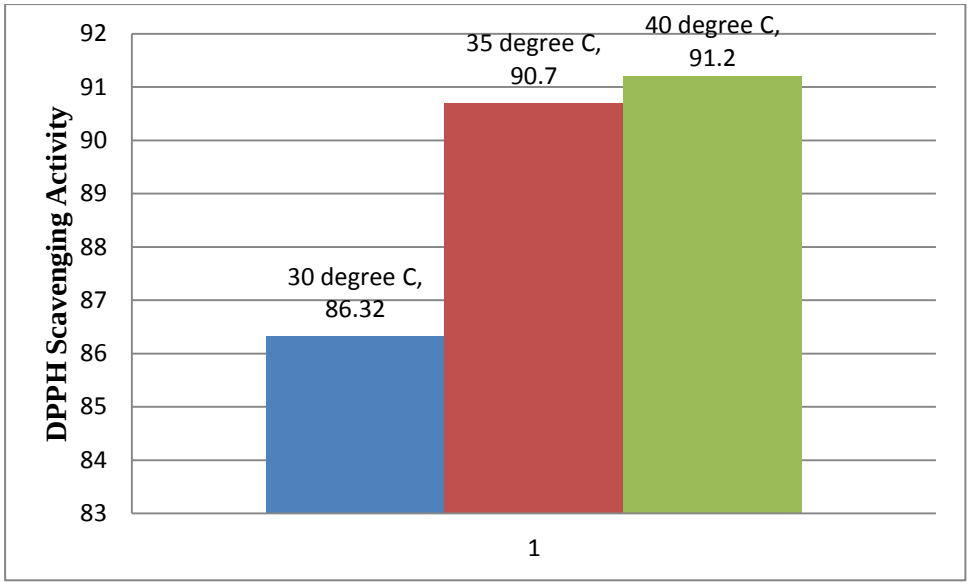

Figure 2: DPPH scavenging activity of the plant extracts with variation in extraction temperature such as 30 ^{o}c, 35 ^{o}C and 40 ^{o}C.

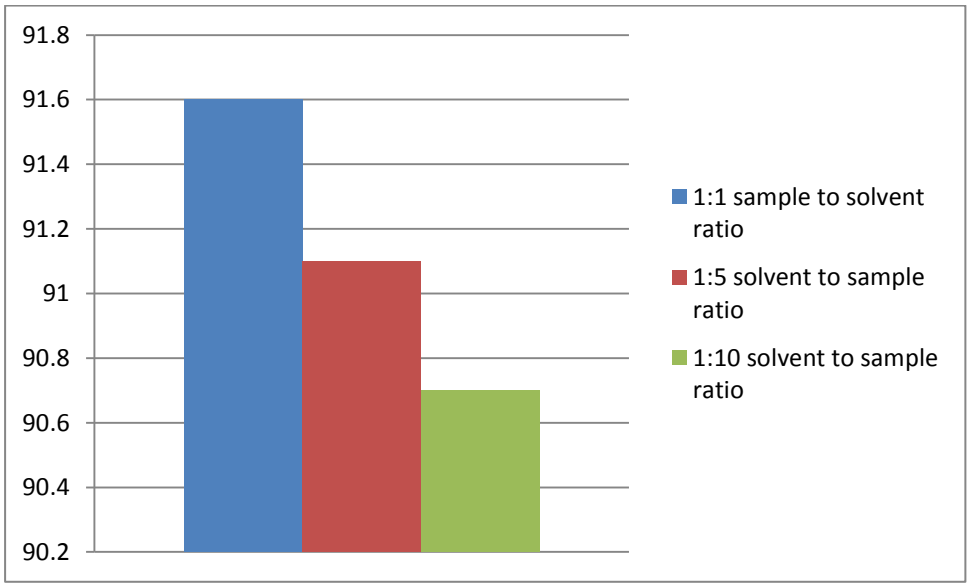

Figure 3: DPPH scavenging activity of the plant extracts with variation in sample to solvent ratio of 1:1, 1:5 and 1:10.

Figure 2 shows that the plant extracts which extraction operated at 40 ^{o}C has a stronger radical scavenging effect compared to the plant extracts which extraction operated at 30 ^{o}C and 35 ^{o}C. It is clearly observed that higher operating temperature of extraction leads to higher DPPH scavenging activity of the *Orthosiphon Stamineus* plant extracts. This can be justified with the study by Chew K.K et. al, 2011 reported that higher temperature (65 ^{o}C) was the best extraction temperature on the recovery of

phenolic compounds and antioxidant capacity of *Orthosiphon stamineus* extracts. Figure 3 shows that the plant extracts with 1:1 sample to solvent ratio has a stronger radical scavenging effect compared to the plant extracts with 1:5 and 1:10 sample to solvent ratio. In other words, lower sample to solvent ratio gives higher DPPH scavenging activity of the *Orthosiphon Stamineus* plant extracts.

3.2 Colour Characteristics of Plant Extracts

Figure 4. Colour characteristisc of *Orthosiphon Stamineus* plant extracts of different operating temperature of extraction (30 ^{o}C, 35 ^{o}C, 40 ^{o}C).

Figure 4 shows the colour characteristics of *Orthosiphon Stamineus* plant of different operating temperature of extraction at 30 ^{o}C, 35 ^{o}C and 40 ^{o}C. From Figure 4, the extracted solution of operating temperature of extraction at 30 ^{o}C shows the lightest colour while the extracted solution of operating temperature of extraction at 40 ^{o}C shows the darkest colour. This may be related to the operating temperature of extraction. In the other words, the higher the operating temperature of extraction, the darker the extracted solution. This can be concluded as higher temperature will results in darker extracted solution. This can be also related to the DPPH radical scavenging activity in previous section that shows that higher operating temperature of extraction will give higher DPPH scavenging activity of the plant extracts.

Figure 5. Colour characteristic of *Orthosiphon Stamineus* plant extracts of different sample to solvent ratio (1:1, 1:5, 1:10).

Figure 5 shows the colour characteristics of *Orthosiphon Stamineus* plant of different sample to solvent ratio, which are 1:1, 1:5 and 1:10. It is clearly shown that the

extracted solution of 1:10 sample to solvent ratio shows the lightest colour while the extracted solution of 1:1 sample to solvent ratio shows the darkest colour. This may be explained by the relationship of the sample to solvent ratio and the extraction. The results show that the least sample to solvent ratio gives the darkest extraction solution. Therefore, the results can be related the DPPH radical scavenging activity in previous section that shows that lower sample to solvent ratio will give higher DPPH scavenging activity of the plant extracts.

3.3 Microscopy Observation of Plant Extracts

Standardization of herbal plants could be categorized into three parts: authenticity, purification and assay. Authenticity of herbal plants is important to enhance the quality of the products in order to ensure the safety and health of the end users. There was study reported that the usage of macroscopic as an approach to identify and authenticating botanical products . Microscopy observation is one of the methods to authenticate the plants materials. The study by Smillie and Khan, 2010 included macroscopic observation authentication of different aspects of the botanical plants products. Figure 4.6 shows the observation of plant extracts at different operating temperatures of extraction at 30 ^{o}C, 35 ^{o}C and 40 ^{o}C.

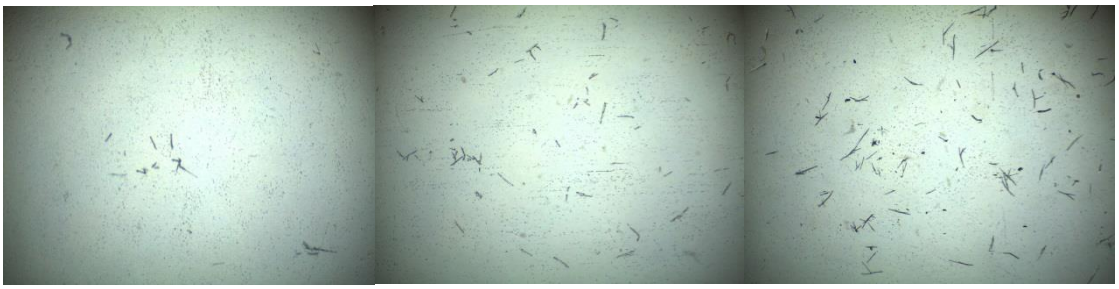

Figure 6: Observation of extracted solution at different operating temperatures of extraction (30 ^{o}C, 35 ^{o}C, 40 ^{o}C).

Figure 6 shows that there are structures of phytochemicals in the extracted solutions under the microscope. Besides, there are less phytochemical structures available in the extracted solution at 30 ^{o}C operating temperature while the extracted solution at 40 ^{o}C has the most phytochemical structures. In the other words, the higher the operating temperature of extraction, the more the phytochemicals available in the extracted solution. This can be concluded as higher temperature will results in more phytochemical structures. The results can be related to the DPPH radical scavenging activity and colour characteristics of plant extracts in previous sections. Figure 7 shows the observation of plant extracts at different sample to solvent ratio of 1:1, 1:5 and 1:10.

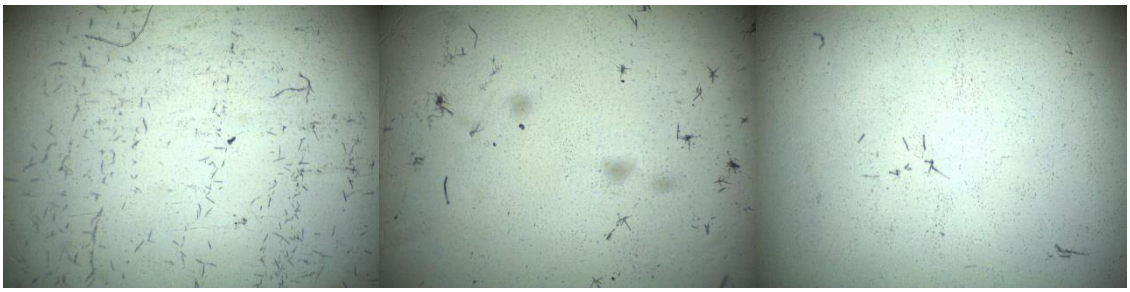

Figure 7: Observation of extracted solution at different sample to solvent ratio (1:1, 1:5, 1:10).

Figure 7 shows that there are less phytochemical structures available in the extracted solution with 1:10 sample to solvent ratio while the extracted solution with 1:1 sample to solvent ratio has the most phytochemical structures. Thus, the lower the sample to solvent ratio, the more the phytochemicals available in the extracted solution. This can be concluded as lower sample to solvent ratio will results in more phytochemical structures. Similarly, the results can be related to the DPPH radical scavenging activity and colour characteristics of plant extracts in previous sections.

4. Conclusion

The effect of operating temperature and the sample to solvent ratio on the extraction of *Orthosiphon stamineus* leaves were investigated based on the resulted extracted solutions. The results show that 4 hours of oven drying is the most appropriate drying duration to obtain minimum moisture content. DPPH radical scavenging activity assay shows that higher operating temperature of extraction leads to higher DPPH scavenging activity of the *Orthosiphon Stamineus* plant extracts while lower sample to solvent ratio gives higher DPPH scavenging activity of the *Orthosiphon Stamineus* plant extracts. The plant extracts achieve 91.2% of DPPH radical scavenging activity at 40 ^{o}C while the plant extracts achieve 91.6% of DPPH radical scavenging activity with 1:1 sample to solvent ratio. The correlation results between the evaluation of colour characteristics of *Orthosiphon Stamineus* plant extracts and microscopy observation of *Orthosiphon Stamineus* plant extracts further justify the results of DPPH radical scavenging activity.

Acknowledgment

The authors would like to thank the School of Engineering, Taylor's University Lakeside Campus for the support and technical assistance.

References

[1] S Gopalakrishnana, R Rajameena, and E Vadivel. (2012). *Journal of Chemical and Pharmaceu-tical Research*, vol. 4, no. 1, pp. 788-794.

[2] Tenni R., Zanaboni G., De Agustini M.P., Rossi A., Bendotti C., Cetta G. (2008). "Effect of the triterpenoids fraction of *Centella asiatica* on macromolecules of the connective matrix in human skin fibroblast cultures", *Italian J. Biochem,* pp. 69-77.

[3] NR Farnsworth.(1998). *Ethnopharmacology and Drug Development. In: Ethnobotany and the search for new drugs*. (pp. 42-59). PA: Wiley.

[4] Sriyana Abdullah, Abdul Razak Shaari, Adli Azimi.(2012). "Effect of Drying Methods on Metabolites Composition of Misai Kucing (*Orthosiphon stamineus*) Leaves", *APCBEE Procedia 2*, pp. 178-182.

[5] P. T. Eisai. (1995).*Medicinal Herb Index in Indonesia*. PA: P. T. Eisai, Jakarta, Indonesia.

[6]Tezuka Y., Stampoulis P., Banskota A.H., Awale S., Tran K.Q., Saiki I., Kadota S.(2000). "Constituents of the Vietnamese medical plant *Orthosiphon stamineus*", *Chemical and Pharmaceutical Bulletin 48 (11)*, pp. 1711-1719.

[7] Akowuah G.A., Zhari I., Norhayati I., Sadikun A., Khamsah S.M.(2004). "Sinensetin, eupatorin, 3'-hydroxy-5,6,7,4'-tetramethoxyflavone and rosmarinic acid contents and antioxidative effect of *Orthosiphon stamineus* from Malaysia", *Food Chemistry 87 (4)*, pp. 559-566.

[8] Chan L.K., Loo P. S..(2006). "Morphological similarities and differences between the two varieties of cat's whiskers (*Orthosiphon stamineus* Benth.) grown in Malaysia", *International Journal of Botany 2(1)*, pp. 1-6.

[9] Akowuah, G.A., et al..(2005). "The effects of different extraction solvents of varying polarities on polyphenols of *Orthosiphon stamineus* and evaluation of the free radical-scavenging activity", *Food Chemistry* 93(2), pp. 311-317.

[10] Adam, Y., et al..(2009). "Diuretic properties of *Orthosiphon stamineus* Benth", *Journal of Ethnopharmacology*, 124(1), pp. 154-158.

[11] Chirinos, R., Rogez, H., Campos, D., Pedreschi, R., Larondelle, Y. (2007). "Optimizatio-n of extraction conditions of antioxidant phenolic compounds from mashua (*Trop-aeolum tuberosum* Ruíz & Pavón) tubers", *Separation and Purification Technolo-gy 55 (2)*, pp. 217-225.

[12] Ncube NS, Afolayan AJ, Okoh AI.(2008). "Assessment techniques of antimicrobial properties of natural compounds of plant origin: current methods and future trends", *African Journal of Biotechnology 7 (12)*, pp. 1797-1806.

[13] Das K, Tiwari RKS, Shrivastava DK. (2010). "Techniques for evaluation of medicinal plant products as antimicrobial agent: Current methods and future trends", *Journal of Medi-cinal Plants Research 4(2)*, pp. 104-111.

[14] Dutia, Pankaj. (2009). " Ethyl Acetate: A Techno-Commercial Profile", *Chemical Week-ly*, pp. 184.

[15] Prashant Tiwari, Bimlesh Kumar, Mandeep Kaur, Gurpreet Kaur, Harleen Kaur. (2011). "Phytochemical screening and Extraction: A Review", *Internationale Pharma-ceutica Sciencia Vol.1 , Issue 1*.

[16] Raymond S. Mouokeu, Rosalie AN Ngono, Paul K. Lunga, Martin M. Koanga, Alambert T. Tiabo, Guy SS. Njateng, Jean DD. Tamokou, Jules-Roger Kuiate. (2004). "Antibacterial and dermal toxicological profiles of ethyl acetate extract from *Crassocephalum bauchiense (Hutch*.) Milne-Redh (Asteraceae)", *BMC Complementary and Alternative Medicine 11*, pp.43.

[17] Prashant Tiwari; Bimlesh Kumar; Mandeep Kaur; Gurpreet Kaur; Harleen Kaur. (2011). "Phytochemical screening and Extraction: A Review.", *Internationale Pharmaceutica Sciencia Vol.1 , Issue 1*, pp 367-369.

[18] Raymond S Mouokeu et al.. (2011). "Antibacterial and dermal toxicological profiles of ethyl acetate extract from *Crassocephalum bauchiense* (Hutch.)

Milne-Redh (Asteraceae)", *BMC Complementary & Alternative Medicine*, 11(26), pp 31-33.

[19] Showkat Ahmad Ganie et al..(2011) "Antioxidant and Protective Effect of Ethyl Acetate Extract of *Podophyllum hexandrum* Rhizome on Carbon Tetrachloride Induced Rat Liver Injury.", *Evidence-Based Complementary and Alternative Medicine*, 11(11), pp. 321-333.

[20] Lacine Aksoy et al..(2013) "Free Radical Scavenging Activity, Total Phenolic Content, Total antioxidant status and Total oxidant status of endemic *Thermopsis Turcica*.", *Saudi Journal of BioScience*, 20(3), pp. 235-239.

[21] D. Krishnaiah; Awang Bono; R. Sarbatly; R.R. Nithyanandam; S.M. Anisuzzaman. (2012). "Optimisation of spray drying operating conditions of Morinda citrifolia L. extract using Response Surface Methodology." *Chem. Eng. Res. Des.*, 90 (5), pp. 14-19.

The Effects of Microwave Sintering on the Properties of CuO doped Y-TZP ceramic

Baapu Shrreraj*, Chinkongleong Jeffrey,

Health Research Group, School of Engineering, Taylor's Lakeside Campus, Malaysia

*raj92.taylors@gmail.com

Abstract

Microwave sintering (MW) is seen as one of the emerging sintering methods which have vast potential in both enhancing the properties of sample material as well as improving productivity of the overall process.MW has exhibited a few advantages like doubling fabricating rate, fast volumetric heating, retarding grain growth and improvement over the densification of the ceramic body to boost the performance of the material [1].The viability of MW approach was proven by obtaining full densification body in lower sintering temperature upon tested using pure Y-TZP powder and Copper oxide(CuO) doped Y-TZP powder. A significantly improvement of relative density of ±99.9% and shrinkage up to 24% is seen in the dense body by applying MW sintering at 1300°C.The doped composition undergoes Ultrasonification followed by Attrition Ball milling aimed to shorten the overall mixing time of the material and strictly maintaining uniform agglomeration of mixing before sintering process. Characterization of the sample was carried out by XRD and SEM. The tetragonal phase of Y-TZP remains undisturbed via MW sintering process. Moreover, a dense and least porous structure with small grain growth was observed in 1300°C sintering of the doped material compared to using pure Y-TZP powder. Hardness of material was tested using Vickers indentation method and is seen to be a significant enhancement via this sintering method at elevated temperature.

Keywords: Microwave sintering (MW), Copper oxide (CuO), Y-TZP, Densification, Tetragonal, Hardness, Enhancement.

1. Introduction

Microwave sintering (MW) is non conventional sintering technique introduced over two decades. However, many failed to see the benefit of this sintering method as its potential of obtaining cost and time effective procedure.MW has short sintering cycle and low sintering temperature which allows it to be ideal for improving the productivity of the current sintering method which involves long sintering time and an overall increase in the cost. Microwave sintering works by inducing microwave radiation into the material whereby helps for a more uniform and volumetric heating. Besides that, MW is believed to be able to improvise the densification behaviors of material. This is because conventional sintering involves high temperature heating which can create Ostwald effect on the samples which induces grain growth. However, practicing a much lower sintering temperature would really benefit the material engineering world.

CuO doped Y-TZP ceramic has shown to demonstrate superplasticity ability and improved mechanical properties compared to pure Y-TZP. This is due to the addition of metal oxides as dopant produces eutectic liquids which cover the grain borders induces it to experience superplasticity nature [6]. Past studies has questioned on the potential of further densification of the doped body without grain growth at relatively low sintering temperature. Hence, non-conventional sintering would be a feasible option. Spark plasma sintering (SPS) is a common non conventional sintering which involves rapid sintering procedure but not suitable to be applied in this study as rapid heating would trigger grain growth [5]. On the other hand, MW is known for a significantly low sintering temperature and short sintering cycle poses more opportunity in solving this challenge.

The nature of the original Y-TZP which poses relatively high fracture toughness is closely related to the transformation toughening mechanism when the material experience failure by stress induced crack .The expansion of volume due at crack tip induces phase transformation of the tetragonal (t) → monoclinic (m) which is able to resist cracking. This mechanism is very essential and effort to retain the tetragonal phase in every sintering sample would necessitate the effort for improved mechanical properties of the ceramic body [2].

The right amount of dopant has a significant effect on improving the overall properties of the ceramic. Besides, the sintering temperature ramp rate has the similar importance as well. It is seen that the best dopant concentration is 0.05% wt and the sintering ramp rate of an increment of 30°C/mins and holding time of 15minutes would suffice the best sintering condition for MW[2].Therefore, applying this similar method in this study would allow to obtain an overall improved doped body in a sustainable manner.

1.1 Objectives

This research aims to apply MW sintering approach in attempt to enhance the Cuo doped Y-TZP ceramic:

i. To study the underlying impact of different sintering additives composition in enhancing the sintering and microstructure of Y-TZP ceramic body.
ii. To identify the best sintering condition for a microwave sintering technique in producing a fully dense body with improved mechanical properties at lower temperature.
iii. To establish micro-structural properties relationship governing the MW sintering of the doped Y-TZP ceramic

2. Methodology

2.1 Materials

Commercial pure Y-TZP powders with initial particle size of 30-40nm from Tosoh Corporation, Japan and Copper (II) Oxide powder with particle size of 5µm from Aldrich Chemicals, Germany was used in this study.

2.2 Powder Preparation

The first step of powder preparation is deciding the best doping composition of copper oxide to be used which was referred as 0.05 wt%. Past research has proved that addition of doping agent below 2 wt% is essential to maintain high tetragonal phase retention for application of low temperature sintering process [2].Hence, both CuO and Y-TZP powders composition were mixed initially using Ultrasonic device (SONICS Vibra-Cell) with pulse 10/2s for 15minutes adjusted up to a set temperature of 24°C.Ultrasonification aims to diminish deagglomeration and deaggregation which would affect the uniformity of processing material.

The mixing process is further extended using Attrition Ball milling whereby the initial ultrasonification sludge is poured for uniform mixing with the presence of 500ml of zirconia ball at a ratio of 1:10. The balls help to crush the powder to help mix the dopant more evenly in attempt to homogenize the mixture. Ball milling is carried out at 500rpm for 30 minutes. The final mixture is sieved and the zirconia balls are filtered away before leaving in a laboratory electric oven overnight at 80°C for drying purpose.

The dried powder is crushed using mortar and pestle before it is sieved at an ultra-fine sieve to obtain fine powders. These powders are then weighed and pressed into disk of 2.5 grams and bar of 3 grams. Then, the pressed samples are placed in latex glove and tightly sealed to avoid contamination with fluid during Cold Isostatic Pressing (CIP) at 200Mpa with holding time of 1minute.

2.3 Sintering Study

The prepared pressed samples are sintered at different temperature of 900°C to 1300°C in the microwave oven using heating ramp chosen to yield best result. The heating ramp is carried out as follows:

(1) From 250°C to 500°C by 15°C/min
(2) From 500°C to required temperature by 30°C/min
(3) 15minutes holding time

2.4 Grinding and Polishing

The disk sintered sample undergoes grinding using silica sandpaper with grit grades of 120, 240, 600, and 800 and 1200 starting with the coarse higher grade of 1200 and slowly moving towards the finer grit sandpaper of 120.Afther that, the samples are polished using 3µ and followed by 1µ diamond paste. The final shiny surface of the samples is used for testing.

2.5 Analysis Method

Density measurement is carried out using Archimedes Water Immersion test by weighing the sample in three different conditions which is weight in air, weight in water and weight in air + water. The temperature of water I also measured to acquire the accurate

density of water which is used together to calculate the relative density, bulk density and shrinkage of the sample using related formulas.

Hardness of the material is measured using Vickers Indentation method by applying required force on sample and analysis on the diagonal indentation size. An initial load ranging from 19.62N to 4.94N was used over a total of 3 indentations made on each samples. Calculations of the values are necessary to obtain the enhanced hardness results. Fracture toughness can also be calculated based on the crack length propagating from the edge of the diagonal indentation. However, due to lack of information on the frequency of doped material has restricted the calculation of Young's modulus as well as the fracture toughness of the material.

Morphology and phase identification of the material is carried out using X-ray diffraction analysis (XRD,X'Pert MPD, PANalytical, with Cu K_1 radiation, λ = 1.542 Å, using 2θ range of 26–34◦ with a step size of 0.02◦. XRD also aimed to observe possibilities of phase tetragonal Zirconia phase change to monoclinic during the MW sintering of doped sample.

The microstructure of the polished surface area of sintered sample is obtained using Scanning Electron Microscope (SEM, Thermo Noran Instruments).The SEM image obtained is used to observe the porosity of the sample at different sintering temperature and acquire understanding in retarding grain growth of the sample at lower temperature.

3. Results and Discussion

3.1 XRD analysis

Fig 1 shows the XRD pattern at 2θ range of 26–34° of the polished doped and pure samples after MW sintering. The major phase that is observed remained as tetragonal zirconia (t-$Zr0_2$). The retention of tetragonal phase would allow the transformation toughening process to occur which signify an overall significant improvement over the mechanical strength of the material due to the resistance over cracking during t → m phase transformation. Generally, the addition of such metal oxide induces the reduction of CuO to Cu which lead to the tetragonal phase retention. The XRD image generated shown only one peak and a relatively stable pattern which would relate to the low sinterability of the dopant due to low sintering temperature. On overall, the XRD pattern (Figure 1) demonstrated a relatively similar pattern on all the pure and doped samples with the retention of tetragonal phase similarly to previous findings (Figure 2)

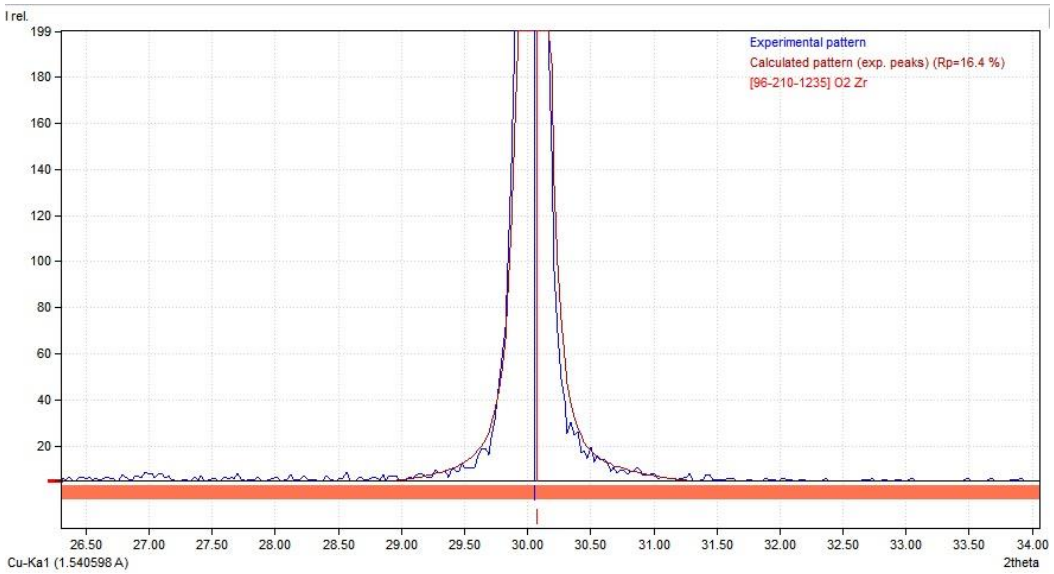

Figure 1: XRD pattern of CuO doped Y-TZP ceramic at 1300°C

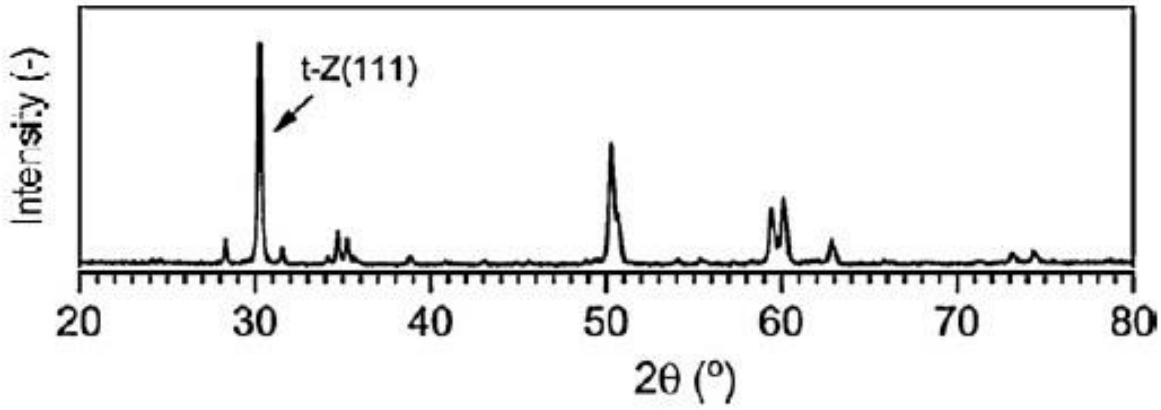

Figure 2: XRD result of past literature on CuO doped Y-TZP ceramic [3]

3.2 Densification

The densification behavior of the samples undergoing MW sintering has exhibit a very favorable result whereby it seen that both the pure and doped sample tend to experience grain densification rapidly in a lower sintering temperature. Figure 3 is a graph which shows the increase of bulk density calculated in both pure and doped samples. The samples increase gradually over the increasing sintering temperature whereby the relative density of the doped ceramic is seen to be the highest up to ±99.94%.

CuO doped Y-TZP exhibits higher densification behavior compared to pure Y-TZP. At 900°C, the densification of the samples intensifies in the doped body. CuO dissolution occurs at low temperature in Y-TZP matrix which increases the ion diffusivity. This result in a high grain boundary diffusion of the matrix whereby inducing rapid rate of densification at low sintering temperature [6].However, the rate of densification drops slightly as the temperature elevates beyond 1000°C. The solid-state reaction between CuO and Yttria

mentioned earlier in this temperature region produces $Y_2Cu_2O_5$ phase which is also responsible for the corresponding drop in the rate of densification. The rate of densification is further retarded until 1100°C when the rapid dissociation of CuO to Cu_2O results in development of large pores. These pores lead to a drop in the density of the sintered sample. A linear increase in densification rate is observed above temperature 1100°C due to the melting of Cu_2O[7].Liquefied Cu_2O spreads and covers the Y-TZP grains resulting in extensive contact point between the dopant and the Y-TZP body. This amplifies the reaction experienced within the matrix and an overall boost in densification rate [8]. Temperature above 1200°C exhibits molten Cu_2O reaction with Yttria resulting in a solid-liquid reaction within the grains. This new reaction produces a liquid Yttria copper oxide phase which substitutes the existing Cu_2O liquid contact area leading to a drop in rate of densification [7].

This proves that the MW sintering does indeed induce volumetric heating in a short period of time which enhances densification without excessive grain growth.

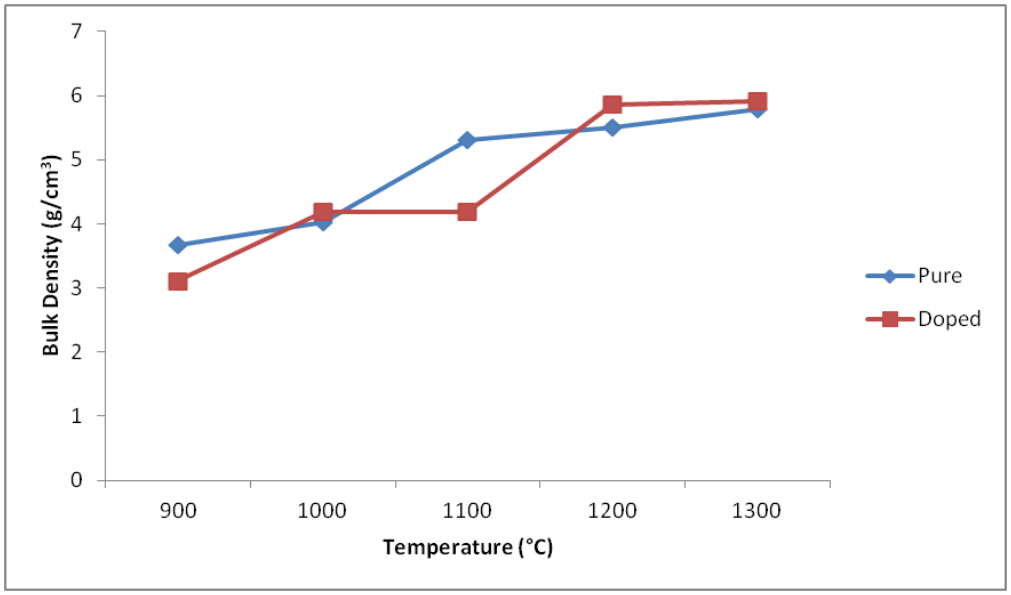

Figure 3: Graph of bulk density against MW sintering temperature

The shrinkage of the sample in Figure 4 has also shown tremendous progress whereby the both the pure and doped sample induce shrinkage of the original material up to a maximum of 24%. Generally, shrinkage of 20% is known to be very effective densification process.

The rate of shrinkage of the sintered samples are said to imitate the same trend similar to the densification behavior observed in bulk density analysis up to the sintering temperature of 1100°C. However, the shrinkage in doped sample is seen to spike above 1100°C whereby the dissolution of CuO to Cu_2O reaction is responsible for the rapid volume shrinkage. Considering the lower theoretical densities and molecular weight of Cu_2O compared to CuO particle has result in an overall reduction of volume by 12%.Therefore, the significant drop in volume result in rapid shrinkage of the doped body suggests an effective densification behavior of the doped sample. However, upon achieving the maximum percentage of shrinkage of 25.15% at 1200°C, the rate of shrinkage dropped resulting in end shrinkage percentage of 24.55%.Similar reduction in shrinkage rate is also recorded for the pure Y-TZP sample at 1300°C.This is related to the inhibition of densification occurring naturally when

the shrinkage rate reaches the maximum accountable percentage whereby the porosity of the structure have significantly been removed.

As such, the MW sintering has further push the limits of enhancing the densification in a low temperature sintering and short sintering cycle.

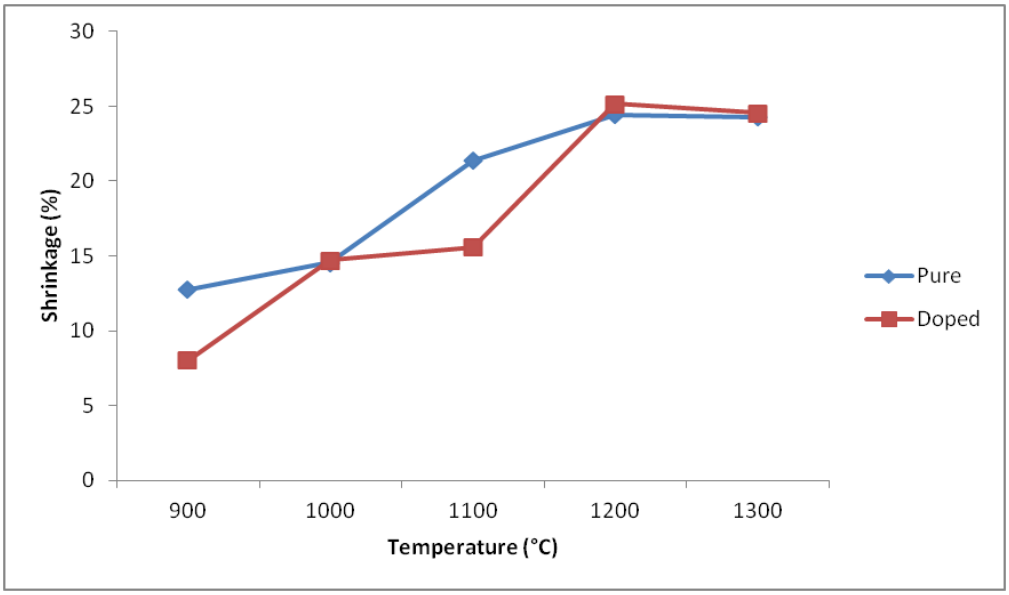

Figure 4: Graph of shrinkage against MW sintering temperature

3.3 Hardness

Improvement over the properties of ceramic body has been part of the concern of this study. Since the limitation of this study in attaining the frequency value for the MW sintered sample has deter the calculation for fracture toughness, the hardness is emphasized in this research. Figure 5 has demonstrate the overall improvement in hardness experience by both the pure and doped sample. However, a sudden drop in the trend line observed for the doped sample sintered at 1000°C and a relatively low hardness recorded at temperature of 1100°C was depicted in figure 5.The justification behind this occurrence relates to the grinding and polishing process underwent by the samples. The intense grinding process carried on the sample sintered at 1000°C at 1100°C is seen to have resulted in reduction of the sample's thickness by halve. Hence, proper polishing could not take place leaving the formation of thin patchy layer on the surface of the sample. This layer exists independently on sample surfaces which are not polished and grinded precisely due to natural deposition of wear debris and are not visible by naked eyes [9]. It is believed that a thin absorption lining present in the layer is responsible for the low hardness value. The lining absorbs the indentation acting on the patchy surface due to its soft nature and affects the accurate hardness value results obtained [9].

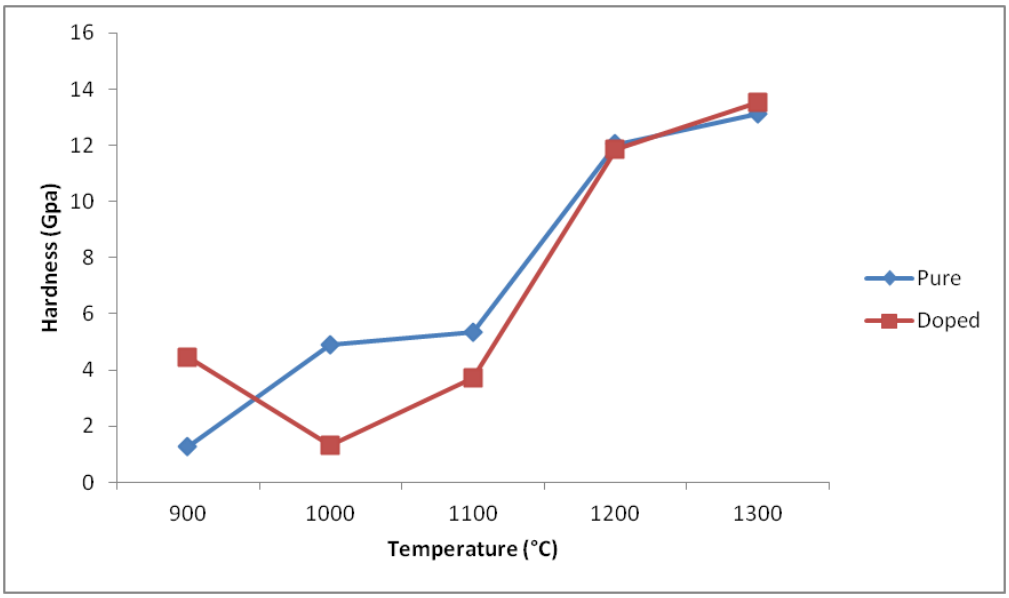

Figure 5: Graph of hardness against MW sintering temperature

3.4 Scanning Electron Microscope (SEM)

It is of interest to study the microstructure of the sample to truly understand the underlying factor and behaviors of the samples after experiencing MW sintering. Figure 6 are SEM images at the initial temperature of 900°C and final temperature of 1300°C for both samples which is used to observe the similarity of the MW effect on the sample. As seen, both the samples demonstrate irregularities and agglomerate structure in the initial sintering temperature whereby the grain are not properly formed and are extremely porous [4]. However, as it reaches the highest MW sintering temperature the grain starts to grow and densify leaving very minimal pores.

Closer analysis of the pure Y-TZP sample at 1300 °C reveal a uniform microstructural grain size growth averaging up to 150nm while the doped samples exhibit non-uniform microstructural grain size growth with a series of tiny grain size of 200nm surrounding larger irregular shape of grain size approximately several μm. The irregularities in grain size growth relates to the CuO content in the doped body. Higher CuO content results in larger grain size growth [7]. Besides, low MW sintering temperature has proven to significantly control grain size growth since both samples range between averages of grain size of 150nm-200nm despite the mixture of irregularities in the doped sample.

This breakthrough in results supports the theory proposed on effect of low temperature sintering on maintaining smaller grain size [1].

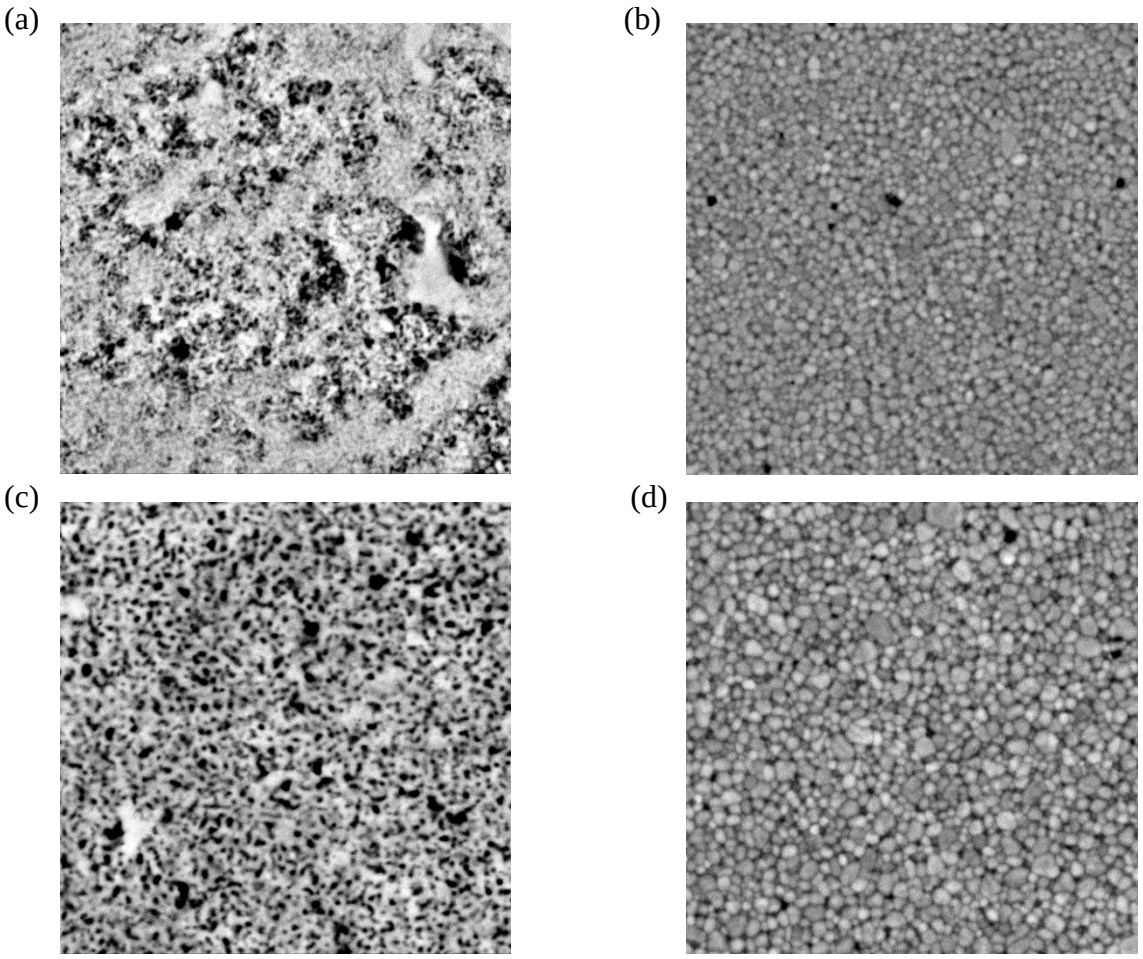

Figure 6: SEM images of pure Y-TZP at (a) 900MW and (b) 1300MW while CuO doped Y-TZP sample at (c) 900MW and (d) 1300MW where each magnification of grain size is 2µm

4. Conclusion

In short, the study has proven that MW is a very competent sintering technique in enhancing the densification of both pure and doped Y-TZP body. The MW samples exhibits retention of tetragonal zirconia phase which is essential for the transformation toughening effect to improve the overall properties of the material. Moreover, the extremely dense material can be obtained through MW sintering procedure which further boosts the potential for high end application through a much more cost efficient and time saving sintering procedure. At the same time, the hardness of the material is also not compromised.

Reference

[1]A. Borrell, M. Salvador, E. Rayón and F. Peñaranda-Foix, 'Improvement of microstructural properties of 3Y-TZP materials by conventional and non-conventional sintering techniques', *Ceramics International*, vol. 38, no. 1, pp. 39-43, 2012.

[2]S. Ramesh, C. Gill and S. Lawson, 'The effect of copper oxide on sintering, microstructure, mechanical properties and hydrothermal ageing of coated 2.5Y-TZP ceramics', *Journal of Materials Science*, vol. 34, no. 22, pp. 5457-5467, 1999.

[3]S. Ran, J. Vleugels, S. Huang, K. Vanmeensel, D. Blank and L. Winnubst, 'Manipulating microstructure and mechanical properties of CuO doped 3Y-TZP nano-ceramics using spark-plasma sintering', Journal of the European Ceramic Society, vol. 30, no. 4, pp. 899-904, 2010.

[4]L. Winnubst, S. Ran, E. Speets and D. Blank, 'Analysis of reactions during sintering of CuO-doped 3Y-TZP nano-powder composites', *Journal of the European Ceramic Society*, vol. 29, no. 12, pp. 2549-2557, 2009.

[5]R. Chaim, M. Levin, A. Shlayer and C. Estournes, 'Sintering and densification of nanocrystalline ceramic oxide powders: a review', *Advances in Applied Ceramics*, vol. 107, no. 3, pp. 159-169, 2008.

[6]S. Ran, L. Winnubst, W. Wiratha and D. Blank, 'Synthesis, sintering and microstructure of 3Y-TZP/CuO nano-powder composites', *Journal of the European Ceramic Society*, vol. 26, no. 4-5, pp. 391-396, 2006.

[7] S. Ran, L. Winnubst, D. Blank, H. Pasaribu, J. Sloetjes and D. Schipper, 'Effect of Microstructure on the Tribological and Mechanical Properties of CuO-Doped 3Y-TZP Ceramics', *Journal of the American Ceramic Society*, vol. 90, no. 9, pp. 2747-2752, 2007.

[8] S. Ran, J. Vleugels, S. Huang, K. Vanmeensel, D. Blank and L. Winnubst, 'Manipulating microstructure and mechanical properties of CuO doped 3Y-TZP nano-ceramics using spark-plasma sintering', *Journal of the European Ceramic Society*, vol. 30, no. 4, pp. 899-904, 2010

[9]L. Winnubst, S. Ran, E. Speets and D. Blank, 'Analysis of reactions during sintering of CuO-doped 3Y-TZP nano-powder composites', *Journal of the European Ceramic Society*, vol. 29, no. 12, pp. 2549-2557, 2009.

Design of Intelligent Bed to Prevent Bedsores

Chan Kar Meng, Andy[1*], Azadeh Ghadimi[1], Mohammad Jaweed[2]

[1]*School of Engineering, Taylor's University Lakeside Campus, Subang Jaya, Malaysia*
[2]*School of Medicine, Taylor's University Lakeside Campus, Subang Jaya, Malaysia*

[*]chan.karmengandy@sd.taylors.edu.my

Abstract
Bedsore is a major issue that frequently occurs on bedridden patients. It can cause serious injury to the skin and/or the tissues underneath. If bedsore is left untreated, it may cause infection to the wound which further increasing the depth of the wound. The treatment to bedsore is very costly according to most of the medical reports, thus the better way to treat bedsore is to prevent bedsore from developing in the first place. Constant pressure and shear stress applying on the skin are the major factors of bedsore development. To eliminate or to reduce these factors, repositioning method was introduced as a part of nursing practice to prevent bedsore. This practice requires caregivers to reposition the sleeping posture of the patient at every few hours. The workload for this practice is heavy considering that the patient has to be moved 6 to 8 times per day. As such, this project is proposed to assist the reposition protocol using an intelligent bed that can imitate the work which the caregivers did. Repositioning method is designed to be done automatically with the help of actuator and computer to track the time interval without any physical assistance from a caregiver. The main focus of the bed design is to reduce pressure and shear stress exerting on the subject. This project only features the designing phase of the bed model, thus no prototyping is involved. The design is first sketched, and then implemented into computer aided design software; 'SolidWorks 2014 SP 4.0'. The final model of the bed design can produce the repositioning process while retaining all the conveniences and comfort that the existing hospital bed has provided.

Keywords: Bedsore, Pressure ulcer, Hospital bed, Design, Patient.

1. Introduction

Bedsore which is also known as pressure ulcer is a localised injury on an area of human skin or/and the underlying tissues [1]. This injury commonly occurs on places which have bony eminence such as the area near coccyx (tailbone), elbows and heels. Bedsore is mainly caused by pressure and shear stress exerting on an area of human skin over a long period of time. When the skin is subjected to pressure and shear stress, blood flow in the soft tissue is restricted [2]. If that situation persists, nutrients will fail to be transferred causing the corresponding tissues to break down, forming an ulcer.

The development of bedsore creates immense amount of pain to the patient. If it is left untreated, the wound might rupture further into the skin, potentially causing infections to the inside body tissues. Therefore, this project was proposed to prevent the development of bedsore in the first place.

The objectives of this project are:

1. To design an ergonomic bed to prevent bedsores without sacrificing the initial comfort and conveniences which the current hospital bed has presented.
2. To implement the design into software for modelling and simulation.
3. To evaluate the design of bed based on the standard needs and by making evaluation using current available design as the benchmark.

2. Theoretical Framework

2.1 Literature review

A study done by Sibbald et al. suggested that the primary cause of bedsore development is the pressure and shear stress acting on the human body [3]. These forces that are applied to an area over a long time will cause the tissue cells to rupture, subsequently injuring the patient. As a preventive measurement, it is recommended to remove or reduce the amount of stresses acting onto the body.

Petzold et al. performed a cohort study of the patients in University Hospital Carl Gustav Carus Dresden in Germany. The sample of study showed that the patients who were admitted into the intensive care unit (ICU) developed a greater risk of acquiring bedsore as compared to those who were admitted to the normal care unit (NCU) [4]. Patients who were admitted into ICU were those who needed constant monitoring and care. The majority of them were not able to make any body movement by themselves due to unconsciousness. Thus, the back of their body were constantly lying on the same position of bed for a long time. According to the statistical study, 21.7% of the patients who developed bedsore had the bedsore on their heel, 19.7% were found at the ischium, 19.5% were discovered near the sacrum, 13.4% were on the gluteus maximus, 3.2% were developed on the ankle, and the remaining 22.5% of the affected patients had bedsore on other different areas of their body.

In accordance to address the issue of bedsore, the National Pressure Ulcer Advisory Panel (NPUAP) had produced a nursing guide that provides useful information to prevent pressure ulcer. In the handbook, it is stated that the patient is at risk of developing a bedsore if his/her body is subjected to a long-term and low stress, or a short-term and high stress exposure [1]. To reduce such exposures, the repositioning method was introduced in the

guidebook. The repositioning method is a method that was advised to be practiced by the caregivers to shift the sleeping position of the patient on a timely basis. Four main sleeping postures were introduced by the NPUAP; there are upright position, leaned to the left, leaned to the right, and sleeping backward. The reason for the frequent shifts on the sleeping posture is to relief the pressure exerting on the same area of body. One important note on this repositioning practice is that the patient should be diligently shifted, not dragged during the repositioning. It is also suggested in the guide that the patient should be tilted at 30 degree angle when s/he is titled to lean to his/her side.

2.2 Hospital Visitation

To further understand bedsore, a hospital visitation had been conducted on the 22nd of November 2014 at Sungai Buloh Hospital, Malaysia. The permission to visit the neurosurgery ward where most ICU patients were placed into was granted. Repositioning method as proposed by NPUAP is practiced by the caregivers at the ward. They initiated a three-hours repositioning interval that consisted of three positions – upfront, left and right-lean sleeping posture. It was observed that when the patient was set to sleep leaning on either side of his/her body, a few towels were folded and placed at the bottom of the patient by the caregivers. The towels were to provide support to the patient's weight and to prevent the patient from falling over from the intended sleeping position. When the caregivers demonstrated the repositioning method, it was observed that the amount of work needed to lift the patient, especially on heavy patient was enormous. Thus the research gap for this project is to design a robotic mechanism that is capable to imitate the repositioning method to ease the workload of the caregivers.

3. Methodology and Data

The key to design the bed is to apply the CDIO framework. The CDIO framework is an innovative framework to develop a new production or technology, and it consists of four stages that made the name. The four stages of CDIO are:

- Conceive
- Design
- Implement
- Operate

In this section, the stages of conceive, design and implement will be discussed as parts of the methodology. The operate stage will be discussed in Section 4.0 Reported Outcomes.

3.1 Conceiving Idea

Conceiving ideas is the first stage of the CDIO framework. It is the stage where various ideas obtained from inspirations are presented. In this stage, the quantity of idea is highly valued over the quality of the idea. The purpose of generating many ideas without evaluating the feasibility is to provide more inspirations so that great ideas can be selected for the design of the bed.

3.2 Design Method

The ideas that had been conceived were realised by adding in structures. Sketches of beds were made with pencils and papers to provide illustrations of the general structures of the beds. Each of the sketches was clearly labelled on its primary functions, and then evaluated for its pros and cons. The advantages from various ideas were merged and the final design was illustrated in Figure 1.

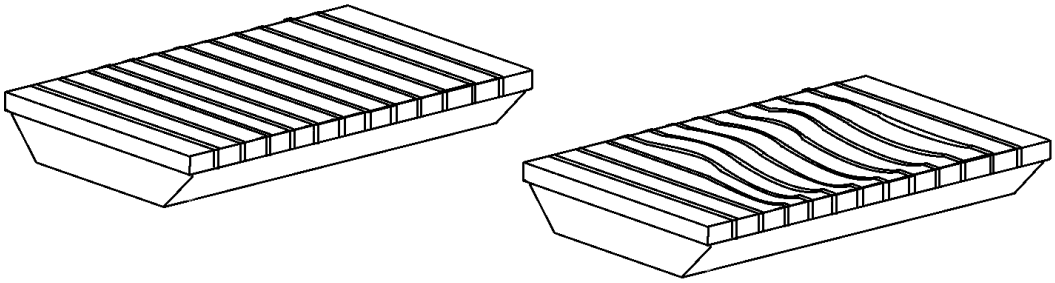

Figure 1. Finalised sketch of the intelligent bed design.

The concept behind the design in Figure 1 is to allow the surface of the bed to move up on one side, and down on the other side. This is to position the patient to lean side way without the need of caregivers' assistance. To do so, the surface of the bed must be flexible enough to move freely. Therefore, rubber strips were the suggested material to build the surface of the intelligent bed. Rubber with soft and elastic property is planned to be implemented into the design because it is easily flexed while providing a level of comfort to the patient. Beneath the rubber strips, there are several actuators and structures that made the mechanism to push the rubber strips in and outwards; replicating the repositioning method. The illustration on the left in Figure 1 shows the original state of the concept bed, whereas the illustration on the right shows the state of the bed when the reposition protocol is executed.

Recalling the first objective of the project is to build a bed without sacrificing the conveniences that the hospital bed had already provided. Therefore, it is essential for the design to retain some of the features of the hospital bed. The features to be included are:

- The design of bed has to fulfil the standard mattress size in Malaysia, which is 1920 mm in length and 910 mm in width.
- Bed must have railings to prevent patient from falling onto the ground.
- Bed can lift the upper body of the patient in the range of 0° to 80°.
- Folding the patient's legs towards his/her pelvic area in the range of 0° to 35°.
- The height of the bed can be adjusted.
- Trendelenburg and reverse Trendelenburg movement (tilting the patient's head up and leg down, and reverse) of 0° to 20°.

3.3 Implementation of Design

The finalised design was modelled in 'SolidWorks 2014 SP4.0', a three-dimensional modelling software for engineering design. The modelling of the bed was done parts by parts so that the final assembly of the model can be articulated. Each of the parts was joined with

bolts and were mated concentrically to generate joints for the desired parts to move. Due to the coding of the software, it was unable to determine the present of collision from structure to structure unless the user specifies them. So to prevent the structure from overturn from how it is supposed to be in practical, ‘angular mate’ was used to restrict the movement of joint, limiting the angle that the intended structure can turn. Figure 2 shows the repositioning mechanism of the bed model which used ‘angular mate’ to define the allowable turning angle of each structural members.

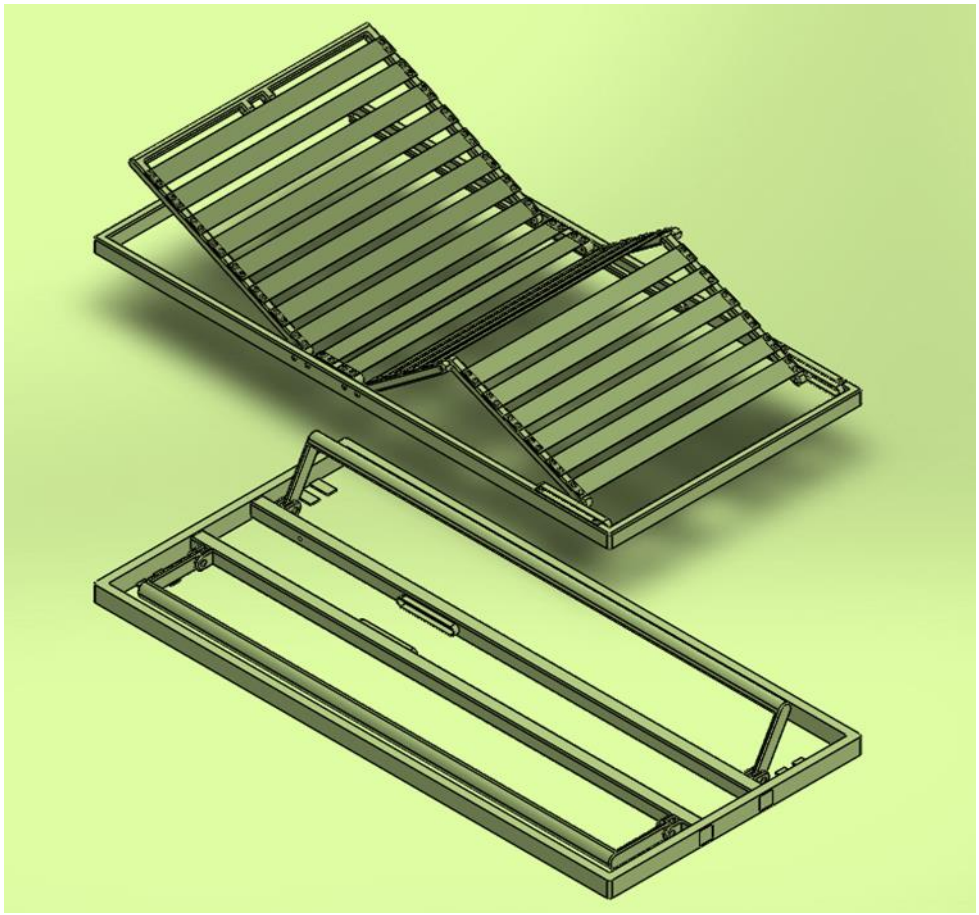

Figure 2. The repositioning mechanisms of the intelligent bed.

In Figure 2, the mechanism of the bed were split into two major parts. The upper part shown in the figure was responsible to imitate the upper body lifting and leg folding motion that the conventional hospital bed had offered. A linear actuator was intended to be used lift the upper body. Similarly, another linear actuator will be used in the leg-folding mechanism. In addition to that, the leg mechanism had a pair of built-in rollers and track so that the leg part can be folded as illustrated. The short length of the roller track also functions to restrict the angle of leg-fold to 35°. The upper part of the mechanism was filled with rubber strips as planned in the finalised sketch.

The lower part in Figure 2 is the main mechanism of repositioning. Two individual beams were placed on the left and on the right side as depicted in the figure. Being the main component of repositioning mechanism, the two individual beams were driven by linear actuators to generate the force to lift the patient to lean towards the side. It was modelled in such a way that when the beams moved upwards, the beam will push the rubber strips, pushing the strips from the side, towards the centre to lift the patient. The length of the beam

was carefully investigated and calculated so that it the movement will not be obstructed by other structures of the bed. As mentioned by the NPUAP, the desired angle of side tilts is 30°. Figure 3 illustrate the maximum side tilting angle that this model can provide.

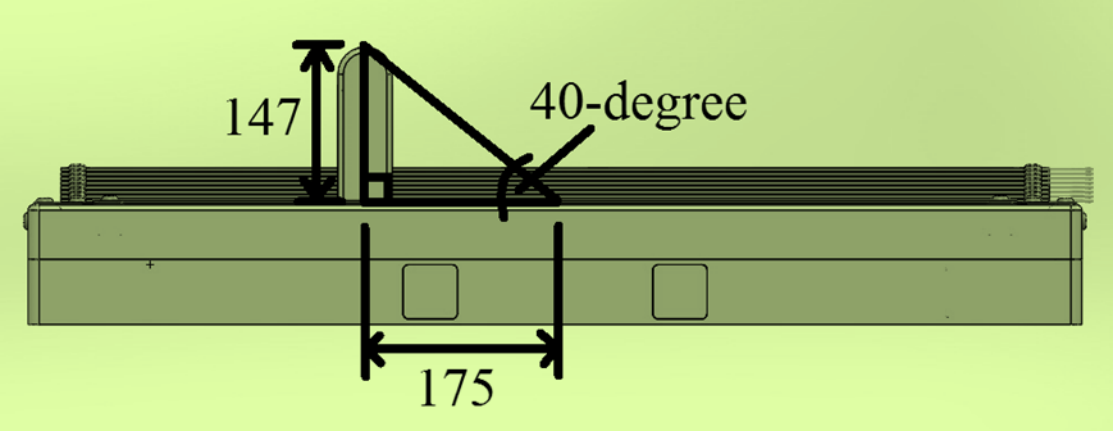

Figure 3. Illustration of maximum side tilt this model can provide.

The model was design to enable a 40° side tilting angle even though the recommended side tilt angle is 30°. This is because the excess angle was needed to successfully turn the patient towards the side. Patient usually sleeps at the centre of the bed. When the patient is lifted from one side, the other side of the patient should remain unlevelled due to the patient's weight. Thus, the angle of side lift in this model was calculated from the centre of the bed to the top of the side-lifting beam as demonstrated in Figure 3. Since the pivot point of the side-lifting beam is 175 mm apart, the length of the beam required to protrude from the rubber surface to simulate approximately 40° side lift is 147 mm at 90° to the base. In this setting where the pivot point of the side-lifting beam was set to 175 mm, it was impossible to generate higher angle side lift. This is because a greater angle side lift would require a longer beam to protrude from the bed surface; and longer beam may collide with other structures of the bed.

The next design criteria which is the Trendelenburg, reverse Trendelenburg, height adjusting and railings were fulfilled as illustrated in Figure 4.

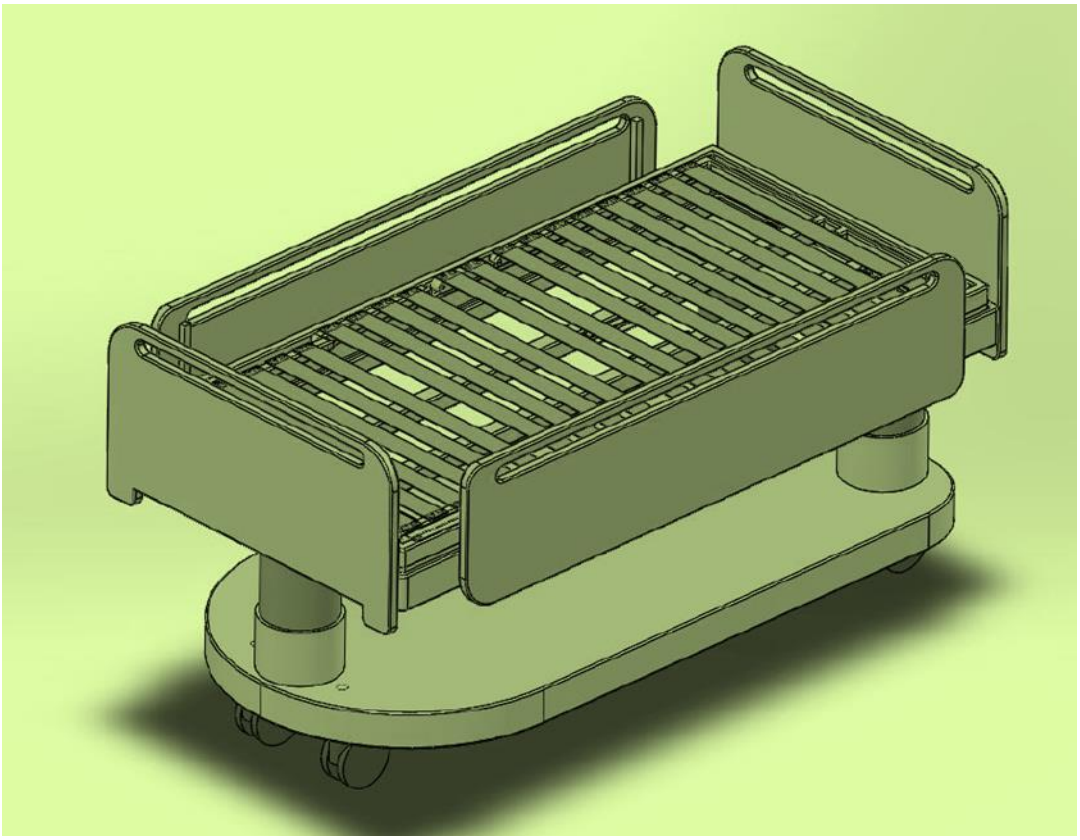

Figure 4. Overall design of intelligent bed.

Trendelenburg movement is used to circulate blood flow from the head to the toe and from the toe back to the head in reverse Trendelenburg. In this design model, three large linear actuators (one is used at the front of the bed and two behind) were used to simulate the Trendelenburg and reverse Trendelenburg movement. Those actuators were as shown as large cylinders in Figure 4. To generate Trendelenburg, the actuators can be set in such a way that the front actuator retracts whereas the back actuators expand. The difference in height will provide the required movement. Besides, the height of the bed can be adjusted by setting both the front and back actuators to extract or retract simultaneously at the same level of height.

On the other hand, the model of the bed was mounted with railings to prevent patient from falling off the bed. The side railings were adjustable, able to be pulled up or pulled down so that patient can be transferred easily during emergency operation. Besides that, the model was also equipped with auxiliary wheels with brakes for portability and mobility.

4. Reported Outcomes

The last stage of CDIO is the operating stage where the model is tested with various measurement. The major component of this model is the reposition mechanism. Therefore, it is important to study the motion of the repositioning process that this model can offer.

4.1 Relation of Actuator Stroke and the Beam Elevation

Similar to most of the moveable structures, the side-lifting beam of the model is also actuated by linear actuator. From the model, the actuator on the side-lifting beam is set to have 0 stroke when the beam is at rest at 0°. The length of the stroke is calculated by setting the angle of the side-lifting beam in SolidWorks. The result is plotted in the graph in Figure 5.

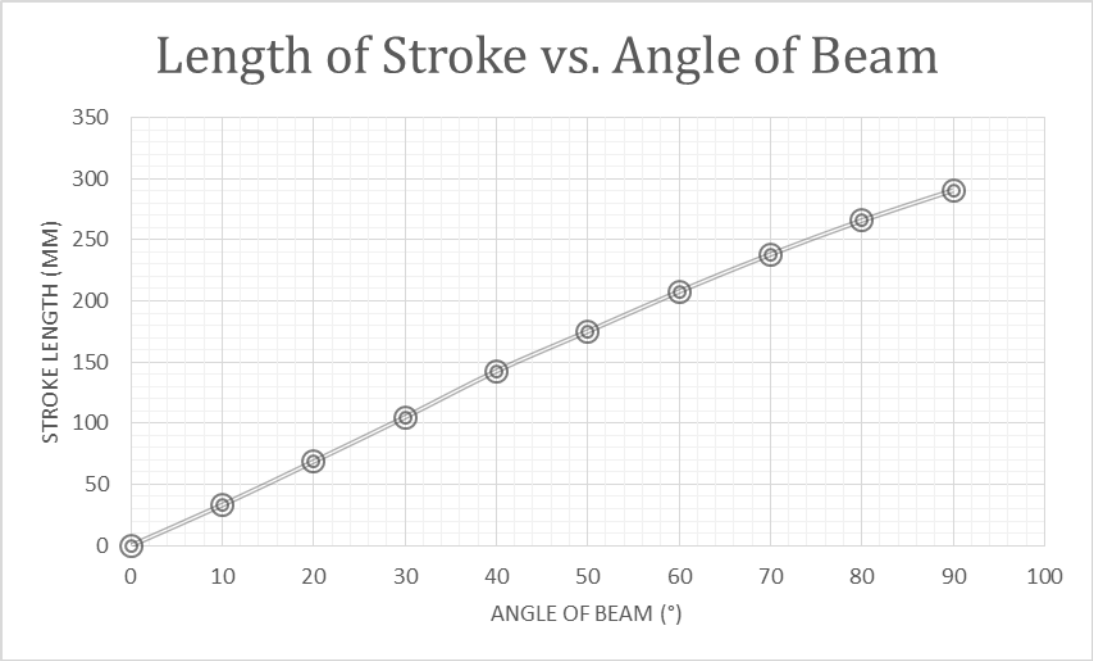

Figure 5. Graph showing the relation of length of stroke of actuator with angle of side-lifting beam.

From Figure 5, it is suggested that the maximum stroke required to reach the maximum angle of beam of 90° is about 291 mm. The trend of the graph showed a uniform increment with an average additional stroke of 33 mm is required for each 10° beam raise.

4.2 Relation of Beam Elevation and Effective Lift Angle

The effective lift angle is the lifting angle of the patient. Figure 6 showed the relation of the beam elevation and the effective lifting angles.

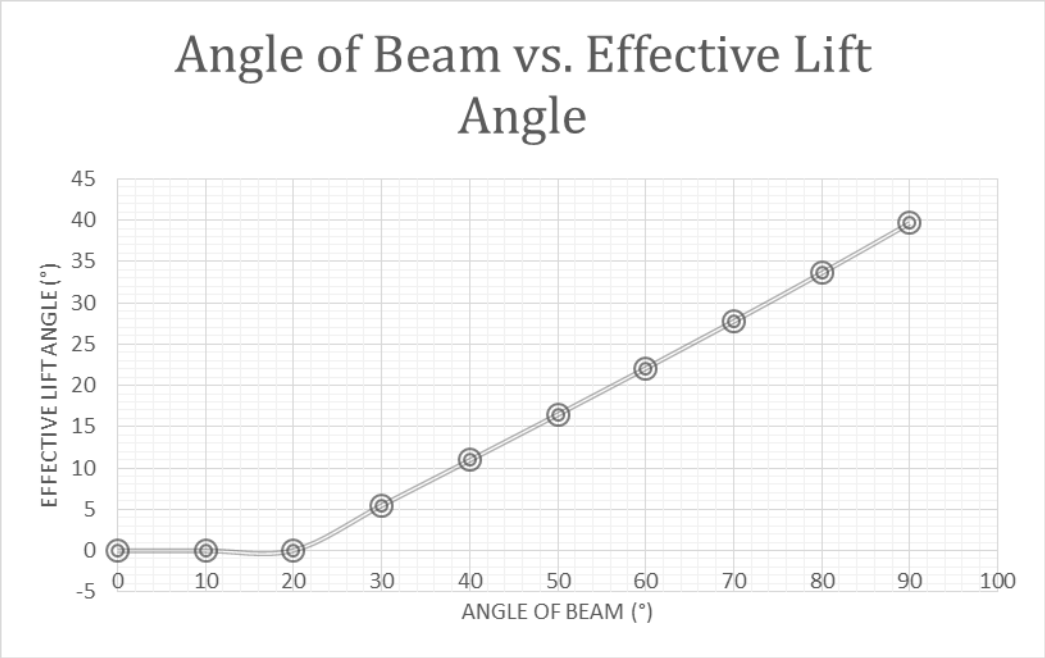

Figure 6. Graph showing the relation of angle of side-lifting beam with the effective angle of lift.

The effective lifting angle starts at 20° of the angle of beam. This showed that the beam does not touch the rubber strips at the beam angle below 20°. Similar to the first graph, the trend of this graph exhibit uniform increment where for every 10° changes in the beam, starting from 20°; there will be 5° of effective lifting on the surface of the bed.

The uniform trend from both the graphs suggested that the effective lifting angle is directly proportional to the actuator stroke. This relation benefits the project as patient can be lifted at a constant angular velocity. The constant velocity is ideal so that the patient will not damage the skin due to sudden movement or acceleration. From the data collected, it is showed that the model can be redesign so that the side-lifting beam is rested at 20° of beam angle. This is to save the unnecessary use of energy in moving the actuator from rest to touching the rubber strips. Approximately 66 mm of actuation stroke can be saved from the redesign.

The study above shows the stroke length required for the actuators to perform 40° tilting towards the patient. However, the effectiveness of this design to tilt the patient is yet to be determined from the software alone. Prototyping and further research need to be conducted to verify the effectiveness of this design.

5. Educational or Field Significance

The model was designed accordingly to suit the needs of the society. The result predicts that the model can be viable to lift the patient slowly from the side, capable to imitate the repositioning protocol effectively. However there might be some factor that affects the reading. For instance, the rubber strips might affect the effective lifting angle result because the weight of the patient may cause the elastic rubber strips to dent inside the bed. Therefore, a prototype of the model is required to validate the result.

The following are the suggestions for future works:

- Create a physical prototype of the model to validate the result further. The prototype also can be used to evaluate the comfort of the bed from various human subject.
- Investigate the possible replacements for rubber strips with materials that can reduce the pressure exerted from body weight such as memo-foam.
- Explore other possible methods to prevent bedsore.
- Conduct various experiment with pressure mapping system, generating a list of diagnosis and prognosis process to predict the factor of bedsore development.

References

[1] European Pressure Ulcer Advisory Panel and National Pressure Ulcer, "Prevention and treatment of pressure ulcers : quick reference guide." Washington DC: National Pressure Ulcer Advisory Panel, 2009.

[2] C. Bauer, "Pressure Ulcer Update for Primary Care," *J. Nurse Pract.*, vol. 9, pp. 729–735, 2012.

[3] R. G. Sibbald, L. Goodman, L. Norton, D. L. Krasner, and E. A. Ayello, "Prevention and Treatment of Pressure Ulcers," *Skin Therapy Lett.*, vol. 17, no. 8, pp. 4–7, 2012.

[4] T. Petzold, M. Eberlein-Gonska, and J. Schmitt, "Which Factors Predict Incident Pressure Ulcers in Hospitalized Patients ? A Prospective Cohort Study *," *Br. J. Dermatol.*, vol. 1, no. 6, pp. 1285–1290, 2014.

Effect of Starch Content in Controlled-Released-Fertilizer in Starch-Derivative-Alginate based Formulation

Har Song Yong[1*], Siew Wei Phang [1,2], Lee Tin Sin [2], Soo Tueen Bee [2], Tiam Ting Tee[2]

[1] *School of Engineering, Taylor's University Lakeside Campus, Malaysia.*

[2]*Department of Chemical Engineering, Faculty of Engineering and Science, Universiti Tunku Abdul Rahman, Kuala Lumpur, Malaysia.*

Lawrence317gg@gmail.com

Abstract

Urea is a fertilizer that bringing huge impact to the agricultural in the sense of economic and human welfare. Due to leaching, decomposition and ammonium volatilization in soil, 70% of the urea fertilizer is lost to the environment that brings eutrophication to the surrounding water sources that affecting aquatic life and nitrous oxide (N2O) production by ammonia-oxidizing bacteria (AOB) through nitrification that causing global warming [1]. Controlled released fertilizer (CRF) of urea, urea will be encapsulated with combinations of sodium alginate (NaAlg), calcium chloride (CaCl2) cross-linker and cassava starch polysaccharide biopolymer formulation set with Taguchi Method of Orthogonal Array of L9 with three possible levels to observe the interaction between each parameters. The coated beads are characterized with FTIR technique to gain insights for the functional group, EDS provide the % wt of compositions on the selected area to find out the composition left after immersion in water for 24h and SEM for surface structural analysis and morphological features of the beads, as well as swelling studies and erosion % of the bead [2]. Result of bead size , yield of the beads , swelling ratio and erosion % results were evaluated with Taguchi analysis method. The parameters of cassava starch, sodium alginate, calcium chloride and urea do show interaction between each other in this study of controlled-released-fertilizer of urea. For example optimizing the yield %, the concentration for cassava starch is 0.08 g/mL, 0.08 g/mL of sodium alginate, 0.2 M of calcium chloride and 0.3 g/mL of urea. Each parameter has its own unique functional groups which provides different degrees of interaction to form the bead which goes to bead of diameter and erosion %. FTIR results show the presence of all four components used in bead formulation. SEM analysis gives a promising structure that slightly affected in high moisture condition for long period of time as will not dissolve immediately as pure urea fertilizer. High surface area which allow water uptake due to the voids surface structure. EDS shows the presence of starch, sodium alginate and calcium chloride composition on the surface of the bead after 24 h in water immersion. No urea can be found on the surface of the bead due to diffusion from high concentration to low concentration water region.

Key Words: Sodium Alginate, Controlled Released Fertilizer (CRF), Cassava Starch, Urea, Beads, Biopolymer, Swelling Ratio, Taguchi Method

1.0 INTRODUCTION

Plantation is considered as agricultural in modern generation that bring huge impact on the economic, environment and welfare of the society at worldwide. In order to well maintain grow of plants and crops, fertilizer is used. Urea is one of the most common nitrogen-release fertilizer used in plantation which is the basic essence of plant for growing and improving the yield.

Excessive usage of urea fertilizer may cause harmful effects to ecosystem, for example the fertilizer is washed off the land by heavy rain into the river or ocean as causing eutrophication that harming aquatic animals and fertilizer burn that resulting leaf scorch [1]. Excessive releasing of hazardous gas such as nitrous oxide by AOB throughout the reduction of nitrite (NO_2) to N_2O via nitric oxide (NO) known as nitrifier or AOB denitrification and N_2O as a side product during incomplete of hydroxylamine (NH_2OH) that potentially resulting ammonia volatilization which cause negative impacts to economic and environment [2].

From Figure 1, the main source of nitrous oxide emissions at U.S. coming from agricultural field which is a greenhouse gas that gives greenhouse effect such as climate warming. The average emission value within 20 years is 150.08 million metric tons carbon dioxide equivalent that stand the highest compared to other fields such as waste management, energy and industry [3]. Based on Figure 2, the agricultural soils gave out the most nitrous oxide emissions compared to animal waste and crop residue burning stand a minor ratio at 2009 in U.S. [3] .

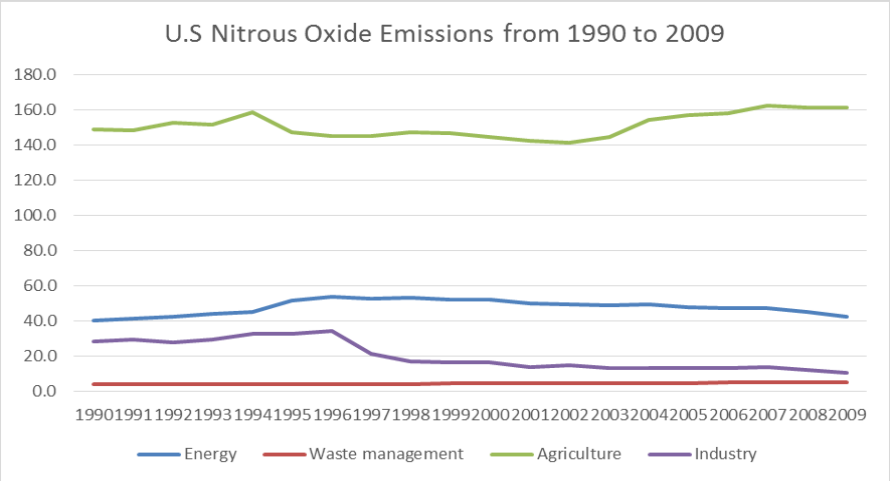

Figure 7: The Nitrous Oxide Emission from 1990 to 2009 for U.S in Different Fields [3]**.**

In engineering, one of the fourteen grand challenges is managing the nitrogen cycle [4]. In addition, unpredictable climate changes give farmers difficulties in plantation such as long term drought causing insufficient water take in by the plant and jeopardize the soil content that required by the crops and plants for growing. Figure 2 shows the outcome of drought for world map in 2000 to 2009 on top diagram, compared with prediction outcome in 2030 to 2039 at diagram below it. Due to this two major issues, controlled release fertilizer (CRF) is introduced to counter them.

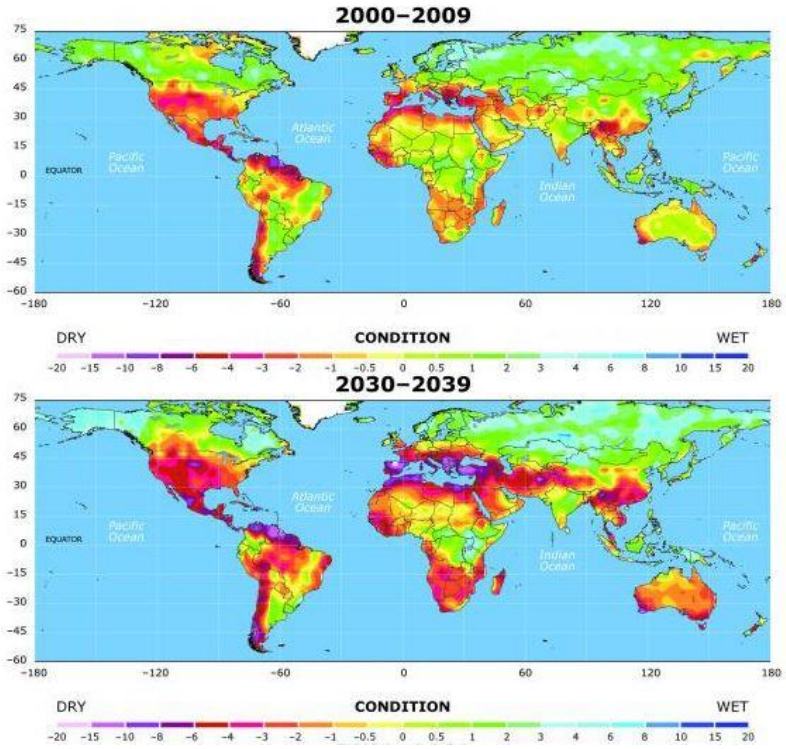

Figure 8: Future Drought Prediction Outcomes [5]**.**

Controlled release fertilizer (CRF) is a design formulation for controlling the release of active fertilizing nutrients, delayed manner in synchrony with sequential needs of plants for nutrients and enhanced nutrient use efficiency along with enhanced yields [6]. The material used for coating the fertilizer preferable to be environmentally friendly macromolecules that can be either natural or semi-natural which help controlling and slowing the release rate [6]. This idea helps saving in economic aspect for reducing the fertilizer apply, watering and frequency of labor for application as needed only in growth season for plants. Moreover, inhibition of nutrient loss, hazardous emissions, dermal irritation, inhalation problems, seed toxicity, leaf burning and provide longer water retention that can be done with the usage of (CRF). However, some of the coating materials are not biodegradable such as polymer based coating materials which will result new pollution to the environment. However, further studies are required to improve the CRF to adapt in various temperature, ambient moisture, bioactivity of the soil and wetting and drying cycles of the soil that affecting the release rate of the nutrients [6].

Some examples will be discussed based on other researchers' studies in lab scale for controlled release formulation with using urea as active ingredient to determine whether it is adaptable in both economically and environmentally ways. The usage of sulfur had been studied as it alone is not able to use as a coating material. However, with the mixture of sealants, binders, plasticizers and protective agents in the formulation to provide coating effects, the process complexity and costs increases [6]. Studies of polymer/superabsorbent materials as coating formulation gives better result in controlled release and water retention, but the high cost and non-environmental friendly side effects stunted industrial scale production [6]. This leads to the research of using starch based formulation in (CRF) because there is relatively small research quantum is currently studied.

Starch is cheap, widely available, biodegradable and renewable but solely depend on starch with hydrophilic nature, weak hydrogen bonding may not give good mechanical properties, stability, and controlled released for desirable outcome. Sodium alginate, NaAlg, will be introduced into the formulation with the combination of a cross-linker calcium chloride, $CaCl_2$, together providing a suitable adaption to study parameters that affecting the ammonia losses from the urea fertilizer such as temperature, soil moisture, soil pH, soil composition and fertilizer coating composition [7][8]. The sodium alginate has the anionic charged polymer factor playing with the intermolecular interaction with starch macromolecular between hydrogen bonding and weak electrostatics forces and cross-linker calcium chloride has the polymer chain providing crosslinking interaction with alginate chains by Ca^{2+} ions to control the solubility that affected the release rate [9].Sodium alginate is a natural polysaccharide with basic structure of linear unbranched polymers with β-(1→4)-linked d-mannuronic acid (M) and α-(1→4)-linked l-guluronic acid (G) residues that presence of di- or tri- cations that gives thermal stability and act as stabilizing agent [10]. There are few encapsulation researches done with the formulation of starch-derivative-alginate formulation. However, thiram is selected to discuss the parameters in research scoop. Thiram is a type of fungicide use to control fungi in the soil to protect the harvested crops

The formulation of starch-alginate beads was used in encapsulation of thiram fungicide [8]. The formulation of beds was prepared as in Table 1 starch (3-15% w/v), alginate (0.5-2.5%, w/v) and calcium chloride (0.1-0.5M) to study their effects on equilibrium swelling, bead size, yield and physical structure etc [8].

Table 1: Formulation Parameters for the Production of Starch-Alginate-Ca^{2+} beads [8]**.**

Formulation Code	Starch (%, w/v)	Alginate (%, w/v)	Thiram (mg)	Crosslinker Concentration (M)	Beads Formed (g)	Yield (%)
SA1	3	1	30	0.1	0.66	64.08
SA2	6	1	30	0.1	1.06	59.55
SA3	9	1	30	0.1	1.42	56.13
SA4	12	1	30	0.1	2.12	64.63
SA5	15	1	30	0.1	2.56	63.52
SA6	12	0.5	30	0.1	No Product	
SA7	12	1.5	30	0.1	2.38	69.79
SA8	12	2	30	0.1	2.44	69.12
SA9	12	2.5	30	0.1	3.18	86.88
SA10	12	1	30	0.2	1.97	60.06
SA11	12	1	30	0.3	2.63	80.18
SA12	12	1	30	0.4	2.7	82.32
SA13	12	1	30	0.5	2.58	78.66

The increase of alginate amount and cross-linker concentration increase the yield of starch-alginate-Ca^{2+} beads due to more available alginate and calcium ions for increasing the crosslinking percentages to form more yields. As starch contents give no much affect to yield of the beads because interaction of between starch and alginate was through hydrogen bonding which limited in SA1 to SA5 formulation where the amount of alginate was constant. As most of the interactions have been used up, no functional moiety was left in alginate to bind the rest of the starch in SA1 to SA5 so not affecting the yield [8]. With amount of alginate of 0.5%, w/v, beads were not formed.

The increasing in starch from 3-12 (%, w/v) with fixed alginate 1 (%, w/v) and cross-linker 1 (M) results in increasing of yield 59.55-64.63%, bead diameter 0.55±0.16 - 1.29±0.23 (mm) and equilibrium swelling 70±5 - 91.67±2.89 (%)[8]. As beyond 12 (%, w/v),

the effect of parameter will be vice versa. Alginate gives same effect as starch in the formulation from 1 - 2.5 (%, w/v), but below 0.5 (%, w/v) of alginate would not give out any product [8]. As for calcium chloride cross-linker, bead diameter and equilibrium swelling (%) will be decreased which due to bivalent calcium ion forming a cavity type of network [8]. However, the thiram properties is different with urea as no precise assumption can be made about the effect of starch-derived-alginate with cross-linker for urea coating.

The studies of swelling properties was done after 24 h of preparation of beads dried in room temperature and results are presented in percentage increase in weight. The increase in starch content in the beads formulation from SA1 to SA5 that can be seen in Figure 14 showed increased the swelling percentage of the beads from 70 % to 93.33 % from starch content of 3 to 15 % (w/v). The hydrophilic nature of starch contribute the swelling properties by increasing the number of interaction of –OH groups between starch and water [8].

Based on Figure 5, the increasing of alginate content resulted in decreasing in swelling percentage from 91.67 % to 76.67 % with SA9 as an irregular trend. This can be explained by increasing in the number of coordination sites cause by increasing in number of COO^- groups based on increasing of alginate content in bead formulation [8].

The increasing of cross-linker concentration from 0.1 M to 0.5 M decreases the swelling percentage of starch-alginate-Ca^{2+} beads from 91.67 % to 65 % because more network were formed in the bead to reduce the surface area and cavity which not retard the absorption ability which can be seen in Figure 6 [8].

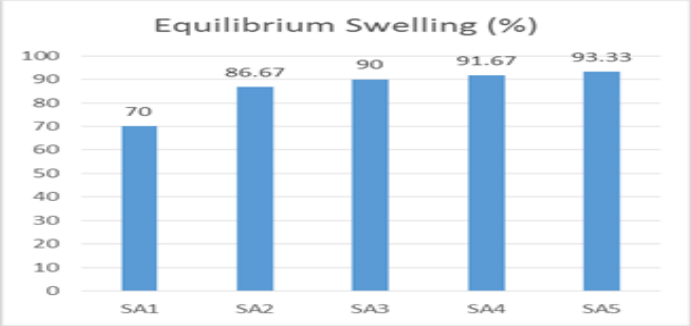

Figure 9: Effect of Various Starch Content in Swelling (%) of starch-alginate-Ca^{2+} beads [8]**.**

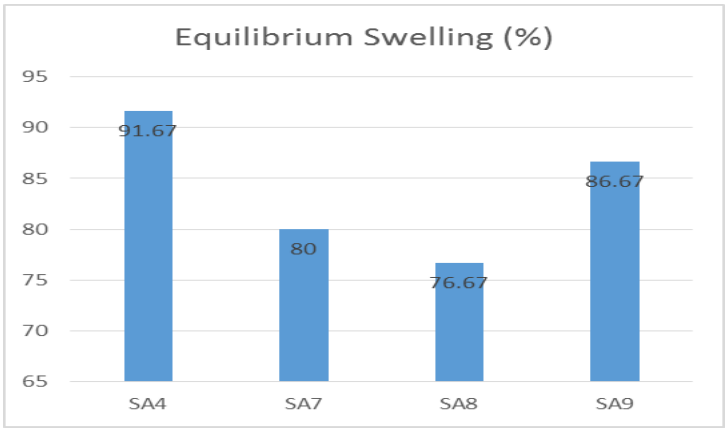

Figure 10: Effect of Various Alginate Content in Swelling (%) of starch-alginate-Ca^{2+} beads [8]**.**

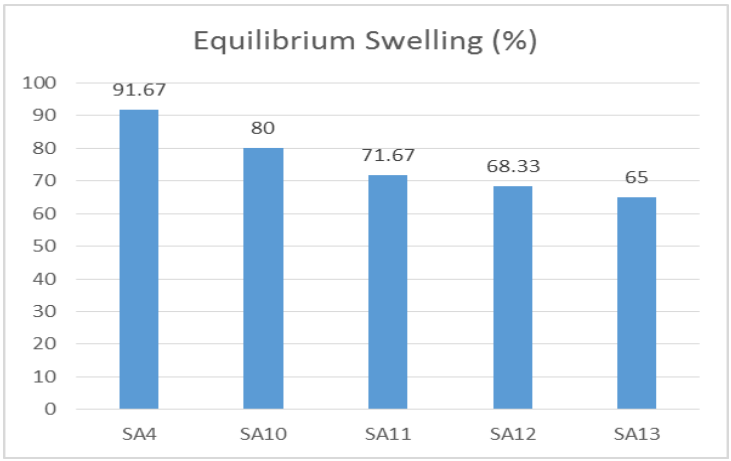

Figure 11: Effect of Various Alginate Content in Swelling (%) of starch-alginate-Ca^{2+} beads [8]**.**

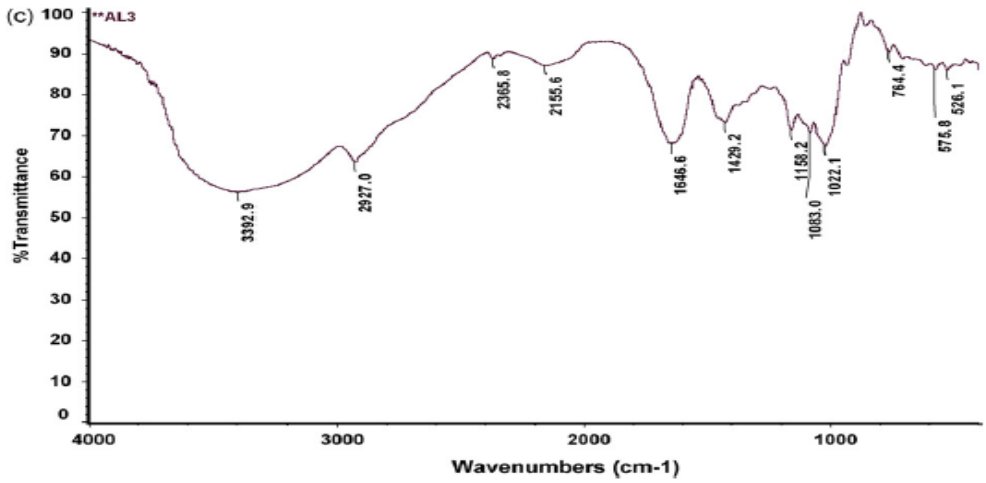

Figure 12: FTIR Spectra of Starch-Alginate-Ca^{2+} bead [8]**.**

For FTIR testing, the characteristics of natural polysaccharides can be seen in figure 7, the strong and broad absorption band can be observed at 3600 and 3200 cm^{-1} due to –OH stretching along some bands in the region of 1200 to 1030 cm^{-1} because of C-O and C-O-C stretching vibration [8]. The vibration modes of pyranose rings of polysaccharides absorption bands can be observed in 930 to 820 cm^{-1} and 785 to 730 cm^{-1} [8]. The carboxylate anion of sodium alginate and calcium alginate shown in Figure 17.a and c is supported by strong asymmetric stretching absorption band at 1650 cm^{-1} and 1620 cm^{-1} and weaker symmetric stretching band around 1420 cm^{-1} [8].

To fully understand the controlled-released-fertilizer of urea, the physical properties, swelling property, yield and morphology of the beads are required to study and analyze in this research [11][12]. The physical properties in this research are affected by this four parameters, sodium alginate (g/L), starch (g/L), calcium chloride cross-linker concentration (M) and urea (M) that will be selected as the manipulate variables for studies [7][8]. One of the objectives of this research is to study the effect of starch-derivative-alginate of urea bead based on the different compositions of starch, sodium alginate, urea and calcium chloride cross-linker content in swelling ratio, erosion % and yield %. Last but not least is to investigate and understand the interaction the physical properties and morphology of the starch-derivative-alginate of urea beads at various concentration of starch, alginate, calcium chloride cross-linker and urea.

2.0 EXPERIMENTAL

2.1 Materials

Sodium alginate, calcium chloride (anhydrous) and urea was purchased from Evergreen Engineering Resources, Malaysia. Sodium alginate was used as receiver, calcium chloride was used as cross-linker and urea will be the active agent. Cassava starch was obtained from SCS Food Manufacturing Sdn. Bhd., Malaysia and distilled water was used throughout the whole experiment.

2.2 Preparation of beads

The formulation of the Starch-Alginate-Ca^{2+} beads was setup with Taguchi Method of Orthogonal Array of L9 by deciding three most affecting level contribute to the study parameters and forming 9 study samples following the Orthogonal Array of L9 arrangement which shown in Table 3. Definite amount of cassava starch, sodium alginate and urea was mixed in 100ml size beaker for 15 min to obtain homogenous solution. After that, syringe with needle size of 12 mm was used to take in the solution and added drop wise into 100 mL of $CaCl_2$ with specific concentration under stirring condition for 15 min. Next, strainer was used to collect the beads formed from the $CaCl_2$ solution and absorb excessive $CaCl_2$ solution from beads surface with filter paper. Lastly, the beads was dried using oven at 40°C for 24hrs and stored in airtight polyethylene bag.

Table 2: The Four Factors Affecting the Behavior of the Beads with Three Possible Levels.

Level	Factor			
	Casava Starch (g/mL)	Sodium Alginate (g/mL)	Concentration of CaCl2 solution (M)	Urea (g/mL)
Low (1)	0.02	0.02	0.2	0.3
Moderate (2)	0.06	0.06	0.5	0.5
High (3)	0.08	0.08	1	0.7

Table 3: Reaction Parameter for the Synthesis of Starch-Alginate-Ca^{2+} beads with Taguchi Method of Orthogonal Array of L9.

Experiment	Factor			
	Casave Starch (g/mL)	Sodium Alginate (g/mL)	Concentration of CaCl2 solution (M)	Urea (g/mL)
SA1	0.02	0.02	0.2	0.3
SA2	0.02	0.06	0.5	0.5
SA3	0.02	0.08	1	0.7
SA4	0.06	0.02	0.5	0.7
SA5	0.06	0.06	1	0.3
SA6	0.06	0.08	0.2	0.5
SA7	0.08	0.02	1	0.5
SA8	0.08	0.06	0.2	0.7
SA9	0.08	0.08	0.5	0.3

2.3 Yield

The percentage of yield of the beads has been calculated as

$$Yield\% = \left(\frac{Amount\ of\ product\ formed\ (g)}{Amount\ of\ reactant\ taken\ (g)}\right) x\ 100 \quad (1)$$

2.4 Bead size measurement

Dried beads for nine samples (SA1 to SA9) were measured for average using 12 cm Vernier Caliper for 6 beads each.

2.5 Characterization of beads

2.5.1 FTIR spectral analysis

Starch-Alginate-Ca^{2+} beads was characterized by Fourier Transform Infrared Spectrophotometer (PerkinElmer Spectrum 100)

2.5.2 Swelling Kinetics

An amount of dried beads were weighted using digital balance (M214Ai, BEL Engineering with a range of 220g with linearity of ±0.003 mg and readability to 0.0001g) before immersed into 50 mL of distilled water. After weighting, beads were immersed at a temperature of 25°C for a range period of time (1h, 2h, 4h, 7h, 24h, 48h, 72h and 168h) for different batch of samples. When the time reaches, strainer was used to collect the beads and using filter paper to remove excessive water and weight using the same digital balance.

$$Swelling\ Ratio\% = \left(\frac{Weight\ of\ swollen\ beads - Weight\ of\ dried\ beads}{Weight\ of\ dried\ beads}\right) x100 \quad (2)$$

2.5.3 Erosion Studies

Erosion of beads is possible because of the water-bio-polymer interaction. To ensure the erosion %, the specific swollen beads based on the immersing time period were dried for 24h to compare with the initial dried beads before immersing into the distilled water.

$$Erosion\ \% = \left(\frac{Weight\ of\ the\ initial\ dried\ beads - Weight\ of\ the\ after\ swollen\ dried\ beads}{Weight\ of\ the\ initial\ dried\ beads}\right) x100 \quad (3)$$

2.5.4 Scanning Electron Microscope (SEM) & Energy Dispersive Spectrometer (EDS)

For SEM (Hitachi Model, S-3400N Variable Pressure SEM; Hitachi Ltd.,Tokyo, Japan) was used to study the morphological characterization of the bead surfaces. Sample were coated with gold before using SEM machine for testing. Energy Dispersive Spectrometer (EDS) was employed to analyze the elements content of the starch-alginate-Ca2+ of urea beads using Cold Field Emission Scanning Electron Microscope (Hitachi Model, SU-8010). The sample was coated with platinum observe with electron beam voltage of 10kV.

3.0 RESULT & DISCUSSION

3.1 Yield %

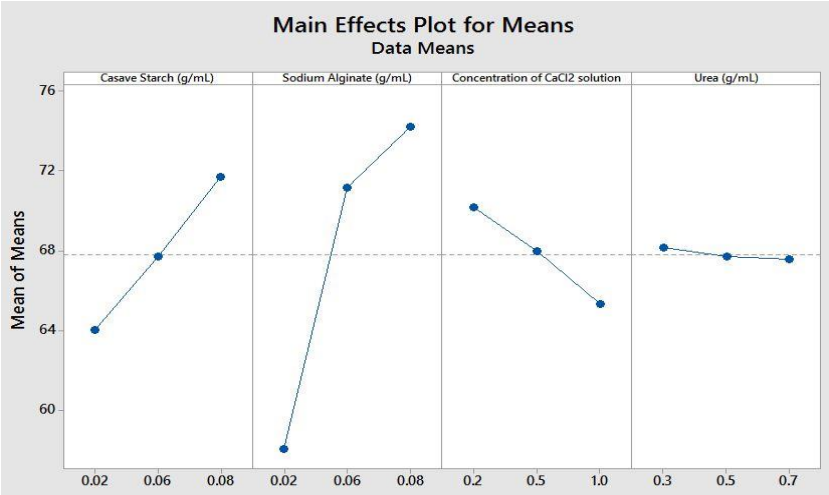

Figure 13: Taguchi Analysis Result of Yield with MiniTab 17.

There are interactions between each parameters for maximize the yield % with using Taguchi analysis. Based on figure 7, sodium alginate and starch at concentration 0.08 g/mL gives highest effect on maximizing the yield %. The amount of sodium alginate and starch must increase together as more functional moiety allow starch to form hydrogen bonding with sodium alginate [8]. If increasing amount of starch while maintaining the amount of sodium alginate at constant, the excessive starch content might not have free functional group to form bonding as fail to maximize the yield %. In this Taguchi interaction analysis method, increasing concentration of calcium chloride cross-linker leads to minimization of yield. When the concentration of starch and sodium alginate is high, only little bit amount of calcium chloride is required as most of the alginate ions are more likely to form bond with starch hydroxyl group. If starch concentration remain constant, calcium ions will be available to cross-linking with alginate ions as maximization of yield % will be possible [13]. Urea do not show much effects on yield %. The best combination to maximize the yield is 0.08 g/mL of cassava starch, 0.08 g/mL of sodium alginate, 0.2 M of $CaCl_2$ and 0.3 g/mL of urea.

3.2 Bead size measurement

Sodium alginate play a major role in providing the spherical shape and diameter of the bead. With low concentration of sodium alginate such as sample SA1, SA4 and SA7 shown irregular shape when dried for 24h. Beads were sticky, having wrinkle surface and forming a cluster which hardly to separate from each other. Three of those samples give very short diameter as longest diameter among this three which is SA7 still shorter than those sodium alginate concentration higher than 0.02 g/mL. Other than the three samples mentioned, all may give spherical bead shape product. From figure 8, sodium alginate has a sharp increment from concentration 0.02 g/mL to 0.06 g/mL as showing it gives huge impact. Starch and $CaCl_2$ do not give interaction and form bonding between each other. Bonding form is mainly depends on sodium alginate as the bridge between starch and $CaCl_2$. Even the concentration of starch and $CaCl_2$ are high but sodium alginate, it is hard to achieve proper spherical shape. The carbonyl group of the sodium alginate form bonding with hydroxyl group from starch and Ca^{2+} ion from $CaCl_2$ cross-linker [8]. Urea has a weak base amides group of lone pair electron tend to form hydrogen bonding with carbonyl group of sodium alginate. However, Ca^{2}+ has a stronger attraction for carbonyl group to form stronger ionic bond compare to amide group from urea to achieve hydrogen bonding [14].

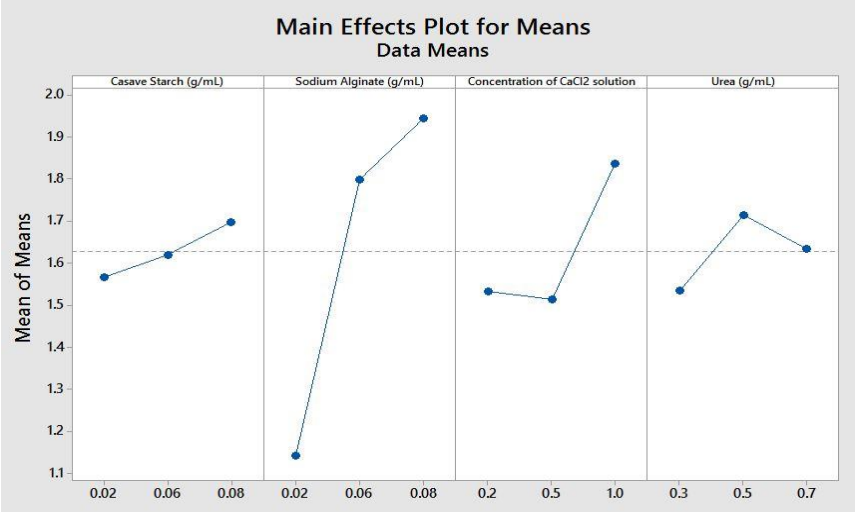

Figure 14: Taguchi Analysis Result of Bead Diameter with MiniTab 17.

3.3 Characterization of beads

3.3.1 FTIR Spectra

Figure 15: FTIR Spectra of Starch-Alginate-Ca^{2+} beads loaded with urea.

The FTIR spectra of urea loaded Starch-Alginate-Ca^{2+} beads for sample SA1 is shown in Figure 9 to ensure the presence of starch, alginate and urea in the bead. 781.7 e functional group identification was done with IR absorption list [15].

The existence of starch content in the bead can be seen from the peak at 3 584.57 cm^{-1} of strong and board O-H stretching as alcohols or phenols 1156.27 iven by glucose unit and 1024.70

1468.29

1024.70 cm^{-1} of strong C-O stretching as carboxylic acid which both is a source of hydrogen ion because the covalent bond between oxygen and hydrogen is very polar as leads to form hydrogen bond with water as providing hydrophilic effect and showing characteristics of natural polysaccharides [16]. The presence of sodium alginate content is shown from peak 3359.59 cm^{-1} of stretching hydroxyl group and medium (-C=C-) stretch of alkene group at 1661.13 cm^{-1} gives better withstand to higher temperature. Due to the non-polar alkene group from sodium alginate, it tends to avoid retard water absorption as the swelling ratio will drop when the concentration of sodium alginate is high. Presence of urea can be proven at peak 1468.29 cm^{-1} of N-H bend of 2^{nd} amines group and 1156.27 cm^{-1} of medium C-N stretch of aliphatic amines group [17]. 2^{nd} amines are more tenable to form hydrogen bond which improve the boiling point of the beads and water attraction, but lower than alcohols group with stronger extent of hydrogen bond. However, increasing of carbons atoms result in chain length increasing as reduces the solubility in water [18]. Aliphatic amines is more likely to be soluble in organic polar solvents such as gasoline and kerosene due to the alkyl chain which showing the immiscibility to the water [18]. Low concentration of urea provide better swelling ratio compared to using high urea concentration.

3.3.2 Swelling Studies

Figure 16: Taguchi Analysis Result of Swelling Ratio with MiniTab 17.

Starch contains the hydrophilic property due to the board and strong O-H stretching of alcohol or phenol group and strong C-O stretching carboxylic as source of hydrogen ion attraction which gives high polarity forming covalent bond with water. By increasing the concentration of starch, swelling ratio may be improved by the increase number of O-H interaction. Calcium chloride ($CaCl_2$) work best at low level concentration. As a crosslinking agent of sodium alginate, bivalent calcium ion creating a cavity type of network resulting reduction in mesh sizes by tightly holding the polymer chain of polymeric bead that retard the movement of water molecules into the bead network [16]. For sodium alginate, increasing of concentration from 0.02 g/mL to 0.06 g/mL shows dropping of swelling ratio %. This can be explained with sodium alginate gives too high polymer fraction as water molecules required to travel longer path and alkene group within it which leads to decrease in swelling ratio. As from 0.06 g/mL to 0.08 g/mL, slight increment is shown in swelling ratio % because the anionic nature of alginate give enhanced repulsion among molecular chain [16]. Due to the hydrophobic aliphatic amines group cause by alkyl chain inhibit in urea, increasing the concentration will result in dropping of swelling ratio [18]. From 0.5 g/mL to 0.7 g/mL of urea provide small contribution in swelling ratio which can be explained by the 2^{nd} amines group with N-H bend that tend to form hydrogen bonding with water. However, limitation is carbon atom in the chain cannot be too high as in vice versa result [17].

3.3.3 Erosion Studies

The erosion % is mainly based on the chemical composition of the surface of the bead and dissolution polymer solvent interaction which is distilled water. From figure 11, it is obvious to see increasing the concentration for starch and sodium alginate at the same time reduces the erosion %. The anionic polymer increasing the number of polar chains causing greater intermolecular interaction between sodium alginate and starch macromolecular, holding it tightly as retarding the penetration of water molecules into surface [16]. Both the components form strong hydrogen bond between carbonyl group of the sodium alginate and hydroxyl

group from the starch. Calcium chloride itself is a high solubility component in water. Increasing the concentration of $CaCl_2$ improves the erosion % as it attracts the water molecules for surface contact when the concentration of starch and sodium alginate is low level concentration as interaction between parameters are required. Ion charges of Ca^{2+} tend to form ionic bond with water molecules, the number of interaction between water molecules and surface of the beads will increase as leading to high erosion %. At high concentration of urea, erosion % seem to increase.

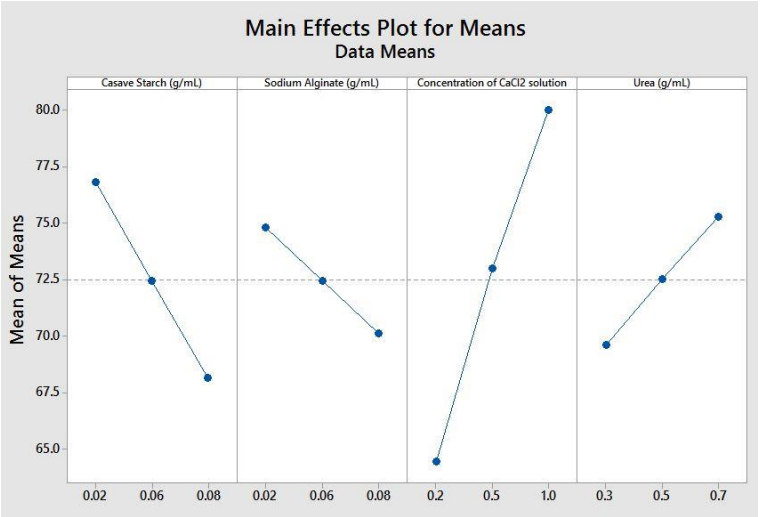

Figure 17: Taguchi Analysis Result of Erosion % with MiniTab 17.

The fact that the 2nd amines group with N-H bend increases with increasing of urea concentration which can be known from swelling ratio section as well [17]. This will cause attraction of water molecules to the bead surface which improved the erosion %.

3.3.4 Scanning Electron Microscope (SEM) & Energy Dispersive Spectrometer (EDS)

The fresh sample SA9 which can be seen in figure 12 (a) shows full spherical structure with surface containing lots of porous-void. This scenario is contributed by starch content acting as filler of the alginate matrix, embedded into the bead surface and retaining their shape as central void [63]. Figure 12 (b) shows clearer surface texture with voids which induce by starch increases tortuous, bumpy surface, roughness and dense packed of structural arrangement to reduce leaching of urea content from the bead. The plane surface was caused by using of clipper to avoid contamination of bead for SEM analysis. In addition, starch may reduce crack formation as no cracking line is shown on the surface and it change the internal.

Comparing both figure 12 (b) and 12 (d), the surface voids structural are more obvious and wrinkle up at the side of the void. This can be explained by the surface layer around the void is going through erosion as it became higher surface layer of the bead as the fresh sample voids are embedded in the surface layer. Moreover, such condition may as well affected during the drying process as all the voids wrinkle up.

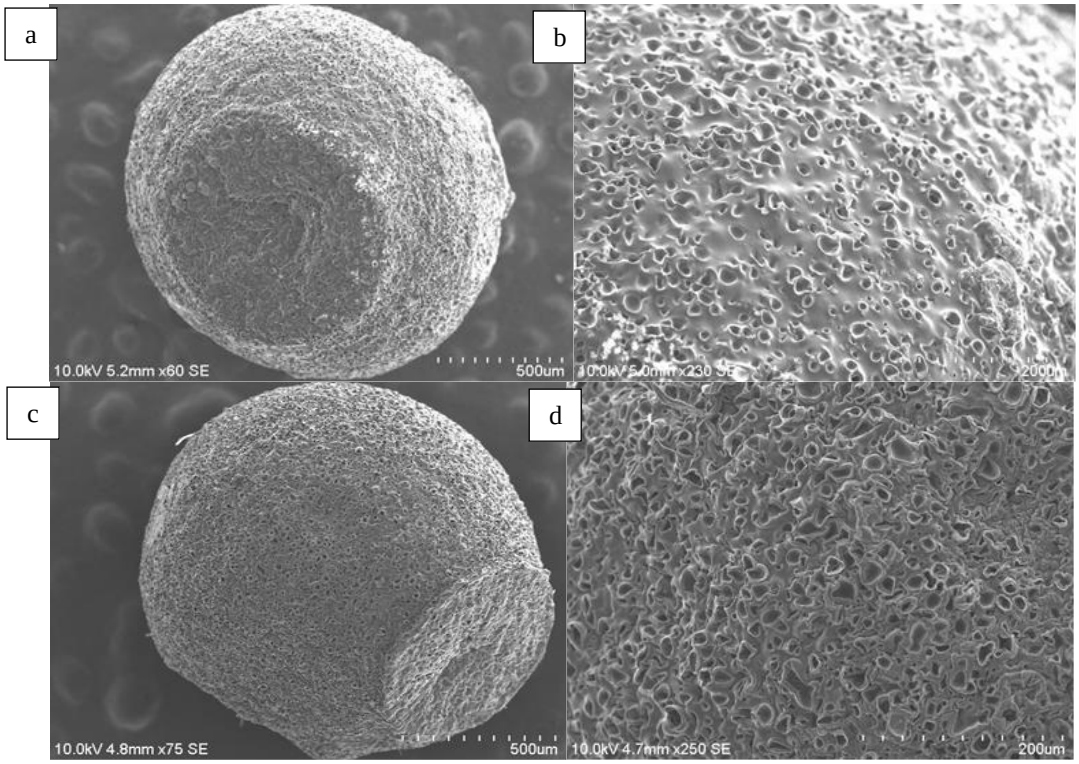

Figure 12: Fresh Sample SA9 of Magnification (a) 60x and (b) 250x and Sample Immersion in water after 1 week time of Magnification (c) 75x and (d) 250x.

For EDS analysis, elemental of carbon and oxygen indicate the presence of starch and alginate on the surface of the bead. Starch is a long polysaccharide contains 20 to 25% linear and helical amylose and 75 to 80% the branched amylopectin [19]. Both amylose and amylopectin itself contain abundant of aldehyde (C=O) carbon molecules showing the abundancy of elemental oxygen and carbon composition. The presence of urea can be indicates by the basic composition of nitrogen [20]. Nitrogen was not found on the surface of the bead. In immersion of water for 24 h, nitrogen will diffuse from high concentration bead external surface to low concentration region water cause by osmotic pressure different.

4.0 Conclusion

The coating of urea is necessary to control the release rate of nitrogen for avoiding losses through denitrification by ammonia-oxidizing bacteria (AOB), leaching due to heavy rain and volatilization. Huge amount of nitrogen loss to the environment will cause a heavy impacts.

The parameters of cassava starch, sodium alginate, calcium chloride and urea do show interaction between each other in this study of controlled-released-fertilizer of urea The parameters are adjustable to achieve the desirable result based on the customers need, for example optimizing the yield %, the concentration for cassava starch is 0.08 g/mL, 0.08 g/mL of sodium alginate, 0.2 M of calcium chloride and 0.3 g/mL of urea. Result in physical properties, swelling property, yield and morphology are majorly depends on the concentration of each parameter. Each parameter has its own unique functional groups which provides different degrees of interaction to form the bead which applicable for erosion %, swelling ratio and size of bead.

FTIR results show the presence of all four components used in bead formulation. SEM analysis gives a promising structure that slightly affected in high moisture condition for

long period of time as will not dissolve immediately as pure urea fertilizer. High surface area which allow water uptake due to the voids surface structure. Last but not least, EDS shows the presence of starch, sodium alginate and calcium chloride composition on the surface of the bead after 24 h in water immersion. No urea can be found on the surface of the bead due to diffusion from high concentration to low concentration water region.

REFERENCES

[1] R. Dupas, M. Delmas, J.-M. Dorioz, J. Garnier, F. Moatar, and C. Gascuel-Odoux, "Assessing the impact of agricultural pressures on N and P loads and eutrophication risk," *Ecol. Indic.*, vol. 48, pp. 396–407, Jan. 2015.

[2] W. Wei, K. Isobe, Y. Shiratori, T. Nishizawa, N. Ohte, S. Otsuka, and K. Senoo, "N2O emission from cropland field soil through fungal denitrification after surface applications of organic fertilizer," *Soil Biol. Biochem.*, vol. 69, pp. 157–167, Feb. 2014.

[3] "EIA - Greenhouse Gas Emissions - Nitrous Oxide Emissions." [Online]. Available: http://www.eia.gov/environment/emissions/ghg_report/ghg_nitrous.cfm. [Accessed: 11-Nov-2014].

[4] R. S. Kalawsky, "The Next Generation of Grand Challenges for Systems Engineering Research," *Procedia Comput. Sci.*, vol. 16, pp. 834–843, Jan. 2013.

[5] "New study puts the 'hell' in Hell and High Water | ThinkProgress." [Online]. Available: http://thinkprogress.org/climate/2010/10/20/206899/ncar-daidrought-under-global-warming-a-review/. [Accessed: 22-May-2015].

[6] B. Azeem, K. Kushaari, Z. B. Man, A. Basit, and T. H. Thanh, "Review on materials & methods to produce controlled release coated urea fertilizer," *J. Control. Release*, vol. 181, pp. 11–21, 2014.

[7] A. B. Pepperman and J. W. Kuan, "controlled release Controlled release formulations of alachlor based on calcium alginate 1," vol. 34, pp. 17–23, 1995.

[8] B. Singh, D. K. Sharma, and A. Gupta, "A study towards release dynamics of thiram fungicide from starch-alginate beads to control environmental and health hazards.," *J. Hazard. Mater.*, vol. 161, no. 1, pp. 208–16, Jan. 2009.

[9] Z. Wu, Y. He, L. Chen, Y. Han, and C. Li, "Characterization of Raoultella planticola Rs-2 microcapsule prepared with a blend of alginate and starch and its release behavior.," *Carbohydr. Polym.*, vol. 110, pp. 259–67, Sep. 2014.

[10] T. Huq, S. Salmieri, A. Khan, R. A. Khan, C. Le Tien, B. Riedl, C. Fraschini, J. Bouchard, J. Uribe-Calderon, M. R. Kamal, and M. Lacroix, "Nanocrystalline cellulose (NCC) reinforced alginate based biodegradable nanocomposite film.," *Carbohydr. Polym.*, vol. 90, no. 4, pp. 1757–63, Nov. 2012.

[11] W. Wang and A. Wang, "Synthesis and swelling properties of pH-sensitive semi-IPN superabsorbent hydrogels based on sodium alginate-g-poly(sodium acrylate) and polyvinylpyrrolidone," *Carbohydr. Polym.*, vol. 80, no. 4, pp. 1028–1036, May 2010.

[12] S. Benavides, R. Villalobos-Carvajal, and J. E. Reyes, "Physical, mechanical and antibacterial properties of alginate film: Effect of the crosslinking degree and oregano essential oil concentration," *J. Food Eng.*, vol. 110, no. 2, pp. 232–239, May 2012.

[13] D. M. Hariyadi, E. Hendradi, T. Purwanti, F. D. G. P. Fadil, and C. N. Ramadani, "Effect of cross linking agent and polymer on the characteristics of ovalbumin loaded alginate microspheres," *Int. J. Pharm. Pharm. Sci.*, vol. 6, no. 4, pp. 469–474, 2014.

[14] W. R. Zheng, Y. Fu, K. Shen, L. Liu, and Q. X. Guo, "Theoretical study on hydrogen bonding interaction of ureas and thioureas with imines," *J. Mol. Struct. THEOCHEM*, vol. 822, no. 1–3, pp. 103–110, 2007.

[15] J. Richardson, "Table of Characteristic IR Absorptions," *Univ. Color. Boulder, Chem. Biochem. Dep.*, vol. 3610, no. m, p. 1, 2011.

[16] A. Roy, J. Bajpai, and a. K. Bajpai, "Dynamics of controlled release of chlorpyrifos from swelling and eroding biopolymeric microspheres of calcium alginate and starch," *Carbohydr. Polym.*, vol. 76, no. 2, pp. 222–231, Mar. 2009.

[17] S. I. Ahmad, I. A. Syed, P. R. Prasad, and A. Ahmad, "Quantitation of urea in urine by Fourier transforms infrared spectroscopy Ibn Sina National College for Medical Studies , Jeddah , Kingdom of Saudi Arabia," vol. i, no. 1, pp. 90–96, 2014.

[18] Boundless, "Amines," Nov. 2014.

[19] R. P. Aquino, G. Auriemma, M. D'Amore, A. M. D'Ursi, T. Mencherini, and P. Del Gaudio, "Piroxicam loaded alginate beads obtained by prilling/microwave tandem technique: Morphology and drug release," *Carbohydr. Polym.*, vol. 89, no. 3, pp. 740–748, 2012.

[20] M. Eichelbaum, A. B. Siemer, R. J. Farrauto, and M. J. Castaldi, "The impact of urea on the performance of metal-exchanged zeolites for the selective catalytic reduction of NOx-Part II. Catalytic, FTIR, and NMR studies," *Appl. Catal. B Environ.*, vol. 97, no. 1–2, pp. 98–107, 2010.

Development of Tissue Engineering Skin Culture System

Nasharudin bin Shaharuddin[1*], Yong Leng Chuan[2], Yap Wei Hsum[3]

[1]*School of engineering, Taylor's University Lakeside Campus, Malaysia*
[2] *School of engineering, Taylor's University Lakeside Campus, Malaysia*
[3]*School of biosciences, Taylor's University Lakeside Campus, Malaysia*

[*]nasharudinshaharuddin@sd.taylors.edu.my

Abstract
The structure of the human skin consists of keratinocytes in the outer layer of the skin and fibroblasts in the medium layer of the skin. Tissue-engineered skin was created as an alternative cure for patients with severe skin cells injuries by culturing keratinocytes and fibroblast in an in-vitro environment and then transferred to the wound site to regenerate the dead skin cells. The patient's period of discomfort can be reduced if the tissue-engineered skin culture time can be reduced. This project involved quantitative research where an innovative culture tray CAD modelling was be done using CAD based software and fabrication of new culture tray was done upon completion. The new culture tray prototype was fabricated out of Acrylonitrile Butadiene Styrene (ABS) using a rapid prototyping machine. This system consists of three section, section one, mechanical section which focuses on the improvement of the conventional culture tray emphasizing on resettling position of different multi-layered cells prior combining utilizing a dual layer removable sliding tray which will reduce the culture time. Section two, the chemical section focusses on the Polycaprolactone (PCL) biocompatibility coating on the internal surfaces of the prototype to make it conducive for cell culture. Lastly, the electrical design section consists of a temperature control. A temperature feedback mechanism is responsible for eliminating the dependency towards an incubator in providing the optimum temperature for cell culture and to reduce irregular growth of cells in the culture tray. Consequently, a new cell culture system with a lower production cost and higher production rate was compared with conventional cell culture technique. Experimentation on the new fabricated culture flask was performed in comparison with the traditional culture tray in terms of heating efficiency and cell density count to assess the efficiency of the prototype. The results show that the prototype heating system is more effective and reliable as compared to conventional method of heating the normal culture tray.

Keywords: skin cell culture, cell culture tray, skin regeneration, Polycaprolactone (PCL), Acrylonitrile Butadiene Styrene (ABS)

1. Introduction

The human skin is responsible for four main purposes that are as a barrier to physical damage, regulation of body temperature, as an immunity system, and lastly prevent the loss of body fluid. When the skin cells are damaged, regeneration of the tissue will only occur if keratinocytes stem cell at that region is adequate. However, chronic scarring and burned wounds prevents this from happening. Hence, Tissue engineered skin was created to culture keratinocytes and fibroblast in an in-vitro environment and then transferred to the wound site to regenerate the dead skin cells. Multi-layer epithelium tissue is cultured by developing fibroblast and keratinocytes seeded onto human fibrin matrix scaffold alongside calcium chloride [1]. Optimization and improvements of skin culture system can be achieved with the application of artificial trypsin derived from animals [2].

The structure of the human skin is mainly keratinocytes in the outer layer of the skin and fibroblast in the medium layer of the skin. At the moment, to engineer skin tissue using in vitro technique, the keratinocytes and fibroblasts are grown separately in a cell culture flask for duration of 3 week and 1 weeks respectively [3]. Once this have been achieved, the fibroblasts cultured cells will be transferred to stack on top of the keratinocytes. Upon success, they will be transferred onto a scaffold that will be implanted on the surgical site of the patient. This exposes the cells to contamination during the resettling stage to combine this two cells. On top of that, the conventional technique of culturing skin cells is time consuming as it requires 2-3 weeks depending on the proliferation rate of the cells and it impose a high cost to the patient and further prolonging the suffering.

The challenges encountered in tissue engineering is to mimic skin cells with proper functionality, durability and at the same time avoiding immunological rejection after implantation on surgical site. Major concern during tissue culture process is the cell-to-cell signalling which defines the specialization in terms of function of that cell itself [3]. In order to achieve this, multiple stages needs to be undergo which contributes to a high cost and time. Moreover, cell culture tray are not reusable thus it needs to be disposed after one session. The commercialize technique of skin grafting which involves firstly culturing the cells in vitro in a petri dish then followed by seeding it onto a scaffold and lastly implantation onto the surgical site imposed low proliferation rate which makes it inefficient and not to forget it has a high cost which does not guarantee 100 percent success rate as it is bound to rejection of the body not only towards the cultured skin graft but also the scaffold itself that may lead to infection.

There are cases where the growth of cells are not uniformly distributed on the substrate surface. This occurrence is due to vibration which causes resonance in the flask that will lead to variations of cell density and leading to wave pattern within the monolayer cell growth [4]. This patterns are called ridges and it can occur even by vibrations made by closing and opening of an incubator door too hard when the flask is in it [4].

Most vertebrate cell grow on an artificial substrate as monolayer when cultured in vitro environment. Thus, the artificial substrate needs to have the correct

charges in order to promote cell adhesion or promote cell attachment factors which will lead to cell spreading and adhesion [4]. Bad cell adhesion will lead to insufficient spreading which will obstruct proliferation of the cells. Majority cell culture vessels nowadays are manufactured from plastic due to simplicity, optical properties, quality and cost. Glass and Pyrex are not regularly used as it contains lead element in it [4].

This research is necessary to bring about improvement to the skin grafting technique currently being used conventionally in the medical field. Optimization of the culture tray is a vital aspect to emphasize on as it will determine the rate of success for the proliferation of skin cell culture. In relation, by improving the conventional culture tray, the medical cost for skin substitution can be reduced to be made more affordable for patients. At the same time, the time required to culture biomimetic skin tissue can be further reduced and the time taken for skin regeneration treatment can be reduced as well.

This project will focus on a few aspects. Firstly, the resettling position of different multi-layered cells prior combining utilizing a dual layer removable sliding stack which will reduce the tendency of cell contamination and to reduce the cell culture time. Secondly, self-independent heating system to achieve the optimum temperature for cell proliferation which will help prevent irregular growth by eliminating the dependency on an incubator. Thirdly, the practicality for storing and space conservation as well as mobility of the culture vessel utilizing stackable design feature.

This project hopes to 3 objectives in comparison with the conventional culture tray, Firstly, a shorter skin cell culture time. Secondly, higher efficiency with regards to cell density count. Thirdly, to substitute the use of an incubator with a more reliable heating system.

2. Methods and Materials

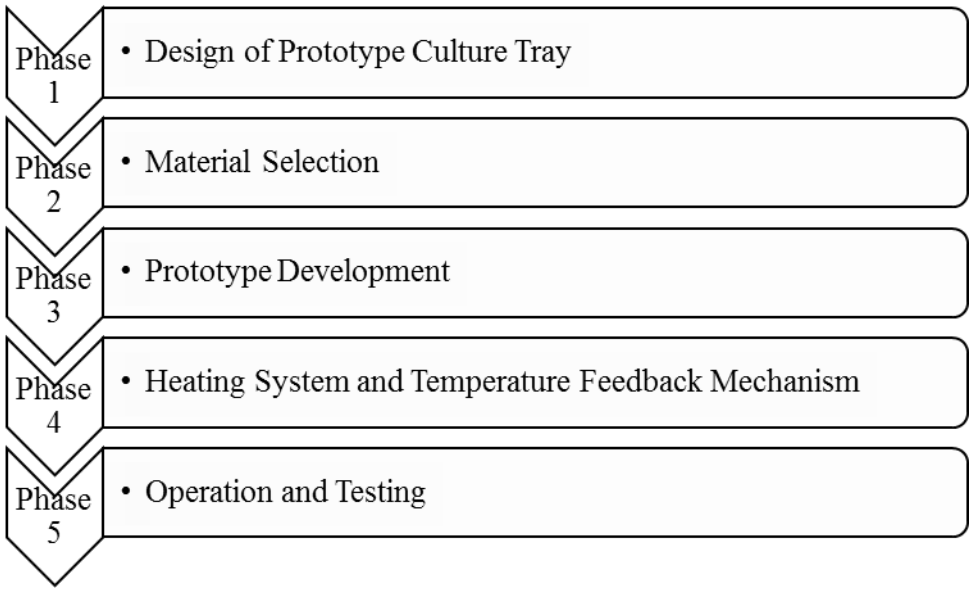

Figure 1. Methodology phases.

The concept behind this research methodology is using the Conceive, Design, Implement and Operate or also known as CDIO based on (Figure 1). This project is divided into two parts

where the Conceive and Design section was performed in the CAD drawing of the prototype and selection of material for the 3D printing process. Implement and operate was performed after the fabrication of the new designed cell culture tray prototype, then assess and compare with the conventional culture tray with the redesigned prototype in aspects of temperature fluctuations and cell density count.

2.1 List of Apparatus Used

Rapid prototyping machine, conventional culture flask, Hemocytometer cell counter, thermocouple, multimeter, Lm-35 temperature sensor, Arduino Uno microprocessor, LCD display screen, fan, and heating coils along with C++ coding inputs which will be key into a laptop having the Arduino software.

2.2 List of Materials Used

Raw Acrylonitrile Butadiene Styrene (ABS), Polycaprolactone (PCL), Human keratinocytes cell lines.

2.3 Design of the Prototype Culture Tray

CAD drawing software is used to simulate the prototype in a 3D architecture format. In order to achieve this, the prototype was drawn using a software called SpaceClaim. This creates a virtual simulation of the prototype appearance and allows improvement or any changes to be made by editing the drawing virtually which will reduce the cost of design. The fabrication process was carried out using the rapid prototyping machine and the prototype was fabricated in ABS

This project can be broken down into 3 parts which is mechanical structural design, chemical biocompatibility coating and lastly electrical system design. For the mechanical structural design, important factors that need to be consider for prototype design including air flow, the internal shape of the prototype, internal spacing and temperature. Secondly, the chemical compatibility coating section is to ensure that the ABS used in the fabrication of the prototype is fully covered with PCL in order to make the surfaces biologically compatible to the cell culture. Lastly, the electrical design system is responsible for eliminating the temperature dependency towards an incubator during the cell culture process. This is because an incubator experiences temperature fluctuations although set at a constant temperature and this affects cell proliferation. In this part, the target is to achieve a controlled and maintained selected temperature of the prototype by utilizing Arduino Uno microprocessor along with C++ coding inputs. The deliverables attained in this stage are CAD drawing of prototype, breakdown analysis of design and selection of chemical coating as well as design of heating system mechanism.

2.4 Material Selection and Prototype Development

Polycaprolactone (PCL) coating to make the surface of the material biocompatible for cell culture as ABS plastic is not biocompatible for cell culture due to its toxicity which will damaged cells that attached to its surface. PCL is a non-toxic, biocompatible and biodegradable aliphatic polyester as reported by Chuan et al. [3]. Experimentation was performed to test the biocompatibility of PCL on human fetal

mesenchymal stem cells and the results obtained was adhesion and proliferation of this cells on PCL surface after 5 days [5]. Besides that, the heating system of this prototype is required to control the temperature within the prototype. This self-independent heating system to achieve the optimum temperature for cell proliferation which will help prevent irregular growth by eliminating the dependency on an incubator. Moreover, the conventional cell culture tray are not reusable thus it needs to be disposed after one session. Hence, the redesigned prototype focusses on reusability as well as practicality for storing and space conservation as well as mobility of the culture vessel utilizing stackable design feature showing sustainability in its design features.

2.5 Heating System and Temperature Feedback Mechanism

In order to maintain the temperature within the prototype at 37 degrees Celsius without the aid of an incubator, a heating system is added along with a feedback mechanism to keep track of the temperature reading within the prototype. The heating system is responsible to heat up the prototype to achieve the optimum temperature for cell culture attachment process which is 37℃. During the detachment process, the temperature within the prototype needs to be reduce to 25℃ and this can be achieved with the heating system as well. The temperature feedback mechanism allows the alteration of temperature within the prototype to the desired value. The heating system and feedback mechanism is constructed utilizing Arduino Uno microprocessor, LM 35 temperature sensor, 2 LCD display screen, fan, and heating coils along with C++ coding inputs which will be key into a laptop having the Arduino software.

2.6 Operation and Testing

The data collected in this project will be obtained experimentally to verify the functionality of the prototype. The time needed to heat up the prototype as compared to a conventional culture tray from 25℃ to 37℃ by the means of an incubator, oven and heating system are recorded and tabulated. In order to view the data clearly, a graph of increase in temperature against time required will be plotted. The variables being altered is the method of heating in order to prove that the heating system of the prototype is more efficient and reliable than the existing method. A thermocouple and multimeter will be used as the apparatus in this experiment to obtain temperature readings inside the prototype while a stopwatch will measure the time taken in intervals of 1 minute to heat up to the desired value. The thermocouple is placed inside the regular culture tray and prototype to detect the temperature changes and the readings are displayed through the multimeter. The experiment is repeated to compare the cooling capability from 37℃ to 25℃ with the same procedures.

In order to prove the cell proliferation rate, the cell density count need to be determined for any cell cultures. The cell culture test will be using human keratinocytes cell lines. The cell density count of the cells grown in the prototype will be compared to the conventional culture tray. In order to perform this experiment, the apparatus and materials needed are ABS prototype, conventional culture flask, keratinocytes cell lines, nutrient medium, and hemocytometer cell counter. The human keratinocytes cell lines will be cultured in 6ml of volume and seeded for 5 days in both trays following cell culture procedures. After 5 days of culture, the cell density count is determined using the hemocytometer. The cell density count is

recorded and comparison will be made based on the observations and results obtained to verify the improvements implemented in the prototype in order to conclude if the prototype have higher efficiency in cell proliferation rate than the traditional culture tray.

3. Results and Discussion

3.1 Acrylonitrile Butadiene Styrene (ABS) Prototype of Redesigned Cell Culture Tray

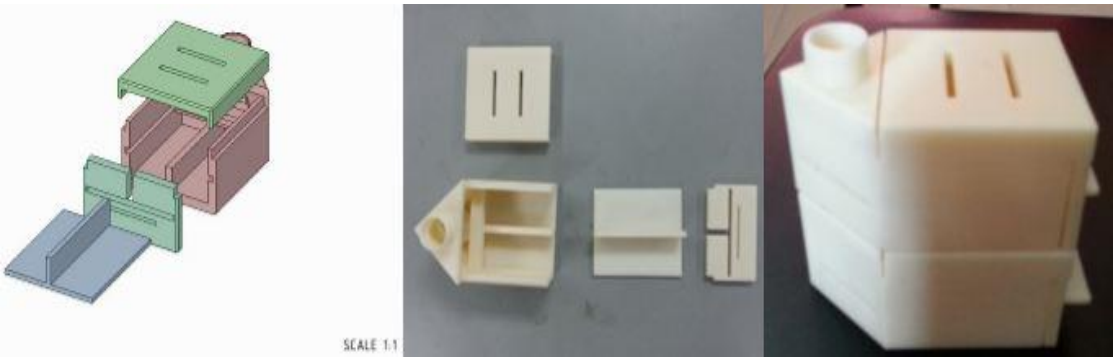

Figure 2. ABS prototype of redesigned cell culture tray.

The redesign of the culture tray targets to maximise space usage by incorporating it with an air flow heating system. The ABS prototype are dual layered whereby the layer can be removed by taking out the sliding tray allowing resettling position of different multi-layered cells prior combining utilizing a dual layer removable sliding stack. The ABS surface was coated with a coating to make the surface of the material biocompatible for cell culture. The coating used was Polycaprolactone (PCL). On the other hand, the slider's surface was coated with N-Isopropylacrylamide (PIPAAm) in order to reduce shear force exerted on the cells during the process of pulling the slider out [6]. The main purpose of the coating is to enhance surface smoothness. This will reduce the chances of damaging the cells when the slider is being pulled out.

The nature of human skin cells itself is a multi-layered structure where several cell culture is vital. This is a key feature needed in skin cell culture as the common practice is that keratinocytes and fibroblast are grown in separate vessel then it is combined manually in a separate culture tray when the cells are mature enough. The slider tray providing the sliding feature for the prototype allows the cells to be combine without the need of interaction thus reducing contamination and physical damage percentage of the cultured cells. By doing this, the proliferation and survival rate is increased and the productivity of cell culture is increased as well as compared to the regular method where the cells are combined manually by transferring them from one tray onto another which is more prone to contamination. The N-Isopropylacrylamide (PIPAAm) coating on the surface of the sliding tray will undertake hydrophilic reaction for cell detachment when temperature is below 32℃ and will undergo hydrophobic reaction when temperature is above 32 ℃ for cell attachment to the surface of the tray. This is to ensure that the removing process of the sliding tray does not damage the cells being cultured which will increase the survival rate of the cells.

The conventional technique of manually transferring and combining the keratinocytes and fibroblast from one culture flask into another increases the mortality rate of the cells and resulting in a longer time needed to achieve the desired cell count. The design of this prototype eliminates the need to manually transfer the keratinocytes onto to fibroblast giving a better efficiency in the resettling stage which will consequently increase the survival rate of the cells resulting in a shorter time required to achieve the desired cell count. Due to that, the time span needed to seed the cells onto the wounded region of the patient is reduced which will reduce the days of suffering for the patient. In addition, using this system the mortality rate of cells is reduced which will reduce number of cells to be cultured in order to achieve the desired cell count and thus reducing the cost of the treatment. Hence, this system will benefit doctors to treat higher number of patients as well as reduce the medical fee and time frame of the treatment for patients.

The practicality for storing and space conservation as well as mobility of the culture vessel utilizing stackable design feature. The prototype is capable of stacking upon one another in order to be user friendly during transportation or handling as well as conserve space during storage.

Due to the limitation of the rapid prototyping machine, the thickness of the prototype parts was set in a range between 2 mm to 5 mm. The fabrication process is incapable of fabrication the prototype parts with thickness of less than 2 mm as it becomes brittle and crack upon dropping or when bending force is applied. The presence of gills in various regions of the prototype allows air to flow in and out in a natural manner without the need to a blower or any device to force air into the vessel. This is needed as most cells need to be exposed to abundant oxygen in order proliferation to occur. The sliding tray feature is infused in the design to allow keratinocytes and fibroblast to combine when prepared by pulling the slider tray out horizontally as well as to eliminate the need to manually layer this two cells together in a separate culture flask. The top cover piece is made removable to allow the user to observe the cultured cells and to ease cell counting as ABS material is not optically transparent. Nonetheless, to incorporate sustainable design in the ABS prototype cell culture tray, the fabrication of the prototype were separated in four individual components to ease cleaning and sterilization process in the cell culture procedure. This allows the ABS prototype tray to be reused unlike the conventional cell culture flask which is limited to one time usage and must be disposed after one session of cell culture.

The prototype design targets cell proliferation which means the vessel interior environment must be biocompatible and optimum for cell spreading and growth. Thus, the two key criteria being considered in the selection of material for fabrication is specific heat capacity and surface roughness as well as chemically stable. In order to achieve that, the prototype was suggested to be fabricated by using polystyrene via injection moulding technique as its properties fall in the desired criteria plus polystyrene is optically transparent which provides easier means for observations and data collection. In addition, Polystyrene is dimensionally stable which makes it physically rigid and tough. Most disposable laboratory apparatus such as petri dish are made from polystyrene. Polystyrene have good chemical resistance against acid and bases but is soluble in halogen and aromatic solvents as well as having a high melting

point of 240℃ which will allow it to undergo sterilization in autoclaving machine at temperatures between 121℃ - 134℃ as compared to the ABS prototype which is unable to do so as its melting point is 105℃ and the PCL coating which have a melting point of 60 ℃ [7]. Both elements will melt if they were to undergo sterilization in the autoclaving machine which was mentioned earlier in the methodology section. Although polystyrene is not naturally biocompatible for cell culture but it can be made so by corona discharge, plasma gas or gamma radiation in order to create a wettable surface conducive for cell culture. This is usually performed during the injection moulding process for production of the conventional culture tray [10]. However, due to the limitation of budget, ABS plastic was used instead.

The regular method to heat up the culture tray is using an incubator where air is heated using convection concept and culture vessel placed in the incubator is heated using the hot air via conduction. Conduction can be modelled using the Eq. (1) below:

$$\dot{Q}conduction = kA\ \frac{\Delta T}{X} \tag{1}$$

$$\dot{Q}convection = hA\Delta T \tag{2}$$

Where K is material conductivity, A is the total surface area of contact, ΔT is the temperature difference within the culture vessel and the outside environment and lastly x is the wall thickness. Theoretically, the thinner the wall thickness, the greater the heat flux of the culture tray and heat transfer via conduction is greater than compared to means of convection shown in Eq. (2).

When incorporating Eq. (1) in the design, ΔT is the same for both ABS prototype and the normal culture tray because it is heated together and by the same method of heating. The variables being altered in the equation is K, A, and lastly x. In order to maximise $\dot{Q}conduction$ output, three criteria needed to be satisfied which was a larger (K) and (A) value along with a small x value. However as mentioned before, the limitation of RPM limiting the ABS prototype thickness which is x to a minimum of only 4 mm. As for the normal culture tray its thickness, (x) is 1 mm. To compensate for the ABS prototype having a higher x value, the thermal conductivity of ABS was higher that is 0.17 W m^{-1} K^{-1} as compared to polystyrene which was 0.115 W m^{-1} K^{-1}. Hence, to increase $\dot{Q}conduction$, the ABS prototype was designed with a higher contact surface area, to allow a higher output of conduction. The ratio comparison below shows the $\dot{Q}conduction$ for both culture trays.

$$Total\ surface\ area\ of\ ABS\ prototype = 0.02033\ m^2$$

$$Total\ surface\ area\ of\ normal\ PS\ culture\ tray = 0.007425\ m^2$$

$$k_{ABS} = 0.17\ Wm^{-1}K^{-1}$$

$$k_{PS} = 0.115\ Wm^{-1}K^{-1}$$

$$x_{ABS} = 0.004\ m$$

$$x_{PS} = 0.001\ m$$

$$\dot{Q}conduction_{ABS} = (0.17)(0.02033)\frac{\Delta T}{0.004}$$

$$\dot{Q}conduction_{PS} = (0.115)(0.007425)\frac{\Delta T}{0.001}$$

$$\frac{Qconduction_{ABS}}{Qconduction_{PS}} = \frac{0.864\ \Delta T}{0.853\ \Delta T}$$

$$\dot{Q}conduction_{ABS} : \dot{Q}conduction_{PS} = 0.864\ W/(m.K) : 0.853\ W/(m.K)$$

Referring to the calculations above, although the ratio difference of $\dot{Q}conduction$ between the ABS prototype and normal culture tray is very small but the significance effect could be seen through the results obtained during the heating test whereby the ABS prototype heats up faster than compared to the normal culture tray in various methods of heating. This is solely due to its higher thermal conductivity of ABS plastic as compared to polystyrene material.

However, the prototype design is not based on means of convection instead it is directly heated by channelling hot air towards it resulting in a faster and better heat transfer than common practice of using incubator. Thus, the heat transfer applies equation based on velocity of fan whereby heat flow is directly proportional to fan speed. Increasing fan speed will increase heat transfer to the prototype. The general formula relating heat transfer and fan speed is illustrated in Eq. (3) below whereby Q_1 is the volume flow capacity of hot air initially when the wheel velocity of the fan is N_1. In addition, Q_2 is the new volume flow capacity of hot air when the fan speed is changed to N_2.

$$\frac{Q_1}{Q_2} = \frac{N_1}{N_2} \quad (3)$$

3.2 Heating of Prototype

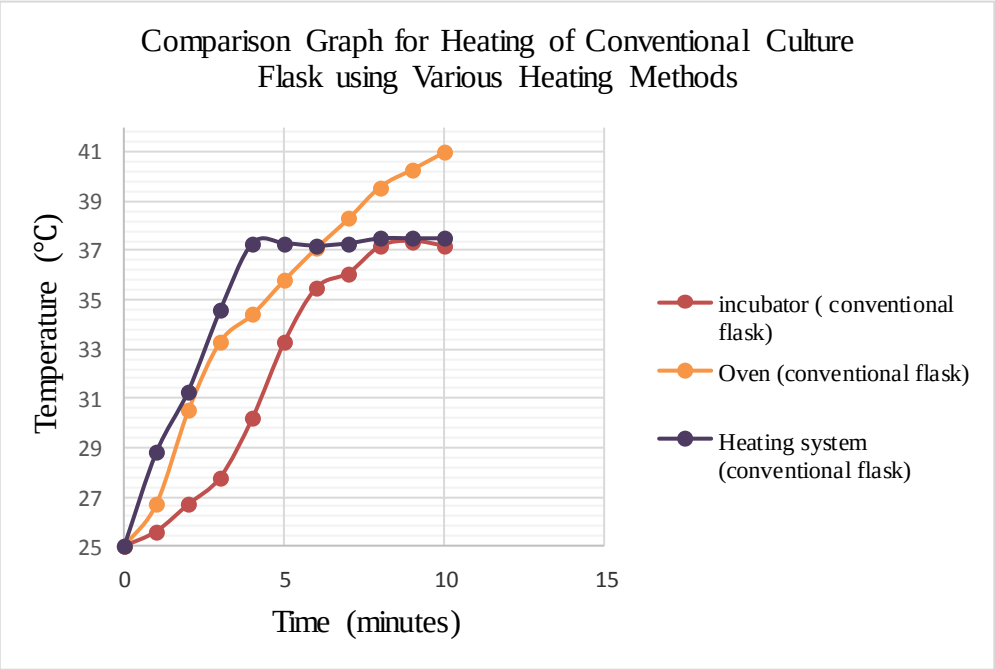

Figure 3. Comparison graph for heating of conventional culture flask using various heating methods.

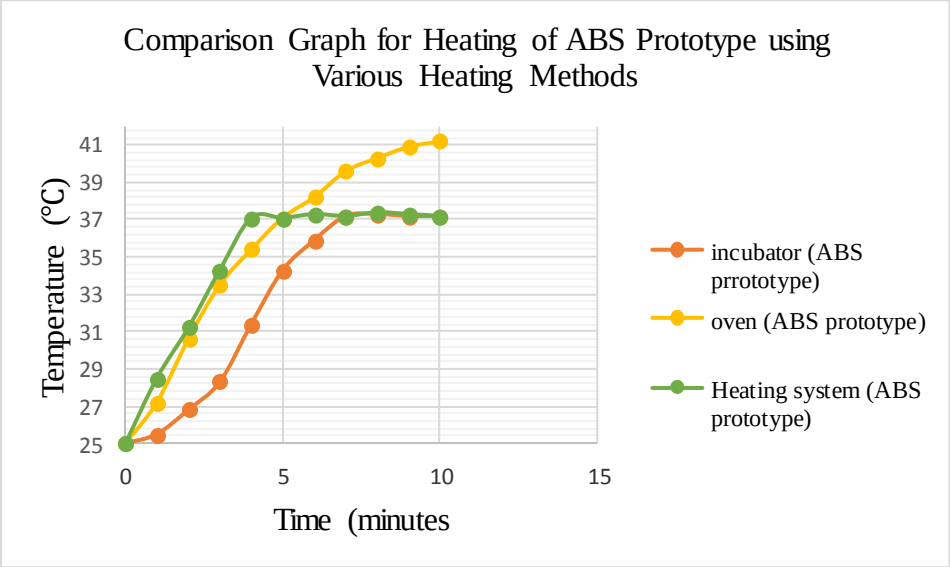

Figure 4. Comparison graph for heating of ABS prototype using various heating methods.

Based on (Figure 3) and (Figure 4), the time required to heat up the conventional polystyrene culture tray to 37 ℃ using an incubator was an average of 8 minutes while the ABS prototype had an average time of 7 minutes. This shows that the ABS prototype heats up faster in an incubator by a difference of 1 minute. Secondly, the time required to heat up conventional polystyrene culture tray to 37 ℃ using an oven was an average of 6 minutes while the ABS prototype had an average

time of 5 minutes. This shows that the ABS prototype heats up faster in an oven by a difference of 1 minute similar to that of the incubator. Lastly, the time required to heat up the conventional polystyrene culture tray and ABS prototype culture tray to 37 ℃ using the prototype heating system was an average of 4 minutes for both.

Based on the results obtained, the similarity that can be observed was the ABS cell culture tray prototype heats up faster as compared to the conventional polystyrene tray when tested with various heating methods. This is because the thermal conductivity of ABS is higher as compared to polystyrene which are 0.17 W m^{-1} K^{-1} and 0.115 W m^{-1} K^{-1} respectively [7]. Due to that, the rate of thermal energy passing through ABS per unit thickness is much higher than polystyrene. As a result, the heat from the incubator is transmitted faster through the walls of ABS plastic than compared to polystyrene [8]. The thermal conductivity of the ABS prototype is higher than the conventional polystyrene flask makes the ABS prototype thermal properties more efficient during the heating process.

An oven is not suitable for the heating of the culture trays because the maximum temperature detected within both the culture trays was 41 ℃ although the temperature of the oven was set to only 37℃. Hence, the use of an oven in cell culture process will exceed the optimum incubation temperature of skin cells and eventually kill the cells due to the exceeded temperature.

Based on (Figure 3) and (Figure 4), the graph line shows irregular temperature variations between 5 to 8 minutes when the heating of the ABS prototype and conventional culture tray is heated using an incubator. This is not suitable for cell proliferation as it will promote irregular growth on the surface of the culture trays.

The prototype heating system allows the cell culture to achieve the desired temperature at a shorter time and maintained it at the optimum temperature of 37℃. This can be seen in the graph in (Figure 4) where the temperature of both culture trays was constant at 37 ℃ after the fourth minute. The graph plotted shows a steady and gradual increment in temperature with low temperature variation as the time increases before it remains constant at 37 ℃ and this will prevent large temperature leap as well as prevent irregular growth of the cells during the heating process in line with the objectives of this project to reduce the dependency on an incubator and to improve the efficiency of the cell proliferation stage.

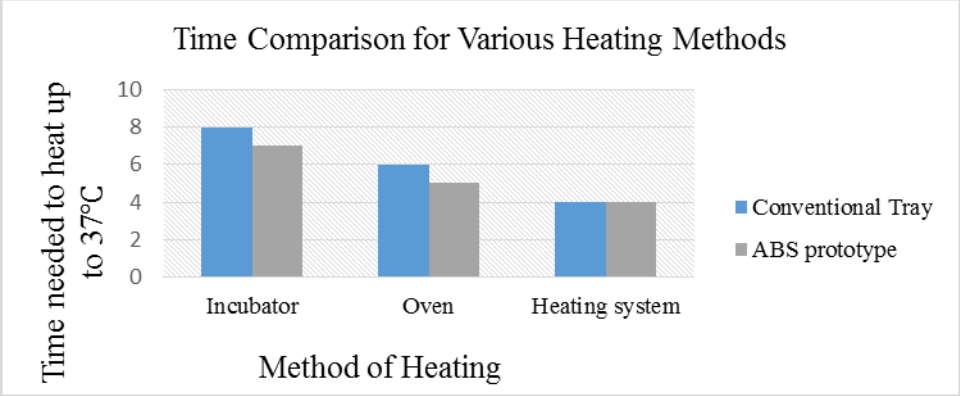

Figure 5. Time comparison bar chart for various heating methods.

Based on (Figure 5), the time needed to heat both the prototype culture tray and the conventional culture flask is the fastest using the heating system prototype, followed by the oven and lastly the incubator. The time taken to heat up both cell culture trays is doubled when using an incubator as compared to the heating system prototype. The incubator take 8 minutes to heat the conventional culture tray while only 4 minutes when using the heating system prototype. As for the ABS culture tray prototype, the incubator requires 7 minutes and the heating system did it in 4 minutes. The prototype heating system is more efficient than the incubator by 50 percent. Thus, the prototype heating system is more efficient than the incubator by 50 percent because cell proliferation is lower at low temperatures which means that if the cell culture tray is able to achieve the temperature of 37 ℃ in a shorter time, the proliferation stage will occur faster at its maximum capability. The design of this prototype tray and the heating system is also applicable to other cell culture stages although the project targets the improvement in the cell proliferation stage only. Nonetheless, the human skin cell structure requires multiple culture process as it is a multi-layered structure and due to that, the accumulated total time to culture the desired cell density will reduce if every stage is reduced by 4 minutes.

The limitation of the heating system is that it is not a closed and expose the cells to bacteria contamination. Thus, the air entering the cell culture trays needs to be pre-filtered with a 0.2μm porosity beforehand. Systematic error resulting from the absence of maintenance of the incubator and oven was reduced by repeating all experiments 3 times and the average readings were calculated which was plotted on the graph.

3.3 Cooling of Prototype

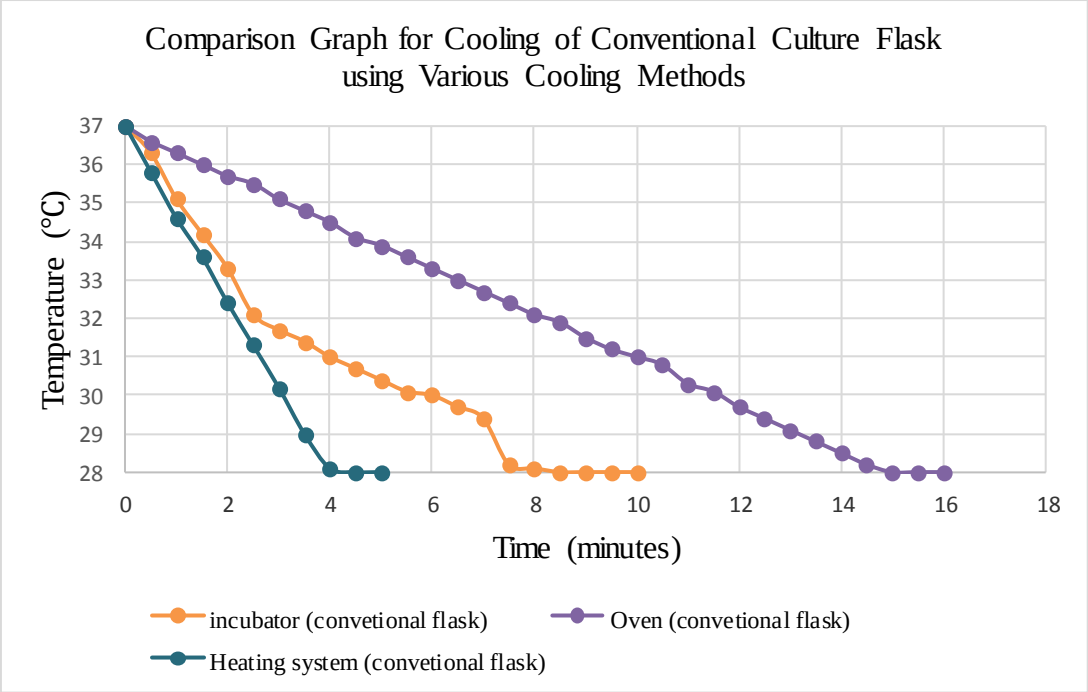

Figure 6. Comparison graph for cooling of conventional culture flask using various cooling methods.

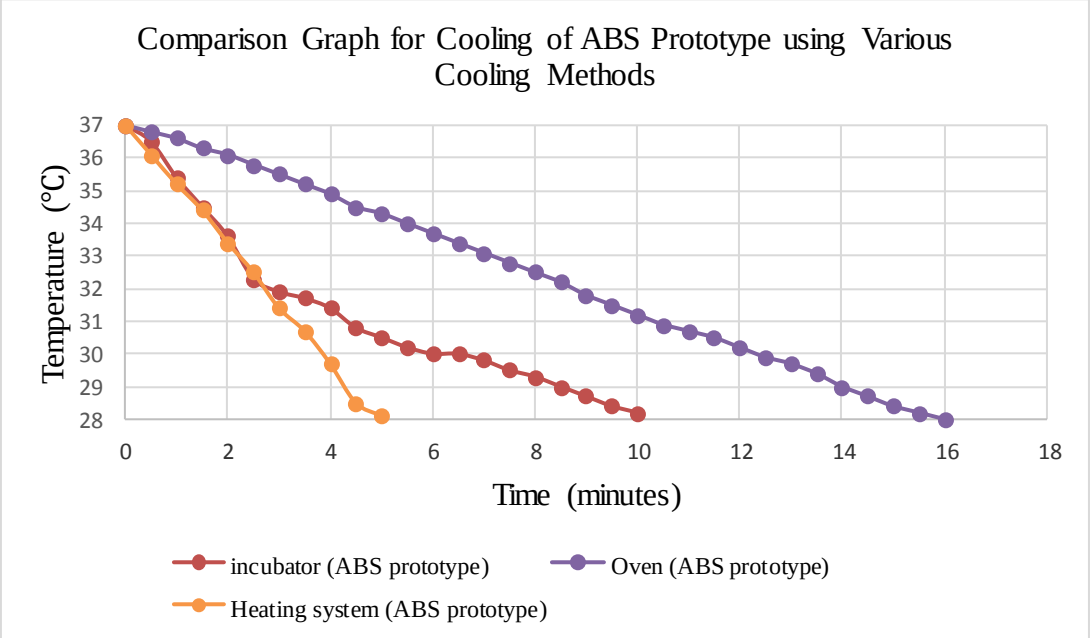

Figure 7. Comparison graph for cooling of ABS prototype using various cooling methods.

The comprehensive coding for the entire system is by having a heating system and temperature feedback mechanism. In order to maintain the temperature within the prototype at 37 degrees Celsius without the aid of an incubator, a heating system is added along with a feedback mechanism to keep track of the temperature reading within the culture trays. The automated heating system was designed for the heating of the ABS prototype to achieve the optimum temperature of 37℃ and maintained it until the switch is turned off which the system will perform the cooling process of the ABS prototype to achieve room temperature for the cells detachment process.

Based on (Figure 6) and (Figure 7), the time required for cooling the conventional polystyrene culture tray to 28 ℃ using an incubator was an average of 7.5 minutes while the ABS prototype had an average time of 10 minutes. This shows that the ABS prototype cools slower in an incubator by a difference of 2.5 minute as compared to the conventional culture tray. Secondly, the time required for cooling conventional polystyrene culture tray to 28 ℃ using an oven was an average of 15 minutes while the ABS prototype had an average time of 16 minutes. . This shows that the ABS prototype cools slower in an oven by a difference of 1 minute. Lastly, the time required for cooling the conventional polystyrene culture tray to 28 ℃ using the prototype heating system was an average of 4 minutes while the ABS prototype had an average time of 5 minutes. . This shows that the ABS prototype cools slower by a difference of 1 minute compared to the normal culture flask.

The reason behind the time difference of the cooling process between the conventional culture tray and the ABS prototype culture tray is because of their specific heat capacity property. The higher the specific heat capacity of the material, the ability to store heat will be greater thus the increase and decrease in temperature will occur slower. Based on (Figure 6) and (Figure 7), the comparison shows that in all of the method of cooling, the conventional culture tray releases heat more rapidly

than compared to the ABS prototype culture tray. This is because the specific heat capacity of polystyrene is lower than that of ABS material which is 1200 j/kg-k and 1400 j/kg-k respectively [7]. The specific heat capacity of the ABS prototype is higher than the conventional polystyrene flask makes the ABS prototype tray cooling process more consistent and gradual decrement in temperature with low temperature variation as the time increases and this will prevent large temperature drop to prevent irregular detachment of cells during the cooling process [6]. Due to that, this makes the ABS prototype thermal properties more efficient during the cooling process.

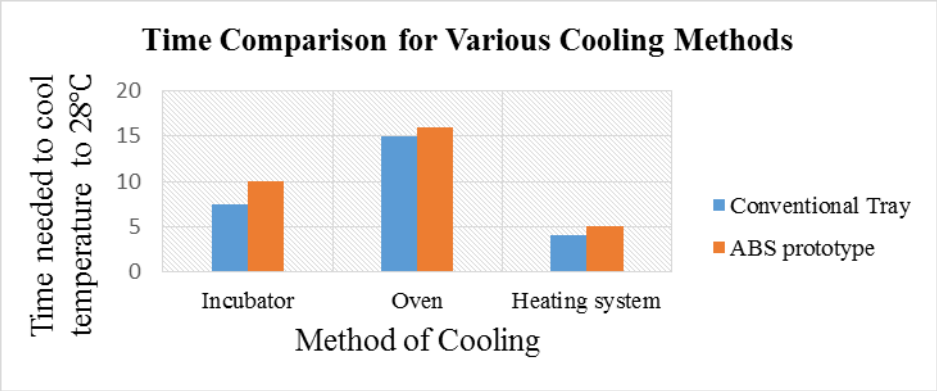

Figure 8. Time comparison bar chart for various cooling methods.

Based on (Figure 8), the cooling process occurs the fastest using the heating system prototype followed by the incubator and lastly the oven. The time taken to cool both cell culture tray is doubled when using an incubator as compared to the heating system prototype. The incubator take 7.5 minutes to cool the conventional culture tray while only 4 minutes when using the heating system prototype. As for the ABS culture tray prototype, the incubator requires 10 minutes and the heating system prototype did it in 5 minutes. The cooling process efficiency is increased by 50 percent and this increases the efficiency of the cell detachment process resulting in a reduction of time in the cell culture process in line with the objective of this project.

The limitation of the heating system is that it is not a closed system and there is will contact with atmospheric air which encourage bacteria contamination of the cells that can result in the death of the cells being cultured. The air entering the cell culture trays needs to be pre-filtered with a 0.2μm porosity beforehand to remove any foreign entities and this should be applied during the heating and cooling process.

There also might be errors in the reading obtained due to systematic error resulting from the absence of maintenance of the apparatus used in the heating and cooling experiment. In order to reduce the systematic error in the results, all experiments was repeated 3 times and the average readings were calculated which was plotted on the graph.

3.4 Cell Viability Count

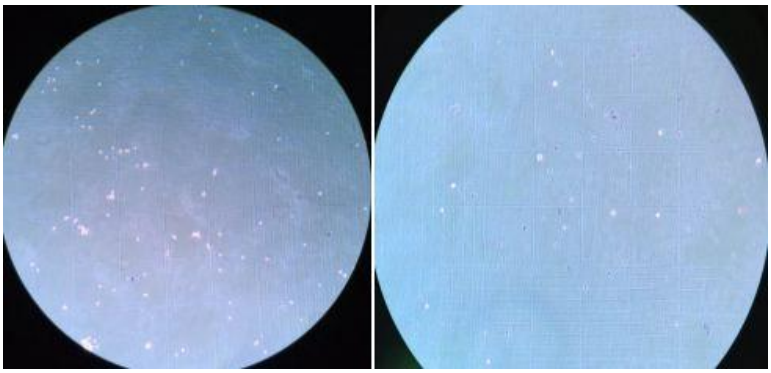

Figure 9. Microscopic view of cells in (left) normal culture flask and (right) ABS prototype.

The experiment was performed to calculate cell viability to compare the percentage of cell viability of the normal culture flask and the ABS culture tray prototype. Trypan blue was used as a staining agent to stained dead cells while viable cells remained white and cell counting was performed using hemocytometer which was viewed under an inverted microscope with 40 times magnification.

Based on (Figure 9), the total viable cell obtained using the normal culture flask was 221 and zero dead cell. The total viable cells obtained using ABS culture tray prototype was 14 and 6 dead cells.

The equation used to calculate percentage cell viability can be seen in Eq. (4) and Eq. (5). The percentage viability calculated for the conventional culture flask was 100% and for ABS prototype was 70%. The difference of percentage cell viability between both trays was 30% showing a 30% reduced efficiency in cell proliferation of the ABS prototype as compared to the conventional culture flask because cell viability is linked directly to cell proliferation. As a result, cell proliferation rate decreases when number of viable cells decreases [9].

When the percentage cell viability is at 100%, the cells seeded are proliferating at its maximum capability which is obtained in the conventional culture flask. As for the ABS prototype, 70% cell viability means the cells seeded in the ABS prototype are proliferating at only 70% which is 30% lower than its maximum capability. In short, lower number of viable cells will cause lower proliferation rate resulting in reduction in percentage cell viability [9].

$$Total\ Cell\ Count = Viable\ Cell\ Count + Dead\ Cell\ Count \tag{4}$$

$$\%\ Cell\ Viability = \frac{Viacle\ Cell\ Count}{Total\ Cell\ Count} \times 100\% \tag{5}$$

The reduction in cell viability by 30% was due to the limitations exerted by the prototype. Firstly, all vents in the ABS prototype needs to be sealed with porosity of 2µm to prevent bacterial contamination of the seeded cells. Secondly, the ABS prototype cannot undergo sterilization using autoclaving machine as the high temperature will exceed the melting point of the Polycaprolactone (PCL) coating

resulting in melting of the Polycaprolactone (PCL) attachment. Due to that, ethanol solution was used to sterilise the ABS prototype which may not fully removed all foreign entities. The leakage of the ABS prototype due to the limitation of the rapid prototyping machine where the prototype needed to be fabricated in four different components and assembled. This resulted in the leakage of the cells and nutrient medium affecting the number of cells seeded. Lastly, the uneven application of the Polycaprolactone (PCL) caused irregularities in the surface for cell attachment to be optimum and this resulted in reduced number of viable cells in the ABS prototype which was a factor proven by Freshney [4]. Due to this factors, the total number of viable cells seeded in the ABS prototype was lower resulting in a lower percentage cell viability as compared to the conventional culture flask.

Furthermore, Random error caused by human in procedures of the cell culture and manual calculation of number of cells contributed to the large difference in the number of viable cell count between both culture trays. This can be improved by performing the experiment three times to obtain an average cell count in order to reduce this error.

4. Conclusions

As a conclusion, this project have reduced the cell culture time by implementing the heating system in its design. The heating system was capable of reducing the heating and cooling process of cell culture to 4 minutes and 5 minutes respectively resulting in a 50% increased efficiency as compared to the conventional method as well as prevent irregular growth of the cells during the heating process in line with the objectives of this project to reduce the dependency on an incubator and to improve the efficiency of the cell proliferation stage through a shorter culture time. Nonetheless, the accumulated total time to culture the desired cell density will reduce if every stage is reduced by 4 minutes. The design of the ABS culture tray prototype eliminates the need to manually transfer the keratinocytes onto to fibroblast giving simplification of cell culture process and a better efficiency in the resettling stage resulting in a shorter time required to achieve the desired cell count and reducing treatment cost. Consequently, reducing days of suffering for patients and benefit doctors to treat more patients. Improvements can be made in the future to overcome the limitations experienced by making the prototype a closed system prevent bacterial contamination of seeded cells. As for future works, the fabrication the prototype using polystyrene material via injection moulding process and chemical coating of internal surface of prototypes to allow non-anchorage cells to be cultured in the prototype and proliferate in suspension as well as testing of the effectiveness of the slider tray of the ABS prototype.

Acknowledgment

The authors would like to acknowledge Taylor’s university for funding the necessary research grant and facilities to conduct the research of this project 2ME10.

References

[1] Mazlyzam, A. L. (2007). Burns: Reconstruction of living bilayer human skin equivalent utilizing human fibrin as a scaffold. *Elsevier Ltd, 1*(33), 355-363.

[2] Manira, M. (2013). Comparison of the effects between animal-derived trypsin and recombinant trypsin on human skin cells proliferation, gene, and protein expression. *Cell Tissue Bank, 1(1),* 1-10.

[3] Hoque, M. E, Chuan, Y. L, Pashby, I. (2011). Extrusion based rapid prototyping technique: An Advanced Platform for Tissue Engineering Scaffold Fabrication. *Wiley Periodicals Inc, 97(2),* 83-87.

[4] Freshney, R. I. (2010). Culture of Animal Cells. (6th Ed.), *A Manual of Basic Technique and Specialized Applications* (pp. 89-98). Hoboken, New Jersey: John Wiley and Sons Inc.

[5] Hoque, M. E, Chuan, Y. L. (2011). Desktop Robot Based Rapid Prototyping System, *An Advanced Extrusion Based Processing of Biopolymers into 3D Tissue Engineering Scaffolds, Rapid Prototyping Technology: Principles and Functional Requirements* (pp. 106-115). Croatia, Rijeka: InTech publications.

[6] Palsson, B., Jeffrey, A., Hubbell, Plonsey, R., Bronzino, J. D. (2003). Principles and Applications in engineering series. (2nd Ed.), *Tissue Engineering* (pp. 4-11). Boca Raton, Florida: CRC Press LLC.

[7] Rosata, D. V., Roasata, D. V., Rosata, M. V. (2004). *Plastic Product Material and Process Selection Handbook.* (pp 40-67). London, United Kingdom: Elsevier science technology.

[8] Zeiger, A. S., Hinton, B., Van Vliet, K. J. (2013). Why the dish makes a difference: Quantitative comparison of polystyrene culture surfaces. *Elsevier Ltd, 9*(7), 7354-7361.

[9] Li, W. et al. (2008). Air Exposure: *Induced Squamous metaplasia of Human Limbal Epithelium,* National Center for Biotechnology Information, *49*(1), 154-162.

[10] Mark, J. E. (2009). *Polymer Data Handbook,* second edition. New York: Oxford University Press, pp. 23-36.

Application of Mean-Shift in Unsupervised Learning for the Identification of Common Household Appliances

Lawrence Ch'ng and Edwin Chung
Taylor's University, Malaysia

lawrencechng92@hotmail.com,chinyau.edwinchung@taylors.edu.my

Abstract

The introduction of new technologies centered upon the usage of electricity has taken its toll on the power grids in Malaysia. The electricity consumption in this region is expected to increase by 30%. Through advancement in smart meters and machine learning techniques, this problem can be reduced by introducing smart energy management in an efficient way called Non-Intrusive Load Monitoring (NILM). This provides an opportunity for Malaysia where efficient energy saving based upon NILM has yet to be implemented. Most NILM conventional methods utilise supervised learning methods which requires a trained database to identify appliance loads which is deemed laborious and costly. The use of an unsupervised learning method such as clustering could be useful in creating a low cost solution. This paper focuses on the usage of mean shift clustering to identify individual load appliances given an aggregated power load obtained from a smart meter in a particular residential home. As a means to validate this, aggregated power load information from an energy audit company website, www.pecanstreet.org was used in this research. Before clustering procedure is carried out, standard NILM steps were carried out which are data acquisition, event detection, and event classification. Once event classification is carried out, the steady state changes are clustered together. Each cluster is assumed to belong to one type of appliance. Once the clusters are determined, it is compared with the main aggregated load signal. The appliance having the closest mean towards the centroids of the cluster is classified under that cluster. Finally a ground truth table is referred to compare the results with the actual value. The results obtained shows that the proposed algorithm is capable of identifying high power loads of over 100 watts with a accuracy of more than 87.5%. This algorithm is however not able to identify smaller loads as their power draw during transitions are similar. It is found that errors in the proposed algorithm are due to purity of the clusters and utilisation of other features is a potential solution to this challenge. As is, the proposed algorithm's ability to identify appliances that consumes high power is beneficial to the user who is concerned about their total power consumption.

Keywords: Non-Intrusive Load Monitoring, Mean-Shift Clustering, Event Detection, Unsupervised Learning, Event Classification.

1. Introduction

Electricity demand around the world is increasing. It is predicted that electric demand will reach its maximum by the year 2035. Research showed that device level feedback can help in providing electrical appliance users to save better. Device level feedback or appliance load monitoring (ALM) started with mass employment of sensors in the home's infrastructure [1, 2]. Each specific electric appliance is attached to these sensors to measure their power consumptions The problems with sensors is they require installation, maintenance, power and current design are very poor aesthetically. To overcome this problem, researchers started to experiment on single point sensing typically at the main power feed and this is termed non-intrusive load monitoring (NILM) as it does not involve anything inside the residential home. These motivations arise solely from the recent advancement of smart meters which enables fast computation of key power consumption values. Most NILM methods use supervised learning due to its simplicity and reliability. Although device level feedback have been around since the late 80s, NILM has yet to reach a large deployment scale due to the need for training used in supervised learning. Training as a pre-requisite in NILM supervised learning methods presents a technique which is extremely tedious as it involves actuating each appliance individually. A common household has many appliances and it is unrealistic to actuate each new appliance in order to obtain information [3]. This problem presents the research gap for this paper.

This paper starts with some past work on this topic followed by the motivation of this paper in solving the issues faced by past research in Section 1. It is then followed with the methods and procedures on non-intrusive load monitoring using unsupervised learning method in Section 2. In Section 3, results and findings are discussed. The paper ends with some key notes for improvements and recommendations for the future are also covered.

1.1.Related Work

The current focus of NILM utilizes supervised machine learning techniques. Researchers which use this technique record the extracted features on a single specific appliance during an occurrence of an event. An event happens when an electrical device is turned on or off. Features are different types of constants related to a particular device during an event. Common features used are real power, reactive power, current harmonics, average current, voltage distortion, and transient power [4]. All supervised learning methods have to perform training as a pre-requisite to solving disaggregation. A standard supervised learning method process starts with:

i) The features are first extracted and classified. This is done by manually actuating individual appliance and acquiring data through a plug or smart meter.

ii) The extracted features are stored in a database in a computer or inside the smart meter itself. This information is then trained by a classifier to identify key features belonging to an appliance. . Some of the techniques used are Artificial Neural Network [5], Bayesian approach [6], and Support Vector Machines [7]. When tested on new aggregated load, the classifier compares key events with known features in the database.

Supervised machine learning techniques can be divided into two major categories which are optimization and pattern recognition.

1.1.1. Optimization

Here extracted feature vectors are compared with known load signatures which had been trained and stored into a database. This extracted feature vector is a transition signature which occurs during a power consumption event such as a device turning on or off. Some of the methods which use optimization include integer programming and genetic algorithms [8].

1.1.2. Pattern Recognition

In pattern recognition, the user uses a classifier to train a database based on distinct features of an appliance when it is turn on or off (an event). As mentioned above, some of the techniques used are Bayesian, Hidden Markov Model, Support Vector Machines and Artificial Neural Network [5, 6, and 7].

1.1.3. Clustering

Clustering falls under the category of unsupervised learning as the procedure tries to classify similar unique events together without the need of a signature database. The most popular method for clustering is K-Means which can be explained with fitness function, detailed in Eq. 1 below, to assess if a solution is a viable candidate [9].

$$CS = \frac{\sum_{k}^{K} \frac{1}{M_k} \sum_{x_i \in C_k} \max_{x_q \in C_k} d(X_i, X_q)}{\sum_{i=1}^{k} \min_{i \neq j} \hat{d}(m_i, m_j)} \quad (1)$$

In equation (1), K is the number of clusters in solution, $M_k$is the number of points in cluster k, X_i is an event, m_i is the real and reactive power (P, Q) and is the coordinates of cluster i in the PQ plane, $d(X_i,X_q)$ is the Euclidean distance between X_i and Xq.

From Eq. 1, the variable K is the number of clusters that need to be provided prior to clustering. Since it is assumed that one cluster belongs to one appliance class, this cannot be adapted into an unsupervised approach for load monitoring as the number of clusters are not known prior to disaggregation. The goal is to solve disaggregation blindly without prior knowledge of appliances class or in this case non-parametric. Table 1.0 shows a list of common household loads as reference to set the predefined threshold for event detection in Section 2.2.

Table 1.0: List of Household Loads [10].

Appliance	Power (watts)
Clock Radio	10
Coffeemaker	900-1200
Clothes Washer	350-500
Clothes Dyer	1800-5000
Dishwasher	1200-2400
Dehumidifier	785
Personal Computer	60 - 270
Laptop	50
Incandescent Lightbulb	40-150
Refrigerator	725
Television (27 inch)	113
Water Heater	4500-5500
Water Pump (Well)	250-1100

1.2 Motivation

It is predicted that electricity demand will double globally by the year of 2035. According to the Southeast Asia Energy Outlook, electricity generation increases by 4.2% on average annually from 696 terawatt-hours at year 2011 to almost 1900 TWh in 2035 [11]. A study concerning electricity knowledge on home users was done which showed that most people are not aware of the most efficient way in reducing energy demand especially electricity [12]. About 55% home users agree that energy saving equipment helps in saving in comparison to only 11% which agrees in the usage of energy-efficient equipment. Another researcher studied the level of understanding of people about electricity. The studied revealed that home users have deeper knowledge of frequency, duration and size of the device in comparison to minimal information on the device's power consumption [13]. One solution is to provide device level feedback which has been around since the late 80s. One reason which prevents device level feedback from expanding to a large scale deployment is the need for training. Training is tedious and requires each appliance class to be actuated as a pre-requisite to load disaggregation. Unsupervised learning methods have become an alternative towards solving disaggregation without training. A conventional unsupervised learning method such as Blind Source Separation and Factorial Hidden Markov Model solves disaggregation using K-Means Clustering and multiple unique features respectively [14, 15] . The problem with using multiple features is the increase cost which does not bode well for commercialization. This paper studies the effectiveness of an unsupervised learning approach using Mean-Shift Clustering for load disaggregation using only one dimensional real active power values with an aim to create a low cost but reliable NILM system.

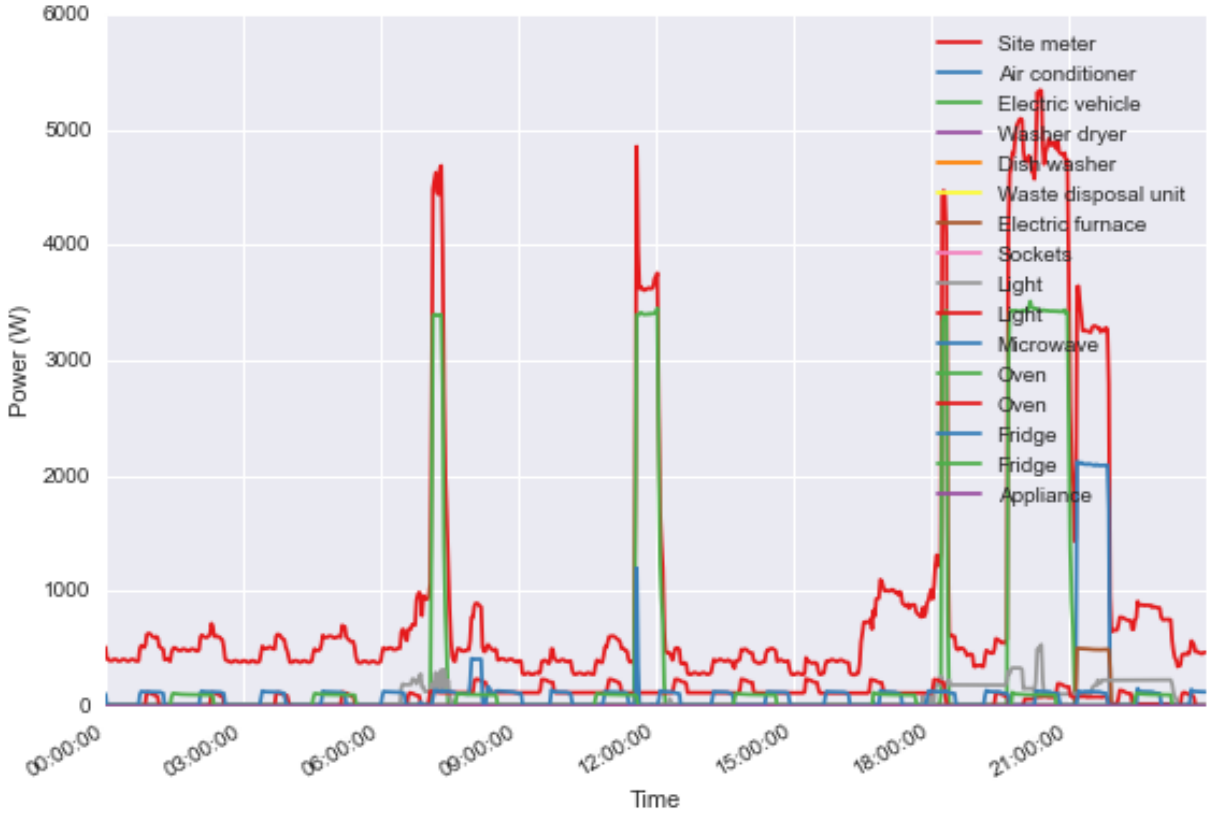

Figure 1: Ground Truth Table

The main dataset was retrieved from an energy management research website called www.pecanstreet.org which promotes research in energy management ranging from electricity, water and gas. Fig. 1 shows the ground truth table of the aggregated load signal. This table was obtained by sequentially turning on and off an appliance manually. An event-detector is then used to label this event. The ground truth is presented because there are no labels in unsupervised learning method and an accuracy metrics is needed to compare the results of the algorithm. The main signal was sampled at 60Hz which is the fundamental frequency in the power lines and translates to a sampling of every 1 second.

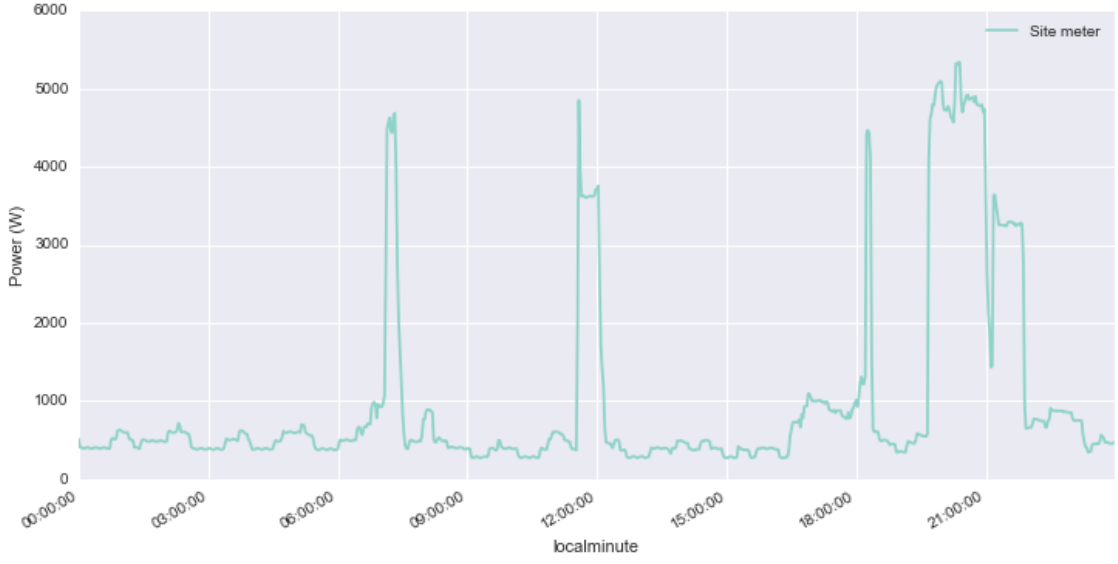

Figure 2: Main load signal

Fig. 2 shows the main aggregated signal obtained at the main power feed of building .This signal will be the test subject of the algorithm. Some notable mentions here is the non-existence of labels of individual appliances and the existence of only active power values. The figure's timeframe starts from "00-00-00" until "24-00-00" indicating one day's sampling.

2.0 Methods

The section details the step by step process of the disaggregation algorithm. The process starts with acquiring and processing the main load signal to obtain only specific features. The step follows by utilizing these features to detect an appliance turning on or off called transitions. By finding similar transitions in terms of magnitude, these transitions are fed into a clustering procedure. Once the centroids (mean) of these clusters are found, they are used for the source reconstruction algorithm which determines the appliances in the main signal.

2.1 Data Acquisition and Post Processing

The data of the main load signal was acquired and filtered out using eGauge current transformer sampled at 60Hz. The data is then processed into raw power data with an interval of 1 second. Once processed, the data is arranged in a systematic format as shown in Fig. 3. Fig. 3 has been cropped for the ease of explanation and viewership. The Pandas Dataframe function from Python has been used. The single column is associated with the only measurement taken which is the real power and indexed by its timeframe.

physical_quantity	power
type	active
localminute	
2014-04-01 00:00:00-05:00	517
2014-04-01 00:01:00-05:00	505
2014-04-01 00:02:00-05:00	410
2014-04-01 00:03:00-05:00	411
2014-04-01 00:04:00-05:00	409
2014-04-01 00:05:00-05:00	401
2014-04-01 00:06:00-05:00	394

Figure 3: Raw power values of main load signal

2.2 Event Detection

An event is said to indicate an appliance turning on or off. The process starts by comparing the current sample with the previous one and calculating the difference. This change is done by a sliding window which goes through each sample. The predefined threshold is set to 15 watts. This means that the difference between two adjacent samples must be greater than 15 watts. The threshold is set to 15 watts based on the lowest consuming device, a clock in Table 1.0. The reason the threshold is not set to 10W instead is, electrical appliances usually consume energy higher than their

rated value during start-up. This event detection process is shown mathematically in Eq.2, Eq.3 and Eq.4 as [10]:

$$l_j = \max_{i \le j \le k} \sum_{i=j}^{k} [\frac{\hat{v_j} \times (y_i - u_{pre})}{\sigma^2} - \frac{\hat{v_j}^2}{2 \times \sigma^2}] \quad (2)$$

In Equation (2), $\hat{v_j}$ is the value of the mean change ($u_{after} - u_{pre}$) at which l_j reaches maximum value. Furthermore, a predefined threshold of 15 watts, v_m is set to discard changes in mean that are below this level. $\hat{v_j}$ can be calculated using equation (3) and (4) as:

$$\hat{v_j} = v_m \quad if\ step\ change\ is < v_m \quad (3)$$

$$\hat{v_j} = \frac{1}{k-j+1} \times \sum_{i=j}^{k} |y_i - u_0| \quad if\ step\ change\ is > v_m \quad (4)$$

Thus, the value of l_j will grow with the change of power above the predefined threshold indicating a potential event of interest. The value of the predefined threshold can be set to the interest of the user in terms of finding which appliances. Since, finding higher power devices are the main target, this threshold is quite flexible. Fig. 4 shows the transitions that happen when there is a true event detected. Altogether there are 98 transitions that occur in this building. One notable mention is unlike their steady states counterparts, it is unsurprising to see that transition values inhibit positive and negative values. The positive value is assumed to happen when an appliance is turned on and vice versa.

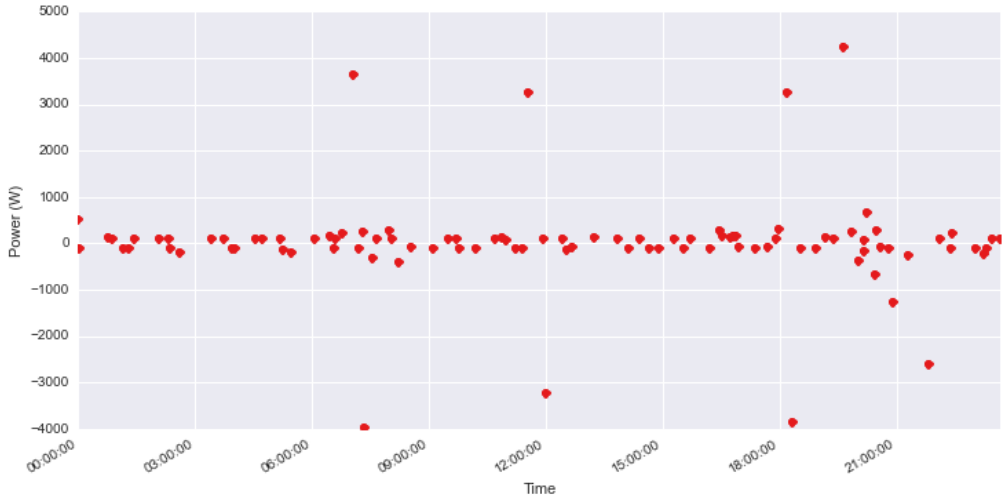

Figure 4: Graph of true transitions

2.3 Event Pairings

Once all transitions have been obtained, similar on and off events are matched together from this list of transitions. The matching is done to find same appliances and group them together in order to infer their whole interval of operation. When checking for a true pair which meets all the assumptions, adjacent transitions are checked first. If true, they are marked and subsequently removed from the table. Then, transitions two entries apart are checked, then three, four and so on until the first and last transitions are checked [16]. Fig. 5 shows a figure of the transition pairings. "T1 Time" states the start of an appliance turning on while "T2 Time" states the ending while "T1 Active" and "T2 Active" are their transitions on/off values respectively.

	T1 Time	T1 Active	T2 Time	T2 Active
0	2014-04-01 05:53:00	92.616071	2014-04-01 06:10:00	-109.758929
1	2014-04-01 05:45:00	121.362126	2014-04-01 06:18:00	-103.317460
2	2014-04-01 07:18:00	107.666667	2014-04-01 07:22:00	-116.000000
3	2014-04-01 07:05:00	114.702703	2014-04-01 07:35:00	-208.432624
4	2014-04-01 08:44:00	98.330144	2014-04-01 08:56:00	-120.659091

Figure 5: The figure shows the first five true pairings.

2.4 Clustering

The clustering procedure produces a number of clusters and their centroids which are the mean of these clusters. These centroids are given to the source reconstruction stage, to find the individual appliances that are active. The clustering method that is being used is the Mean-shift clustering. Instead of the popular k-Means clustering, this method does not need prior setting of the number of clusters. Mean-Shift has the advantage in this case as it is non-parametric, independent of the underlying distribution and indirectly contains a mode-seeking algorithm. Each cluster found is assumed to belong to one appliance class. Since the purpose of this paper is to find appliances without labels, the numbers of appliances in the aggregated load are unknown [17]. Mean-shift clustering does not require the user to impute the number of clusters which implies that the individual appliances are found blindly without any prior information. Based on Eq.5, given a set of data points in a plane, Mean Shift clustering tries to find the point of highest density within the plane. x in Mean-Shift term is the mean of the clusters and it seeks for convergence by subtracting each sample x^i in the plane. It finally converges when the gradient of density becomes zero. The clustering result in Fig. 6 produces 3 clusters. These centroids will be used as guidelines for the source reconstruction algorithm.

$$\nabla f(x) = \frac{2c_{k,d}}{nh^{d+2}}\left[\sum_{i=1}^{n} g\left(\left\|\frac{x-x^i}{h}\right\|^2\right)\right]\left[\frac{\sum_{i=1}^{n} x_i g\left(\left\|\frac{x-x^i}{h}\right\|^2\right)}{\sum_{i=1}^{n} g\left(\left\|\frac{x-x^i}{h}\right\|^2\right)} - x\right] \quad (5)$$

In Equation (5), $\nabla f(x)$ is the gradient of the density estimator, the first term is proportional to the density estimate at *x* and the second term is the mean shift.

$$Average\ of\ individual\ pairing = \frac{T1\ Active + T2\ Active}{2} \quad (6)$$

	(power, active)
0	115.677191
1	671.083333
2	3243.837500

Figure 6: Clustering Results

2.5 Source Reconstruction Algorithm

The algorithm now uses the newly obtained clusters to find hidden appliances. From the main signal, the transitions are obtained again using the same event detection method. The absolute values of these transitions are subtracted with the centroids of each cluster, in this case three and the absolute minimum value is chosen. The algorithm also looks for transitions greater and lesser than zero as it is assumed that a transition greater than zero would mean an appliance turning on and vice versa. Going through each iteration of transitions, a positive transition would result in a value of 1 in the table while a negative transition would result in a value of 0 [10]. All transitions are taken into account. Fig. 7 shows the initial setup to find hidden appliances from the load signal. For viewing purposes the figure consist of the first five minutes. The total 24 hours still applies. The columns of 0, 1, and 2 belong to the 3 different clusters. For this setup, the database values are set to negative one (-1) indicating that no appliance has been detected yet.

	0	1	2
localminute			
2014-04-01 00:00:00-05:00	-1	-1	-1
2014-04-01 00:01:00-05:00	-1	-1	-1
2014-04-01 00:02:00-05:00	-1	-1	-1
2014-04-01 00:03:00-05:00	-1	-1	-1
2014-04-01 00:04:00-05:00	-1	-1	-1

Figure 7: Initial setup

```
   (power, active)
0         2.886493
1       558.292636
2      3131.046802
   (power, active)
0         5.684936
1       549.721207
2      3122.475374
   (power, active)
0        23.061119
1       578.467262
2      3151.221429
   (power, active)
0         5.918262
1       561.324405
2      3134.078571
   (power, active)
0        12.359730
1       567.765873
2      3140.520040
```

Figure 8: Absolute values of centroids after subtracting with each transition value

```
                                  active transition
2014-04-01 00:02:00-05:00        -112.790698
```

Figure 9: Reminder of first value transition

Fig. 8 shows the absolute value after subtracting the centroids with the transition value at each iteration. Taking the first iteration as an example seen at Fig. 9 the first transition of the steady state value was recorded at time “00:02:00” with a value of -112.8. This value is then subtracted with each cluster values taking the absolute value of the result. Thus, the first iteration results as shown in the first cluster in Fig. 8. Once the absolute value is obtained, the index belonging to the minimum value among the three clusters is taken. 0 belongs to the first cluster, 1 belongs to the second cluster and 2 belong to the third cluster.

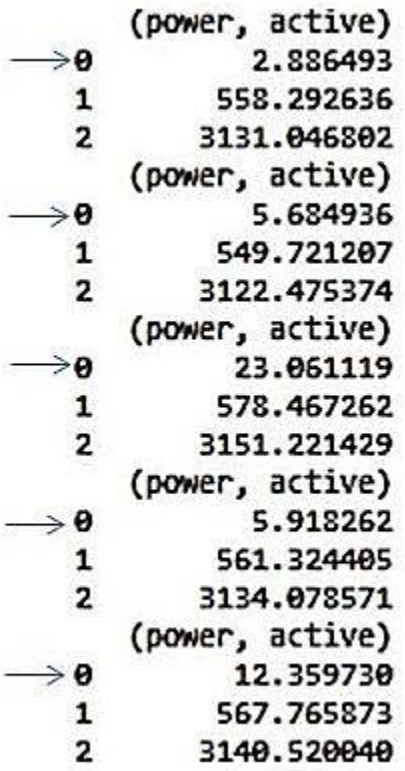

Figure 10: The indexes of the minimum value are chosen

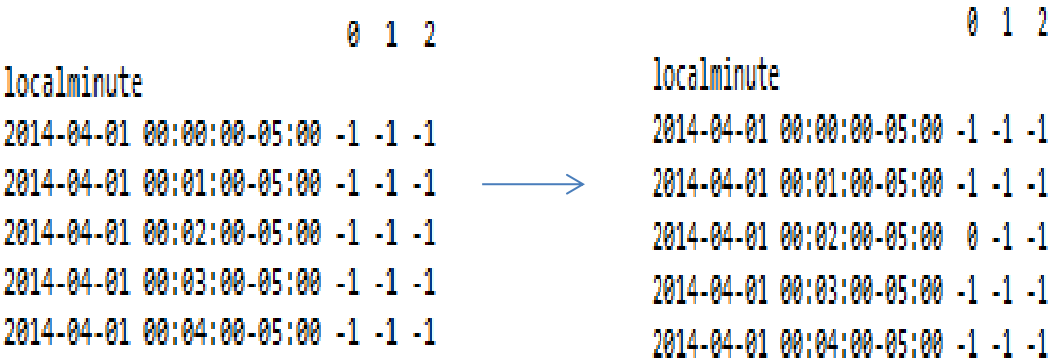

Figure 11: Initial setup vs Modified Setup

Fig. 10 shows that the minimum value of the first five iterations falls in the first cluster corresponding with the arrows pointing at zero. With this information, the initial setup can now be modified. Based on Fig. 11, database on the left shows the initial setup while the right shows the modified version after finding the minimum values and subsequently editing the values. Once this modified setup is completed, it is time to assign power values to it. An appliance is assumed to turn on indicated by the number "1" and continues to turn on until a number "0" appears. Therefore, the algorithm starts with one cluster and goes through the length of transitions associated with that cluster. As it goes through the length it tries to find the first "1" since "1" is assumed to be an appliance turning on. Once a "1" is found the following length from then onwards are assigned the power values of the cluster itself regardless of the value until it finally meets a "0" which is assumed to be an appliance turning off. If initially,

any other symbol or number besides "1" is found, no power values are assigned to it. This algorithm is done on each cluster separately. The power values that will be assigned are the values of the original clusters centers itself.

3.0 Results

Since this is an unsupervised way of solving disaggregation, there are no labels for the learnt appliances. There is no accuracy metrics that can be used thus the only way to study and compare the results is through the ground truth table as seen in Fig. 1 manually.

3.1 First Appliance Reconstruction based on cluster one

From the ground truth table and its appliances power values, the first cluster seems like a good match for a fridge.

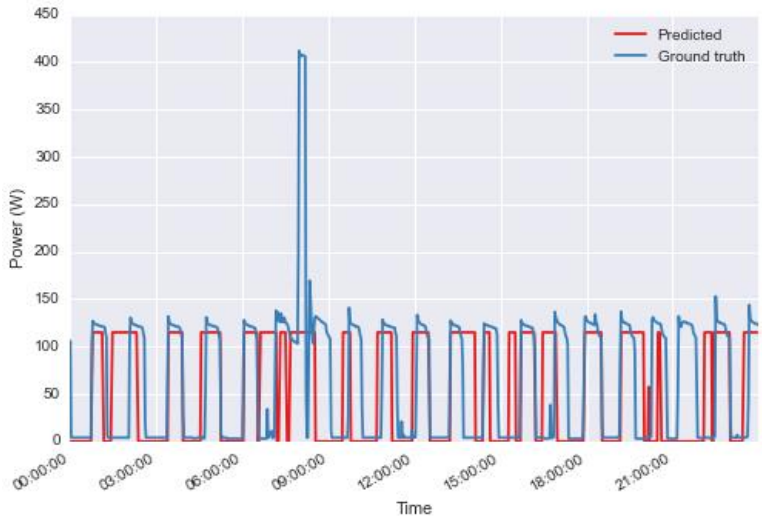

Figure 12: Graph of predicted value and ground truth of the fridge class

From Fig. 12, it can be seen that the power values for the predicted and ground truth are almost identical. The spike in power for the ground truth occurring at roughly time "09:00:00" could be caused by a surge in current and a standard method like clustering could not identify this error. Since the algorithm used in the source reconstruction stage assigns fix power values, a surge as shown could not be detected. The slight offset is due to the smaller power consuming items that are not identified and thus contributing to the overall on time for the fridge.

3.2 Second Appliance Reconstruction based on cluster two

Comparing with the ground truth, the appliance's power values and load signature resembles an electric furnace. From Fig. 13, the power values and timing are off by quite a big margin.

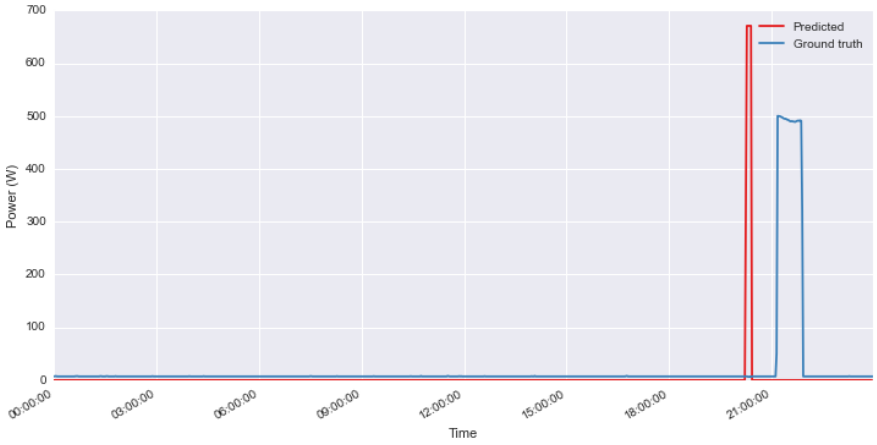

Figure 13: Graph of predicted value and ground truth of the electric furnace class

3.3 Third Appliance Reconstruction based on cluster three

T last cluster looks like it belongs to the electric vehicle class. The predicted and ground truth values of cluster number three and electric vehicle are respectively plotted.

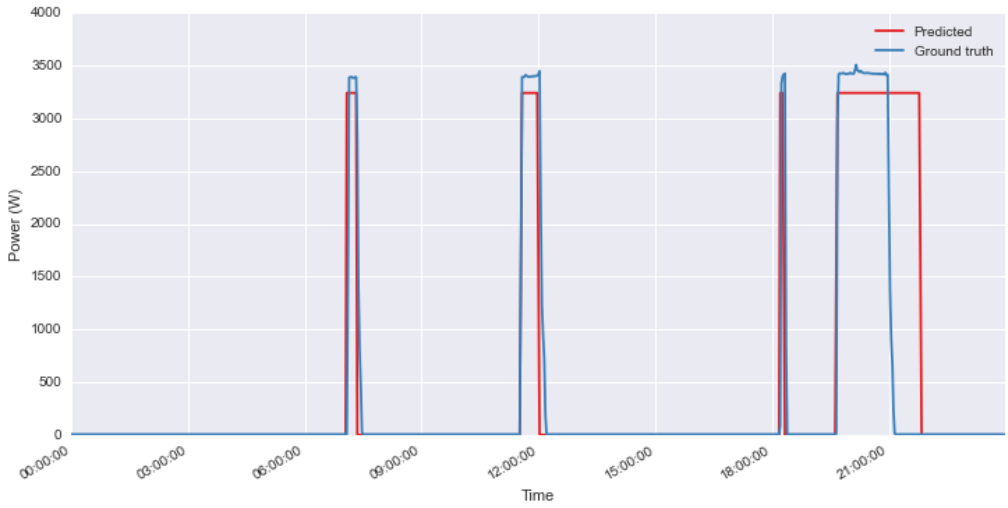

Figure 14: Graph of predicted value and ground truth of the electric vehicle class

According to Fig. 14, the timing seems impeccable until the end at time “21:00:00. This is due to the interference of smaller unidentified loads. The small loads occurring at that time contributes some offshoot power to the electric vehicle class. Besides that, the power values has a little offshoot from the real ground truth values.

3.4 Several Days Test

To test its effectiveness, the algorithm was tested on the same dataset but on several different days. The results were tabulated in Table 2.0.

Table 2.0: Results of algorithm on several days' data

Appliance Class	Ground Truth Power	Ability for Detection
Fridge	125W	Yes
Electric Furnace	500W	No
Electric Vehicle	3450W	Yes
Air Conditioner	2150W	Yes
Dish Washer	1220W	Yes

3.5 Overall Discussion

From the three different comparisons of predicted appliances with their ground truth in day one, it can be seen that this method is not the most accurate method in disaggregating all loads. The algorithm was only able to locate loads having power draw of more than 100W. There are some offshoot in terms of timing and power values. One of the main reasons is due to the clustering procedure which clusters distinct active power values together. Therefore different appliances having similar power draw will be clustered together. Since Mean-Shift Clustering takes into account the mean of all the data points within the cluster, data points not belonging to the correct appliance is also taken into account. The algorithm uses these centroids as reference to compare with the transitions of the main signal. If the centroids are inaccurate in the first place, the matching results will also be the same. This discrepancy creates the offshoot in the center of the clusters (centroids). Besides that, the results show that only three appliances class were detected. Referring to the ground truth table in Fig. 1, there are other active appliances contributing towards the main signal. One clear characteristic of these other appliances is that they each have low power values. Therefore, the clustering procedure could not detect similar power value appliances together and differentiate them. The small power appliances are clustered together with the fridge which results in the offshoot in terms of timing and power magnitude. In terms of identification, the algorithm works wonderfully in finding high power consuming devices. From the three days, all high loads which draw powers of 300 watts and more were successfully identified. Out of 8 results obtained, 7 predicted outcomes matches with the ground truth giving a percentage of 87.5%.

3.6 Recommendations and Future Work

In order to prevent the problem of overshooting in terms of power and time, steps are required to address the problems of small power loads detection which is affecting the results of the clusters. One solution is to introduce a time and day feature in conjunction with the real power features. Since some appliances are used mostly at a specific time of the day, this information can be gathered and fed into the algorithm as

an additional feature vector. As an example, the washing machine is used mostly during the morning while the television is used at night when people finished their work. There are appliances which also work concurrently with one another. Appliances such as television and DVD recorder also operate together. This kind of information can be used to disaggregate loads better. Furthermore, although smaller power loads inherit similar active power consumption, sampling at higher frequency of range 10 kHz and above could determine more subtle attributes such as their transient states and harmonics. By acquiring this information as well as active power, this could provide a framework of a multidimensional plane. The result of this action would provide a more robust clustering procedure. The disadvantage of high frequency sampling is the additional cost needed. However, as the current dataset only contain active power, these steps are very much for future improvement. Besides that, the algorithm has to be more robust in terms of handling multi-state and varying power appliances [18]. The current method only takes into account appliances that have two states (on and off). One of the ways of handling this is by applying some supervised learning such as Artificial Neural network and Bayesian Probability with this unsupervised learning algorithm together [5, 6].

Conclusions

Mean Shift clustering was used as a means to disaggregate a given aggregated load signal that differs with existing supervised learning methods by not requiring prior knowledge on the set of preset appliances. The validation of the results was done on the dataset acquired online which comes with a ground truth table over a span of 24 hours. The results obtained gave a good indication that the clustering method using only real power features were able to detect higher power appliances substantially well with an accuracy of 87.5%. The inabilities to detect smaller appliances were due to the clustering procedure joining them together. The research was mainly due to interest in solving load disaggregation using an unsupervised approach given only real power features. The algorithm can be said an achievement as users is more concern of higher power consuming appliances

References

[1] K. Ehrhardt-Martinez, K. A. Donnelly and J. A. “Skip” Laitner, 'Advanced Metering Initiatives and Residential Feedback Programs: A Meta-Review for Household Electricity-Saving Opportunities', ACEEE, 2010.

[2] Tapia, E.M., Intille, S.S., Larson, K. 'Accurate activity recognition in a home setting', in *Proceedings of the 10th international conference on Ubiquitous computing*, Ubiquitous Computing, 2015, pp. 1-9.

[3] M. Zeifman and K. Roth, 'Nonintrusive appliance load monitoring: Review and outlook', *IEEE Transactions on Consumer Electronics*, vol. 57, no. 1, pp. 76-84, 2011.

[4] Du, Y.; Du, L.; Lu, B.; Harley, R.; Habetler, T. 'A Review of Identification and Monitoring Methods for Electric Loads in Commercial and Residential Buildings', in *In Proceedings of IEEE Energy Conversion Congress and Exposition (ECCE)*, Atlanta, GA, USA, 2010, pp. 4527–4533.

[5] Ruzzelli, A.G.; Nicolas, C.; Schoofs, A.; O'Hare, G.M.P. 'Real-Time Recognition and Profiling of Appliances through a Single Electricity Sensor', in *In Proceedings of the 7th Annual IEEE Communications Society Conference on Sensor, Mesh and Ad Hoc Communications and Networks*, Boston, MA, USA, 2010, pp. 1–9.

[6] M. Zeifman,'Disaggregation of home energy display data using probabilistic approach', *IEEE Transactions on Consumer Electronics*, vol. 58, no. 1, pp. 23-31, 2012.

[7] D. Srinivasan, W. Ng and A. Liew, 'Neural-Network-Based Signature Recognition for Harmonic Source Identification', *IEEE Trans. Power Delivery*, vol. 21, no. 1, pp. 398-405, 2006.

[8] Suzuki, K.; Inagaki, S.; Suzuki, T.; Nakamura, H.; Ito, K. 'Nonintrusive Appliance Load Monitoring Based on Integer Programming', in *In Proceedings of SICE Annual Conference*, Tokyo, Japan, 2008, pp. 2742–2747.

[9] C. Chou, M. Su and E. Lai, 'A new cluster validity measure and its application to image compression', *Pattern Analysis and Applications*, vol. 7, no. 2, 2004.

[10] L. Pereira and N. Jardim Nunes, 'Low Cost Framework For Non-Intrusive Home Energy Monitoring And Research', in *1st International Conference on Smart Grids and Green IT Systems (SMARTGREENS 2012)*, 2015.

[11] 9 rue de la Fédération, 'Southeast Asia Energy Outlook 2012', IEA, Paris, 2013

[12] S. Z.Attari, 'Public perceptions of energy consumption and savings', 15213, 2015

[13] Y. Chisik, 'An image of electricity: towards an understanding of how people perceive electricity', in *INTERACT'11 Proceedings of the 13th IFIP TC 13 international conference on Human-computer interaction - Volume Part IV*, Berlin, Heidelberg, 2015, pp. 100-117

[14] Goncalves, H.; Ocneanu, A.; Berges, M.; Fan, R.H. .'Unsupervised Disaggregation of Appliances ´ Using Aggregated Consumption Data', in *In Proceedings of KDD 2011 Workshop on Data Mining Applications for Sustainability*, San Diego, CA, USA, 2011.

[15] Kim, H.; Marwah, M.; Arlitt, M.; Lyon, G.; Han, J. 'Unsupervised Disaggregation of Low Frequency Power Measurements', in *In Proceedings of the 11th SIAM International Conference on Data Mining*, Mesa, AZ, USA, 2011.

[16] G. Hart, 'Nonintrusive appliance load monitoring', *Proc. IEEE*, vol. 80, no. 12, pp. 1870-1891, 1992.

[17] Das, S. & Abraham, A. & Konar, A. 'Automatic Clustering Using an Improved Differential Evolution Algorithm', in *Journal IEEE Transactions on Systems, Man, and Cybernetics, Part A: Systems and Humans*, NJ, USA, 2015, pp. 218-237.

[18] Berges, M.; Rowe, A. 'Poster Abstract: Appliance Classification and Energy Management Using Multi-Modal Sensing', in *In Proceedings of the 3rd ACM Workshop on Embedded Sensing Systems for Energy-Efficiency in Building*, Seattle, WA, USA, 2011.

Development of Image Processing Methodology to Analyze Cancer Cell Images

Leong Mun Loong[1*], Suresh Manic Kesavan[1], Chew Wei Jen[1]

[1] *School of Engineering, Taylor's University, Lakeside Campus, Box.47500 Subang Jaya, Malaysia.*

[*] *munloong92@hotmail.com*

Abstract

Image processing has risen in popularity in the medical industry in recent years. The increase in popularity of image processing can be credited to the harmful effects patients suffer from prolong usage of x-ray while using image processing on biopsy images, patients do not suffer from such drawback. Thresholding is a widely considered method in the field of image processing. Otsu's thresholding method which uses the maximum between class variance criteria is a popular image processing tool used to locate the optimal thresholds. In this work, the maximum between class variance is used as the objective search function to locate the optimal threshold value with the aim of improving the visibility of cancer cells in the processed image to help improve the detection and analysis of cancer cells. The Particle Swarm Optimization (PSO) method is used alongside Otsu's method in this work. The Darwinian Particle Swarm Optimization (DPSO) and Fractional Order Darwinian Particle Swarm Optimization (FODPSO) methods based on PSO is also used to segment six 896x768 sized colour cancer cell images. Using information from the histogram obtained from the images, the optimal threshold value is obtained. The performance of these algorithms are evaluated using well-known image performance indices such as Root Mean Square Error (RMSE) and PSNR. From the segmented images, it is clear that as the dimension search value increases, the visibility of cancer cells in the segmented images increases. Based on the results, it can be seen that in most cases FODPSO offers the best results.

Keywords: Multi-level thresholding, Otsu, PSO, DPSO, FODPSO.

1. Introduction

The enhancements achieved in digital imaging and computing technology has allowed image processing to play a pivotal role in many fields such as navigation, surveillance, environment modelling and medical [1]. Image processing is now considered a core part in cancer cell detection procedures as despite the advancements gained in the medical field, for the last three decades the death toll caused by cancer has not reduced [2,3].

Image segmentation is one of the popular image processing methods where images are divided into non-overlapping, homogenous areas containing similar properties [4]. One of the popular method of segmentation is called thresholding. The reason this method is widely considered is due to its accuracy, simplicity and robustness. A bi-level thresholding happens when the input image is divided into two classes known as background and object of interest. The level of thresholds can be increased when work requiring more levels is needed and is called multi-level thresholding [5,6].

For bi-level thresholding applications, the use of traditional methods has proven to work well. However, as the complexity of the problem increases, the number of thresholds required also increases which inevitably increases the computational time exponentially. In order to overcome this issue, recently researchers have proposed heuristic multilevel thresholding algorithms such as Particle Swarm Optimization (PSO), Bacterial Foraging Optimization (BFO), Cuckoo Search (CS) and many more for grey scale [7-13] and RGB images [12,13]. These methods are proposed to not only improve the final results but to reduce the computational time required to do so compared to traditional methods [2]. Despite the proposed methods, colour/RGB image segmentation is considerably more difficult when compared to grey scale images.

RGB images is chosen in this work because RGB images provide more details such as cell structure, abnormality in the cell or DNA and nuclei when compared to grey scale images. This helps in improving the rate of detection and analysis for cancer cells for it gives physicians more information to better diagnose the patient which is important as earlier the detection leads to higher chances of successful treatment.

In this paper, histogram based RGB image segmentation procedure proposed by Rajinikanth and Cuoceiro in 2014 [2] is adopted along with Otsu's maximum between class variance function as objective functions to segment the colour breast cancer cell images for heuristic dimension search 'm' = 2, 3, 4 and 5 using Particle Swarm Optimization (PSO), Darwinian Particle Swarm Optimization (DPSO) and Fractional Order Darwinian Particle Swarm Optimization (FODPSO) optimization methods. The proposed method is tested on breast cancer cell images. The images can be found in an online database at [14]. The proposed method aims to improve visibility of cancer cells in the images so that greater results can be obtain when the images are sent for cancer cell detection and analysis. The performance of considered algorithms were evaluated using statistical analysis based on well-known performance measurements.

The remainder of this paper is organized as follows: section 2 will be showing an overview of Otsu's based maximum between class variance function as well as discusses the heuristic algorithms considered in this paper. The research finding are presented in section 3. Section 4 concludes the results of the present research work.

2. Research Methodology

2.1 Otsu

Originally proposed by Otsu in 1979, the Otsu's method remains one of the most popular and used image segmentation methods [15]. The Otsu's method locates the optimal threshold available by maximizing the between class variance function. The function is shown below [16, 17] :

For any RGB image, let L represent the intensity level of the images in the range of {0,1,2,…,L-1}. While the probability distribution, P_i^C is defined as:

$$p_i^C = \frac{h_i^C}{N} \qquad \sum_{i=0}^{L-1} p_i^C = 1 \tag{1}$$

here *i* represents the specific intensity level from a range of { $0 \le i \le$ L-1 } while C represents {R,G,B}, total number of pixels in the image is represented by N, and H_i^C represents the number of pixel according to the intensity level *i* within component C.

Total mean of each component can be calculated through:

$$\mu_T^C = \sum_{i=0}^{L-1} \mathrm{i} p_i^C = 1 \tag{2}$$

The *m* – level thresholding shows *m*-1 threshold levels as t_j^C, where *j* = 1,2,…,*m*-1, and the operation is as below:

$$F^C(x,y) = \begin{cases} 0, & f^C(x,y) \le t_1^C \\ \frac{1}{2}(t_1^C + t_2^C), & t_1^C < f^C(x,y) \le t_2^C \\ \vdots & \vdots \\ \frac{1}{2}(t_{m-2}^C + t_{m-1}^C), & t_{m-2}^C < f^C(x,y) \le t_{m-1}^C \\ L-1, & f^C(x,y) > t_{m-1}^C \end{cases} \tag{3}$$

Here, the width and height of a pixel within the image of size H x W is represented by *x* and *y* denoted by $f^C(x,y)$ with L intensity levels for each component.

The chances of classes $D_i^C, \ldots, D_m^C$ is occurring is represented by the probability of occurrence denoted as w_j^C, as shown as:

$$w_j^C = \begin{cases} \sum_{i=0}^{t_j^C} p_i^C, & j = 1 \\ \sum_{i=t_j^C - 1 + 1}^{t_j^C} p_i^C, & 1 < j < m \\ \sum_{i=t_j^C - 1 + 1}^{L-1} p_i^C, & j = m \end{cases} \tag{4}$$

While the mean of each class μ_j^C, can be found through:

$$\mu_j^C = \begin{cases} \sum_{i=0}^{t_j^C} \frac{p_i^C}{w_j^C q}, & j = 1 \\ \sum_{i=t_j^C-1+1}^{t_j^C} \frac{p_i^C}{w_j^C}, & 1 < j < m \\ \sum_{i=t_j^C-1+1}^{L-1} \frac{p_i^C}{w_j^C}, & j = m \end{cases} \quad (5)$$

For each component, the Otsu's between class variance is shown as:

$$\sigma_B^{c^2} = \sum_{j=1}^{m} w_j^C \left(\mu_j^C - \mu_T^C \right)^2 \quad (6)$$

With W_j^C representing the probability of occurrence and μ_j^C representing the mean.

In the end, the *m* – level thresholding can be summarized as an optimization problem locating t_j^C. This is achieved through the maximization of the objective function of each image component C. The equation can be shown as:

$$\varphi^C = \max_{1<t_i^C<,\cdots,L-1} \sigma_B^{c^2}(t_j^C) \quad (7)$$

2.2 Heuristic Algorithm

For the last decade, heuristic or meta-heuristic algorithms are being used as powerful tools for solving optimization problems. This is mainly because of various advantages such as higher speed, accuracy and adaptability that heuristic algorithms have when compared to traditional methods. Hence, heuristic algorithms are adopted for this work.

In this work, the segmentation of colour cancer cell images is conducted with the use of well-known heuristic algorithms such as, PSO, DPSO and FODPSO.

2.2.1 PSO

Initially invented by Kennedy and Eberhart in 1995, the PSO is an evolutionary optimization technique which was inspired by movements made from flocks of birds and school of fishes [17]. The PSO algorithm is based on the two equations known as velocity update and position update which is represented below as:

$$V_i(t+1) = W^t . V_i^t + C_1 R_1 (P_i^t - S_i^t) \quad (8)$$

$$X_i(t+1) = X_i^t + V_i(t+1) \quad (9)$$

Base on the equations, W^t represents the inertia weight and is usually assigned as 0.75 while current velocity of the particle is represented as V_i^t with $V_i(t+1)$ representing the updated particle velocity. X_i^t indicates the current position of particle while X_i (t + 1) represents the updated position of the particle with R1 and R2 being random numbers ranging

between {0,1}. C1 and C2 represents the cognitive coefficient and social coefficient with C1 normally set at a value of 2.1 while C2 is usually set at 1.8 [17].

2.2.2 DPSO

The DPSO is an evolution of the PSO algorithm formulated by Tillett et al. in 2005, which inserts the concept of survival of the fittest into the algorithm to enhance the algorithms ability to escape from local optima [18]. This method is mostly used when solving Otsu related issues involving multi-level thresholding values and overcoming issues related to the trapping of local optima and high computational time [18].

In DPSO, a swarm in the algorithm is used as a comparison to multiple similar swarms in order to judge the ability of the algorithm to escape local optima [18]. Generally, DPSO optimization is suited for searches conducted within a discrete time space [18].

2.2.3 FODPSO

For optimization problems involving higher level of segmentation with less computational time, FODPSO is considered by many as the better algorithm for it is able to do so with better stability [19].

FODPSO operates using the same principle as DPSO. By having multiple swarms, the particles within the swarm of the algorithm all strive to survive by locating the best solution available. The most distinct difference between the particles of FODPSO when compared to DPSO is the particles within the swarms of the FODPSO algorithm possess memories hence are able to recall past decisions [19].

2.3 Implementation

In this work, Otsu's maximum between class variance will be used as the objective function in order to segment the images through thresholding. The PSO, DPSO, and FODPSO algorithms are used alongside the Otsu's method that acts as an enhancer. This is because the PSO, DPSO and FODPSO are heuristic optimization methods

When the method and 'm' value is determined, the test image is broken down into three histogram each representing a layer of colour as it is a RGB image. From the histogram, vital information such as the optimal threshold values can be obtained from the histogram.

The figure 1 shows the process flow of the segmentation process.

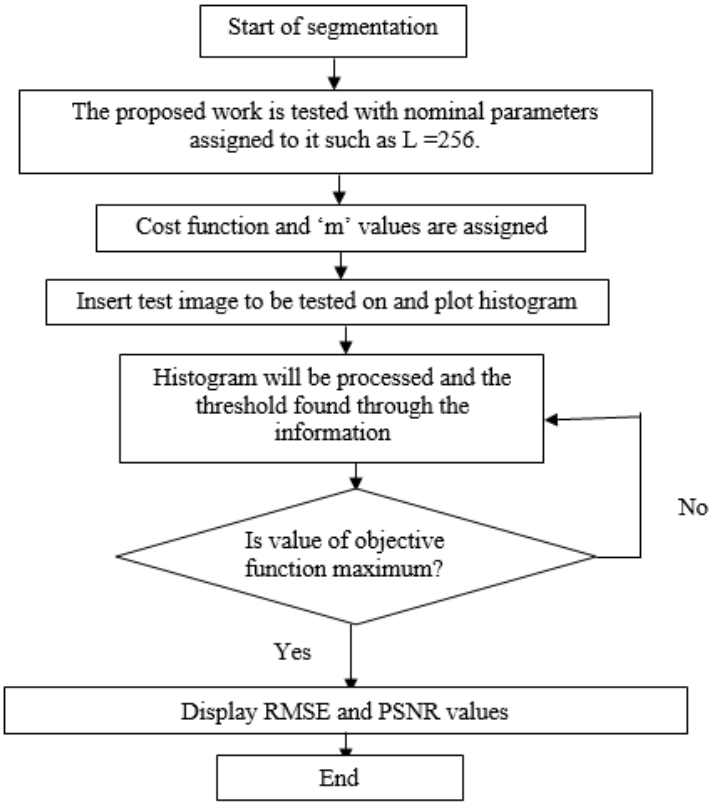

Figure 1. Flow chart of segmentation process.

2.4 Performance measurements

In order to judge the performance of the algorithms, popular image quality measurements such as Peak Signal to Noise Ratio (PSNR) and Root Mean Square Error (RMSE) is used. The mathematical equations of both performance measurements is shown below:

$$\mathrm{PSNR}_{(x,y)} = 20\log_{10}\left(\frac{255}{\sqrt{MSE_{(x,y)}}}\right); dB \tag{10}$$

$$RMSE_{(x,y)} = \sqrt{MSE_{(x,y)}} = \sqrt{\frac{1}{MN}\sum_{i=1}^{H}\sum_{j=1}^{W}[x(i,j)-y(i,j)]^2} \tag{11}$$

In the equation above, MSE is known as the Mean Square Error obtained between the original (x) and segmented (y) images.

3. Results and Discussions

Six 896x768 sized cancer cell images, three of which is benign and the other three malignant, is segmented using Otsu guiding PSO, DPSO and FODPSO thresholding

techniques. The simulation work is executed on a work station with Intel Dual Core 1.6 GHz with 1.5GB of RAM and equipped with MATLAB R2010a software.

The three benign images were used to determine the range of 'm' value in this work. This is done by comparing the PSNR value obtained for each image using all three heuristic algorithms using 'm' values ranging from 2 to 10.

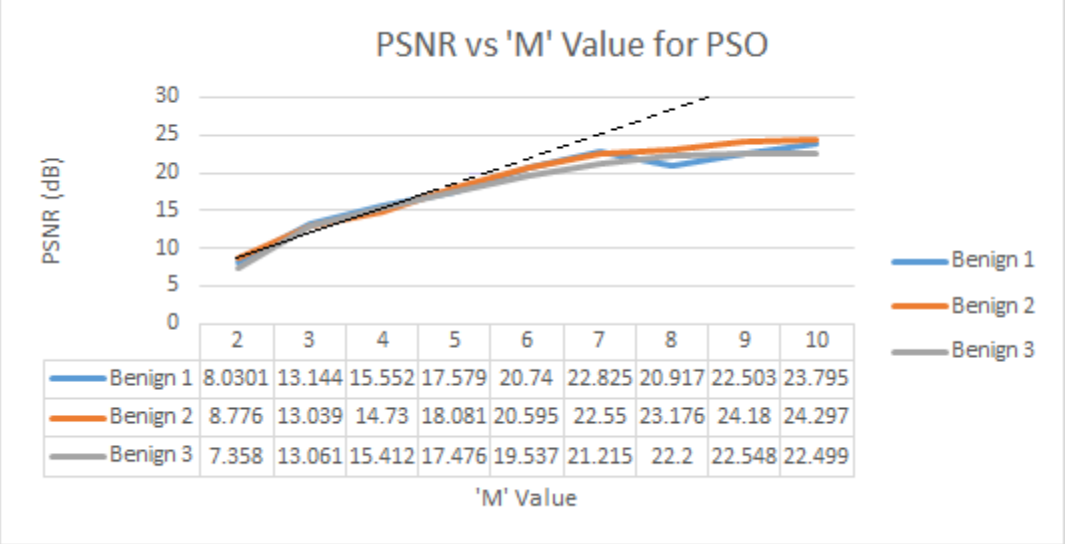

	2	3	4	5	6	7	8	9	10
Benign 1	8.0301	13.144	15.552	17.579	20.74	22.825	20.917	22.503	23.795
Benign 2	8.776	13.039	14.73	18.081	20.595	22.55	23.176	24.18	24.297
Benign 3	7.358	13.061	15.412	17.476	19.537	21.215	22.2	22.548	22.499

Figure 2: PSNR value obtained from three benign images through PSO method with 'm' values from 2 to 10

From figure 2, using the dotted line as a linear gradient, it can be seen that after the 'm' value passes 5, the increase in PSNR is minimal and will gradually hover around there. The same experiment on the images was conducted using DPSO and FODPSO and the results were similar, hence the range of 'm' value for this work is set at 2 to 5. Table 1 to 3 shows the segmented images obtained using PSO, DPSO and FODPSO. Table 4 shows the computational time needed for each method to segment the images at the various 'm' values. While table 5 and 6 shows the PSNR and Root Means Square Error (RMSE) of the dataset based on the applied 'm' levels for benign and malignant images respectively.

Table 1. Original and Segmented Image for 'm' = 2, 3, 4, and 5 using PSO.

	Original Image	Segmented Image	
Benign 1	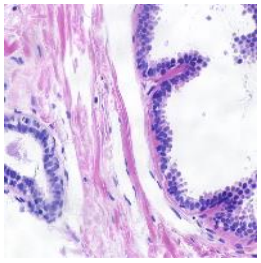	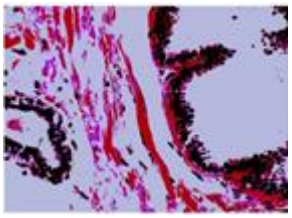 m = 2	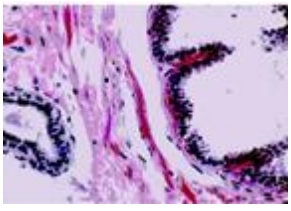 m = 3

		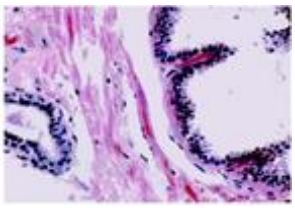 m = 4	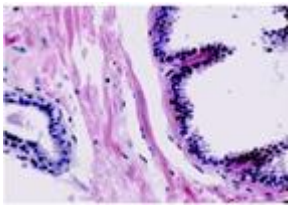 m = 5
Benign 2	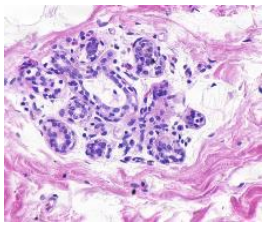	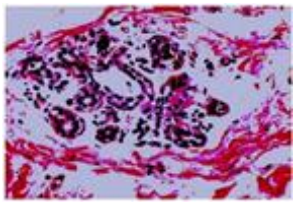 m = 2	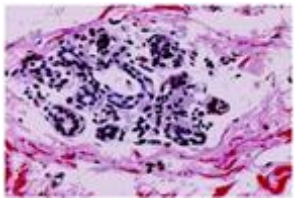 m = 3
		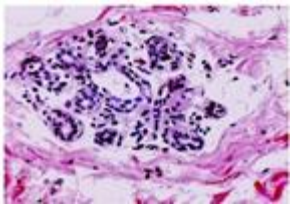 m = 4	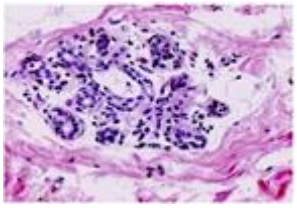 m = 5
Benign 3	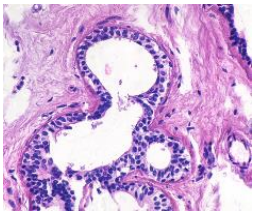	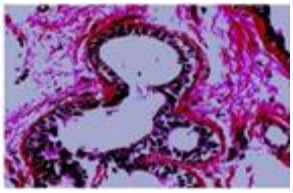 m = 2	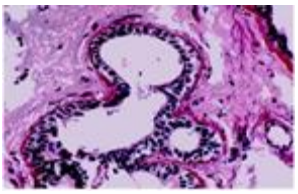 m = 3
		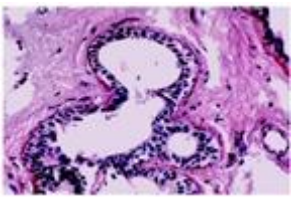 m = 4	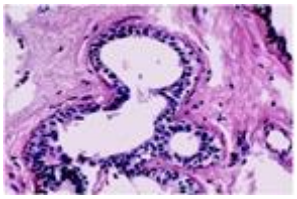 m = 5
Malignant 1	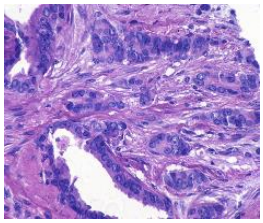	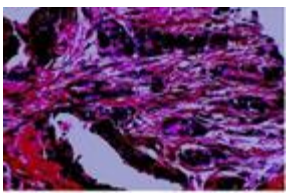 m = 2	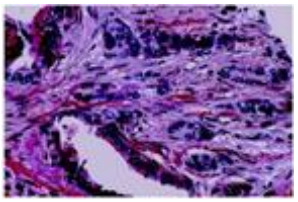 m = 3
		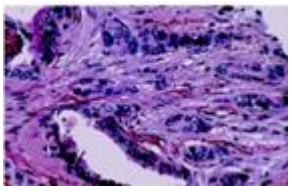 m = 4	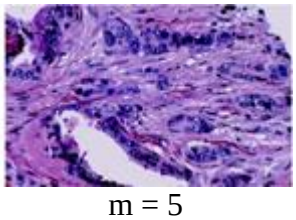 m = 5

Malignant 2	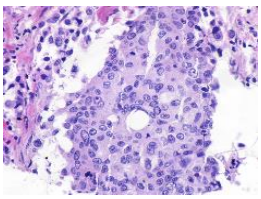	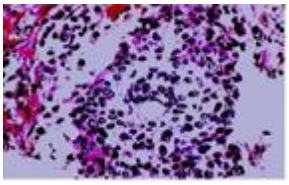 m = 2	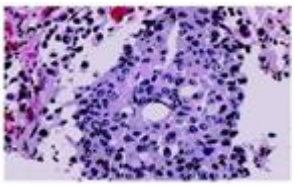 m = 3
		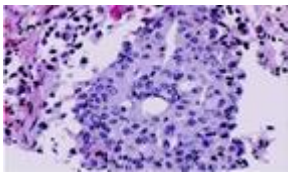 m = 4	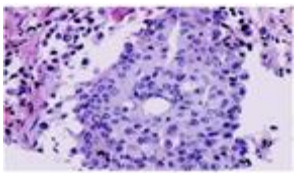 m = 5
Malignant 3	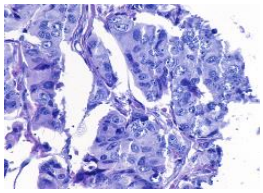	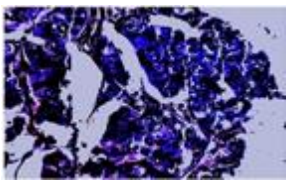 m = 2	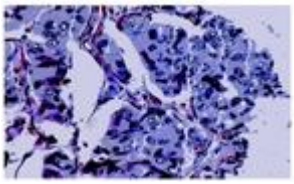 m = 3
		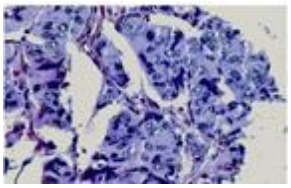 m = 4	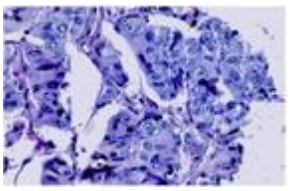 m = 5

Table 2. Original and Segmented Image for ‘m’ = 2, 3, 4, and 5 using DPSO.

Image		Segmented Image	
Benign 1	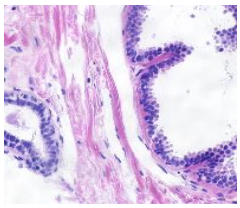	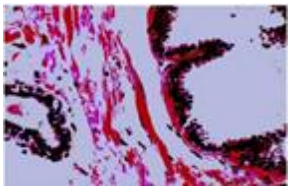 m = 2	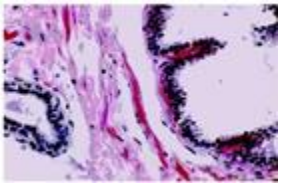 m = 3
		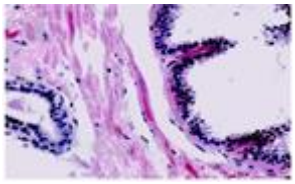 m = 4	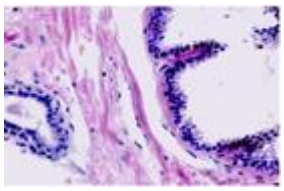 m = 5

Benign 2	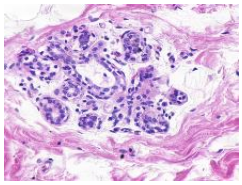	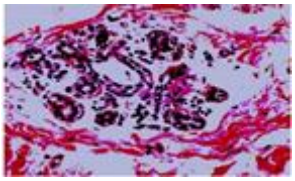 m = 2	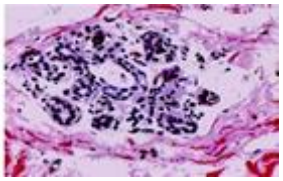 m = 3
		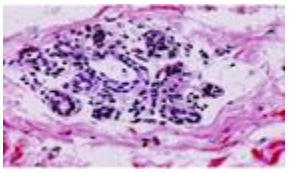 m = 4	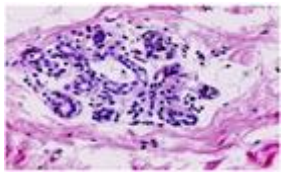 m = 5
Benign 3	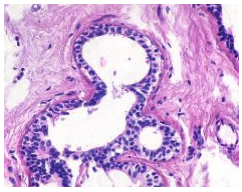	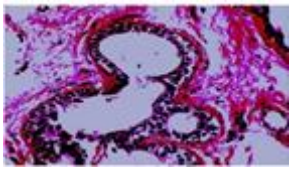 m = 2	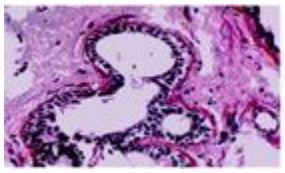 m = 3
		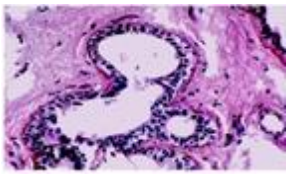 m = 4	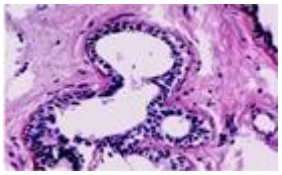 m = 5
Malignant 1	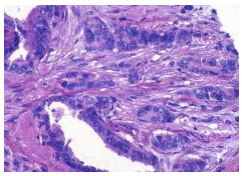	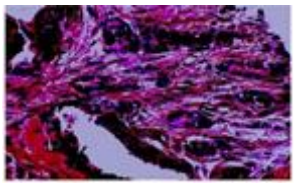 m = 2	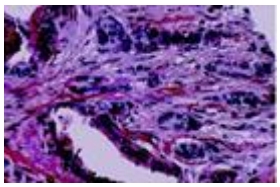 m = 3
		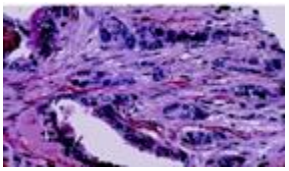 m = 4	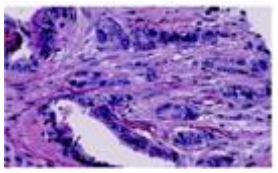 m = 5
Malignant 2	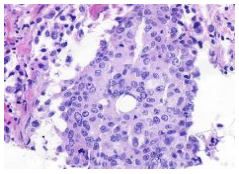	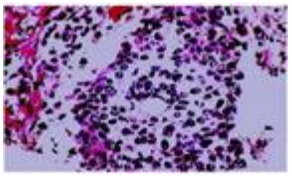 m = 2	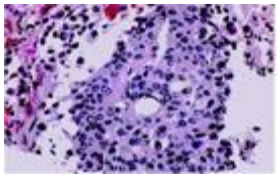 m = 3

		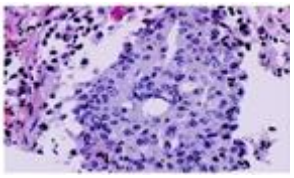 m = 4	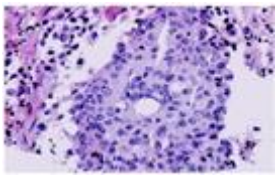 m = 5
Malignant 3	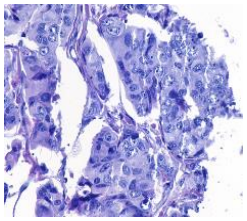	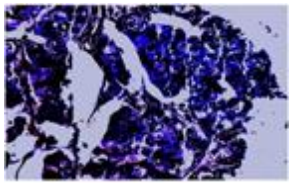 m = 2	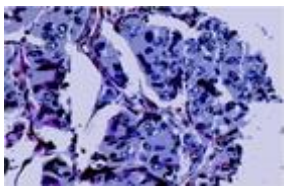 m = 3
		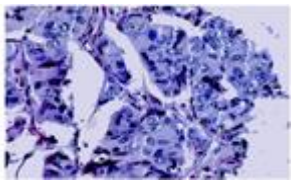 m = 4	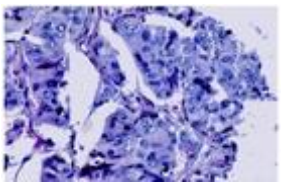 m = 5

Table 3. Original and Segmented Image for ‘m’ = 2, 3, 4, and 5 using FODPSO.

Image		Segmented Image	
Benign 1	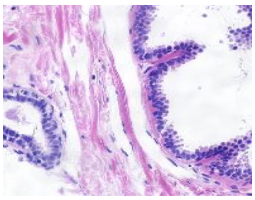	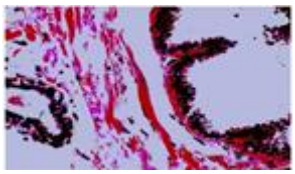 m = 2	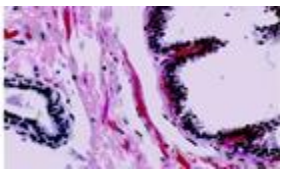 m = 3
		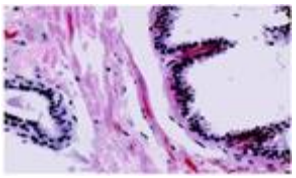 m = 4	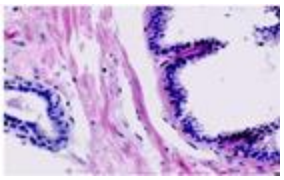 m = 5
Benign 2	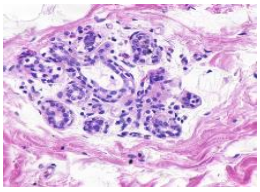	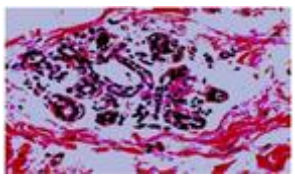 m = 2	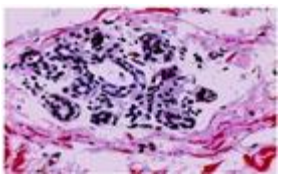 m = 3
		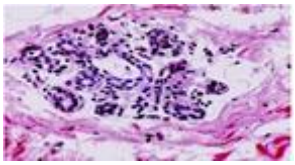 m = 4	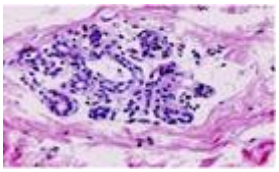 m = 5

Benign 3	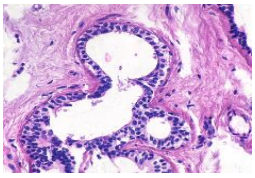	 m = 2	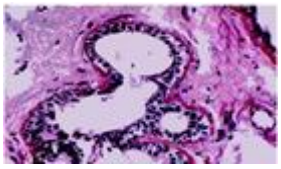 m = 3
		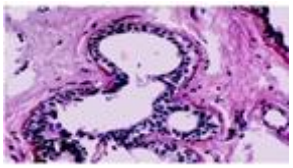 m = 4	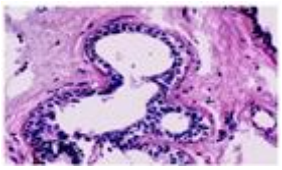 m = 5
Malignant 1	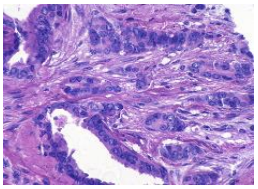	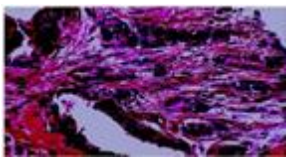 m = 2	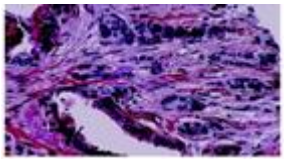 m = 3
		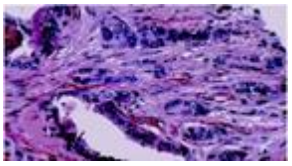 m = 4	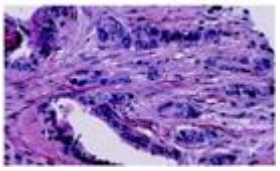 m = 5
Malignant 2	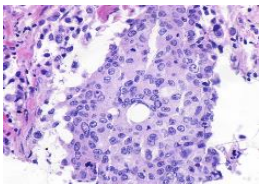	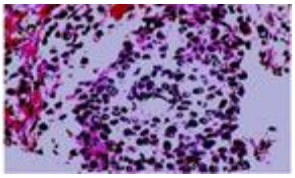 m = 2	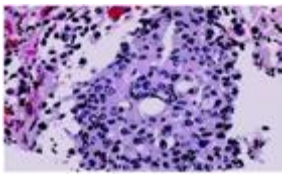 m = 3
		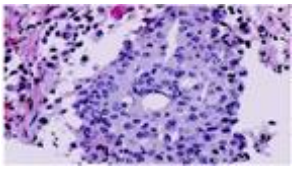 m = 4	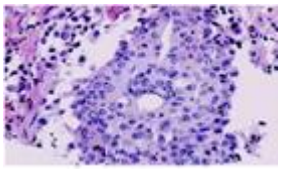 m = 5
Malignant 3	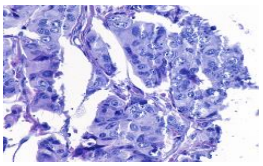	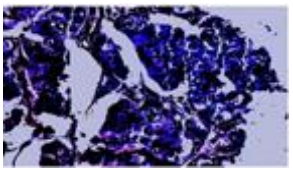 m = 2	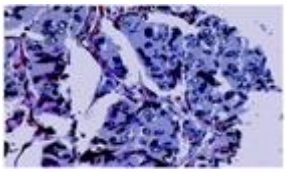 m = 3
		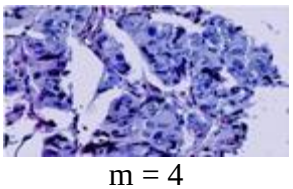 m = 4	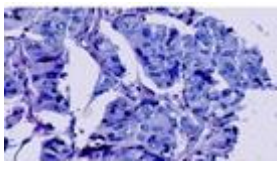 m = 5

Table 4. Computational Time needed to segment the images.

Image	m	Computational Time (s)		
		PSO	DPSO	FODPSO
Benign 1	2	3.061	1.907	1.967
	3	4.299	3.766	4.191
	4	5.563	6.207	6.243
	5	6.83	7.394	7.68
Benign 2	2	3.248	1.796	1.796
	3	4.231	3.877	4.077
	4	5.631	5.834	6.063
	5	6.873	7.498	7.558
Benign 3	2	3.013	2.036	1.846
	3	4.223	3.862	3.959
	4	5.46	5.955	5.916
	5	6.872	7.706	7.651
Malignant 1	2	3.017	1.951	1.952
	3	4.908	3.6	3.891
	4	5.622	5.869	6.076
	5	7.023	7.408	7.68
Malignant 2	2	2.987	1.843	1.983
	3	4.223	3.869	4.024
	4	5.424	5.922	5.941
	5	6.674	7.954	7.262
Malignant 3	2	3.034	2.034	1.846
	3	4.263	3.581	3.952
	4	5.483	5.801	6.121
	5	6.753	7.494	7.497

Table 5. PSNR and RMSE values of benign images when ‘m’ = 2, 3, 4, 5 using PSO, DPSO and FODPSO.

Image	m	PSNR (dB)			RMSE		
		PSO	DPSO	FODPSO	PSO	DPSO	FODPSO
Benign 1	2	8.0301	9.0198	9.0198	102.674	90.2178	90.2178
	3	13.144	13.047	13.038	56.151	56.782	56.84
	4	15.552	15.805	16.012	42.928	41.343	40.398
	5	17.579	18.274	18.605	34.211	31.155	30.007
Benign 2	2	8.776	8.738	8.738	92.994	93.248	93.248
	3	13.039	12.945	12.923	56.829	57.459	57.595
	4	14.73	15.774	15.836	48.581	41.485	41.213
	5	18.081	18.194	18.65	31.889	31.395	29.799
Benign 3	2	7.358	8.9609	8.9609	111.554	90.886	90.886
	3	13.061	12.928	12.931	56.702	57.652	57.544
	4	15.412	15.58	15.731	43.378	42.417	41.691
	5	17.476	17.661	17.826	34.189	33.386	32.774

Table 6. PSNR and RMSE values of malignant images when 'm' = 2, 3, 4, 5 using PSO, DPSO and FODPSO.

Image	m	PSNR (dB)			RMSE		
		PSO	DPSO	FODPSO	PSO	DPSO	FODPSO
Malignant 1	2	6.979	7.233	7.233	114.501	110.895	110.895
	3	10.169	10.693	10.675	79.956	74.454	74.609
	4	13.234	13.444	13.643	56.072	54.247	53.024
	5	15.855	15.989	16.744	41.33	40.499	37.129
Malignant 2	2	8.963	8.744	8.744	91.837	93.189	93.189
	3	11.881	12.129	12.113	65.869	63.107	63.227
	4	15.799	15.945	15.977	41.452	40.675	40.541
	5	17.995	18.58	18.679	32.443	30.048	29.698
Malignant 3	2	6.791	6.882	6.882	117.478	115.464	115.464
	3	12.08	12.005	11.977	63.468	64.018	64.224
	4	14.73	15.532	15.586	48.961	42.652	42.391
	5	16.721	18.01	18.258	38.266	32.078	31.7639

Based on results shown in tables 1 to 3, the segmented test images obtained from the proposed PSO, DPSO and FODPSO algorithms with various 'm' threshold values, shows improved quality and visibility when compared to the original test images for the tissue layers and cancer cells are more visible in the segmented images. This shows through the image segmentation technique, the visibility of cancer cells in the images increases regardless of the method applied.

While table 4 shows the computational time needed for each algorithm to segment each image at various 'm' values. Based on the results obtained, it can be seen that when the 'm' values are low at 2 or 3, the DPSO or the FODPSO method needs the least computational time. However, when the 'm' value increases, the PSO method is the method that needs the least computational time. Despite that, from the table it is observed that the difference in computational time between DPSO and FODPSO is near indistinguishable as both are separated by only few tenths of a second at most. This is also observed when the 'm' values are at 3, 4 and 5 where the computational time between all three heuristic algorithm is only separated by a few tenths of a second making it almost impossible to distinguish. When 'm' value is 2 that is where the most obvious difference between performance in computational speed of PSO against DPSO and FODPSO as the PSO often is always more than one second slower.

Based on this observation, it can be said that the performance of algorithm in computational time only matters when 'm' value is at 2 for when the 'm' value increase the computational times between the algorithms are barely distinguishable. When the value of 'm' is higher, the performance of the algorithms are more focused on the quality of the segmented image.

The best RMSE and PSNR values of the benign and malignant test images are highlighted in tables 5 and 6. Based on the results it is noticed that for most of the time the FODPSO method is the best method available but when the 'm' value is 2 which represents a simple two dimensional optimization problem, more traditional methods such as PSO and DPSO could provide better results.

4. Conclusion

In this paper, the cancer cells within RGB breast cancer cell images is enhanced by using histogram assisted bi-level and multi-level segmentation techniques. Here Otsu's maximum between class variance is used as the objective function implemented alongside optimization algorithms PSO, DPSO and FODPSO. The performance of the proposed methods are evaluated using six test images (896 X 768) by comparing the values of performance measurements such as PSNR and RMSE with 'm' = 2, 3, 4 and 5. From this study, it is shown that for simple optimization problems, older methods such as PSO and DPSO at times provide better results. However, most of the time and especially when the optimization problem becomes complex, FODPSO provides better results.

The results also shows an improvement in visibility of cancer cells in the images when compared to the original image regardless of which algorithm implemented. This increases the accuracy of detection and analyzing of the cancer cells. Other image processing techniques such as edge detection or filters can also be used to further improve the quality of the image.

References

[1] M. Sezgin, and B.Sankar, "Surveyover Image Thresholding Techniques and Quantitative Performance Evaluation," Journal of Electrical Imaging, Vol. 13, No.1: pp. 146-165, 2004.

[2] V. Rajinikanth and M. S. Couceiro, "Multilevel Segmentation of Colour Image using Levy driven BFO Algorithm," Proceddings of the ICONIAAC' 14, No.19 : pp. 1-8, 2014.

[3] G. B. Patil and S. N. Jain, "Cancer Cells Detection Using Digital Image Processing Methods," International Journal of Latest Trends in Engineering and Technology (IJLTET), Vol. 3, No.4 : pp. 45-49, 2014.

[4] M. Maitra, A. Chatterjee, "A hybrid cooperative–comprehensive learning based PSO algorithm for image segmentation using multilevel thresholding", Expert Systems with Applications, Vol. 34, No.2, pp.1341–1350, 2008

[5] S.U. Lee, S.Y. Chung, and R.H Park, "A Comparative Performance Study Techniques for Segmentation, Computer Vision, Graphics and Image Processing," vol. 52, no2, pp. 171-190, 1990.

[6] N.R. Pal, and S. K. Pal, "A review on image segmentation techniques, Pattern Recognition," vol.26, no.9, pp. 1277-1294, 1993.

[7] P.D. Sathya, and R. Kayalvizhi, "Modified bacterial foraging algorithm based multilevel thresholding for image segmentation," Engineering Applications of Artificial Intelligence, vol. 24, pp. 595–615, 2011.

[8] P.D. Sathya, and R. Kayalvizhi, "Optimal multilevel thresholding using bacterial foraging algorithm," Expert Systems with Applications, vol. 38, pp.15549–15564, 2011.

[9] N. Otsu, "A Threshold selection method from Grey-Level Histograms," IEEE T. on Systems, Man and Cybernetics, vol. 9, no.1,pp. 62-66, 1979

[10] B. Akay, "A study on particle swarm optimization and artificial bee colony algorithms for multilevel thresholding," Applied Soft Computing, vol.13, no.6, pp. 3066–3091, 2013.

[11] K.Charansiriphaisan, S. Chiewchanwattana, and K. Sunat, "A comparative study of improved artificial bee colony algorithms applied to multilevel image thresholding," Mathematical Problems in Engineering, Vol. 2013, Article ID 927591, 17 pages, 2013.

[12 P.Ghamisi, M.S. Couceiro, J.A. Benediktsson, and N. M. F. Ferreira, "An efficient method for segmentation of images based on fractional calculus and natural selection," Expert Syst. Appl., vol. 39, no.16, pp. 12407– 12417, 2012.

[13] V. Rajinikanth, N. Sri Madhava Raja, and K. Latha, "Optimal Multilevel Image Thresholding: An Analysis with PSO and BFO Algorithms," Aust. J. Basic & Appl. Sci., vol. 8, no. 9: pp. 443-454, 2014.

[14] http://bisque.ece.ucsb.edu/client_service/view?resource=http://bisque.ece.ucsb .eu/data_service/dataset/2145442, Accessed at 10th Sept 2014.

[15] P. Moallem, and N. Razmjooy, "Optimal Threshold Computing in Automatic Image Thresholding using Adaptive Particle Swarm Optimization", Journal of applied research and technology, 10(5): 703-712, 2012.

[16] A. A. Yahya, Tan. Jieqing, and MinHu, "A novel model of image segmentation based on Watershed Algorithm". Advances in multimedia 2013, article 5,pp.5 2013.

[17] Y. Yang, J. Ming and Y. Nenghai, "Color Image Quality Assessment on CIEDE2000.".Advances in Multimedia vol. 2013, 10 pg, 2013.

[18] P.Ghamisi, M.S.Couceiro, and J.A. Benediktsson, "Classification of hyperspectral images with binary fractional order Darwinian PSO and random forests," SPIE Remote Sensing, 88920S-88920S-8, 2013.

[19] P.Ghamisi, M.S. Couceiro, F.M.L. Martins, and J.A. Benediktsson, "Multilevel image segmentation based on fractional-order Darwinian particle swarm optimization," IEEE T. on Geoscience and Remote sensing, vol. 52, no.5, pp.2382-2394, 2014.

Double Rotor Switched Reluctance Machine with reduced Torque Ripple

Muhammad Aiman Ismail, Aravind C.V*

Computer Intelligence Applied Research Cluster
Taylor's University, School of Engineering, Malaysia

*aravindcv@ieee.org

Abstract
Reluctance machine is one type of electrical machine which does not possess any permanent magnet to operate. Basically, Switched Reluctance Machine (SRM) operates by using the first electromagnetic principle; attraction and repulsion force concept. The air gap between stator pole and rotor pole gives a huge effect on the reluctance variation. Therefore, dual air-gap is introduced by making a double rotor structure design which can give a higher torque density production. In the previous development of novel double rotor switched reluctance machine which using a dual air-gap concept has a little drawback which can be improvised. Suppose the Double Rotor Switched Reluctance Machine (DRSRM) able to give a smooth transient curve for generated torque production when compared to conventional switched reluctance machine. However, the previous double rotor switched reluctance machine does not give a higher torque production compared to classic switched reluctance machine. The circular hole design in the stator pole of the switched reluctance machine could lower torque ripple and reduce the acoustic noise. Thus, double rotor switched reluctance machine is proposed which improvising torque production and lower the torque ripple. In this paper, a few machine designs are devised, then, the performance of machine designs are compared and evaluated through the computer simulation and numerical analysis. From the simulation result, the motor constant square density of new double rotor switched reluctance machine is improved by 140% compared to DRSRM. The ripple torque is reduced to 18.5% compared to SRM and 64.5% compared to DRSRM.

Keywords: dual air-gap, double rotor, switched reluctance, motor constant square density, torque ripple.

1. Introduction

Switched reluctance machine has high operational efficiency, large torque to inertia ratio, cheap and simple construction which clearly shows that this machine is chosen over other conventional machine for various applications like variable speed drives [1], wind energy [2], automotive [3-4], and elevator [5]. Basically, the operation of switched reluctance machine begins when the phase current passes through stator windings. When the stator pole gets excited, the closest rotor pole attracts to the corresponding stator pole due to the electromagnetic attraction and magnetic reluctance variation.

Nowadays, the switched reluctance machine has very high demand in many application due to expensive permanent magnet. Most people are making a research on increase the average torque density of switched reluctance machine over wide speed range of the operating system [6-7]. Besides that, there are other different approaches that could optimized the switched reluctance machine that could give a huge benefit to the industry and society as well. Switched reluctance machine properties can be improved by ripple torque reduction [8], machine design optimization [9] and current control [10].

An improved novel switched reluctance machine design can be produced by making the previous switched reluctance machine design based on its development and improvement as a guideline which presented in [8-10]. The previous developed switched reluctance machine design in [10] is assessed. From the assessment made, the torque density production in normal switched reluctance machine relies on distance of air gap between stator and rotor. The torque production is inversely proportional to the total length of air-gap. Thus, the dual air-gap magnetic circuit is introduced at the double rotor switched reluctance machine design [11]. Since the total length air gap remains the same, the length for each air-gap is reduced and the torque density generation is increased. Conversely, the volume of the double rotor switched reluctance machine much bigger and the average torque density is lower compared to normal switched reluctance machine. Although dual air-gap magnetic circuit has little disadvantages, it offers some improvements in other features for switched reluctance machine, thus, gives a huge opportunity for used in industrial application. The previous novel switched reluctance machine design which has a circular hole in the stator pole is evaluated and presented in [12]. It has been identified the torque ripple is lower compared to conventional switched reluctance machine. In this paper, a dual air-gap with circular hole magnetic circuit is proposed. An improved novel double rotor switched reluctance machine design with a better torque density capability and lower torque ripple is introduced. To determine and evaluate the machine performance, the finite element analysis is used and motor constant square density of all the machines are being compared where the size and volume for all machine should be same for experimental purpose. The main objective of this research project is improvising the performance of the previous double rotor switched reluctance machine in terms of torque density and torque ripple especially by using the electro-magnetic principles. Huge demand on the market for double rotor switched reluctance machine and it is used in many application due to its smooth operation and interesting features which injects a motivation to design an improved double rotor switched reluctance machine.

2. Theoretical Framework

2.1 Magnetic Circuit Design for Double Rotor Switched Reluctance Machine

The switched reluctance machine operates based on the first electromagnetic principle; attraction and repulsion of the magnetic force. The torque production capability relies on the electromagnetic force in the air gap flux linkage between stator and rotor. As the torque density of reluctance is directly proportional to the air-gap flux linkage, the double rotor switched reluctance machine which has two air-gap in the machine structure is introduced. The dual air-gap magnetic circuit used in the double rotor switched reluctance machine are presented in Fig. 1 as,

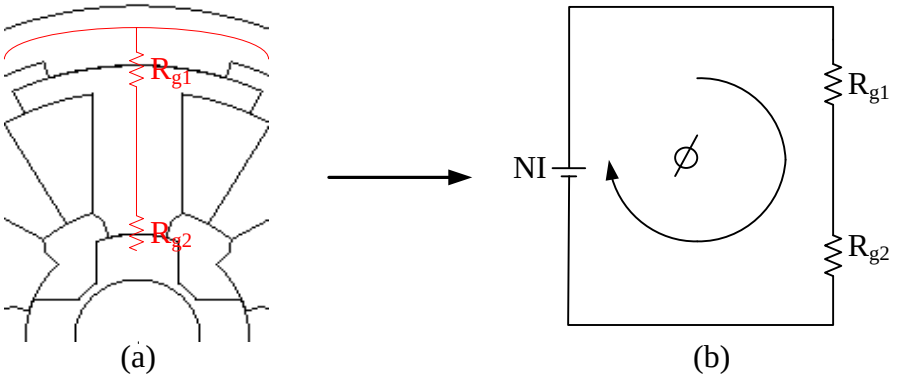

Fig. 1. Double Rotor Switched Reluctance Machine

(a) Magnetic Reluctance (b) Equivalent Magnetic Circuit

The total magnetic reluctance for conventional double rotor switched reluctance machine is given in Equation (1) as,

$$R_t = R_{g1} + R_{g2} \tag{1}$$

where R_t is the total magnetic reluctance, R_{g1} is the first magnetic reluctance at the air-gap and R_{g2} is the second magnetic reluctance at the air-gap. The magnetic flux production for conventional double rotor switched reluctance machine is given in Equation (2) as,

$$NI = \emptyset\left(R_{g1} + R_{g2}\right) \tag{2}$$

where N is the number of turns per phase, I is the phase current and $\emptyset$ is the magnetic flux.

2.2 Magnetic Circuit Design for Proposed Double Rotor Switched Reluctance Machine

Although, torque density of reluctance machine is improved with dual air-gap magnetic circuit, the ripple torque of reluctance is increased which causes a mechanical vibration and acoustic noise. The circular hole in the tip of stator pole is introduced which can guide the flux linkage direction to the machine rotation.

The circular hole is designed instead of square hole or triangle hole due to its-shaped. Circular hole occupies large volume compared to other shapes in the same size. Besides that, it does not have edges which can obstruct the flux linkage direction. The dual air-gap with circular hole magnetic circuit used in the double rotor switched reluctance machine are presented in Fig. 2 as,

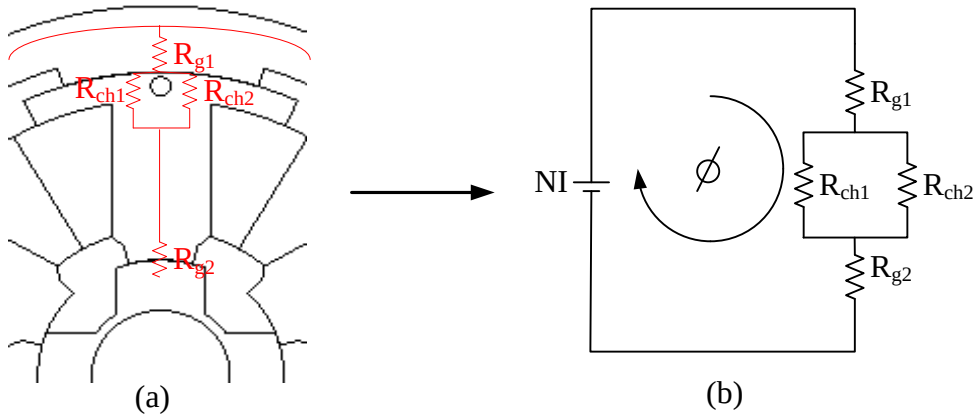

Fig. 2. Proposed Double Rotor Switched Reluctance Machine

(a) Magnetic Reluctance (b) Equivalent Magnetic Circuit

The presence of circular hole on the stator structure makes the magnetic circuit has two magnetic reluctances in parallel. The total magnetic reluctance for conventional double rotor switched reluctance machine is given in Equation (3) and (4) as,

$$R_t = R_{g1} + R_{g2} + (R_{ch1} || R_{ch2}) \tag{3}$$

$$R_t = R_{g1} + R_{g2} + \frac{R_{ch1} \times R_{ch2}}{R_{ch1} + R_{ch2}} \tag{4}$$

where R_{ch1} is the first magnetic reluctance at the circular hole and R_{ch2} is the second magnetic reluctance at the circular hole. The magnetic flux production for conventional double rotor switched reluctance machine is given in Equation (5) as,

$$NI = \emptyset \left(R_{g1} + R_{g2} + \frac{R_{ch1} \times R_{ch2}}{R_{ch1} + R_{ch2}} \right) \tag{5}$$

3 Research Methodology

Few machine structures have been designed and simulated in the JMAG® software. All machine structures are designed in the same size and equal magnetic circuit. The first approach is making a few double rotor switched reluctance machines and select the machine design which can give the best torque density. The second approach is determining the circular hole radius and length between its center point and tip of stator pole. The proposed machine design plan flow chart is presented in Fig. 3 as,

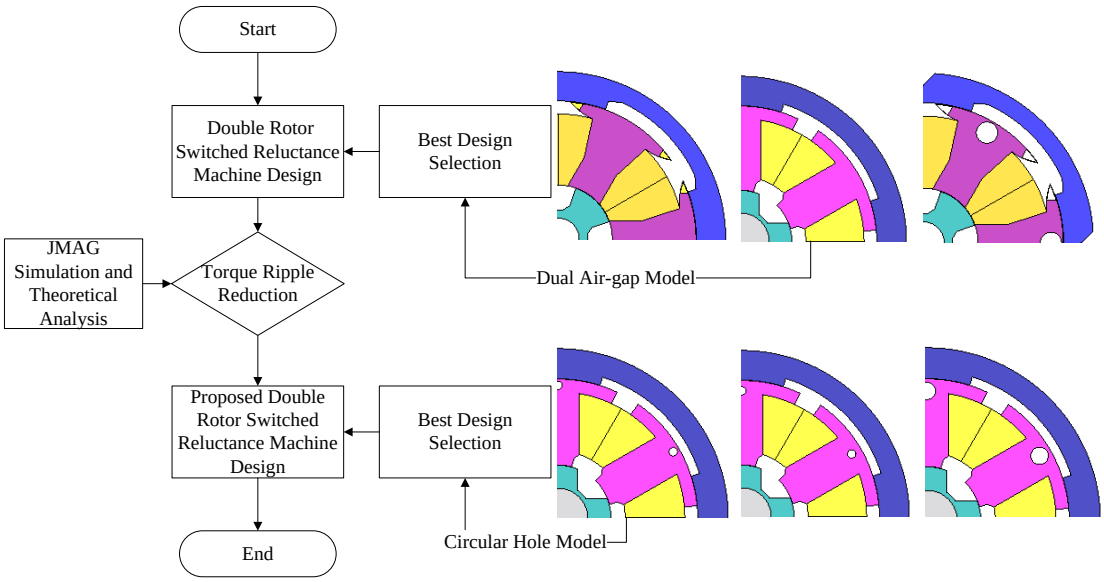

Fig. 3. Proposed Design Plan Flow Chart

The structural dimension of the proposed machine is presented in Table 1 and the 3D model design of the proposed double rotor switched reluctance machine is presented in Fig 4.

TABLE 1. PROPOSED STRUCTURE SPECIFICATION

Parameter	Value
Machine diameter	80 mm
Inner air-gap length	0.05 mm
Outer air-gap length	0.05 mm
Outer rotor pole arc	35°
Inner rotor pole arc	42°
Outer stator teeth pole arc	50°
Inner stator teeth pole arc	30°
Circular hole diameter	1 mm
Number of turns per phase	116 turns

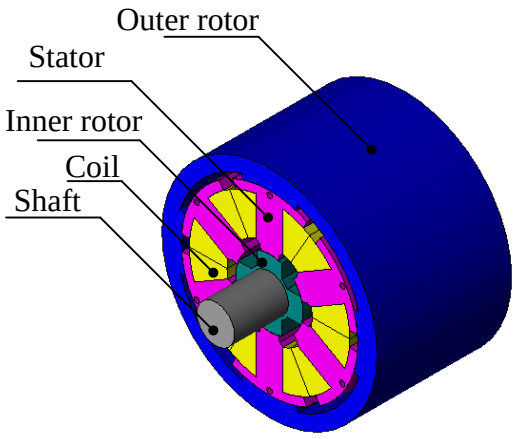

Fig. 4. Proposed Double Rotor Switched Reluctance Machine

4 Finite Element Analysis (FEA)

A Finite Element Analysis (FEA) method has been done on this machine design in order to determine and identify the torque production of the machine design. In research based, the finite element analysis is use as a basic analysis material or object in order to identify the applied stress that occurs in the machine design. It is commonly used as an identifier of potential magnetic vector regardless the magnetic circuit complexity as well as non-linear properties of its magnetic material. In this machine design experiment the finite element analysis of the proposed machine is identified based on the JMAG software. The proposed machine magnetic flux characteristics is presented in Fig. 4 as,

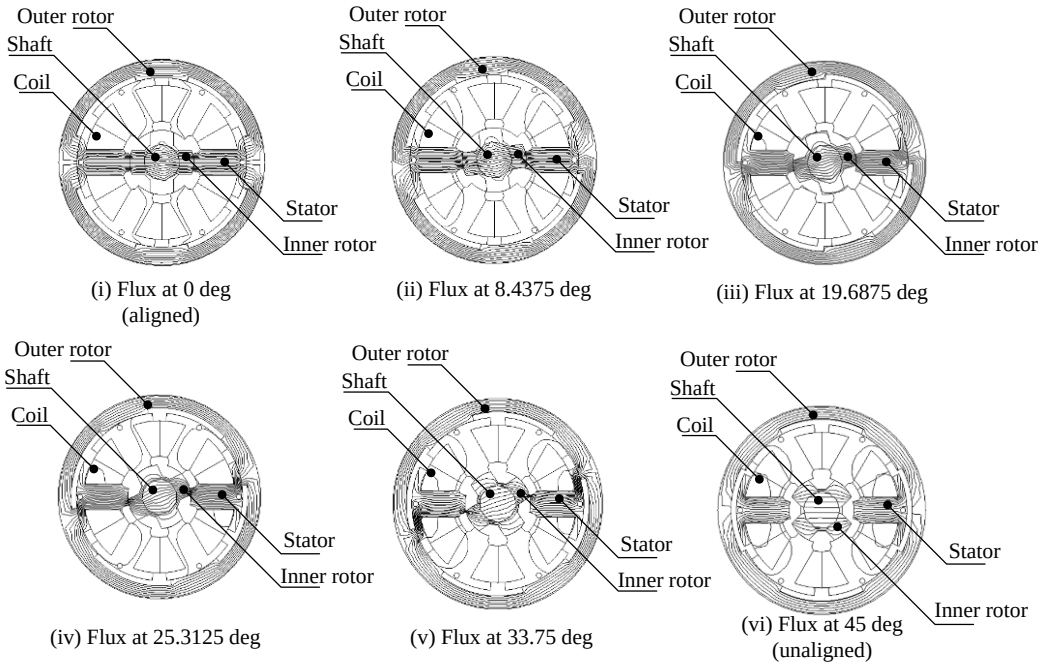

Fig. 5. Proposed Double Rotor Switched Reluctance Machine Circuit

Fig. 5 above shows the magnetic flux characteristics for proposed model design. The current on coil winding on this simulation is a single phase supply and its value is 7 A. Fig. 5(i) illustrates the complete non-overlap flux line. It means the torque is not been generated yet, thus, the long flux line is shown horizontally. There is a quite large number of magnetic flux line on this proposed machine design. Fig. 5 (ii)-(v) shows the variation behavior of magnetic flux line on the proposed machine design. Fig. 5(vi) shows a flux line at the unaligned position. A small increment angle leads to a single step for torque density increment.

5. Results and Discussion

5.1 Evaluation Parameters

The motor constant square density (G) calculation has been used in order to evaluate and compare the performance between conventional and proposed machine design. This calculation is very reliable as it consists of the power, torque density and

volume of structure design. The motor constant square density (G) is shown in the Equation (5).

$$G = \frac{{K_m}^2}{V} \tag{5}$$

where K_m is the machine constant in $[Nm/A/W^{-(1/2)}]$, V is the machine volume $[m^3]$. The machine constant is given as in the Equation (6).

$$K_m = \frac{{K_m}^2}{\sqrt{P}} \tag{6}$$

where K_T is the torque constant $[Nm/A]$ and P is the power input to the winding coil $[W]$. The torque constant can be expressed in the Equation (7).

$$K_T = \frac{T_{avg}}{I} \tag{7}$$

where T_{avg} is the average torque $[Nm]$ and I is the maximum input current to the machine $[A]$.

Besides that, the calculation for ripple torque is done to identify and compare the ripple torque of machine design. The ripple torque (T_r) equation is given in the Equation (8).

$$T_r = \frac{T_{max} - T_{min}}{T_{avg}} x\ 100\% \tag{8}$$

where T_{max} is the maximum torque density $[Nm]$ and T_{min} is the minimum torque density $[Nm]$.

4.2 I-Ps Characteristics

In the I-Ps characteristics experiment the physical phenomena analysis of the magnetic circuit is created using static analysis model for the simulation of the circuit model from the coil drive circuit are presented in Fig. 6. The result from the I-Ps characteristics experimental analysis for the current value of $7A$ at unaligned and aligned position is presented.

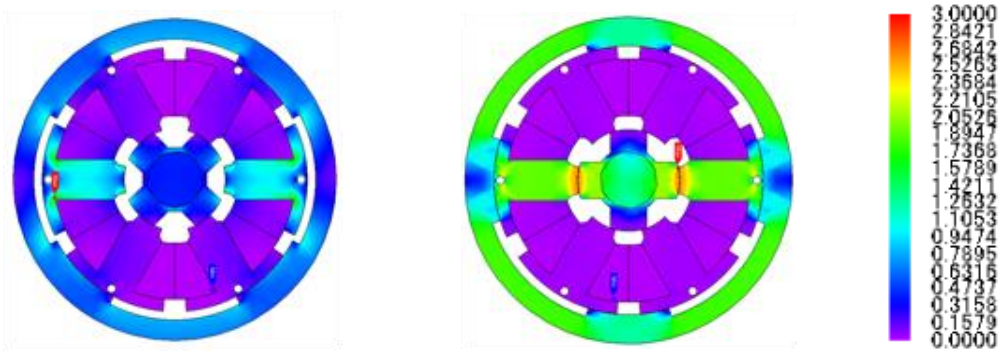

(a) unaligned position (b) aligned position Unit: T

Fig. 6. Double Rotor Position for Magnetic Flux Linkage

The Fig. 6 displays the magnetic flux linkage of proposed machine at unaligned position (a) and aligned position (b). As the proposed machine at unaligned position (a), the maximum value of magnetic flux linkage produces by the machine is $1.44T$ and when the proposed machine at aligned position (b), the maximum value of magnetic flux linkage produces by the machine is $2.48T$. This phenomena is happened as the machine at aligned position has higher number of flux line along the machine compared to the machine at unaligned position. As the number of flux line is gradually increases, the magnetic flux linkage is increases as well.

4.3 Comparative Evaluations

In the static characteristics experiment, the torque analysis model for three different switched reluctance machine structure with coil drive circuit is presented in the Fig. 7. The static characteristics shows that the proposed machine has higher torque generation in comparison to conventional switched reluctance machine and previous novel double rotor switched reluctance machine.

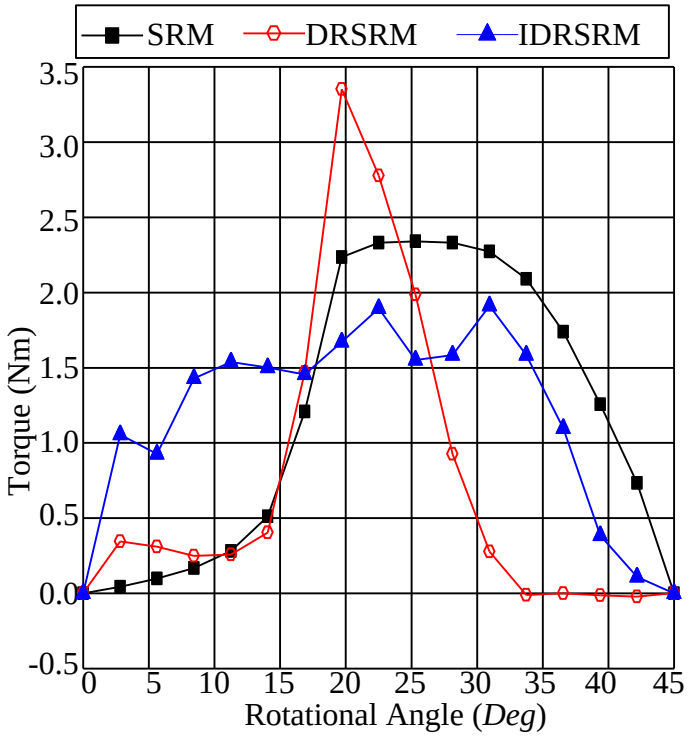

Fig. 7. Static Characteristics

The comparative evaluation for motor constant square density and torque ripple between typical switched reluctance machine, previous novel double rotor switched reluctance machine, and improved double rotor switched reluctance machine in the same size is shown in the table 2.

TABLE 2. COMPARISON ON FIGURE OF MERIT

Figure of Merit	*SRM*	*DRSRM*	*Improved DRSRM*
$I\ [A]$	7	7	7
$V\ [m^3]$	$2.13e^{-3}$	$1.99e^{-3}$	$2.11e^{-3}$
$T_{avg}\ [Nm]$	1.1555	0.7243	1.1584
$K_t\ [Nm/A]$	0.1651	0.1035	0.1655
$K_m\ \left[Nm/A/W^{-\left(\frac{1}{2}\right)}\right]$	0.0165	0.0104	0.0166
$G\ [Nm^2/A^2/W/m^3]$	0.1278	0.0544	**0.1306**
$T_{max}\ [Nm]$	2.3395	3.3504	1.9127
$T_{min}\ [Nm]$	$-2.28e^{-7}$	-0.0223	$-2.44e^{-5}$
$T_r\ [\%]$	202.47	465.65	**165.12**

It is clearly seen the improved double rotor switched reluctance machine shows a better average torque density and higher motor constant square density compared to two conventional reluctance machines. The improved DRSRM has the lowest ripple torque in comparison to other two conventional switched reluctance machine which obviously shows a promising results in the reluctance machine research dimension.

5. Conclusion

The flux assisted of the improved double rotor switched reluctance machine is designed based on the double rotor structure and circular hole in the stator pole structure. The
I-P characteristics and static characteristics of the machine structure design are analyzed using a standard laboratory simulation, finite element analysis and comparative results are presented. The new double rotor switched reluctance machine are compared to conventional switched reluctance machine and previous novel double rotor switched reluctance machine in terms of motor constant square density and ripple torque at the same size of machine. There is a huge improvement of the improved double rotor switched reluctance machine. The motor constant square density of new double rotor switched reluctance machine is increased by 140% compared to double rotor switched reluctance machine. The ripple torque of new double rotor switched reluctance machine is reduced greatly by 18.5% compared to conventional switched reluctance machine and 64.5% compared to double rotor switched reluctance machine. Therefore, the proposed double rotor switched reluctance machine can be applied in the industrial application like electric vehicle as it gives high torque density and operate smoothly.

References

[1] H.M.B. Metwally, W.R. Anis, "Performance Analysis of PV Pumping Systems using Switched Reluctance Motor Drives," *Energ. Convers. Mgmt*, vol. 38, no. 1, pp. 1-11, 1997.

[2] C.A. Ferreira, S.R. Jones, B.T. Drager, W.S. Heglund, "Design and Implementation of a Five Horsepower, Switched Reluctance Fuel-Lube, Pump Motor Drive for a Gas Turbine Engine," *IEEE Transactions on Power Electronics*, Vol. 10, No. 1, pp. 55-61, Jan. 1995.

[3] N. Abut, B. Cakir, U. Akca, N. Erturk, "Fuzzy Control Applications of SR Motor Drive for Transportation System," *Proceedings ITSC '97, the IEEE Conference on Intelligent Transportation System,* pp.135-140, 9-12 Nov. 1997.

[4] Y. Yang, N. Schofield, A. Emadi, "Double-Rotor Switched Reluctance Machine (DRSRM)," *IEEE Transactions on Energy Conversions,* pp. 1-10, 2015.

[5] T. D. Kumar, A. Nagarajan, "Design of Switched Reluctance Motor for Elevator Application," *Journal of Asian Scientific Research,* No. 3, pp. 258-267, 2013.

[6] R. Krishnan, Switched Reluctance Motor Drives: Modelling Simulation, Analysis, Design, and Applications. BocaRaton, FL: CRC Press, 2001.

[7] Aravind CV, G. P. Ramesh, M. Aiman, "Electromagnetic Design of a Novel Double Rotor Switched Reluctance Machine," *International Journal of Applied Engineering Research,* Vol. 10, No. 17, pp. 12856-12861, 2015.

[8] Ozoglu. Y., Guzelbeyoglu, N., et al. 2005. Torque Ripple Reduction in Switched Reluctance Motors by Pole Tip Shaping. *Electric Power Systems Research* 74 (1): 955-103.

[9] Matsuo, T. 1994. "Rotor Design Optimization of Synchronous Reluctance Machine." *IEEE Transactions on Energy Conversion*, Vol.9, No.2, June 1994.

[10] Zaskalicky, P. and Zaskalicka, M. 2008. "Analytical Method of Calculation of the Current and Torque of a Reluctance Stepper Motor using Fourier Complex Series." *Power Electronics and Motion Control Conference, 2008. EPE-PEMC 2008. 13th*. 889-902.

[11] C.V. Aravind, "Design and Development of Double Rotor Switched Reluctance Motor using Magnetic Circuit Analysis," Ph.D thesis, Universiti Putra Malaysia, Selangor, Malaysia, 2013.

[12] Jawad Faiz, "Performance Improvement of a Switched Reluctance Motor," *Progress In Electromagnetics Research Symposium (PIERS) Proceedings,* KL, Malaysia, pp. 728-732, 27-30 March 2012.

Effect of Moisture on Electrical Response of Soil under High Impulse Voltage Applications

Mohd Syariffuddin Bin Johari[1*], Siow Chun Lim[2]
[1*, 2]Department of Electrical and Electronic Engineering, School of Engineering, Taylor's University, Malaysia

*Syariffuddin_91@yahoo.com

Soil plays an important role when designing the grounding system because it is one of the three major factors that affect the efficiency of the grounding system besides conductivity and arrangement of the electrode and contact surface area between the electrode and the soil. Engineers normally consider only the soil resistivity under normal condition when designing the grounding system. Under certain circumstances such as lightning, the electrical response of the soil will change accordingly and thus the grounding system will be affected. The purpose of the study is to investigate the effect of moisture content on the electrical behavior of sand and clay under high impulse voltage condition. At first, both soil samples was dried in the vacuum oven at 110 ± 5°C to remove the water content until became 0%. Then the sample was subjected to 30 shots of standard (1.2/50μs) lightning impulse voltage generated by the Marx generator for both positive and negative impulse polarities. This study is followed by moistening the sample with 5% amount of water over the volume of the samples. The corresponding $V_{50\%}$ breakdown voltage for both sand and clay are calculated and the value obtained was converted to standard atmospheric condition. Statistical analysis was done for the voltage at breakdown and time to breakdown of the soil sample. It is found that the breakdown voltage for sand is higher than clay for both positive and negative impulse polarity in which the moisture content and physical properties of sand and clay have an effect on the breakdown voltage of sand and clay under high impulse voltage condition.
Keywords: grounding system, soil resistivity, breakdown voltage, impulse voltage.

1. Introduction

In any electrical system, it is crucial to have a good grounding system where it has the capability of channeling the excessive or unwanted charges from the system in order to avoid the risk of equipment failure whenever there are faults occurred. Efficiency of grounding system is highly dependent on the soil characteristic namely the soil resistivity in which it varies from one type of soil to another. However, under high frequency and high voltage phenomena such as lightning, the soil characteristic is significantly different form its static behavior [1].

Based on the literature, one way to characterize the soil behavior under high impulse voltage condition is by analyzing its 50% breakdown voltage which can be used to indicate the ability of soil in discharging high impulse voltage. In other words, soil with lower 50% breakdown voltage is expected to be more conductive. Other than 50% breakdown voltage, two more interesting parameters which can be analysed is the time to breakdown and voltage at breakdown of the soil sample.

Several papers have done similar studies [2, 3]. However there are very few which have studied these two parameters statistically. It is well known that moisture affects soil resistivity. However effect of moisture on the soil under this high impulse voltage condition is still very limitedly discussed in the literature. Most of the past studies have been done on sand [1, 4] due to the fact that it is the most common type of soil used in construction of building and is easy to be handled. In this paper, the studies are focused on sand and clay. Clay is chosen due to the fact that its physical properties are opposite to sand especially in terms of resistivity and porosity [5].

The objective of this research is to analyse and compare the electrical behavior of both sand and clay in terms of 50% breakdown voltage, time to breakdown and voltage at breakdown under high impulse voltage condition since sand and clay have distinct values in term of soil resistivity [6]. This will give better understanding on how sand and clay react under high impulse voltage condition given different amount of moisture. Based on the result obtained, it will provide the design engineer with more information in designing the grounding system.

2. Research Methodology

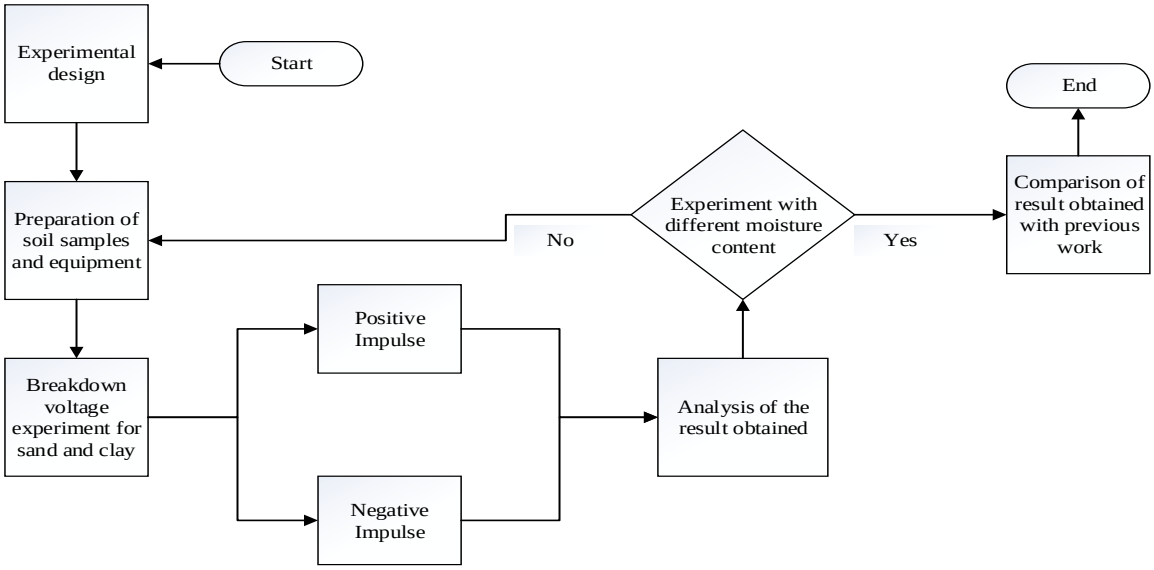

Figure 1: Research Methodology

Figure 1 outlines the flow of this research project. It consists of 3 major stages namely experimental design stage, experiment stage and experimental data analysis stage. Each soil sample was subjected to up and down analysis to determine the breakdown voltage for both positive and negative impulse polarities. The experiment was done for 0% moisture content followed by 5% of moisture content.

2.1 Experimental Design Stage

The design setup is shown in Figure 2. The experiment was performed on a cylindrical acrylic container with inner diameter of 242mm and height of 105mm with the copper rod having an approximate dimension of 15mm diameter and 300mm height. The thickness of the soil sample inside the acrylic container is set to be 65mm. A cylindrical metal plate with diameter of 240mm and thickness of 5mm is placed inside and at the bottom of the acrylic container to serve as a medium to channel the impulse current directly to the ground through a ground wire whenever there is breakdown occurred.

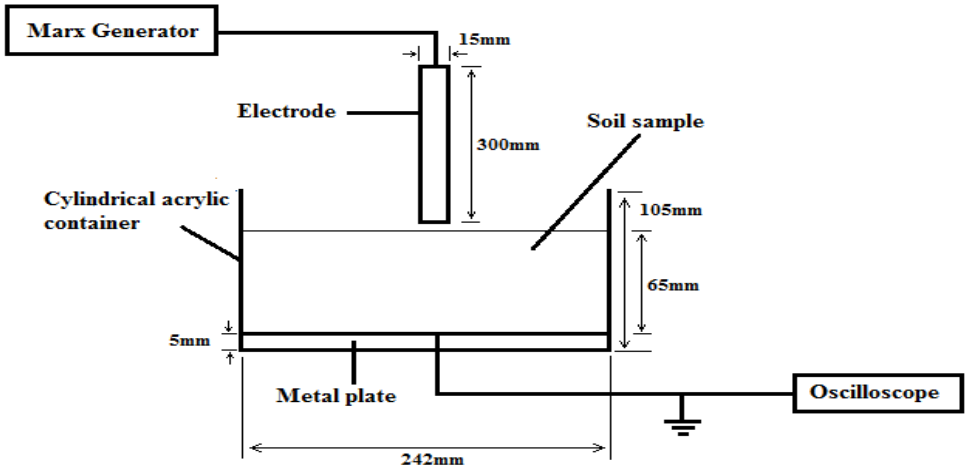

Figure 2: Setup of the experiment

2.2 Experimental Stage

Two types of soil samples were used. The sand was filtered to remove the pebbles in order to get pure coarse sand. As for the clay, it was crushed into powder form. Both samples were dried in the oven approximately 16 hours at the temperature of 110 ± 5 °C [7] using a metal container in order to have approximately 0% moisture content of soil sample followed by adding water based on the specified moisture content (0% and 5%) to the soil and mix them as uniform as possible in the cylindrical acrylic container as shown in Figure 3.

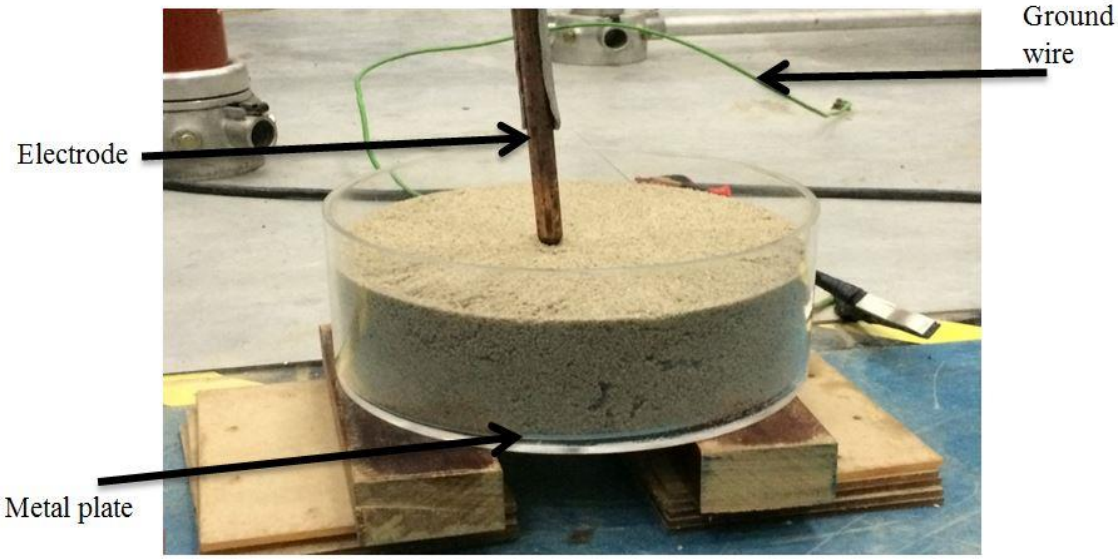

Figure 3: Soil sample inside acrylic container

The 0% and 5% moisture content were quantified based on the volume of the of the soil sample inside the acrylic container using the formula:

$$V = \pi r^2 h \quad (1)$$

Where: V = Volume for cylindrical container (soil sample)
r = Radius of the cylindrical container
h = Thickness of soil sample

The volume V was 2.989 mm^3 and the corresponding 5% added water was 0.1495mm^3. The volume for 5% moisture content was used to calculate the height of measuring cylinder where the radius is known for easy transfer of water to the soil sample. The temperature and relative humidity were measured before the experiment began to apply standard reference atmospheric condition as discussed in the next section.

The impulse voltage was generated using the Marx Generator as shown in Figure 4 having the capability of producing standard high impulse voltage (1.2/50μs) following the standard [8] up to magnitude of 260kV (2 stages of configuration) with a range of 0V to 130kV per stage of configuration. Each sample was subjected to 30 shots of impulse voltage with approximately 90 seconds interval between each shot for both polarities. This interval is to ensure that the soil regained its initial properties before the next shot is applied.

Figure 4: Marx Generator

The voltage signal was captured on a DSO09104A Agilent Infiniium 9000 Series Oscilloscope that has the specifications of 1 Ghz, 4 channels and has the analog sample rate of 5GSa/s.

2.3 Experimental Data Analysis Stage

The soil sample was subjected to random impulse voltage in order to determine the minimum breakdown voltage of the sample. Up and down analysis was used in this experiment for both positive and negative impulse polarities in which after the minimum breakdown voltage is obtained, it is then followed by stepping up whenever there was breakdown and stepping down whenever there was no breakdown with a step voltage of 2kV. The result from Up and Down analysis was used to calculate the $V_{50\%}$ of each soil sample using the formula [9]:

$$V_{50\%} = V_0 + \Delta V \left(\frac{A}{k} \pm \frac{1}{2}\right) \quad (2)$$

Where: V_0 = Minimum breakdown voltage (kV)
ΔV = Step voltage (kV)
k = The number of breakdown voltage occurred in that particular event
$A = \sum_{i=1}^{r} ik_i$; k_i is the number of events concerned at the i^{th} step

The standard deviation for the breakdown voltage for each soil sample was calculated using the formula [9]:

$$s = 1.62\, x\, \Delta V \left(\frac{kB - A^2}{k^2} + 0.029\right) \quad (3)$$

Where: ΔV = Step voltage
k = The number of breakdown voltage occurred in that particular event
$B = \sum_{i=1}^{r} i^2 k_i$; k_i is the number of events concerned at the i^{th} step.
$A = \sum_{i=1}^{r} ik_i$; k_i is the number of events concerned at the i^{th} step.

The result of the breakdown voltage and time to breakdown obtained was analyzed statistically using the independent samples T-test method in the SPSS

software in which this method comparing the means of two unrelated groups and evaluates them. In other words, this test verifies whether the sand and clay is significantly different from each other by comparing the means between sand and clay soil sample in terms of voltage at breakdown and time to breakdown.

3. Result and Discussion

3.1 Breakdown Voltage

The result of breakdown voltage for both positive and negative impulse polarities given 0% and 5% moisture content are depicted in Table 1. The values shown are the values which have been converted to their corresponding breakdown voltage values under standard atmospheric condition as stated in [10] where temperature, T_0 = 20°C (293 K), absolute air pressure, P_0 = 1,013 hPa (1,013 mbar) and absolute humidity, h_0 = 11 g/m^3. The result in Table 1 shows that the value of breakdown voltage for positive impulse is higher than the negative impulse and sand has higher breakdown voltage for both polarities compared to clay given the same amount of moisture content. This clearly indicates that clay is more efficient in discharging high impulse voltage.

Table 1: Breakdown voltage of sand and clay at standard condition

Applied Voltage, kV	**Percentage of moisture content over the volume of the sample (%)**	**Sample A (Sand)**		**Sample B (Clay)**	
		Breakdown Voltage (V50%) , kV	**Standard Deviation, kV**	**Breakdown Voltage (V50%) , kV**	**Standard Deviation, kV**
Positive impulse	0	61.2	4.9	46.2	4.2
	5	35.6	2.9	34.4	4.8
Negative impulse	0	50.7	4.7	41.2	2.6
	5	34.2	2.9	32.3	2.5

The comparison between the voltage traces for both no breakdown and breakdown voltage is shown in Figure 5, 7, 9 and 11 for positive impulse and Figure 6, 8, 10 and 12 for negative impulse. Whenever breakdown occurs, a sudden drop of voltage appears which indicates that the soil sample becoming conductive at that particular of time where the impulse current can pass through the soil and directly discharge through the grounding wire.

Positive Impulse **Negative Impulse**

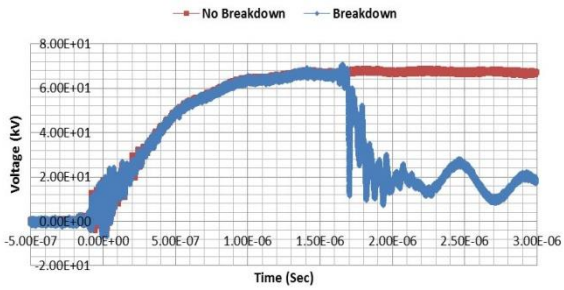

Figure 5: Sand 0% moisture

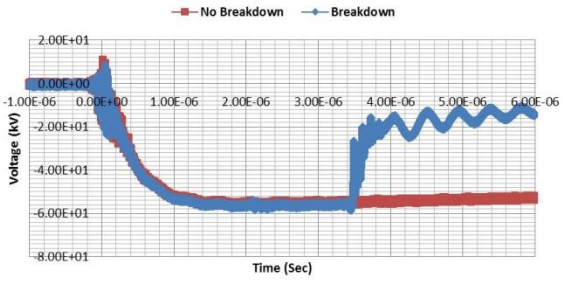

Figure 6: Sand 0% moisture

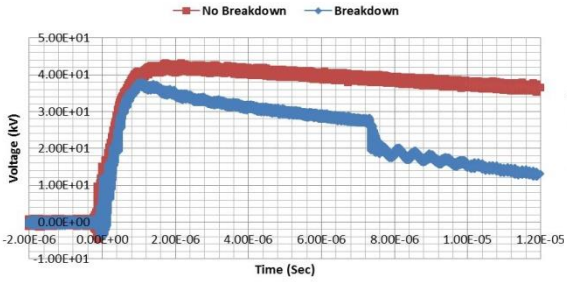

Figure 7: Sand 5% moisture

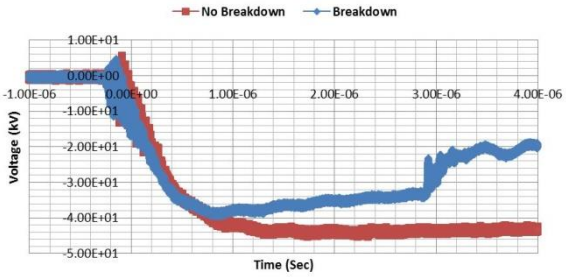

Figure 8: Sand 5% moisture

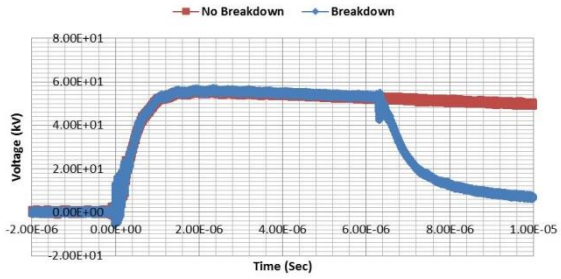

Figure 9: Clay 0% moisture

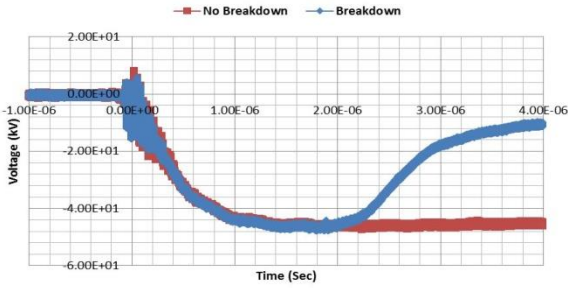

Figure 10: Clay 0% moisture

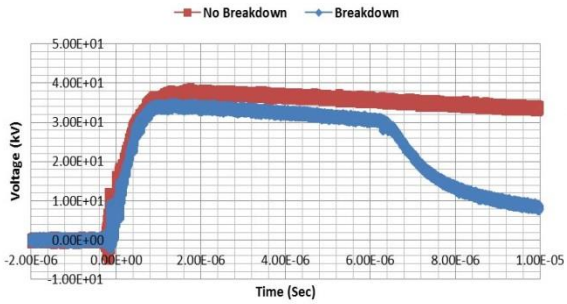

Figure 11: Clay 5% moisture

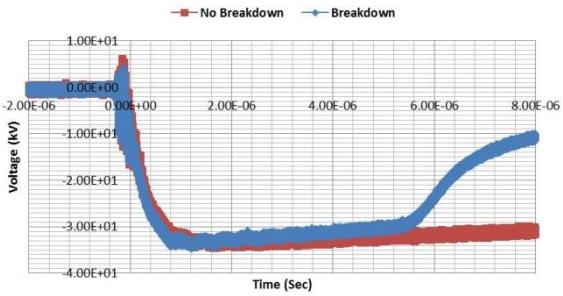

Figure 12: Clay 5% moisture

It is observed that, the breakdown voltage for positive polarity is higher than negative polarity for all the voltage traces (Figure 5 – Figure 12). Meanwhile, the voltage traces show reduction in breakdown voltage between sand 0% and sand 5% (Figure 5 – Figure 8) for both polarities. The same result can be observed for clay 0%

and clay 5% (Figure 9 – Figure 12). The reduction in the breakdown voltage is due to the effect of moisture added to the soil sample which has caused the soil resistivity to decrease thus increasing the tendency for the soil sample to be more conductive. When a comparison is done between sand and clay for both 0% (Figure 5, 6, 9, 10) and 5% (Figure 7, 8, 11, 12) moisture content for both polarities, it is found that sand has higher breakdown voltage than clay. This is referring to the fact [6] that the soil resistivity in sand is higher than clay. Note that the above mentioned are based on the physical observation. Statistical analysis will be outline in the next sub-section.

When 5% amount of moisture is added to the sample, the sand and clay experience lower breakdown voltage in which the efficiency of discharging the impulse voltage is higher than 0% moisture content. This is due to some of the energy from the impulse voltage are being absorbed by the water. It is found that there is a gap exists between no-breakdown and breakdown voltage as shown in Figure 7, 8, 11 and 12. The reason why the gap for sand is bigger than clay is probably due to the porosity level of clay which is higher than sand. Meaning that, clay particle absorb more water than sand particle [11] thus the amount of water left to fill the void (outside the clay particle) between the clay particle is lesser than sand. This caused the energy absorption by water in clay is smaller than the energy absorption by water in sand. In addition, the presence of moisture has caused a higher amount of reduction of 50% breakdown voltage in sand than clay under both polarities. A possible explanation is again due to the porosity of sand which allows more moisture to remain as moisture in the sand sample. Therefore, a significant portion of the impulse current will flow through the moisture in sand.

It can be seen that in sand 0% for both impulse polarities, the graph for breakdown voltage oscillates before it reaches stable state. This oscillation decreases as an amount of water is added to the sand. This oscillation is probably due to the breakdown of the small air particle occupied between the sand particles before it reaches the metal plate connected to the grounding wire. When 5% of moisture is added to the sand, the water particles replaced the air to fill the void. Based on [12], the breakdown voltage of water is five times smaller compared to air in which it can be seen clearly in the graph that oscillation for sand 5% is much smaller than sand 0%.

Table 2: Size of particle [11]

Particle Name	**Size Range**
Sand	2mm – 0.05mm
Clay	<0.002mm

In clay 0% and 5%, there are no traces of oscillation in the breakdown graph. This is due to the particle size of clay which is twenty five times smaller compared to (Table 2) that caused clay for having less air gap to be filled by air. Thus, this indicates the reason why clay does not have any oscillation after the breakdown.

3.2 Statistical Analysis

Independent T-test was done to statistically analyse both the breakdown voltage and the time to breakdown among sand and clay to verify whether there are any significant differences among the selected combinations of samples. The independent T-test was divided into two categories which are positive impulse and negative impulse and the combinations of the test samples are the same for both categories; Sand 0% - Sand 5%, Sand 0% - Clay 0%, Clay 0% - Clay 5%, and Clay 5% - Sand 5%. The confidence level was set to be 95% in which when the computed P

value is less than 0.05, it shows that there is statistical significant difference between the compared test samples. The result of the test for both impulse polarities are shown in Table 3 and Table 4.

Table 3: Positive impulse independent sample T-test

Positive Impulse				
Independent T-test	P-value of Voltage at breakdown	Significant Difference	P-value of Time to breakdown	Significant Difference
Sand 0% - Sand 5%	0.000	Yes	0.000	Yes
Sand 0% - Clay 0%	0.000	Yes	0.000	Yes
Clay 0% - Clay 5%	0.000	Yes	0.690	No
Clay 5% - Sand 5%	0.091	No	0.638	No

Table 4: Negative impulse independent sample T-test

Negative Impulse				
Independent T-test	P-value of Voltage at breakdown	Significant Difference	P-value of Time to breakdown	Significant Difference
Sand 0% - Sand 5%	0.000	Yes	0.000	Yes
Sand 0% - Clay 0%	0.000	Yes	0.107	No
Clay 0% - Clay 5%	0.000	Yes	0.000	Yes
Clay 5% - Sand 5%	0.008	Yes	0.012	Yes

The statistical analysis result shows that there is statistical significant difference for sand 0% and sand 5% for both polarities. This indicates that the moisture does have an effect on both voltage at breakdown and time to breakdown for these two samples. As for clay 0% and clay 5%, it is found that, the moisture only has an effect for both voltage at breakdown and time to breakdown for negative polarities. But for positive polarities, it only has an effect for voltage at breakdown. Meanwhile, for comparison between sand and clay, it is found that, the moisture content does have an effect for voltage at breakdown for both 0% and 5% moisture content at both polarities. As for the time to breakdown, the moisture only has an effect for the combination of Sand 0% - Clay 0% for positive impulse and Clay 5% - Sand 5% for negative impulse. At present moment, these findings are yet to be understood.

4. Conclusion

In conclusion, sand has higher breakdown voltage compared to clay for both impulse polarities which indicates that clay has lower soil resistivity than sand and the voltage for positive impulse polarities is higher than the voltage for negative impulse polarities for both type of soil with 0% and 5% moisture content. It is found that, when 5% of moisture was added to both soil samples, the graph of the breakdown voltage is lowered from the no-breakdown graph is due to reduction of resistivity,

according to the influence of moisture and salt content. When analyzing the traces of the breakdown voltage, it can be seen clearly that right after the breakdown event, the voltage waveform for sand 0% is oscillatory and as 5% moisture is added, the oscillation reduced. As for the clay, there is no oscillation found after the breakdown. This suggests that the physical property of soil which is in this case is the particle size has an effect on the trend of the breakdown voltage traces as discussed on the result and discussion section.

Based on this research, it gave better understanding on the electrical behavior of sand and clay under different amount of moisture content when subjected to high impulse voltage. The gathered knowledge is useful for setting experimental test. These understanding can be further increase in the future by comparing other type of soil sample with the same amount of moisture under high impulse voltage condition and the influence of oscillation should be considered for evaluating ground potential rise of grounding systems along with the existing of gap between the no-breakdown and breakdown voltage waveform when moisture is added to the soil sample. Another experiment should be conducted in the future by considering increments of moisture from 0% until saturation.

References

[1] N. Mohamad Nor, A. Ramli, "Electrical properties of dry soil under high impulse current", *Journal of Electrostatics*, 65, pp.500-505, 2007.

[2] F. E. Asimakopoulou, I. F. Gonos, I. A. Stathopulos, "Experimental Investigation on Soil Ionization", *Proceedings of the 16th International Symposium on High Voltage Engineering*, 2009.

[3] N. M. Nor, A. Hadad, H. Griffths, "Characterization of Ionization Phenomena in Soils under Fast Impulses", *IEEE Transactions on Power Delivery*, vol.21, no.1, pp. 353-361, Jan 2006.

[4] M. Cabrera, S. Lundquist, V. Cooray, "On the Physical Properties of Discharges in Sand under Lightning Impulses", *Journal of Electrostatics*, Vol. 30, pp. 17-28, 1993.

[5] E. B. Joffe, K-S. Lock, *Grounds for Grounding*, New Jersey: WILEY, 2010.

[6] H. Markiewicz, A. Klajn, *Earthing system – Fundamentals of Calculation and Design*, United Kingdom: Copper Development Association (CDA), 2003.

[7] Department of Transportation, "*Test procedure for determining moisture content in soil materials",* August. 1999. [Online] Available from: http://ftp.dot.state.tx.us/pub/txdot-info/cst/TMS/100-E_series/pdfs/soi103.pdf [Accessed: Oct. 8, 2014].

[8] IEC-60-1, *Guide on high-voltage testing technique*, Standard, 1989.

[9] R. Campos, *Guide to the laboratory on insulation coordination*, Uppsala, 1995.

[10] W. Hauschild, E. Lemke, *High-Voltage Test and Measuring Technique.* New York: Springer-Verlag Berlin Heidelberg, 2014.

[11] R. Whitlow, *Basic Soil Mechanics*, 4th Edition. England: Pearson Prentice Hall, 2001.

[12] Y.S. Jin et al, "Long Gap Discharge in Water", *Journal of the Korean Physical Society*, Vol. 59, No. 6, pp. 3640-3643, (2011)

EURECA 2015 – Conference Paper
Paper in Session B3

Mastering Programmable Logic Controller: A Self-Directed Learning Approach

Sarowar M. S., Ijaz Ali and Gobbi.R

Faculty of Engineering, Multimedia University (MMU), Cyberjaya Campus

gobbi@ieee.org

Abstract

A Programmable Logic Controller (PLC) is a smart industrial and technical control device, which provides a smooth, transparent and simple but powerful mechanism of controlling production and dynamic operations. Because of their flexibility, constancy and low cost, PLCs are by far the most preferred control system used by manufacturing trade of all extents for motion control, environment control and regulation, food processing and management, and automated test machinery. Yet even though PLCs are massively used by industry, they are not taught in undergraduate level especially in Malaysian Universities. This paper mainly covers the following topics in the manner of self-directed learning approach: PLC program control instructions, PLC hardware components, developing fundamental PLC wiring diagrams, basics of PLC programming, timers, counters, PLC installation, debugging, editing and troubleshooting. This paper discusses three different design projects aided with PLCs to solve practical process, control, automation and machinery problems in industrial environments for undergraduate level students. Since all the details and procedures are explained as a self-directed learning approach, students are expected to observe the operation of the ladder logic program and make necessary modifications and alterations as necessary. After finishing all three projects, students should have learned all the basic PLC programming instructions and the working principle of ladder logic program. It is an excellent time to boost up their proficiency, expertise and knowledge in rational and practical problem solving by working on these simple but effective design projects using PLCs.

Keywords: Programmable Logic Controller (PLC), Ladder Logic Program, Undergraduate Students, Self-Directed learning.

1. Introduction

A programmable Logic Controller (PLC) is an industrial computer used for the control and operation of fabrication process and machinery. It has a programmable memory, which stores instructions and execute functions including turning on and off control, counting, data handling, arithmetic, timing and sequencing. PLCs are used in almost every attitude of industry to outspread and enhance production and manufacturing. In older automated systems hundreds or thousands of electromechanical relays were used but now they are replaced with a PLC. The performance of the PLC has emerged over the years to include potentialities beyond ordinary relay control. Sophisticated motion control, control and automation, distributive regulation systems, and multiplex networking have now been combined to the PLC's activity. Therefore, PLCs contribute many superiorities over conventional relay sort of control, including more authenticity, more flexibility, less expenditure, and transmissions capability, faster feedback time and painless to troubleshoot [1-2].

All the manufacturing and construction industries are moving to cost-effective technologies to advance their competitiveness, productivity and fertility. Certainly, idea of how to automate and control the system including applying PLC in production lines is crucial in most engineering, modeling, and manufacturing program. Thus, schooling, coaching and training in the field of control and automation are on the upswing across most colleges and universities in the world [3].

Since the use of automation escalates in the manufacturing and distribution industry, considering this technology is vital for those related to engineering technology students. The PLC is extensively practiced in industry to automate manufacturing process, to boost constancy and flexibility, rebate expenditure, and gain sustainability.

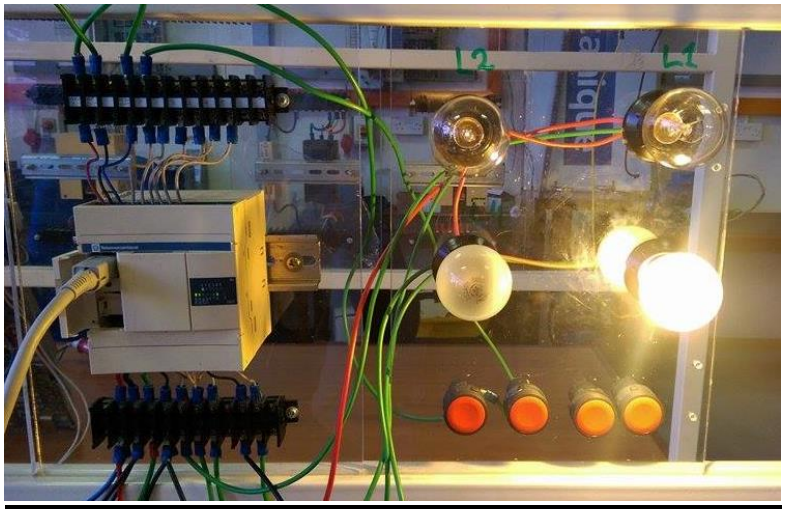

Figure 1. Sequential blinking of 4 bulbs using PLC

A few electrical, mechanical and industrial engineering along with numerous technology programs have incorporated with some introduction to PLCs into their curriculum, where they are usually conferred as a factor of a workshop or laboratory course. However, considerable programs have started offering courses devoted to schooling and practicing PLCs. In contrast, very minor electrical engineering program offers any disclosure to PLCs all through the curriculum. Still, they stand the most accepted and beneficial part in regulating manufacturing mechanism and machinery. Electrical and mechanical engineers need to master how issues of control and automation can affect their models and ideas of new machines and driver interfaces. Regrettably, many engineers lack knowledge and ideas in the field of cross-discipline knowledge. They become specialized in their own area to the fault of not bearing in mind (or even knowing) how, their performance in a project affect the other colleague. If engineering students can achieve a robust understanding of how to implement control and automation theory in real-world applications, they will spread out their knowledge and can communicate and design more efficiently and impressively [4].

The key objective of this paper is to review the self-directed learning approach and the basic use of PLC in undergraduate level. This paper discusses how problem based learning can be used to enhance the students learning experience in programmable logic controller. Although, PLCs are widely used in industries, but the teaching of such programming in undergraduate level is not sufficient for electrical, mechanical and telecommunication engineering programs especially in control and automation theory concepts.

In Malaysia very few universities have included the PLC programming in undergraduate level. For example University Teknikal Melaka, Malaysia include control instrumentation and automation course in their undergraduate level which includes PLC lessons.

Recently a project named as "Do It by Yourself (DIY) PLC Trainer" was completed in Multimedia University (MMU), Cyberjaya Campus for the electrical students in undergraduate curriculum. By doing this projects the students will be able to install, program and implement automation projects without the need for formal classroom coaching. The details of the projects are given in subsequent sections.

2. Self-directed Learning

The growing demands of technological advance in an age of exploding information challenges highlight the increasingly growing need for continuous, day-to-day maintenance and boosting of one's knowledge, skills, and attitudes. The visions of lifelong learning and the autonomous knowledge that have rise in most Western countries over the last 50 years, the literature in the relevant fields of adult education, vocational training and educational psychology has evidenced a powerful growth of interest in self- learning concepts.[5] Scholars working in the area of self-directed learning have clearly identified the fact that a new learner access, use, and re-craft resources through multiple sources and methods, to help their learning goals without the involvement of formal educational institutions [6].

A widely accepted conceptual foundation of Self-directed learning is Knowles' (in1975) definition: In its deepest meaning, self-directed learning express a process in which individuals take the action, with or without the assistance of others, in analyzing their learning needs, formulating learning goals and aims, identifying human and material resources for learning, choosing and carry out suitable learning strategies, and figure out learning outcomes. Twenty years later, in year1991 Long concurred: "I define self-directed learning as a personally directed purposive mental process usually accompanied and supported by behavioral activities involved in the identification and searching out of information" . [5]

Learning tasks in challenging situations boost students to recognize their strengths and weaknesses and motivate them to complete the given task. The volume of independent study at university demands that students have self- directed learning skills.
There are several motivation steps in self-directed learning for students which are given below:

- Carry out personal and group learning task plan and schedule.
- Develop tables, drawings, activities, etc. and present learning outcomes in various ways.
- Connect learning tasks to real-life situations.
- Set own experience-based learning evaluation criteria and cooperate with others during learning
- Establish self-planning and self- management.
- Convert emotions to practical activities.
- Choose problem-solving strategies and resources.
- Collaboration and self-realization of factors contributing to successful studies.
- Self-evaluation of process and outcomes.[7]

However in year 2000 Clardy identified three types of learning projects: induced, voluntary and synergistic. Induced projects are undertaken because of some perceived imbalance between current

and needed skills; voluntary projects are those undertaken because of a personal desire to learn; while synergistic projects "arise in situations where there are new enabling organizational conditions that ignite a latent employee readiness to act and learn. [3]

The stages or degrees of movement from entirely teacher-directed learning toward self-directed learning include the following:

- *Incidental self-directed learning:* The casual introduction of self-directed learning activities into courses or programs that are otherwise teacher-directed (e.g. individual projects, stations, or brief introduction of any other forms of self-directed learning on the spectrum) begins the journey toward self-direction.
- *Learning to think independently:* Facilitating students' independent thinking is gifted through courses or programs that highlight the personal pursuit of meaning through research, investigation, problem-solving, and creative activity (e.g. debates, case studies, investigations, trials, dramatizations, fieldwork).
- *Self-managed learning:* Programs or courses can be presented through learning guides that students complete independently.
- *Self-planned learning:* Even if the outcomes are preset, students can pursue course outcomes through activities they design themselves.
- *Self-directed learning*: In self-directed learning, students choose the outcomes, design their own activities and pursue them in their own ways (Based on Gibbons, 2002, 2004, 2008).[1]

In 2014 Merriam and Bierema recommend that learners exercise self-determination in that they are responsible for both what learning will occur and how it will occur, but these learning opportunities are "intervene by opportunities they find in their own environments" .Furthermore, in 2011 Kasworm notes it may be that the environment of people, supports, and experiences all can provide a significant "holding environment" to aid the learner's journey towards a more evolved state of cognitive complexity or of consciousness[8].

This research was designed to explore the opportunities and development of self-directed learning on programming logic controller (PLC). The goal is to examine and illustrate the potential of students in undergraduate level in order to facilitate the processes of promoting and building knowledge. Moreover, this paper will focus on the concept of self-directed learning, as described by researchers namely: "initiative and persistence in learning, high degree of interest, and viewing problems as challenges" to clarify and understand the self-directed nature of learning context. [8]

Student's feedback on these projects was very positive. They valued the practical experience and would have enjoyed more time to learn and practice ladder logic. The software language created for PLCs, called "ladder logic," retained a very similar look to the wiring diagrams that were used for the physical components it replaced. This software design enabled students to quickly understand and update the logic as changes were needed with minimal additional training.

3. Methodology

Experiences, knowledge from the authors and the lecturers who are teaching ladder logic programming, students face difficulties with, how to design a ladder diagram from a provided statement. There are two simple approaches to ladder logic programming: empirical which is based on observation rather than theory and Functional Block Diagram. Observing that the empirical method is ideal for small-scale applications. Prolonged planning and improvement time of the programming needs for this approach but extremely scale-downs the performance and troubleshooting of problems in programming. But the handiest approach to ladder logic programming is "I/O mapping". At the beginning of the modeling, every system input and output are diagrammed independently on a surface. Then we are supposed to draw the links between inputs and outputs, which they affect. Finally, develop

a Boolean expression for every output, which facilitate a simpler interpretation into programming rungs. The authors present some basic self-learning approaches for undergraduate students that will help to understand and give them head start in learning PLC.

Three simple projects have been designed to demonstrate and help the undergraduate students in a self-directed learning approach. These projects have been designed according to lower difficulties level to higher.

4. Projects for Self-Directed Learning

This project helps the students the basic understanding and the working principles of PLC. In this project students will be using lights as an output and turning on /off through PLC ladder diagram. First of all students need to download the twido software from the following website links.

After installation the students are supposed to click on the Twido Suite icon and then choose PROGRAMMING MODE. Then click on the PROJECT and create a new project. Then click on DIRECTORY and choose where the program files to be saved. After that click on DESCRIBE and students will see catalog on the right top corner of the screen. Below catalog click on BASES and then click on COMPACT. Then students will see all the PLC model numbers and choose the respective one. A telemecaniqe brand's PLC TWLCAA10DRF, which has 6 inputs and 4 outputs. Now by clicking on the model no, students will see a PLC image below and drag the image into the page one (right sided).

Finally, clicking on PROGRAM (top left corner), students will see all the inputs and outputs under CONFIGURE THE HARDWARE section

4.1 Project 1: Turning ON and OFF one light:

This project helps the students the basic understanding and the working principle of PLC. In this project students will be using light as an output and will control it's on /off through PLC. The procedures are listed below.

Under CONFIGURE HARDWARE section students will see a table for inputs and outputs. So for the project 1 configure the table same as the figure shown below.

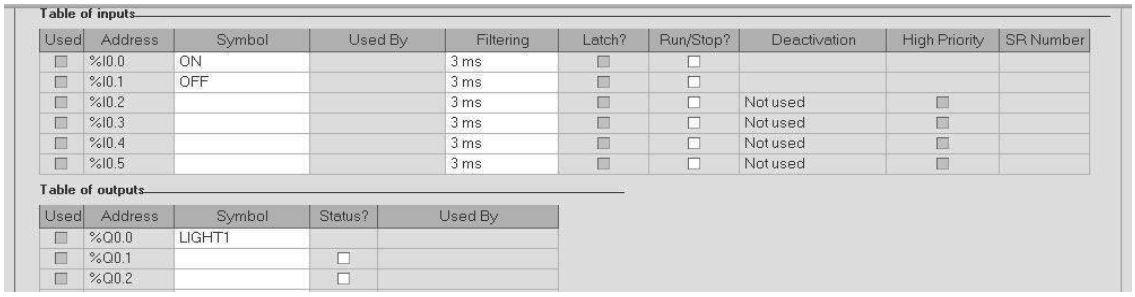

Table of inputs

Used	Address	Symbol	Used By	Filtering	Latch?	Run/Stop?	Deactivation	High Priority	SR Number
☐	%I0.0	ON		3 ms	☐	☐			
☐	%I0.1	OFF		3 ms	☐	☐			
☐	%I0.2			3 ms	☐	☐	Not used	☐	
☐	%I0.3			3 ms	☐	☐	Not used	☐	
☐	%I0.4			3 ms	☐	☐	Not used	☐	
☐	%I0.5			3 ms	☐	☐	Not used	☐	

Table of outputs

Used	Address	Symbol	Status?	Used By
☐	%Q0.0	LIGHT1		
☐	%Q0.1		☐	
☐	%Q0.2		☐	

Figure 2 Configuration for project 1

Then students are supposed to click on PROGRAM and will see INSERT A SECTION TO BEGIN. Below PROGRAM students will see a Ladder section bar and click the first icon (add a section) then RUNG 0 will be appeared on the screen.

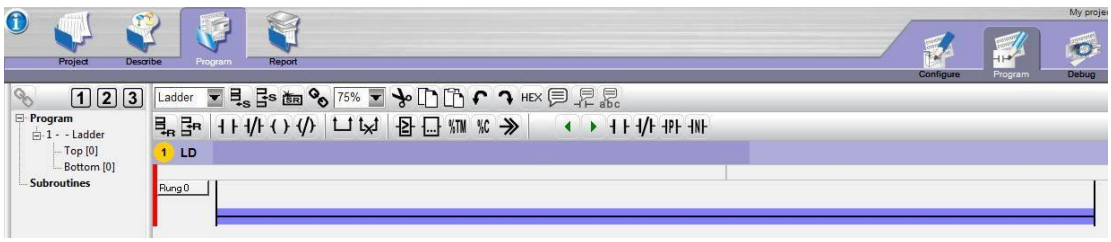

Figure 3 Ladder section bar with all icons.

Then click on NORMALLY OPEN CONTACTOR and then NORMALLY CLOSE CONTACTOR and also insert a COIL which can be used as a light. Normally open contact can be used as ON button and normally close contact as OFF button which are shown in the below figure. To latch the output click in between of the 2 contactor and drag it to the left contactor line same as in the figure below. To simulate the program, click on the **S icon** right below of the screen which is meant for Simulation. Then a simulation MENU will pop up. Click on the RUN icon and if any pop up menu comes just click on OK. There is a black controlling menu by which outputs can be controlled. By clicking on 0, normally open contact will be close and the output will get power hence the light will be turned on.

Figure 4 Ladder diagram of Project 1.

And when students click on 1, then normally close contact will be opened and the output will not get any power hence the light will be turned off. To DEBUG, click on the DEBUG option (right top corner) and click on OK to establish the connection between the PLC and the Computer. Two options will be displayed as (PLC to Computer) and (Computer to PLC) to receive and transmit the data.

4.2 Project 2: Turning ON and OFF Multiple lights dependency.

In this project the students will be using two light1 and light2. Light2 on/off will be depended on light1 while the light 1 on/off is independent of light2.

This project is a bit more advance from project 1. Here we use 4 inputs and 2 outputs.

Used	Address	Symbol	Used By	Filtering	Latch?	Run/Stop?	Deactivation	High Priority	SR Number
☑	%I0.0	ON1	user logic	3 ms	☐	☐			
☑	%I0.1	OFF1	user logic	3 ms	☐	☐			
☑	%I0.2	ON2	user logic	3 ms	☐	☐	Not used	☐	
☑	%I0.3	OFF2	user logic	3 ms	☐	☐	Not used	☐	
☐	%I0.4			3 ms	☐	☐	Not used	☐	
☐	%I0.5			3 ms	☐	☐	Not used	☐	

Table of outputs

Used	Address	Symbol	Status?	Used By
☑	%Q0.0	LIGHT1		user logic
☑	%Q0.1	LIGHT2	☐	user logic
☐	%Q0.2		☐	
☐	%Q0.3		☐	

Figure 5. Configuration for project 2

In this project we use 2 rung because of application purposes. For better understanding take a look at the figure shown below.

To DEBUG click on the DEBUG option (right top corner) **and** click on OK to establish the connection between the PLC and the Computer. Two options will be displayed as (PLC to Computer) and (Computer to PLC) to receive and transmit the data.

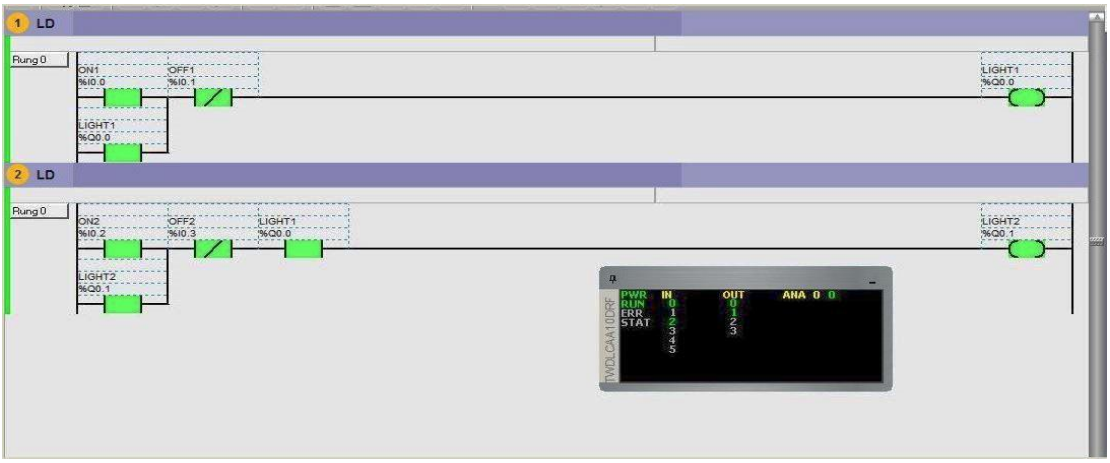

Figure 6. Ladder diagram of project 2

4.3 Project 3: Continuous LIGHT blinking system with maintaining the sequence.

In this project students are supposed to make a sequential LIGHT blinking but the LIGHTs will be continuously blinking while maintaining the sequence. For this purpose students will be using Hold option from the PLC simulator and SET and RESET option of the output. Electromagnetic latching relays are designed to hold the relay closed after power has been removed from the coil. Latching relays are used where it is necessary for contacts to stay open and/or closed even though the coil is energized only momentarily.

This project is more advanced than the project 2. In this project students are supposed to make a sequential LIGHT blinking but the LIGHTs will be continuously blinking with maintaining the sequence. For this purpose students have to use Hold option from the PLC simulator and SET and RESET option of the output. Electromagnetic latching relays are designed to hold the relay closed after power has been removed from the coil. Latching relays are used where it is necessary for contacts to stay open and/or closed even though the coil is energized only momentarily.

Under CONFIGURE HARDWARE section inputs and outputs table can be seen. So for the project 3 configures the table same as the figure shown below. First click on program and choose CONFIGURE THE DATA (right top corner) to configure the memory for HOLD option. Then under OBJECT CATAGORIES students will see FUNCTION BLOCK then configure the timers as shown in the figure below. We use TIMER to delay the output and students can choose whatever time delay they want. For this project students have to use multiple RUNGs with multiple TIMERs and SET and RESET options. For better understanding refer to the ladder diagram shown in figure 7.

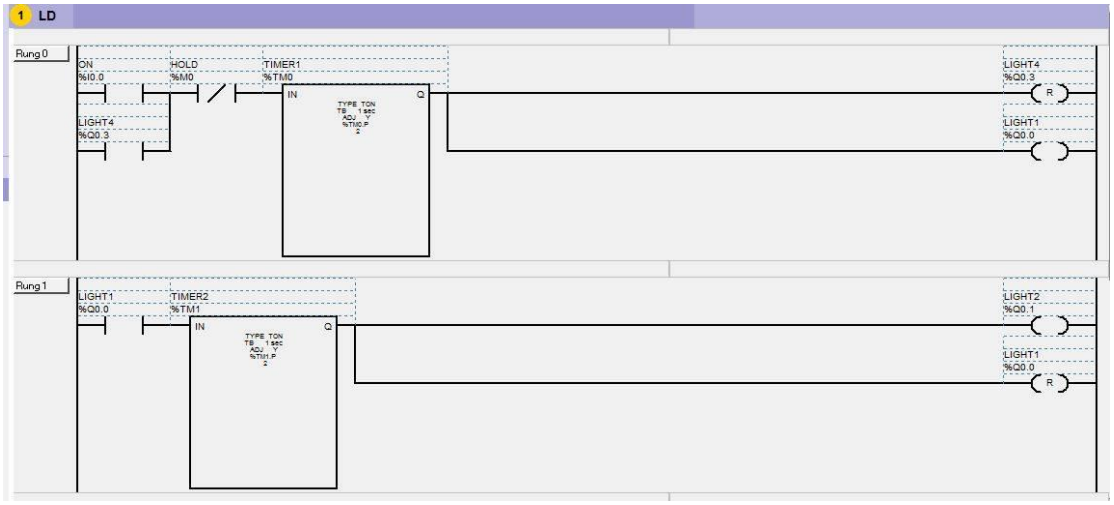

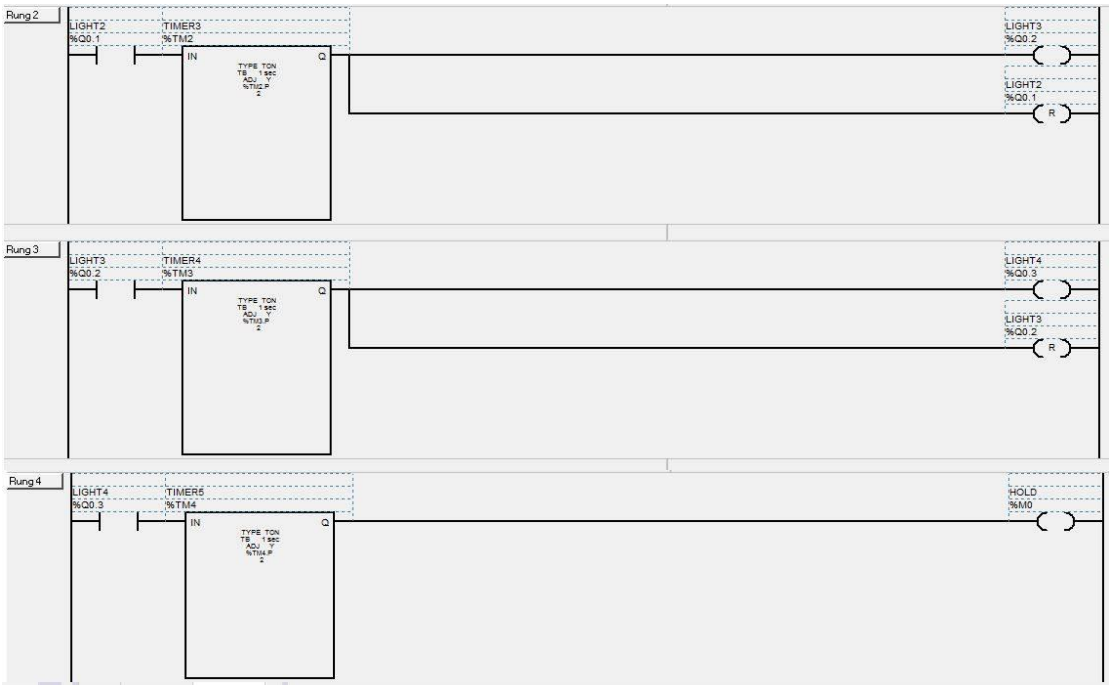

Figure7 Ladder logic diagram for project 3

5.0 Discussion & Conclusion

There is an indisputable need for a more comprehensive approach to control and automation system education for undergraduate electrical engineering students. These basic three projects devoted to the modeling and software implementation is in its early phase. All the projects are explained as a self-learning approach so that any undergraduate can easily learn and practice PLC ladder logic programming.

Around 40 electrical engineering students were selected to test the projects. They are mostly third year students who do not have any experience in PLC. They worked in a group of two. They were given 30 minutes to complete each projects. Table 1 shows the results for the completion of projects by the groups.

Table 1: Results of project completion

Projects	Completed <30 min	Completed >30 min	Not able to complete	Total
1	12 (60)	7 (35)	1 (5)	20 (100)
2	10 (50)	8 (40)	2 (10)	20 (100)
3	9 (45)	8 (40)	3 (15)	20 (100)

From the table, it was found that more than 80% of students able to complete all projects based on the self-directed approach. Almost 50% of them are able to complete within 30 minutes which shows that the students able to quickly understand and design the ladder diagram.

From the authors' experiences and the examples of projects given in this paper in teaching ladder logic programming, students struggle with how to structure a ladder diagram from a given problem statement. These projects have included a specific focus on non-continuous (on/off) control commonly used in industrial environments.

At the end of the session, the students we also requested to fill up a simple questionnaire particularly to get feedback on the project procedures, the steps and diagrams. The objective of this questionnaire study was to verify if the existing procedures were well written to encourage self-directed learning.

Table 2: Feedback on projects procedures.

Questions	Project 1		Project 2		Project 3	
	Qty.	%	Qty.	%	Qty.	%
The projects procedures are quite confusing	7	17.5	7	17.5	5	12.5
The project procedures are clear but not in a proper order	6	15	10	25	25	62.5
The project procedures are very systematic and easy to follow	27	67.5	23	57.5	10	25
Total	40	100	40	100	40	100

The result shows that more than 50% agree that the procedures are good for project 1 and 2. However, students found it difficult to follow the procedures for project 3. This is simply due to the difficulty level of project 3. The procedures may need a few round of revisions.

We wish that these hands-on experiences, maturity and participation will strengthen, inspire and encourage students to feel about how their own expertise and skills can be used in an entrepreneurial way to improve the lives of others. Also we have been planning to build student proficiency by designing some of the learning modules in a very funny and interesting way such as games and puzzles where students can work or solve collaboratively or competitively to deal with PLC programming challenges.

6.0 Acknowledgement

The authors would like to thank Schneider Electric (industries) Malaysia for donating PLCs and components. We would also grateful to Mr. Ngu Su Jin, a PLC specialist from Schneider Electric, Malaysia for guiding us throughout this project.

7.0 References

[1]. F. D. Petruzella, Programming Logic Controllers, McGraw Hill, 2005.
[2]. C.D. Johnson, Process Control Instrumentation technology, Prentice Hall, 2006
[3]. J. Rehg, "PLC laboratories – the next generation", 2002 ASEE Annual Conference & Exposition, June 2002.
[4]. Ahmad Fairuz Muhd Amin, MohdAriff Mat and Hanafiah,MarizanSulaiman, "Problem Based Learning Approach in Programmable Logic Controller "Malaysia:, Regional Conference on Engineering Education, 2005.
[5]. Laurent Cosnefroy and Philippe Carré, "self-regulated and self- directed learning: why don't some neighbors communicate?" International Journal of Self-Directed Learning Volume 11, Number 2, Fall 2014.pp. 1-12
[6]. Dirk Morrison and Jennifer X. Seaton, "Exploring self-directed learning in an online; Do it yourself forum",International Journal of Self-Directed Learning Volume 11, Number 2, Fall 2014. Pp. 29- 45

[7]. GunarsStrods, "Promotion of student self- direction through cooperative learning in teacher training", International Journal of Self-Directed Learning Volume 11, Number 2, Fall 2014, pp 13-28

[8]. Maurice Taylor, David Trumpower, SaitAtas, and Edward Purse," Exploring the attributes of social capital and self-directed learning for adults with low skills", International Journal of Self-Directed Learning Volume 11, Number 2, Fall 2014. Pp 46-58

[9]. Dutch et al., The power of problem based learning: "A practical how-to for teaching undergraduate courses in any discipline", Stylus Publishing, 2001

[10]. R.A. Cox, Technicians Guide to Programmable Logic Controllers. 4th ed., Delmar Thomson Learning,Inc.2001

[11]. Blakley , J.J., And Irvine, D.A. (2000),Teaching Programmable Controllers Using Multimedia-Based Courseware, International Journal of Electrical Engineering Education.

[12]. Wen-JyeShyr, "Enhancement of PLC programming learning based on a virtual laboratory," World Transactions on Engineering and Technology Education, vol.8, No.2, 2010, pp. 196-202.

[13]. L.A. Bryan and E.A. Bryan. "Programmable Controllers: Theory and Implementation," Industrial Text, Chicago, IL, 1988, pp. 20 – 40.

[14]. R.W. Lewis, Programming industrial control system using IEC 1131-1, IEE Press, 1998.

[15]. G. Warnock, Programmable Controllers: Operation and Application, Prentice Hall, 1988

Dynamic Bandwidth Allocation For Fiber Wireless

C.Y. Liang[1], N. I. Hassan [2]
[1]*liang_chui@yahoo.com*
[2]*NurmalaIrdawaty.Hassan@taylors.edu.my*

Abstract

Fiber Wireless access network architectures are basically combination of two sections, named front end and back end system. First consider the back end, the major technology was used in the system is the passive optical network (PON), where all the fiber optics links are directed from the optical line terminals (OLTs) from the central server to optical network units (ONUs) which is closer to the users. Follow by the back end, there are optic fiber links from the central server all the way to end user, and the front end is the wireless routers taking over for providing internet access to the users. On the other side the front end, many topologies and radio frequencies technologies such as IEEE 802.11 or Worldwide Interoperability for Microwave Access (WiMAX) and others can be used in this system. However, there is limitation on wireless communication network which is interference in between each of the network. To ensure everyone have high bandwidth of communication network, QoS is essential to be implemented into the system to improve the Quality of Experience (QoS). Therefore, in this research on Dynamic Bandwidth Allocation (DBA) algorithm on fiber wireless network which can utilize the bandwidth and to improve the terms of QoS. This QoS-aware dynamic bandwidth allocation scheme provide the bandwidth fairness at the Optical Network Unit (ONU) base station level. The purpose of this project is to simulate a DBA algorithm that can improve the performance characteristics of fiber wireless in the terms of QoS as well as the QoE of the end users. There are four major stages in the design and development. First of all, the research will be working on the practically studies on the research project. Furthermore, at this stages the specific area of this recommended application in the DBA will be determined, as the objective of this project is to utilize the bandwidth and to support the QoS in the communication system by using DBA. Through the simulated results of this dynamic bandwidth allocation, this show that the effectiveness of dynamic bandwidth allocation on fiber wireless network.

Keywords: Dynamic Bandwidth Allocation (DBA), Fiber Wireless, Quality of Experience (QoS)

1. Introduction

In this new era, communication network is very important for human. Communication network is generally to provide access to the information and communicate around the globe. With the increasing demand for media rich applications and bandwidth intensive services due to the increasing number of technology smart devices, the communication network is needed to be improved with more advanced technologies to provide high mobility and high capacity communication system. From the statistics in Figure 1, it can be seen that the number of internet users is the world has dramatically increased over the years.

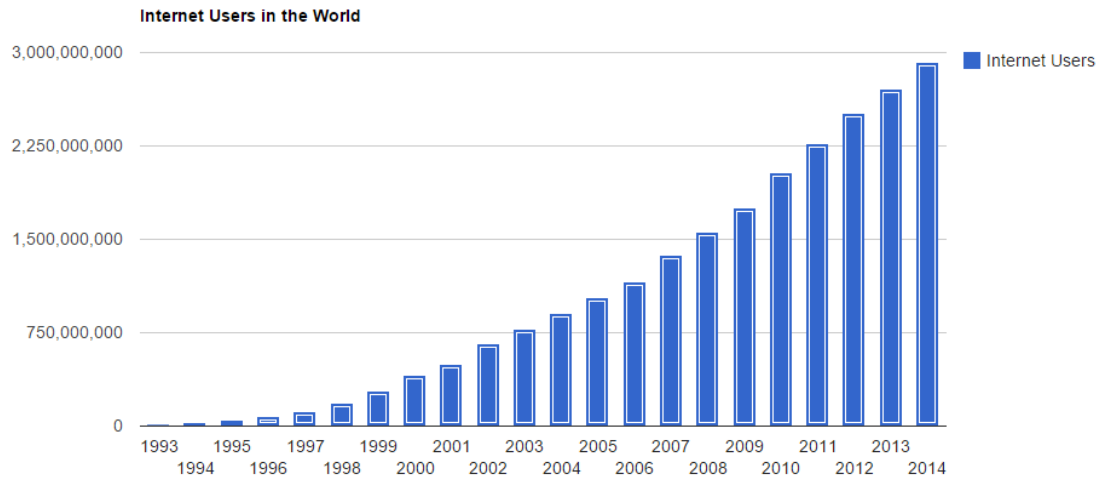

Figure 1: Statistics of internet users in the world [1].

Here comes the importance of fiber wireless network and wireless optical broadband access network (WOBAN) [2], both fiber optical and broadband wireless network that combines high capacity, robustness, reliability of fiber optic network and the high mobility, cost saving and ubiquity of wireless networks [3]. It is crucial to replace the current legacy copper wire cable and microwave backhaul technology with this integrated fiber wireless access network.

Fiber Wireless Access Network architectures are basically combination of two sections, named front end and back end system. Firstly, consider the back end, the major technology was used in the system is the passive optical network (PON), where all the fiber optics links are directed from the optical line terminals (OLTs) from the central server to optical network units (ONUs) which is closer to the users. Then, followed by the front end is the wireless router or access point taking over for providing internet access to the users. On the other side, the front end have many topologies and radio frequencies technologies such as IEEE 802.11 or Worldwide Interoperability for Microwave Access (WiMAX) and so on, can be used in this system as shown in Figure 2 [3].

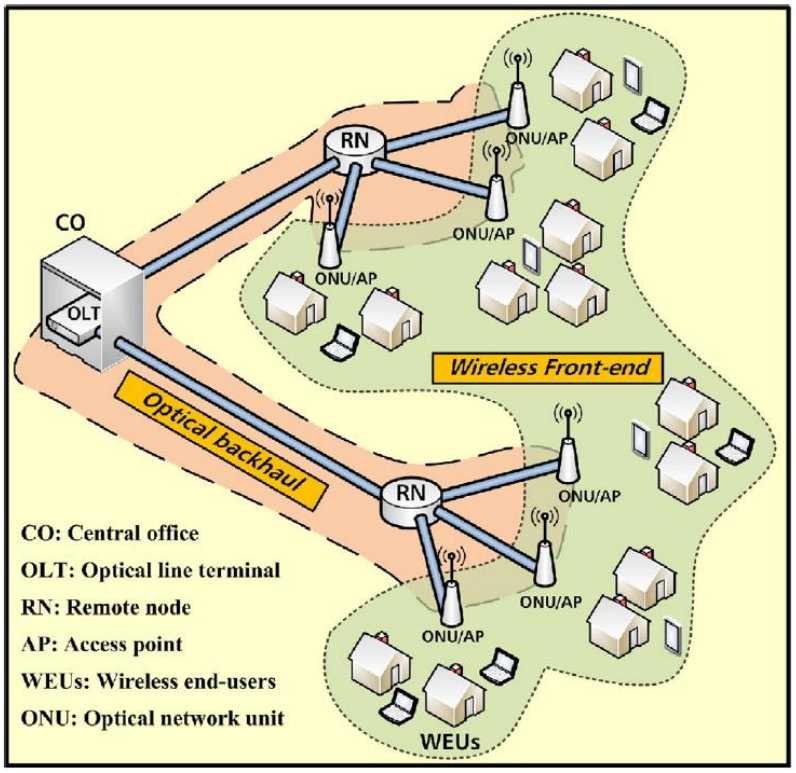

Figure 2: Architecture of Fiber Wireless access network [4].

The fiber wireless access network seems to be the technology of future, but there are some challenging issues that still needs to be addressed. This is because the limitation of standalone optical fiber as well as the wireless network to provide the optimal services to the end users leads to the application of fiber wireless network. Therefore, Quality of Service (QoS) and Quality of Experience (QoE) play a very important role in providing the various multimedia services and applications over the fiber wireless network [5]. Here, the focus is to assure that the QoS over a fiber wireless network, which is vital to offer a satisfactory service. Due to the popularity of peer-to-peer (P2P) application, and also the social network and video streaming site such as Facebook and YouTube are growing rapidly. It is necessary for service providers to have an efficient mechanism such as dynamic bandwidth allocation to improve the performance of fiber optics based on the demand of the users' requirement [6]. For this reason, QoS might be provided with expanding the bandwidth supplemented by long distance communication in addition to cost savings. The network performance with high bandwidth is restricted is due to the interferences of communications. Thus, the QoS is typically relies on a dynamic bandwidth allocation (DBA) algorithm to solve and reduce the challenges along with optimization and utilization [7]. The DBA scheme is to enables a smooth data transmission across the wireless and optical networks. This QoS-aware DBA system supports the bandwidth fairness in the ONU layer to the users of the wireless network [8].

1.1 Project Objective

This project objectives are:

1. To study specific area of application of the Dynamic Bandwidth Allocation (DBA) in fiber wireless.

2. To analyze the overall performance of the fiber wireless communication system with DBA.

2. Methods

FiWi access network is in high demand in this developing country to enhance their technology advancement and improve the communication system. FiWi is best fit for them, as FiWi fits with the wired as well as wireless networks therefore it is best to cover the stationary and mobile communication system [8]. However, there is limitation on wireless communication network which is interference in between each of the network. To ensure everyone have high bandwidth of communication network, QoS is essential to be implemented into the system to improve the QoE. Therefore, the purpose of this project is to research the characteristics of DBA which can utilize the bandwidth and to improve the terms of QoS [9]. This QoS-aware dynamic bandwidth allocation scheme provide the bandwidth fairness at the Optical Network Unit (ONU) base station level and improve the QoE of the end user equally [10].

PONs is a point to multipoint optical fiber network without active component in the optical distribution networks (ODNs) [11], thus this is called as "passive". With this PON technology, it is greatly reduces the complexity as well as the cost of the maintenance and deployment of the network infrastructure [11].

Table 1 : xPON standards [12]

Types	Standard	Wavelength (nm)	Reach	Speed
APON	ITU-T G.983	1550/1310 1490/1310	20 km	155 Mbps – 622 Mbps
BPON	ITU-T G.983	1550/1310 1490/1310	20 km	155 Mbps – 622 Mbps
EPON	IEEE/EFM 802.3ah	1490/1310	20 – 60 km	1 Gbps
GPON	ITU-T G.984	1490/1310	10 – 20 km	1.25 Gbps upstream 2.25 Gbps downstream

PON network are typically based on the tree topology branching from OLT to ONUs can be seen from Figure 3:

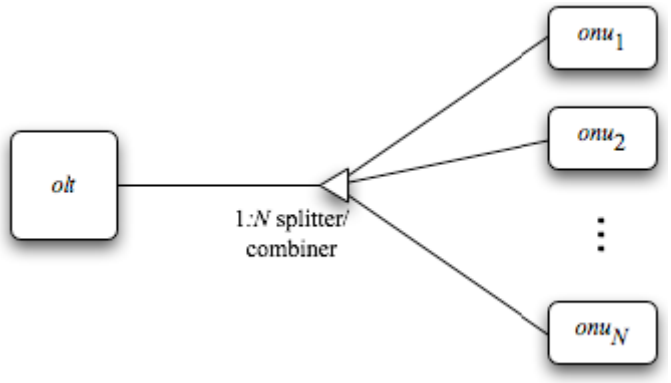

Figure 3: Typical PON Architecture [12]

The OLT is placed at the central office server and connects the access to the international backbone. On the other side, ONU is link to the end user location such as home or building. In this tree topology which also called as point to multipoint topology and all ONUs sharing the same transmission channel. Thus, to avoid the interferences among the data from other different ONUs, a Medium Access Control (MAC) mechanism is required in the upstream flow. In order to make ONU to send the data at the specified timeframe normally, a uniform clock is required to synchronize each of the ONUs [12].

2.1 Dynamic Bandwidth Allocation

For the performance of EPON delay on the package, network load utilization, and the quality of service, EPON dynamic bandwidth allocation (DBA) is the primary factor. DBA is generally defined as the process of contributing statistical multiplexing between all the ONUs [13]. In access to the network, it is established each link between single users or a small network of users with intermittently data sources traffic, for example, web browsing data, video packetized data and, etc. Thus the nature of the intermittent traffic, and bandwidth requirements usually it varies widely with the passage of time. Consequently, the allocation of fixed bandwidth per subscriber in PON topology leads to inefficient use of bandwidth and high delay of package. There is a need dynamic allocation bandwidth that can be continuous assign bandwidth requirements for the use of high bandwidth utilization and low delay of package. Usually, DBA algorithm is the polling process works in the Optical Line Terminal (OLT), which is responsible for contributing statistical multiplexing. The ONUs will constantly reporting on the sizes of queue right away under the control and dissemination of this bandwidth requirements information for OLT through the PON. OLT and calls for instantaneous information bandwidth requirements of each ONU to make access decision before send them back to the ONU. Conversely it is because of the delay in the propagation to the network, and this is why, it is impossible to be precise bandwidth required information. Average estimation of the propagation delays is up to 100μsec, much superior to the 12.3μsec, and transmission time of the peak size of Ethernet frame [14].

However the design of DBA to transmission upstream in EPON has received considerable attention, not the formation of a comprehensive framework for the classification of the elements and mechanisms DBA.

DBA mechanisms is classified with three factors:

- Grant scheduling framework (α), which is characterized by the event triggering the allocation of bandwidth.
- Grant sizing (β), which determines the size of the transmission window allocated to the ONU upstream.
- Grant scheduling policy (γ), which determines the temporal order of several windows transmission scheduled at one time.

With this classification, and it can be seen every DBA has a three-layered of (α, β, γ) [19].

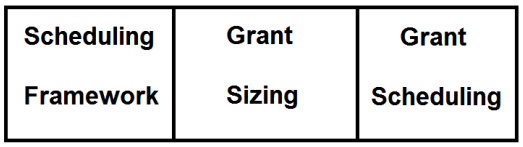

Figure 4: Structure components of DBA

2.1.1 Grant framework scheduling

Grant framework scheduling determines when OLT to make admission decisions and send grants to allocate ONUs. We can discern between the frameworks according to the scheduling of the event that triggers the production of the grant schedule.

To characterize the difference of frame scheduling, and let N represent the number of ONUs, k as denoted as k^{th} ONU in grant cycle, t_g denote as guard time between transmission ONU, t_G is to be the time of transmission of a GATE message, t_{start} (k, j) begins from the start of transmission granted window of the k^{th} ONU in grant cycle, t_{poll} (k, j) denote as the polling time of the k^{th} ONU in grant cycle j, G (k, j) to be the length of transmission granted window of the k^{th} ONU in grant cycle j, τ (i) represent as a propagation delay symmetric between ONU and OLT i, and [k, j] denote as a factor that returns a number, i, of the k^{th} ONU in grant cycle j, t_{end} (k, j) represent the end of this is time that the grant to the k^{th} ONU in grant cycle [14] .

$$t_{end}(k, j) = t_{start}(k, j) + G(k, j) \quad (2.1)$$

Let t_a (k, j) represent the time of upstream channel is available when OLT programs transmission window for granted as the k^{th} ONU in the grant cycle j. Upstream channel becomes free time guard after the end of the transfer granted to the previous window of the ONU.

$$t_a(k, j) = \begin{cases} t_{end}(N, j-1) + t_g, k = 1 \\ t_{end}(k-1, j) + t_g, k \neq 1 \end{cases} \quad (2.2)$$

Let t_{sched} (k, j) denote as the time of the OLT schedules the transmission window k^{th} ONU in the grant cycle j. Thus, the time to start of the granted transmission window of the k^{th} ONU in the grant cycle would be

$$t_{start}(k, j) = \max\{(t_{sched}(k, j) + t_{poll}(k, j)), t_a(k, j)\} \qquad (2.3)$$

Different polls, frame schedule and orders ONUs differently. As a result, the values of t_{start} (k, j) the beginning, t_{poll} (k, j), and [k, j] vary.

2.1.2 Grant Sizing

Grant sizing problem is how they should be given a large amount of bandwidth for each ONU to OLT when allocating bandwidth, and it can be classified 5 main types are: Exhaustive grant sizing with queue size prediction, Limited grant sizing with excess distribution, Limited grant sizing, Gated grant sizing and Fixed grant sizing.

To express a different way grant sizing, following notation are going to be used: G (i, j) to represent the window along the granted transmission for the ONU i grant cycle, R (i, j) represents the size of the reported of ONU i in the cycle j. Gmax (i) denotes as the maximum grant size ONU i's, P (i, j) denoted as expected traffic queue for ONU i in the period between REPORT message is sent out from ONU to the OLT and the end of the granted transmission window sent from OLT to ONU i grant the cycle [14]. The formula of Grant Sizing will be:

$$G(i, j) = f[R(i, j), G_{max}(i)] + E(i, j) + P(i, j) \qquad (2.4)$$

2.1.3 Grant Scheduling Policy

Grant Scheduling Policy in EPON of Medium Access Control (MAC) level is concerning in both the Intra ONU scheduling and Inter ONU scheduling. Intra ONU scheduling apprehension the scheduling different queues at each of the ONU for transmission within the granted transmission window, while the Inter ONU scheduling apprehensive in scheduling grants among different ONUs. This division of the schedule if referred to as hierarchical scheduling [14].

2.2 Simulation Scenario

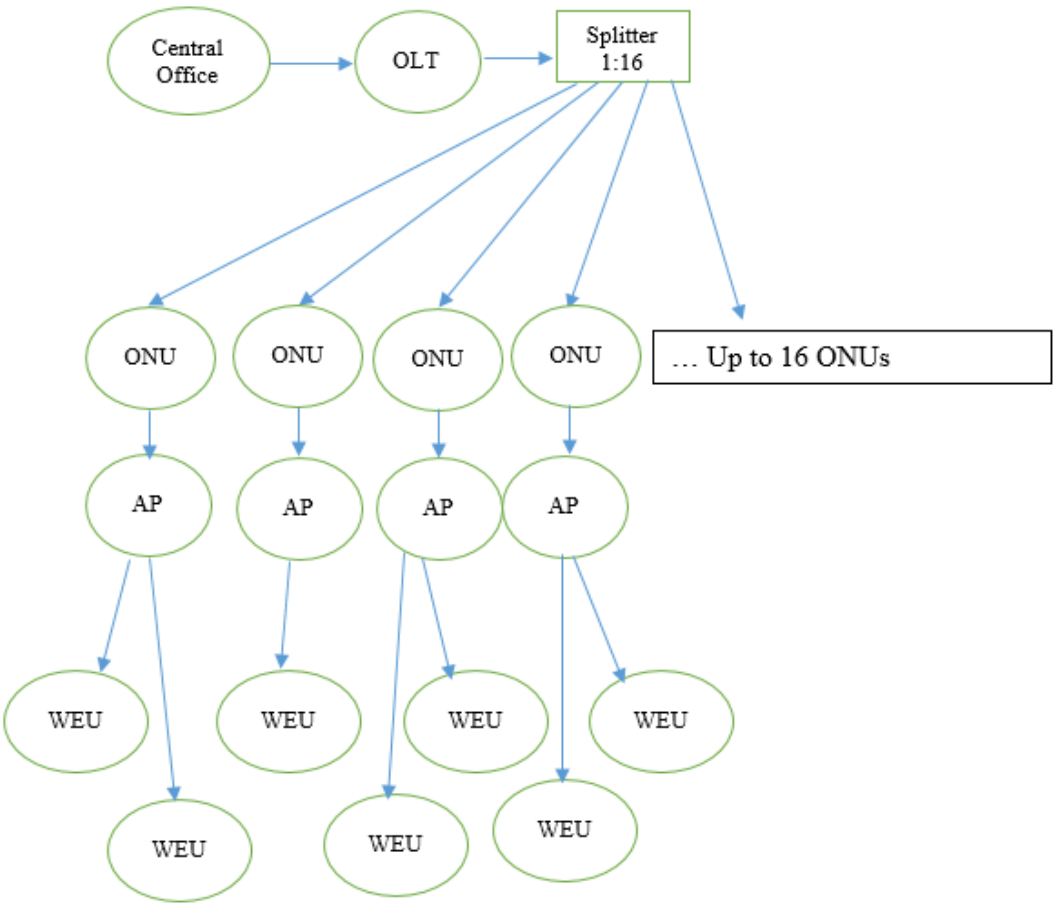

Figure 5: Fiber Wireless architectures design integrated with EPON and WiMAX

OLT: Optical Line Terminal

ONU: Optical Network Unit

AP: Access Point – WIMAX

WEU: Wireless End User

Figure 10 shows the Fiber Wireless network simulation scenario which will be includes the path from OLT to the WEU. In this simulation will also have 16 ONU splitting from 1 OLT incoming.

2.3 Dynamic Bandwidth Allocation Evaluation Parameters

Three main parameters for evaluate the performance characteristic of DBA. The three criteria are interconnected.

- Latency – the duration of a packet waits at an ONT upstream queue before transmission
- Fairness – the capability to fairly satisfy or dissatisfy of Service Level Agreement (SLA) on each ONTs
- Utilization – the percentage of usable data transmission in the upstream channel

An efficient dynamic bandwidth allocation algorithm is to attempts to attain high bandwidth utilization at the same time it will still substantial the typical traffic requirement such as throughput, jitter and delay. Upstream efficiency is introduced to provides more vision to the operation of dynamic bandwidth allocation algorithm and the real reason of losses of throughput in EPON

$$\frac{\sum_{i,j} B_{i,j}^{\text{sent}}}{\sum_{i,j} (B_{i,j}^{\text{grant}} + B^{\text{guard}} + B^{\text{Control}})},$$

Where B^{Grant} represents the packet size of the bandwidth accept from the OLT for the *j*th ONU in the *i*th polling cycle, whereas B^{sent} represent the packet size of the bandwidth from the ONU that are used to send Ethernet frames based on the granted supplied by the OLT in the *i*th polling cycle. In EPON there is no unused slots reminders (USRs) and frame fragmentation can be caused by the difference between B^{Grant} and B^{sent} [13].

Table 2: Fiber Wireless Simulation Parameters

Ethernet Passive Optical Network	
Speed – OLT to ONUs	1 Gb/s
Numbers of ONUs in system	16
OLT- ONU distance	20 km
Buffer Size	10 MB
Cycle and guard time	2ms , 1µs
WiMAX	
Number of Station – from ONU	16
WiMAX channel capacity	20MHz
WiMAX Duplexing and Frame Duration	TDD,5ms
Propagation delay	10 µs

3. Results and Discussion

Performance parameters are numerically evaluated, using MATLAB software. Where the bandwidth requested of each ONUs is classified into 3 different types, which is Expedited Forwarding (EF), Assured Forwarding (AF), and Best Effort (BE), where EF is Voice service highest priority, follow by AF is Video service medium priority and lastly the BE is Data service lowest priority. However the service of EF is the voice is very stable and very low burst, but normal data service would have more burst, so three different categories of service cannot use the same prediction system and parameters. Conversely, and the different services have different requirements from the allocation of bandwidth, so the DBA algorithm to sign these services on the basis of three different priorities in order to ensure quality of service. In contrast, it contains a status report on the message queue length of three information service, which provides multi-service conditions of comfort to predict. Therefore, for the OLT should create three independent predicted network for matching three service differentiate in the first phase after the discovery and the ONUs registration process.

```
r1EF = [27750000;  34750000;  31250000;  31250000;  31250000;  31250000;  31250000;  31250000;
r1AF = [24975000;  31275000;  28125000;  28125000;  28125000;  28125000;  28125000;  28125000;
r1BE = [2775000;   3475000;   3125000;   3125000;   3125000;   3125000;   3125000;   3125000;
```

Figure 6: Bandwidth Requested of each ONUs in MATLAB

Case 1 – Balanced Bandwidth load

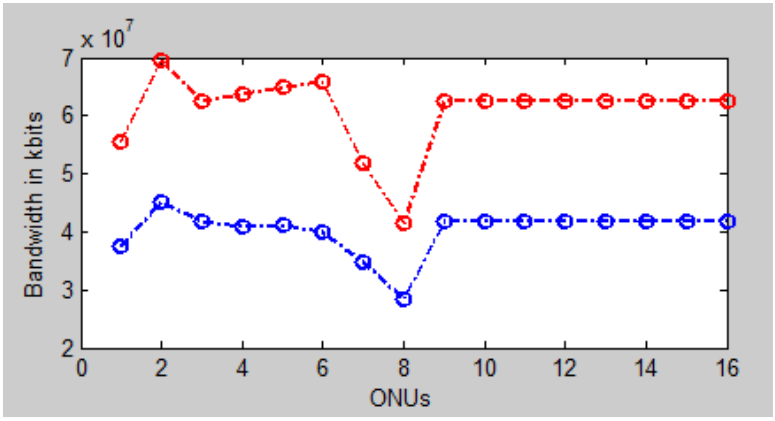

Figure 7: Bandwidth Allocated in kbits (blue), Bandwidth Requested (red)

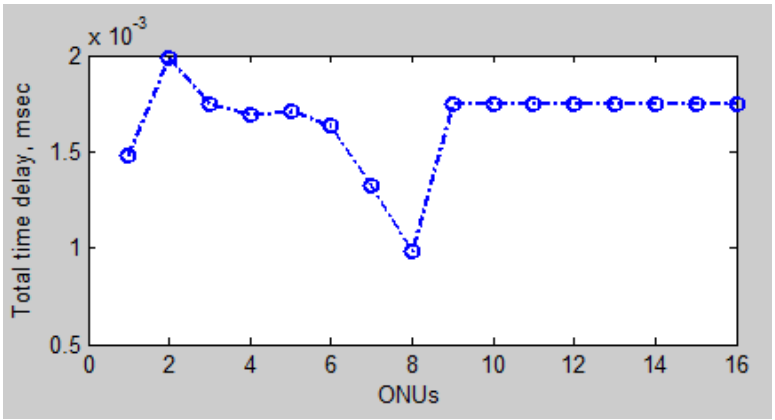

Figure 8: Total time delay to allocate bandwidth

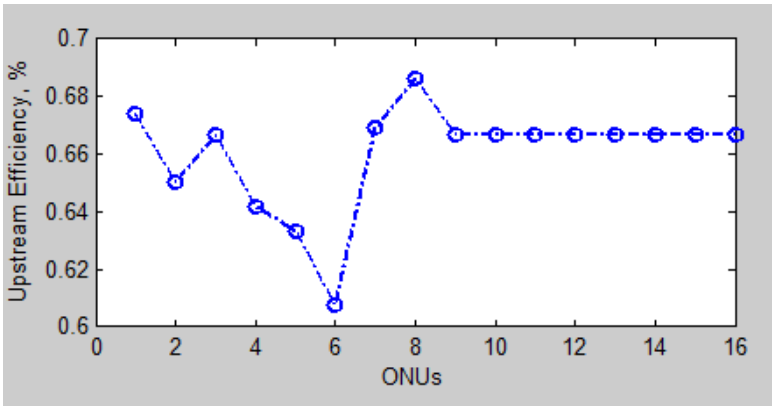

Figure 9: Total Upstream Efficiency

Case 2 – High Bandwidth Load

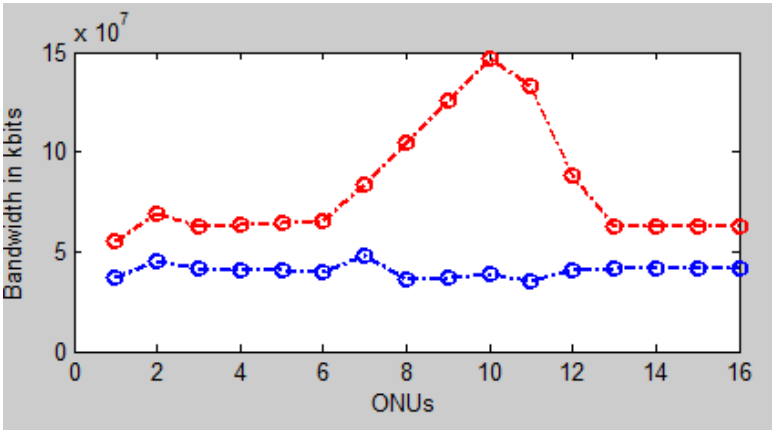

Figure 10: Bandwidth Allocated in kbits (blue), Bandwidth Requested (red)

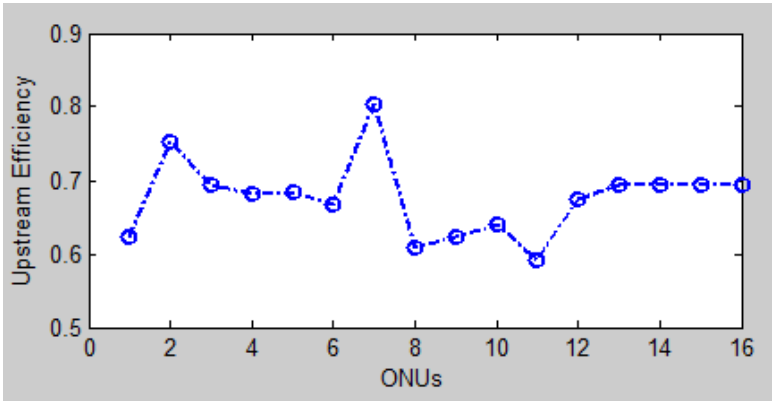

Figure 11: Total Upstream Efficiency

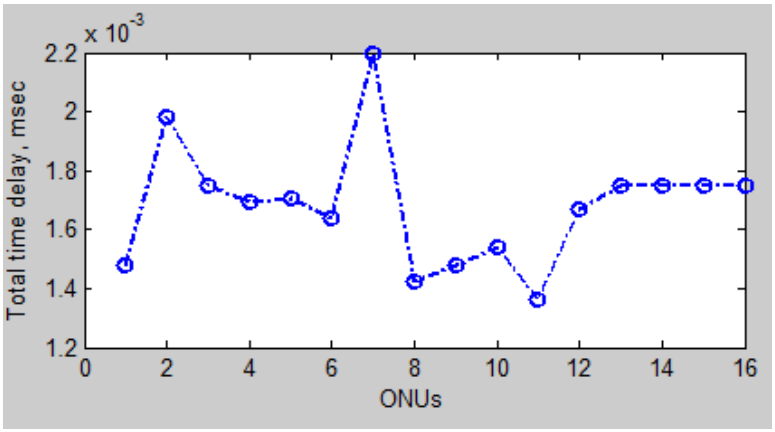

Figure 12: Total time delay to allocate bandwidth

Based on the simulated results above, which it consist of 2 cases, one is balanced bandwidth load and second is the high bandwidth load. For the balanced bandwidth load which can see in figure 9, the total upstream efficiency have an average at 66% and in figure 7 bandwidth is not limited because of the bandwidth requested is not higher than the maximum bandwidth of each ONUs. Whereas for the high bandwidth load which can see in figure 11, the maximum total upstream efficiency is up to 80% and in figure 10 showing that the bandwidth is limited at the ONU 8 to ONU 12, this is because the total bandwidth requested is not higher than the maximum bandwidth of each ONUs, therefore bandwidth is limited to have Fairness of bandwidth to provide the capability to fairly satisfy or dissatisfy of Service Level Agreement (SLA) on each ONTs. On the other hand, in figure 8 and figure 11 also shows that the total time delay is a responsive variable to the bandwidth allocated, as the bandwidth allocated is high, thus the total time delay increases. From the results, can conclude that the dynamic bandwidth allocation method for fiber wireless is able to improve the fairness and data utilization of the bandwidth in terms of the QoS.

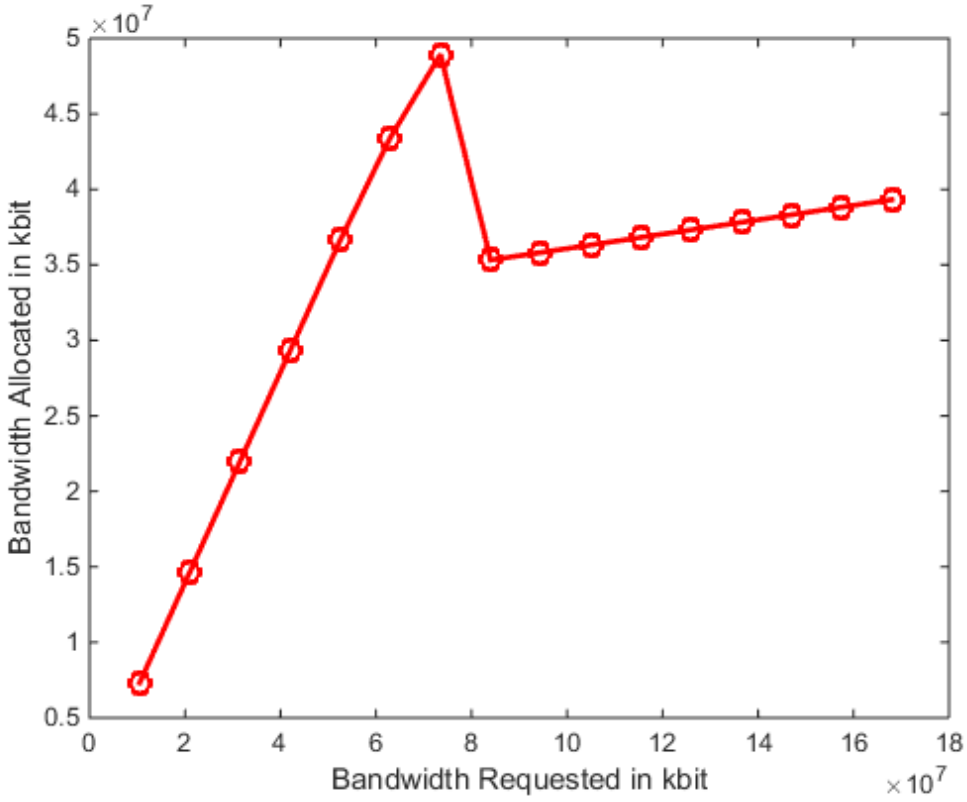

Figure 12: Graph bandwidth requested against bandwidth allocated

Table 3: Data of bandwidth requested and allocated in Mbit (A)

Bandwidth Requested (Mbit)	10.5	21.0	31.5	42.0	52.5	63.0	73.5	84.0
Bandwidth Allocated (Mbit)	7.327	14.654	21.981	29.308	36.635	43.440	48.940	35.320

Table 4: Data of bandwidth requested and allocated in Mbit (B)

Bandwidth Requested (Mbit)	94.5	105.0	115.5	126.0	136.5	147.0	157.5	168.0
Bandwidth Allocated (Mbit)	35.820	36.320	36.820	37.320	37.820	38.320	38.820	39.320

Another graph plotted in figure 12 bandwidth requested against the bandwidth allocated, and here the bandwidth is set to increases uniformly by 10.5Mbit each interval, the results has shown in Figure above. The result above shown the bandwidth is allocated up to 50Mbit and had slow down to 35 Mbit, this is due to the limitation of the OLT and the algorithm here is reacted to ensure the fairness of bandwidth for all the user, therefore the average allocated bandwidth is at 35Mbit and have only slight increase after across the limit.

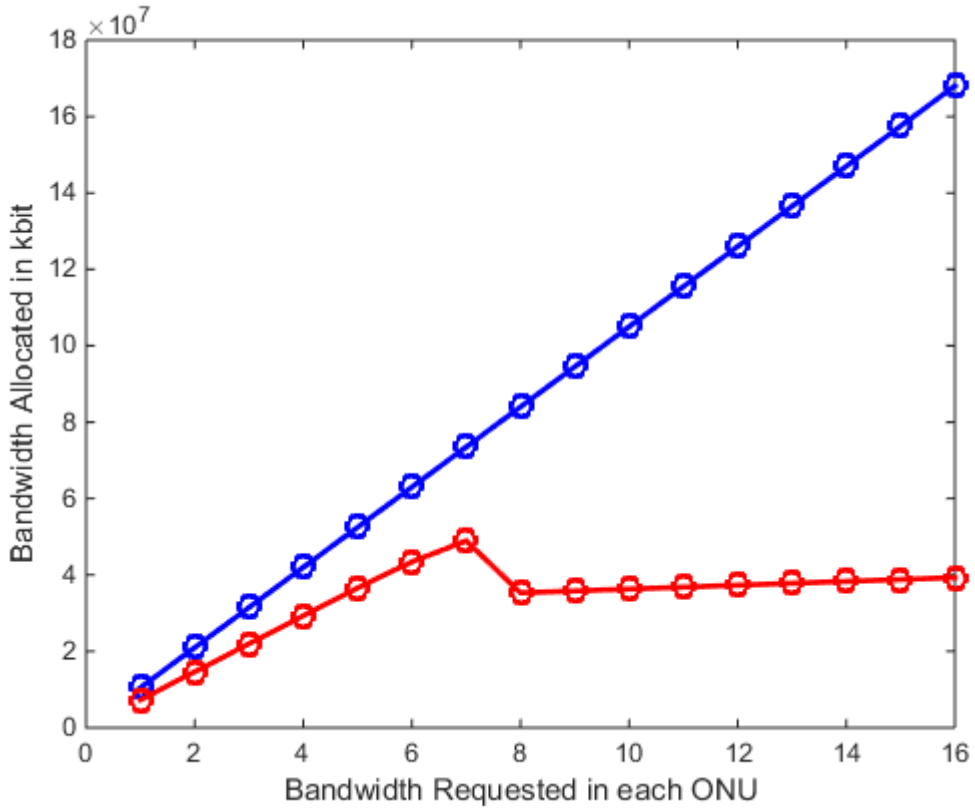

Figure 13: Graph bandwidth requested in each ONU against bandwidth allocated

Table 5: Data of bandwidth requested and allocated in Mbit (A)

ONU	1	2	3	4	5	6	7	8
Bandwidth Requested (Mbit)	10.5	21.0	31.5	42.0	52.5	63.0	73.5	84.0
Bandwidth Allocated (Mbit)	7.327	14.654	21.981	29.308	36.635	43.440	48.940	35.320

Table 6: Data of bandwidth requested and allocated in Mbit (B)

ONU	9	10	11	12	13	14	15	16
Bandwidth Requested (Mbit)	94.5	105.0	115.5	126.0	136.5	147.0	157.5	168.0
Bandwidth Allocated (Mbit)	35.820	36.320	36.820	37.320	37.820	38.320	38.820	39.320

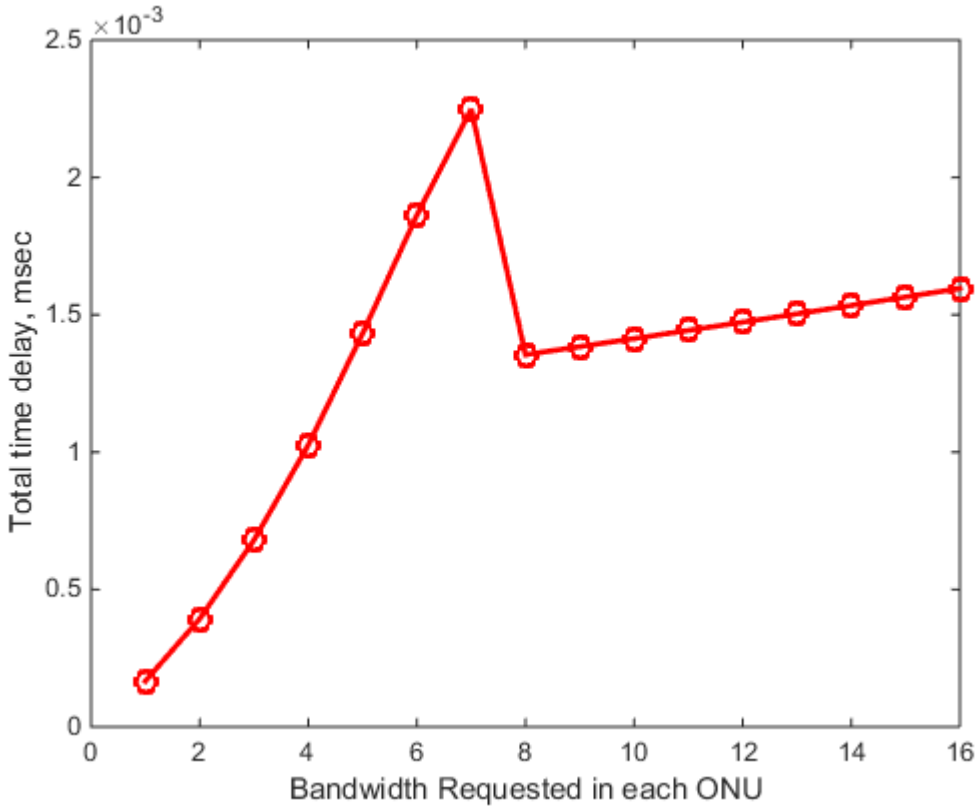

Figure 14: Total time delay to allocate bandwidth

Based on the figure 13 showing that, the bandwidth requested is also set 10.5Mbit increases on each of the ONUs up to 168Mbit and start from ONU 7 the bandwidth is limited at 49Mbit and start from ONU 8 the bandwidth is drop to 35Mbit and will only increase gradually as the bandwidth requested increases. From the calculation the total bandwidth allocated in one OLT is 538 Mbit. On the other hand, graph is plotted in figure 14 show total graph total time delay against the bandwidth requested in each ONU, same case of data is used on this graph, as clearly see the total time delay is reacted same condition as the bandwidth requested. Therefore, another graph is plotted in figure 15 below, which proven as the bandwidth allocated is increases then the total time delay also increases, thus the bandwidth allocated is directly proportional to the total time delay. In this case, the sum total time delay on all 16 ONU 21.1 msec.

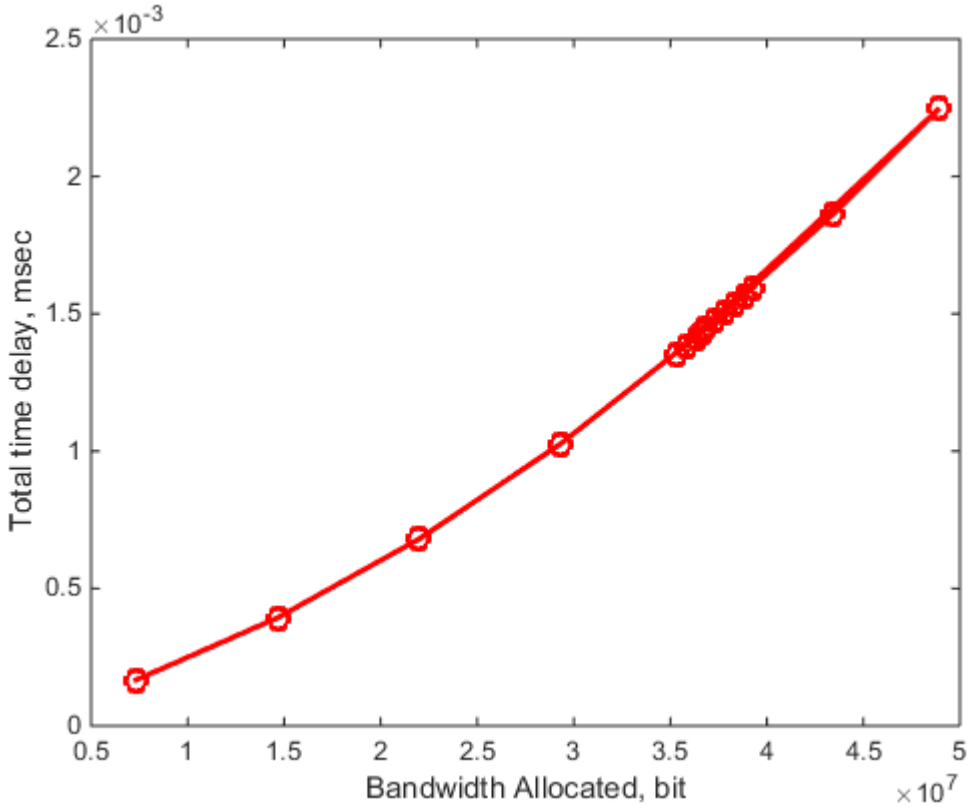

Figure 15: Bandwidth Allocated against Total time delay

Table 7: Data of Total Time Delay and allocated bandwidth in Mbit (A)

Total Time Delay, Msec	0.2	0.4	0.7	1.0	1.4	1.9	2.2	1.4
Bandwidth Allocated (Mbit)	7.327	14.654	21.981	29.308	36.635	43.440	48.940	35.320

Table 8: Data of Total Time Delay and allocated bandwidth in Mbit (A)

Total Time Delay, msec	1.4	1.4	1.4	1.5	1.5	1.5	1.6	1.6
Bandwidth Allocated (Mbit)	35.820	36.320	36.820	37.320	37.820	38.320	38.820	39.320

4. Conclusion

In conclusion, you are given a comprehensive introduction and background knowledge of Ethernet Passive Optical Network and Fiber Wireless network. Moreover, this paper also provide an extensive study and novel classification and notation of EPON on Dynamic Bandwidth Allocation components. From the results, can see that the bandwidth allocated will not exceed the overall bandwidth supply by the OLT. Moreover, the results also shows that as the bandwidth allocated is increases then the total time delay also increases, thus the bandwidth allocated is directly proportional to the total time delay Therefore, here can conclude that the dynamic bandwidth allocation method for fiber wireless is able to provide the fairness and data utilization of the bandwidth in terms of the QoS. In this research, the student also learned the fundamental of the dynamic bandwidth allocation on the fiber wireless network and also to analyze the performance characteristics and validate the overall performance of the fiber wireless communication system with dynamic bandwidth allocation.

For the future work to done after the bandwidth allocation is well developed would be to include the implementation of the proposed dynamic bandwidth allocation to the Fiber Wireless access network which the performance will be evaluated based on the QoS and QoE. Furthermore, further studies on research will be done for further improve the latency, fairness and the data utilization, this is because the drawback of current dynamic bandwidth algorithm is as the bandwidth allocated increases, the bandwidth also increases.

5. References

[1] *Measuring Information Society*. (2013). Viewed on Oct 16, 2014 ISBN: 978-92-61-14401-2, International Telecommunication Union.

[2] J. Coimbra, G. Schütz, and N. Correia, "A game-based algorithm for fair bandwidth allocation in Fibre-Wireless access networks," *Opt. Switch. Netw.*, vol. 10, no. 2, pp. 149–162, Apr. 2013.

[3] M. Maier and N. Ghazisaidi, "QoS Provisioning Techniques for Future Fiber-Wireless (FiWi) Access Networks," *Futur. Internet*, vol. 2, no. 2, pp. 126–155, Apr. 2010.

[4] M. Mirahmadi and A. Shami, "Traffic-prediction-assisted dynamic bandwidth assignment for hybrid optical wireless networks," *Comput. Networks*, vol. 56, no. 1, pp. 244–259, Jan. 2012.

[5] D. Ren, H. Li, and Y. Ji, "Demonstration of QoS-aware wireless protection scheme for video service in fiber-wireless access network," *Opt. - Int. J. Light Electron Opt.*, vol. 124, no. 14, pp. 1827–1831, Jul. 2013.

[6] R. Q. Shaddad, A. B. Mohammad, A. M. Al-Hetar, S. a. Al-Gailani, and M. a. Elmagzoub, "Fiber-wireless (FiWi) access network: Performance evaluation and scalability analysis of the physical layer," *Opt. - Int. J. Light Electron Opt.*, vol. 125, no. 18, pp. 5334–5338, Sep. 2014.

[7] Moradpoor, N., Parr, G., McClean, S., Scotney, B., & Owusu, G. (2011). Hybrid optical and wireless technology integrations for next generation broadband access networks. *12th IFIP/IEEE International Symposium on Integrated Network Management (IM 2011) and Workshops*, 1013–1020.

[8] Roberts, K., Borowiec, A., & Laperle, C. (2011). Technologies for optical systems beyond 100G. *Optical Fiber Technology*, *17*(5), 387–394.

[9] Xia, T. J. (2011). Optical channel capacity – From Mb/s to Tb/s and beyond. *Optical Fiber Technology*, *17*(5), 328–334.

[10] Bai, X., Shami, A., & Assi, C. (2006). On the fairness of dynamic bandwidth allocation schemes in Ethernet passive optical networks. *Computer Communications*, *29*(11), 2123–2135.

[11] Wang, C.-H., & Luh, H. P. (2011). Analysis of bandwidth allocation on end-to-end QoS networks under budget control. *Computers & Mathematics with Applications*, *62*(1), 419–439.

[12] Kadhim, D. J. (2013). Performance Analysis of xPON Network for Different Queuing Models, *44*(1), 1131–1137.

[13] M. Mcgarry, M. Reisslein, and M. Maier. Ethernet passive optical network architectures and dynamic bandwidth allocation algorithms. *Communications Surveys Tutorials, IEEE*, 10(3):46 –60, quarter 2008.

[14] D. Zhao. Ethernet Passive Optical Network Dynamic Bandwidth Allocation Study. *A Thesis Presented in Partial Fulfillment of the Requirements for the Degree Master of Science, ARIZONA STATE UNIVERSITY*, December 2011

The Fundamental Study on Antioxidant Activity and Stability of Bioactive Compounds in Betel Leaves (*Piper Betle*) Extract

Chia Wan Teng[1*], Rebecca Lim Xiao Yien[1], Puteri Farah Wahida[1]

[1]*School of Engineering, Taylor's University, Jalan Taylor's, Subang Jaya, Malaysia*

[*]chiawanteng@gmail.com

Abstract

Traditional herbal medicine has been used worldwide since antiquity to date due to the bioactivity of herbs such as antioxidant activity which provides health benefits such as prevention of diseases and anti-aging. Therefore, natural products which are rich in bioactive compounds with antioxidant properties have attracted a lot of interests ranging from cosmetic industries, dietary supplement manufacturers to pharmaceutical companies. Betel leaf (*Piper betle*) is one of the common herbs that has been used for medicinal purposes due to its significant antioxidant capability. This study investigated the effects of three solvents (95% ethanol, 50% ethanol and water) on extraction yield of bioactive compounds that contribute to high antioxidant activity and stability of antioxidant activity at room temperature during one month of storage period. Solvent extraction was used to extract the bioactive compounds from betel leaves (*piper* betel) and the result showed water had the highest extraction yield which is 29%. Stability of total phenolic content was analysed by Fast Blue BB (FBBB) reagent where 95% ethanol extract had the least degradation rate after a month. Stability of antioxidant activity was analysed by Diphenyl-1-Picrylhydrazyl (DPPH) and 95% ethanol extract possessed the highest antioxidant activity of 96% after a month. The stability of Eugenol (EU) concentration in 95% ethanol extract has been analysed by High Performance Liquid Chromatography (HPLC) and it showed a significant degradation rate of 73% after a month in room temperature storage condition. The overall results suggest that the use of 95% ethanol as solvent is suitable for extraction of bioactive compounds that contribute to high antioxidant activity value from betel leaves (*piper* betle). It also possesses the highest stability of antioxidant activity of piper betel leaves extract at room temperature storage condition for a month with the least degradation of less than 5% which has potential application in the pharmaceutical or nutraceutical industries.

Keywords: *Piper Betle* Leaf, Antioxidant Activity, Fast Blue BB, Eugenol, Stability

1. Introduction

Traditional herbal medicine has been used worldwide since antiquity to date. About 3.4 billion people in the developing world depend on plant-based traditional medicines (Pradhan, Suri, & Biswasroy, 2013). This represents about 88 per cent of the world's inhabitants, who mainly rely on traditional plant-based medicine due to their bioactivities (Doughari, 2012).

Betel leaf (*Piper betle*) belongs to the species *Piper* of the family *Piperaceae* (Chakraborty & Shah, 2011; Pin et al., 2010). This plant originates from central and eastern Peninsular Malaysia and is locally called *sirih* (Pin et al., 2006). Various studies have reported that betel leaves extract has shown anti-mutagenic, anti-carcinogenic, anti-diabetic, anti-inflammatory, antioxidant, and antibacterial bioactivities (Hoque et al., 2012; Pin et al., 2010; Tan & Chan, 2014). Besides that, betel leaf has also known to have healing properties such as reduce body odor and bad breath, throat and lung problems, cough prevention, reduce unwanted vaginal secretion and to prevent itching caused by fungus and bacteria (Guha, 2006; Pin et al., 2010). Studies have confirmed that the bioactive compounds in betel leaves are the main contributor to all the therapeutic properties mentioned above (Othman et al., 2014; Paranjpe et al., 2013; Pin et al., 2010).

Among all the bioactivities mentioned earlier, the bioactive compounds in betel leaves extract exhibit significant antioxidant activity that attracts intense interest from the researchers (Othman, Mukhtar, & Ismail 2014; Paranjpe et al., 2013; Pin, 2009). Antioxidant agent is a molecule that has ability to slow down or prevent the oxidation process. In biological system, the antioxidant molecule protects cells from damage. Besides, it also helps to provide support for immune system and protect cells from premature (Chakraborty & Kumar, 2009). Eugenol (EU) is found in betel leaf and it contributes to significant antioxidant activity and has been commonly used as herb drug or general pain relief (Lin, Ni, & Kokot, 2014; V. A. Parthasarathy, Chempakam, & Zachariah, 2008) Hence, bioactive compounds in piper betel leaf have the potential to be used as ingredients in dietary supplements, medicine, preservatives in food and cosmetics. Moreover, It can also be used in industrial processing to prevent the degradation of rubber and gasoline caused by oxidation (Hamid et al.,2010).

For the extraction process of betel leaves, solvent has significant effect on extraction efficiency, bioactive compound profile and biological activity (Nguyen et al., 2015). In this study, three solvents (95% ethanol, 50% ethanol ad water) were used to extract the bioactive compounds that contribute to high antioxidant activity from betel leaf. From a study done by Pin et al (2010), water had the highest extraction yield, phenolic content and antioxidant activity compared to ethanol. However, according to the results obtained by Nouri et al (2014), 90% ethanol was the most effective solvent which had the highest total phenolic content and antioxidant activity compared to water. Both studies had different findings on the effectiveness of ethanol and water in extracting the bioactive compounds from betel leaf which contribute to high antioxidant activity. Thus, the selection of solvents is crucial in the extraction of betel leaf.

Bioactive compounds degrade due to high temperature, or inappropriate storage condition (Queiroz et al., 2011). There were several stability studies done on different plants to investigate the shelf life and the storage condition to prevent degradation. However, to date, there are limited studies on stability of antioxidant activity in betel leaves extracts. Hence, this study was aimed to investigate the effects of various solvents on the bioactive compounds that contribute to antioxidant activity from betel leaf as well as the stability of total phenolic content, concentration of bioactive compound (Eugenol) and antioxidant activity of betel leaves extracts with different solvents (95% ethanol, 50% ethanol and water) at room temperature storage condition. The results provided information for the selection of solvent for the antioxidant activity and stability of bioactive compounds in piper betel leaves extract for potential application in the pharmaceutical or nutraceutical industries.

2. Materials and Methodology

2.1 Materials

Fresh betel leaves were purchased from Sirih Enterprise located at Banting, Selangor in December 2014. Distilled water, 95% Ethanol from HmbG Chemicals, Sodium Hydroxide from Friendemann Schmidt, Fast Blue BB purchased from Sigma-Aldrich, Deionized Water from Biology Lab, Taylor's University, Gallic Acid from Merck, HPLC Grade Methanol purchased from VWR PROLACO, Eugenol standard from Sigma-Aldrich and DPPH from Sigma-Aldrich.

2.2 Washing and Drying of Fresh Betel Leaves

Betel leaves were washed with running tap water followed by distilled water in order to remove the excess soils and dusts. After that, the leaves were dried for 4 days at temperature of 50 ^{o}C by using Forced-Air-Convection Oven (FAC-350, 3508711-608, Tech-Lab Scientific Sdn Bhd). The main purpose of drying is to lower the moisture content of the leaves to 10% in order to prevent contamination and fungi infection (Pin et al., 2011).

2.3 Crushing and Blending of Dried Betel Leaves

Dried betel leaves were then crushed by using cleaned hands with gloves into smaller pieces. Crushed betel leaves were then further ground by using electrical blender (Hand Blender HB680, Kenwood, Malaysia) into powder form. The dried betel leaves powder will be used for the extraction process. The purpose of grinding betel leaves into powder form is to reduce the particle size in order to obtain larger surface area. Particles with larger surface areas can easily contact with the solvents during the extraction process and achieve higher extraction yield.

2.4 Extraction Process

After drying and blending process of betel leaves, betel leaves powders are prepared to be extracted by 95% ethanol, 50% ethanol and water. The ratio of solvent to solid (betel leaves powder, W_s) to process duration used in the extraction were 30 ml: 1 g: 1 hour respectively at temperature of 50 ^{o}C and 250 rpm by using magnetic stirrer. After extraction, the mixture was then filtered by using filter paper (Whatman). The filtered extract was being further evaporated to remove the solvent from the

extract by using rotary evaporator (RV10BASIC, 07.196068, Lee Hung Scientific Sdn Bhd) under vacuum at 50^{o}C in order to obtain betel leaves crude extract (Pin et al., 2010; Sowndhararajan & Kang, 2013). However, in this study, 95% ethanol extract was dried at 80^{o}C; water and 50% ethanol extract were dried at 105 ^{o}C due to the limitation of equipment. The weight of the dried crude extracts (W_d) were measured and substituted into Eq. (1) below. The crude extracts were transferred into Petri disc and stored at room temperature (estimated 25 ^{o}C) for stability study. The extraction yield of each solvent can be calculated by using the equation below:

$$Yield = \frac{W_d}{W_s} \times 100\% \quad (1)$$

W_d is weights of dried extract (g)
W_s is weight of raw material (betel leaf) (g)

2.5 Stability of Fast Blue BB (FBBB) Total Phenolic Content (TPC) Assay

Fast Blue BB (FBBB) was assayed according to Lester et al (2012) and Medina (2011). The ratio of betel leaves extract and deionized water is 1:20 (Lester et al., 2012). A 0.1 ml aliquot of 0.1% FBBB was added to samples, and then 0.1ml of 5% Sodium Hydroxide (NaOH) was added into the samples after 1 minute. The reaction was allowed to take place at room temperature for 90 min. After that, the absorbance values of samples were measured at 420 nm by using UV spectrophotometer. The absorbance values of each sample were recorded and referred to the gallic acid calibration curve to obtain the equivalent concentration of gallic acid. Thus, the total phenolic content of samples was measured against the gallic acid calibration standard and the results were expressed as gallic acid equivalents (GAE) (Lester et al., 2012; Medina, 2011). The TPC results were plotted against week for a month in order to study the stability of betel leaves extracts.

2.6 Stability of DPPH Antioxidant Assay

The antioxidant assay system evaluates the extracts based on the scavenging activity of the stable DPPH radical according to the method described by Pin et al (2010). The DPPH stock solution was prepared in methanol at a concentration of 1 mM. The reaction mixture, consisting of 4 ml of methanol, 2 mg of dried betel leaves extract and 1 ml of DPPH was kept in universal bottle. The reaction mixture was shaken and left to stand at room temperature for 30 min. After that, the reaction mixture was then subjected to UV spectrophotometer with 520nm wavelength in order to indicate the absorbance value (Pin et al., 2010). The absorbance of negative control (4 ml methanol and 1 ml DPPH) and positive control (replacing betel leaves extract with gallic acid) was obtained. The percentage of inhibition can be calculated by using Eq. (2) below:

$$\%\ Inhibition = \frac{Ab_{c,-ve} - Ab_S}{Ab_{c,-ve} - Ab_{c,+ve}} \times 100\% \quad (2)$$

Ab_s is absorbance of sample
$Ab_{c,-ve}$ is absorbance of negative control
$Ab_{c,+ve}$ is absorbance of positive control

The DPPH antioxidant activity analysis will be carried out weekly to record the inhibition percentage of the betel leaves extracts samples for a month to find out the

stability of antioxidant activity of the bioactive compounds in betel leaves extract with different solvents.

2.7 Stability of Concentration of Eugenol (EU) Using HPLC

2.7.1 High Performance Liquid Chromatography (HPLC) Analysis and Condition

The HPLC analysis of the extract samples were performed by using HPLC (Model 1260, Agilent Technologies) and Hypersil GOLD column C_{18} with 250 x 4.6 mm.

2.7.2 Method Development

The ratio of mobile phase for HPLC method is HPLC grade methanol to deionized water is 70:30. The column oven was set as 28^{o}C, Flow rate was 0.7 ml/min, wavelength was 280 nm, the injection volume was 10 µl and the duration was set as 10 minutes.

2.7.3 HPLC Analysis on Betel Leaves Extract

Stability study of the concentration of eugenol in betel leaves extracts can be determined by using HPLC. To measure the betel leaves extract from water, 4 mg of dried extracts from water were dissolved in 4 ml of distilled water. 4 mg of dried extracts from 95% ethanol and 50% ethanol were dissolved in 4 ml of HPLC grade methanol (Pin et al., 2010). 2 ml of the solutions were filtered by using syringe filter and injected into HPLC for analysis to determine the concentration of eugenol. The concentration of eugenol at room temperature was plotted against week in order to study the stability of eugenol in betel leaves extracts.

3. Results and Discussion

3.1 Effects of Solvents on Extraction Yield and Stability of TPC

3.1.1 Extraction Yield

Extraction yield refers to the betel leaves crude extracts obtained from dried betel leaves through various solvent extractions. Figure 1 shows the comparison of extraction yields for three types of solvents. The increasing order of extraction yield for the solvents is: 95% ethanol < 50% ethanol < water. Water possesses the highest extraction yield, 29%. The extraction yield of 50% ethanol is 25% which is slightly lower than water, whereas 95% ethanol has the lowest extraction yield which is only 6%. These data are in good agreement with the results that reported by Pin et al (2010) and Nguyen et al (2015) that water has the highest extraction yield in the extraction of betel leaves and xao tam phan (*paramignya trimera*) respectively. This indicates that water possesses better dissolution of phenolic compounds present in betel leaves due to the interactions of hydrogen bonds between the phenolic compounds and water (Boeing et al., 2014; Pin et al., 2010).

Although both water and ethanol able to form hydrogen bonding with phenolic compounds, water is more effective in extracting the phenolic compounds because it has higher polarity of 9.0 compared to ethanol which is 5.2 (Pin et al., 2010; Sadek,

2002; Torres, Velasquez, & Brito-Arias, 2011). These characteristics explain the difference between the extraction yield of water and 95% ethanol, which water is about 4.7 times greater than ethanol. The result obtained by Xu and He (2007) showed that the extraction yield of water had 4 times greater than ethanol of *Pueraria lobata* (Willd.) Ohwi (kudzu vine). These results indicate that the extraction yield of betel leaves was greatly affected by the polarity and type of solvents used (Nguyen et al., 2015; Nouri et al., 2014).

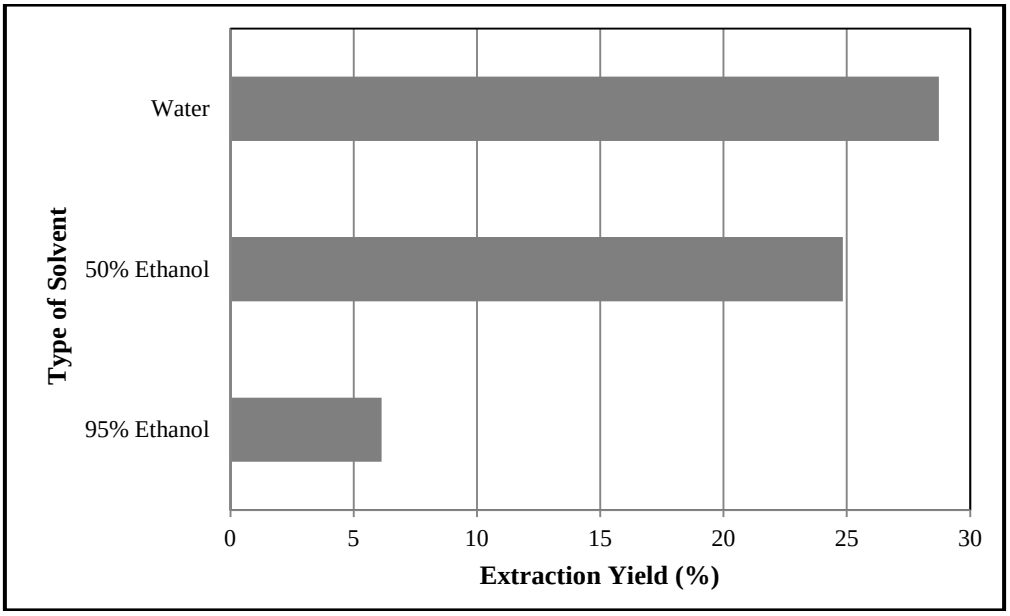

Figure 1. Comparison of Extraction Yield for Three Solvents

3.1.2 Stability of Total Phenolic Content (TPC) by Fast Blue BB (FBBB)

Phenolic compounds contribute to antioxidant activity to prevent diseases by scavenging the free radicals which have ability to damage cells produced by oxidation reaction. In order to evaluate the antioxidant capacity of betel leaves extracts, the phenolic content in the extract is utmost important. From this study, the betel leaves extract of water contains 104 mg GAE/g dried extract, while 95% ethanol contains 818 mg GAE/g dried extract. Nouri et al (2014) reported that 90% ethanol has higher total phenolic content (202.92 mg GAE/g dry weight) compared to water (71.30 mg GAE/g dry weight) by using Folin-Ciocalteu (FC) reagent. However, 95% ethanol analyzed by using FBBB provides higher amount of total phenolic content compared to Nouri et al (2014) FC method. This finding is in agreement with Bliss (2015) who reported that FBBB method provides a higher and more accurate estimation of total phenolics than FC method due to its direct reaction.

Figure 2 shows the percentage of total phenolic content remains in betel leaves extracts with three types of solvents stored at room temperature (estimated 25^{o}C) which was analyzed by using Fast Blue BB (FBBB) reagent for a month. The increasing order of stability on total phenolic compounds among the three samples is: water < 50% ethanol < 95% ethanol. 95% ethanol extract stored at room temperature has the highest stability on total phenolic compounds among other solvent extracts, which has a range from 818 mg GAE/g dried extract to 258 mg GAE/g dried extract (degraded 68%) after a month. 50% ethanol extract has a range from 434 mg GAE/g

dried extract to 133 mg GAE/g dried extract (degraded 69%) in a month. Water extract stored at room temperature has the lowest stability on total phenolic compounds, which ranged from 104 mg GAE/g dried extract to 31 mg GAE/g dried extract (degraded 70%) in a month. The drastically degradation rates of three betel leaves extracts which ranged from 68% to 70% shows that most of the phenolic compounds degraded rapidly. The significant degradation rate of the extracts may be due to the storage condition such as storage temperature, light exposure or type of storage containers.

A recent finding published by Jaiswal et al (2014) indicated that solvent has high polarity was found to have lesser amount of total phenol content (Jaiswal, Patel, Saxena, & Naik, 2014). In earlier extraction yield results, water had the highest extraction yield but possessed the lowest stability (highest rate of degradation) of total phenolic content; whereas ethanol had the lowest extraction yield but possessed the highest stability (lowest rate of degradation) of total phenolic content. Hence, this result is in good agreement with Jaiswal et al (2014). To date, limited studies have focused on the analysis of stability on total phenolic content using FBBB method for betel leaves extracts. From this study, it shows that FBBB method provides a higher and more accurate estimation of total phenolics than FC method as well as the stability of total phenolic content from betel leaves extract is greatly affected by the type of solvents used.

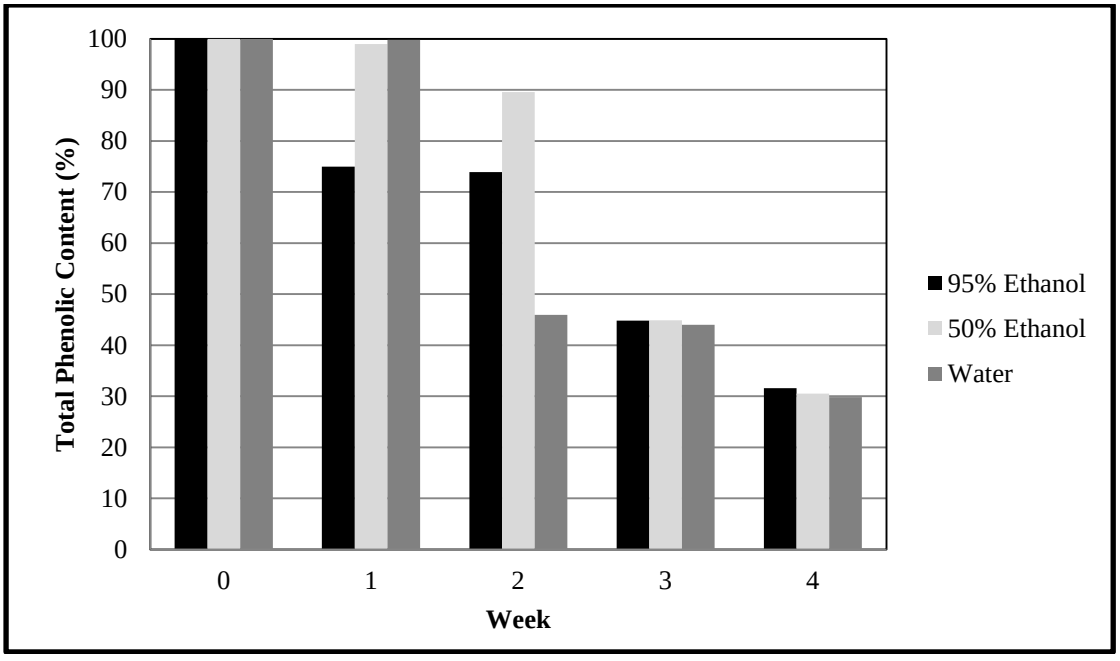

Figure 2. Total Phenolic Content of Various Betel Leaves Extracts for a Month

3.2 Stability of Betel Leaves Extract DPPH Antioxidant Activity

From this study, it can be observed that solvent applied in extraction process affects the stability of antioxidant activity of betel leaves extract at room temperature. Figure 3 illustrates the antioxidant activity of three solvent extracts stored at room temperature for a month. The betel leaves extracts with various solvents show an increasing order in the percentage inhibition of antioxidant activity for the first week

as follow: water (84.5%) < 50% ethanol (86.9%) < 95% ethanol (89.8%). 95% ethanol extract has the highest antioxidant activity compared to water. This result is similar to Nouri et al (2014), who reported that 90% ethanol betel leaves extract has the highest antioxidant activities than water extract.

Combining the finding in Section 3.1, this indicates that the total phenolic content presents in 95% ethanol extract (818 mg GAE/g dried extract) contributes to significant antioxidant activity. This result coincides with Soares et al (2013) who reported that the phenolic content of c.citratus and other plant matrices are dependent on the solvent that used to extract them; this is most likely due to the different profiles of phytochemicals for different extracts (Soares et al, 2013). Furthermore, Xu and Chang (2007) had also reported that the total phenols content in soybeans and the effect on DPPH assay may vary with the choice of extraction solvent. These results are supported by Rahman et al (2013), Nouri et al (2014) and Nguyen et al (2015).

After a month, the betel leaves extracts of various solvents have an increasing order in the antioxidant stability as follow: water < 50% ethanol < 95% ethanol. The 95% ethanol extract has the highest antioxidant activity and stability among all the solvents used with degradation of 3.5% for antioxidant activity. Water exhibited the lowest stability for antioxidant activity, with degradation rate of 6.2%. Total phenolic content decreases drastically within a month with 70% of degradation rate but antioxidant activity remains stable with only 6% of degradation rate. This finding shows the remaining 30% of phenolic compounds in betel leaves extract contribute to high and stable antioxidant activity for a month.

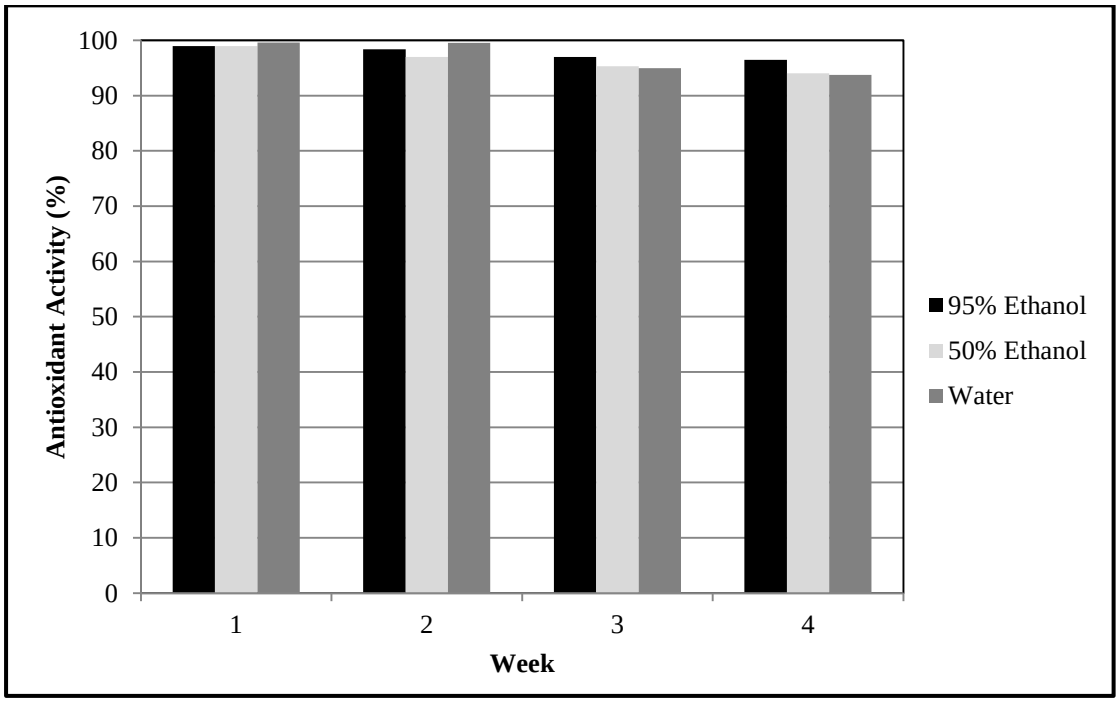

Figure 3. DPPH Antioxidant Activity of Various Betel Leaves for a Month

3.3 Stability of Betel Leaves Extract Component – Eugenol (EU)

The targeted bioactive compound, Eugenol (EU) was only detected in 95% ethanol extracts among the solvents used. The absence of EU could be due to the high temperature used for evaporation (100^{o}C) of 50% ethanol and water, which caused the fast degradation of EU. From HPLC results, 38 ng/µl of EU concentration was found in 95% ethanol extract and degraded to 10 ng/µl in a month. Figure 4 illustrates the EU concentrations in 95% ethanol extract stored at room temperature for a month. It shows that only 27% of EU remains in 95% ethanol extract after one month. From a study conducted by Girisgin et al (2014), it showed that the level of EU from clove oil in 1 g of sample beeswax completely degraded from 3.1 mg/g to 0 mg/g within 28 days. The fast degradation is due to high volatility of EU, and it is sensitive to light and heat (Woranuch & Yoksan, 2013).

The main purpose of detecting EU in betel leaves extracts is to study the stability and capability of EU in contributing antioxidant activity. By combining the findings from Section 3.1 and 3.2, the amount of total phenolic compounds remain in 95% ethanol extract is only 32% and the concentration of EU is 27%, but it possesses 96% of high antioxidant activity after a month. The results showed that the presence of EU had less enhancing effect on the antioxidant activity in 95% ethanol extract. There might have some other phenolic compounds present in the betel leaf which also contribute to antioxidant activity such as Hydroxychavicol (HC) (Gundala et al., 2014; Pin et al., 2010).

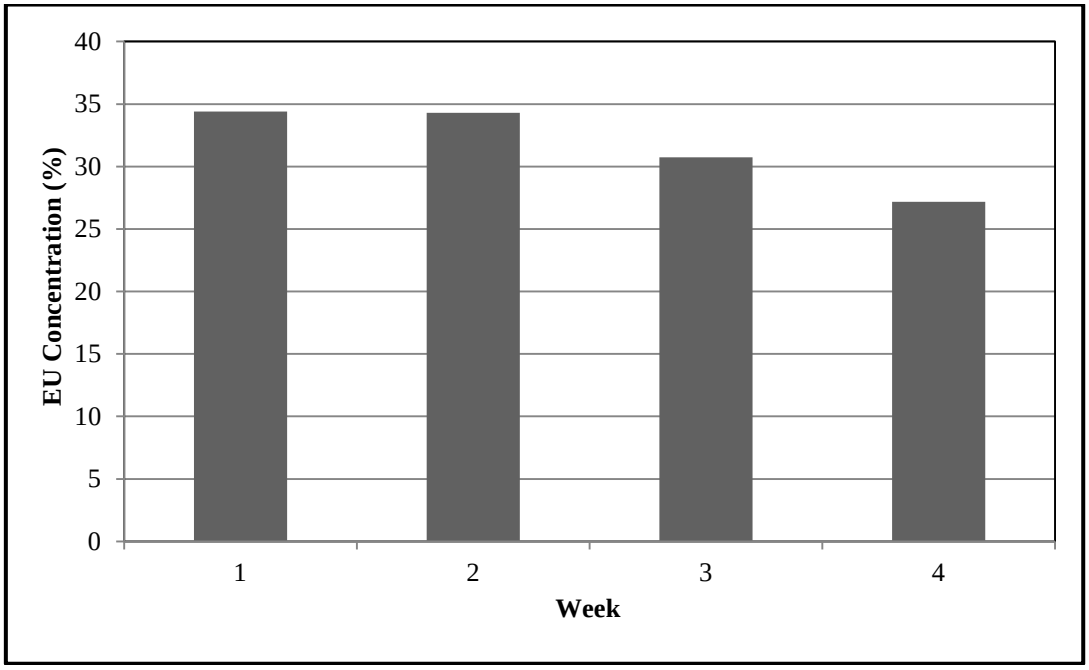

Figure 4. Concentration of Eugenol (EU) in 95% Ethanol Extracts for a Month

4. Conclusion

This study demonstrated that type of solvent had great effect on the extraction yield, stability of total phenolic content, antioxidant activity as well as concentration of EU in betel leaves extracts. Among the three solvents (95% ethanol, 50% ethanol and water), 95% ethanol was the best selection in extracting the bioactive compounds that contributed to high antioxidant activity and stability even though it had the lowest extraction yield. From the findings, the stability of total phenolic compounds and concentration of EU remained in 95% ethanol extract were low, but the stability of antioxidant activity was high after a month. It showed that the presence of EU had less enhancing effect on the antioxidant activity in 95% ethanol extract. There might have some other phenolic compounds present in the betel leaf which also contribute to antioxidant activity such as hydroxychavicol. As a conclusion, 95% ethanol possessed high stability on antioxidant activity and has potential for application in the pharmaceutical or nutraceutical industries. Investigation on product stability during storage is crucial when considering the production of food, beverage or dietary supplements, as the antioxidant activity may be affected. In further study, more bioactive compounds will be investigated for stability of other biological activity in betel leaves (*piper betle*).

Acknowledgment

The author would like to thank Dr Rebecca, Ms Puteri and Ms Lithness for supporting and providing advices and suggestions.

References

Boeing, J. S., Barizão, E. O., E Silva, B. C., Montanher, P. F., de Cinque Almeida, V., & Visentainer, J. V. (2014). Evaluation of solvent effect on the extraction of phenolic compounds and antioxidant capacities from the berries: application of principal component analysis. *Chemistry Central Journal*, *8*(1), 48. doi:10.1186/s13065-014-0048-1

Chakraborty, D., & Shah, B. (2011). Antimicrobial, Anti-Oxidative and Anti-Hemolytic Activity of Piper Betel leaf Extract. *International Journal of Pharmacy and Pharmacuetical Sciences*, *3*(1923).

Chakraborty, P., & Kumar, S. (2009). Role of Antioxidants in Common Health Diseases. *Research J. Pharm. and Tech.*, *2*(2), 238–244.

Doughari, J. H. (2012). Phytochemicals : Extraction Methods , Basic Structures and Mode of Action as Potential Chemotherapeutic Agents. In Dr Venketeshwe Rao (Ed.), *Phytochemicals - A Global Prespective of Their Role in Nutrition and Health* (pp. 1–33). INTECH.

Guha, P. (2006). Betel Leaf : The Neglected Green Gold of India. *J. Hum. Ecol*, *19*(2), 87–93.

Gundala, S. R., Yang, C., Mukkavilli, R., Paranjpe, R., Brahmbhatt, M., Pannu, V., … Aneja, R. (2014). Hydroxychavicol, a betel leaf component, inhibits prostate cancer

through ROS-driven DNA damage and apoptosis. *Toxicology and Applied Pharmacology*, *280*(1), 86–96. doi:10.1016/j.taap.2014.07.012

Hamid, A. A., Aiyelaagbe, O. O., Usman, L. A., Ameen, O. M., & Lawal A. (2010). Antioxidants : Its medicinal and pharmacological applications. *African Journal of Pure and Applied Chemistry*, *4*(August), 142–151.

Hoque, M. M., Rattila, S., Shishir, M. A., Bari, M. L., Inatsu, Y., & Kawamoto, S. (2012). Antibacterial Activity of Ethanol Extract of Betel Leaf (Piper betle L.) Against Some Food Borne Pathogens. *Bangladesh Journal of Microbiology*, *28*(2), 58–63. doi:10.3329/bjm.v28i2.11817

Jaiswal, S. G., Patel, M., Saxena, D. K., & Naik, S. N. (2014). Antioxidant Properties of Piper Betel (L) Leaf Extracts from Six Different Geographical Domain of India, *2*(2), 12–20.

Lester, G. E., Lewers, K. S., Medina, M. B., & Saftner, R. A. (2012). Journal of Food Composition and Analysis Comparative analysis of strawberry total phenolics via Fast Blue BB vs . Folin – Ciocalteu : Assay interference by ascorbic acid. *Journal of Food Composition and Analysis*, *27*(1), 102–107. doi:10.1016/j.jfca.2012.05.003

Lin, X., Ni, Y., & Kokot, S. (2014). Electrochemical mechanism of eugenol at a Cu doped gold nanoparticles modified glassy carbon electrode and its analytical application in food samples. *Electrochimica Acta*, *133*, 484–491. doi:10.1016/j.electacta.2014.04.065

Medina, M. B. (2011). Determination of the total phenolics in juices and superfruits by a novel chemical method. *Journal of Functional Foods*, *3*(2), 79–87. doi:10.1016/j.jff.2011.02.007

Nguyen, V. T., Bowyer, M. C., Vuong, Q. Van, Altena, I. A. V., & Scarlett, C. J. (2015). Phytochemicals and antioxidant capacity of Xao tam phan (Paramignya trimera) root as affected by various solvents and extraction methods. *Industrial Crops and Products*, *67*, 192–200. doi:10.1016/j.indcrop.2015.01.051

Nouri, L., Mohammadi Nafchi, A., & Karim, a. a. (2014). Phytochemical, antioxidant, antibacterial, and α-amylase inhibitory properties of different extracts from betel leaves. *Industrial Crops and Products*, *62*, 47–52. doi:10.1016/j.indcrop.2014.08.015

Othman, A., Mukhtar, N. J., Ismail, N. S., & Chang, S. K. (2014). Phenolics , flavonoids content and antioxidant activities of 4 Malaysian herbal plants. *International Food Research Journal*, *21*(2), 759–766.

Paranjpe, R., Gundala, S. R., Lakshminarayana, N., Sagwal, A., Asif, G., Pandey, A., & Aneja, R. (2013). Piper betel leaf extract: anticancer benefits and bio-guided fractionation to identify active principles for prostate cancer management. *Carcinogenesis*, *34*(7), 1558–66. doi:10.1093/carcin/bgt066

Pin. (2009). Drying and Solid-Liquid Extraction of Hydroxychavicol and Eugenol Betel Leaves (Piper Betel L.). *Universsity Putra Malaysia*, 1–3.

Pin, K. Y., Chuah, A. L., Rashih, A. A., Mazura, M. P., Fadzureena, J., & Vimala, S. (2010). Antioxidant and anti-inflammatory activities of Extracts of betel leaves (Piper betle) from solvents with different polarities. *Journal of Tropical Forest Science*, *22*(4), 448–455.

Pin, K. Y., Chuah, T. G., Abdul Rashih, a., Rasadah, M. ., & Choong, T. S. Y. (2006). Aqueous Extraction of Hydroxychavicol from Piper Betle L . Leaves. *1St International Conference on Natural Resources Engineering & Technology 2006*, (July), 146–152. Retrieved from http://eprints.utm.my/184/1/KYPin2006_Aqueous_extraction_of_hydroxychavicol_from.pdf

Pin, K. Y., Luqman Chuah, a., Abdull Rashih, a., Rasadah, M. a., Law, C. L., & Choong, T. S. Y. (2011). Solid-Liquid Extraction of Betel Leaves (Piper Betle L.). *Journal of Food Process Engineering*, *34*(3), 549–565. doi:10.1111/j.1745-4530.2009.00395.x

Pradhan, D., Suri, K. A., & Biswasroy, P. (2013). Golden Heart of the Nature : Piper betle L . *Journal of Pharmacognosy and Phytochemistry*, *1*(6), 147–167.

Queiroz, C., Lopes, M. L. M., Fialho, E., & Valente-Mesquita, V. L. (2011). Changes in bioactive compounds and antioxidant capacity of fresh-cut cashew apple. *Food Research International*, *44*(5), 1459–1462. doi:10.1016/j.foodres.2011.03.021

Sadek, P. (2002). Solvent Miscibility and Viscosity Chart. *The HPLC Solvent Guide Wiley-Interscience*, 2.

Soares, M. O., Alves, R. C., Pires, P. C., Oliveira, M. B. P. P., & Vinha, A. F. (2013). Angolan Cymbopogon citratus used for therapeutic benefits: Nutritional composition and influence of solvents in phytochemicals content and antioxidant activity of leaf extracts. *Food and Chemical Toxicology*, *60*, 413–418. doi:10.1016/j.fct.2013.07.064

Sowndhararajan, K., & Kang, S. C. (2013). Free radical scavenging activity from different extracts of leaves of Bauhinia vahlii Wight & Arn. *Saudi Journal of Biological Sciences*, *20*(4), 319–25. doi:10.1016/j.sjbs.2012.12.005

Tan, Y. P., & Chan, E. W. C. (2014). Antioxidant, antityrosinase and antibacterial properties of fresh and processed leaves of Anacardium occidentale and Piper betle. *Food Bioscience*, *6*, 17–23. doi:10.1016/j.fbio.2014.03.001

Torres, L. G., Velasquez, A., & Brito-Arias, M. A. (2011). Ca-alginate spheres behavior in presence of some solvents and water-solvent mixtures. *Advances in Bioscience and Biotechnology*, *02*(February), 8–12. doi:10.4236/abb.2011.21002

V. A. Parthasarathy, Chempakam, B., & Zachariah, T. J. (2008). *Chemistry of Spices* (First.). CABI.

Woranuch, S., & Yoksan, R. (2013). Eugenol-loaded chitosan nanoparticles: I. Thermal stability improvement of eugenol through encapsulation. *Carbohydrate Polymers*, *96*(2), 578–585. doi:10.1016/j.carbpol.2012.08.117

Drying Characteristics and Product Quality of Medicinal Herbs

Sze Ting Goh, Chien Hwa Chong

Health Research Group, School of Engineering, Taylors University,
No 1, Jalan Taylor's, 47500 Subang Jaya, Selangor Malaysia

**Corresponding author E-mail: ChienHwa.Chong@taylors.edu.my*

Abstract
The objectives of this study were to investigate the drying characteristics and assess the retention of total phenolic compounds of dried *Vernonia Amygdalina* leaves (VA). 100 g of VA were dried at 60ºC, 70ºC and 80ºC until the moisture content reached equilibrium stage when three consecutive weights obtained. Empirical models such as the Page model, the Newton model and the Henderson and Pabis model were selected to model the drying kinetics of VA. Further to this, total phenolic compounds of VA dried using different temperature were analysed using an UV Spectrometer at 420 nm. Referring to the results obtained, only first falling rate period found in the drying characteristics curve. Transient period, constant rate period and 2nd falling rate period did not exist in drying of VA from 60 to 80 ºC. The drying kinetics of VA dried from 60 to 80ºC was best fitted to the Newton model. It was found that drying rate of VA dried at 80ºC was 37% faster than 70ºC and 387.5% faster than 60ºC. In terms of total polyphenol content, the mean of the total phenolic compound of dried bitter leaves for 80ºC was 186.22 mg GAE/100 g sample, for 70ºC was 190.2 mg GAE/100 g sample and for 60ºC was 188.54 mg GAE/100 g sample. However, based on the two-tailed distribution test, it was found that there was no significant difference (p>0.05) when VA were dried from 60ºC to 80ºC.

Keywords: Drying characteristics; Total phenolic compounds; Drying kinetics; *Vernonia Amygdalina*

1. Introduction

Vernonia Amygdalina is a green leafy plant with height of 5 m and is well known with its other name, bitter leaf. It is rich in various polyphenolic compound such as Chlorogenic acid, Luteolin-7-O-glucoside, 1,5-Dicaffeoyl-quinic acid and Dicaffeoyl-quinic acid (Ong *et al.*, 2011). The extract of *Vernonia Amygdalina*'s leaf shows an antidiabetic effect activity. There is a reduction of 0.4% of blood glucose concentration in human who has normal fasting blood glucose concenration and body health condition (Nwangozi *et al.*, 2013). Other than that, the *Vernonia Amygdalina'*s leaf is used to test on the anti-obesity effect. Rats are used as specimen and the result shows that there is a decrease of 12.78% and 38.51% in body weight gain for rats that is fed with 5% and 15% of *Vernonia Amygdalina*'s leaf powder for 4 weeks (Atangwho *et al.*, 2012). There are vast research on the vernonia species but the drying kinetics of speficially on the leaf of *Vernonia Amygdalina* is rather scarce.

Drying industry has been through revolution for decades. There are different types of dryers that use different mechanism such as convective, conduction and radiation. Researches often use these methods to obtain the optimized quality for their products. As an example, microwave drying of the *coriander foliage* to 12% moisture wet basis was around 10 times faster than hot air convective drying but the color change of the coriander foliage was greater for convective drying as the convective dried samples had higher L value than the microwave dried samples (Shaw *et al*., 2007). Different type of dryers gave various results for different products. Drying of fruits had been studied intensely by a lot of researches to maintain the quality of the dried product in terms of nutrient and physical structure. For instance, the residual ratio of AsA (vitamin) content inside a kiwi when dried using a hot air dryer is 0.75 to 0.88 while dried using a microwave dryer is 0.90 to 0.99, which showed that microwave dryer can retained higher amount of AsA (vitamin) component inside a kiwi than the hot air dryer (Orikasa *et al*., 2014). In this paper, the drying method used was forced convective hot air drying. 100 g of *Vernonia Amygdalina L*. was put into the oven and dried at 60ºC, 70ºC and 80ºC until Equilibrium Moisture Content (EMC) was achieved.

On the other hand, parameters such as pressure, air velocity, relative humidity and chamber temperature also affect the drying characteristics and product quality of samples. Many researches have been conducted to investigate the effects of drying on herbs as it is a heat sensitive biomaterial. Adapa & Schoenau (2005) recommended to keep the drying temperature from 30ºC to 35ºC. This is because Diaz-Maroto *et al*., (2002) found that small losses of volatile compunds can be found in air-drying of bay leaves. Lemon myrtle plant leaves dried using fluidized bed dryer at temperature at 30ºC, 40ºC, and 50ºC shows that the volatile compound (citral) of the leaves percentage of retention as high as 90% (Buchaillot *et al*., 2009). In forced convective air drying, drying temperature is the major driving force to remove the moisture content compared to relative humidity and air velocity. Furthermore, some researchers reported the optimization and design of convective drying units (Shaw *et al.*, 2007). Additional parameter needs to be considered in drying of herbs such as moisture measurement standards (Shaw *et al*., 2005). In this context, the only parameter that will be manipulated in this research was the drying temperatures of the oven, which were set at 60ºC, 70ºC and 80ºC.

The main objective of this research is to determine the drying characteristics and product qualities of *Vernonia Amygdalina L.*. Three drying temperatures (60ºC, 70ºC, and 80ºC) were used to test on the drying kinetics and to test on the effects of drying temperature on the Total Phenolic Compound in the *Vernonia Amygdalina L.*. Empirical drying models were formulated using the experimental data obtained and the best fitting model was

determined using the coefficient of determination (R^2), root mean square error (RMSE) and reduced chi-square (χ^2).

2. Methodology

2.1 Preparation of Samples

VA was purchased from TKC Herbal Nursery Sdn Bhd located at Seremban, Negeri Sembilan, Malaysia. The leaves were cleaned using water to remove soils. 100 g of bitter leaves was stored inside the refrigerator (2D-DC, SN:121204) operating at 2º - 8ºC before subjected to drying.

2.2 Drying Process

A bag of 100 g bitter leaves was taken out from the refrigerator and was left to recover to room temperature. The initial weight of the leaves was then measured using weighing balance (PA4102, SN:8329520028) to be exact before evenly distributed onto the oven tray. The forced air convective oven (FAC-350) was pre heated to the desired temperature before inserting the tray of leaves. The temperatures used to dry the leaves are 60ºC, 70ºC, and 80ºC. For the first hour the weight of the leaves are measured every 15 minutes and every 30 minutes after the first hour until three consecutive reading are taken. The moisture content of the leaves can be calculated by equation (1):

$$MC = \frac{M_t - M_{BDW}}{M_{BDW}} \quad (1)$$

where MC is the moisture content (kg $H_2O \cdot kg^{-1}$ DM), M_t is the weight at specific time (g) and M_{BDW} is the bone dry weight of the leaves (g). The moisture ratio can be calculated by using equation (2):

$$MR = \frac{M_T - M_E}{M_O - M_E} \quad (2)$$

where MR is the moisture ratio, M_T is the mass of leaves at time T (g), M_E is the final mass of the leaves (g) which is also the equilibrium moisture content (EMC) and M_o is the initial mass of the leaves (g). The drying rate of the samples was calculated by using equation (3):

$$DR = \frac{M_t - M_E}{M_E \, x \, \Delta t} \quad (3)$$

where DR is the drying rate (kg $H_2O \cdot kg^{-1}$ DM min^{-1}), M_t is weight of leaves at time t (g), M_E is the weight of leaves at Equilibrium Moisture Content (g) and Δt is the total drying time (minutes).

2.3 Mathematical Modeling and Curve Fitting

Three empirical drying models are used in this research to do a curve fitting onto the drying data obtained from the experiments. The empirical models are(Mohamed *et al.*, 2005; Jamali *et al.*, 2006; Midilli & Kucuk 2003; Lahsasni *et al.*, 2004):

Newton Model:

$$MR = \exp(-kt) \quad (4)$$

Page Model:

$$MR = \exp(-kt^n) \quad (5)$$

Henderson and Pabis Model:

$$MR = a\exp(-kt) \quad (6)$$

Where MR is the moisture ratio, k is the drying rate constant (min^{-1}), *a* and *n* are dimensionless coefficients of the model. The fitness of the models onto the experimental data is evaluated by using coefficient of determination (R^2), root mean square error (RMSE) and the reduced chi-square (χ^2). The R^2 can be determined from the graph plotted while RMSE and χ^2 are determined by using equation (7) and (8):

$$RMSE = \sqrt{\frac{1}{N}\sum_{i=1}^{N}(MR_{exp,i} - MR_{pre,i})^2} \quad (7)$$

$$\chi^2 = \frac{\sum_{i=1}^{N}(MR_{exp,i} - MR_{pre,i})^2}{N-n} \quad (8)$$

Where N is the total number of observation, n is the number of constant, $MR_{pre,i}$ is the ith predicted moisture ratio and $MR_{exp,i}$ is the ith experimental moisture ratio.

2.4 Total Phenolic Content Analysis

The total phenolic content analysis is based on the research done by Dr. Pin(Pin *et al.*, 010). The dried bitter leaves from the drying process were ground using a blender to smaller size particles. The leaves are extracted by using 95% ethanol as solvent. The ratio of solvent to solid is 30 ml: 1 g and the duration of extraction is 1 hour. 10 g of crushed bitter leaves are used in this extraction process. After 1 hour of extraction the mixture is filtered by using filter paper and the permeates was poured into a rotary evaporator to evaporate off the solvent to obtain a purer extract.

The dried extract is liquefied by mixing with de-ionized water with a ratio of 20 ml: 1 g. The liquid extract is then added with 1ml of NaOH and waited for 1 minute before adding FBBB reagent. The solution is then analyzed by using UV Spectrometer at 420nm wavelength 90 minutes after adding the FBBB reagent. The absorbance value is converted to Gallic Acid Equivalent (mg GAE/100 g of sample) by using Gallic Acid calibration curve. A two-tailed z-test is done to evaluate the significance difference between the results obtained.

3. RESULTS AND DISCUSSION

3.1 Drying Kinetics of *Vernonia Amygdalina L.*

In this study, a forced convective hot air dryer was used to dry the leaves. The drying kinetics of the leaves were determined by calculating the moisture content, moisture ratio, and drying rate of the leaves using equation (1), (2), (3) and the drying data obtained from the experiment. Graph of moisture ratio in the leaves (% Dry Basis) against time (min) and graph of drying rate of the leaves (kg H_2O/kg DM min) against moisture content of the leaves (kg H_2O/kg DM) were plotted and discussed.

The drying temperature affects the drying duration of the leaves of *Vernonia Amygdalina* significantly. Based on Figure 1, *Vernonia Amygdalina L*. started at the same moisture ratio but the steepness of the drying curve was different due to different temperatures. At 80ºC, the leaves reaches equilibrium moisture content at 60 min, 70ºC at 90 min and 60ºC at 210 minutes. This shows that 80ºC is 50% faster than 70ºC and is 250% faster than 60ºC to reach Equilibrium Moisture Content. Furthermore, at the first 15 minutes, 80 ºC shows a huge drop of moisture ratio inside the leaves compared to 70ºC and 60ºC. This is because 80ºC provides higher driving force, which is the temperature difference (Chong *et al.*, 2008).

The drying curve of *Vernonia Amygdalina L*. was steeper at the beginning of the experiment and gradually decreases along the drying process. The freeze drying of Javanese pepper, microwave convective drying of Parsley leaves and fluidized bed drying of kaffir lime leaves also shows similar drying kinetics where the moisture ratio dropped in a decreasing manner (Tambunan, 2001; Śledź *et al.*, 2013; Tasirin *et al.*, 2014). The effects of drying temperatures on drying kinetics of the leaves can be further distinguished based on the gradient of the lines in Figure 1. Drying temperature at 80ºC has the steepest line followed by 70ºC and then 60ºC. The initial moisture contents of the samples were around 3.5 kg H_2O/kg DM but the initial drying rate are different. At 80ºC, the drying rate was at 0.078 kg H_2O/kg DM min, at 70ºC it was at 0.057 kg H_2O/kg DM min and at 60ºC it was at 0.016 kg H_2O/kg DM min. This indicated that the drying rate at 80ºC was 37% faster than 70ºC and 387.5% faster than 60ºC.

Based on Figure 2, there was no transient period and constant rate period in the drying of the leaves of *Vernonia Amygdalina L.*. There was only first falling rate period shown in the graphs without the second falling rate period when the leaves achieved equilibrium moisture content. This phenomenon indicates that there is no boundary and restriction from the internal moisture to diffuse out from the leaves. Constant rate period was absent in this drying kinetic probably because the constant rate period was too fast and short. The interval for the weight of the leaves to be measured is 15 minutes at first for the first hour. The constant rate period probably fall at the first few minutes of the drying process hence it is undetectable.

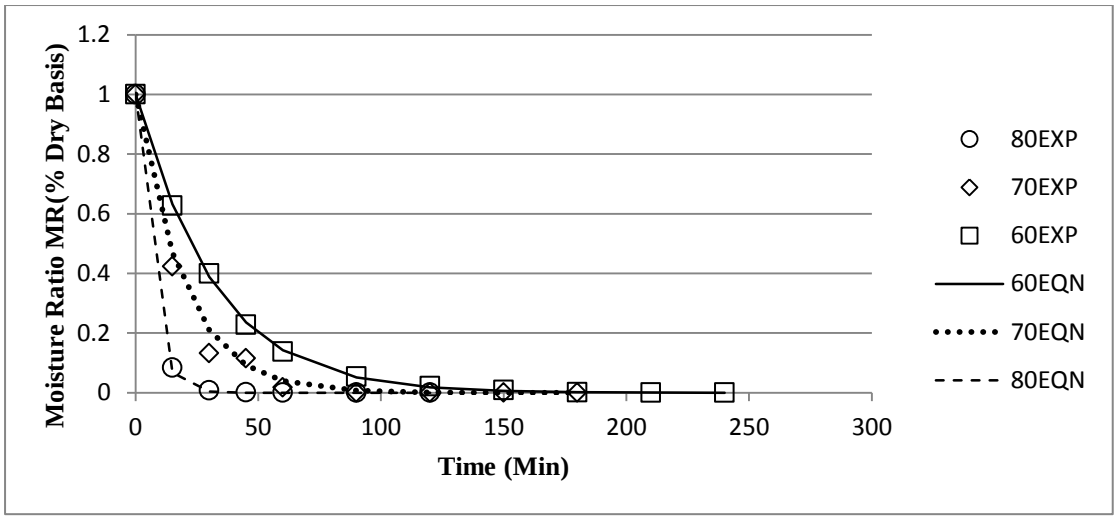

Figure 1. The Drying Kinetics of *Vernonia Amygdalina L*.

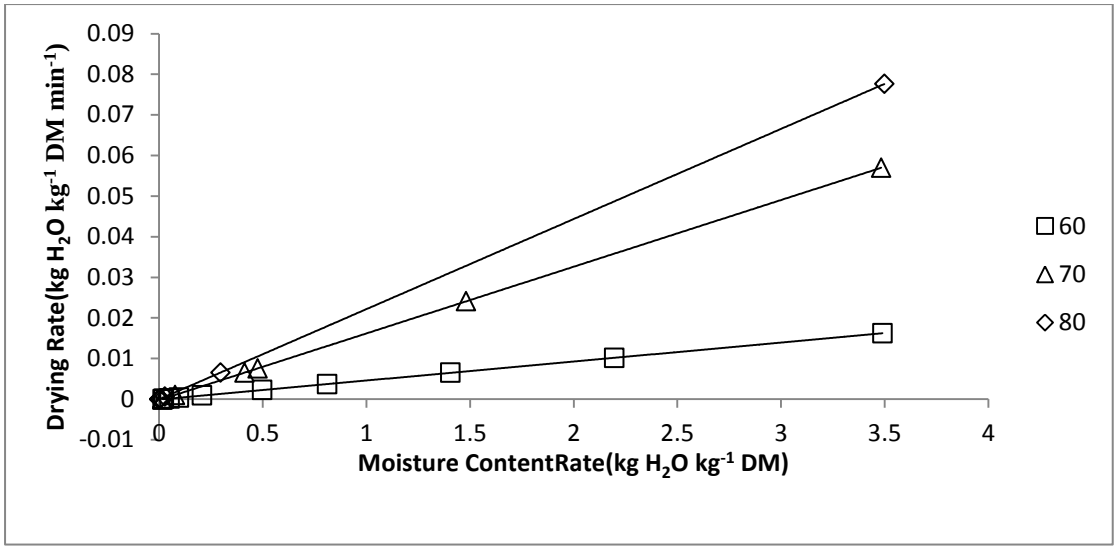

Figure 2. Drying Characteristics of *Vernonia Amygdalina L*. at 60ºC, 70ºC and 80ºC

3.2 Mathematical Modelling

The drying kinetics data were used to formulate three empirical mathematical modelling for *Vernonia Amygdalina L*., which is by referring to Newton Model, Page Model, and Henderson and Pabis Model. The fitness of the equation model is by having the highest coefficient of determination (R^2), lower Root Mean Square Error (RMSE) and lower chi-square value (χ^2).

The Newton Model was chosen to represent the drying kinetics of the leaves of *Vernonia Amygdalina L*.. The statistical data from Newton, Page, and Henderson and Pabis drying models were tabulated in Table 1. Model with High R^2, low RMSE and low χ^2 was chosen as the best fit model. Based on the data tabulated, Newton model and Henderson and Pabis model have the highest R^2, which are 0.9999. This shows both the model had good fitness onto the experimental data.

However, Newton model had lower RMSE value, which were 0.0148, 0.0353 and 0.0132 for 60ºC, 70ºC and 80ºC compared to Henderson and Pabis model which had 0.0155, 0.0366 and 0.0151 for 60ºC, 70ºC and 80ºC. Furthermore, the χ^2 value for Newton model was lower than the Henderson and Pabis model, which were 4.2943 and 4.8124 at 70ºC for instance. Hence, the Newton model was chosen to be the best drying model to be fitted onto the drying kinetics of *Vernonia Amygdalina L*..

Table 1. Forced Convective Air Drying model constants and statistical parameters of *Vernonia Amygdalina*

Model	Temperature (ºC)	k (min^{-1})	n	a	R^2	RMSE	χ^2
Newton	60	0.0323	-	-	0.9999	0.0148	0.5346
	70	0.0574	-	-	0.9999	0.0353	4.2943
	80	0.1450	-	-	0.9999	0.0132	1.2617
Page	60	0.0273	1.043	-	0.9997	0.0119	0.2596
	70	0.0450	1.043	-	0.9997	0.0587	0.0011
	80	0.1599	1.043	-	0.9997	0.0082	0.4934
Henderson and Pabis	60	0.0320	-	1.005	0.9999	0.0155	0.4688
	70	0.0577	-	1.005	0.9999	0.0366	4.8124

	80	0.1450	-	1.005	0.9999	0.0151	1.5601

3.3 Total Phenolic Compound Analysis

The dried samples were crush into smaller using a blender in order to increase the surface area for the extraction process. The extracts were contained in a petri dish wrapped with aluminium foil to avoid the contact of the extracts with UV light. All the extracts were stored in a refrigerator, hence before each analysis the extracts were allowed to reach room temperature first.

Figure 3 shows box plot of the total phenolic compound of *Vernonia Amygdalina L*. dried at different temperature. 10 readings were taken and converted to Gallic Acid Equilibrium concentration. The mean of the total phenolic compound of dried bitter leaves for 80ºC was 186.22 mg GAE/100 g sample, for 70ºC was 190.2 mg GAE/100 g sample and for 60ºC was 188.54 mg GAE/100 g sample. The results distribution for 70ºC had wider range compared to 80ºC and 60ºC. Referring to the statistical analysis, total phenolic compound of *Vernonia Amygdalina L*. dried at 60ºC, 70ºC and 80ºC have no significant difference (p>0.05). All the results obtained from the analysis fall at the non-rejection region.

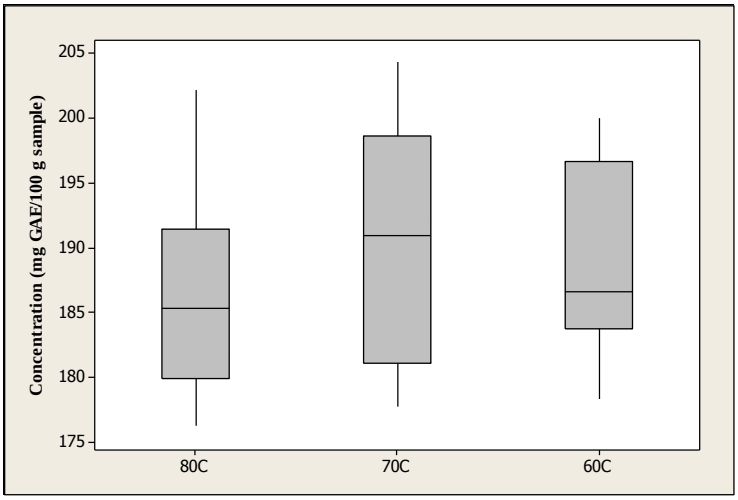

Figure 3. Box Plot of Total Phenolic Compound of *Vernonia Amygdalina L*. Extract at different drying temperatures (ºC)

4. Conclusions

Forced convective air drying of VA was conducted at 60ºC, 70ºC and 80ºC. It was found that the drying rate was highest at 80ºC. The best fitted empirical model to the drying kinetics of dried VA was the Newton Model. In term of drying characteristics, only 1st falling rate period exist. No transient period, constant rate period and 2nd falling rate period found in the drying characteristics curve. Further to this, total phenolic compounds found were ranged from 186 to 190 mg GAE/100 g sample. There were not significantly differences in total phenolic compound of VA dried from 60 to 80ºC. Hence, it can be concluded that 70ºC is the best drying temperature for VA because the drying rate was moderate and the total phenolic compounds retained was highest.

References

Atangwho, I.J., Edet, E.E., Uti, D.E., Obi, A.U., Asmawi, M.Z. and Ahmad, M., 2012. Biochemical and histological impact of Vernonia amygdalina supplemented diet in obese rats. *Saudi journal of biological sciences*, 19(3), pp.385–392.

Buchaillot, A., Caffin, N. & Bhandari, B., 2009. Drying of Lemon Myrtle (Backhousia citriodora) Leaves: Retention of Volatiles and Color. *Drying Technology*, 27(3), pp.445–450.

Chong, C.H., Law, C.L., Cloke, M., Hii, C.K., Abdullah, L.C. and Daud, W.R.W., 2008. Drying kinetics and product quality of dried Chempedak. *Journal of Food Engineering*, 88(4), pp.522–527.

Jamali, A., Kouhila, M., Mohamed, L.A., Jaouhari, J.T., Idlimam, A. and Abdenouri, N., 2006. Sorption isotherms of Chenopodium ambrosioides leaves at three temperatures. *Journal of Food Engineering*, 72(1), pp.77–84.

Lahsasni, S., Kouhila, M., Mahrouz, M. and Jaouhari, J.T., 2004. Drying kinetics of prickly pear fruit (Opuntia ficus indica). *Journal of Food Engineering*, 61(2), pp.173–179.

Midilli, A. and Kucuk, H., 2003. Mathematical modeling of thin layer drying of pistachio by using solar energy. *Energy Conversion and Management*, 44(7), pp.1111–1122.

Mohamed, L.A., Kouhila, M., Jamali, A., Lahsasni, S., Kechaou, N. and Mahrouz, M., 2005. Single layer solar drying behaviour of Citrus aurantium leaves under forced convection. *Energy Conversion and Management*, 46(9-10), pp.1473–1483.

Nwangozi, P., Ejike, C.E.C.C, Godwin, C.D., and Awazie, S.O., 2013. Synergistic postprandial blood glucose modulatory properties of Vernonia amygdalina (Del.), Gongronema latifolium (Benth.) and Occimum gratissimum (Linn.). *agris.fao.org*, 65(6), pp.759–765.

Ong, K.W., Hsu, A., Song, L.X., Huang, D.J. and Tan, B.K.H, 2011. Polyphenols-rich Vernonia amygdalina shows anti-diabetic effects in streptozotocin-induced diabetic rats. *Journal of ethnopharmacology*, 133(2), pp.598–607.

Orikasa, T., Koide, S., Okamoto, S., Imaizumi, T., Muramatsu, Y., Takeda, J., Shiina, T. and Tagawa, A., 2014. Impacts of hot air and vacuum drying on the quality attributes of kiwifruit slices. *Journal of Food Engineering*, 125, pp.51–58.

Pin, K.Y., Chuah, A.L., Rashih, A.A., Mazura, M.P., Fadzureena, J., Vimala, S., & Rasadah, M.A., 2010. Antioxidant and anti-inflammatory activities of extracts of betel leaves (Piper betle) from solvents with different polarities. *Journal of Tropical Forest Science*, 22(4), pp.448–455.

Shaw, M., Meda, V., Jr. L.T. and Opoku, A., 2007. Drying and color characteristics of coriander foliage using convective thin-layer and microwave drying. *Journal of Microwave Power and Electromagnetic Energy*, 41(2), pp.56-65.

Shaw, M., Meda, V. & Jr, L.T., 2005. Development and Trends in Drying of Herbs and Specialty Crops in Western Canada. , (05), pp.1–14.

Śledź, M., Nowacka, M., Wiktor, A., Witrowa-Rajchert, D., 2013. Selected chemical and physico-chemical properties of microwave-convective dried herbs. *Food and Bioproducts Processing*, 91(4), pp.421–428.

Tambunan, A. H., 2001. Freeze Drying Characteristics of Medicinal Herbs. *Drying Technology*, 19(2), pp.325–331.

Tasirin, S.M., Puspasari, I., Lun, A.W., Chai, P.V., & Lee, W.T., 2014. Drying of kaffir lime leaves in a fluidized bed dryer with inert particles: Kinetics and quality determination. *Industrial Crops and Products*, 61, pp.193–201.

The Effect of Solvent Type and Its Concentration on Linalool Extraction from *Coriandrum Sativum* Seeds

Melissa Chin Wei Ling*, Mohamed H Nassir, Chong Chien Hwa

[1]*School of Engineering, Taylor's University, Malaysia*

*chin.melissaweiling@sd.taylors.edu.my

Abstract

Herbal plants have been popular and widely used by humans since the ancient times. These herbs serve various purposes mainly as a food source, preservative, medication and cosmetics. However, medical practitioners have yet to explore the full potential of these herbs as a form of medication. Coriander (*Coriandrum Sativum L.*) is a plant that originated from the Mediterranean and Middle Eastern countries. It is used as a spice, has an aromatic fragrance and possesses medicinal properties. The active ingredient that contributes to the anti-fungal and anti-bacterial property of coriander is linalool which constitutes about 70% of the compounds in coriander. Solvent extraction using water bath was selected as a method of extraction using ethanol and hexane as solvent and the extract material was evaporated by the rotary evaporator and oven. The solid-to-solvent ratios (1:2, 1:4, 1:6) were selected as parameters for study in this research. The extract obtained was analysed with Gas Chromatography (GC) to obtain a chromatogram for the concentration of linalool. The objective of this research is to investigate the effect of these parameters on the yield of linalool and the performance of the solvents. The results obtained in this research clearly show that hexane is a better solvent at extracting linalool compared to ethanol by obtaining a comparative yield of about 16% to 32% depending on the volume of the solvent. This study also displays interesting results as the effectiveness of the hexane and ethanol varies beyond the 300 mL solution. Hexane slows down the extraction process at this level while ethanol continues its performance of extracting linalool.

Keywords: Solid-to-solvent ratio, Ethanol, Hexane, Linalool, Concentration

1. Introduction

The history of herbal medicines dates back to the beginning of mankind and there were vast evidences indicating that the Greeks, Chinese, Native-Americans and others have used herbal medicines to treat many diseases [1]. Many countries have incorporated the usage of herbs as part of their tradition a long time ago [2]. Throughout the human history, herbs were used as a source of food, preservative, cosmetics, medicine and other purposes [1]. For some of these uses, herbs should be treated to serve certain functions. Though herbal medications have been popular back in the ancient times, it is still poorly understood by the society and medical practitioners [2]. Examples of various herbs that have been utilized since the ancient times are summarized in **Table 1** below.

Table 1: Examples of the Usage of Herbs Since Ancient Times

Common Name	Usage	References
Aloe Vera	Control skin burn, sun burn, injury	[3]
Garlic	Promotes skin healing, anti-bacterial	[4]
Neem	Antiseptic agent, cure wounds, ulcers, skin diseases	[3]
Gingko Biloba	Treats hypertension, dementia, depression	[5]
Ginseng	Stimulate blood flow to skin, anti-oxidant	[6]

Coriander is selected as the center of this research and the parameters affecting the concentration of active ingredient in coriander is studied. Coriander (Coriandrum Sativum L.) or more commonly known as "cilantro" is a plant that originated from the Mediterranean and Middle Eastern countries. It is used as a spice, is aromatic and possesses medicinal properties [7]. The active ingredient that contributes to the anti-fungal and anti-bacterial property of coriander is linalool.

Coriander seeds contain essential oil that ranges from 0.3% to 1.1% [8]. Sreelatha *et al.* and Zoubiri *et al.* have shown that the extracted essential oil from coriander possesses anti-bacterial, anti-diabetic, anti-cancerous, anti-mutagenic, anti-oxidant, and free radical scavenging activities [9, 10]. Their healing property is another depth added to the importance of coriander as well. Based on the study conducted by Wangensteen *et al.*, coriander seeds are used as a drug to treat indigestions, against worms, rheumatism and joint pain [11]. Apart from that, Jabeen *et al.* stated that coriander is used as a remedy for common diseases such as gastrointestinal diseases, healing rheumatism, curing inflammation as well as possesses antiseptic and nerve-soothing property [12]. Besides that, coriander is also recognized for its carminative and cooling properties [13]. One of the most important features of coriander is that it is clinically accepted as a memory-enhancing herb [14]. Coriander plants contain linalool, monoterpenes, limpene, citronella, and essential oils as its constituents [15]. However, the main component responsible for the contribution of these properties is a monoterpenoid known as linalool [16].

The extract from coriander seeds can be obtained by subjecting the seeds through several processes to obtain the extract and its compounds. Extraction is one of the very known and famous processes, traditionally and historically. It is commonly used to isolate a product with the presence of an organic solvent. Various methods can be utilized to carry out the extraction process, mainly hydrodistillation, steam distillation and solvent extraction [17]. The process of extracting herbs is termed as herbal extraction [18]. The commonly used organic solvents in herbal extraction are methanol, ethanol, hexane, ethyl acetate and acetone. During the extraction, there are several parameters (extraction time, solvent ratio, type of solvent) that need to be taken into account to ensure a high yield and purity of the product [19]. The herbs that have been acquired can undergo the distillation, extraction or infusion process to produce the natural product [19].

Certain parameters play an important role in yield of the extract; for example, the amount of solvent, heating or extraction time and power. The type of parameters selected will vary depending on the type of extraction process used. One of the parameters that play a crucial role in the extraction process is the solvent ratio [20] . Also, the type of solvent used must also be appropriate with the extract. The selection of the solvent adheres by the *'like dissolves like'* theory whereby the polar diluents will remove the polar substance and vice versa [20]. In general, a combination of alcohol and water in different quantities can contribute to high extraction yields [20]. This combination is also known as a hydro-alcoholic solvent [20]. Ethanol, water and methanol are most commonly used as

solvents in the extraction process due to their high polarity index value [20]. The polarity of a solvent is dependent on the hydroxyl group. This hydroxyl group contributes to the hydrophilic property of the solvent [21]. Due to their polar property, a high extraction yield can be obtained during the extraction process [21].

Coriander is selected in this research to undergo some analysis regarding the yield of the active ingredient, linalool. The reason behind this selection is based on its availability because coriander seeds are easily attainable from local supermarkets. Different solvents will be selected and the volumes will be varied to study the effect of these parameters on the yield of linalool.

Studies have shown that using Soxhlet extraction with ethanol as a solvent produces the greatest amount of yield as compared to hydrodistillation and supercritical fluid extraction (SFE) [22]. The yield of the active ingredient is highly dependent on the type of solvent used and the polarity of the compound that is selected for extraction. [8]. Sreelatha *et al.* and Zoubiri *et al.* have shown that the extracted essential oil from coriander possesses anti-bacterial, anti-diabetic, anti-cancerous, anti-mutagenic, anti-oxidant, and free radical scavenging activities [9, 10]. It is also proven that just a small concentration of linalool in coriander is capable of inhibiting the HEPG2 cells (Liver cancer cells) from replicating up to 100% and thus destroying the cancer [23]. Thus the objective of this research is to investigate the effect of solid-to-solvent ratio, type of solvent on the concentration of linalool in coriander and analysis of the concentration of linalool using Gas Chromatography (GC-FID).

2. Research Methodology

The methodology is divided into two main sections, namely the extraction process to obtain the coriander extract and the analysis of extract using Gas Chromatography (GC-FID). The flow chart in Fig. 1 depicts the general procedure of the entire research. Details about the methodology will be further elaborated later.

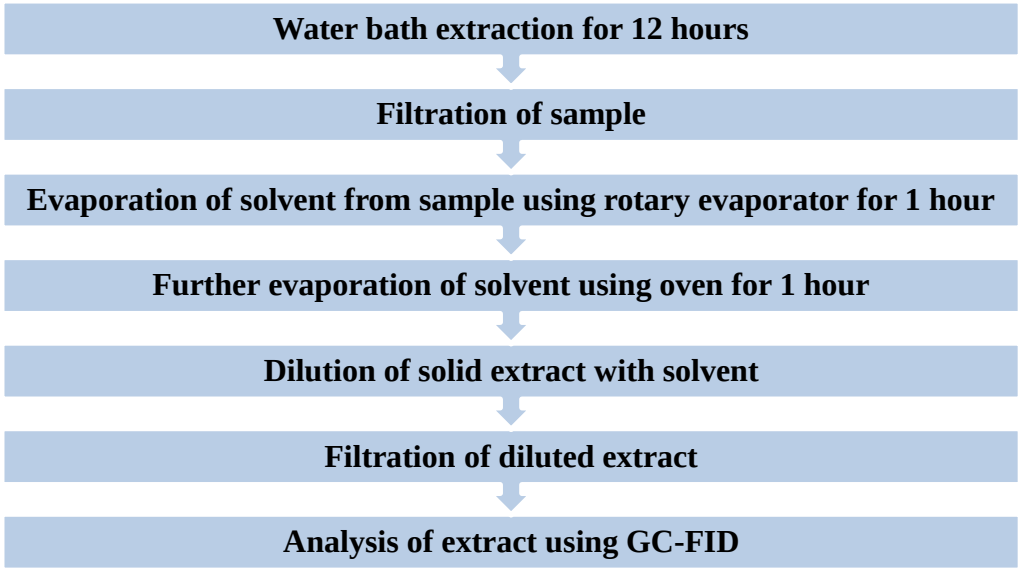

Figure 1. Flow Chart of General Procedure

2.1 Plant Materials

Coriander seeds (*Coriander sativum*) were purchased from Giant Hypermarket in Subang Jaya and were stored in the desiccator to prevent moisture from entering the packaging. The seeds were finely grounded using a blender before transferring the samples into a conical flask.

2.2 Chemicals

All chemicals purchased were of analytical grade. Hexane (2.5 L) and ethanol (2.5 L) (Brand: R&M), with a purity of 95% were purchased from Evergreen Engineering & Resources prior to the extraction process. Linalool standard (5 mL) was purchased from Sigma Aldrich Canada and shipped over to Malaysia.

2.3 Solvent Extraction using Water Bath

50 g of coriander seeds was weighed and measured using a weighing balance (Model: PA4102, U.S.A). The seeds were transferred into a blender (Model: Moulinex) and were grounded finely to increase the surface area. The grounded seeds were then transferred into a 400 mL of conical flask. 100 mL of hexane was measured using a measuring cylinder and poured into the flask containing the sample. A solid-to-solvent ratio of 1:2 was used.

The conical flask was placed into the water bath (Daniel Digital Water Bath). A mercury thermometer was placed into the flask to measure the temperature inside the flask. The water bath was set to a temperature of 60℃ and further adjusted until the temperature in the flask shows 60℃. Then the sample is left to extract for 12 hours. The experiment is repeated with a ratio of 1:4 and 1:6 for hexane and ethanol with a ratio of 1:2, 1:4 and 1:6. For ethanol, the temperature of the water bath is set to 70℃. All experiments are repeated twice.

After obtaining the crude hexane extract, it was filtered into another conical flask using a filter paper (Brand: WHATMAN) placed onto a filter funnel to remove the solid samples. The filtered crude samples are then stored in Schott bottles provided by the laboratory and labeled accordingly.

2.5 Evaporation of Solvent

The filtered crude samples were then subjected to evaporation to remove the solvent with the help of a rotary evaporator (Model: IKA RV 10 BASIC). The crude samples were poured into the rotating flask and the flask was lowered into the silicon oil until it covers the samples. The temperature of the silicon oil was set to 95℃ and the rotation speed of the flask was set to 30 rpm. The samples were left to evaporate for 1 hour. The evaporated samples were transferred back into their respective Schott bottles.

The Schott bottles containing the evaporated samples were then placed into the air forced convection oven (Model: MEMMERT UN 75) for further evaporation for another 1 hour. The bottle caps were removed to aid in the evaporation process. For samples with hexane, the temperature of the oven is set to 70℃ and for samples

containing ethanol, the temperature of the oven is set to 80℃. The Schott bottles were left to cool and then sealed with paraffin film (Brand: PARAFILM 'M') before refrigerating them at 4℃ prior to analysis.

2.6 Dilution of Solid Extract with Solvent

A reference sample containing 0.1% (synthetic) linalool in hexane for calibration was prepared and the coriander extract that was previously extracted with hexane was diluted to 2% in hexane (20 mg in 1 mL). Dilution was repeated using ethanol as solvent. The extract that was extracted with the particular solvent was diluted again with the same solvent respectively.

2.7 Filtration of Diluted Extract

All extracts containing the solvent were then filtered using a 0.2 μm syringe (Brand: WHATMAN) to remove any traces of solid and 1 μL of sample was injected manually into the GC-FID using a 10 μL syringe (Brand: Agilent).

2.8 Analysis of Extract Using Gas Chromatography (GC-FID) [24]

GC-FID analyses of the extracts were conducted using a GC Agilent instrument (Model: 7820A Agilent) equipped with a DB-1 column (**30 m × 0.53 mm i.d., × 3 μm**). Nitrogen was used as the carrier gas at the constant flow of 1.1 ml/min. The oven temperature was raised from 60°C to 250°C at a rate of 5°C/min. The injector and detector (FID) temperatures were kept at 250°C and 280°C, respectively. The chromatograms plotted using the software was compared with the calibration curve plotted earlier to determine the concentrations of the extracts.

3. Results and Discussion

The calibration curve shown in **Figure 2** is plotted by injecting the linalool standard (95%) into the gas chromatography (GC). The concentrations injected are 2, 4 and 6 ppm, respectively. A straight line of $y = mx + b$ is obtained where x represents the amount of linalool injected and y represents the corresponding peak/area. The straight line equation has a gradient of $m = 34194.22930$ and intercept $b = -3411.39688$, with a R^2 correlation of 0.99842 and a residual standard deviation of 6084.6384.63857. The calibration curve below is used to calculate the respective concentrations of the extract obtained.

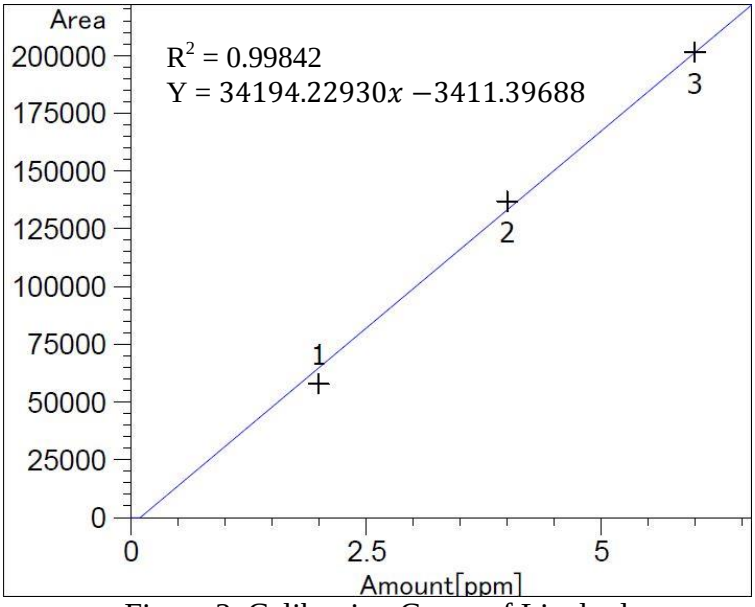

Figure 2. Calibration Curve of Linalool

The solution extracted from each trial was evaporated using a rotary evaporator at 95℃ and rotational angular speed of 30 rpm. Further evaporation was carried out by placing the remaining solution into the oven at 70℃ for hexane and 80℃ for ethanol. 1 μL of sample is injected into the GC column from each extracted sample of hexane and ethanol solvent. A chromatogram of the sample as shown in **Figure 3** is obtained. The results from the chromatogram show that there are many peaks depending on the retention time. By trial and error, the retention time of linalool is found to be around 25 minutes. Therefore, any compound that appears on the 25 minute mark as denoted by the circle is linalool. Different GC columns display different retention times due to there several factors affecting the time such as the length and diameter of the column, the temperature profile, the split injection, the carrier gas and the type of compound. However, the retention time here is in agreement with Saim *et al*. and Ahmad *et al.* [17, 25].

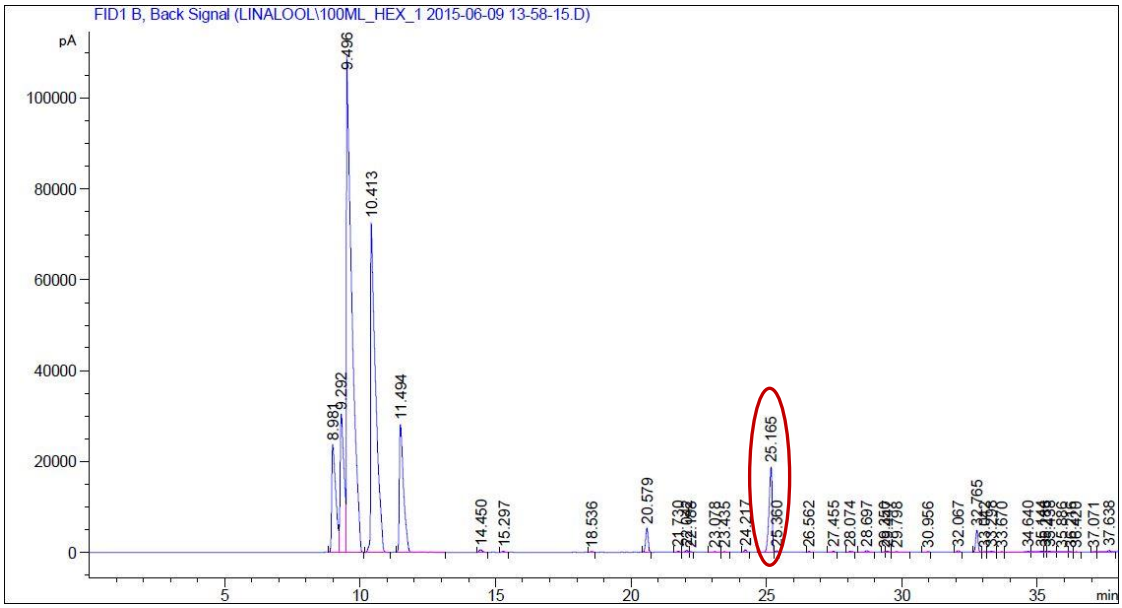

Figure 3. Chromatogram for 100 mL Hexane

The amount of the samples evaporated by the rotary evaporator was not standardized to a certain mass or volume because of the difficulty in obtaining the same volume and/or mass for all samples under consideration. Therefore, a simple approach was conducted in order to standardize all measurements. The weight of each extracted solution was measured and the results were tabulated in the sixth column in **Table 2**.

Since the injection of 1 μL taken from each extract was the key factor of calculating the ppm amount by using the calibration curve, this ppm amount has to be standardized for all samples in this study. By taking the ppm amount measured by the GC and dividing it by the mass of the extract, a new ppm amount is equally developed for all the samples regardless of the mass (volume) of the extract because the ppm is measured with respect to 1 g of the extract. Column seven in **Table 2** shows the new *x* values which serves as the standard for further and upcoming calculations. The new sets of *x* values obtained will be utilized in the calibration curve to represent the actual ppm amount in each sample.

Table 2. New Peak Areas and Concentration Per Gram

Solvent	Volume (mL)	x: Amount (ppm)	y: Peak Area	Amt/Area ($\times 10^5$)	Mass of Solution (g)	x (new) ppm/g	y (new) peak area
Ethanol	100	4.31	143919.23	2.99	4.87	0.88	26822.67
		1.14	35691.41	3.2	1.38	0.83	25027.01
	Avg.	**2.73**	**89805.32**	**3.04**	**3.12**	**0.87**	**26427.50**
	200	2.60	85445.73	3.04	2.57	1.01	31149.91
		6.56	220786.15	2.97	6.28	1.04	32311.60
	Avg.	**4.58**	**153115.94**	**2.99**	**4.42**	**1.03**	**31974.01**
	300	2.15	69958.14	3.07	1.48	1.45	46330.66
		2.36	77136.53	3.05	1.58	1.49	47439.57
	Avg.	**2.26**	**73547.33**	**3.06**	**1.53**	**1.47**	**46904.87**
Hexane	100	4.51	150841.51	2.99	3.58	1.26	39700.09
		3.99	132907.66	3.00	3.24	1.23	38688.37
	Avg.	**4.25**	**141874.58**	**3.00**	**3.41**	**1.25**	**39219.47**
	200	1.43	45557.48	3.14	0.90	1.58	50757.71
		3.52	116938.95	3.01	2.27	1.55	49723.42
	Avg.	**2.48**	**81248.21**	**3.05**	**1.58**	**1.56**	**50018.46**
	300	4.24	141541.02	2.99	2.29	1.85	59969.63
		3.58	119102.77	3.01	2.20	1.63	52352.90
	Avg.	**3.91**	**130321.89**	**3.00**	**2.24**	**1.74**	**56237.71**

Having standardized the measurements, a comparison between the effectiveness of ethanol and hexane on linalool extraction is shown in Figure 4. The comparison yield between hexane and ethanol is calculated using the following equation:

$$Comparative\ Yield\ of\ Linalool(\%) = \frac{extract_{hexane} - extract_{ethanol}}{extract_{\ hexane}} \times 100 \qquad (1)$$

Based on this equation, the yield due to hexane clearly outperforms the yield due to ethanol by 32% for 100 mL of solution, 36% for 200 mL of solution, and 17% for 300 mL of solution respectively. The general trend of the better extract by hexane is in agreement with Kansal *et al.* [13] and Majapelo *et al.* [26]. The solvent adheres by the *'like dissolves like'* theory whereby the polar diluents will remove the polar substance and vice versa [20]. Linalool is a very non-polar compound and hexane is a non-polar solvent. By obeying the theory, hexane acts as a better solvent compared to ethanol which is a polar solvent, thus extracting more linalool. This is proven from the yield calculated above. The yield rapidly increases from 32% to 36% but declines to 17% as the volume of the solution increases to 300 mL. Seemingly, there is a limit at which the effectiveness of the solvent decreases because there is no material to be extracted. Within the concept of this result, it is expected that there is a critical ratio of mass to solvent ratio at which the performance of the extractor is maximized. It is possible that this critical point lies between 200 mL and 300 mL volume of solvent.

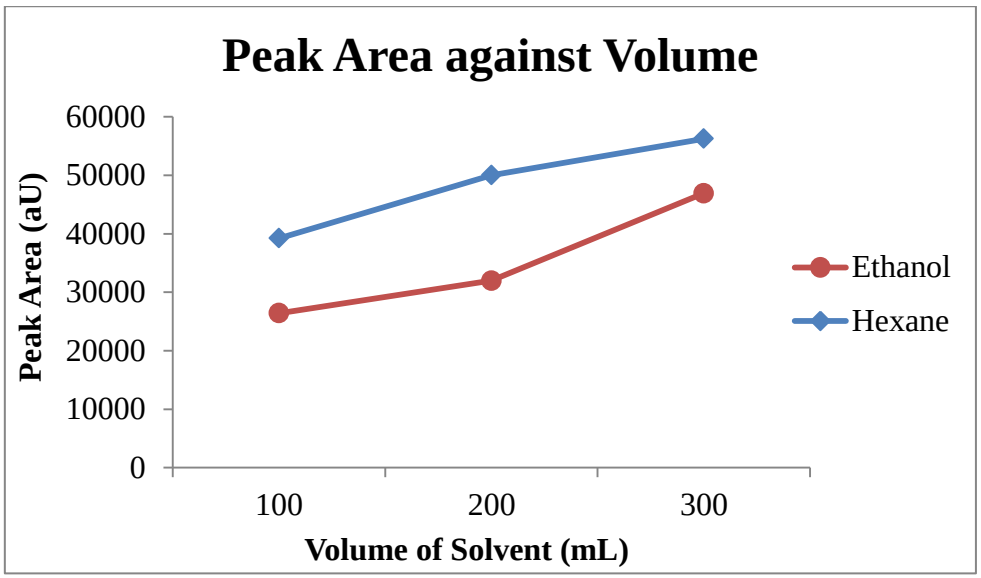

Figure 4. Comparison of Peak Areas of the Extract with Different Volumes

To analyze the effectiveness of the solvent on linalool extraction, the concentration of linalool is expressed by plotting the area against the volume of solvent as shown in Figure 5. For ethanol, the amount of linalool extracted decreases with 200 mL compared to 100 mL, however, the extract increases again when 300 mL of solvent was used. Hexane, on the other hand shows a different behaviour. The linalool extract increased with 200 mL compared to 100 mL and decreased as the solvent volume becomes 300 mL. The results obtained from both solvents depict that with 200 mL of solvent, coriander, or linalool extract reaches a critical value which might be connected to the nature of the solvents. It is well-known that ethanol is a polar solvent and is soluble in water while hexane is a non-polar solvent and is insoluble in water.

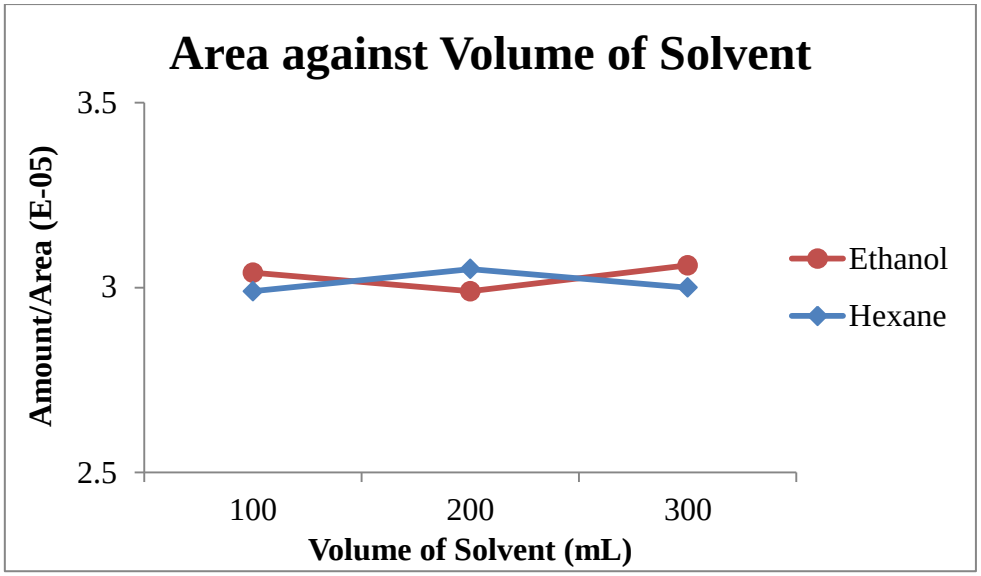

Figure 5. Effect of Volume and Type of Solvent on the Yield of Linalool

The performance of ethanol and the hexane as a solvent to extract linalool from coriander is illustrated in **Figure 6 and 7**. The effectiveness of the sample could be calculated using the following equation:

$$Performance\ of\ Solvent\ on\ Linalool\ (\%) = \frac{yield_{hexane} - yield_{ethanol}}{yield_{hexane}} \times 100\% \quad (2)$$

The calculated performances are 30%, 33%, and 15% at 100 mL, 200 mL and 300 mL respectively. Again, the results here are in agreement with the previous results and it shows clearly that there is an abundance of unused solvent at 300 mL where the extra solvent has lesser effect on the extraction process.

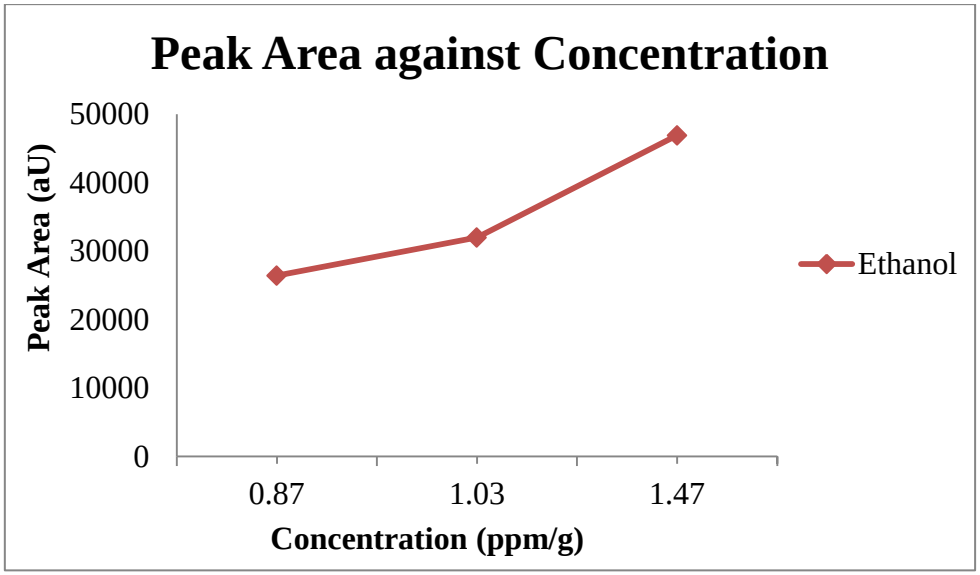

Figure 6. Performance of Ethanol on Linalool

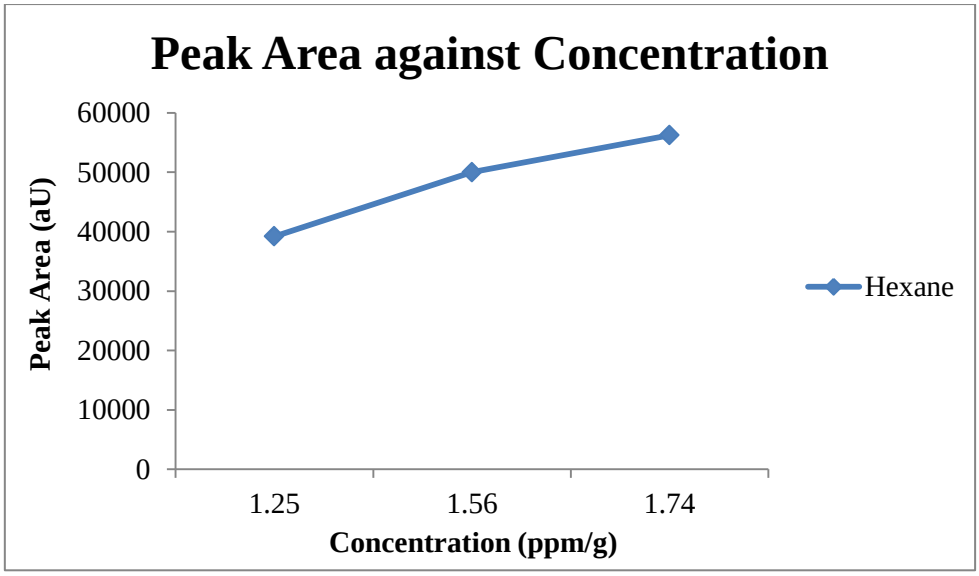

Figure 7. Performance of Hexane on Linalool

5. Conclusion

Based on the results obtained, the study shows the effectiveness of ethanol and hexane on the linalool extraction process. The extraction is carried out using 100, 200, and 300 mL volume of solvents. The research clearly shows that hexane is a better extraction solvent than ethanol to extract linalool. However, the results here indicate that at 300 mL, hexane slowed down the effectiveness and decreased the yield. On the other hand, ethanol did not show similar behavior and the effectiveness continued to increase even when the solvent is at 300 mL. This behaviour is worthy of a comprehensive study because as the performance of the solvent starts to slow down, it is economically not desirable.

References

[1] J. N. Caroline Foley, and Marcus A. Webb, *new Herb Bible*. United States: Viking Studio, 2002.

[2] I. A. f. R. o. Cancer, *EVALUATION OF CARCINOGENIC RISKS TO HUMANS - Some Traditional Herbal Medicines, Some Mycotoxins, Naphthalene and Styrene* vol. 82. Lyon, France: IARC Press, 2002.

[3] V. P. Kapoor, "Herbal Cosmetics for Skin and Hair Care," *National Product Radiance*, vol. 4, pp. 306-314, 2005.

[4] S. K. Gediya, R. B. Mistry, U. K. Patel, M. Blessy, and H. N. Jain, "Herbal Plants: Used as a Cosmetics," pp. 24-32, 2011.

[5] D. S. Jain Amit, Gupta Alka, Kannojia Pushpendra, Tomar Vivek, "Potential of Herbs as Cosmaceuticals," *International Journal of Research in Ayurveda & Pharmacy*, vol. 1, pp. 71-77, 2010.

[6] S. V. Kumar Sumit, Sharma Sujata, Baldi Ashish, "Herbal Cosmetics: Used for Skin and Hair," *Inventi Rapid: Cosmeceuticals,* vol. 2012, pp. 1-7, 2012.

[7] S. Mildner-Szkudlarz, R. Zawirska-Wojtasiak, W. Obuchowski, and M. Gośliński, "Evaluation of antioxidant activity of green tea extract and its effect on the biscuit lipid fraction oxidative stability," *Journal of Food Science,* vol. 74, pp. 362-370, 2009.

[8] M. Neffati, J. Sriti, G. Hamdaoui, M. E. Kchouk, and B. Marzouk, "Salinity impact on fruit yield, essential oil composition and antioxidant activities of Coriandrum sativum fruit extracts," *Food Chemistry,* vol. 124, pp. 221-225, 2011.

[9] S. Zoubiri and A. Baaliouamer, "Essential oil composition of Coriandrum sativum seed cultivated in Algeria as food grains protectant," *Food Chemistry,* vol. 122, pp. 1226-1228, 2010.

[10] S. Sreelatha, P. Padma, and M. Umadevi, "Protective effects of Coriandrum sativum extracts on carbon tetrachloride-induced hepatotoxicity in rats," *Food Chemistry Toxicology,* vol. 47, pp. 702-708, 2009.

[11] H. Wangensteen, A. B. Samuelsen, and K. E. Malterud, "Antioxidant activity in extracts from coriander," *Food Chemistry,* vol. 88, pp. 293-297, 2004.

[12] Q. Jabeen, S. Bashir, B. Lyoussi, and A. Gilani, "Coriander fruit exhibits gut modulatory, blood pressure lowering and diuretic activities," *Journal of Ethnopharmacology,* vol. 122, pp. 123-130, 2009.

[13] L. Kansal, V. Sharma, A. Sharma, S. Lodi, and S. H. Sharma, "Protective role of Coriandrum sativum (Coriander) extracts against lead nitrate induced oxidative stress and tissue damage in the liver and kidney in male mice," *International Journal of Applied Biology and Pharmaceutical Technology,* vol. 2, pp. 65-83, 2011.

[14] V. Anju, S. Pandeya, S. K. Yadav, S. Singh, and P. Soni, "A Review on Coriandrum sativum (Linn.): An Ayurvedic Medicinal Herb of Happiness," *Journal of Advanced Phamaceutical Health Research,* vol. 1, pp. 24-48, 2011.

[15] P. N. L, K. S. B, B. N. M, and R. J. D, "Phytopharmacological Properties of Coriander Sativum as a Potential Medicinal Tree: An Overview," *Journal of Applied Pharmaceutical Science,* vol. 1, pp. 20-25, 2011.

[16] M. H. Eikani, F. Golmohammad, and S. Rowshanzamir, "Subcritical water extraction of essential oils from coriander seeds (Coriandrum sativum L.)," *Journal of Food Engineering,* vol. 80, pp. 735-740, 2007.

[17] N. Saim, "Subcritical Water Extraction of Essential Oil from Coriander (*Coriandrum sativum L.*) Seeds," *The Malaysian Journal of Analytical Sciences,* vol. 12, pp. 22-24, 2008.

[18] M. N. Pandey Shivanand*, D.Viral, "Herbs Play an Important Role in the Field of Cosmetics," *International Journal of PharmTech Research*, vol. 2, pp. 632-639, 2010.

[19] D. M. Ioannis. (2011). *Medicinal Herbs and Bee Products in The Development of Natural Cosmetics*.

[20] M. N. V. K. Ankit Gupta, "Modern Extraction Methods for Preparation of Bioactive Plant Extracts," *International Journal of Applied and Natural Sciences (IJANS)*, vol. 1, pp. 8-26, 2012.

[21] A. C. Kumoroa, M. Hasana, and H. Singh, "Effects of Solvent Properties on the Soxhlet Extraction of Diterpenoid Lactones from *Andrographis Paniculata* Leaves," *ScienceAsia*, vol. 35, pp. 306-309, 2009.

[22] K. Y. F. Kawase, C. G. Mothé, F. A. Furtado, and G. L. Vieira, "Changes in Essential Oil of *Origanum Vulgare* L. Affected by Different Extraction Methods," *International Journal of Research and Reviews in Applied Sciences (IJRRAS)*, vol. 14, pp. 238-247, 2013.

[23] J. Usta, S. Kreydiyyeh, K. Knio, P. Barnabea, Y. Bou-Moughlabaya, and S. Dagher, "Linalool decreases HepG2 viability by inhibiting mitochondrial complexes I and II, increasing reactive oxygen species and decreasing ATP and GSH levels," *Chemico-Biological Interactions*, vol. 180, pp. 39-46, 2009.

[24] R. Jamshidi, Z. Afzali, and D. Afzali, "Chemical Composition of Hydrodistillation Essential Oil of Rosemary in Different Origins in Iran and Comparison with Other Countries," *American-Eurasian J. Agric. & Environ. Sci.*, vol. 5, pp. 78-81, 2009.

[25] A. Ahmad, A. F. M. Alkarkhi, S. Hena, and L. H. Khim, "Extraction, Separation and Identification of Chemical Ingredients of Elephantopus Scaber L. Using Factorial Design of Experiment," *International Journal of Chemistry*, vol. 1, pp. 36-49, 2009.

[26] N. Mojapelo, M. Mollagee, E. Muzenda, and L. L. Mguni, "Effect of Moisture Quantity on Non-Distillation Oil Extraction from SCG using Methanol," *Int'l Journal of Research in Chemical, Metallurgical and Civil Engg*, vol. 1, pp. 115-118, 2014.

Immobilization of Metal Species from Water Sludge by Porous Clay

Ng Zi Shin[1], Cheah Wee Keat[1], Yeoh Fei Yee[1*]
[1]School of Materials and Mineral Resources Engineering, Universiti Sains Malaysia, Engineering Campus, 14300, Nibong Tebal, Pulau Pinang, Malaysia
[*]feiyee@usm.my

Abstract
Sludge is a by-product produced from water treatment plant. The major metal element found in the sludge, which is aluminum, is harmful to human beings and the environment. Due to safety issues, disposal of sludge to the water source, which is river, is prohibited by the government. Thus, the sludge is suggested to be reused as one of the clay raw material in order to produce a ceramic product. This is because the intercalated structure of clay is potentially able to entrap the aluminum from the sludge. In this project, the sludge obtained is from Sungai Dua Water Treatment Plant. The metal capture capability by porous clay was studied. Samples with formulated clay derived from sludge in clay powder and clay blocks were formed. The aim of this project is to study the potential of clay body to trap the aluminum from the sludge. By using the method of Inductively Coupled Plasma-Atomic Emission Spectrometry, 4 samples were studied and compared with the sludge powder. The metal leaching from glazed and unglazed ceramic products were also evaluated. X-Ray Diffraction analysis was applied to study the changes of mineral phase before and after firing process. Results from Inductively Coupled Plasma-Atomic Emission Spectrometry testing show that formulated clay products were able to capture the aluminum from the sludge; glazed ceramic products can also reduce the metal leaching from the sludge. X-Ray Diffraction results showed that mullite and quartz were the major phase for the final clay product after the firing process with temperature 1100°C with 6 hour soaking.

Keywords: sludge, metal leaching, formulated clay body, glazed ceramic body.

1. Introduction

Sludge is a by-product generated from water treatment plant (WTP). During the water treatment process, coagulant is added in the raw water to precipitate the fine particles of soil and slowly accumulate at the bottom of the water tank. Finally, clean water will be produced at the top layer of the mix and thus, the by-product that left at the bottom of the water tank is known as sludge. In Malaysia, alum is the most used coagulant in water treatment plant for coagulation-flocculation processes [1].

The use of alum as coagulant has resulted in higher concentration of aluminum in the treated water compare to the raw water [2-5]. The high concentration presence of aluminum in sludge gives a serious impact to threat the raw water quality and aquatic biota [6]. The maximum acceptable value for aluminum in drinking water is 0.2 mg/L [7]. In Malaysia, sludge has been classified as "scheduled waste" under First Schedule of the Environmental Quality (Scheduled Waste) Regulation 2005 of the Environment Quality Act (EQA) 1974 [8]. The WTP sludge can no longer be directly discharge to the water sources. The current practice used in Malaysia is dewatering of sludge. The dewatered sludge will be further processed by the application of landfill, exemption or dispose according to the method of code Scheduled Waste 204 (SW204).

Due to high cost of operation and maintenance, a proposal to reuse the sludge in ceramic products is considered to be an economic and environmental sound manner. The use of sludge as a clay raw material is due to the similar mineralogical composition of sludge and commercial ceramic products. The potential uses of sludge include brick manufacturing [3, 5, 9-11], cement developing [12], roof tiles [13], tiles [14] and ceramic making [15-18]. Magalhães et. al. applied MANOVA statistical test to study the effect of the three independent variables on the clay body: thermal treatment (two levels - control and firing); kind of leaching solution (four levels: water, NH_4Cl, acetic acid, H_2SO_4), and the percentage of sludge in the clay matrix (three levels: 10, 50 and 100 %) in the release of metals from each of their clay body samples [2].

One of the reasons that sludge can be utilized as raw material for clay products is the mineral and structure of clay. The structural arrangement of tetrahedral unit leaves a net charge of negative, -1 per unit while octahedral unit leaves a total of 2 negative charges per unit [19]. Since clay particles carry a net negative charge on their surface, the clay particles can attract the positive charged particles. Sludge contains most of the cations such as Al^{3+}, Fe^{3+} and Si^{4+} and thus it is expected that the clay atoms are able to attract and immobilize the metals element from sludge to prevent the metal leakage.

In this project, the sludge obtained from Sungai Dua Water Treatment Plant (SDWTP) and clay raw materials will be characterized by X-Ray Diffraction (XRD). The clay body with the addition of bentonite powder into a formulated clay composition was studied in order to compare the amount of metal leaching from sludge, formulated unglazed and glazed ceramic products. On top of that, the XRD result for final products will be evaluated to determine the mineral phases in the ceramic body.

2. Objectives

1. To produce formulated clay and ceramic products derived from water sludge.
2. To investigate metal leaching from unglazed and glazed ceramic products.
3. To study metal capability of constituent clay components.

3. Methodology

In this project, the sludge source from SDWTP was dried, followed by grinded and sieved to obtain fine powder of sludge. The powders prepared were characterized by using XRD. Next is the preparation of clay body with formulated clay composition. 13 samples with different weight ratio composition of raw materials were mixed with distilled water until homogenous and formed slurry. By using the method of slip casting, samples with shaped green body were formed. Then, the green products were dried and bisque fired. After that, glaze was applied to the 3 samples of the bisque fired body and finally sintered. Lastly, final products brought into Inductively Coupled Plasma (ICP) Test, and analyzed by XRD.

3.1 Preparation of Sludge Powder and Raw Materials Characterization

Raw sludge was dried in oven at 100 °C for 24 hours to remove the moisture in the sludge to avoid from agglomeration instead of forming fine powder. After that, every 400 g of dried sludge was grinded for 30 minutes by using Pestle & Mortar Mill Pascal until powders form obtained. Sludge powder was sieved by using a sieve shaker of siever size 425 μm for 5 minutes with amplitude 1.5 mm. Fine sludge powder was produced. In order to characterize the sludge powder, XRD analysis was carried out. The scanning range (2θ°) was set from 10° to 90° with the step size of 0.030° and 38.4 seconds as the step time. The software of X'pert Highscore Plus were used to illustrate the graph of XRD and indicated the mineral phases exist in the sludge and clay powder. The results were identified and analyzed.

3.2 Preparation of Green Clay Body

Bentonite content was set as the parameter in this project. A formulated clay body composition is shown in the Table **1** with constant weight percentage (wt%) ratio of sludge: ball clay: potash feldspar: silica powder in 20:35:30:15 which termed as α in this research. The reason to decide the ratio as stated is evaluated based on the optimum research results obtained from Tham [15], Lim [16] and Rahman [17]. Weight ratio of bentonite was set from 0, 10, 20 and 30 wt% and labeled as B0, B10, B20, and B30 respectively as shown in Table 1.

Table 1: Formulated clay mixture by setting parameter for the content of bentonite.

Sample	Weight Percentage (wt%)	
	α	Bentonite
B0	100	0
B10	90	10
B20	80	20
B30	70	30

The formulated clay composition as shown in the Table 1 mixed with 40 wt% of distilled water and sodium nitrate deflocculant was added until slurry is formed. The mixture was stirred at 600 rpm for 20 minutes in order to achieve a homogenous mixture. The slurry was then poured into a Plaster of Paris (POP) mould to form into a desired shape green body.

3.3 Formation of Final Products and Final Products Analysis

Green clay bodies produced from slip casting method were air dried for at least 48 hours. The purpose of drying is to remove the moisture from the green body to avoid a thermal shock during firing which may lead to crack happening. Next, dried bodies were brought to bisque firing at 900 °C and soaked for 2 hours. The heating and cooling rate was set as 5 °C/min. The bodies were cooled down in the furnace and taken out from the furnace when room temperature reached. After that, the bisque fired samples were grinded with Silicon Carbide grinding paper of 600 through 2000 grit size. The purpose of grinding is to ensure the weight of 13 samples were the same for ICP testing purpose. 3 of the bisque fired samples were glazed and sintered at 1150 °C. The furnace was set the soaking condition for 6 hours, heating and cooling rate as 5 °C/min. Lastly, the final products were analyzed by using XRD and ICP testing.

4.Results and Discussion

In this research, the result will be categorized in three sections which are raw material characterization and final products properties analysis. The analyses explain in Section 4.1 and 4.2.

4.1 Raw Materials Characterization

4.1.1 Qualitative Mineralogical Analysis by X-Ray Diffraction (XRD)

Figure 2 shows the XRD diffractograms for each of the raw materials. The major mineral phase exist in ball clay are kaolinite ($Al_2Si_2O_5$) which contains 84.1%, quartz (SiO_2) contains 15.4 % while 0.5 % is phase of magnetite (Fe_3O_4). For bentonite, the major phase is tridymite (SiO_2) with content of 69.5 %, followed by cristobalite (SiO_2) which contains 25.9 % and 4.5 % of quartz. 77.9 % of microcline ($KAlSi_3O_8$) phase was detected in the potash feldspar followed by 22.1 % of sanidine $K(AlSi_3O_8)$ phase. Silica powder contained high amount of quartz which is 97.9 % with 2.3 % of zeolite (SiO_2). The water sludge contains 86.7 % of dickite, 8.7 % of quartz, 3.5 % of kaolinite and 1.1 % of hematite (Fe_2O_3). Based on the previous research from Oh [18], Tham [15] and Lim [16], the mineral phases found from the water sludge which obtained from SDWTP were almost similar.

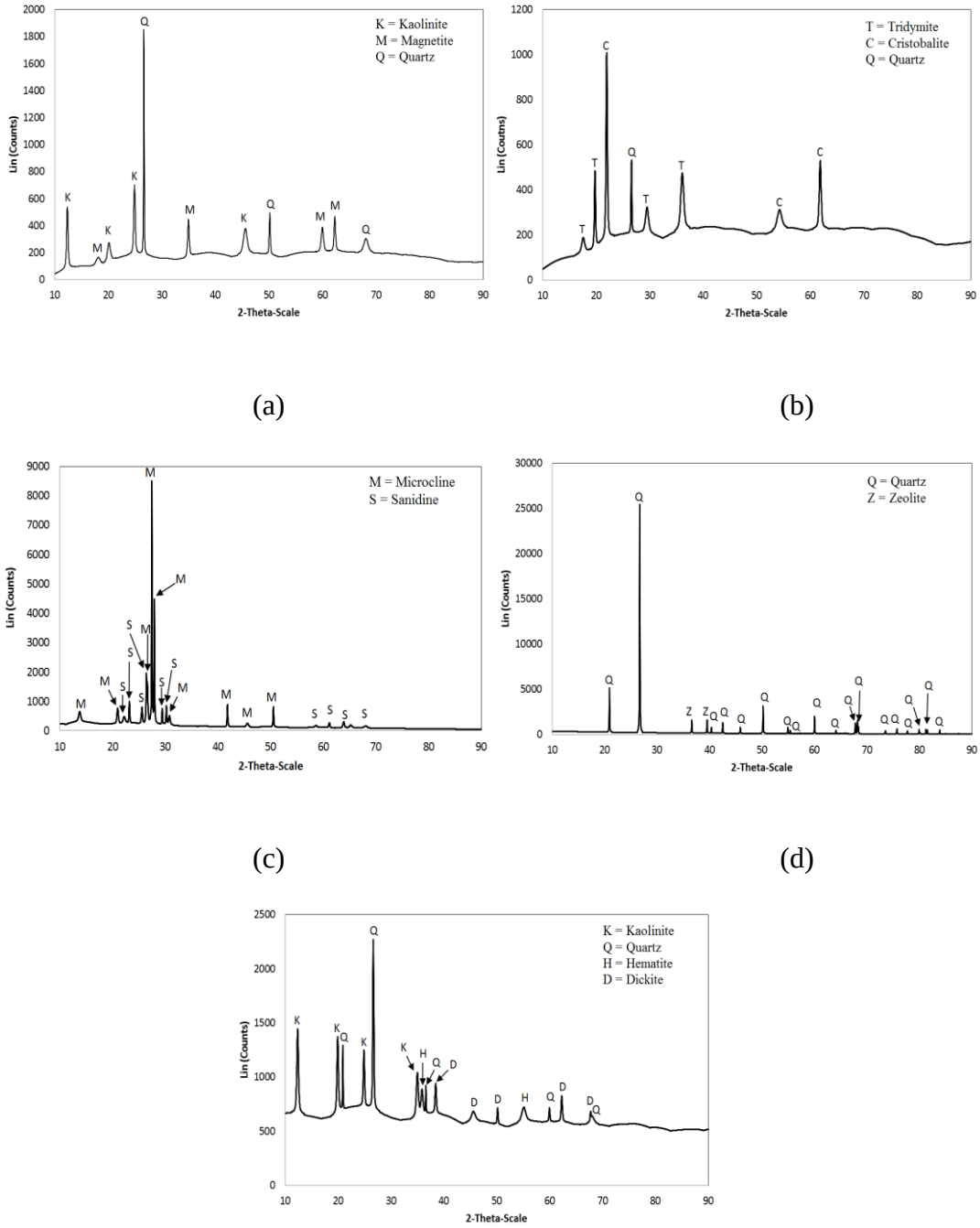

Figure 2: XRD pattern of (a) ball clay, (b) bentonite, (c) feldspar, (d) silica, (e) sludge.

4.2 Final Product Analysis

4.2.1 X-Ray Diffraction Analysis

The purpose of XRD analysis on the final product is to determine whether any new phase exist in the final ceramic body. Figure 3 shows the result of XRD pattern for sample B30. A major phase found from the XRD patterns is mullite ($Al_6Si_2O_{13}$), 61.5 % found in sample B30. The second major phase found in the sample B30 is quartz, which are 42.8 %. In this research, the final stage of firing temperature was

1100 °C and soaking for 6 hours. During firing, the main crystalline phases corresponding to minerals such as feldspar in the unfired ceramic body disappear and new crystalline phase will formed. Thus, when the clay body fired until 1100 °C, a boundary reaction of the silica and potash feldspar begins and a melt is formed. During the heating, needle like mullite crystals crystallize formed at relatively low temperatures from this melt [20] and the quartz in this ceramic body remain as quartz.

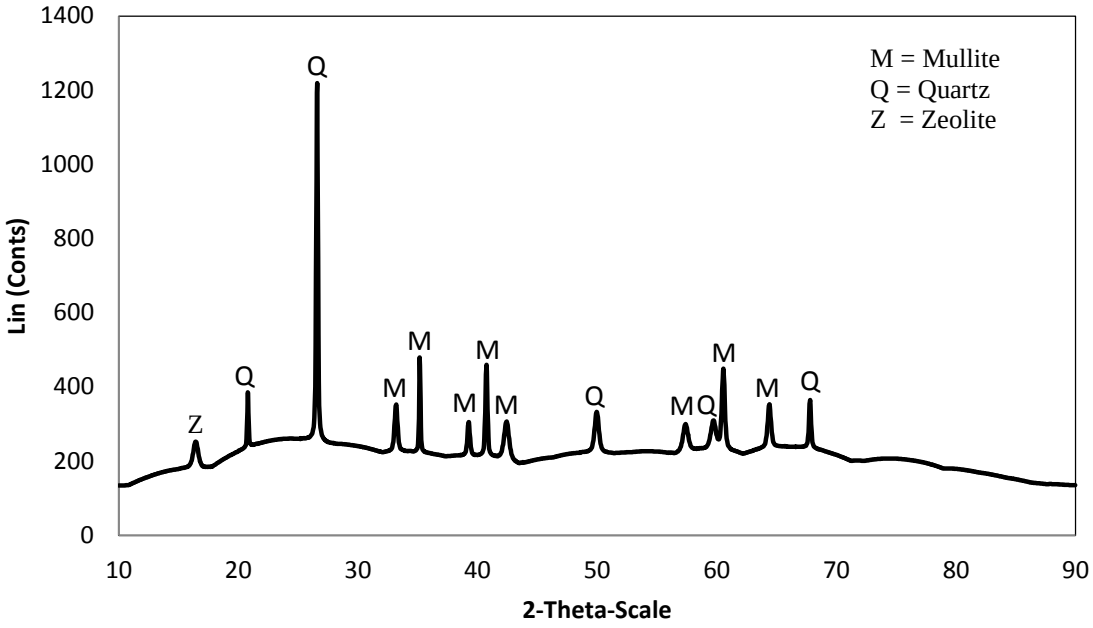

Figure 3: XRD pattern for sample B30.

4.2.2 Aluminum Leaching Analysis by ICP Method

All aluminum leaching analysis results show a similar trend to that of exponential growth. The amount of aluminum dissolved increases until reaching a plateau. The rate of leaching after equilibrium is close to zero, i.e. little or no leaching is observed once equilibrium is achieved. Thus, the leaching analysis data are fit according to the exponential growth fit. The result from Figure 4 shows the exponential growth fit using software of Origin 8.0 for the data sludge powder analysis. The concentration of aluminum achieves equilibrium at the 0.1126 ppm which is lower than the maximum acceptable from Ministry of Health Malaysia [7], 0.2000 ppm. Although the concentration is lower than the maximum acceptable range but still it is harmful to human. The concentration may increase over the limit when the higher amount of aluminum existed in the sludge. This can be seen from the result by Lim [16], the amount of aluminum dissolved in the solution is 0.9000 ppm. This value is over the acceptable limit by Ministry of Health Malaysia [7] and thus formulated ceramic products were investigated through ICP test to reduce the risk of harmful.

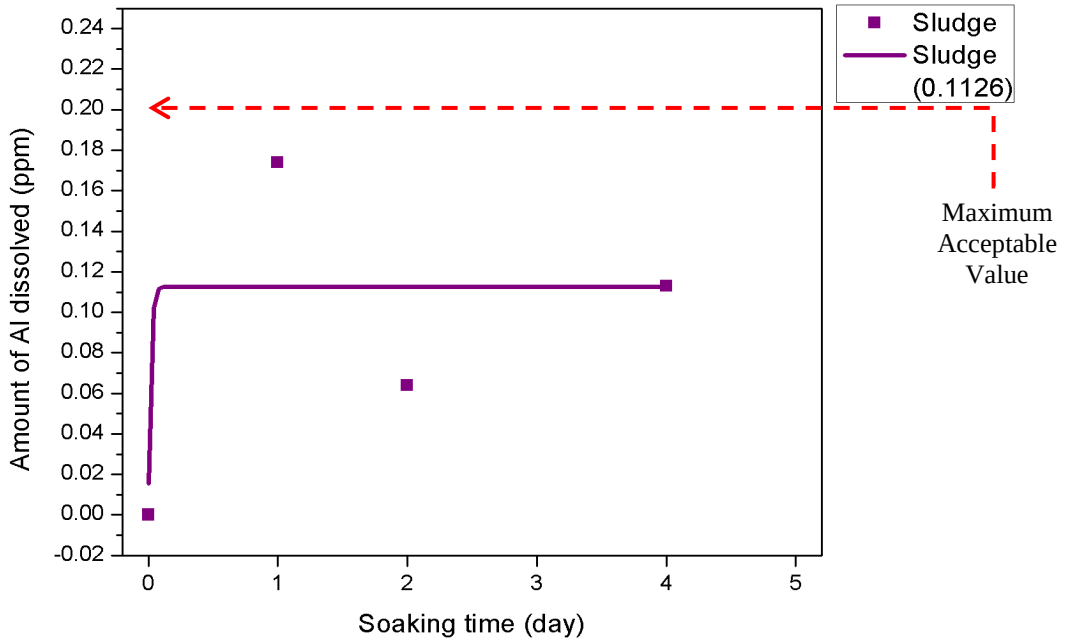

Figure 4: Amount of aluminum (Al) dissolved in the solution at 1, 2, 3, 4 and 5 soaking days for the raw sludge powder.

Figure 5 shows the results for aluminum dissolved in the solution for samples B0, B10, B20, B30 and GB10. The value shown in the legend from Figure 5 was obtained from the exponential growth fit by using the software Origin 8.0. For the comparison between the samples with and without bentonite composition, the amount of aluminum dissolved for sample B0 is highest with 0.0430 ppm as compared with samples of B10, B20 and B30 which are 0.0223 ppm, 0.0232 ppm and 0.0226 ppm respectively. This shows that with the addition of bentonite to the clay body helped to immobilize the aluminum from water sludge. Moreover, an impressive result obtained from the sample GB10, which the sample covered with a layer of glaze, the concentration of aluminum dissolved is reduced to 0.0183 ppm. This value indicated that ceramic body with a layer of glaze improved the capability of the ceramic body to entrap the aluminum instead of leaching to the solution. This is also proven by Rahman [17], the dissolved metal element concentration for ceramic product with bentonite content is lower than the product without bentonite content.

Glaze is a layer of glass applied to the ceramic body. Practically, the glaze has zero porosity [21]. Therefore, when the glazed sample GB10 immersed in the solution, the water will not be able to penetrate into the sample and the metal element will not react with the solution and stay inside the ceramic body. In this case, the ICP was able to trace the aluminum in the solution is because the glaze layer that applied on the samples have defects of crawling and pinholes obtained from the samples GB10. The defect of glaze will give an opportunity to the metal to leach from the ceramic body.

Figure 6 shows the comparison between sludge powder, unglazed ceramic products of sample B0, B10, B20, B30 and glazed product, GB10. Sample GB10 gives the lowest value of amount Al dissolved.

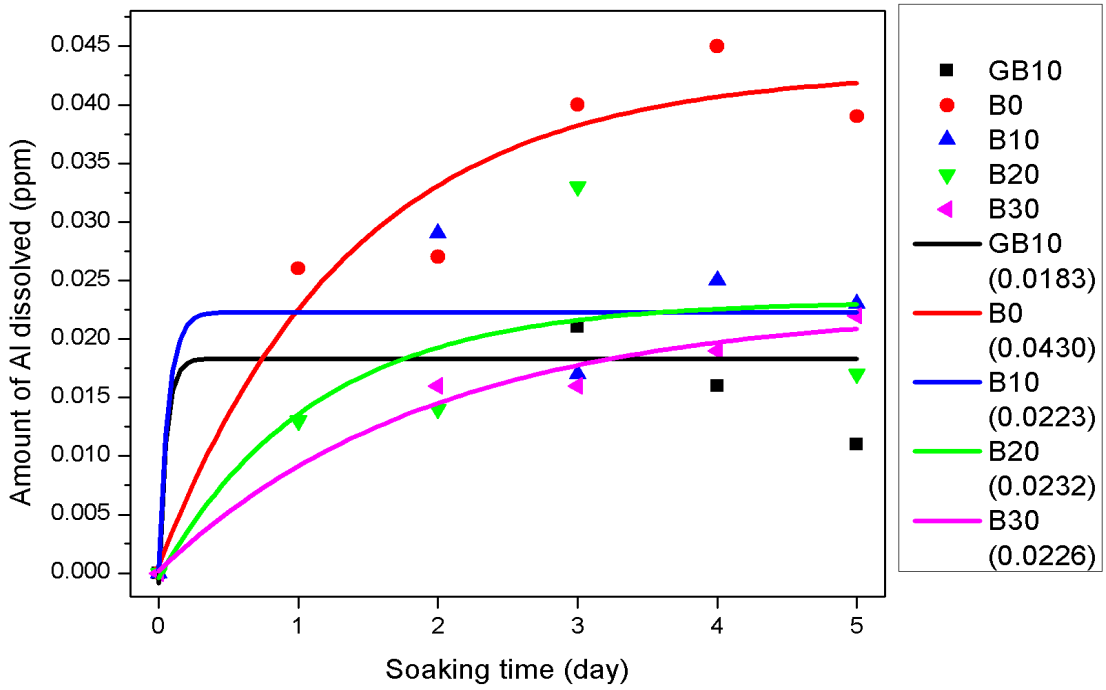

Figure 5: Amount of Al dissolved at 1, 2, 3, 4 and 5 soaking days for samples GB10, B0, B10, B20 and B30 with respective equilibrium achieved value.

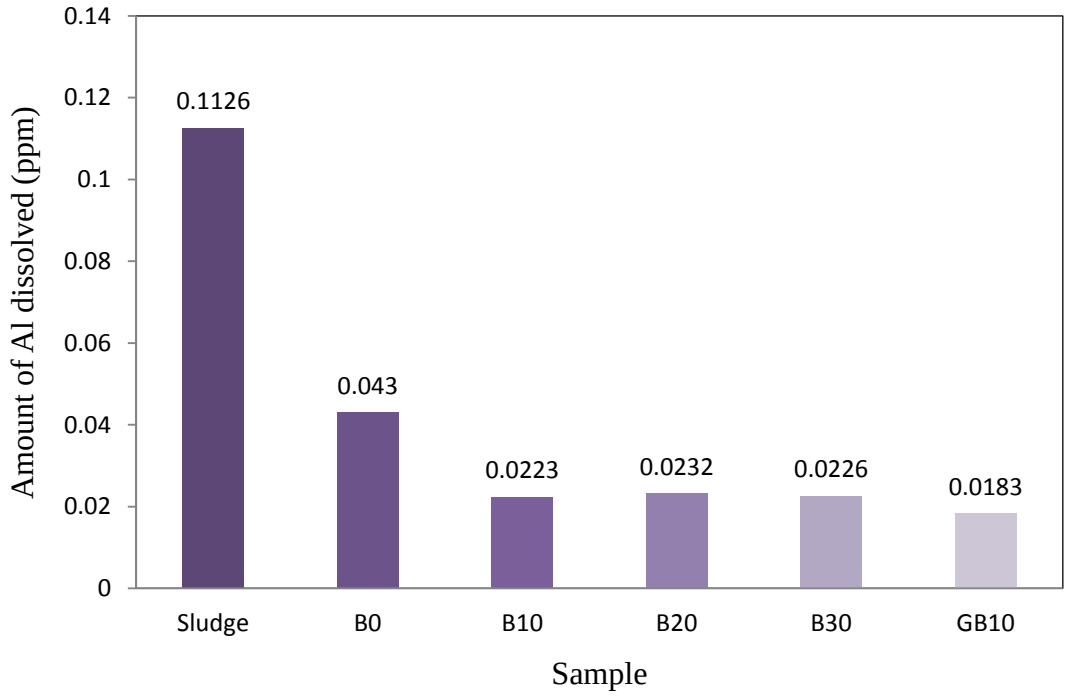

Figure 6: Comparison between the samples about the amount of Al dissolved.

5. Conclusion

In this research, the aim is to produce formulated clay blocks and ceramic products derived from water sludge. Research also investigated metal leaching from unglazed and glazed ceramic products. Metal capture capability of constituent clay components have been studied. From the results of XRD, a new phase of mullite was formed after sintered the clay body. Through the testing of ICP, the metal capture capability of formulated clay components was investigated. As compared with the sludge powder, the formulated clay products were able to capture the metal form the sludge and reduce the leaching of metal to the solution. With the addition of bentonite, amount of aluminum leaching to the solution further reduced. Glazed ceramic product is able to reduce the metal leaching from the sludge as compared with unglazed ceramic product. The defects of the glaze layer will also affect the amount of metal leaching to the solution. Thus, a good layer of glaze is necessary in order to minimize the amount of metal leaching.

References

1. Fukushi, K., *Southeast Asian Water Environment 4*. 2010: IWA Publishing.
2. Magalhães, J.M., et al., *Kinetic study of the immobilization of galvanic sludge in clay-based matrix.* Journal of Hazardous Materials, 2005. **121**(1): p. 69-78.
3. Hegazy, B.E.-D.E., H.A. Fouad, and A.M. Hassanain, *Brick manufacturing from water treatment sludge and rice husk ash.* Australian Journal of Basic and Applied Sciences, 2012. **6**(3): p. 453-461.
4. Babatunde, A., et al., *From" fills" to filter: insights into the reuse of dewatered alum sludge as a filter media in a constructed wetland.* 2007.
5. Monteiro, S., et al., *Incorporation of sludge waste from water treatment plant into red ceramic.* Construction and Building Materials, 2008. **22**(6): p. 1281-1287.
6. Sales, A. and F.R. de Souza, *Concretes and mortars recycled with water treatment sludge and construction and demolition rubble.* Construction and building materials, 2009. **23**(6): p. 2362-2370.
7. Ministry of Health Malaysia. *Drinking Water Quality Standard*. 2010 5th March 2015]; Available from: http://kmam.moh.gov.my/public-user/drinking-water-quality-standard.html.
8. Law of Malaysia, *Environmental Quality Act 1964*. 2001.
9. Saijun, Z. and S. Chang. *Experiment on making autoclaved sludge bricks with water-treatment plant sludge*. in *Electric Technology and Civil Engineering (ICETCE), 2011 International Conference on*. 2011. IEEE.
10. Victoria, A.N., *Characterisation and Performance Evaluation of Water Works Sludge as Bricks Material.* International Journal of Engineering, 2013. **3**(3): p. 8269.
11. Ramadan, M.O., H.A. Fouad, and A.M. Hassanain, *Reuse of water treatment plant sludge in brick manufacturing.* J. Appl. Sci. Res, 2008. **4**(10): p. 1223-1229.
12. Hsieh, H.-N. and D. Raghu. *Characterization of water treatment residuals and their beneficial uses*. in *GeoCongress 2008@ sGeotechnics of Waste Management and Remediation*. 2008. ASCE.
13. Al-Hamati, M.F. and F.G. Faris, *Reuse of Alum Sludge In Clay Roof Tiles Manufacturing.* JOURNAL OF APPLIED SCIENCES RESEARCH, 2008. **4**(10): p. 1223-1229.
14. Alqam, M., A. Jamrah, and H. Daghlas, *Utilization of cement incorporated with water treatment sludge.* Jordan Journal of Civil Engineering, 2011. **5**(2).
15. Tham, R.H., *Investigation of Sludge from Water Treatment Plant for Pottery Clay Formulation*. 2012, Universiti Sains Malaysia.
16. Lim, S.M., *Immobilization of Hazardous Metals in Water Treatment lant SLudge through Formulations of Pottery Clay*. 2013, Universiti Sains Malaysia.
17. Rahman, M.F.b.A., *Development of Ecoclay Products from Water Treatment Sludge through Slip Casting and Throwing Method*. 2014, Universiti Sains Malaysia.
18. Oh, S.K., *Tiles Fabrication from Sludge of Water Treatment Plant*. 2011, Universiti Sains Malaysia.

19. Murthy, V.N.S., *Geotechnical Engineering: Principles and Practices of Soil Mechanics and Foundation Engineering*. 2002: Taylor & Francis.
20. Schüller, K., *Reactions between mullite and glassy phase in porcelains.* Trans. Br. Ceram. Soc, 1964. **63**(2): p. 102-17.
21. Bengisu, M., *Engineering ceramics*. 2001: Springer Science & Business Media.

Synthesis and Characterization of Graphene Materials from Cellulose Acetate Tape

'Aqilah Ghazali[1], CheeHeongOoi[1], YeohFei Yee[1*]
[1]School of Materials and Mineral Resources Engineering, Universiti Sains Malaysia, Engineering Campus, 14300, NibongTebal, Pulau Pinang, Malaysia
[*]feiyee@usm.my

Abstract
A simple method for the synthesis of graphene is demonstrated via the coating of cellulose acetate tape (carbon source) on copper foil and followed by post annealing process. The coating of cellulose acetate tape on the metal catalyst layer was done without undergoing cold lamination process. The uniform graphene layer could be grown on the copper catalyst layer due to the uniformity of the solid carbon source layer. The thickness of graphene layer was controlled by varied the annealing temperatures and durations. The synthesis of grapheme on the copper foil was done without involving explosive gaseous carbon sources, which is used in CVD methods. Raman spectroscopy, Scanning Electron Microscope (SEM) and Energy Dispersive X-Ray Spectroscopy (EDS) and Fourier Transform Infrared Spectroscopy (FTIR) is used for characterize the graphene growth. Amongst the samples 800-2-B (sample type B annealed at 800^{O}C for 2 minutes) shows the graphene's characteristics in early nucleation stage and incomplete crystallization. The present of impurity in the sample also caused the interruption in nucleation point.

Keywords: Graphene, Carbon, Cellulose acetate, Annealing, Raman spectra

1. Introduction

Geim and Konstantin kicked a new field of nanoparticle research into gear when they identified many interesting properties of graphene. Their findings show that graphene has astounding properties that had never been observed in other materials.[1]

Graphene sheet is a layer of sp^2-bonded carbons where the thickness is dependent on size of carbon atom. It is interesting that carbon with sp^2 hybridization is able to form the two-dimensional graphene, the planar local structure in the closed polyhedral of the fullerene family and the cylinder-shaped carbon nanotubes, all with different physical properties (Table 1). Thus, keeping the sp^2 hybridization, the 2D carbon can be wrapped up into 0D fullerenes, rolled into 1D nanotube, or stacked into 3D graphite.[2]

Table 1: Important parameters of carbon materials of different dimensionalities [2]

Dimension	0D	1D	2D	3D
isomer	Fullerene	Nanotube	Graphene	Diamond
Hybridization	sp^2	sp^2	sp^2	sp^3
Density	1.72	1.2-2.0	2.26	3.52
Bond length	1.40 (C=C) 1.46(C-C)	1.44 (C=C)	1.42(C=C)	1.54 (C-C)
Electronic Properties	Semiconductor	Metal/Semiconductor	Semiconductor	Insulator

Graphene has a large specific surface area (up to 2630 $m^2\ g^{-1}$),[1] high intrinsic mobility (200 000 $cm^2\ v^{-1}\ s^{-1}$), [3,4] high Young's modulus (1.0 TPa)[5] and thermal conductivity (5000 $Wm^{-1}\ K^{-1}$). Its excellent optical transmittance (~ 97.7%) and electrical conductivity merit attention for application in transparent conductive electrodes [6,7]. Furthermore, graphene has been utilized in applications such as transistors [8], transparent electrodes [9–11], liquid crystal devices [12], ultracapacitors[13], and ultra-tough paper [14].

The fabrication of graphene sheets with large surface area and high quality has become an important challenge. Studies have carried out by converting food, insects, and waste into graphene e.g. carbon-containing materials was used without purification (cookies, chocolate, grass, plastics, roaches, and dog feces) to grow grapheme directly on the backside of a copper foil at 1050 °C under H_2/Ar flow [15]. Graphene also can be grown on a metal catalyst layer adhered with a cellulose acetate laminate film (CALF) by post-annealing process. Cellulose acetate tape consists of a backing to which an adhesive substance is affixed for the purpose of joining materials with a surface bond. The film of cellulose provides the backing for adherends made from chemically treated petroleum byproducts that create the tape's stickiness [16]. In the manufacturing process, natural cellulose that comes from wood pulp (consists of high carbon content) is reacted with acetic anhydride to produce cellulose acetate tape [17]. The cellulose acetate tape which is made from natural cellulose can be utilized as a low cost and effective carbon-containing precursor for the synthesis of graphene.

In this study, the possibility of using new precursor for graphene production was investigated. Cellulose acetate tape(carbon source) was coated on copper foil and undergone post-annealing process at different temperatures and durations. The post-annealing process was carried out under argon gas flow without involving explosive gaseous carbon sources such as methane. The produced grapheme was characterized to determine the possible application for the industry.

2. Experimental

2.1. Synthesis of graphene samples

Graphene was grown by annealing a copper foil (100µm) coated with the CALF product(cellulose acetate (CA) tape with 58 µm thick). Then the copper foil was cut to the dimension of 2cm x 2cm.Tube furnace was used to carry out the post-annealing process at temperature varied from 700^{O}C to 900^{O}C with different soaking time (120s, 180s and 240s)under argon gas flow (700 cm^{3}/minute). After annealing, the samples were rapidly cooled to room temperature by removing the samples from the hot zone to room temperature. After that, the graphene on Cu foil was transferred onto glass as substrate.

The general idea of the transfer is to attach a polymer to the graphene and then removing the layers on the opposite side. A polymer (often poly(methyl methacrylate), or PMMA for short) is deposited onto the metal foil, and the polymer binds the graphene on the surface of the metal. In this experiment, 5 wt% PMMA dissolved in toluene was spin coated on the samples at 2000 rpm for one minute and then the sample were heated on a hot plate at 180 ^{O}C for one minute.

Several steps were then used to remove the metal from the polymer and graphene. There are multiple ways to do this, but each method must remove both the graphene on the opposing side and the metal growth substrate. The $FeCl_3$ solution was used as the copper etchant and 2% of hydrochloric acid (HCl) has been added on to obtain the strong acid. But the strong acid will degrade the sample if the samples dip too long.

The final step of this method was to remove the polymer from the top of the graphene. Depending on the polymer used, different procedures are required where some need heat, while others require an acetone bath. Our method uses an acetone bath and we were careful not to disturb the film on top of the final substrate in adding and removing the acetone. In order to do this, the glass was placed on an empty dish and acetone was slowly added to allow it covered completely on glass. After soaking the sample in acetone overnight, acetone was removed from the dish carefully, and isopropyl alcohol (IPA) was added carefully in order to prevent any staining from the acetone. After the IPA is removed, the resulting film should be uniform over the final substrate, but often is not.

2.2. Measurement and characterization

After the transferring the graphene to the glass substrate properties of the sample were characterized using Raman Spectroscopy by using Ranishaw in Via Raman microscope. Scanning Electron Microscope (SEM) and Energy Dispersive X-ray Spectroscopy (EDS) was carried out atthe sample surfaces at 100x and 1000x magnification. EDS was conducted to determine the elemental composition of sample at the interested area. Fourier Transform Infrared Spectroscopy (FTIR) spectra were recorded by a FTIR spectrometer (Perkin-Elmer) using KBr method.

3. Results and Discussion

Raman spectroscopy is a powerful tool to determine the number of graphene layers and the quality of graphene[18]. In order to analyze these properties, Raman spectroscopic analysis (Ranishaw in Via Raman microscope at 633nm) was carried out. Figure 1 shows the Raman spectra of the graphene grown from the CA-tape annealed at various temperatures. For all samples, Raman spectra show the typical feature of graphene. Two peaks are observed at 1320 cm^{-1} and 1595 cm^{-1}, corresponding to the D peak indicates graphene signifies sp2 hybridization and, G peak indicates disorder due to the defects induced on the sp2 hybridized hexagonal sheet of the carbon respectively. The important aspects that need to be concerned on analyzing the number of graphene layer are the shape of the 2D peak, the full width half maximum (FWHM) of the 2D peak, and the intensity ratio of the 2D to G peak are very important to analyze the number of graphene layers. First, for the intensity ratio of the 2D to G peak higher than 2, from 1 to 2, and lower than 1 indicated the monolayer, bilayer, and few layer graphene respectively. Second, the full width half maximum (FWHM) of the 2D peak lower than 45 cm^{-1}, from 45 to 60 cm^{-1}, and higher than 60 cm^{-1} suggests monolayer, bilayer, and a few layer graphene, respectively. Third, the shape of the 2D peak of the monolayer graphene can be fitted with a single Lorentzian curve and is symmetric. While, the shape of the 2D peak of the bilayer graphene cannot be fitted with a single Lorentzian, but with four Lorentzian curves and is asymmetric. The few-layer grapheme show the 2D peak shape cannot be fitted with a single Lorentzian curve and is asymmetric [19].

The excitation wavelength that has been used slightly can affect the Raman spectra result but if compared the excitation for 514nm and 633nm they shows a minor shiftin 2D band[18]. It proves that, 2D band still exist in Raman spectra, while in our case the 2D band just exist for sample 800-2-B but not at 200cm^{-1}. These features are attributed to incomplete crystallization and edge-state dominance at this very early stage of nucleation [20]. So, the sample type B annealed at 800^{O}C for 2 minutes can be considered as the optimum sample compared to others

.

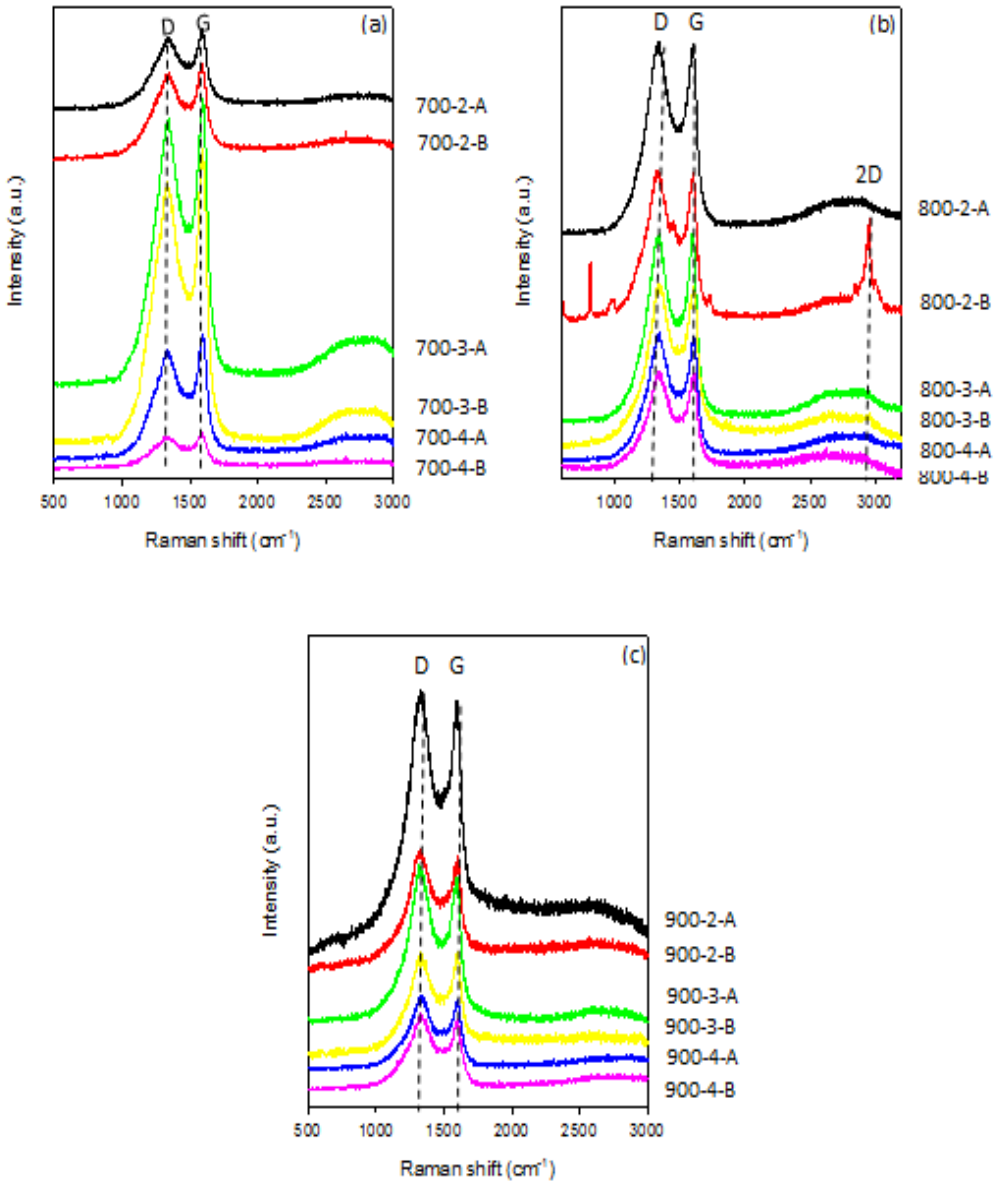

Figure 1: Raman spectra of (a) 700 batch, (b) 800 batch and (c) 900 batch graphene samples

The peak position, peak intensity and the intensity ratio between D band and G band (I_D/I_G) for the graphene samples were found identical and summarized in Table 1. The intensity ratio of the D to G peak is an important index to identify the quality of the graphene because the D peak originates from defects present in graphene. Even though sample 800-2-B shows the graphitic characteristics but sample 700-4-A is better in terms of formation grapheme quality. Supposedly, when the annealing temperature increasing, high quality graphene was grown on copper foil [19]. In fact the crystalline size (L_a) also can be calculated using the ratio intensity of the D to G peak. It is important to understand what the maximum of I_D/I_G vs L_α means. I_D will keep on increasing until the contribution from each defect sums independently [21].

$$\frac{1}{L_\alpha} = D(\lambda)\left(\frac{I_D}{I_G}\right), \text{ where } D(\lambda) = \text{constant, depends on Raman laser source used} = 633 \text{ nm}$$

Table 1: Peak position, peak intensity and I_D/I_G) for the D band and G band of graphene samples

Sample	Peak Position (cm^{-1})		Peak Intensity (counts)		I_D/I_G
	D-band	G-band	I_D	I_G	
700-2-A	1329	1591	3783	4127	1.091
700-2-B	1320	1591	4403	4888	0.901
700-3-A	1327	1595	12142	13178	0.921
700-3-B	1327	1595	12337	13618	0.906
700-4-A	1334	1597	5158	5757	0.896
700-4-B	1322	1596	1816	1977	0.919
800-2-A	1326	1598	8707	8619	1.010
800-2-B	1322	1599	6884	6888	0.999
800-3-A	1320	1599	8170	8317	0.982
800-3-B	1329	1606	8147	8045	1.013
800-4-A	1339	1608	5505	5408	1.018
800-4-B	1351	1606	4140	4178	0.991
900-2-A	1318	1597	10648	10420	1.022
900-2-B	1319	1598	4928	4454	1.107
900-3-A	1319	1594	5221	4957	1.053
900-3-B	1324	1599	4254	4129	1.030
900-4-A	1320	1600	2319	2189	1.059
900-4-B	1329	1598	2408	2263	1.064

This experiment was carried out until 240s soaking time based on the previous research that uses cellulose acetate lamination film (CALF) as the solid carbon source and neglecting other factor like impurity [19]. The presence of impurities and defects (Figure 2) on the surface of a substrate affected the nucleation behavior. So, high temperature treatments of the substrate revealed to be helpful for the reduction of volatile impurities, contaminants, and defects on a copper surface, thus hindering of graphene nucleation. Prolong of annealing (3 h) time was also attempted by Wang and co-workers[23] to reduce the nucleation density on copper foils resulting in large hexagonal domains about 0.4 × 0.4 mm^2. In other hand, Gao and co-workers have demonstrated the importance of surface defect that shows the graphene nucleation rate near a step edge may be 104−107 times greater than that on a terrace due to a significantly lower nucleation barrier [22].

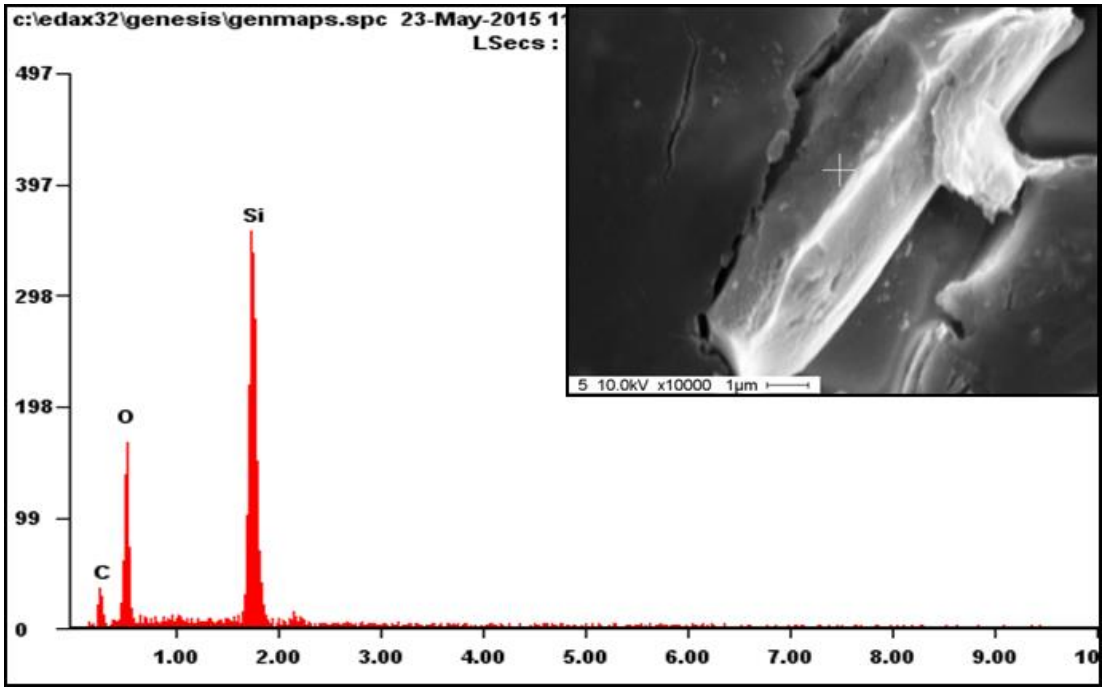

Figure 2: EDS data that shown the impurity element in sample

Fourier transform infrared spectroscopy (FTIR)was used to characterize the functional groups in the films shown in Figure 3. When the sample undergoes increase annealing temperature, many functional groups can be introduced in the graphene samples. A particular group which has a peak at approximately 3,410 cm^{-1} arises from the OH stretching vibrations. Bands at 2928cm^{-1} and 2865 $cm^{-1}$are representing the C-H stretch vibrations of the methylene group. Other peaks that can be observed are 1,730 cm^{-1} (carboxyl C=O), 1,620 cm^{-1} (C-C groups), 1,400 cm^{-1} (O-H), and 1,100 cm^{-1} (alkoxy C-O).

When samples was annealed at 700^{O}C, the peak at 2928 cm^{-1} and 2865 cm^{-1} became slightly flat but the peak became extremely sharp when it went through annealing temperature at 800^{O}C and 900^{O}C. The situation shows the formation of graphene start to take placed when the peak that representing graphene oxide at 1711 cm^{-1} C=O disappears after undergoes reduction of graphene oxide to graphene and arise the new bands at 2918 and 2865 cm^{-1} [24].

Annealing temperature is the main factor that affected the amount of carbon diffusing into the copper foil. The number of carbon atoms that diffuse from the cellulose acetate tape into copper foil is given by:

$$J_c = -D_c \frac{\partial C_c}{\partial x}\ atoms\ m^{-2}s^{-1} \quad (1)$$

where Dc is the diffusion coefficient, C_c is the concentration of carbon, and x is the position. This equation is known as Fick's first law of diffusion. The diffusion coefficient is closely related to the temperature. This can be simplified to an Arrhenius-type equation, that is

$$D_c = D_{co} \exp\left(-\frac{Q_{ID}}{RT}\right) \quad (2)$$

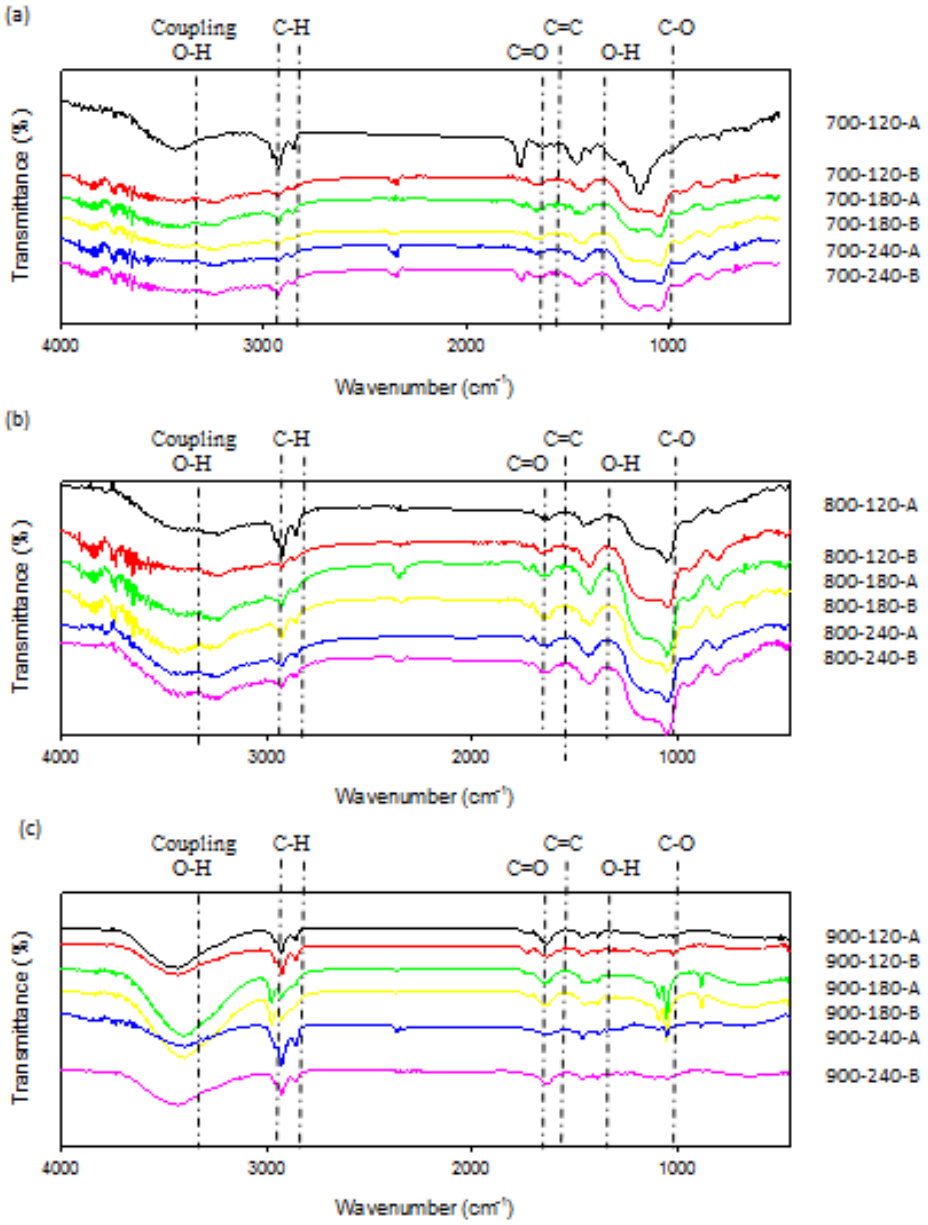

Figure 3: FTIR spectra for samples undergo (a) 700^{O}C, (b) 800^{O}C and (c) 900^{O}C at various duration and cellulose acetate tape type.

where D_{co} is the maximum diffusion coefficient at infinite temperature and Q_{ID} is the activation enthalpy for the diffusion. The diffusion coefficient increases exponentially with temperature. [25] Therefore a higher annealing temperature allows a larger amount of carbon to diffuse into the copper, which 5.86×10^{-12} m^2/s for 900^{O}C. Subsequently, a large amount of carbon diffuses and precipitates on the copper surface during annealing, resulting in an increase in the area of thicker graphene. Therefore, it is obvious that the amount of graphene precipitated on copper surface increased at higher annealing temperature. Due to the increased area of graphene

precipitated, one can see lower sheet resistance and transmittance with higher annealing temperature.

4. Conclusion

In summary, a simple and low cost method has been demonstrated for synthesis of graphene on a copper foil. The cellulose acetate tape was easily coated on the large-area metal catalyst layer. The post-annealing process shows the large surface area of graphene layer could be grown on the copper catalyst layer due to the uniform thickness of the solid carbon source layer and various annealing temperature and duration. We suggested that the annealing time must be prolonged to 5 minute with temperature 800^{O}C for the high quality of graphene production. Our results also highlight the potential importance of unintentional carbon sources, which must be considered when developing models for graphene growth.

References

1. Geim a K, Novoselov KS, Geim A. K. *et al.* The rise of graphene. *Nat Mater* 2007:183–91.

2. Kroto HW, Heath JR, O'Brien SC *et al.* C60: Buckminsterfullerene. *Nature* 1985;**318**:162–3.

3. Bolotin KI, Sikes KJ, Jiang Z *et al.* Ultrahigh electron mobility in suspended graphene. *Solid State Commun* 2008;**146**:351–5.

4. Morozov S V., Novoselov KS, Katsnelson MI *et al.* Giant intrinsic carrier mobilities in graphene and its bilayer. *Phys Rev Lett* 2008;**100**:11–4.

5. Lee C, Wei X, Kysar JW *et al.* Measurement of the elastic properties and intrinsic strength of monolayer graphene. *Science* 2008;**321**:385–8.

6. Cai W, Zhu Y, Li X *et al.* Large area few-layer graphene/graphite films as transparent thin conducting electrodes. *Appl Phys Lett* 2009;**95**:3–5.

7. Li X, Magnuson CW, Venugopal A *et al.* Graphene films with large domain size by a two-step chemical vapor deposition process. 2010:13.

8. Echtermeyer TJ, Lemme MC, Baus M *et al.* Non-volatile switching in graphene field effect devices. 2008:14.

9. Eda G, Fanchini G, Chhowalla M. Large-area ultrathin films of reduced graphene oxide as a transparent and flexible electronic material. *Nat Nanotechnol* 2008;**3**:270–4.

10. Wang X, Zhi L, Müllen K. Transparent, conductive graphene electrodes for dye-sensitized solar cells. *Nano Lett* 2008;**8**:323–7.

11. Kim KS, Zhao Y, Jang H *et al.* Large-scale pattern growth of graphene films for stretchable transparent electrodes. *Nature* 2009;**457**:706–10.

12. Blake P, Brimicombe PD, Nair RR *et al.* Graphene-based liquid crystal device. *Nano Lett* 2008;**8**:1704–8.

13. Stoller MD, Park S, Yanwu Z *et al.* Graphene-Based ultracapacitors. *Nano Lett* 2008;**8**:3498–502.

14. Dikin DA, Stankovich S, Zimney EJ *et al.* Preparation and characterization of graphene oxide paper. *Nature* 2007;**448**:457–60.

15. Ruan G, Sun Z, Peng Z *et al.* Growth of graphene from food, insects, and waste. *ACS Nano* 2011;**5**:7601–7.

16. Dunning HR, Martin LF. *Pressure Sensitive Adhesives: Formulations and Technology*. Noyes Data Corp., 1977.

17. Performance H, Compatible E. Cellulose Acetate Film and Sheet Cellulose Acetate Film and Sheet High Performance , Environmentally Compatible. 2008;**44137**.

18. Ferrari AC, Meyer JC, Scardaci V *et al.* Raman spectrum of graphene and graphene layers. *Phys Rev Lett* 2006;**97**, DOI: 10.1103/PhysRevLett.97.187401.

19. Kim D, Han JY, Lee D *et al.* Facile conversion of a cellulose acetate laminate film to graphene by a lamination process and post-annealing. *J Mater Chem* 2012;**22**:20026.

20. Matthews M, Pimenta M, Dresselhaus G *et al.* Origin of dispersive effects of the Raman D band in carbon materials. *Phys Rev B* 1999;**59**:R6585–8.

21. Cançado LG, Jorio A, Ferreira EHM *et al.* Quantifying defects in graphene via Raman spectroscopy at different excitation energies. *Nano Lett* 2011;**11**:3190–6.

22. Gao J, Yip J, Zhao J *et al.* Graphene nucleation on transition metal surface: Structure transformation and role of the metal step edge. *J Am Chem Soc* 2011;**133**:5009–15.

23. Wang H, Wang G, Bao P *et al.* Controllable synthesis of submillimeter single-crystal monolayer graphene domains on copper foils by suppressing nucleation. *J Am Chem Soc* 2012;**134**:3627–30.

24. Naebe M, Wang J, Amini A *et al.* Mechanical Property and Structure of Covalent Functionalised Graphene/ Epoxy Nanocomposites. 2014:1–7.

25. Porter DA, Easterling KE. *Phase Transformations in Metals and Alloys*., 1992.